36th conference with international participation

COMPUTATIONAL MECHANICS 2021

PROCEEDINGS OF COMPUTATIONAL MECHANICS 2021

November 8 - 10, 2021

HOTEL SRNÍ
CZECH REPUBLIC

FACULTY OF APPLIED SCIENCES
UNIVERSITY OF WEST BOHEMIA

PILSEN REGION

ČSM

IFToMM

cea cm
Central European Association for Computational Mechanics

PROCEEDINGS OF COMPUTATIONAL MECHANICS 2021

ISBN 978-80-261-1059-0

Published by
University of West Bohemia, Univerzitní 8, 301 00 Plzeň, Czech Republic, IC 49777513

Edited by
Vítězslav Adámek
Alena Jonášová
Stanislav Plánička
Martin Zajíček

Conference secretariat
Jana Nocarová
Department of Mechanics
Faculty of Applied Sciences
University of West Bohemia
Univerzitní 8
301 00 Plzeň
Czech Republic

phone: +420 377 632 301
e-mail: vm@kme.zcu.cz

PREFACE

The proceedings contain 86 conference papers presented at the 36th conference **Computational Mechanics 2021**, which was held at the Hotel Srní in Srní, Czech Republic, on November 8 – 10, 2021. This annual conference, which was attended by over one hundred participants from the Czech Republic, Slovakia and from abroad, was organised by the Department of Mechanics, Faculty of Applied Sciences of the University of West Bohemia under the auspices of

- Miloš Železný, the Dean of the Faculty of Applied Sciences,
- Ilona Mauritzová, the President of the Pilsen Region,
- Czech Society for Mechanics,
- Czech National Committee of IFToMM,
- Central European Association for Computational Mechanics.

The main objective of this traditional conference is to bring together academicians, researchers and industrial partners interested in relevant disciplines of mechanics including

- solid mechanics,
- dynamics of mechanical systems,
- mechatronics and vibrations,
- reliability and durability of structures,
- fracture mechanics,
- mechanics in civil engineering,
- fluid mechanics and fluid-structure interaction,
- thermodynamics,
- biomechanics,
- heterogeneous media and multiscale problems,
- experimental methods in mechanics,

to create an opportunity for meeting, discussion and collaboration among the participants. As in the previous years, the three best papers presented at this conference were awarded the Czech Society for Mechanics Award for young researchers under 35 years of age.

To all conference participants, we offer the possibility to publish their peer-reviewed full papers in the international journal **Applied and Computational Mechanics** indexed by Scopus. This journal has been published by the University of West Bohemia since 2007 (see https://www.kme.zcu.cz/acm/).

We would like to express our gratitude to all the invited speakers for their significant contribution to the conference and the time and effort they put. Considerable acknowledgement belongs also to the members of the Organising Committee for their important work.

We strongly believe that all participants of the CM2021 enjoyed their stay in the beautiful nature of the Šumava region in a meaningful way despite the ongoing COVID-19 restrictions. Finally, we would like to invite you all to come to the next conference CM2022.

Jan Vimmr
University of West Bohemia
Chairman of the Scientific Committee

Vítězslav Adámek
University of West Bohemia
Chairman of the Organising Committee

SCIENTIFIC COMMITTEE

Chairman:

Jan Vimmr
University of West Bohemia, Faculty of Applied Sciences, Czech Republic

Members:

Miroslav Balda
Research and Testing Institute Plzeň, Czech Republic

Jiří Burša
Brno University of Technology, Faculty of Mechanical Engineering, Czech Republic

Jan Dupal
University of West Bohemia, Faculty of Applied Sciences, Czech Republic

Václav Dvořák
Technical University of Liberec, Faculty of Mechanical Engineering, Czech Republic

Jiří Fürst
Czech Technical University in Prague, Faculty of Mechanical Engineering, Czech Republic

Miroslav Holeček
University of West Bohemia, Czech Republic

Jaromír Horáček
Institute of Thermomechanics, Czech Academy of Sciences, Czech Republic

Michal Kotoul
Brno University of Technology, Faculty of Mechanical Engineering, Czech Republic

Jiří Křen
University of West Bohemia, Faculty of Applied Sciences, Czech Republic

Vladislav Laš
University of West Bohemia, Faculty of Applied Sciences, Czech Republic

Justín Murín
Slovak University of Technology in Bratislava, Faculty of Mechanical Engineering, Slovak Republic

Milan Naď
Slovak University of Technology in Bratislava, Faculty of Materials Science and Technology in Trnava, Slovak Republic

Jiří Náprstek
Institute of Theoretical and Applied Mechanics, Czech Academy of Sciences, Czech Republic

Miloslav Okrouhlík
Institute of Thermomechanics, Czech Academy of Sciences, Czech Republic

Luděk Pešek
Institute of Thermomechanics, Czech Academy of Sciences, Czech Republic

Jindřich Petruška
Brno University of Technology, Faculty of Mechanical Engineering, Czech Republic

Jiří Plešek
Institute of Thermomechanics, Czech Academy of Sciences, Czech Republic

František Pochylý
Brno University of Technology, Faculty of Mechanical Engineering, Czech Republic

Pavel Polach
Research and Testing Institute Plzeň, Czech Republic

Eduard Rohan
University of West Bohemia, Faculty of Applied Sciences, Czech Republic
Josef Rosenberg
University of West Bohemia, Faculty of Applied Sciences, Czech Republic
Milan Růžička
Czech Technical University in Prague, Faculty of Mechanical Engineering, Czech Republic
Milan Sága
University of Žilina, Faculty of Mechanical Engineering, Slovak Republic
Petr Sváček
Czech Technical University in Prague, Faculty of Mechanical Engineering, Czech Republic
Zbyněk Šika
Czech Technical University in Prague, Faculty of Mechanical Engineering, Czech Republic
Michael Valášek
Czech Technical University in Prague, Faculty of Mechanical Engineering, Czech Republic
Jaroslav Zapoměl
VŠB – Technical University of Ostrava, Faculty of Mechanical Engineering, Czech Republic
Vladimír Zeman
University of West Bohemia, Faculty of Applied Sciences, Czech Republic

Table of Contents

COMPUTATIONAL MECHANICS 2021
36th conference with international participation
Srní
November 8 - 10, 2021

Unsteady vortex lattice method for an active morphing airfoil

A. Balon[a], P. Beneš[a], Z. Šika[a]

[a] *Department of Mechanics, Biomechanics and Mechatronics, Faculty of Mechanical Engineering, Czech Technical University in Prague, Technicka 4, Praha 6, Czech Republic*

The concept of a morphing wing is characterized by continuous surface changing its shape to perform various maneuvers. Additionally, such wing can alter its shape to an optimal shape determined by given flight conditions. This ability leads to improved lift to drag ratio and fuel consumption among other advantages. To model the aerodynamics several methods can be used. This extended abstract will focus only on panel methods based on potential flow to derive aeroelastic models that will be used for control design and optimization in our ongoing research of morphing wings.

The potential flow is characterized by the assumption of inviscid and irrotational flow where the velocity field is obtained as a gradient of a scalar field [1], [2], [3]. This model is applicable to attached flows with large Reynolds number and so it can be used to model the flow around a wing (airfoil) with low angles of attack. Panel methods are boundary element methods that discretize the surface of a body into discrete panels with singularity elements (source, doublet, point vortex) that are solutions to Laplace equation which describes an incompressible flow. Then the boundary condition of flow tangency on these panels is prescribed and the flow is described by linear combination of individual singularity element solutions that satisfies the boundary condition. When only a lifting surface is considered instead of a lifting body the approach is usually called a lattice method [2].

There are two approaches to unsteady potential flow modeling for lifting surfaces. The doublet lattice method (DLM) which uses an acceleration potential to relate the normal velocity at an oscillating lifting surface, described by natural modes, to pressure difference across the surface [1], [3]. DLM is the industry standard for aeroelastic analysis. The results of DLM are in frequency domain and can be transformed into time domain via rational function approximation [3]. The other approach is the unsteady vortex lattice method (UVLM) which uses the velocity potential to describe velocity field of the flow and is directly derived in time domain [2], [3]. However, unlike DLM which only models the lifting surface, UVLM must model the lifting surface and the wake produced by this surface, because the wake influences the velocity field around the wing in unsteady flows (Fig. 2) [2], [3]. This necessity greatly increases the number of states needed to describe the system. However, our goal is to use this high order nonlinear model to generate data which would be used for methods like dynamic mode decomposition, which reduces the model order, to obtain a linear dynamical system for the controller. The aeroelastic model is obtained by using the pressure distribution from aerodynamic model as load in structural model, then the structural deformations are used to adjust the aerodynamic mesh geometry.

Unfortunately, at the time of writing this extended abstract the aeroelastic model isn't working as intended so only the aerodynamic part is presented. The full aeroelastic model of an active morphing airfoil will be presented at the conference. The UVLM aerodynamic model is applied to a sudden acceleration of a flat plate, which can also be viewed as a step

change from zero angle of attack. Theoretical lift response of this step change is described by the Wagner function [2]. The normalized lift simply means $L(t)/L(t=\infty)$ and nondimensional time is the distance traveled in terms of wing chords. The comparison of lift responses between various models is shown on Fig. 1, while Fig. 2 shows the wake rollup of the UVLM model and the comparison to starting trailing vortex visualized by Prandtl.

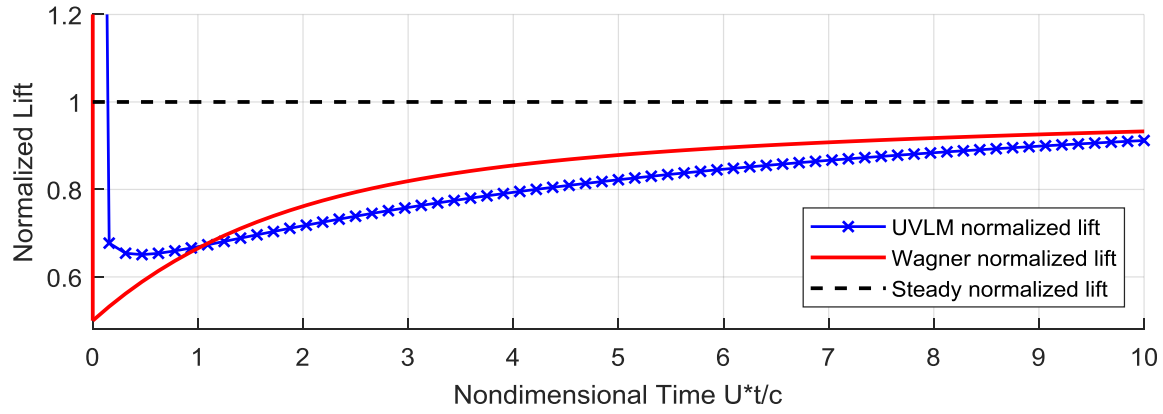

Fig. 1. Comparison of normalized lift response during sudden flat plate acceleration

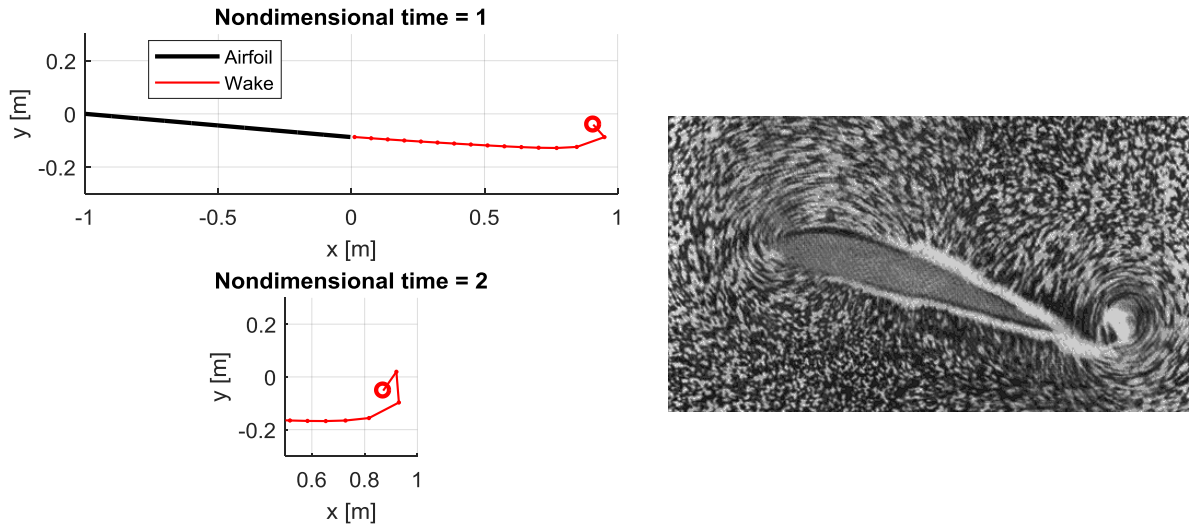

Fig. 2. Wake rollup during sudden flat plate acceleration (left), flow visualization of starting trailing vortex by Prandtl (right)

Acknowledgements

The work has been supported by the Czech Science Foundation, project GA19-16772S Aerodynamic bodies with actively controlled morphing.

References

[1] Blair, M., A compilation of the mathematics leading to the doublet lattice method, Wright lab Wright-Patterson AFB OH, 1992.
[2] Katz, J., Plotkin, A., Low-speed aerodynamics, Cambridge university press, 2001.
[3] Werter, N., Aeroelastic modelling and design of aeroelastically tailored and morphing wins, TU Delft, 2017.

COMPUTATIONAL MECHANICS 2021
36th conference with international participation
Srní
November 8 - 10, 2021

Vault principle in joining robots

V. Bauma [a], M. Valášek [a]

[a] *Department of Mechanics, Biomechanics and Mechatronics, Faculty of Mechanical Engineering, Czech Technical University in Prague, Technická 4, 16607 Praha 6, Czech Republic*

A major problem with serial kinematic structures, such as serial industrial robots, is their low stiffness. They cannot generally be used for more precise operations, such as CNC milling. One way how to increase their stiffness is to use more mutually connected such robots in the end-effector. In the article [1] it is stated that by connecting two robots it is possible to increase the stiffness of robots about 3.5 times. This is an experimentally determined result, which has not yet been computationally verified nor explained.

For verification, we chose a planar model of a robot, consisting of five flexible arms, interconnected by four flexible joints (Fig. 1). The lower part of the robot is fixed to the base frame. After loading the robot, the end-effector moves in both the horizontal and vertical directions and it also rotates. In the Fig. 2 are two such robots mutually connected. If we model them as springs, then after joining their stiffness should be doubled. Fig. 3 shows

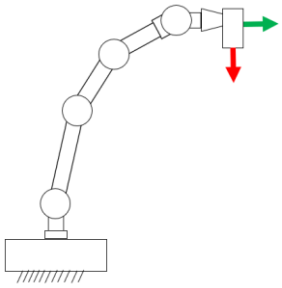

Fig. 1. One robot

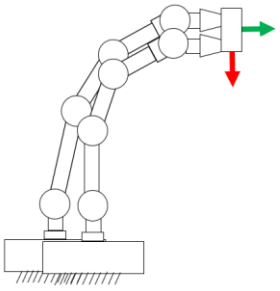

Fig. 2. Two robots

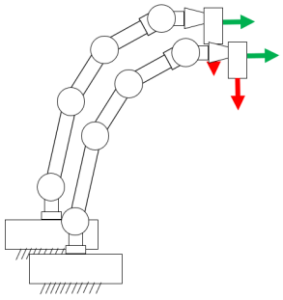

Fig. 3. Two parallel robots

another variant of connecting two robots in a configuration where the corresponding arms are permanently parallel. If we also connect the end-effectors by a rod with joints (Fig. 7), we get a multi-parallelogram, the stiffness of which will depend mainly on the stiffness of the joints. The greatest rigidity will probably be shown by two interconnected symmetrical robots (Fig. 4), in which horizontal, as well as rotational, deformations will be compensated under symmetrical loading. After their connection, the principle of the vault appears (Fig. 5).

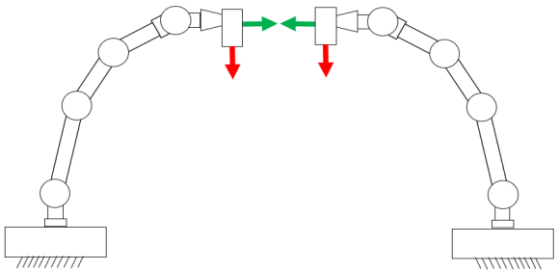

Fig. 4. Two symmetrical robots

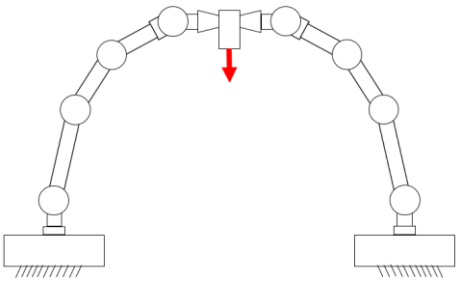

Fig. 5. „Vault“

Calculations were performed by FEM only in one robot(s) position. The arms were modeled by beam elements, the flexible joints were modeled by connecting matrixes, where the only considered flexibility was rotational flexibility.

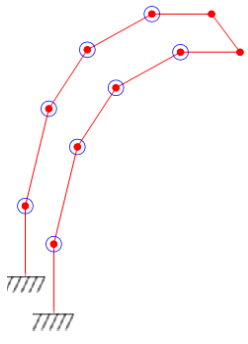

Fig. 6. Parallel – welded end-effectors

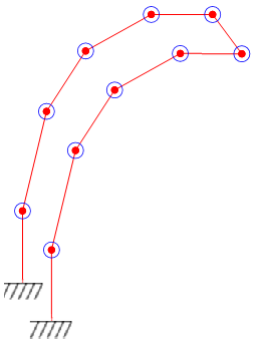

Fig.7. Parallel – joint connection of end-effectors

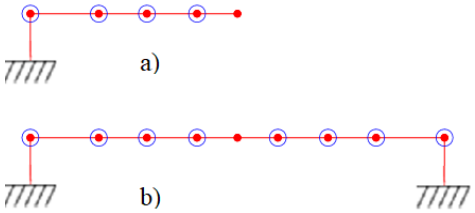

Fig. 8. Horizontal positions

The comparison of the stiffnesses of the individual variants is performed relatively in percentages with respect to the stiffness of one robot (its partial stiffnesses each represent 100 percent). During the verification of the "vault", a significant increase of stiffness was confirmed and further that, in contrast to the classic concave vault in the construction industry, the convex "vault" also works here and gives the same stiffness. For comparison, the horizontal positions of one and two connected robots were also investigated. The result of the comparison is in Table 1. Finally, we verified our assumption that the effect of the vault will be even more pronounced for more flexible joints.

Table 1. Comparison of stiffness at the effector location (due to the stiffness of one robot)

Kinematic scheme according to Stiffness	Fig. 1	Fig. 2	Fig. 6	Fig. 7	Fig. 5	Fig. 8a	Fig. 8b
Horizontal [%]	100	243	246	205	1092	51279	104220
Vertical [%]	100	301	472	339	8337	51	475
Rotational [%]	100	266	492	289	1608	100	914

The work showed that the connection of two robots can significantly increase the resulting rigidity. The highest effect is achieved using the vault principle. It will probably not be possible to use this in the whole workspace, but it will be possible to identify suitable areas, for example for machining. Research could continue by acquiring stiffness maps or extended ideas into space.

Acknowledgements

This work was supported by the European Regional Development Fund under the project Robotics for Industry 4.0 (reg. no. CZ.02.1.01/0.0/0.0/15 003/0000470).

References

[1] Valášek, M., Nečas, M., Mráz, L., Increase of stiffness in physically cooperating robots, Proceedings of the 8th ECCOMAS Thematic Conference on Multibody dynamics, Prague, Czech Republic, CTU Publisher, 2017, pp. 577-585.

COMPUTATIONAL MECHANICS 2021
36th conference with international participation
Srní
November 8 - 10, 2021

Solving the moving mass problem on large finite element models with modal analysis – estimation of the discrete movement error

J. Bayer[a]

[a]*Institute of Theoretical and Applied Mechanics of the Czech Academy of Sciences, Prosecká 809/76, 190 00 Prague 9, Czech Republic*

1. Introduction

Solving transient dynamic problems on large finite element (FE) models using a direct integration requires a high sampling rate and therefore also considerable computing times because of the large system matrices. Movement of a mass on a FE model has to follow the discrete pattern of the FEs, and is therefore of a discrete character. This introduces an unknown error into the analytical results. Applying modal analysis (MA) reduces the number of equations used in the subsequent numerical integration by orders of magnitude. Resampling of the mode shapes to the required sampling rate makes it possible to solve the moving mass problem much more quickly and quasi-continuously. The performed comparative analytical study using ANSYS and MATLAB showed that using a discrete movement on the FE mesh when solving a moving mass problem can cause a considerable error.

The problem of moving vehicles on bridges is practically as old as the first railway bridges. Theoretical studies were in focus until around the late 1950s. Since that time, numerical methods have prevailed. The problem of a moving vehicle on a structure can be formulated as a coupled or uncoupled system, or by using Lagrange multipliers.

The difficulty of the problem lies in the changing inertia relations in the system during the passage of the vehicle across the bridge. This means that the natural frequencies and the mode shapes of the system in fact change during the movement of the mass. If only a force travels, a closed form solution exists [5], and it can be solved using Duhamel's Integral. A closed-form solution for a moving mass on a beam has been around since 1985 [4], using operational calculus to obtain eigenfunctions, finally leading to an integral equation.

The closed-form solution is however not applicable for more complicated practical problems, and the FE method must then be applied. Discussions about discretisation problems with moving loads started in the 90-ties [3]. An efficient way of attaining quasi-continuous solutions using FE analysis and post-processing in MATLAB is applied in the article. This approach makes it possible to estimate the discrete movement error, which is difficult to estimate when only using FE programs. It is demonstrated that even a rather fine FE mesh can cause a considerably biased transient solution of the moving mass problem. This is considered to be the main contribution of the presentation next to the description of the model transfer from ANSYS into MATLAB.

Discrete movement is not only the problem with using software like ANSYS and similar, but also of all stepper motors frequently used nowadays. The solution of moving mass requires modification of the system mass matrix at each integration step. In addition, the system matrices are large (unless model reduction is applied), and therefore long solution times are required.

2. Theoretical background

According to the well-known principles of modal analysis [1], the dynamic behaviour of common building structures can be described with FE models using the following equations (1, 4-7).

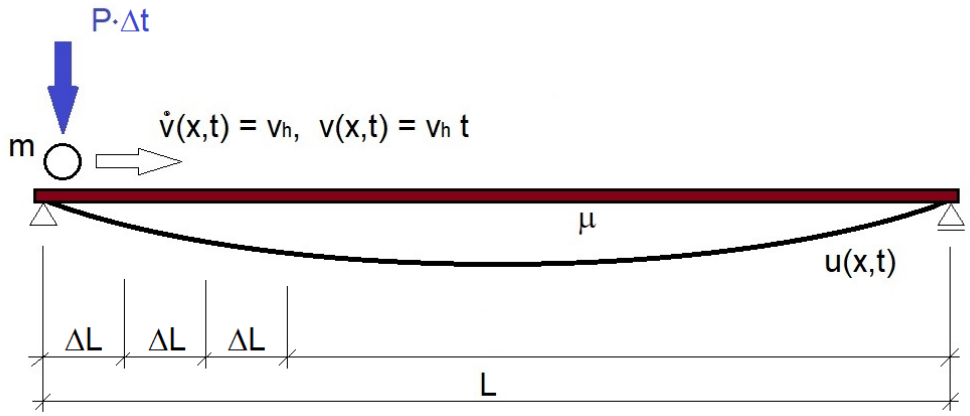

Fig. 1. Schema of the coupled system "Structure – Mass"

$$M \cdot \ddot{u} + C \cdot \dot{u} + K \cdot u = F \,, \tag{1}$$

where *F* and *u* are time-dependent. Formulation for the coupled system shown in Fig. 1 changes the equation (1) to

$$\mathrm{M} \cdot \ddot{u} + \mathrm{C} \cdot \dot{u} + \mathrm{K} \cdot u = -\delta_j \cdot \left(m \cdot g - \mathrm{m} \cdot \ddot{u}_j - \mathrm{m} \cdot v_h^2 \cdot u''_j - \mathrm{m} \cdot 2 \cdot v_h \cdot \dot{u}'_j - F_{st} \right). \tag{2}$$

The terms on the right hand side represent the mass weight, the inertia force, the centripetal force, the Coriolis force and the F_{st} is inertia force due to the static deformations (from the curved path of the mass). For the vertical movement of the mass it holds that

$$w = \delta_j \cdot \mathrm{u}_j \,, \tag{3}$$

where δ_j is the Kronecker delta. The following expressions are valid for the natural modes

$$\emptyset^T \cdot M \cdot \emptyset = I; \qquad \emptyset^T \cdot C \cdot \emptyset = D; \qquad \emptyset^T \cdot K \cdot \emptyset = \Omega \,. \tag{4a-c}$$

$$u = \emptyset \cdot \mathrm{Q} \,; \qquad \dot{u} = \emptyset \cdot \dot{\mathrm{Q}} \,; \qquad \ddot{u} = \emptyset \cdot \ddot{\mathrm{Q}} \,; \tag{5a-c}$$

$$u'' = \frac{d^2\emptyset}{dx^2} \cdot \mathrm{Q} \,; \qquad \dot{u}' = \frac{d\emptyset}{dx} \cdot \dot{\mathrm{Q}} \,; \tag{5d-e}$$

$$\mathrm{Q} = \left[q_1; \ldots; q_n \right], \tag{6}$$

$$\emptyset = \left[\varphi_{1,1}; \ldots; \varphi_{p,n} \right], \tag{7}$$

where *n* is the number of modes used, and *p* is a number of finite element nodes.

From rewriting (2) using (4) – (7) it follows that

$$\mathrm{I} \cdot \ddot{\mathrm{Q}} + \mathrm{D} \cdot \dot{\mathrm{Q}} + \Omega \cdot \mathrm{Q} = \emptyset^T \cdot \left(\delta_j \mathrm{m} \cdot \left(-\mathrm{g} - \emptyset_{..j} \ddot{\mathrm{Q}} - 2 v_h \frac{d\emptyset_j}{dx} \dot{\mathrm{Q}} - v_h^2 \frac{d^2\emptyset_j}{dx^2} \mathrm{Q} \right) - F_{sw} \right), \tag{8}$$

$$\ddot{u}_j(\mathrm{x},\mathrm{t}) = \sum_{i=1}^{n} \varphi_{i,j} \cdot \ddot{q}_i = \emptyset_{..j} \cdot \ddot{\mathrm{Q}} \,, \tag{9}$$

$$\mathrm{I} \cdot \ddot{\mathrm{Q}} + \mathrm{D} \cdot \dot{\mathrm{Q}} + \Omega \cdot \mathrm{Q} = -\delta_j \cdot \mathrm{m} \cdot \emptyset^T \cdot \left[\left(\emptyset_j \cdot \ddot{\mathrm{Q}} - \mathrm{g} - a_{sw} \right) - \left(\frac{d\emptyset}{dx} \cdot \dot{\mathrm{Q}} \right)_j - \left(\frac{d^2\emptyset}{dx^2} \cdot \mathrm{Q} \right)_j \right]. \tag{10}$$

Because $a_{sw} = F_{sw}/\mathrm{m}$ can usually be neglected, eq. (10) can be written as

$$\left(\mathrm{I} + \mathrm{m} \cdot \emptyset_{\mathrm{j}}^{\mathrm{T}} \cdot \emptyset_{\mathrm{j}}\right) \cdot \ddot{\mathrm{Q}} + \left(\mathrm{D} + \mathrm{m} \cdot \emptyset_{\mathrm{j}}^{\mathrm{T}} \cdot \frac{\mathrm{d}\emptyset}{\mathrm{dx}}\right) \cdot \dot{\mathrm{Q}} + \left(\Omega + \mathrm{m} \cdot \emptyset_{\mathrm{j}}^{\mathrm{T}} \cdot \frac{\mathrm{d}^2\emptyset}{\mathrm{dx}^2}\right) \cdot \mathrm{Q} = -\delta_{\mathrm{j}} \cdot \mathrm{m} \cdot \mathrm{g} \cdot \emptyset_{\mathrm{j}}^{\mathrm{T}}. \quad (11)$$

The vertical displacement under the moving mass is

$$w = \delta_j \cdot \emptyset_j \cdot \mathrm{Q} = \mathrm{diag}(\emptyset \cdot \mathrm{Q}^T). \quad (12)$$

Only s selected degrees of freedom (DOFs, $s < p$) can be imported from the FE model. But the imported set $\emptyset_a$ must contain all the DOFs on the driving path and can also contain other nodes of interest $\emptyset_b$ like e.g. measured nodes

$$\emptyset = \begin{bmatrix} \emptyset_a \\ \emptyset_b \end{bmatrix}. \quad (13)$$

The damping matrix D can be assumed to be proportional, and therefore also of the diagonal form

$$\mathrm{D} = \alpha \cdot \mathrm{I} + \beta \cdot \Omega. \quad (14)$$

The quasi continuous solution is achieved through resampling of the $\emptyset_a$ using a spline interpolation from the model resolution into the resolution resulting from the horizontal moving velocity and the applied sampling frequency.

Eq. (11) is a nonlinear system of n differential equations of the second order with a time dependent mass matrix. Solving it is generally not an easy task. However, under the assumption that the mass matrix changes only marginally between two successive time steps, numerical integration using the Hilber–Hughes–Taylor-α method (HHT-α) solver [2] with fixed integration stepping can be applied.

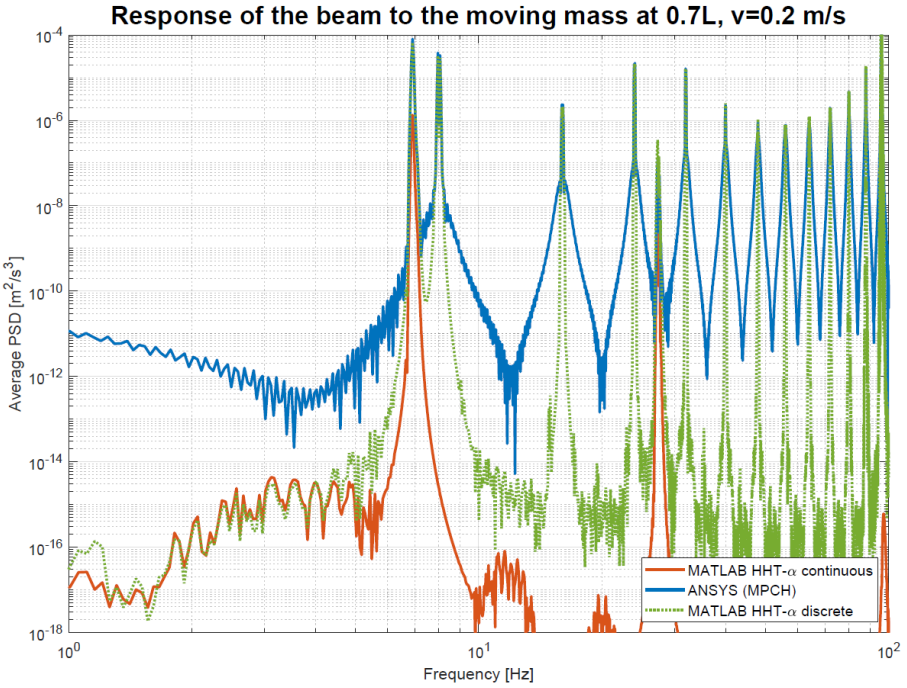

Fig. 2. Comparison of the solutions obtained from ANSYS and the above described procedure

3. Numerical Simulations

For demonstration purposes, an FE model was assembled in the ANSYS program. The applied model corresponded to Fig. 1, with a span of 3.975 m, made from U-Jäckel steel 210x50x4 mm, and weighting 33.3 kg. The moving mass was 0.5 kg, thus the mass ratio between the structure

and the moving mass was only ca. 1.5 %. The first natural frequency of the beam without the moving mass was 6.98 Hz. Two passing velocities were considered: v_h = 0.2 m/s, and v_h = 0.16 m/s. The relatively low driving speed was chosen due to practical requirements. Proportional damping was used with the mass multiplier $\alpha = 0.1$ and a stiffness multiplier of $\beta = 2*10^{-5}$.

The FE model was assembled in ANSYS 17. A resolution of 160 nodes per driving path was chosen in order to minimise the discrete steps in movement of the mass, forming a model of ca 2600 nodes and about 2400 SHELL181 elements.

The first seven natural modes with distinct amplitudes on the driving path (bending modes) in the frequency band 0-200 Hz were exported from ANSYS into MATLAB using the APDL commands. The solution then followed the schema described above.

Fig. 2 compares the average acceleration power spectral density (PSD) obtained from ANSYS and MATLAB. The discrete solution obtained in MATLAB complies well with the ANSYS solution, showing that the transfer of the modal model into MATLAB was successful. The continuous solution however has a considerably lower response at the peaks corresponding to the natural frequencies, and the harmonic peaks caused by the discrete motion are missing entirely. The difference in amplitudes at the first natural frequency is approximately 10 times lower in the case of the continuous solution than with the discrete movement.

4. Conclusions

The described approach offers an efficient tool for solving interaction problems between structures and moving bodies, reducing the required computing time by orders of magnitude. If a continuous movement is solved as if it were a discrete movement, a considerable error can be expected in the transient analysis. This has to be considered also in application of stepper motors drives.

Acknowledgements

The sponsorship from grant GACR 21-32122J of the Czech Science Foundation and of the joint research project 109WFD0410468 of Taiwan's Ministry of Science and Technology are very much appreciated.

References

[1] Ewins, D.J., Modal testing, theory, practice, and application, 1984. ISBN-10: 0863802184
[2] Hughes, T.J.R., Analysis of transient algorithms with particular reference to stability behaviour, Computational Methods for Transient Analysis (1983) 67–155.
[3] Rieker, J.R., Lin, Y-H., Trethewey, M.W., Discretization considerations in moving load finite element beam models, Finite Elements in Analysis and Design 21 (1996) 129-144.
[4] Stanišič, M.M., On a new theory of the dynamic behaviour of the structures carrying moving masses, Ingenieur-Archiv 55 (1985) 176–185.
[5] Yang, Y.B., Yau, J-D.,Wu, Y.S., Vehicle-bridge interaction dynamics, World Scientific Publishing Co. Pte. Ltd., Singapore, 2004. ISBN 981-238-847-8

COMPUTATIONAL MECHANICS 2021
36th conference with international participation
Srní
November 8 - 10, 2021

Comparison of computational approaches for the efficient analysis of airfoil dynamics

M. Bělohoubek, M. Hajžman, J. Vimmr

Faculty of Applied Sciences, University of West Bohemia, Univerzitní 8, 301 00 Plzeň, Czech Republic

The analysis of the interaction of the flowing fluid with the enveloped body became of great importance, since it can induce structural instability. The most typical example of this type of instability is the so-called flutter representing a self-excited oscillation of the structure due to fluid flow, which in the extreme case can lead to the structural destruction. The problem is very complex and even with the current computational power it cannot be solved efficiently using the commonly available computational tools. From this point of view, there is still a motivation to find an efficient tool that would allow real-time optimization of structures with respect to flutter safety. This paper deals with the first step of the methodology and aims to compare different approaches to investigate the effect of forces acting on the stationary airfoil geometry and also the airfoil vibration response to flow field excitation.

The first performed analysis is a comparison of the force effects acting on a stationary and a fully rigid airfoil geometry in 2D. The main analysis tools chosen were the panel method represented by the XFoil software [2] and the complex CFD analysis implemented in the ANSYS Fluent software. The XFoil combines a potential flow panel method and an integral boundary layer formulation for the analysis of the flow around thin airfoils. The code is suitable for low Reynolds numbers and its convergence is reached through the iteration between the inner and outer flow solutions on the boundary layer displacement thickness. The CFD analysis was carried out using ANSYS Fluent software for comparison, which is based on solving the

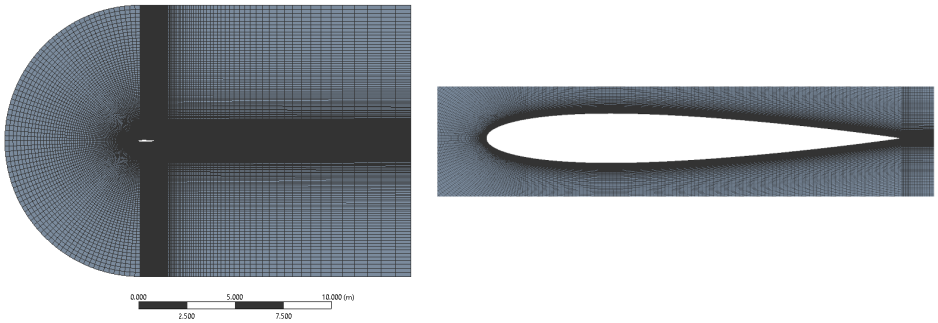

Measured quantity	Value	Measured quantity	Value
Elements	96400	Orthogonal quality (avg)	0.99531
Skewness (avg)	0.03313	y^+ (max)	7.17

Fig. 1. Illustration of the computational domain, including mesh detail in the encircled airfoil and an overview of the basic mesh quality indicators

nonlinear Reynolds-averaged Navier-Stokes equation (RANS) system using the Finite Volume Method (FVM). In the case of this analysis, the pressure-based solver was chosen. Two types of turbulent models were chosen to define the viscous behavior of the flow field, namely the two-equation Shear-Stress Transport (SST) $k-\omega$ and the one-equation Spalart-Allmaras (SA).

The analysis of force effects was performed for two types of airfoils, specifically for symmetric NACA0012 (see Fig. 1) and non-symmetric NACA4412 (see for example [5]), different values of Reynolds number in the range $\mathrm{Re} \in \langle 5 \times 10^5, 6 \times 10^6 \rangle$ and different values of angle of attack ($\theta \in \langle -15°, 15° \rangle$). In all cases, the flow medium was atmospheric air with density $\rho = 1.225\,\mathrm{kg.m^{-3}}$ and dynamic viscosity $\mu = 1.789 \times 10^{-5}\,\mathrm{Pa.s}$. The air flow was modeled as incompressible and the airfoil was then modeled as a fixed solid. In particular, the lift force L and drag force D were analyzed and converted into the dimensionless form of force coefficients C_L and C_D based on the following relations for comparison with experimental data $C_L = \frac{L}{qcs}$, $C_D = \frac{D}{qcs}$, $q = \frac{1}{2}\rho U_\infty^2$, where U_∞ is the flow speed, c is the airfoil length and s is the considered wingspan, and for both these quantities in all tested cases $c = s = 1\,\mathrm{m}$ is assumed. The dependence between Re and U_∞ is then described by the expression $\mathrm{Re} = \frac{\rho U_\infty c}{\mu}$.

As can be seen from the results summarized in Fig. 2 (for NACA0012, $\mathrm{Re} = 5 \times 10^5$), all analyzed approaches achieve good agreement with the experimental data, especially on the interval $\theta \in \langle -10°, 10° \rangle$. Outside this interval, the turbulent character of the flow becomes more evident and the accuracy of the numerical approaches decreases slightly. However, the difference between experiments also increases.

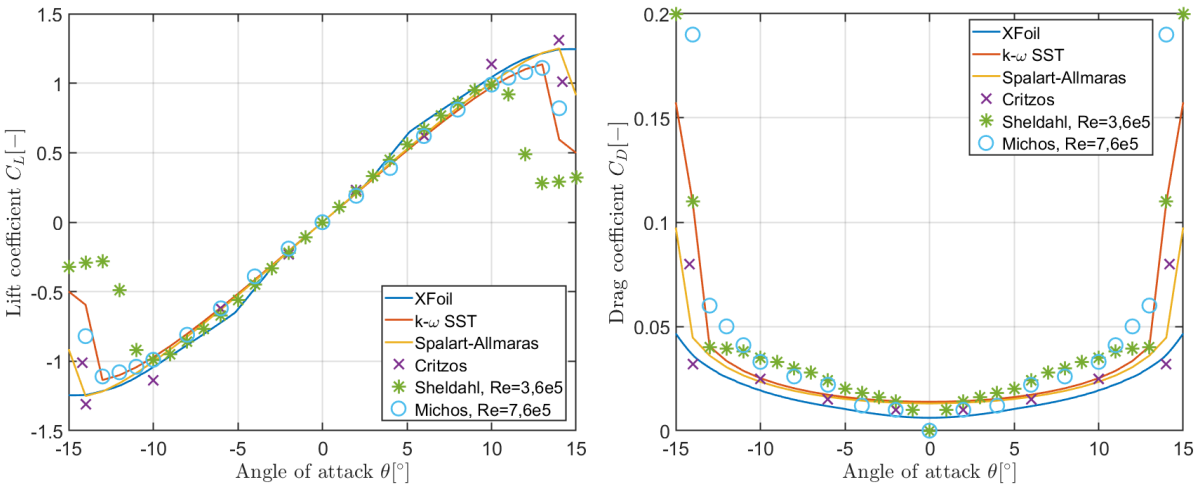

Fig. 2. Comparison of the aerodynamic force effects on a stationary airfoil for test mode No. 2 (i.e. NACA0012, $\mathrm{Re} = 5 \times 10^5$). The experimental data are taken from the literature [1, 3, 4]

It can be concluded from the presented results that all the analyzed approaches represent a comparably accurate tool for defining the force effects acting on a stationary 2D airfoil in a flow field. In terms of computational complexity (the computation of a single test mode interval at identical sampling $0.1°$ would be 10 h for Fluent and 30 s for XFoil), XFoil proves to be a very efficient tool that can be used to solve a given type of real-time problem with minimal loss of output accuracy.

The second analysis shown in this paper deals with the comparison of the system response in time domain for an elastically suspended rigid airfoil geometry with one or two degrees of freedom wrapped with fluid (Fig. 3). The elasticity of the system is represented by torsional and translational springs, and the system is further considered without direct material damping.

The shear center of the geometry is chosen at a distance of 18.6 % leading edge of the airfoil. The investigated approaches are an analytical method (implemented in MATLAB) based on the calculation of the forces from Quasi-Steady theory (with term $\frac{\mathrm{d}C_L}{\mathrm{d}\theta}$ calculation using XFoil or thin airfoil theory) and a fully non-stationary solution calculated using ANSYS Fluent software. The defined initial condition are the initial pitch angle (identical to the initial AoA) θ_0, the heave h_0 or the initial velocities $\dot{\theta}_0$ and $\dot{h}_0$. In terms of outputs, the force effects over time and the kinematic quantities of the position and velocity of the mass center of the profile are mainly investigated.

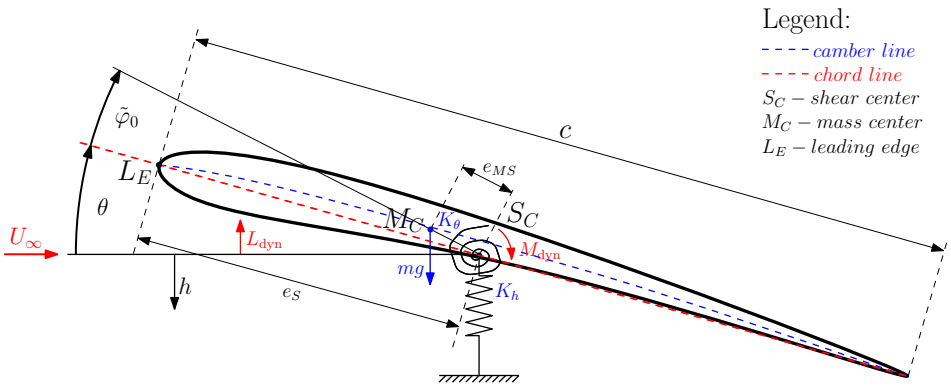

Fig. 3. Scheme of the analyzed airfoil profile with two DOF including the marked force effects acting on the system

In case of the analytical approach with force effects based on Quasi-Steady theory, the solution of the ODE system was based on the explicit Runge-Kutta formulation with the Dormand-Prince pair. Concerning the solution in ANSYS Fluent, the used mesh, solver settings and turbulent models were identical to the first analysis comparing force effects on a fixed body. Regarding the newly chosen parameters, an implicit solver of second-order of accuracy was chosen in terms of time discretization. A sensitivity analysis was carried out to adjust the time step Δt appropriately, which showed that the choice of the time step has a negligible effect on the accuracy of the results when the condition $\Delta t \leq \frac{T}{80}$ is satisfied, where T is the period length of the oscillating motion of the airfoil, thus also satisfying the basic assumption on the sampling frequency given by the Nyquist-Shannon sampling theorem. For larger values of the time step Δt, the system exhibited some degree of numerical dissipation. The stop condition for convergence at each time step was again set by the maximum size of the residual in the continuity equation, namely, to a value of 3×10^{-5}, or a maximum number of 150 iterations.

The analysis of the time response of the system was carried out on asymmetric profile NACA0012 with one DOF, with the absence of gravitational acceleration ($g = 0\,\mathrm{m.s^{-2}}$), for the value of Reynolds number $\mathrm{Re} = 0.94 \times 10^5$ ($U_\infty = 8.802\,\mathrm{m.s^{-1}}$) and different initial conditions (non-zero θ_0, $\dot{\theta}_0$, h_0 or $\dot{h}_0$). In all cases, the airfoil was modeled as a rigid body with length $c = 0.156\,\mathrm{m}$, and the assumed span was $s = 1\,\mathrm{m}$. The force term C_L was approximated by a polynomial of 5th degree when solved with XFoil software. A total of four regimes were tested. As can be noted from the graphical outputs in Fig. 4, the outputs of all models are similar. The greatest agreement is achieved by the two models computed with Fluent software, and the highest dissipation in all cases tested is achieved by the analytical model combined with XFoil. Bigger differences between the approaches are generally detectable in the case of longitudinal oscillations, but mainly in the amplitude domain, with little effect on the value of the frequency f from the different modelling approaches. In terms of computational efficiency, the calculation of one presented time response in the Fluent software corresponded to approximately 3 h, while

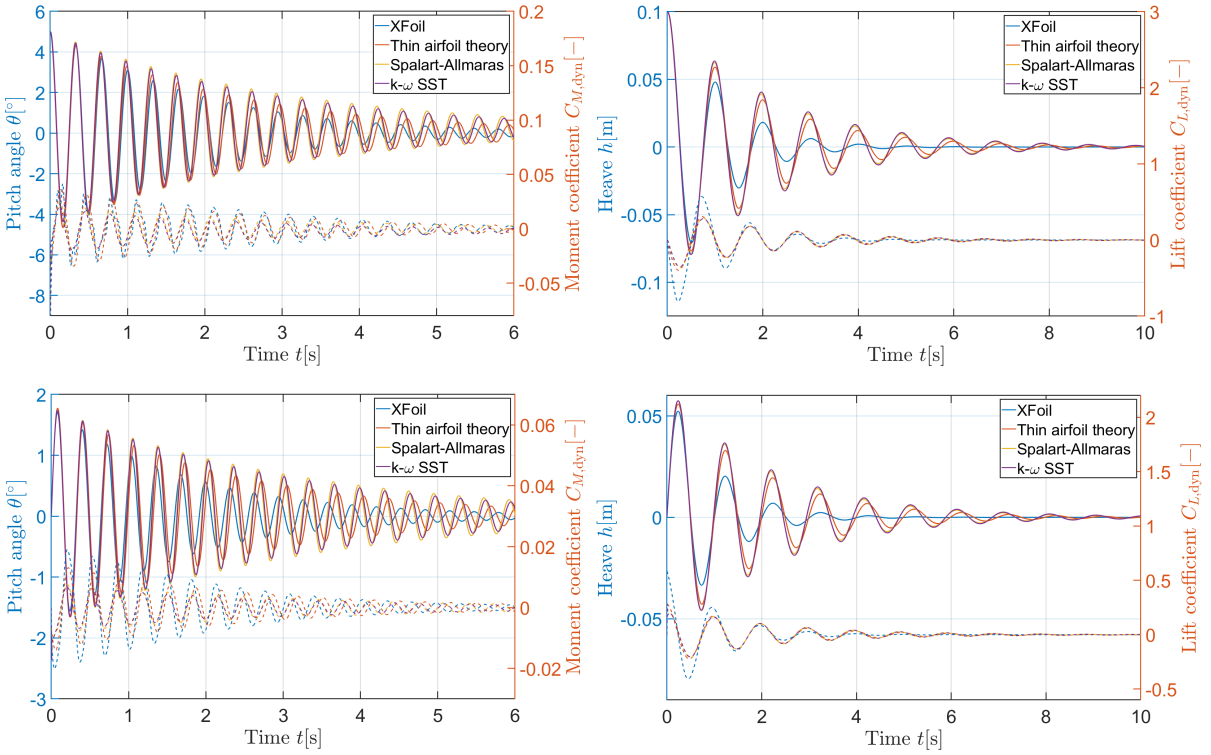

Fig. 4. Comparison of the response of a rigid airfoil with one DOF to IC and flow field excitation. Graphical dependencies of position and force coefficients over time are plotted. The evaluated oscillation frequency corresponds to values $f = 3\,\mathrm{Hz}$ for rotation and $f = 1\,\mathrm{Hz}$ for longitudinal deflection

the analytical calculation took about 10 s.

Two analyses presented in this paper show that despite the currently available computational power in combination with complex numerical software, analytical methods based on semi-empirical assumptions still have their indispensable place in FSI problems. These methods offer a high level of computational efficiency while maintaining sufficient accuracy of the generated outputs, especially at the level of one-sided interaction.

Acknowledgements

This research work was supported by project SGS-2019-009 of the Czech Ministry of Education, Youth and Sport, and by the Czech Science Foundation project number 20-26779S.

References

[1] Critzos, C. C., Heyson, H. H., Boswinkle, R. W., Aerodynamic characteristics of NACA 0012 airfoil section at angles of attack from 0° to 360°, Report NACA TN3361, Washington, 1955.

[2] Drela, M., XFOIL – An analysis and design system for low Reynolds number airfoils, T. J. Mueller (Ed.), Low Reynolds number aerodynamics, Springer-Verlag, Berlin, 1989, pp. 1–12.

[3] Michos, A., Bergeles, G., Athanassiadis, N., Aerodynamic characteristics of NACA 0012 airfoil in relation to wind generators, Wind Engineering 7 (4) (1983) 247-262.

[4] Shedahl, R., Kilmas, P., Aerodynamic characteristics of seven symmetrical airfoil sections through 180-degree angle of attack for use in aerodynamic analysis of vertical axis wind turbines, Report SAND-80-2114, Sandia National Labs., Albuquerque, 1981.

[5] UIUC Applied Aerodynamics Group, https://m-selig.ae.illinois.edu/.

COMPUTATIONAL MECHANICS 2021
36th conference with international participation
Srní
November 8 - 10, 2021

Improving dexterity of tensegrity structures using a set of local linear models

P. Beneš[a], J. Zavřel[a], M. Jílek[a], Z. Šika[a]

[a] *Faculty of Mechanical Engineering, CTU in Prague, Technická 4,160 00 Praha 6, Czech Republic*

The paper deals with the research of future robotic-type mechatronic structures based on tensegrities [4]. The aim is to replace serial robots with tensegrity mechanisms and to maintain a large collision-free workspace while significantly improving the ratio between stiffness and weight and the overall variability of the robot.

Tensegrity structure has typically more degrees of freedom than its end-effector. The set of local linear models is used to find the optimal configuration of these redundant degrees of freedom. The goal is to maximize dexterity throughout the workspace.

The dexterity optimization was performed on a simulation model of planar 3-stage tensegrity tower [2] shown in three different positions in the left part of Fig. 1. The structure consists of 6 bars and 22 tendons of variable length. The centre of mass of the upper left bar was selected as the working point (end effector). The workspace was defined using 100 predefined positions of this working point.

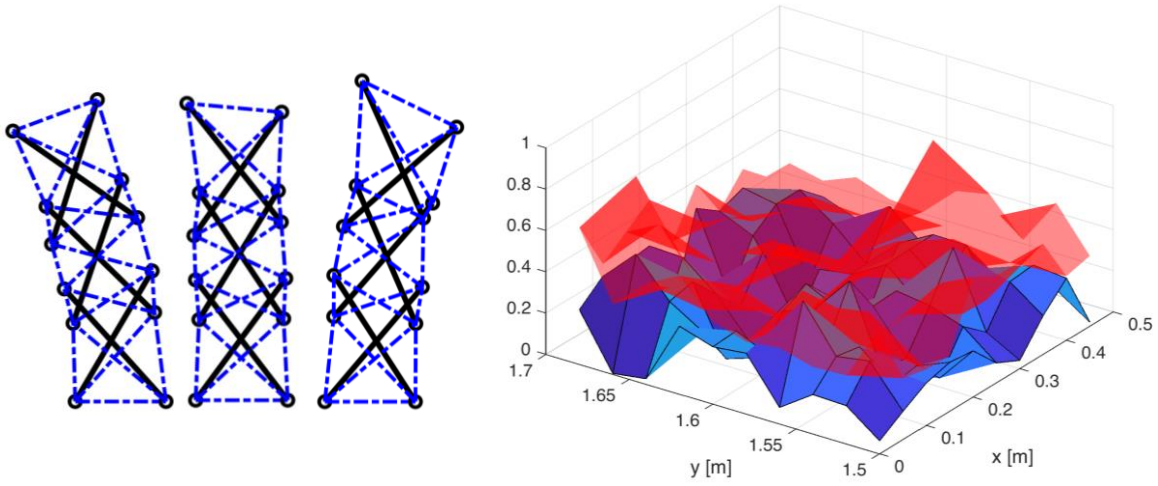

Fig. 1. Different positions of controlled tensegrity structure (left), comparison of optimized and nominal dexterity throughout predefined workspace (right)

Dexterity quantifies the ability to control the end-effector using available actuators. We describe it mathematically as

$$D = \frac{1}{cond(\boldsymbol{J})}, \tag{1}$$

where $\boldsymbol{J}$ is a Jacobi matrix describing the transfer between velocities of actuators/tendons $\dot{\boldsymbol{l}}$ and velocity of the end effector $[\dot{x}_S, \dot{y}_S]^T$

$$\boldsymbol{J} \cdot \dot{\boldsymbol{l}} = \begin{bmatrix} \dot{x}_S \\ \dot{y}_S \end{bmatrix}. \tag{2}$$

The structure in Fig. 1 is described using 15 independent coordinates. The positions of the end effector x_S and y_S were prescribed and the remaining 13 coordinates represents optimization parameters that were optimized to maximize dexterity in defined workspace points [1]. The subsequently calculated tendon lengths were used as input to the local linear model tree algorithm (LOLIMOT) [3]. The whole workspace was divided by this algorithm into 46 sub-areas, in which a linear model was created for each tendon, Fig. 2. These models are represented in the approximated model by the validity function and the membership function. The product of all validity and membership functions is then equal to one in the whole domain of the model. The resulting model is then given by the sum of the individual local linear models with the corresponding validity and membership function.

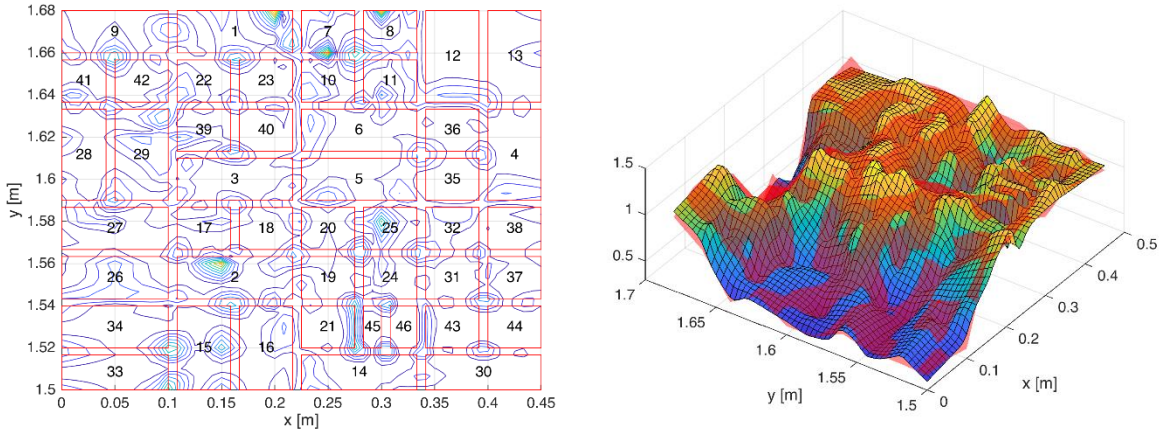

Fig. 2. Workspace division using LOLIMOT and model error (left), comparison of LOLIMOT approximation with exact values (right)

In the right part of Fig. 1 is the resulting comparison of dexterity when the redundant degrees of freedom are controlled using the set of local linear models (red surface) and the nominal configuration of tensegrity taken from a form-finding approach. There is an obvious improvement throughout the entire workspace. The simulation experiments confirmed that the set of local linear models is a suitable approximator for finding rules for controlling the length of tendons even in positions between optimized points.

Acknowledgements

The work has been supported by the Czech Science Foundation project GA20-21893S - Mechatronic Tensegrities for energy efficient light robots.

References

[1] Balon, A., Optimalizace a řízení mechatronické tensegrity pro robotiku, Master thesis. ČVUT, Praha, 2019. (in Czech)
[2] Jílek, M., Zlepšení manipulovatelnosti tensegritických struktur využitím sítě lokálních lineárních modelů, Master thesis. ČVUT, Praha, 2021. (in Czech)
[3] Nelles, O., Local linear neuro-fuzzy models: fundamentals. In: Nonlinear System Identification. Springer, Berlin, Heidelberg, 2001.
[4] Skelton, R.E., de Oliveira, M., Tensegrity systems, Springer-Verlag US, 2009.

COMPUTATIONAL MECHANICS 2021
36th conference with international participation
Srní
November 8 - 10, 2021

Some solutions to crack growth effects in metallic materials - crack shape progress and plasticity induced crack closure simulation

P. Brož[a], D. Dobiáš[b]

[a]Faculty of Applied Sciences, University of West Bohemia in Pilsen, Univerzitní 8, 301 00 Plzeň, Czech Republic
[b]Klokner Institute, Czech Technical University in Prague, Šolínova 7, 166 08, Praha 6, Czech Republic

1. Introduction

One of the main contemporary challenges being pertinent to the subject given is the prediction of fatigue crack propagation components made of ductile metallic matter. Owing to the high stresses round the crack tip, strips of constantly deformed material occur along the opposite crack faces in the course of the crack growth [1]. These strips contact each other through portion of the loading cycle, yielding a wedge result known as Plasticity Induced Crack Closure (PICC). It is a basic aspect of the mechanics of propagating cracks that clarifies diverse effects referred to the fatigue crack propagation, such as the effect of stress ratio, mean stress and specimen thickness. Moreover, PICC affects the crack shape evolution (CSE), causing a larger growth retardation (wedging effect) close to face surfaces. The matter is an independent analysis of both events PICC and CSE.

2. Motivation

PICC was studied for established crack shapes, either straight or curved. Among others, elastic-plastic material simulations were considered and followed the strategy that comprises the successive release of nodes after attaching specific load cycles. This tactics permits to develop the plastic wake as the crack grows and to stipulate the crack opening load or stress (P_{op}/P_{max}, S_{op}/S_{max}) which can be employ for estimating the value of a crack driving force such as the effective stress intensity factor extent ($\Delta K_{eff} = K_{max}\,(1–P_{op}/P_{max})$).

The objective of this research is to develop and validate a methodology for the modelling plasticity induced crack closure and crack form evolution rested on elastic-plastic fracture parameters. In this treatise, the plastic crack tip opening displacement extent ($\Delta CTOD_p$) is choosen as the crack driving force, since its relationship with the fatigue crack growth rate is linear and so that, the fatigue CSE and PICC can be predicted along the crack without experimental profile of the crack growth ratio.

3. Methodology

The intended methodology permits to model PICC and CSE concurrently by solving iteratively an elastic-plastic finite simulation which retains the load history information by remeshing and mapping methods and carries out the crack increase by node releasing. The principal phases of the methodology are demonstrated in the flow diagram presented in Fig. 1.

Above all, the linear elastic qualities and hysteretic conduct of the material must be explained. In this work the Von Mises yield criterion was employed together with the

Chaboche hardening law that is correct for symbilizing metals which show kinematic hardening

$$\mathrm{d}\mathbf{X} = C_x \left[X_{\mathrm{sat}} \frac{\boldsymbol{\sigma}' - \mathbf{X}}{\bar{\sigma}} - \mathbf{X} \right] \mathrm{d}\bar{\varepsilon}^{\mathrm{p}} \tag{1}$$

X is the backstress tensor and σ' is the deviatoric component of the Cauchy stress tensor ε^p and σ are the equivalent plastic strain and the equivalent stress, respectively, whereas C_x and X_{sat} are fitting parameters that can be stipulated by the optimization algorithm.

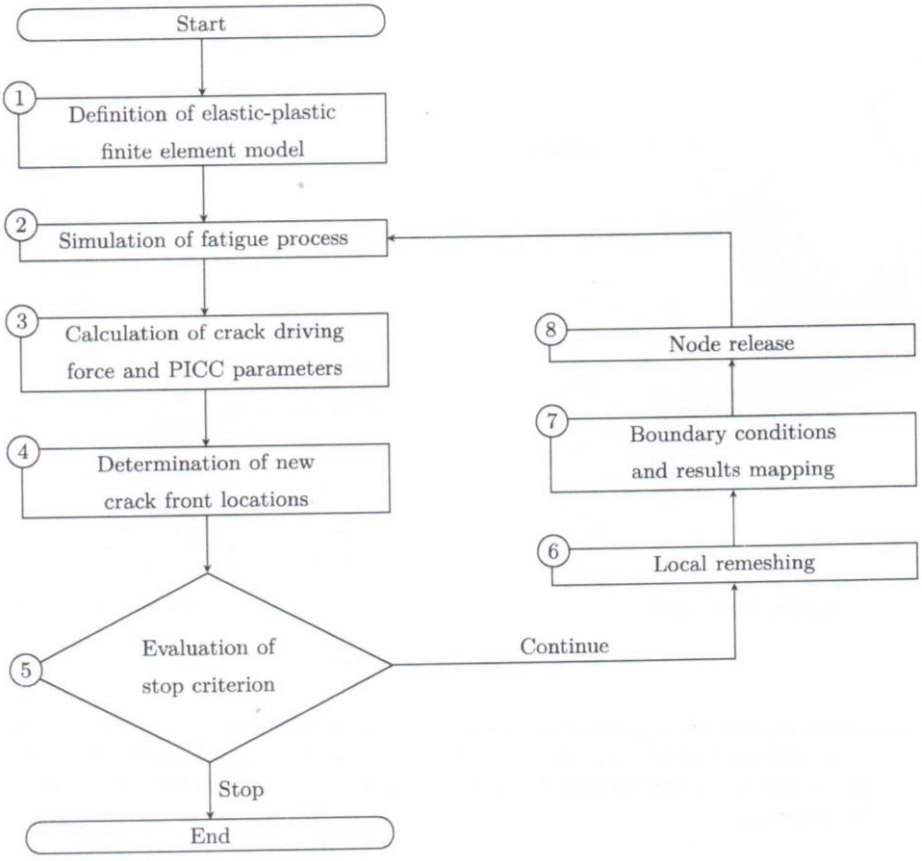

Fig. 1. Flow diagram of the intended methodology [1]

4. Modelling fatigue process

The loading history is now modelled by using the boundary conditions and cyclic loading in question (Fig. 2). Typically, several cycle should be modelled so that to consolidate the material response and get stationary values of the studied variables ($\Delta CTOD_p$ and P_{op}/P_{max}). The optimal number of cycles is still indistinct, because it can be inferred from the different values acquired in the literature, and is often limited by the available computer capacities.

5. Crack driving force and PICC parameters calculation

CTOD is explained as the vertical displacement of the immediate vicinity node behind each crack-front node (Fig. 3), whereas the mesh dependence brought in by such definition can be prevented by consistent in the alternative of the same crack-tip element dimension in description and prediction crack compositions. Δ $CTOD_p$ is taken out from the last loading ramp before the note releases. So as to, the initial elastic region portion is identified, a linear fit is carried out to get the elastic constituent and the difference between complete CTOD and elastic CTOD is received at maximum load. This simple procedure confronts with energetic

methods applied for calculating stress intensity factors that mean the evaluation of domain integrals over contours of elements round the crack front.

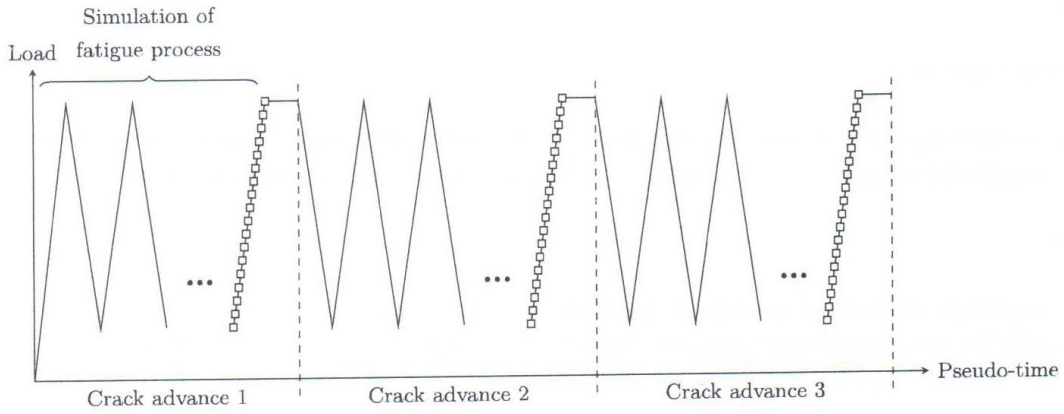

Fig. 2. Schematic example of the applied load cycles [1]

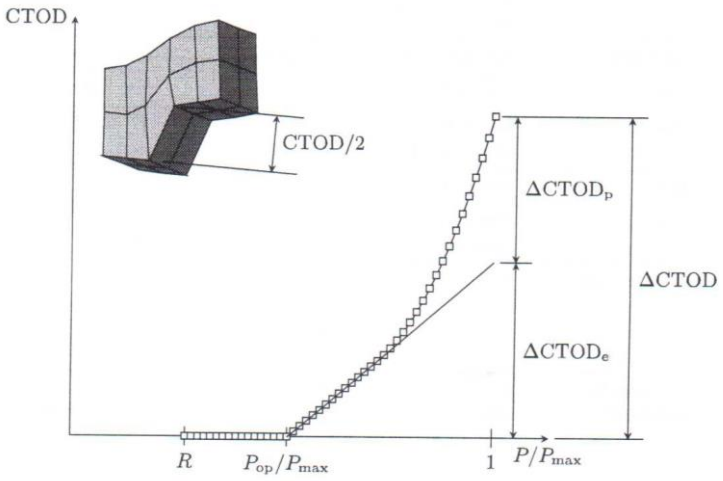

Fig. 3. Crac tip opening displacement measured in the firs node behind the crack front in the last loading ramp

6. Conclusion

It is relevant to compare the results gained in the analysis given with the tendencies watched for other driving forces, such as ΔK_{eff}, that was employed by several authors to do simultaneous modelling PICC and CSE.

For example, Gardin et al [2] modelled the growth of an initially straight through-crack in a compact tension sample, by though about – fixed straight and evolving curved forms.

Shifting to the crack opening load (P_{op}/P_{max}) Branco et al discovered that the crack closure developed next to the surface resulted in an increase of the crack opening load as the crack grows. The principal newness was the using an elastic-plastic fracture parameter rather than the broadly employed effective stress intensity factor range (ΔK_{eff}) what means two pertinent advantages: (a) a lower numerical endeavour, (b) a wider suitability, as large scale yielding scenarios may be analyzed.

It was inferred:

- The suggested methodology is valid, founded on the good numerical – experimental correlation of crack forms and the high arrangement between the watched fracture and PICC tendencies and the literature.
- Δ $CTOD_p$ is an effective crack driving force, since it allows to predict crack forms accurately.
- Δ $CTOD_p$ is an efficient crack driving force, because it demonstrates faster convergence with attached load cycles than the crack opening load. In actual fact, only one cycle has to be attached between note releases so that to stipulate the realistic crack form evolution.

Acknowledgement

The authors gratefully acknowledge the financial support of the presented research by the University of West Bohemia in Pilsen.

References

[1] Escalero, M., Muniz-Calvente, M., Zabala, H., Urresti, I., Suitability of constraint and closure models for predicting cracks growth in generic configurations, Engineering Fracture Mechanics 225 (15) (2020) 106808.

[2] Gardin, C., Fiordalisi, S., Sarrazin-Baudoux, Ch., Gueguen, M., Petit, J., Numerical prediction of crack front shape during fatigue propagation considering plasticity-induced crack closure, International Journal of Fatigue 88 (7) (2016) 68-77.

COMPUTATIONAL MECHANICS 2021
36th conference with international participation
Srní
November 8 - 10, 2021

Fast blade shape optimization based on a neural-network-predicted flow field

O. Bublík, A. Pecka, V. Heidler

Faculty of Applied Sciences, University of West Bohemia, Univerzitní 8, 301 00 Plzeň, Czech Republic

The optimization of the geometrical shape of the blade in turbo machinery is generally a computationally demanding task. The optimization algorithms usually use the gradient descent method, which require to compute the flow fields many times to slightly modify the geometry. The use of the neural networks can significantly improve the speed of the optimization process by predicting flow fields extremely quickly [4, 5].

In this work a neural network architecture for prediction of viscous compressible fluid flow in blade cascade was developed. The focus of the architecture is an autoencoder based on the convolutional neural network that transforms a structured computational mesh into the resulting flow field. Periodic boundary conditions were achieved by periodic padding. The developed neural network also contains Mach number as an input parameter. The neural network was implemented using the Python programming language with the help of Keras [3] and TensorFlow [1] libraries.

The developed neural network was trained on 136 randomly generated geometries, where the input Mach number was varied in the range $[0.5, 1]$. The numerical computation of the specimens was performed with open-source CFD software FlowPro [2]. The considered blade profile consist of six design points, where the cubic spline forms the shape of the profile, see Fig. 1. The design points on the tip and the end of the profile are fixed, while the rest of the points can by optimized by finding a maximum of the functional

$$f(\boldsymbol{x}) = \frac{c_L(\boldsymbol{x})}{1 + c_D(\boldsymbol{x})}, \qquad c_L = \oint_\Gamma p\, n_y, \;\; c_D = \oint_\Gamma p\, n_x, \tag{1}$$

where $\boldsymbol{x} = [x_1, y_1, x_2, y_2, x_3, y_3, x_4, y_4]$ are positions of the design points, c_L and c_D are lift and drag coefficients and Γ is the profile surface.

The developed neural network was tested on the problem of blade profile optimization for the mach number $M = 1$. In the first step, the optimization algorithm roughly searches the state space for a combinations of the design-point positions, as shown at Fig. 1 (left). The red squares defines the permissible area for the position of free design points. At each of square a nine possible positions were considered (blue points) which lead to a $9^4 = 6561$ combinations. At each of square a nine possible positions were considered (blue points) which lead to a $9^4 = 6561$ combinations. The evaluation of all combination took 13.3s of CPU time on common desktop PC. In the second step, 100 steps of gradient descent method (32s of CPU time) is started to obtain the more precise solution, see Fig. 1 (right). Fig. 2 shows the comparison between predicted and computed pressure and velocity fields for optimized profile.

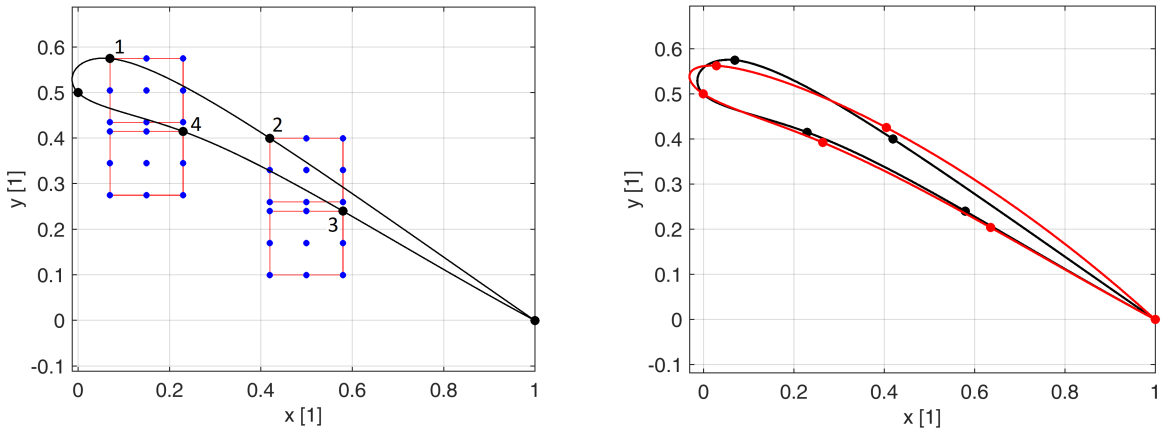

Fig. 1. *Left:* Blade profile with designed points (black dots). Red squares denote the searching area with admissible values (blue points). *Right:* Red color show the optimized profile shape after 100 gradient descent iterations.

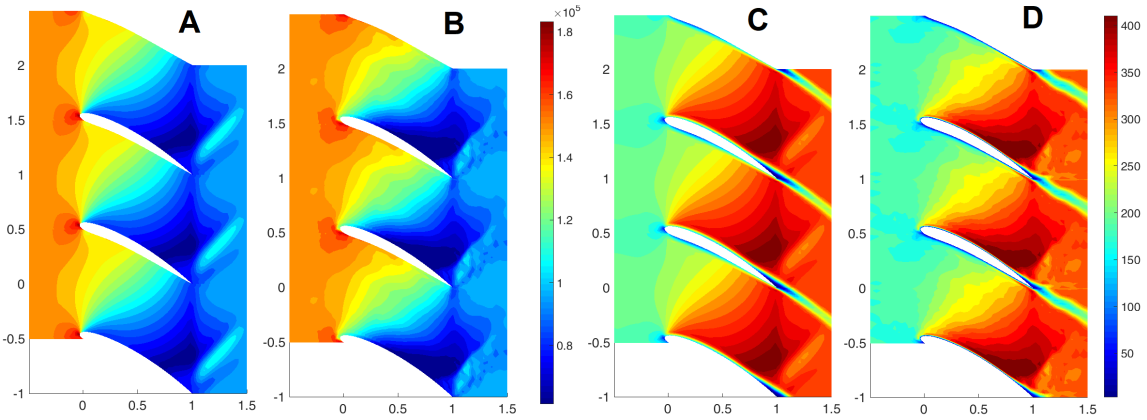

Fig. 2. A: computed pressure field, B: predicted pressure field, C: computed velocity field, D: predicted velocity field

Acknowledgements

This research is supported by project "Fast flow-field prediction using deep neural networks for solving fluid-structure interaction problems" GA21-31457S of the Grant Agency of the Czech Republic and by the internal student grant project SGS-2019-009.

References

[1] Abadi, M., Agarwal, A., et al., TensorFlow: Large-scale machine learning on heterogeneous systems, Software, 2015, https://www.tensorflow.org/.

[2] Bublík, O., Pecka, A., Vimmr, J., FlowPro – multipurpose CFD software written in Java, Proceedings of the conference Computational mechanics 2017, Srní, 2017, pp. 13-14.

[3] Chollet, F. et al., Keras, 2015, https://keras.io.

[4] Guo, X., Li, W., Iorio, F., Convolutional neural networks for steady flow approximation, Proceedings of the ACM SIGKDD International Conference on Knowledge Discovery and Data Mining, 2016, pp. 481-490.

[5] Hennigh, O., Lat-Net: Compressing lattice Boltzmann flow simulations using deep neural networks, 2017, https://arxiv.org/abs/1705.09036.

COMPUTATIONAL MECHANICS 2021
36th conference with international participation
Srní
November 8 - 10, 2021

Influence of various constraints in topology optimization of tensegrity structures using mixed integer linear programming

R. Bulín[a], M. Hrabačka[b], M. Hajžman[a,b]

[a] NTIS – New Technologies for the Information Society, Faculty of Applied Sciences, Technická 8, 301 00 Plzeň, Czech Republic
[b] Department of Mechanics, Faculty of Applied Sciences, University of West Bohemia, Univerzitní 8, 301 00 Plzeň, Czech Republic

The definition of a tensegrity structure is not unique, but the word tensegrity itself is composed from words "tension" and "integrity". This implies, that some continuous network of tension is needed to maintain the structure's integrity [4]. In general, the tensegrity is a pre-stressed structural system that has a great potential to reach favorable strength to weight ratio. There are various types of tensegrities and they can be found throughout several different fields, such as architecture (e.g., lightweight self-supporting roofs, bridges or towers), biology (e.g., tensegrity cell model, skeleton with muscles) or engineering (lightweight manipulators, human exoskeletons, space deployable structures). From the perspective of mechanical engineering and robotics, the tensegrity structures are interesting systems in terms of their mechanical properties, such as stability, modal properties or controllability and dexterity. The first step before an utilization of tensegrity structure as a part of a mechanical system is to find suitable topology and form of a tensegrity. In this paper, the tensegrity topology optimization using mixed integer linear programming is briefly summarized and the influence of various optimization constraints is further discussed.

The topology optimization of tensegrity structures is based on the ground structure method [1] which is commonly used for topology optimization of truss pin-jointed structures. This method is based on the definition of nodes positions and on the definition of candidate members, each member connects two nodes. In case of tensegrity structures, each candidate member can be a strut, cable or it can be completely omitted. To distinguish the type of member, two binary optimization variables x_i, y_i for each member are used [2]. Since these variables can have only integer values 0 or 1 and commonly also other continuous variables are used, the whole optimization problem is formulated as a mixed integer linear programming (MILP) problem [1]. The linear programming is mainly used because of computational efficiency of numerical methods, that can operate with binary variables. The whole problem can utilize a large number of optimization variables (even for simple structures it can be more than thousand) and a large number of optimization constraints (again, more than thousand constraints for simple structures), so any nonlinearity can lead to difficulties with convergence in acceptable computational time.

Since the MILP formulation is used, the objective function is linear. The common optimization objectives are: (a) a minimization of number of cables used in the tensegrity, (b) a minimization of the total length of all cables [2], (c) a minimization of the overall structure weight [5], (d) a maximization of the sum of pre-stress forces in the structures [4]. First two objectives are similar and practical, because with the lower number of cables (or total cable length), the whole structure can be easier to manufacture. Since the pre-stress forces can be

negative (compressive force) or positive, the fourth objective tends to generate a stiff and stable tensegrity structure.

The basic MILP formulation for the topology optimization of tensegrity structures is [2]

$$\min_{\mathbf{x},\mathbf{y},\mathbf{q}} \sum_{i \in E} y_i, \tag{1}$$

$$\text{s.t.} \quad \mathbf{Hq} = \mathbf{0}, \tag{2}$$

$$-q_s^U x_i \leq q_i \leq -q_s^L x_i + q_c^U (1 - x_i), \quad \forall i \in E, \tag{3}$$

$$q_c^L y_i - q_s^U (1 - y_i) \leq q_i \leq q_c^U y_i \quad \forall i \in E, \tag{4}$$

$$\sum_{i \in E(j)} x_i \leq n \quad \forall j \in V. \tag{5}$$

Eq. (1) represents the objective function, which evaluates a number of cables in the whole structure. The optimization variables are binary variables $\mathbf{x}$ and $\mathbf{y}$ and they determine the type of member: if $(x_i,\ y_i) = (1,\ 0)$, the member i is strut, if $(x_i,\ y_i) = (0,\ 1)$, the member i is cable, if $(x_i,\ y_i) = (0,\ 0)$, the member is not used in the structure. Optimization variable $\mathbf{q}$ represents the pre-stress forces in members. Eq. (2) is the static equilibrium condition, where $\mathbf{H}$ is the equilibrium matrix [2]. Eqs. (3) and (4) ensure, that if member i is a cable, it will be in tension, and if member i is a strut, it will be in compression. Constants q_s^U, q_s^L, q_c^U and q_c^L represent upper (U) and lower (L) boundaries on forces in strut members (s) and cable members (c). Eq. (5) expresses so called discontinuity conditions and it ensures, that in one structure node there will end n or less struts. For classical tensegrities, there is only one end of strut in one node, thus $n = 1$. Symbol E denotes a set of candidate members, V is set of nodes and $E(j)$ is a set of members, that ends in node j.

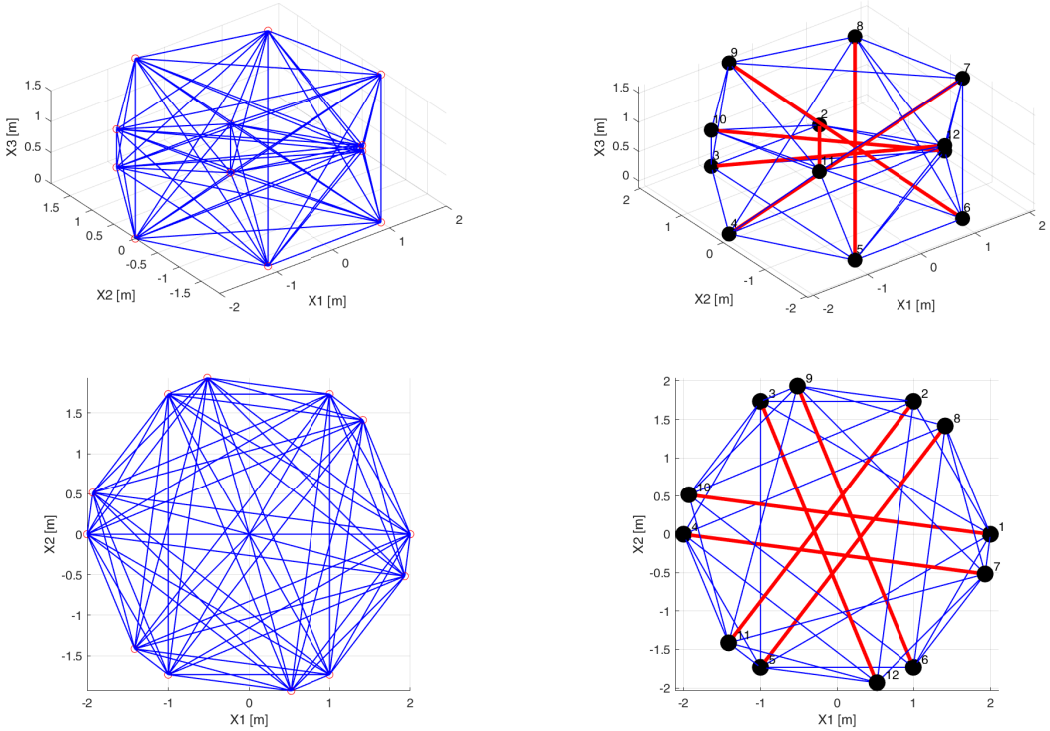

Fig. 1. *Left:* Ground structure of two hexagons (blue - candidate member); *Right:* Resulting tensegrity structure using struts with the same lengths (red - strut, blue - cable)

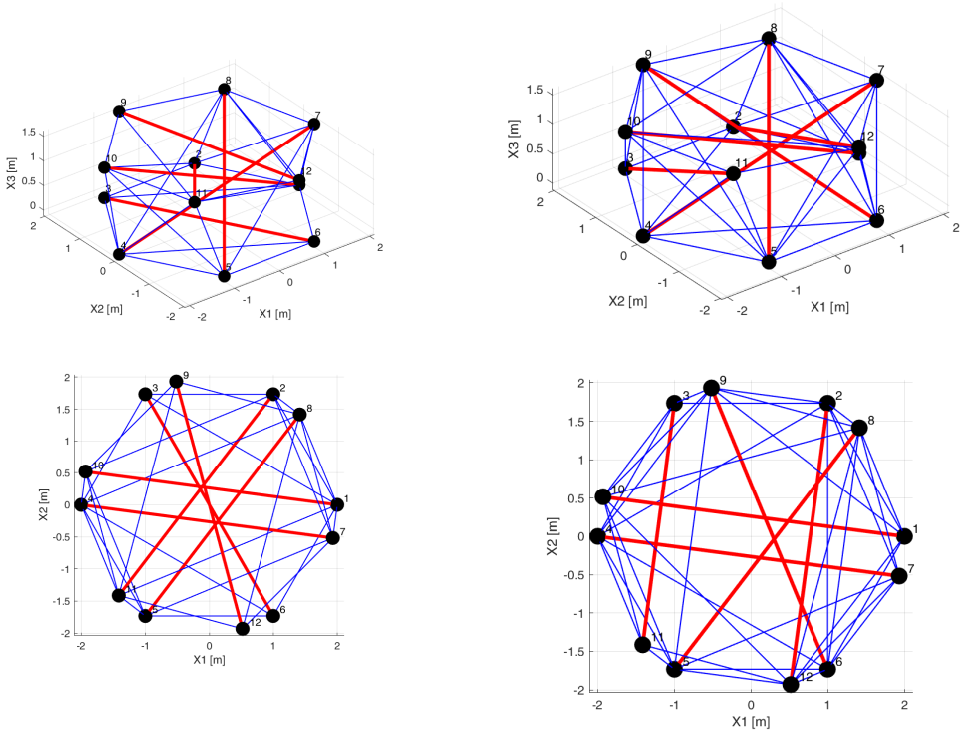

Fig. 2. *Left:* Resulting tensegrity structure using two different strut lengths (red - strut, blue - cable); *Right:* Resulting tensegrity structure using three different strut lengths (red - strut, blue - cable)

The optimization process does not often lead to satisfying results using Eqs. (1)–(5) only, thus many other additional constraints, that can also require to add other optimization variables, can be employed to obtain desired results. The additional constraints can be generally divided into two groups: practical constraints and properties constraints. Essential practical constraints are: constraints to avoid intersecting members [3], constraints on the number of strut length groups used [2] (this requires to sort the potential members by length and to create groups with similar length), constraints on kinematic and static indeterminacy [2] or constraints on the number of cables in one node. The tensegrity properties constraints are: constraints on the structural deformation when externally loaded [3] or constraints on the member forces to prevent buckling [5].

The influence of the number of strut length groups on the structure of hexagonal tensegrity is shown in Figs. 1 and 2. On the left side of Fig. 1 the ground structure with all candidate members is shown. The right side of Fig. 1 shows the structure after the topology optimization, where all the used struts belong to the same length group, thus they have the same length. The structure has a nice level of symmetry. In Fig. 2 the resulting structure with two resp. three strut length groups are shown.

In Fig. 3, the topology optimization of tensegrity tower is illustrated. At first, the counter-clockwise twisted triangular tensegrity is shown in order demonstrate one layer of the tensegrity tower. Then, the ground structure that is composed from two layers and the resultant topology after optimization are shown. The bottom layer of the tower is the counter-clockwise twisted triangular tensegrity and the upper layer is clockwise twisted triangular tensegrity. These results demonstrate, that the topology optimization reached the expected results. In addition, the constraints on the structure deformation were used in the optimization. It allows to specify the load in the nodes (in this case, nodes 10, 11 and 12 were loaded). In the results of the opti-

mization, the forces in members that equalize the external loads are also obtained, which is an advantage in comparison with classical form-finding methods. It can be concluded, that the topology optimization of tensegrity structures using MILP formulation provides also practical results, such as total forces in the used members. By a combination of various constraints in topology optimization of tensegrity structures, different results can be obtained.

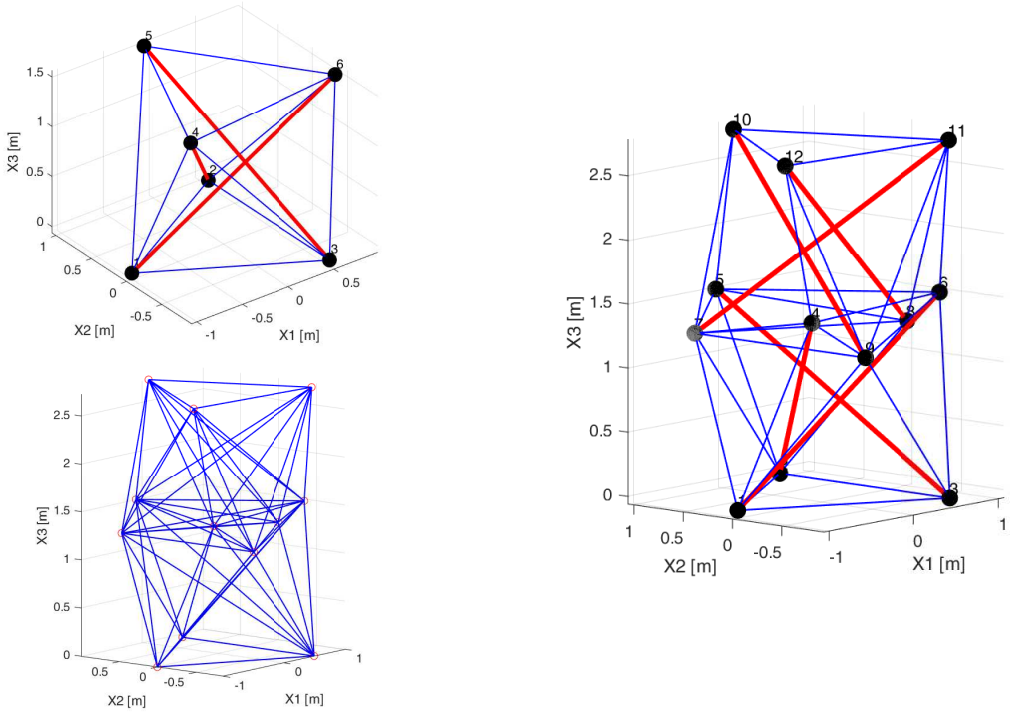

Fig. 3. Counter-clockwise triangular tensegrity, ground structure for tensegrity tower and resultant topology of tensegrity tower

Acknowledgement

The work was supported by the Czech Science Foundation project number 20-21893S.

References

[1] Ehara, S., Kanno, Y., Topology design of tensegrity structures via mixed integers programming, International Journal of Solids and Structures 47 (2010) 517-579.

[2] Kanno, Y., Exploring new tensegrity structures via mixed integer programming, Structural Multidisciplinary Optimization 48 (2013) 95-114.

[3] Kanno, Y., Topology optimization of tensegrity structures under self-weight loads, Journal of the Operations Research Society of Japan 55 (2) (2012) 125-145.

[4] Liu, K., Paulino, G. H., Tensegrity topology optimization by force maximization on arbitrary ground structures, Structural and Multidisciplinary Optimization 59 (2019) 2041-2062.

[5] Xu, X., Wang, Y., Luo, Y., Hu, D., Topology optimization of tensegrity structures considering buckling constraints, Journal of Structural Engineering 144 (10) (2018) No. 04018173.

COMPUTATIONAL MECHANICS 2021
36th conference with international participation
Srní
November 8 - 10, 2021

Shape optimization of nonlinear Gao beam

J. Burkotová[a]

[a] Department of Mathematical Analysis and Applications of Mathematics, Faculty of Science, Palacký University, 17. listopadu 12, 771 46 Olomouc, Czech Republic

The contribution is devoted to an optimal shape design problem of a nonlinear stepped elastic beam. The nonlinear Gao beam model [2] is motivated by a limitation of the Euler-Bernoulli beam model for relatively small deformations. The governing equation for the Gao beam reads as follows

$$E\mathcal{I}w'''' - E\,\alpha\,(w')^2\,w'' + P\,\mu\,w'' \;=\; f, \quad \text{in } (0,L),$$

where $$\mathcal{I} \;=\; \frac{2}{3}\,t^3\,b, \quad \alpha \;=\; 3\,t\,b\,(1-\nu^2), \quad \mu \;=\; (1-\nu^2), \quad f \;=\; (1-\nu^2)\,q.$$

Here E denotes the elastic modulus of the material, $\mathcal{I}$ is the area moment of inertia of the beam's cross-section, w is the transverse displacement of the beam, ν is the Poisson ratio, P is the axial force acting at the point $x \;=\; L$, q is the distributed vertical load, $2t$, b and L represent the height, the width and the length of the beam, respectively. Here the modified integral constant μ is used in the governing equation, see [5]. The existence analysis of the state problem was studied in [4].

The objective of the design problem is to find the thickness distribution minimizing compliance of the beam represented by the functional

$$J(w(t)) = \int_I f w(t) \mathrm{d}x,$$

where $w(t)$ is a solution of the state problem for a given admissible thickness distribution t. The volume of the beam is preserved and fixed during the optimization. Therefore, a set of admissible thicknesses U^{ad} is defined by

$$U^{ad} = \left\{ t \in L^\infty(I) : 0 < t_{min} \le t \le t_{max} \text{ in } I,\ t|_{I_i} = t_i \in P_0(I_i)\,\forall i, \int_I t(x)\mathrm{d}x \;=\; \gamma \right\},$$

where the stepped beam is represented by an interval $I = (0, L)$ composed of r mutually disjoint subintervals $I_1, I_2, \ldots I_r$. Finally, the thickness optimization problem reads

$$\begin{cases} \text{Find } t^* \in U^{ad} \text{ such that} \\ J(w(t^*)) = \min\limits_{t \in U^{ad}} J(w(t)). \end{cases}$$

The concept of shape optimization in the context of the linear Euler-Bernoulli model is well understood, see [3]. The corresponding analysis for the nonlinear Gao beam model is provided in [1] where the existence of a solution to the optimization problem is proved and the convergence analysis of the discretization using the finite element approach is covered.

For illustration, we consider a propped cantilever beam and a simply supported beam composed of 8 elements subject to the constant vertical load $q = -10^6\,\mathrm{Nm}^{-1}$ and no axial force. The material and geometric parameters are defined as follows: $L = 1\,\mathrm{m}, b = 0.1\,\mathrm{m}$, $E = 21 \cdot 10^{10}\,\mathrm{Pa}$, $\nu = 0.3$, $t_{min} = 0.01\,\mathrm{m}$, $t_{max} = 0.08\,\mathrm{m}$, $\gamma = 0.0425\,\mathrm{m}^2$. The initial thickness distribution is constant $t_i = 0.0425\,\mathrm{m}, \forall i$.

The results for the optimal thickness distribution of the Gao beam are shown in Fig. 1. The optimal thickness distribution of the Gao beam plotted with a solid line is compared with the reference constant thickness distribution plotted with a dashed line, left above for the propped cantilever beam and right above for the simply supported beam. Similarly, the deflection of the beam with the optimal thickness distribution is plotted with a solid line and the deflection of the beam with the initial constant thickness distribution is plotted with a dashed line below.

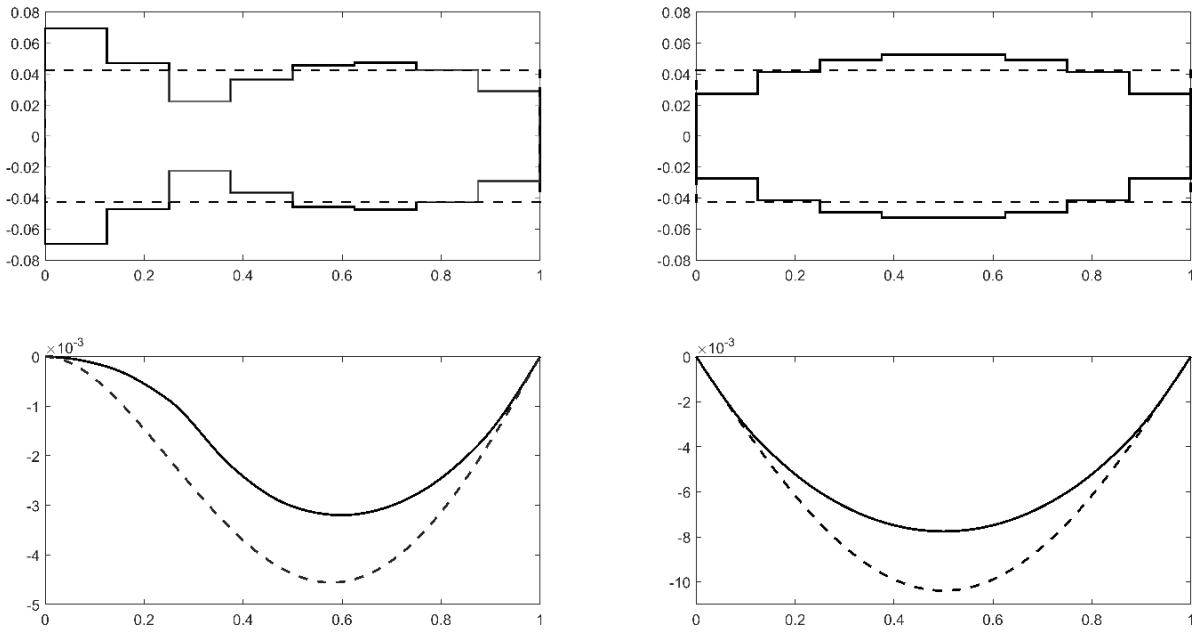

Fig. 1. Optimal thickness distribution and resulting deflection of the nonlinear Gao beam

The value of the compliance cost functional decreases from $2393\,\mathrm{Nm}$ for the reference beam with the constant thickness distribution to $1617\,\mathrm{Nm}$ for the beam with the optimal thickness distribution in the case of the propped cantilever beam and from $6044\,\mathrm{Nm}$ for the reference beam to $4840\,\mathrm{Nm}$ for the optimized beam in the case of the simply supported beam.

References

[1] Burkotová, J. Machalová, J., Radová, J., Optimal thickness distribution of stepped nonlinear Gao beam, Mathematics and Computers in Simulation 189 (2021) 21-35.

[2] Gao, D.Y, Nonlinear elastic beam theory with application in contact problems and variational approaches, Mechanics Research Communications 23 (1) (1996) 11-17.

[3] Haslinger, J., Mäkinen, R.A.E., Introduction to shape optimization: Theory, approximation and computation, SIAM, 2003.

[4] Machalová, J., Netuka, H., Control variational method approach to bending and contact problems for Gao beam, Applications of Mathematics 62 (6) (2017) 661-677.

[5] Machalová, J., Netuka, H., Comments on the large deformation elastic beam model developed by DY Gao, Mechanics Research Communications 110 (2020) No. 103607.

COMPUTATIONAL MECHANICS 2021
36th conference with international participation
Srní
November 8 - 10, 2021

Electrolyte flow through piezoelectric porous media and its application to two-scale cortical bone modeling

J. Camprová Turjanicová[a,b], E. Rohan[a,b]

[a] *Faculty of Applied Sciences, University of West Bohemia, Univerzitní 8, 301 00 Plzeň, Czech Republic*
[b] *NTIS – New Technologies for the Information Society, Univerzitní 8, 301 00 Plzeň, Czech Republic*

In biomechanics, electrochemical interactions between ions and negatively charged surfaces of the porous material occur in a few types of biological tissues. Our interest lies in the modeling of the cortical bone porous structure, where the transport of the ions in the proximity of charged collagen-apatite matrix has shown to play a role in bone regrowth and remodeling. Upon stress, bone tissue generates an electrical potential that directly influences the activity of bone cells. With this in mind, we derive the model of electrolyte flow through piezoelectric porous media and apply it to simulate the processes in cortical bone.

The cortical bone is a strictly hierarchical system with a complicated porous structure on different scale levels. The cortical bone tissue comprises a system of approximately cylindrical sub-units called osteons, see Fig. 1. Each osteon has a radius of approximately 100-150 μm, [5], with a hollow canal in its center. It is called the Haversian canal (HC) and contains blood vessels and nerves with rest of the space occupied by the bone fluid. The walls of the HC are covered by bone cells. Behind this bone cell layer, the walls of the HC are perforated by a network of small interconnected channels known as canaliculi, [5]. The canaliculi network connects the HC and lacunae, which are ellipsoidal cavities containing one bone-creating cell each, i.e., an osteocyte. The lacunar-canalicular network (LCN) is also saturated by bone fluid that transports nutrients and information about mechanical loading.

The cortical bone consists of two phases at the microscopic scale: the collagen-hydroxyapatite matrix and the bone fluid that fills the LCN. For modeling, we imagine the bone fluid as a salt-

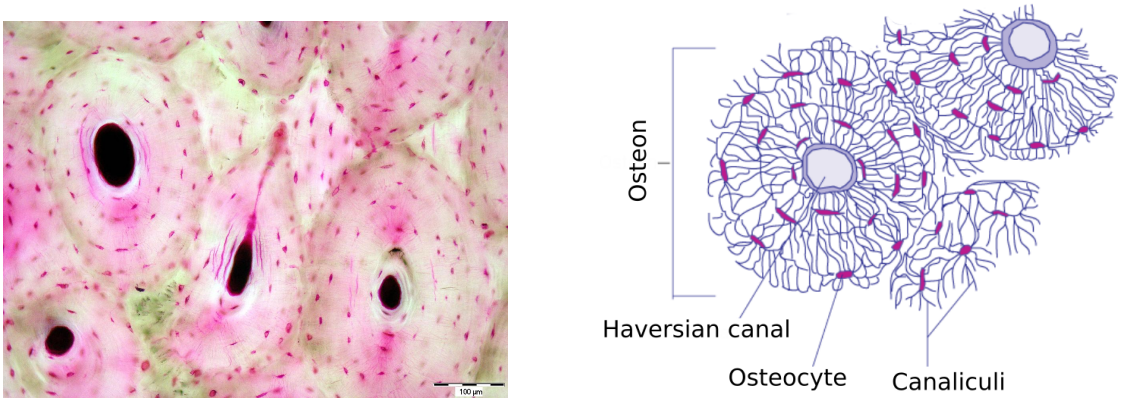

Fig. 1. Cortical bone structure: (*left*) the osteonal structure in cortical bone tissue, scale of 100 μm; (*right*) the illustration of lacunar-canalicunar network in the osteonal structure

water solution. Thus, there are two types of ions (further indexed by $\alpha = 1, 2$) with opposite polarization and that are defined by their respective diffusivity coefficients D_α^0. The bone fluid is an incompressible Newtonian fluid characterized by dynamic viscosity η_f.

Due to the presence of collagen, the bone matrix is deformable. Moreover, it exhibits piezoelectric behavior that was first reported by [2]. Biopolymers, such as collagen-hydroxyapatite, usually have the specific symmetry type: the piezoelectric coupling tensor $\boldsymbol{g}$ and dielectric tensor $\boldsymbol{d}$ are defined by their components g_{14}, $g_{25} = -g_{14}$, and d_{11}, $d_{22} = d_{11}$, d_{33}. Elastic properties of this type of material are transversal isotropic with the elastic tensor characterized by Young's moduli E_1, E_3, shear modulus G_{13} and Poisson's ratios ν_{12}, ν_{31}, [3].

The modeling of cortical bone tissue presents a unique challenge because of its highly hierarchical structure and complex interaction between phases. To simulate such material by direct modeling of its whole microstructure in its complexity would be very taxing on the computational memory requirements and not practical for bigger and more complex simulations. Instead, the material's heterogeneity is dealt with by applying a suitable homogenization method, such as unfolding homogenization (UFH). The UFM also respects the microstructure of the porous medium and, through the introduction of scale separation formulae, provides us with tools to reconstruct the macroscopic solution on the microscopic scale.

To successfully apply the UFH, we assume that the cortical bone tissue occupies domain Ω. The domain Ω is decomposed into solid and fluid phase, Ω_s and Ω_f, that have designated parts of the external boundary, $\partial_{\text{ext}}\Omega_s$ and $\partial_{\text{ext}}\Omega_f$, and interface $\Gamma = \partial\Omega_s \cup \partial\Omega_f$. Domain Ω is generated by periodical repeating copies of representative volume element (RVE) Y scale by ε. The RVE Y is decomposed into solid and fluid phase, Y_s and Y_f, with interface $\Gamma_Y = \bar{Y}_s \cup \bar{Y}_f$.

The homogenization procedure yields the expressions for computing the effective tensors that describe the behavior at the macroscopic scale. The tensors relevant to the ionic transport are tensor of permeability $\boldsymbol{\mathcal{K}}$, migration-diffusion tensors $\boldsymbol{\mathcal{J}}^\beta$, Onsager tensors $\boldsymbol{\mathcal{L}}^\beta$, diffusivity tensors $\boldsymbol{\mathcal{D}}^{\alpha\beta}$ and two new tensors $\boldsymbol{\mathcal{Q}}^{\alpha\beta}$ and $\boldsymbol{\mathcal{S}}^{\alpha\beta}$. Further, it gives tensors related to the piezoelectricity, which are piezoelasticity tensor $\boldsymbol{\mathcal{A}}$, modified Biot's tensor $\boldsymbol{\mathcal{B}}$, and ionic potential tensor $\boldsymbol{\mathcal{C}}^\alpha$. Then, the dimensionless macroscopic homogenized system of equations, where the external electrical field is omitted, reads: Find global pressure P^0, displacement $\boldsymbol{u}^0$ and ionic potentials $\Phi_\alpha^0, \alpha = 1, 2$, such that

$$
\begin{aligned}
\nabla_x \cdot \left[\boldsymbol{\mathcal{K}}(\boldsymbol{f} - \nabla_x P^0) + \sum_{\beta=1}^{2} \boldsymbol{\mathcal{J}}^\beta \nabla_x \Phi_\beta^0 \right] + \mathcal{M}\partial_t P^0 - \boldsymbol{\mathcal{B}} : e_x\left(\partial_t \boldsymbol{u}^0\right) - \mathcal{N}^\beta \partial_t \Phi_\beta^0 = 0, \\
\sum_{\beta=1}^{2} (\boldsymbol{\mathcal{Q}}^{\alpha\beta} + \boldsymbol{\mathcal{S}}^{\alpha\beta}) \partial_t \Phi_\beta^0 + \nabla_x \cdot \left[\boldsymbol{\mathcal{L}}^\alpha (\boldsymbol{f} - \nabla_x P^0) + \sum_{\beta=1}^{2} \boldsymbol{\mathcal{D}}^{\alpha\beta} \nabla_x \Phi_\beta^0 \right] = 0, \qquad (1) \\
-\nabla_x \cdot \boldsymbol{\mathcal{A}} e_x\left(\boldsymbol{u}^0\right) + \nabla_x \cdot \left[\boldsymbol{\mathcal{B}} P^0 - \sum_{\beta=1}^{2} \boldsymbol{\mathcal{C}}^\alpha \Phi_\beta^0 \right] = \boldsymbol{f}
\end{aligned}
$$

for $\alpha = 1, 2$ and completed by boundary conditions given below. We can distinguish the fluid seepage velocity $\boldsymbol{w}^0$, the ionic diffusion fluxes $\boldsymbol{j}_\alpha^0, \alpha = 1, 2$, and the porous body stress $\boldsymbol{\sigma}^0$,

$$
\begin{aligned}
\boldsymbol{w}^0 &= \sum_\beta \boldsymbol{\mathcal{J}}_\beta \nabla_x \Phi_\beta^0 - \boldsymbol{\mathcal{K}}(\nabla_x P^0 - \boldsymbol{f}) \quad \text{in } \Omega, \\
\boldsymbol{\sigma}^0 &= \boldsymbol{\mathcal{A}} e_x(\boldsymbol{u}^0) - P^0 \hat{\boldsymbol{\mathcal{B}}} + \sum_\beta \boldsymbol{\mathcal{C}}^\beta \Phi_\beta^0 \quad \text{in } \Omega, \qquad (2) \\
\boldsymbol{j}_\alpha^0 &= \sum_\beta \boldsymbol{\mathcal{D}}_{\alpha\beta} \nabla_x \Phi_\beta^0 - \boldsymbol{\mathcal{L}}_\alpha (\nabla_x P^0 - \boldsymbol{f}) \quad \text{in } \Omega, \quad \alpha = 1, 2.
\end{aligned}
$$

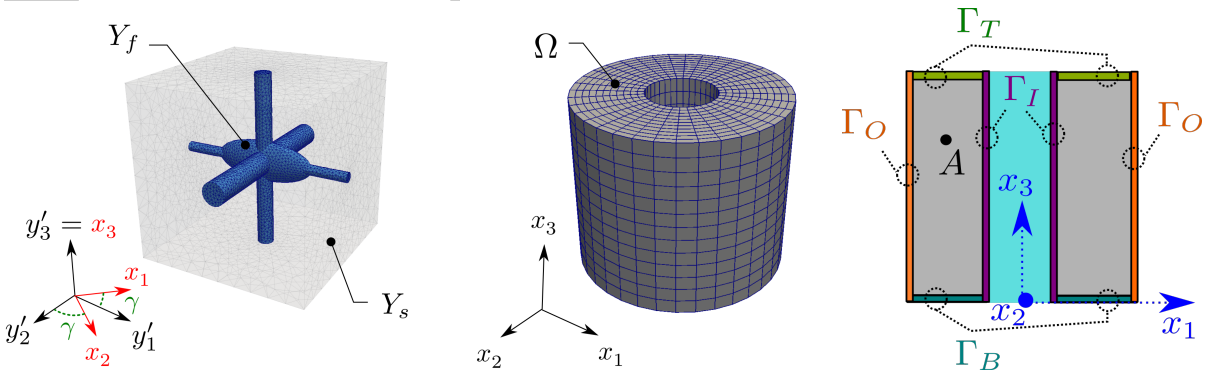

(a) (b) (c)

Fig. 2. (a) Mesh representation of RVE Y; (b) mesh representation of single bone osteon, i.e., domain Ω; (c) definition of boundaries of domain Ω

The system (1) needs to be completed by a set of boundary conditions given below.

For numerical modeling, we simplify the bone structure into two structural levels and propose their geometry representation, as follows:

- The microscopic level represents the LCN filled with bone fluid. The cubic RVE Y represents three channels with a single ellipsoidal lacuna, see Fig. 2a. The three channels have a cross-sectional area corresponding to the sum of cross-sectional areas of all the canaliculi in the given direction to preserve the flow rate between lacunae, [1].
- The macroscopic level is represented by a single osteon which has an approximately cylindrical shape with a hollow canal in its center, see Fig. 2b.

To respect the orientation of LCN in osteon, the computed effective coefficients are circumferentially rotated around the x_3-axis of the central canal.

We consider the inner osteonal wall Γ_I to be non-permeable. The gradual compression is applied at the top of the osteon, i.e., at Γ_T. This is realized through the following boundary value problem (BVP), which is defined by (1) and by the boundary conditions of Neumann and Dirichlet type. The boundary conditions are applied to the parts of macroscopic specimen boundary, in the following manner (for all $t \in]0, T[$):

- $u_1 = u_2 = 0, \quad u_3(t) = \bar{u}(t)t, \quad \boldsymbol{n} \cdot \boldsymbol{j}_\alpha = 0, \quad \boldsymbol{n} \cdot \boldsymbol{w} = 0$ on Γ_T,
- $\boldsymbol{u}(t) = \boldsymbol{0}, \quad \boldsymbol{n} \cdot \boldsymbol{j}_\alpha = 0, \quad \boldsymbol{n} \cdot \boldsymbol{w} = 0$ on Γ_B,
- $\boldsymbol{n} \cdot \boldsymbol{j}_\alpha = 0, \quad \boldsymbol{n} \cdot \boldsymbol{w} = 0, \quad \boldsymbol{n} \cdot \boldsymbol{\sigma}_s^p = 0$ on Γ_O,
- $P = \bar{P}, \quad \Phi_1 = \bar{\Phi}_1, \quad \Phi_2 = \bar{\Phi}_2, \quad \boldsymbol{n} \cdot \boldsymbol{\sigma}_s^p = 0$ on Γ_I,

where $\boldsymbol{\sigma}, \boldsymbol{w}$ and $\boldsymbol{j}_\alpha, \alpha = 1, 2$, are given by (2) and $\bar{u}(t) = 0.1t$. The prescribed values of boundary conditions are $\bar{P} = 1.0, \bar{\Phi}_1 = -0.01, \bar{\Phi}_2 = 0.01$.

Initial conditions are taken from the steady-state solution (i.e., for $t = 0$) of the macroscopic problem (1) with a set of boundary conditions given above. The numerical implementation of the homogenized model completed by suitable choice of initial and boundary conditions was made in python-based FEM software *SfePy*. Let us note that the macroscopic problem is solved in its dimensionless form. However, its results can be easily dimensionalized. Thus, all the following results are in dimensionalized form denoted by $\sqcup^{\text{eff}}$.

All the presented results are axially symmetric, which is the direct consequence of the circumferential orientation of the microstructure in the macroscopic specimen. Thus, Fig. 3 shows the distribution of macroscopic solution $(p^{\text{eff}}, \boldsymbol{u}^{\text{eff}}, \Phi_\alpha^{\text{eff}})$, $\alpha = 1, 2$, of BVP at $t = T$ along the radial axis that passes through the point A, see Fig. 2c.

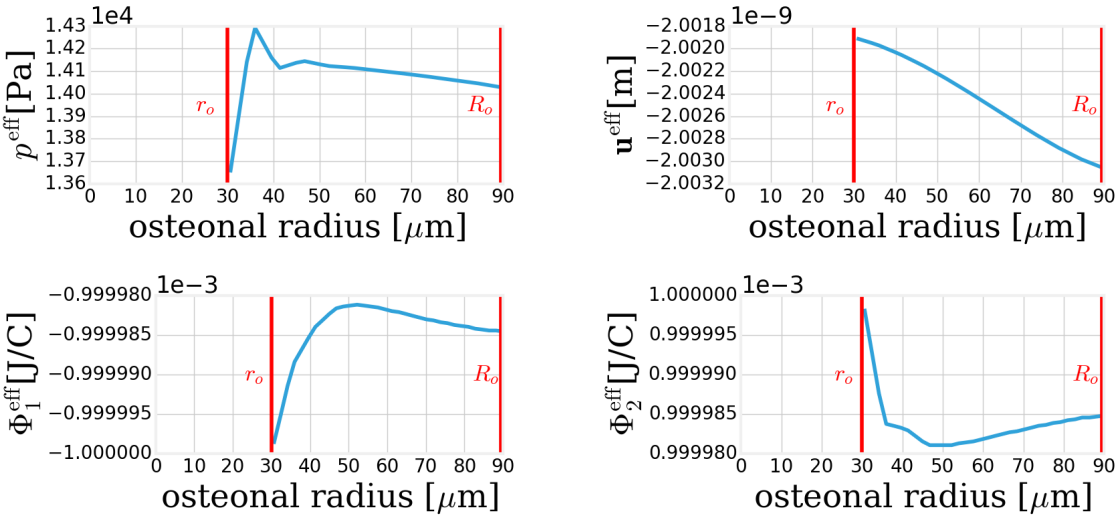

Fig. 3. BVP IV: Distribution of macroscopic fields $(p^{\text{eff}}, \boldsymbol{u}^{\text{eff}}, \Phi_\alpha^{\text{eff}})$, $\alpha = 1, 2$, at $t = T$ along the radial axis. The values of radius of HC r_o and radius of osteon R_0 are denoted by red vertical lines

The presented model computational model can be used not only for studying processes in the cortical bone but also for a wide range of other applications due to the derivation of equations in general dimensionless form. The chosen homogenization method also enables us to study the effect of the macroscopic fields on the microscale. This work is the extension of our previous research, so we refer to it for more details, [4].

Acknowledgements

The work was supported in part by the project GACR 19-04956S of the Scientific Foundation of the Czech Republic, by the European Regional Development Fund-Project "Application of Modern Technologies in Medicine and Industry" (No. CZ.02.1.01/0.0/0.0/17 048/0007280), and the project SGS-2019-002.

References

[1] Beno, T., Yoon, Y.J., Cowin, S.C., Fritton, S.P., Estimation of bone permeability using accurate microstructural measurements, Journal of biomechanics 39 (13) (2006) 2378-2387.

[2] Fukada, E., Yasuda, I., On the piezoelectric effect of bone, Journal of the Physical Society of Japan 12 (10) (1957) 1158-1162.

[3] Silva, C., Thomazini, D., Pinheiro, A., Aranha, N., Figueiro, S., Góes, J., Sombra, A., Collagen–hydroxyapatite films: Piezoelectric properties, Materials Science and Engineering: B 86 (3) (2001) 210-218.

[4] Turjanicová, J., Rohan, E., Lukeš, V., Homogenization based two-scale modelling of ionic transport in fluid saturated deformable porous media, Computers & Mathematics with Applications 78 (9) (2019) 3211-3235.

[5] Yoon, Y. J., Cowin, S. C., The estimated elastic constants for a single bone osteonal lamella, Biomechanics and Modeling in Mechanobiology 7 (1) (2008) 1-11.

COMPUTATIONAL MECHANICS 2021
36th conference with international participation
Srní
November 8 - 10, 2021

Aeroelastic response analysis of turboprop aircraft including effects of powerplant rotating mass

J. Čečrdle[a]

[a] Czech Aerospace Research Centre (VZLU), Beranových 130, 199 05 Praha Letňany, Czech Republic

Aeroelastic certification analyses of turboprop aircraft are required to take in account the dynamic and aerodynamic effects of rotating masses, such as a propeller or a gas turbine engine rotor. These effects are usually considered with respect to the aeroelastic stability (whirl flutter). Nevertheless, the mentioned effects also influence the dynamic behaviour of the structure with respect to the dynamic (aeroelastic) response, especially the response of engines. Contrary to flutter, the key issue is not a structural integrity, but the issues related to static strength or fatigue life of specific structural parts (e.g. engine suspension) as dynamic responses generate dynamic loads.

Physical principle is outlined on a simple mechanical system with two degrees of freedom. A flexible engine mounting is represented by two rotational springs of stiffnesses K_Ψ and K_Θ, as illustrated in Fig. 1.

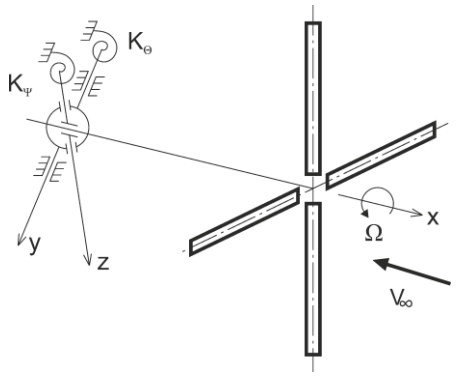

Fig. 1. Gyroscopic system with propeller

Such a system has two independent mode shapes (yaw and pitch) with angular frequencies ω_Ψ and ω_Θ. For a propeller rotation with angular velocity Ω, the gyroscopic effect causes both independent mode shapes to merge into a whirl motion. The axis of rotation of the propeller exhibits an elliptical movement. The orientation is backward relative to the propeller rotation for the mode with the lower frequency (backward whirl mode) and forward relative to the propeller rotation for the mode with the higher frequency (forward whirl mode). The gyroscopic motion results in changes in the propeller blades' angles of attack, consequently leading to unsteady aerodynamic forces. These forces may induce the instability. If the air velocity is lower than the critical speed, the system is stable, and the gyroscopic motion is damped (Fig. 2a). If the airspeed exceeds the critical speed, the system becomes unstable, and the gyroscopic motion is divergent (Fig. 2b).

Contrary to flutter, the right-hand side of aeroelastic response equations of motion is non-zero. Instead, frequency dependent loading is applied. Loading origin may be aerodynamic (gust, turbulence), dynamic (landing impact, store ejection, gun firing) or

combined (control surface deflection). Loading may be either in frequency domain (frequency response) or in the time domain (transient response). In both cases, the primary analysis is performed in the frequency domain. In the case of transient analysis, Fourier Transform Technique is employed to convert loads into the frequency domain and computed quantities are then converted back using Inverse Fourier Transform Technique. For both types of analysis, modal solution is employed.

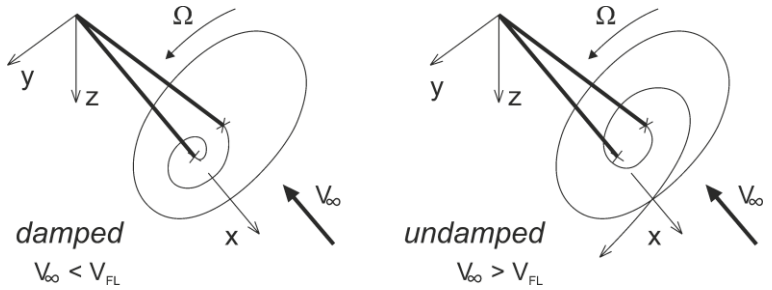

Fig. 2. Stable (a) and unstable (b) states of gyroscopic vibrations for the backward whirl mode

Matrix equation for the above-mentioned case with engine pitch and yaw modes become

$$\left[-\omega^2\left[M\right]+j\,\omega\left(\left[D\right]+\left[G\right]+qF_p\frac{D_p}{V}\left[D^A\right]\right)+\left(\left[K\right]+qF_pD_p\left[K^A\right]\right)\right]\left\{\begin{matrix}\overline{\Theta}\\ \overline{\Psi}\end{matrix}\right\}=\left\{P(\omega)\right\}\,, \qquad (1)$$

where left-hand side include mass matrix, structural damping matrix, structural stiffness matrix, gyroscopic matrix representing the dynamic effect of rotating mass, and finally aerodynamic damping and stiffness matrices representing the aerodynamic effect of rotating mass. Vector of modal deformation include generalised pitch and yaw angles. Right-hand side include frequency dependent load vector.

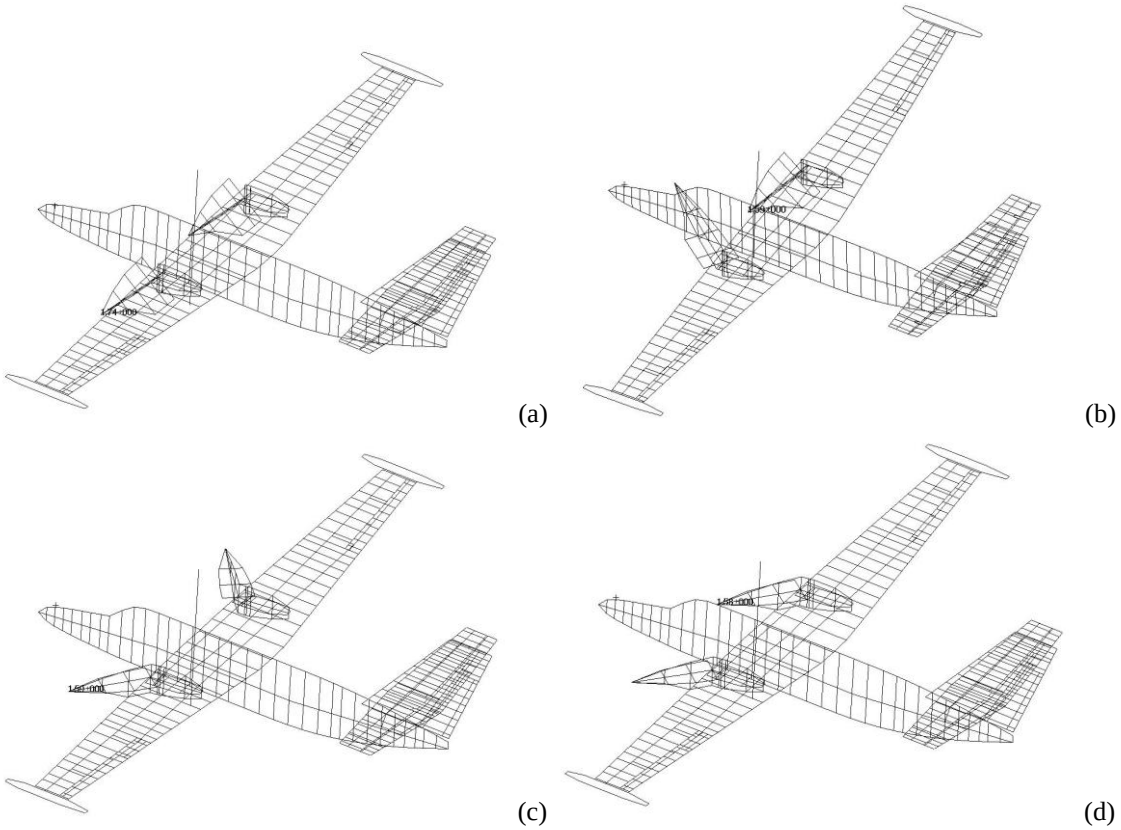

Fig. 3. Engines vibration mode shapes: (a) SΘ, (b) AΘ, (c) SΨ and (d) AΨ

Solution is based on a rigid propeller in a windmilling mode. Unsteady aerodynamic forces on a propeller are calculated by Strip Theory. Unsteady aerodynamic forces on a residual structure (wing and nacelles) are calculated by Wing Body Interference Theory.

Presented calculations represent analyses of a twin-engine turboprop aircraft for 19 passengers. Parameters of analyses were following: Flight altitude 4267 m, Mach number 0.493, damping ratio 0.02, flight velocities 100, 200 and 300 m/s, propellers rpm 2080. Both identical and inverse rotations of both propellers were considered. For the nominal stiffness of engines suspension, the engines show the following vibration modes: Symmetric pitch (SΘ) 8.14 Hz, antisymmetric pitch (AΘ) 9.89 Hz, symmetric yaw (SΨ) 10.43 Hz and antisymmetric yaw (AΨ) 12.21 Hz. These modes are shown in Fig. 3.

In the following examples, the displacement of the starboard engine front point is presented. First example demonstrates the frequency response to the harmonic force excitation applied to both engines. The airflow velocity was 100 m/s. Specific relations of forces were used to excite appropriate gyroscopic movement. Fig. 4 demonstrates the coupling of SΘ and AΨ modes. Fig. 4a shows the case with no propeller rotation in which two independent modes are present while Fig. 4a shows the case with CW-CW rotations of both propellers, in which both modes merge to the gyroscopic motion. Backward whirl mode has elliptical trajectory with dominating pitch deformation (T2) and the frequency is lower compare to the frequency of the uncoupled SΘ mode. Forward whirl mode has elliptical trajectory with dominating yaw deformation (T3) and the frequency is higher compare to the uncoupled AΨ mode. Similarly, Fig. 5 demonstrates the coupling of AΘ and AΨ modes. Fig. 5a shows the case with no propeller rotation in which two independent modes are present while Fig. 5a shows the case with CW-CCW rotations of both propellers, in which both modes merge to the gyroscopic motion. Backward whirl mode has elliptical trajectory with dominating pitch deformation and the frequency is lower compare to the frequency of the uncoupled AΘ mode. Forward whirl mode has elliptical trajectory with dominating yaw deformation and the frequency is higher compare to the uncoupled AΨ mode.

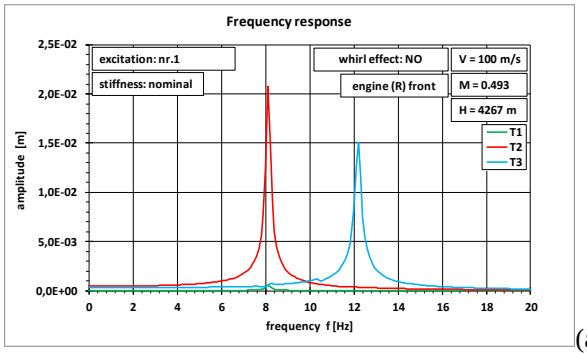

(a)

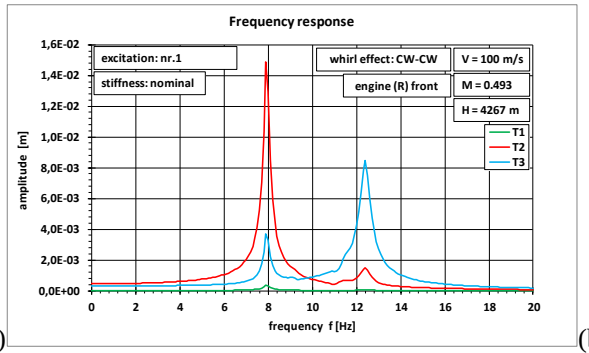

(b)

Fig. 4. Frequency response, V = 100 m/s, starboard engine front point, excited modes: SΘ, AΨ. Propellers rotation (a) no, (b) CW-CW

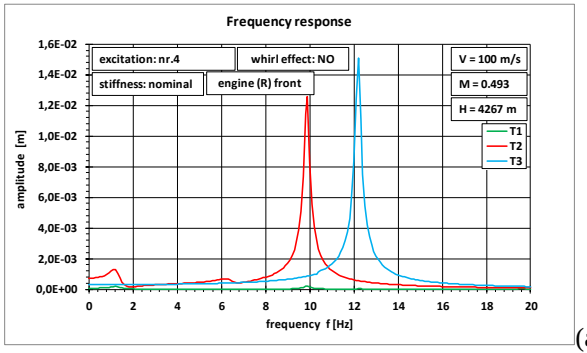

(a)

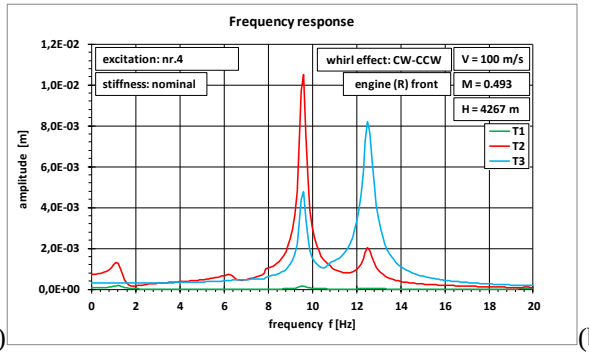

(b)

Fig. 5. Frequency response, V = 100 m/s, starboard engine front point, excited modes: AΘ, AΨ. Propellers rotation (a) no, (b) CW-CCW

The second example demonstrates the transient response to the landing impact at the velocity of 50 m/s. The excitation is realised as enforced displacement obtained from the main landing gear drop test. Fig. 6a shows the case with no propeller rotation. Fig. 6b then demonstrates the comparison of pitch displacement (T2) of the cases with no rotation, CW-CW rotation and CW-CCW rotation. Increase in damping as well as decrease in frequency can be found for both cases including rotation compare to the no rotation case.

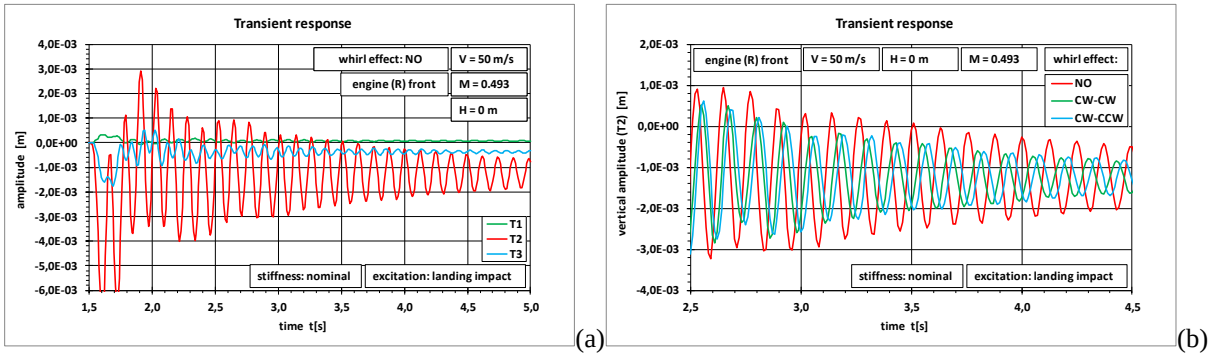

(a) (b)

Fig. 6. Transient response, V = 50 m/s, starboard engine front point, landing impact excitation. (a) no propellers rotation, (b) pitch displacement (T2), comparison

The last example demonstrates the transient response to the delta impulse applied at the centre of gravity. The airflow velocity was 200 m/s. Reduced stiffness was applied to demonstrate the state of neutral stability in this example. Fig. 7a shows the response for the case with no propeller rotation in which the response is damped and both pitch (T2) and yaw (T3) deformations are independent and frequencies of pitch and yaw vibrations are diverse. Fig. 7b shows the case with CW-CW rotation in which the response is (almost) harmonic and the damping of the system is (almost) zero showing the state of the neutral stability. Also, the change in the frequency and coupling of both pitch and yaw deformations (phase shift) can be found compare to the no rotation case.

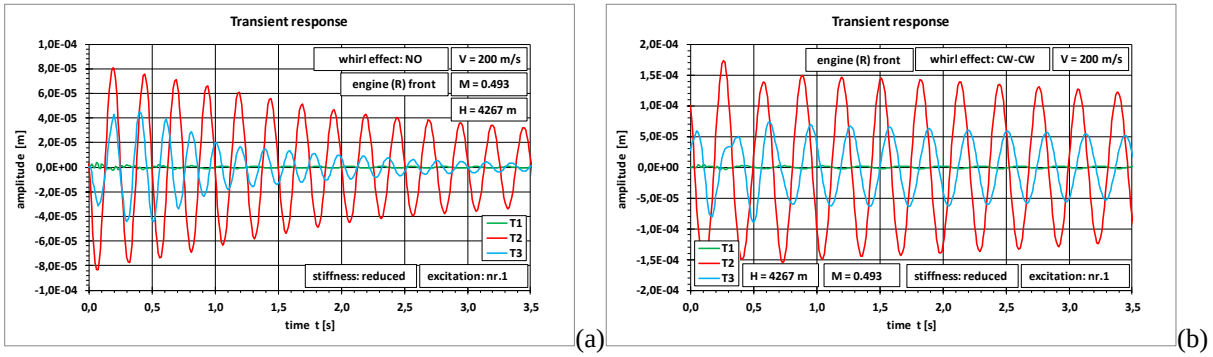

(a) (b)

Fig. 7. Transient response, V = 200 m/s, starboard engine front point, delta impulse excitation. Propellers rotation (a) no, (b) CW-CW

References

[1] Čečrdle, J., Whirl flutter of turboprop aircraft structures, Elsevier Science, Oxford, 2015.

[2] Giessing, J.P., Kalman, T.P., Rodden, W.P., Subsonic steady and oscillatory aerodynamics for multiple interfering wings and bodies, Journal of Aircraft 9 (1972) 693-702.

[3] Rodden, W.P., Bellinger, E.D., Aerodynamic lag functions, divergence, and the British flutter method, Journal of Aircraft 19 (1982) 596-598.

[4] Theodorsen, T., General theory of aerodynamic instability and the mechanism of flutter, NACA Report 496, 1935.

COMPUTATIONAL MECHANICS 2021
36th conference with international participation
Srní
November 8 - 10, 2021

Conveyor belts - predictive maintenance

M. Čermák

Deloitte Czech Republic, Italská 67, 120 00 Praha, Czech Republic

Conveyor belts and their maintenance make a significant cost item in the sectors of mineral extraction and processing and energy. Deloitte, thanks to a combination of industrial maintenance expertise and an advanced data analytics team, has developed a unique solution in the field of predictive maintenance of conveyor belts. The solution was verified by a pilot project.

For the purposes of the pilot project, we identified a belt conveyor of our client, which on the one hand lies on the critical supply route of key raw material and its performance is not backed up. In the event of its failure, it is therefore a major reduction in the production of the entire company. As part of the pilot project, we used the data from the installed “Schenck” belt weigher, as well as the measurement of the current load of the drive in the client's substation, and we carried out the data transmission using IoT SigFox.

The principle of the solution is an online monitoring and continuous evaluation of the dependence of two basic parameters of conveyor belts, which are, on the one hand, the aggregate weight of the transported raw material and also the instantaneous current load of the belt conveyor drive.

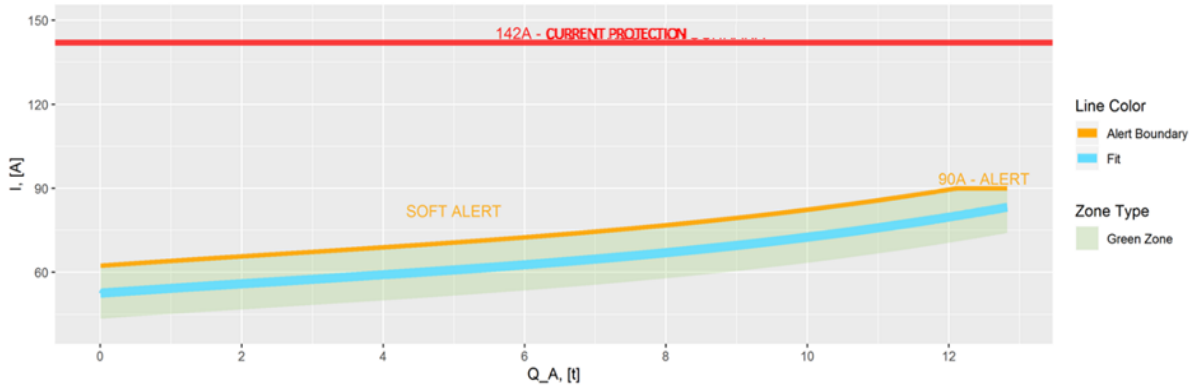

Fig. 1. Dependence of the current load on the aggregate weight

Fig. 1 shows the optimal dependence (blue) of the weight of the transported material and the current load. The green field includes 99% of the measured values during the weekly operation of the belt in optimal condition. The yellow curve represents the limit of optimal operation. Crossing the yellow border indicates an anomaly that will lead to failure.

The principle of the solution is that the system is able to identify and alert the operator to a non-standard development of the independence of the current load on the aggregate weight of the transported raw material before damage to the belt or steel structure of the conveyor or backfill occur or, as the case may be, before the conveyor is shut down by the intervention of current protection.

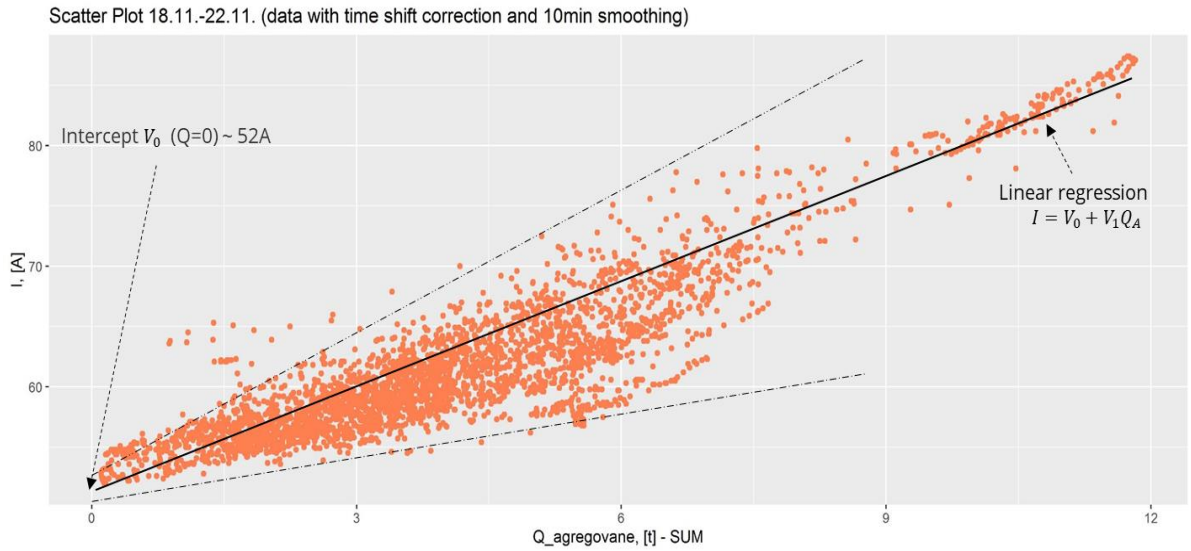

Fig. 2. Intercept and slope - theory

In addition to the basic dependence between the aggregated mass, it is appropriate to observe the intercept - ie the place where the linear regression line intersects the y-axis and also the slope - ie the slope of the linear regression line, see Fig. 2.

Fig. 3. Intercept and slope in a robust linear model estimated within a four-hour sliding window

The graphs in Fig. 3 show the results of monitoring the intercept and slope of linear regression of the aggregate mass and current load - linear regression in a 4-hour sliding window. Both quantities show a relatively high correlation rate - 66%. The marked places correlate with the detected damage to the belt conveyor.

The solution benefit is the estimated savings in maintenance costs in the following areas:

- Rollers and cylinders - longer service life - approx. 20-40%
- Conveyor belt - approx. 40-60%
- Steel structure, slips, shifters, side guides and wiper blades – approx. 30-50%
- Drive, transmission - about 20%

Another, no less significant effect is the possibility of reducing the frequency of preventive inspections, which leads to FTE savings, and the advantage is also the elimination of unplanned conveyor outages.

COMPUTATIONAL MECHANICS 2021
36th conference with international participation
Srní
November 8 - 10, 2021

Assessment of Python tensor contraction packages in the context of finite element evaluations

R. Cimrman[a,b]

[a] New Technologies Research Centre, University of West Bohemia, Univerzitní 8, 306 14 Plzeň, Czech Republic
[b] Faculty of Applied Sciences, University of West Bohemia, Univerzitní 8, 306 14 Plzeň, Czech Republic

Fast evaluation of the weak formulation integral forms in finite element calculations is of crucial importance, especially when using a higher order approximation of the unknown and test fields. The integral forms are usually evaluated using nested loops over elements, and over quadrature points. Many such forms (e.g. all linear or multi-linear) can be written using a single tensor contraction expression using the Einstein summation convention. This convention, abbreviated as *einsum* in the following text according to the eponymous function of NumPy [7], allows a concise ways of writing tensor expressions.

Unlike large tensor networks in machine learning or quantum physics calculations, see e.g. [5, 11], the einsum expressions in the FE context consist usually of only several tensors and the contractions have low numerical intensity. This complicates use of modern computer architectures and is subject to an ongoing research [13]. Nevertheless, einsums are successfully used, for example, in the pure finite element package scikit-fem [6].

In the contribution we will comment on our recent results published in [2], where we assess several Python scientific computing packages implementing optimized tensor contractions. The tested packages are

- NumPy [7], with the basic implementation and some optimizations from opt_einsum;
- opt_einsum [12], with state-of-the-art contraction optimization strategies;
- Dask [4], which allows parallel out-of-core calculations with very large data.
- JAX [1], with JIT compilation[1] and possible parallel execution or automatic GPU transfer.

In [2] we proposed a simple "weak form to einsum" transpiler[2] from generalized einsum-like expressions (see Table 1). The transpiler allows simple definitions of multi-linear finite element weak forms as evidenced in Table 2. It supports several einsum evaluation backends implemented using the packages listed above, arbitrary memory layout of operands, easy automatic differentiation due to (multi-)linearity of the considered weak forms and various evaluation modes.

The transpiler based weak forms are available in SfePy from version 2021.1, allowing a rapid prototyping of multi-physical finite element models and subsequent calculations in diverse fields such as biomechanics of liver [10] or solid state physics [9]. All data used in [2] are available online [3].

[1] JIT compilation = Just in time compilation.

[2] A transpiler translates input in a language to another language that works at approximately the same level of abstraction, unlike a traditional compiler that translates from a higher level programming language to a lower level programming language.

Table 1. The generalized einsum-like notation

symbol	meaning	example
`0`	scalar	p
`i`	i-th vector component	u_i
`i.j`	gradient: derivative of i-th vector component w.r.t. j-th coordinate component	$\frac{\partial u_i}{\partial x_j}$
`i:j`	symmetric gradient	$\frac{1}{2}(\frac{\partial u_i}{\partial x_j} + \frac{\partial u_j}{\partial x_i})$
`s(i:j)->I`	vector storage of symmetric second order tensor, I is the vector component	Cauchy strain tensor $e_{ij}(\underline{u})$

Table 2. Examples of multi-linear weak form definitions

description	definition	weak form expression
vector dot product	`('i,i', v, u)`	$\int_T v_i u_i$
weighted vector dot product	`('ij,i,j', M, v, u)`	$\int_T v_i M_{ij} u_j$
weak Laplacian	`('0.i,0.i', v, u)`	$\int_T \frac{\partial v}{\partial x_i} \cdot \frac{\partial u}{\partial x_i}$
Navier-Stokes convection	`('i,i.j,j', v, u, u)`	$\int_T v_i \frac{\partial u_i}{\partial x_j} u_j$
Stokes coupling	`('i.i,0', v, p)`	$\int_T \frac{\partial v_i}{\partial x_i} p$
transposed Stokes coupling	`('i.i,0', u, q)`	$\int_T q \frac{\partial u_i}{\partial x_i}$
divergence operator	`('i.i', v)`	$\int_T \frac{\partial v_i}{\partial x_i}$
linear elasticity	`('IK,s(i:j)->I,s(k:l)->K', D, v, u)`	$\int_T D_{ijkl}\, e_{ij}(\underline{v}) e_{kl}(\underline{u})$
Cauchy stress	`('IK,s(k:l)->K', D, u)`	$D_{ijkl}\, e_{kl}(\underline{u})$

The calculation speed and memory requirements of the transpiled weak forms, in comparison with the original C implementation of those forms as available in SfePy, will be presented. To provide a broader context, the serial performance of the reference SfePy implementation will be also compared to the finite element framework FEniCS [8].

Acknowledgement

The work was supported from European Regional Development Fund — Project "Application of Modern Technologies in Medicine and Industry" (No. CZ.02.1.01/0.0/0.0/17_048/0007280).

References

[1] Bradbury, J., Frostig, R., et al., JAX: Composable transformations of Python+NumPy programs, https://github.com/google/jax, 2021. Ver. 0.2.9

[2] Cimrman, R., Fast evaluation of finite element weak forms using python tensor contraction packages, Advances in Engineering Software 159 (2021) No. 103033.

[3] Cimrman, R., Performance measurements of Python tensor contraction packages in the finite element context, Data set, Zenodo, 2021, doi: 10.5281/zenodo.4750560.

[4] Dask Development Team, Dask: Library for dynamic task scheduling, 2016.

[5] Gray, J., Kourtis, S., Hyper-optimized tensor network contraction, Quantum 5 (2021) No. 410.

[6] Gustafsson, T., McBain, G., Scikit-fem: A Python package for finite element assembly, Journal of Open Source Software 5 (52) (2020) No. 2369.

[7] Harris, C. R., Millman, K. J., et al., Array programming with NumPy, Nature 585 (7825) (2020) 357-362.

[8] Logg, A., Mardal, K. A., Wells, G. (editors), Automated solution of differential equations by the finite element method: The FEniCS book, Lecture Notes in Computational Science and Engineering, Berlin Heidelberg, Springer-Verlag, 2012.

[9] Novák, M., Vackář, J., Cimrman, R., Evaluating Hellmann–Feynman forces within non-local pseudopotentials, Computer Physics Communications 250 (2020) No. 107034.

[10] Rohan, E., Turjanicová, J., Lukeš, V., Multiscale modelling and simulations of tissue perfusion using the Biot-Darcy-Brinkman model, Computers & Structures 251 (2021) No. 106404.

[11] Schindler, F., Jermyn, A. S., Algorithms for tensor network contraction ordering, Machine Learning: Science and Technology 1 (3) (2020) No. 035001.

[12] Smith, D. G. A., Gray, J., opt_einsum – a python package for optimizing contraction order for einsum-like expressions, Journal of Open Source Software 3 (26) (2018) No. 753.

[13] Świrydowicz, K., Chalmers, N., et al., Acceleration of tensor-product operations for high-order finite element methods, The International Journal of High Performance Computing Applications 33 (4) (2019) 735-757.

COMPUTATIONAL MECHANICS 2021
36th conference with international participation
Srní
November 8 - 10, 2021

Investigation of critical rotor revolution in rotating space

J. Dupal[a]

[a] *Faculty of Applied Sciences, University of West Bohemia in Pilsen, Univerzitní 8, 301 00 Plzeň, Czech Republic*

1. Introduction

The rotating space can be advantageously used for modelling rotating structures as e.g. rotors, turbine blades etc. This approach can be very useful especially in case of rotors having isotropic bearings and non-symmetrical cross sections. In such case result of modelling is time independent mathematical model with constant matrices of stiffness, mass, membrane and gyroscopic forces. It suggests itself a question what is the meaning of complex eigenvalues and mode shapes obtained from model corresponding to rotating space and how can be these quantities used for determining of critical angular rotor speed.

2. Mathematical model

As a starting point of modelling we can use expression of kinetic and potential energy to create conservative mathematical model of the rotor with circular cross section. According to

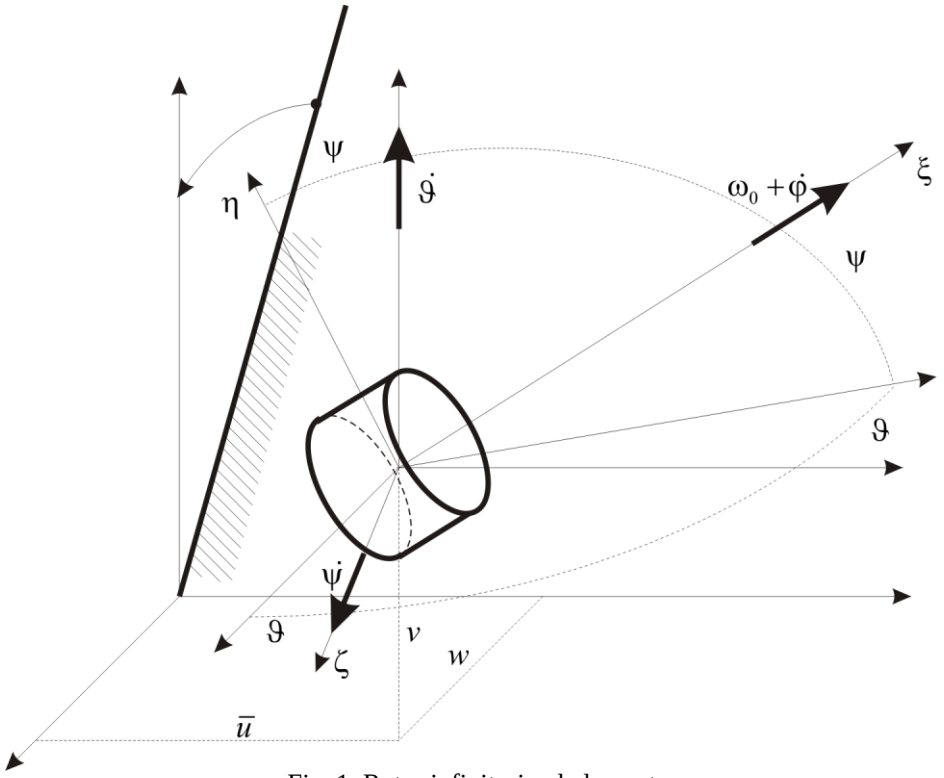

Fig. 1. Rotor infinitesimal element

Fig. 1, we can express displacement and velocity vectors of the gravity centre of an infinitesimal element in form

$$\mathbf{u}_S = \begin{bmatrix} \bar{u} \\ v \\ w \end{bmatrix}, \quad \mathbf{v}_S = \dot{\mathbf{u}}_S = \left.\frac{d\mathbf{u}_S}{dt}\right|_{\xi\eta\zeta} + \boldsymbol{\omega} \times \mathbf{u}_S \doteq \begin{bmatrix} \dot{\bar{u}} \\ \dot{v} - \omega w \\ \dot{w} + \omega v \end{bmatrix}, \tag{1}$$

where

$$\boldsymbol{\omega} = \begin{bmatrix} \dot{\varphi} + \omega + \dot{\vartheta}\psi \\ \dot{\vartheta} \\ \dot{\psi} \end{bmatrix}, \quad f^{\backslash} = \frac{\partial f}{\partial \xi}, \quad \dot{f} = \frac{\partial f}{\partial t}. \tag{2}$$

Vector $\boldsymbol{\omega}$ expresses resulting angular velocity of the infinitesimal element. Using FEM for modelling we can take these common used functions for displacement approximations

$$v(\xi) = \boldsymbol{\Phi}(\xi)\mathbf{S}_1^{-1}\mathbf{q}_1, \quad \psi(\xi) = \frac{\partial v}{\partial \xi} = \boldsymbol{\Phi}^{\backslash}(\xi)\mathbf{S}_1^{-1}\mathbf{q}_1, \; \bar{u}(\xi) = \boldsymbol{\Psi}(\xi)\,\mathbf{S}_3^{-1}\mathbf{q}_3, \quad \varphi(\xi) = \boldsymbol{\Psi}(\xi)\mathbf{S}_3^{-1}\mathbf{q}_4,$$

$$w(\xi) = \boldsymbol{\Phi}(\xi)\mathbf{S}_1^{-1}\mathbf{P}\mathbf{q}_2, \; \vartheta(\xi) = -\frac{\partial w}{\partial \xi} = -\boldsymbol{\Phi}^{\backslash}(\xi)\mathbf{S}_1^{-1}\mathbf{P}\mathbf{q}_2, \tag{3}$$

where

$$\mathbf{S}_1 = \begin{bmatrix} 1 & 0 & 0 & 0 \\ 0 & 1 & 0 & 0 \\ 1 & l & l^2 & l^3 \\ 0 & 1 & 2l & 3l^2 \end{bmatrix}, \quad \mathbf{P} = diag\{1, \; -1, \; 1, \; -1\} \Rightarrow \mathbf{P}^{-1} = \mathbf{P},$$

$$\boldsymbol{\Phi}(\xi) = \left[1, \; \xi, \; \xi^2, \; \xi^3\right], \; \boldsymbol{\Psi}(\xi) = \left[1, \; \xi\right],$$

$$\mathbf{q}_1 = \left[v_1, \; \psi_1, \; v_2, \; \psi_2\right]^T, \; \mathbf{q}_2 = \left[w_1, \; \vartheta_1, \; w_2, \; \vartheta_2\right]^T, \; \mathbf{q}_3 = \left[\bar{u}_1, \; \bar{u}_2\right]^T, \; \mathbf{q}_4 = \left[\varphi_1, \; \varphi_2\right]^T.$$

Respecting foregoing relations and Fig. 1 we can express kinetic and potential energy of one finite rotor element by means of rotatory system coordinates in form

$$E_K = \frac{1}{2}\int_0^l \rho A \mathbf{v}_S^T \mathbf{v}_S d\xi + \frac{1}{2}\int_0^l \rho\, \boldsymbol{\omega}^T \mathbf{J} \boldsymbol{\omega}\; d\xi, \quad \mathbf{J} = diag\left\{J_o, \frac{1}{2}J_o, \frac{1}{2}J_o\right\}. \tag{4}$$

Respecting (1) and (2) we can come to

$$\begin{aligned} E_K = {} & \frac{1}{2}\int_0^l \rho A\left(\dot{\bar{u}}^2 + \dot{v}^2 - 2\omega\dot{v}w + \omega^2 w^2 + \dot{w}^2 + 2\omega\dot{w}v + \omega^2 v^2\right)d\xi + \\ & + \frac{1}{2}\int_0^l \rho J_o\left(\dot{\varphi}^2 + \omega^2 + \underline{\dot{\vartheta}^2\psi^2 + 2\dot{\varphi}\omega + 2\dot{\varphi}\dot{\psi}\psi} + 2\omega\dot{\vartheta}\psi + \frac{1}{2}\dot{\vartheta}^2 + \frac{1}{2}\dot{\psi}^2\right)d\xi. \end{aligned} \tag{5}$$

The highlighted terms can be left out. J_o, ρ, A is cross section polar moment of inertia, density and cross section area, respectively. To express finite element potential energy of deformation we take into account displacement and strains of arbitrary point

$$u(\xi,\eta,\zeta) = \bar{u}(\xi) - \eta\psi(\xi) + \zeta\vartheta(\xi) = \bar{u}(\xi) - \eta v^{\backslash}(\xi) - \zeta w^{\backslash}(\xi), \tag{6}$$

$$\varepsilon(\xi,\eta,\zeta) = \frac{\partial u(\xi,\eta,\zeta)}{\partial \xi} = \bar{u}^{\backslash}(\xi) - \eta v^{\backslash\backslash}(\xi) - \zeta w^{\backslash\backslash}(\xi), \; \gamma(\xi,r) = r\varphi^{\backslash}(\xi) = \sqrt{\eta^2 + \zeta^2}\,\varphi^{\backslash}(\xi), \tag{7}$$

$$E_{Pd} = \frac{1}{2}\int_0^l \iint_A \boldsymbol{\varepsilon}^T \mathbf{E}\,\boldsymbol{\varepsilon}\, dA\, d\xi,\ \boldsymbol{\varepsilon} = \begin{bmatrix} \varepsilon \\ \gamma \end{bmatrix},\ \mathbf{E} = \begin{bmatrix} E & 0 \\ 0 & G \end{bmatrix}. \tag{8}$$

Substituting approximation relations (3) and applying Lagrange's equation we can come to coefficient matrices of one finite element [1-2]. Assembling individual finite element matrices into global ones we obtain equation of motion of the whole rotor in form

$$\mathbf{M}\ddot{\mathbf{q}}(t) + (\mathbf{B} + \omega\mathbf{G})\dot{\mathbf{q}}(t) + (\mathbf{K} + \omega^2\mathbf{K}_D)\mathbf{q}(t) = \mathbf{0}, \tag{9}$$

where $\mathbf{M}, \mathbf{B}, \omega\mathbf{G}, \mathbf{K}, \omega^2\mathbf{K}_D$ mark matrix of mass, damping, gyroscopic forces, stiffness and membrane forces, respectively.

3. Critical angular speed investigation

Let us remind meaning of Campbell diagram. It is dependence of imaginary parts of eigenvalues on angular rotor speed (revolution). Let us say what is it critical rotor speed (in stationary coordinate space). It is such revolution, which are equal to imaginary part of some eigenvalue. It means that critical speed corresponds to intersection of quadrant axis with imaginary part of some eigenvalue dependence on revolution. It can be written down $\mathrm{Im}\{\lambda_i(\omega)\} = \omega$. Corresponding mode shape is complex vector which can be animated as bending curve rotating about rotor axis by angular speed ω (forward whirl-FW-increasing branch of dependence) or $-\omega$ (backward whirl-BW-decreasing branch of dependence). What does it mean in rotating space by ω? This mean that bending curve is standing ($\omega = 0$) for FW and rotating by -2ω for BW. For the reason of symmetricity of Campbell diagram about the axis $\mathrm{Im}\{\lambda_i(\omega)\} = 0$ we will seek intersection of decreasing branch of $\mathrm{Im}\{\lambda_i(\omega)\}$ with straight line $\mathrm{Im}\{\lambda_i(\omega)\} = 0$ (FW) and increasing branch with straight line $\mathrm{Im}\{\lambda_i(\omega)\} = 2\omega$. It can be shown by means of simple example. Let us find critical speed of very simple rotor modelled by means of FEM in stationary and rotatory spaces and depicted in Fig. 2.

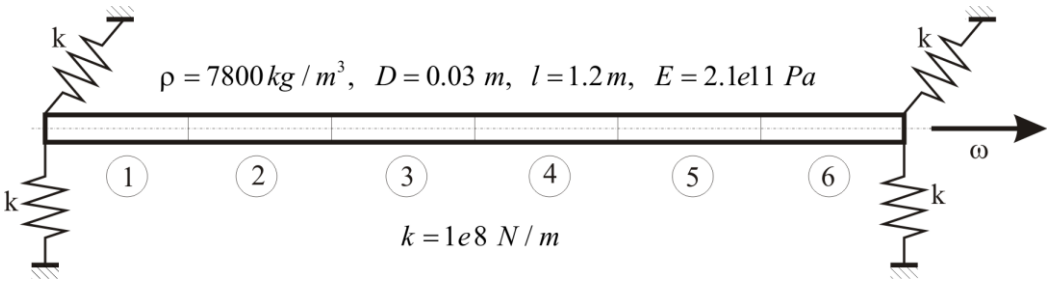

Fig. 2. Subdivision of rotor to finite elements

Campbell diagram of the rotor modelled in stationary coordinate system with zoom is depicted in Fig. 3. The following Fig. 4 presents Campbell diagram of the rotor modelled in rotatory coordinate system.

The critical speeds (intersections in Fig. 4) can be found by means of iteration rules

$$\omega_i^{(r)} = \frac{1}{2}\left|\mathrm{Im}\left\{\lambda_i^{(r-1)}\right\}\right|, \quad \text{(backward whirl)} \tag{10}$$

$$\omega_i^{(r)} = \omega_i^{(r-1)} + \mathrm{Im}\left\{\lambda_i^{(r-1)}\right\}, \quad \text{e.g.} \quad \omega_i^{(0)} = 10\ rad/s. \quad \text{(forward whirl)} \tag{11}$$

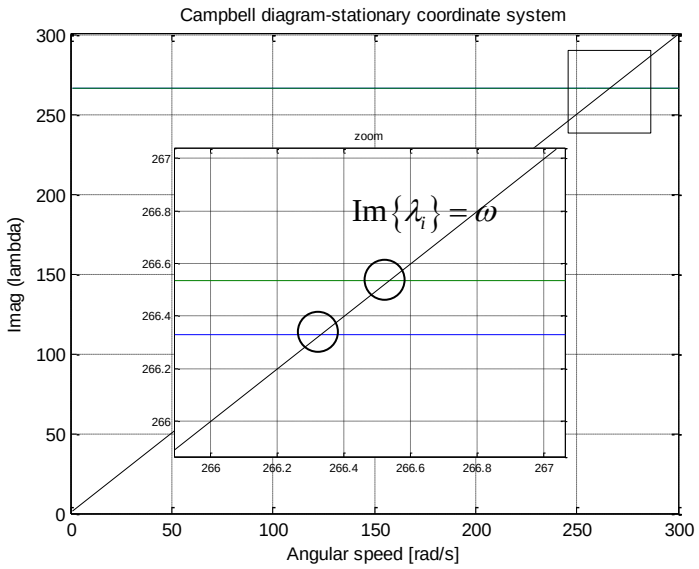

Fig. 3. Campbell diagram for rotor model in stationary coordinate system

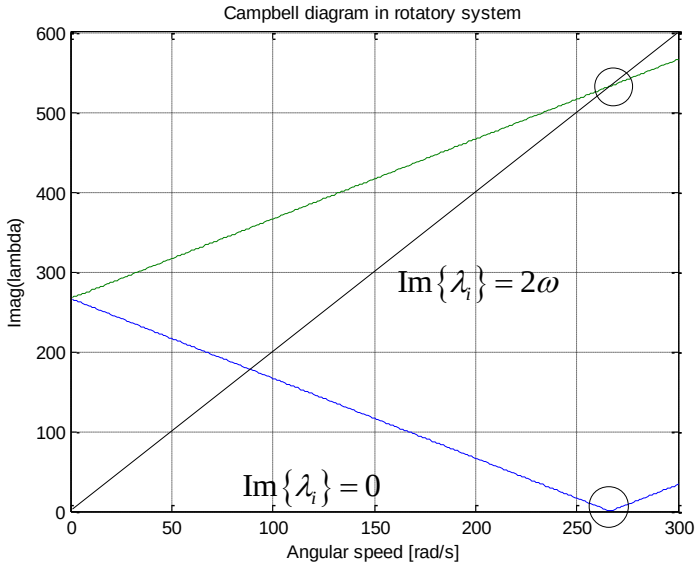

Fig. 4. Campbell diagram for rotor model in rotatory coordinate system

4. Conclusion

The relation (10) and (11) need not be convergent in some cases because imaginary parts of some eigenvalues can change its order in the iteration process. For this reason, the recommendation of the paper author is use Campbell diagram and zoom of the intersections.

References

[1] Byrtus, M., Hajžman, M., Zeman, V., Dynamics of rotating systems, University of West Bohemia in Pilsen, 2010. (in Czech)
[2] Dupal, J., Computational methods of mechanics, University of West Bohemia in Pilsen, 1999. (in Czech)

COMPUTATIONAL MECHANICS 2021
36th conference with international participation
Srní
November 8 - 10, 2021

In-silico study of flow-mediated thrombosis in portal vein reconstructions

V. Dušková[a], A. Jonášová[a], S. Plánička[a], J. Vimmr[a]

[a] *Faculty of Applied Sciences, University of West Bohemia, Univerzitní 8, 301 00 Plzeň, Czech Republic*

Surgical treatment of advanced pancreatic cancer is often accompanied by removal and consequent replacement of adjacent portal vein segments infiltrated by tumour cells. In accordance with the general consensus in vascular surgery, harvested autografts are recognised as the best grafting material, which, unfortunately, is not always available or of adequate quality. Thus, finding a clinically reliable alternative to this type of grafts has become one of the main tasks within the medical community and as such led to various experimental and clinical studies. Notable in this regard is the recent experimental study by Pálek et al. [3] that explored the possible use of various allogeneic venous grafts in portal vein reconstructions of pig models, Fig. 1.

According to the observations made in the study, some types of implanted allografts showed susceptibility to thrombotic events resulting in graft occlusions and failures. Because the occurrence of these events could not be explained by technical errors of the performing surgeon, it was hypothesised that they are of hemodynamic origin and as such induced by the altered vessel geometry. Although the following computational analysis of the hemodynamic environment could explain some of the observed tendency to form blood clots [3], it showed that the problem is of much more complex origin than initially thought, thus, triggering the need for a more in-depth study.

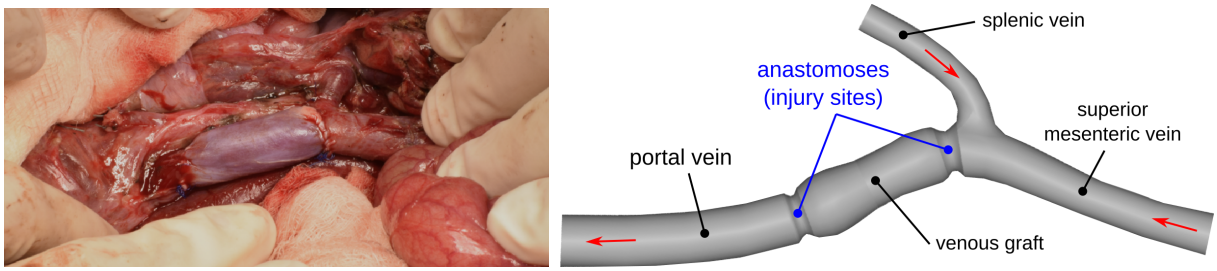

Fig. 1. Porcine portal vein reconstruction (*left*) and its computational counterpart (*right*)

The present work brings the first results of this study, whose aim was to provide an in-silico insight into the post-surgical development of intravascular thrombosis in portal vein reconstructions, particularly in relation to several key factors. These factors were selected to reflect the relationship between the blood clot growth and the direct and indirect stimuli such as the trigger level or injury extent. For the intended simulations of flow-mediated thrombosis, a special computational model was proposed in the form of three interlinked submodels (Fig. 2), each representing a process crucial for the in-vivo formation of a stable blood clot. In other words, compared to other similar studies, which were mainly limited to the modelling of the generally accepted blood clotting mechanism (haemocoagulation), the present mathematical model

also recognises the need for the formation of a platelet plug as a primary thrombus [2, 5] and introduces a moment-based submodel governing the polymerisation and cross-linking of fibrin monomers up to the formation of a secondary thrombus [1, 4]. Because of the overall model complexity and the need for a robust CFD solver to ensure the two-way interaction between the growing blood clot and portal haemodynamics, the proposed model of thrombosis was implemented and numerically solved in the Ansys Fluent software by means of user-defined functions (UDFs) written in the C programming language.

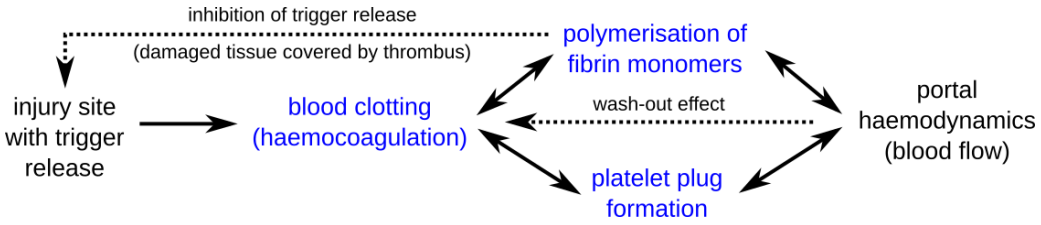

Fig. 2. Submodels of the thrombosis model (in blue) and their interaction with the vessel environment

The numerical results obtained for various scenarios (normal/elevated trigger levels, injury position etc.) allowed for several interesting observations. Particularly notable in this regard is the key role of platelets during the initial phase of clot formation, which is demonstrated by the results shown in Fig. 3. The left set of pictures corresponds to a thrombosis model without the inclusion of platelets (formation of a pure fibrin clot), whereas the right set was obtained for a complete model as listed in Fig. 2. Aside from the significantly dissimilar thrombus shapes in both scenarios, it should be pointed out that the presence of platelets, particularly the bound ones at injury sites, allowed for simulations of much higher blood flow velocity than when these blood cells were completely omitted (compare velocity ranges in Fig. 3). Note that this behaviour is in full agreement with experimental observations [2] due to the fact that high velocity haemodynamics tends to significantly dilute the concentration of activated coagulation

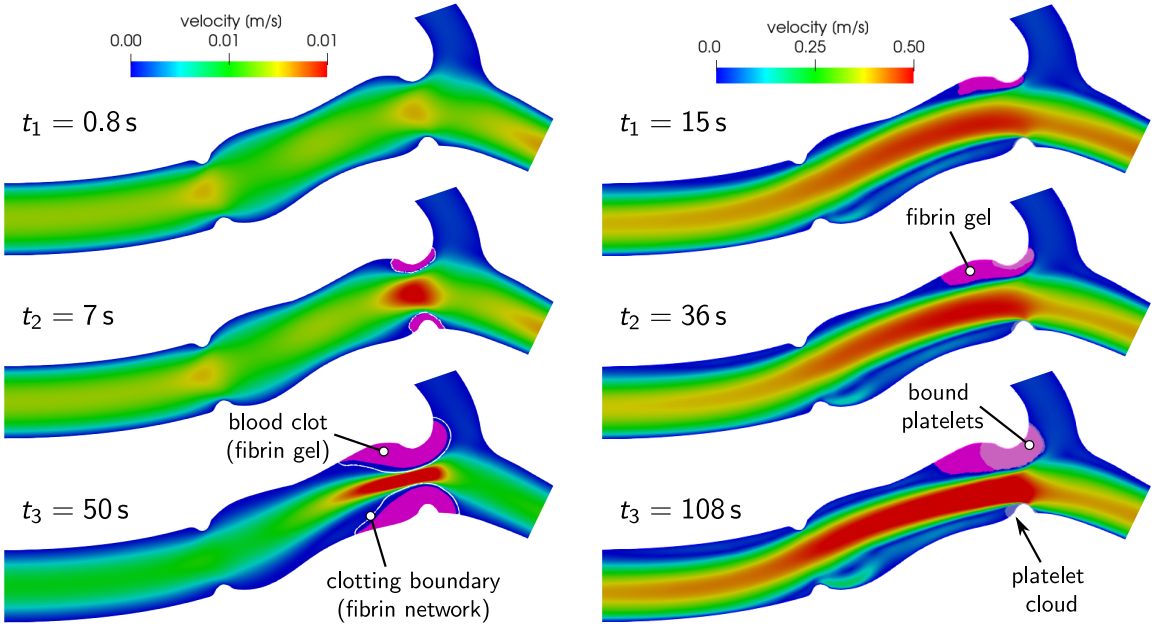

Fig. 3. Blood clot formation within the flow field of a portal vein reconstruction with the coagulation trigger located at the upstream anastomosis – (*left*) model without platelets, (*right*) complete model

factors (the so-called "wash-out effect"). In other words, the blood clotting mechanism requiring chemical species of certain concentration cannot be started properly, requiring so a drastic decrease in blood flow velocity in order to be able to observe the formation of a fibrin clot.

Acknowledgements

The study was supported by the European Regional Development Fund-Project "Application of Modern Technologies in Medicine and Industry" (No. CZ.02.1.01/0.0/0.0/17_048/0007280). Computational resources were supplied by the project "e-Infrastruktura CZ" (e-INFRA CZ ID:90140) supported by the Ministry of Education, Youth and Sports of the Czech Republic.

References

[1] Guria, G. T., Herrero, M. A., Zlobina, K. E., A mathematical model of blood coagulation induced by activation sources, Discrete & Continuous Dynamical Systems 25 (1) (2009) 175-194.

[2] Link, K. G., Sorrells, M. G., Danes, N. A., Neeves, K. B., Leiderman, K., Fogelson, A. L., A mathematical model of platelet aggregation in an extravascular injury under flow, Multiscale Modeling & Simulation 18 (4) (2020) 1489-1524.

[3] Pálek, R., Jonášová, A., Rosendorf, J., Mik, P., Bajcurová, K., Hošek, P., Moulisová, V., Eberlová, L., Haidingerová, L., Brzoň, O., Bednář, L., Kříž, T., Dolanský, M., Třreška, V., Tonar, Z., Vimmr, J., Liška, V., Allogeneic venous grafts of different origin used for portal vein reconstruction after pancreaticoduodenectomy – Experimental study, Anticancer Research 39 (12) (2019) 6603-6620.

[4] Rukhlenko, O. S., Dudchenko, O. A., Zlobina, K. E., Guria, G. T., Mathematical modeling of intravascular blood coagulation under wall shear stress, PLOS One 10 (7) (2015) No. e0134028. https://doi.org/10.1371/journal.pone.0134028

[5] Seo, J. H., Abd, T., George, R. T., Mittal, R. A coupled chemo-fluidic computational model for thrombogenesis in infarcted left ventricles, American Journal of Physiology-Heart and Circulatory Physiology 310 (11) (2016) H1567-H1582.

COMPUTATIONAL MECHANICS 2021
36th conference with international participation
Srní
November 8 - 10, 2021

Frequency lock-in phenomenon in structures with aeroelastic couplings

Š. Dyk[a], M. Byrtus[a,b]

[a] NTIS, Faculty of Applied Sciences, University of West Bohemia, Univerzitní 8, 301 00 Plzeň, Czech Republic
[b] Department of Mechanics, Faculty of Applied Sciences, University of West Bohemia, Univerzitní 8, 301 00 Plzeň, Czech Republic

Flexible structures exposed to the airflow can induce so-called *fluid-structure interaction* (FSI) – a complex process that needs highly sophisticated computational approaches to be dealt with. In some cases, shedding vortices can produce a phenomenon called *vortex-induced vibrations* (VIV). Moreover, if vortex frequency comes close to the natural frequency of the system, *frequency lock-in* possibly occurs in a small range of the velocity flow [1, 2]. This phenomenon is also often discussed e.g. in the field of rotating systems together with *crossing* or *veering* phenomena in Campbell diagrams.

The contribution focuses on the reduced phenomenological model of the flexible body exposed to airflow. The structure is represented by the damped linear oscillator and aero-elastic coupling is described by the van der Pol oscillator [3]. The linearized analysis is performed with respect to show interesting lock-in regimes as well as stability issues. These phenomena are studied considering a single-degree-of-freedom (sdof) system and a cyclic structure corresponding to the bladed disc exposed to the steam flow.

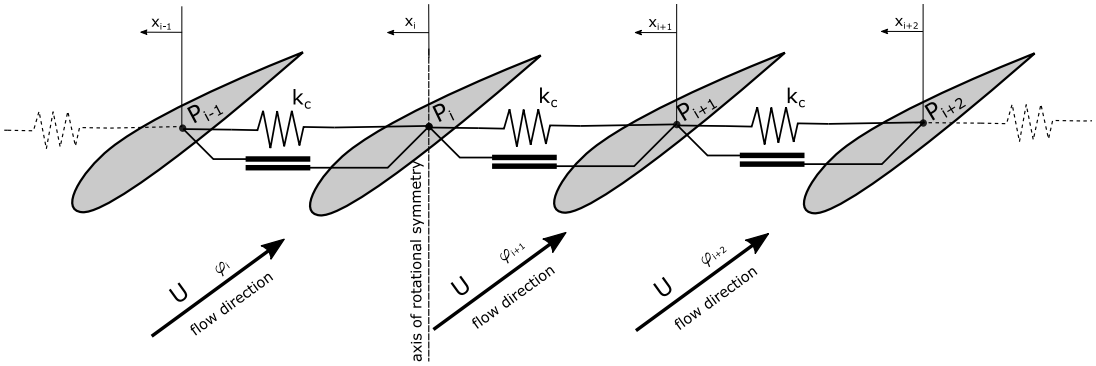

Fig. 1. Cyclic structure formed by a blade cascade with internal couplings and friction dampers between neighboring profiles

Let us focus on the multiple-degrees-of-freedom case shown in Fig. 1. A corresponding mathematical model is nonlinear due to the van der Pol terms. However, for the preliminary analyses and for the purposes of lock-in areas estimation, a linearized model is sufficient. A general mathematical model of the linearized and homogeneous system can be written in the form

$$\mathbf{M}_{BD}\ddot{\mathbf{q}}_{BD} + (\mathbf{B}_{BD} + \mathbf{B}_{fric})\dot{\mathbf{q}}_{BD} + (\mathbf{K}_{BD} + \mathbf{K}_C)\mathbf{q}_{BD} = \mathbf{0}, \tag{1}$$

where $\mathbf{q}_{BD} = [\ldots, \varphi_i, x_i \ldots] \in \mathbb{R}^{2N_B}$ is vector of generalized coordinates which includes displacements x_i and van der Pol coordinate φ_i of i-th profile. $\mathbf{M}_{BD}, \mathbf{B}_{BD}, \mathbf{K}_{BD} \in \mathbb{R}^{2N_B, 2N_B}$

are mass, damping and stiffness matrices, respectively, and $\mathbf{K}_C \in \mathbb{R}^{2N_B,2N_B}$ is coupling matrix representing elastic couplings between neighbouring profiles. Matrix $\mathbf{B}_{fric}) \in \mathbb{R}^{2N_B,2N_B}$ stands for equivalent linearized damping matrix corresponding to the friction couplings between neighbouring blades.

Modal analysis of such a system was performed with respect to the vortex shedding frequency which affects modal properties. For this purpose, system matrix $\mathbf{A}$ was defined in the form

$$\mathbf{A} = -\begin{bmatrix} \mathbf{0} & -\mathbf{I} \\ \mathbf{M}^{-1}\left(\mathbf{K}_{BD}+\mathbf{K}_C\right) & \mathbf{M}^{-1}\left(\mathbf{B}_{BD}+\mathbf{B}_{fric}\right) \end{bmatrix}. \tag{2}$$

Since stiffness and damping matrices are shedding-frequency-dependent ($\mathbf{K}_{BD} = \mathbf{K}_{BD}(\Omega_{aa})$, $\mathbf{B}_{BD} = \mathbf{B}_{BD}(\Omega_{aa})$), also eigenvalues of $\mathbf{A}$ are frequency-dependent. Moreover, due to the presence of damping forces, modal analysis produces complex values representing eigenfrequencies (imaginary part) and stability (real part). Results of the modal analysis are shown in Fig. 2 for two chosen values of the damping between profiles. It shows lock-in areas and its degeneration with changing damping.

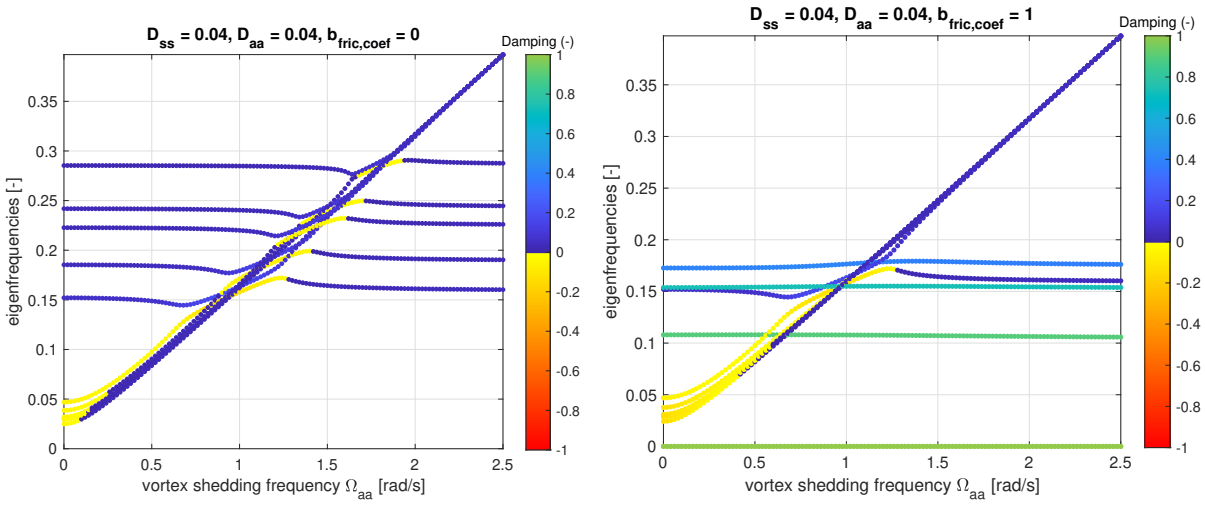

Fig. 2. Resulting eigenfrequency charts of the cyclic structure with five profiles; stability is denoted by the colour code

Acknowledgements

This work was supported by the GA CR project No. 20-26779S *Study of dynamic stall flutter instabilities and their consequences in turbomachinery application using mathematical, numerical and experimental methods.* Validation would not be possible without the AVL Excite software, which is available in the framework of the University Partnership program of AVL List GmbH and whose usage is greatly acknowledged.

References

[1] Byrtus, M., Dyk, Š., Hajžman, M., Non-synchronous vibration and lock-in regimes in coupled structures using reduced models, ASME IDETC/CIE-66815, August 2021.

[2] de Langre, E., Frequency lock-in is caused by coupled-mode flutter, Journal of Fluids and Structures 22(6) (2006) 783-791.

[3] Hoskoti, L. A. D. A., Misra, A., Sucheendran, M. M., Frequency lock-in during nonlinear vibration of an airfoil coupled with van der pol oscillator, Journal of Fluids and Structures 92 (2020) No. 102776.

COMPUTATIONAL MECHANICS 2021
36th conference with international participation
Srní
November 8 - 10, 2021

Some aspects of isogeometric analysis discretization of the incompressible fluid flow problem

J. Egermaier, H. Horníková

Department of Mathematics and European Centres of Excellence New Technologies for the Information Society, Faculty of Applied Sciences, University of West Bohemia, Univerzitní 8, 301 00, Plzeň, Czech Republic

1. Introduction

We focus on efficient numerical solution of the incompressible Navier-Stokes equations using our in-house solver based on the isogeometric analysis (IgA) approach. IgA uses the isoparametric approach, i.e., the same basis functions are used for description of the computational domain geometry and also for representation of the solution. The primary goal of using isogeometric analysis is to be always geometrically exact, independently of the discretization, and to avoid generation of computational meshes which is often a very time-consuming step for finite element (FEM) and finite volume (FVM) methods. Since the computational domains are usually designed as B-spline or NURBS objects in the industrial practice, IgA relies on B-spline/NURBS basis for representation of the solution. The B-spline/NURBS discretization basis has several specific properties different from standard finite element basis, most importantly a higher interelement continuity leading to denser matrices. Our aim is also to developed efficient solver of these systems by a preconditioned Krylov subspace method. Therefore, the efficiency of the ideal and approximate versions of suitable state-of-the-art block preconditioners for the Navier-Stokes equations is also discussed.

2. Navier-Stokes equations

The mathematical model is based on the incompressible Navier-Stokes equations. Let $\Omega \subset \mathbb{R}^d$ be a bounded domain, d being the number of spatial dimensions, with the boundary $\partial\Omega$ consisting of two complementary parts, Dirichlet $\partial\Omega_D$ and Neumann $\partial\Omega_N$. The steady-state incompressible Navier-Stokes problem is given as a system of $d+1$ differential equations together with boundary conditions

$$\begin{aligned} -\nu\Delta\mathbf{u} + (\mathbf{u}\cdot\nabla)\mathbf{u} + \nabla p &= \mathbf{0} \quad \text{in } \Omega, \\ \nabla\cdot\mathbf{u} &= 0 \quad \text{in } \Omega, \\ \mathbf{u} &= \mathbf{g}_D \quad \text{on } \partial\Omega_D, \\ \nu\tfrac{\partial\mathbf{u}}{\partial\mathbf{n}} - \mathbf{n}p &= \mathbf{0} \quad \text{on } \partial\Omega_N, \end{aligned} \tag{1}$$

where $\mathbf{u}$ is the flow velocity, p is the kinematic pressure, ν is the kinematic viscosity and $\mathbf{g}_D$ is a given function. If the velocity is specified everywhere on the boundary, the pressure solution is only unique up to a hydrostatic constant.

3. Numerical model

The nonlinear problem (1) is linearized by Picard method and discretized using isogeometric analysis approach, see [1] for details. IgA is a relatively new discretization approach [2] based on Galerkin method, where the basis of the discrete solution space is taken from the B-spline/NURBS representation of the computational domain Ω. We limit ourselves to the B-spline discretization basis in this work. The discretization, similarly to finite element method, leads to a sparse non-symmetric linear system of saddle-point type

$$\begin{bmatrix} \mathbf{F} & \mathbf{B}^T \\ \mathbf{B} & \mathbf{0} \end{bmatrix} \begin{bmatrix} \mathbf{u} \\ \mathbf{p} \end{bmatrix} = \begin{bmatrix} \mathbf{f} \\ \mathbf{g} \end{bmatrix}, \tag{2}$$

where $\mathbf{F}$ is block diagonal with the diagonal blocks consisting of the discretization of the viscous term and the linearized convective term, $\mathbf{B}^T$ and $\mathbf{B}$ are discrete gradient and negative divergence operators, respectively. An efficient iterative solver is necessary for solving large systems (2) because direct solvers are very time and memory consuming. Krylov subspace methods are the most commonly used in similar applications and can be very efficient if combined with a good preconditioning technique. Since our matrices are non-symmetric, we choose a Krylov subspace method GMRES.

4. Preconditioning techniques

In contrast of standard finite element method, the B-spline basis is generally of higher continuity across the element boundaries. This leads to denser matrices, which makes the linear system more expensive to solve. We are interested in the convergence behavior of the preconditioned GMRES with several block preconditioners, which were developed for finite element discretizations, especially its dependence on the B-spline basis degree and continuity.

Due to the form of linear system (2) we use some block preconditioners based on the decomposition

$$\begin{bmatrix} \mathbf{F} & \mathbf{B}^T \\ \mathbf{B} & \mathbf{0} \end{bmatrix} = \begin{bmatrix} \mathbf{I} & \mathbf{0} \\ \mathbf{B}\mathbf{F}^{-1} & \mathbf{I} \end{bmatrix} \begin{bmatrix} \mathbf{F} & \mathbf{0} \\ \mathbf{0} & \mathbf{S} \end{bmatrix} \begin{bmatrix} \mathbf{I} & \mathbf{F}^{-1}\mathbf{B}^T \\ \mathbf{0} & \mathbf{I} \end{bmatrix}, \tag{3}$$

where $\mathbf{S} = -\mathbf{B}\mathbf{F}^{-1}\mathbf{B}^T$ is the Schur complement, which is approximated in different ways. The tested precoditiners are LSC (Least-Squares Commutator), PCD (Pressure Convection-Diffusion), AL (Augmented Lagrangian) and SIMPLE (Semi-Implicit Method for Pressure Linked Equations) type preconditioners. An overview of these preconditioners can be found e.g. in [3].

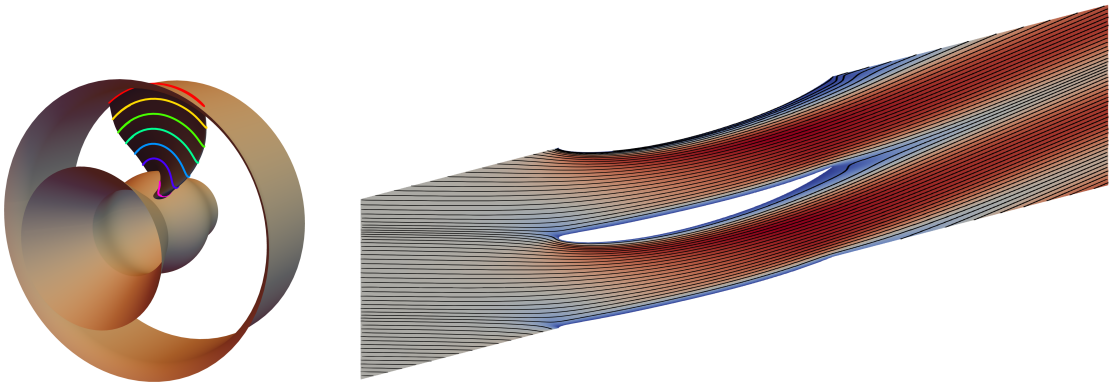

Fig. 1. Blade cascade flow

5. Numerical experiments

We chose several test problems to show and compare convergence properties of GMRES method with the particular preconditioners, especially dependence on the mesh refinements, Reynolds number, the degree of continuity of the solution across the element interfaces, etc.

One of the test examples is the 2D laminar blade profile cascade flow, see Fig. 1 (right). The computational domain is constructed by unfolding a cylindrical slice of the runner wheel domain, see Fig. 1 (left). The second test example is the 3D flow over a backward facing step domain. Both the steady and unsteady cases have been considered.

In Fig. 2 we can see example of convergence properties of selected preconditioners - residual norm of the solution dependency on the numbers of iterations over three levels of uniform mesh refinements. Third-order B-splines with C^2 interelement continuity are considered.

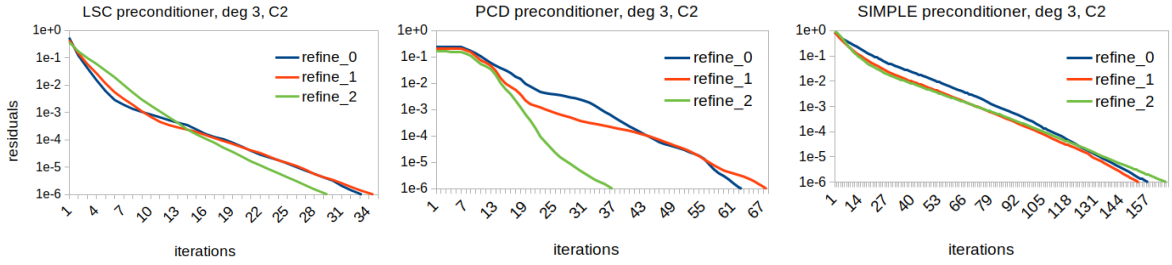

Fig. 2. Sensitivity of convergence to uniform mesh refinement of 2D blade profile domain

6. Conclusions

We tested the block preconditioners on several test problems discretized using B-spline basis of various degree and continuity. Based on these experiments, we can conclude, that higher interelement continutity of the discretization, which is typical for IgA, does not have a negative impact on the convergence of the preconditioned GMRES. Moreover, the opposite seems to be true in many cases. For example, some tested preconditioners were less sensitive to uniform mesh refinement for discretizations of high continuity. In the unsteady case, higher continuity even improves the convergence of GMRES for most preconditioners.

Acknowledgements

This work was supported by the Czech Science Foundation (GA ČR) grant No. 19-04006S.

References

[1] Bastl, B., Brandner, M., Egermaier, J., Michálková, K., Turnerová, E., Isogeometric analysis for turbulent flow, Mathematics and Computers in Simulation 145 (2018) 3-17.

[2] Hughes, T., Cottrel, J., Bazilevs, Y., Isogeometric analysis: CAD, finite elements, NURBS, exact geometry and mesh refinement, Computer Methods in Applied Mechanics and Engineering 194 (2005) 4135-4195.

[3] Segal, A, Rehman, M, Vuik, C., Preconditioners for incompressible Navier-Stokes solvers, Numerical Mathematics: Theory, Methods and Applications 3 (2010) 245-275.

COMPUTATIONAL MECHANICS 2021
36th conference with international participation
Srní
November 8 - 10, 2021

Ejector-boosted transcritical R744 refrigeration system

A. F. A. Elbarghthi, V. Dvořák

Department of Applied Mechanics, Technical University of Liberec Studentská 1402/2, 46117 Liberec, Czech Republic

The conventional refrigeration systems are mainly driven by electricity and are usually categorized by high energy consumption. Transcritical refrigeration systems have been verified to be very energy efficient, reliable, and more attractive, especially as the world becomes more energy-sentient. The properties of CO_2 as a refrigerant have made the transcritical refrigeration systems cost-effective and efficient. In contrast, working at supercritical pressure and high gas cooler outlet temperature leading to significant exergy destruction lies in the throttling process impacting the overall system performance. The use of ejector allows for overcoming the significant exergy destruction lays on the expansion processes of the cooling systems and led to spark improvement in the system performance by recovering some of the expansion work [3]. This study addresses the impact of utilizing the expansion ejector on the CO_2 transcritical refrigeration system by recovering some expansion work and reducing power consumption. The ejector profile was described by a comprehensive experimental study, and its performance was validated with approximation functions by Elbarghthi et al. [1, 2]. In the analysis, the ejector boosted system was compared with the parallel compression configuration representing the baseline system layout. The ejector cartridge type CTM ELP60 by Danfoss was used; it proposed the smallest profile with a motive nozzle throat diameter of 0.71 mm. The schematic diagram of the system supported with an ejector is represented in Fig. 1. The system consists of a base-load compressor, gas cooler, evaporator, and HPV with a metric expansion valve. The system is supplied with a supplementary compressor denoted as a parallel compressor to draw the vapour from the liquid separator to the gas cooler.

In refrigeration systems, the energy efficiency of the cycle can be quantified by assessing the coefficient of performance as the ratio between the cooling capacities into the total gross energy input to the cycle based on the first law of thermodynamic. The analysis was performed at exit gas cooler pressure of 90 bar and temperature of 20°C and 35°C. The cooling system was tested at a -6°C evaporation temperature with an outlet evaporator superheat of 10 K. Semi-hermetic reciprocating compressors manufactured by Dorin type CD1400H and CD380H were incorporated into the analysis presenting the base-load and parallel compressors. The compressor supplier provides polynomial functions to calculate each compressor's mass flow rate and electric power consumption. The calculation considers that the pressure drop in the piping and all heat exchangers are neglected with a totally isolated system. The analysis was conducted at steady-state conditions, and the potential and kinetic energies were not considered.

Fig. 2 represents the impact of the ejector profile on the overall system COP improvement and the reduction of power consumption. The left side shows the COP improvement via different cooling loads at pressure lift of 6 bar and exit gas cooler of 20°C and 35°C. The result revealed a significant COP improvement when running the system with the ejector at low system cooling capacity. The highest COP improvement recorded was 8.5% when implementing

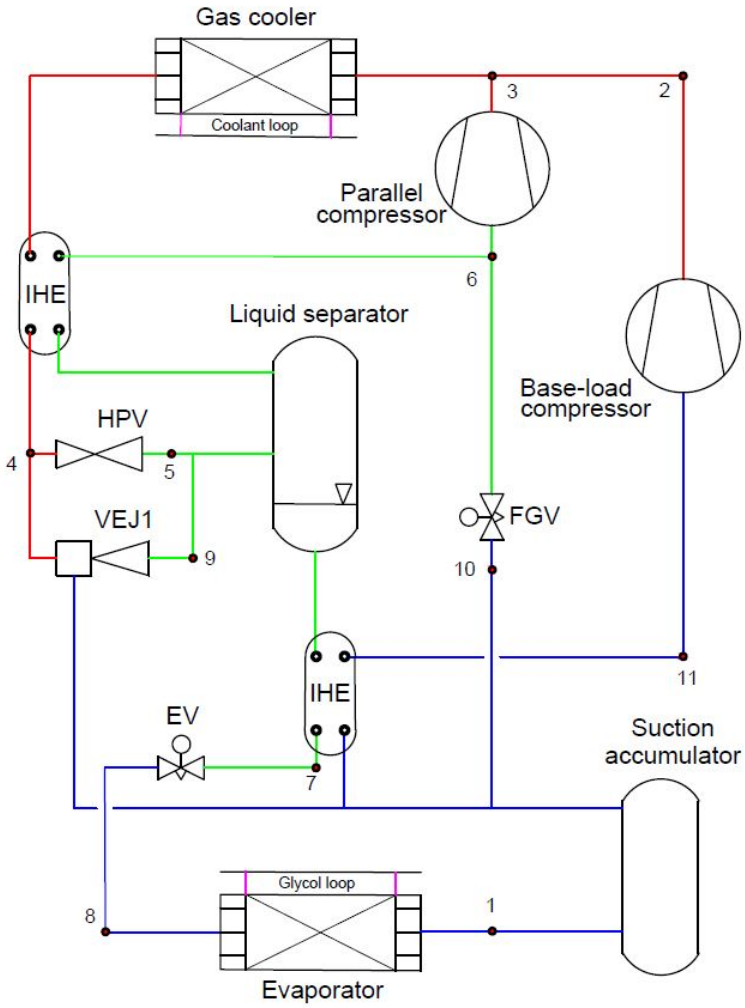

Fig. 1. The schematic diagram of the proposed ejector-boosted cooling system

the ejector comparing with operating in parallel configuration baseline at $T_{gc,out}$ = 20°C while the system improved by 3.36% under the same cooling load of 4 kW at $T_{gc,out}$ = 35°C. As long as the system cooling load increased, the effect of the ejector reduced. For example, COP improvement dropped to less than half when the cooling load grew to 10 kW.

Moreover, implementing the ejector to the system assisted in saving some of the energy needed for the compressors. Based on the result illustrated in the right side of Fig. 2, for the calculation of the power consumption at pressure left of 5 bar and $T_{gc,out}$ = 20°C, the ejector could reduce the input power for the compressors up to 5.3% and 13.45% at the cooling capacity of 10 kW and 4 kW respectively. The peak where the system could reach the highest possible power-saving when utilizing the ejector is a function of the ejector efficiency, which is interpreted as the amount of the total power applied to compress the entrained flow isentropically to the ejector outlet over the maximum theoretical work recovery potential. Therefore, operating with an ejector should be regulated with a specific pressure lift that can improve the system's performance.

In conclusion, applying the ejector in the R744 transcritical refrigeration system as a flashing device will recover the expansion work and reduce the overall input power. It is worth highlighting that understanding the ejector characteristics and the optimum operation conditions will lead to the ideal overall system performance.

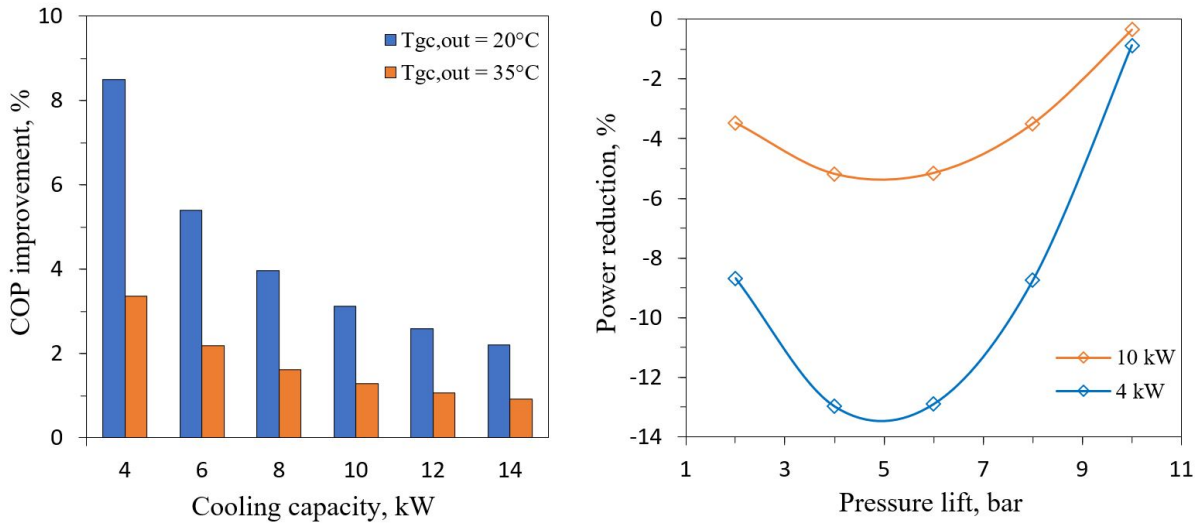

Fig. 2. The impact of the ejector profile on the system: COP improvement versus cooling load (*left side*), and the power reduction as a function of the different pressure lift (*right side*)

Acknowledgement

The work was supported by the Student Grant Competition of the Technical University of Liberec under the project No. SGS-2021-5063.

References

[1] Elbarghthi, A. F. A., Dvorak, V., Hafner, A., Banasiak, K., The potential impact of the small-scale ejector on the R744 transcritical refrigeration system, Energy Conversion and Management (2021) No. 114860.

[2] Elbarghthi, A. F. A., Hafner, A., Banasiak, K., Dvorak, V., An experimental study of an ejector-boosted transcritical R744 refrigeration system including an exergy analysis, Energy Conversion and Management 238 (2021) No. 114102.

[3] Shestopalov, K. O., Huang, B. J., Petrenko, V. O., Volovyk, O. S., Investigation of an experimental ejector refrigeration machine operating with refrigerant R245fa at design and off-design working conditions. Part 2. Theoretical and experimental results, International Journal of Refrigeration 55 (2015) 201-211.

COMPUTATIONAL MECHANICS 2021
36th conference with international participation
Srní
November 8 - 10, 2021

Macroscopic constitutive model for NiTi shape memory alloys: Formulation, numerical implementation, and application in materials research

M. Frost, P. Sedlák

Institute of Thermomechanics, Czech Academy of Sciences, Dolejškova 5,182 00 Praha, Czech Republic

1. Introduction

Shape memory alloys (SMA) are metallic materials with the ability to undergo reversible phase solid-to-solid phase transformation between a high-symmetry and a low-symmetry phase. In addition to temperature variation, the phase transition may be induced by applying stress on the high-symmetry phase. The most common and practically utilized example are the alloys with nickel and titanium as the dominant constituents, known as NiTi-based SMA.

From the viewpoint of mechanics, an exciting feature of NiTi SMA polycrystals is the ability to be strained up to 10% deformation and, after unloading, to fully recover the original shape; this is called *superelasticity*, and it manifests itself at higher temperatures. If the material is deformed at low temperatures and then its shape-change is constrained, it generates relatively high force (called recovery force) against the constraint. Finally, loaded SMA structure can perform work when cycled between high and low temperatures.

All these features gave rise to many smart and useful applications of NiTi SMA [5]. It is not surprising that soon after their discovery, SMA attracted the attention of a wide engineering community. Since 1980s, there has been a continuous effort to develop a complex constitutive model capable of reproducing the specific mechanical response. Because of many additional peculiarities, e.g., the pronounced asymmetry of the response in tension and compression, anisotropy of some physical properties, or the inclination towards strain localization, a robust and comprehensive constitutive model tailored even for the commercially most successful NiTi alloy is still sought.

2. Constitutive model and its numerical implementation into finite element software

The inherent challenge for constitutive modeling is that multiple microstructural processes can be simultaneously activated in the material, and these processes are mutually interdependent, i.e., activation of one process can influence the progress of another one and *vice versa*. Most of them are *dissipative*, which indicates thermodynamic irreversibility. For such situations, continuum thermodynamics offers some powerful modeling tools. The model presented in this contribution is developed within the so-called *generalized standard materials* framework [4], which employs only two potential functions – energy function and dissipation function – as determinants for the complete evolution of the system. So-called internal (state) variables serving as the descriptors of the present material state complement the conventional state variables (e.g. strain and temperature) in the functions' definitions. Let us note that the particular choice

of internal variables and the form of the two functions are tightly linked to the knowledge and understanding of the material system by the authors of the model.

The constitutive (evolutionary) equations are determined via a mathematical relation between generalized forces obtained from the energy function and (generalized) gradients of the dissipation function. Under some (relatively weak) conditions, this relation may be derived from a suitable thermodynamic extremum principle [3]. The variational character of the framework then allows for the exploitation of incremental energy minimization approaches in the numerical implementation of the model.

The numerical implementation of the boundary value problems typical for computational mechanics involves a spatial discretization (the finite element method is usually the first-choice tool) and a temporal discretization. For the common backward Euler implicit scheme, the latter corresponds to a time-incremental problem of determining the state-update of the material at a time instant t_{n+1} based on the known state at the time instant t_n and some prescribed disturbance of that state. The microstructural processes behind the characteristic effects of SMA (athermal phase transformation, crystal twinning) are, similarly to the conventional flow plasticity, in a good approximation *rate-independent* (i.e., the dissipation function is homogenous first order in rates of internal variables). Most of the common methods for the solution of the resulting time-incremental problem can be classified as "check and treat" strategy: first, the possibility that the inelastic process is not active is checked and, if it is not the case, the process is considered as active, and the evolution is resolved. These methods are usually quite flexible and easy to implement; however, with an increasing number of involved inelastic processes and their mutual coupling, searching for the set of active processes turns into a complex and elaborate task.

The minimization problems stemming from the variational formulation can also be dealt with "check and treat" strategies; however, they also allow for employing direct minimization procedures or algorithms of mathematical programming. The former option was used for resolving the constitutive equations of the model introduced in [6], implemented within the user material (UMAT) subroutine of the commercial finite element solver Abaqus, and it has been successfully employed in three-dimensional computational simulations as demonstrated on the example in the following section.

3. Computational simulation of experiments on NiTi helical spring

A computational simulation employing the constitutive model [6] was used as a tool for analysis and interpretation of experimental data obtained on a NiTi helical spring by diffraction/scanning computational tomography. Let us note that this experimental method allows for in situ reconstruction of the spatial distribution of microstructural heterogeneities within probed samples, see details in [1]. A helical spring was chosen as the object of this study since it allows for simple manufacturing and direct utilization in actuating devices and, at the same time, when stretched to higher strokes, two deformation modes – twisting and bending – are simultaneously active and naturally result in a heterogeneous, non-proportional deformation within any cross-section.

In the experimental part, a helical spring was manufactured from a NiTi wire, its superelastic response (at room temperature) was measured (see the upper inset in Fig. 1), and a series of X-ray diffraction scanning runs was performed at two distinct deformation states, denoted S1 and S2 hereinafter. The computational tomography algorithms were then employed to resolve the spatial distribution of volume fractions of phases in the cross-section of the spring at the two states (see Fig. 2). More details can be found in [2].

In the computational simulation, a structural model of a one-coil spring (dimensions corre-

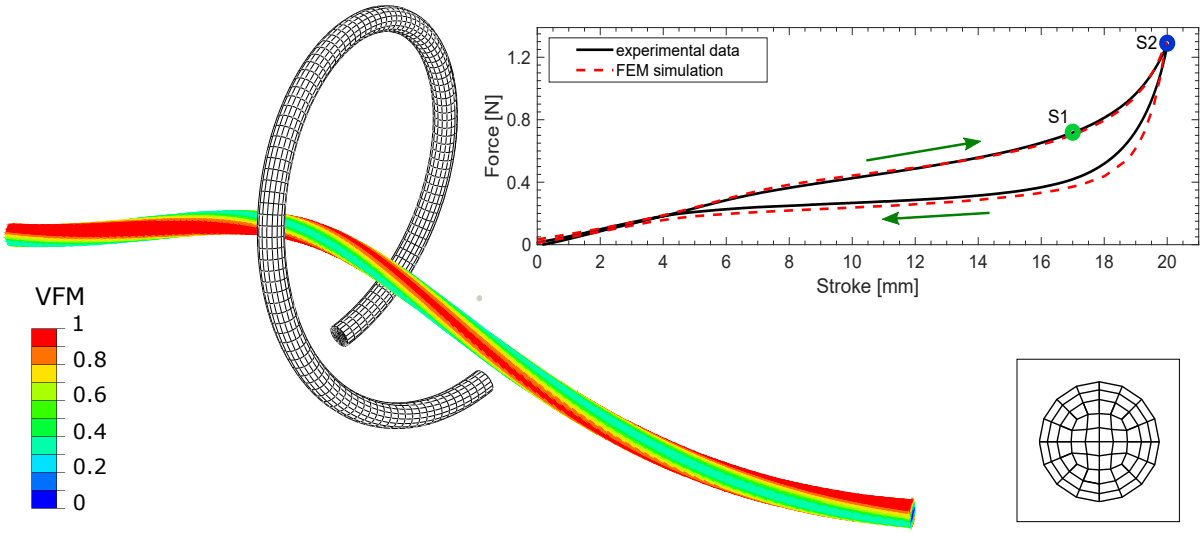

Fig. 1. Finite element model of the helical spring. The free-standing mesh is in grey; the mesh layout in an arbitrary cross-section is shown in the lower inset. The deformed configuration corresponding to the maximum stroke (S2) is in colors displaying the computed volume fraction of the low-symmetry phase (see the colorbar). The upper inset (graph) compares measured (black line) and simulated (red dashed line) dependence of total force on stroke obtained from the FE simulation. Marked points S1 and S2 correspond to strokes at which the diffraction scanning was performed

spond to the spring used in experiments) was constructed and meshed into 120 equivalent cross-sectional element layers with 64 elements per layer. In Fig. 1, the complete mesh is depicted on the undeformed configuration; the arrangement of 64 elements within an arbitrary layer is shown in the lower square inset. The computation was performed with eight-node linear hexaedral elements with centroid integration (C3D8R). Geometric nonlinearities were accounted for via *NLGEOM settings. Stretching of the spring was simulated by a gradual, symmetrical change of prescribed x-displacement (parallel with the coil axis) of the central nodes at both ends of the coil, displacement in other directions of these nodes were fixed, and the rigid body motion of the whole coil was prevented. The periodic boundary conditions with shifted x-displacement are imposed via *EQUATION functionality of Abaqus FEA at the remaining nodes of both ends of the segment (infinite spring approximation). Material parameters serving as the model's input were determined from a standardized experimental dataset measured on the constituent wire.

Fig. 1 also shows the deformed configuration of the coil corresponding to the maximum stretch of the real spring (S2). The distribution of computed volume fraction of martensite on the wire surface (see the colorbar) complies with the symmetry of the model. The upper inset compares the force-stroke response obtained in the experiment (black line) with the simulation (red dashed line). The overall excellent match is observed (with respect to experimental errors).

The main aim of the computational part was to reveal the spatial distribution of the quantities representing volume fractions of phases within the cross-section of the spring so that it can be directly compared with the results of the computational tomography employing the diffraction experiment. This comparison is presented in Fig. 2 for the volume fraction of the high-symmetry phase (austenite) denoted as VFA there. Distributions are shown for both deformation stages S1 and S2. Let us note that the inclination of the spring wire to the probing plane results in the ellipticity of the cross-sections.

The comparison of results provides valuable information from the computational modeling point of view. First, it confirms plausible parametrization of the model via the internal variables:

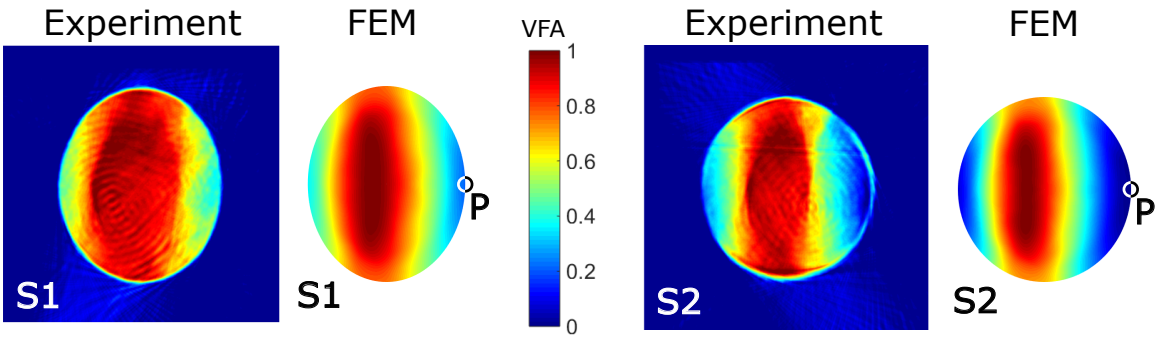

Fig. 2. Spatial distribution of the volume fraction of austenite (VFA) within the spring cross-section determined from scanning experiments compared with its equivalent computed in the finite element simulation (an arbitrary cross-section of the structural model) at two deformation states S1 and S2 (cf. Fig. 1). The same colorbar applies to all phase distributions. The coil axis is directly to the right from the center of the cross-sections; hence, point P lies on the most inner material fiber of the coil

phase gradients existing in the material are very well (considering also experimental errors) detected and even quantified by the model. Second, the main features of the phase pattern can be interpreted in the terms of advanced features of the model; e.g. the obvious asymmetry of the pattern with respect to the "neutral axis" of bending is due to the so-called tension-compression asymmetry of the material response implemented in the model. Third, the variation of the model parameters can help determine the physical characteristics (parameters) of the material which can be difficult to obtain directly through experiments. For instance, the tension-compression asymmetry parameter can be obtained via its variation in the model so that the best correspondence between the simulation and experimental patterns is reached. Finally, the model provides distributions of state variables, e.g., components of the stress tensor, which are difficult or even impossible to gain through conventional experimental techniques.

Acknowledgements

The financial support via project No. GA18-03834S provided by the Czech Science Foundation is acknowledged as well as the provision of experimental beamtime at the beamline ID 15A within experiment No. MA2114 by European Synchrotron Radiation Facility in France.

References

[1] Àlvarez-Murga, M., Bleuet, P., Hodeau, J., Diffraction/scattering computed tomography for three-dimensional characterization of multi-phase crystalline and amorphous materials, Journal of Applied Crystallography 45 (6) (2012) 1109-1124.

[2] Frost, M., Ševčík, M., Kadeřávek, L., Šittner, P., Sedlák, P., Reconstruction of phase distributions in NiTi helical spring: comparison of diffraction/scattering computed tomography and computational modeling, Smart Materials and Structures 29 (2020) No. 075036.

[3] Hackl, K., Fischer, F. D., On the relation between the principle of maximum dissipation and inelastic evolution given by dissipation potentials, Proceedings of The Royal Society A – Mathematical Physical and Engineering Sciences 464 (2008) 117-132.

[4] Halphen, B., Nguyen, Q. S., On generalized standard materials, Journal de Mécanique 14 (1975) 39-63. (in French)

[5] Mohd Jani, J., Leary, M., Subic, A., Gibson, M. A., A review of shape memory alloy research, applications and opportunities, Materials & Design 56 (2014) 1078-1113.

[6] Sedlák, P., Frost, M., Benešová, B., Šittner, P., Ben Zineb, T., Thermomechanical model for NiTi-based shape memory alloys including R-phase and material anisotropy under multi-axial loadings, International Journal of Plasticity 39 (2012) 132-151.

COMPUTATIONAL MECHANICS 2021
36th conference with international participation
Srní
November 8 - 10, 2021

Numerical simulation of flows in discharge objects with siphon

J. Fürst[a], T. Halada[a], M. Sedlář[b], T. Krátký[b], P. Procházka[c], M. Komárek[b]

[a] *Faculty of Mechanical Engineering, Czech Technical University in Prague, Karlovo nám. 13, 121 35 Praha, Czech Republic*
[b] *Centre of Hydraulic Research, Jana Sigmunda 313, 783 49 Lutín, Czech Republic*
[c] *Institute of Thermomechanics, Czech Academy of Sciences, Dolejškova 1402/5, 182 00 Praha, Czech Republic*

The paper deals with the numerical simulations of free-surface flows in discharge objects with siphon. The goal of the work is to investigate the applicability of the lattice Boltzmann method (LBM) for numerical simulations of the problem. The results of the LBM simulations are compared to numerical results obtained with the standard finite volume method in the Volume-of-Fluid formulation and with the experimental data obtained in the hydraulic laboratory with water circuit [4].

We consider a free-surface flows in a test channel depicted in Fig. 1. The water enters through the siphon at the left hand side of the channel and leaves the channel through an adjustable gate at the right hand side. The numerical solution is calculated in a computational domain corresponding to left part of the channel.

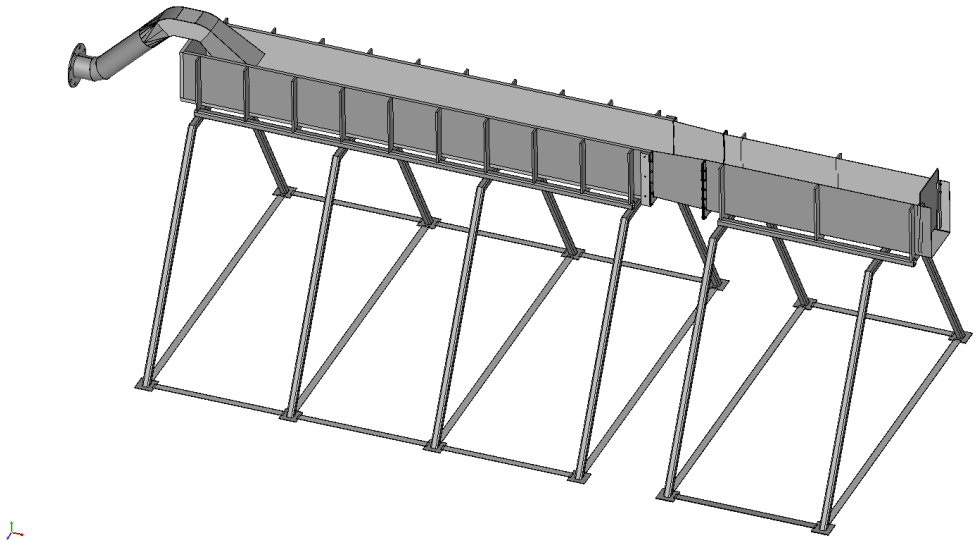

Fig. 1. Test channel with siphon

The numerical solution is obtained with the free surface LBM method proposed in [2] and carried out with an in-house code based on the open source LBM framework Palabos [3]. The motion of the liquid is described by the system of advection-reaction PDEs for the so-called discrete density distribution functions $f_i(\vec{x}, t)$

$$\frac{\partial f_i}{\partial t} + \vec{c}_i \cdot \nabla f_i = \frac{1}{\tau_c}\left(f_i - f_i^{(eq)}\right) + F_i, \tag{1}$$

where $\vec{c}_i$ are the discrete velocities of the D3Q19 model (see [2]), τ_c is the relaxation time, F_i represent the contribution of the external forces and $f_i^{(eq)}$ are the equilibrium distribution functions for incompressible fluid

$$f_i^{(eq)} = w_i \left[\rho + \frac{\vec{c}_i \cdot \vec{u}}{3} + \frac{(\vec{c}_i \cdot \vec{u})^2}{18} - \frac{\vec{u} \cdot \vec{u}}{6} \right], \tag{2}$$

where w_i are the weights of the D3Q19 model. The free-surface extension is described in [2]. The relaxation time τ_c is a function of the effective viscosity including the molecular and eddy viscosity calculated with the Smagorinsky model, for more details see [1].

The problem was solved using a Cartesian mesh with uniform spacing $\Delta x = \Delta y = \Delta z = 2\,\mathrm{mm}$ with staircase approximation of boundary and with constant time step $\Delta t = 5 \times 10^{-5}\,\mathrm{s}$. Although the staircase approximation with standard bounce-back boundary conditions impairs the overall accuracy of the method, the current study focuses mainly on the flow structures in the channel with straight boundaries. The parabolic velocity profile with given volumetric flow rate is prescribed ad the inlet and simple extrapolation is used at the outflow. The desired water level in the channel is kept using an adjustable gate near the outlet. The model does not use any local mesh refinement near the wall neither any wall functions. This simplification partially impairs the accuracy of the model near the wall and the fails to predict correct wall shear stresses. Nevertheless, the dynamics structure of the flow field further from wall corresponds very well to the numerical results obtained with the finite volume approach using the ANSYS CFX software and to the experimental data acquired with the laser particle image velocimetry (PIV) method.

Fig. 2 shows the outline of the domain and the water level calculated with LBM for prescribed flux rate $q = 13.81/\mathrm{s}$.

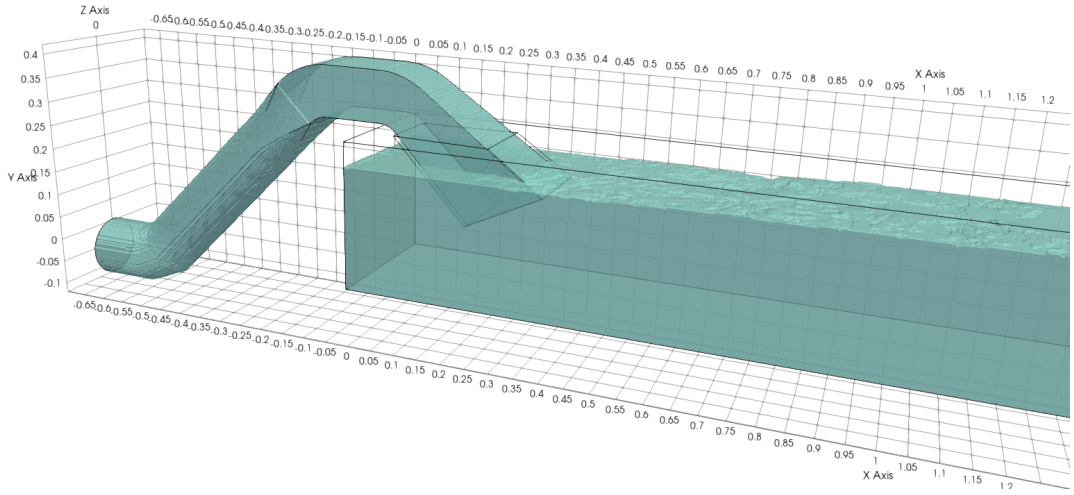

Fig. 2. LBM, water level at time $t = 30\,\mathrm{s}$ for flux rate $q = 13.81/\mathrm{s}$

Fig. 3 shows the instantaneous magnitude of 2D velocity projection in vertical symmetry plane and the structure of the flow field using the line integral convolution (LIC) method. Since the method corresponds to LES approach, the calculated instantaneous flow field contains a lot of turbulent vortices. Therefore, the results were post-processed using standard time averaging over a time window $T = 15\,\mathrm{s}$ to $20\,\mathrm{s}$ and the time averaged results are plotted in Fig. 4.

Fig. 5 shows the results of PIV measurements. One can see very similar flow features, namely the vortex near the bottom at $x \approx 350\,\mathrm{mm}$ and the attachment point at $x \approx 500\,\mathrm{mm}$.

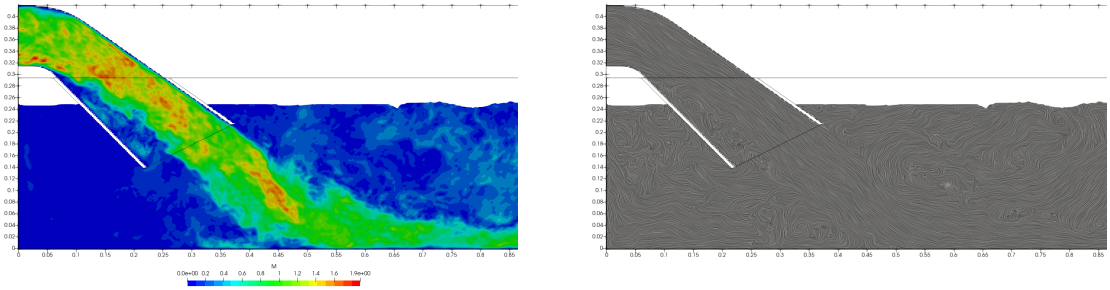

Fig. 3. Instantaneous 2D velocity magnitude (*left*) and flow field structure (*right*) in the symmetry plane

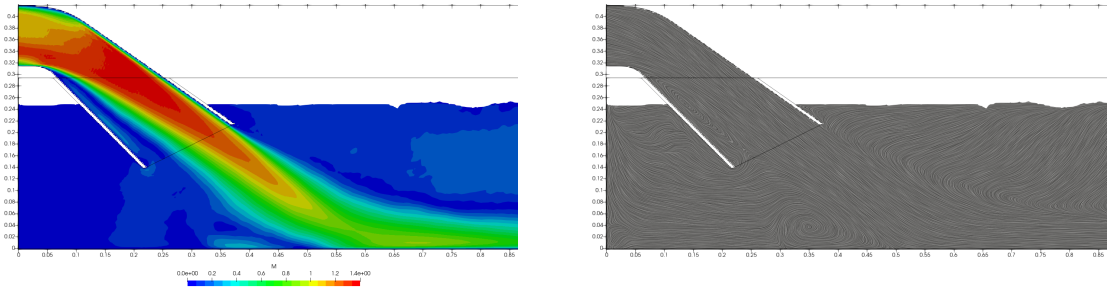

Fig. 4. Time averaged 2D velocity magnitude (*left*) and flow field structure (*right*) in the symmetry plane

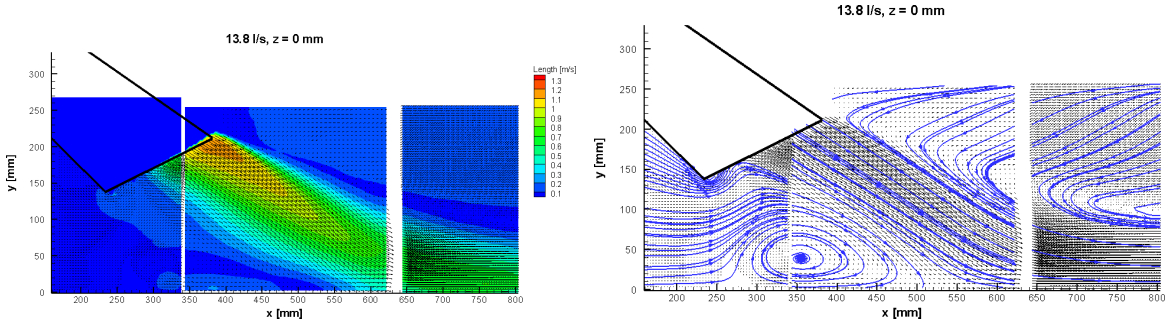

Fig. 5. PIV, 2D velocity magnitude and streamlines in the vertical symmetry plane $z = 0\,\mathrm{mm}$

Figs. 6 and 7 compare the calculated time averaged flow field with the PIV data in the horizontal plane $10\,\mathrm{mm}$ above the channel bottom. One can clearly see that the flow is non-symmetric. See, e.g., the position of the critical point ($x \approx 480\,\mathrm{mm}$). Note that the flow is highly unsteady and the calculated and measured positions of the critical point depend (among others) on the time averaging interval.

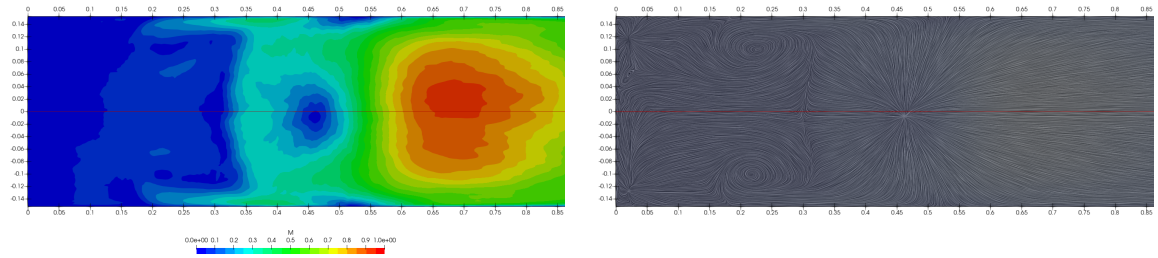

Fig. 6. Time averaged 2D velocity magnitude (*left*) and flow field structure (*right*) in the horizontal plane $10\,\mathrm{mm}$ above the bottom

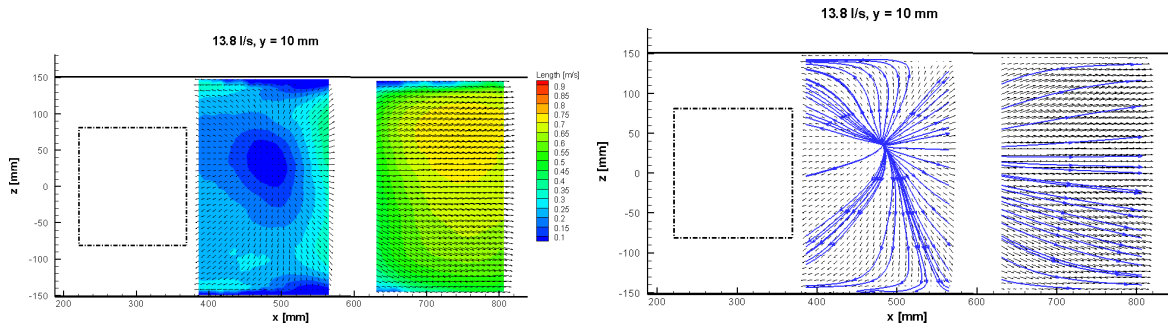

Fig. 7. PIV, 2D velocity magnitude and streamlines in the horizontal plane $y = 10\,\mathrm{mm}$

The paper shows that the free-surface LBM method provides a viable alternative to standard finite volume method (FVM) for given problem. The advantage of LBM over the FVM is its simplicity especially in the pre-processing phase. Moreover, the LBM is extremely easy to parallelize and can exploit modern CPU/GPU architectures. On the other hand, the implementation of boundary conditions in the case of non-planar boundaries becomes more difficult. Moreover, the current software package does not use any wall model (e.g., wall functions) and therefore it does not handle the very near wall flows correctly.

Acknowledgements

The work was supported by the Grant Agency of the Czech Technical University in Prague, grant No. SGS19/154/OHK2/3T/12 and by the Grant Agency of the Czech Technical University in Prague, grant No. SGS19/154/OHK2/3T/12.

References

[1] Fürst, J., Halada, T., Sedlář, M., Krátký, T., Procházka, P., Komárek, M., Numerical analysis of flow phenomena in discharge object with siphon using lattice Boltzmann method and CFD, Mathematics 9 (15) (2021) No. 1734.

[2] Körner, C., Thies, M., Hofmann, T., Thürey, N., Rüde, U., Lattice Boltzmann model for free surface flow for modeling foaming, Journal of Statistical Physics 121 (2005) 179-196.

[3] Latt, J., Malaspinas, O., Kontaxakis, D., Parmigiani, A., Lagrava, D., Brogi, F., Ben Belgacem, M., Thorimbert, Y., Leclaire, S., Li, S., Marson, F., Lemus, J., Kotsalos, C., Conradin, R., Coreixas, C., Petkantchin, R., Raynaud, F., Beny, J., Chopard, B., Palabos: Parallel lattice Boltzmann solver, Computers & Mathematics with Applications 81 (2021) 334-350.

[4] Sedlář, M., Procházka, P., Komárek, M., Uruba, V., Skála, V., Experimental research and numerical analysis of flow phenomena in discharge object with siphon, Water 12 (12) (2020) No. 3330.

COMPUTATIONAL MECHANICS 2021
36th conference with international participation
Srní
November 8 - 10, 2021

Temperature variations of microfiber textiles subject to DC voltage

A. Guran[a], A. Vahidi-Shams[a], A. Sapietová[b], M. Ságа[b]

[a] *Institute of Structronics, Canada*

[b] *Department of Applied Mechanics, Faculty of Mechanical Engineering, University of Žilina, Žilina, Slovakia*

In recent years, thermal conductivity of micro and nano carbon textiles has been studies for possible manufacturing of cold weather protective clothing, window defrosting, road de-icing, medical instrumentation, and functional textiles [1-5]. The present paper sets out to investigate the thermal properties of a 30mmX130mm Carbone microfiber cloth.

1. Experimental setup

Figure 1 shows the experimental set up. A 30mm x130mm carbon micro fibre cloth is connected to a 1amp adaptor with 1.5 to 12V voltage. The temperature at the midspan of the strip is measured by a noncontact infrared thermometer.

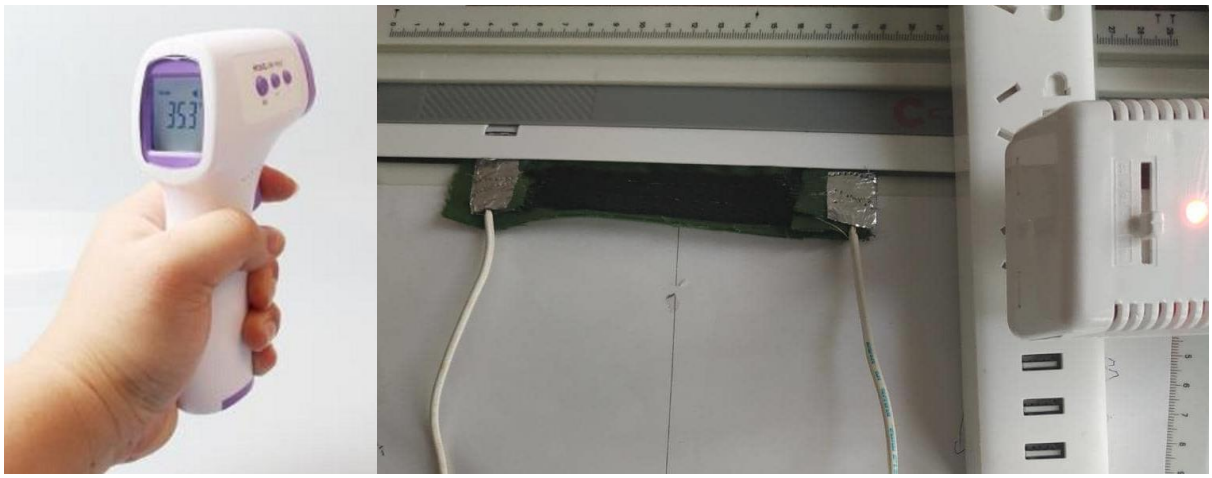

Fig. 1. Experimental set up

2. Results

Fig. 2 shows the temperature variations of the mid-point of the strip. For each voltage the temperature variant curve increases with high rate and then the rate decreases till the temperature reaches a plateau, T_{max}. Fig. 3 shows the variations of temperature at the mid-point of the strip under 12V voltage. The temperature increases from room temperature To and reaches a plateau, T_{max}. We turn off the voltage at t_{cr} denoting the measured temperature at this point of time t_{cr} with T_{cr}. It can be shown

$$T = (T_0 - T_{max})\, e^{-\alpha t} + T_{max}\,, \tag{1}$$

where

$$\alpha = \frac{1}{t_{cr}} \ln\left(\frac{T_{max} - T_0}{T_{max} - T_{cr}}\right). \tag{2}$$

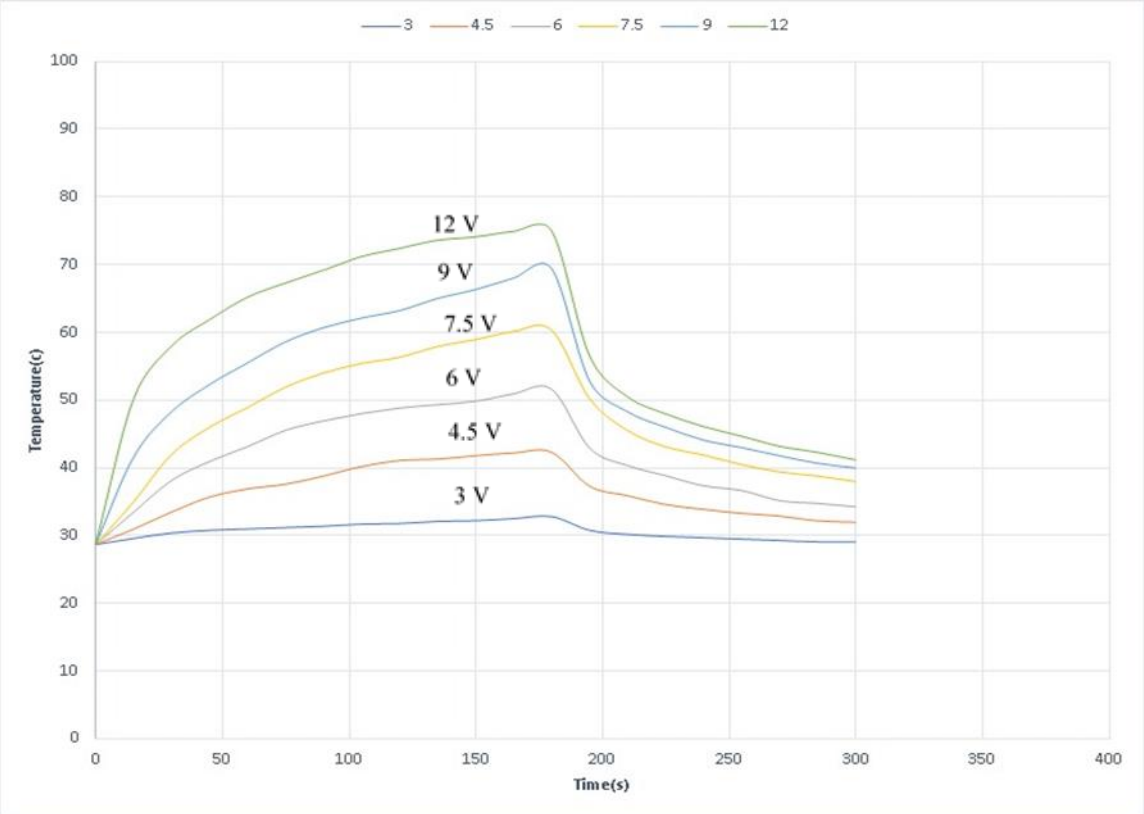

Fig. 2. Temperature variations of the mid-point of the strip for each voltage

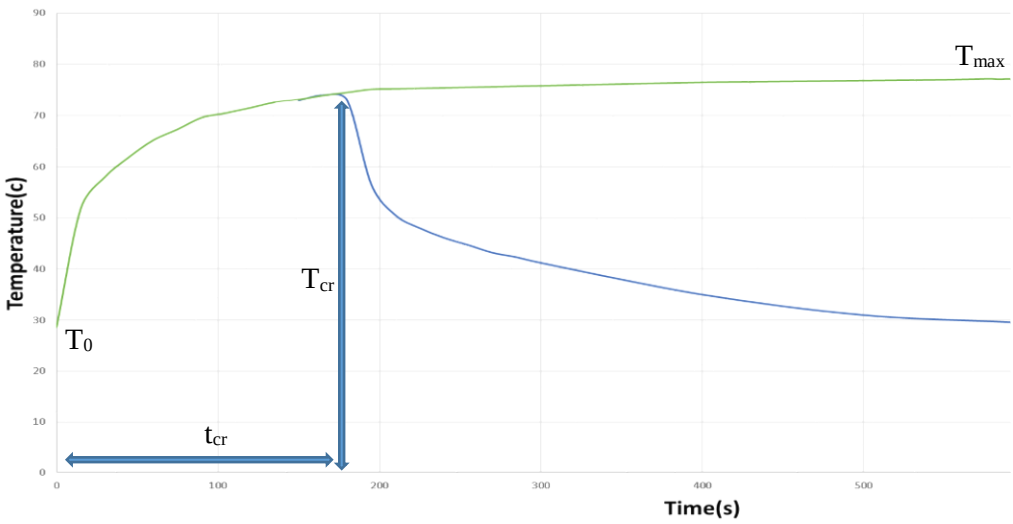

Fig. 3. Shows the variations of temperature at the the mid-point of the strip under 12 V voltage

Fig. 4 shows the maximum possible temperature as a function of the voltage of two ends of the strip. Table 1 shows the time series of the temperature for 15 second time step.

3. Conclusions

From the foregoing discussions and results we conclude there is an electrical and a mechanical analogy with the thermal system investigated in this paper. The variations of the temperature at the midspan of the strip is exactly the same way as the voltage across a capacitor in an

electrical circuit with a capacitor and resistor or the velocity across the spring in a mechanical vibrator with a damper and a spring.

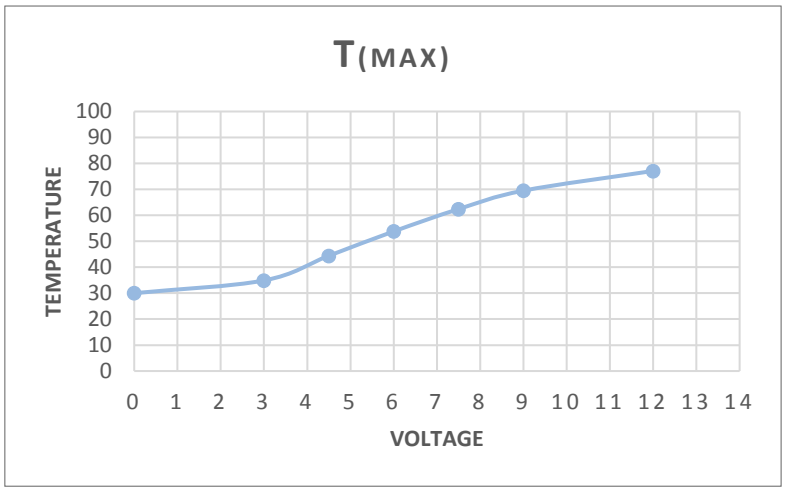

Fig. 4. Variations of T_{max} as a function of the difference in voltages of the two ends of the strip

Table 1. Time series of the temperature

Time(s)	V=3	V=4.5	V=6	V=7.5	V=9	V=12
0	28.7	28.7	28.7	28.7	28.7	28.7
15	29.6	31	32.5	35	41.6	51.8
30	30.3	33.5	36.2	42	48.3	58
45	30.7	35.7	40	46	52.3	61.9
60	31	37.2	42.2	48.9	55.5	65.2
75	31.2	38.6	44.6	51.9	58.6	67.3
90	31.4	39.8	46	54	60.7	69.6
105	31.7	40.4	47.5	55.4	62.1	70.5
120	31.8	41.1	48.9	56.9	64.2	71.5
135	32.1	41.3	49.4	57.9	65	72.6
150	32.2	41.8	50.5	58.9	66.3	73.1
165	32.5	42.2	51	60.1	67	73.9
180	32.8	42.3	51.7	60.3	67.4	74.5
195	32.9	42.4	51.8	60.4	67.5	75.1
210	33	42.5	51.9	60.5	67.6	75.2
225	33.1	42.6	52	60.6	67.7	75.3
240	33.2	42.7	52.1	60.7	67.8	75.4
255	33.3	42.8	52.2	60.8	67.9	75.5
270	33.4	42.9	52.3	60.9	68	75.6
285	33.5	43	52.4	61	68.1	75.7
300	33.6	43.1	52.5	61.1	68.2	75.8
315	33.7	43.2	52.6	61.2	68.3	75.9
330	33.8	43.3	52.7	61.3	68.4	76
345	33.9	43.4	52.8	61.4	68.5	76.1
360	34	43.5	52.9	61.5	68.6	76.2
375	34.1	43.6	53	61.6	68.7	76.3
390	34.2	43.7	53.1	61.7	68.8	76.4
405	34.3	43.8	53.2	61.8	68.9	76.5
420	34.35	43.85	53.25	61.85	68.95	76.55
435	34.4	43.9	53.3	61.9	69	76.6
450	34.45	43.95	53.35	61.95	69.05	76.65
465	34.5	44	53.4	62	69.1	76.7
480	34.55	44.05	53.45	62.05	69.15	76.75
495	34.6	44.1	53.5	62.1	69.2	76.8
510	34.65	44.15	53.55	62.15	69.25	76.85
525	34.7	44.2	53.6	62.2	69.3	76.9
540	34.75	44.25	53.65	62.25	69.35	76.95
555	34.8	44.3	53.7	62.3	69.4	77
570	34.85	44.35	53.75	62.35	69.45	77.1
585	34.9	44.4	53.8	62.4	69.5	77.1
600	33.95	43.45	52.85	61.45	68.55	76.1

References

[1] Guran, A., Yousefghahari, B., Invited speakers, I-9: Modal analysis of carbon nano tubes (Cnt) by means of finite element technique, Cell Journal (Yakhteh) 13 (2) (2011) 7-7.

[2] Guran, A., Yousefghahari, B., Bayranvand, M., Vahidi-Shams, A., Feasibility of using nanotextiles for hypothermia or applied to a part of the body for warmth, Cell Journal (Yakhteh) 13 (2) (2011) 7-7.

[3] Hao, Y., Tian, M., Zhao, H., Qu, L., Zhu, S., Zhang, X., Chen, S., Wang, K., Ran, J., High efficiency electrothermal graphene/tourmaline composite fabric joule heater with durable abrasion resistance via a spray coating route, Industrial & Engineering Chemistry Research 57 (40) (2018) 13437-13448.

[4] Wen-Jin, S., Ling, X., Li-Chuan, J., Chang-Ge, Z., Yang, X., Ru-Hua, Y., Ding-Xiang, Y., Jian-Hua, T., Zhong-Ming, L., Highly conductive and stretchable carbon nanotube/thermoplastic polyurethane composite for wearable heater, Composites Science and Technology 181 (2019) 107695.

[5] Yan, J., Jeong, Y., Synergistic effect of hybrid carbon fillers on electric heating behavior of flexible polydimethylsiloxane-based composite films, Composites Science and Technology 106 (2015) 134-140.

COMPUTATIONAL MECHANICS 2021
36th conference with international participation
Srní
November 8 - 10, 2021

Effect of multiple pantographs on their dynamic interaction with a catenary system

M. Hajžman[a], R. Bulín[a], J. Očenášek[b]

[a] *Faculty of Applied Sciences, University of West Bohemia, Univerzitní 8, 301 00 Plzeň, Czech Republic*
[b] *New Technologies – Research Centre, University of West Bohemia, Univerzitní 8, 301 00 Plzeň, Czech Republic*

The collection of electric current during the operation of electric rail vehicles is provided by pantographs, which should be in contact with a catenary system conducting current. The motion of the vehicle with pantographs causes various dynamic effects related to the interaction of pantographs and catenaries. It is the issue for all types of vehicles ranging from low-speed trams to high-speed trains. The authors of this paper started to develop the in-house DynPAC software for the analysis of the dynamic interaction between catenary systems and pantographs [1]. The main problem was to create the software in order to fulfil the requirements of particular European Standard EN 50318:2002 called "Railway applications – Current collection systems – Validation of simulation of the dynamic interaction between pantograph and overhead contact line" [2]. This standard defines a special benchmark problem and criteria on numerical results in order to validate developed software tools. Currently, new edition of this standard EN 50318:2008 is valid and brings many new requirements on the simulation software. As a results of this standard update, the authors developed the DynPAC 3 software reflecting the substantial changes of the standard. This paper deals with the dynamical analysis of two pantographs running on one catenary system and with the effects of various operational and design parameters on this interaction.

Main components of the catenary system are shown in Fig. 1. Static problems have to be solved in the course of catenary system design. It is affected by a tension of particular wires, by the gravity force acting on the wires and mainly by the length of droppers. The modelling approach used in this paper applies the discretization of the wire by the beam finite

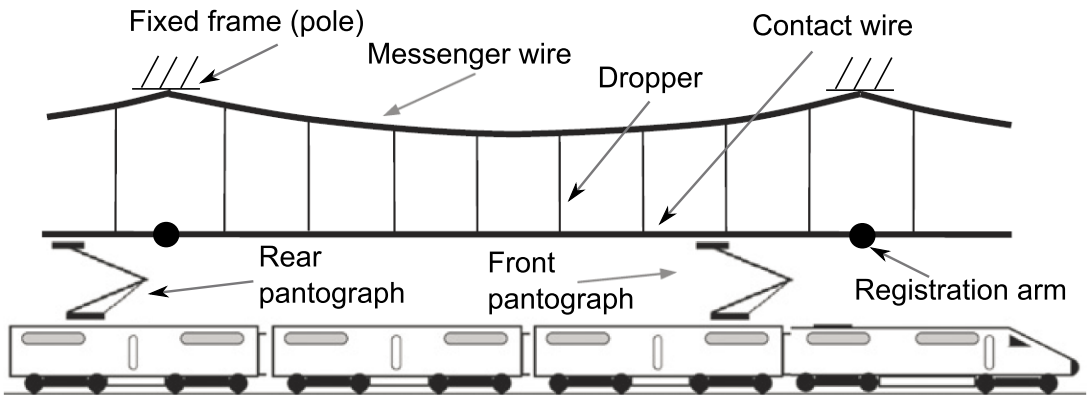

Fig. 1. Scheme of a general pantograph-catenary problem with its main components

elements with two nodes [3] and respecting bending and pretension of the wire. The whole mathematical model of the pantograph-catenary system, which is the basis of the DynPAC software, is assembled in this form

$$\begin{bmatrix} \mathbf{M}_{pF} & \mathbf{0} & \mathbf{0} & \mathbf{0} \\ \mathbf{0} & \mathbf{M}_{pR} & \mathbf{0} & \mathbf{0} \\ \mathbf{0} & \mathbf{0} & \mathbf{M}_{cw} & \mathbf{0} \\ \mathbf{0} & \mathbf{0} & \mathbf{0} & \mathbf{M}_{mw} \end{bmatrix} \begin{bmatrix} \ddot{\mathbf{q}}_{pF} \\ \ddot{\mathbf{q}}_{pR} \\ \ddot{\mathbf{q}}_{cw} \\ \ddot{\mathbf{q}}_{mw} \end{bmatrix} + \begin{bmatrix} \mathbf{B}_{pF} & \mathbf{0} & \mathbf{0} & \mathbf{0} \\ \mathbf{0} & \mathbf{B}_{pR} & \mathbf{0} & \mathbf{0} \\ \mathbf{0} & \mathbf{0} & \mathbf{B}_{cw} & \mathbf{0} \\ \mathbf{0} & \mathbf{0} & \mathbf{0} & \mathbf{B}_{mw} \end{bmatrix} \begin{bmatrix} \dot{\mathbf{q}}_{pF} \\ \dot{\mathbf{q}}_{pR} \\ \dot{\mathbf{q}}_{cw} \\ \dot{\mathbf{q}}_{mw} \end{bmatrix} +$$

$$+ \begin{bmatrix} \mathbf{K}_{pF} & \mathbf{0} & \mathbf{0} & \mathbf{0} \\ \mathbf{0} & \mathbf{K}_{pR} & \mathbf{0} & \mathbf{0} \\ \mathbf{0} & \mathbf{0} & \mathbf{K}_{cw} & \mathbf{0} \\ \mathbf{0} & \mathbf{0} & \mathbf{0} & \mathbf{K}_{mw} \end{bmatrix} \begin{bmatrix} \mathbf{q}_{pF} \\ \mathbf{q}_{pR} \\ \mathbf{q}_{cw} \\ \mathbf{q}_{mw} \end{bmatrix} = \begin{bmatrix} \mathbf{f}_{pF} \\ \mathbf{f}_{pR} \\ \mathbf{0} \\ \mathbf{0} \end{bmatrix} + \begin{bmatrix} \mathbf{0} \\ \mathbf{0} \\ \mathbf{f}_{cw} \\ \mathbf{f}_{mw} \end{bmatrix} + \tag{1}$$

$$+ \begin{bmatrix} \mathbf{0} \\ \mathbf{0} \\ \mathbf{f}_{dr}^{(cw)}(\mathbf{q}_{cw}, \mathbf{q}_{mw}) \\ \mathbf{f}_{dr}^{(mw)}(\mathbf{q}_{cw}, \mathbf{q}_{mw}) \end{bmatrix} + \begin{bmatrix} \mathbf{f}_{c}^{(pF)}(\mathbf{q}_{pF}, \mathbf{q}_{cw}) \\ \mathbf{f}_{c}^{(pR)}(\mathbf{q}_{pR}, \mathbf{q}_{cw}) \\ \mathbf{f}_{c}^{(cwF)}(\mathbf{q}_{pF}, \mathbf{q}_{cw}) + \mathbf{f}_{c}^{(cwR)}(\mathbf{q}_{pR}, \mathbf{q}_{cw}) \\ \mathbf{0} \end{bmatrix}.$$

Variables denoted by $\mathbf{M}$ are mass matrices, $\mathbf{B}$ are damping matrices and $\mathbf{K}$ are stiffness matrices. Vectors $\mathbf{q}$ are vectors of generalized coordinates. Pantographs are indicated by subscript pF for front and pR for rear pantograph. They are represented by lumped models with two or three degrees of freedom according to the standard. Force vectors $\mathbf{f}_{pF}$ and $\mathbf{f}_{pR}$ contains designed uplift forces of pantographs. Finite element matrices of pretensioned wires are denoted by subscripts cw for contact wire and mw for messenger wire. Vectors $\mathbf{f}_{cw}$ and $\mathbf{f}_{mw}$ represent gravity load of the wires, while vectors $\mathbf{f}_{dr}^{(cw)}$ and $\mathbf{f}_{dr}^{(mw)}$ represent nonlinear dropper forces between both wires. The interaction between pantographs and contact wire is described by nonlinear force vectors $\mathbf{f}_c$ with particular superscripts. The contact forces act on the contact wire as a moving load with the defined speed of the train. This huge system of nonlinear equations of motion have to be numerically integrated in time. The implemented software allows to automatically create the finite element mesh of the wires and also to evaluate the important results of the numerical solution with respect to the standard. The simulation results are used for the evaluation of the effects of various operational and design parameters on the contact force, motion of pantographs and vibration of wires.

Acknowledgement

The work was supported from European Regional Development Fund-Project "Research and Development of Intelligent Components of Advanced Technologies for the Pilsen Metropolitan Area (InteCom)" (No. CZ. 02.1.01/0.0/0.0/17_048/0007267).

References

[1] Hajžman, M., Očenášek, J., Benchmark problem for the pantograph and catenary numerical simulations, Proceedings of Colloquium Dynamics of Machines, Prague, Institute of Thermomechanics AS CR, 2014, pp. 37-44.

[2] EN 50318:2002 Railway applications – Current collection systems – Validation of simulation of the dynamic interaction between pantograph and overhead contact line, International Technical Standard, 2002.

[3] Przemieniecki, J. S., Theory of matrix structural analysis, Dover, New York, 1985.

COMPUTATIONAL MECHANICS 2021
36th conference with international participation
Srní
November 8 - 10, 2021

Design, modelling and analysis of concepts of planar serial robots based on tensegrity structures

V. Halamka[a], Z. Šika[a], M. Valášek[a]

[a] *Faculty of Mechanical Engineering, Czech Technical University in Prague, Technická 4, 166 07 Praha, Czech Republic*

The term tensegrity originated from the shortening of the phrase tensional integrity. These are stable structures composed of pressure-stressed elements that do not touch in the case of first-class tensegrities (in higher-class tensegrities, some elements are connected by joints) and a network of tensile-stressed elements. This concept was introduced by the architect Buckminster Fuller in the second half of the 20th century.

The great advantage of these structures, e.g. Fig. 1, is the fact that all elements are stressed only by tension or pressure. Since it is not necessary to dimension the individual elements for bending or torsional stresses, a rigid structure can be achieved by using elements with a lower weight than conventional structures. The load-bearing capacity of the structure is then proportional to the prestressing of the ropes.

The stability of tensegrity does not depend on gravity, which implies the possibility of arbitrary orientation in space. Unlike serial robots, the load is distributed over the entire structure, so there is no accumulation of load at critical points, [1].

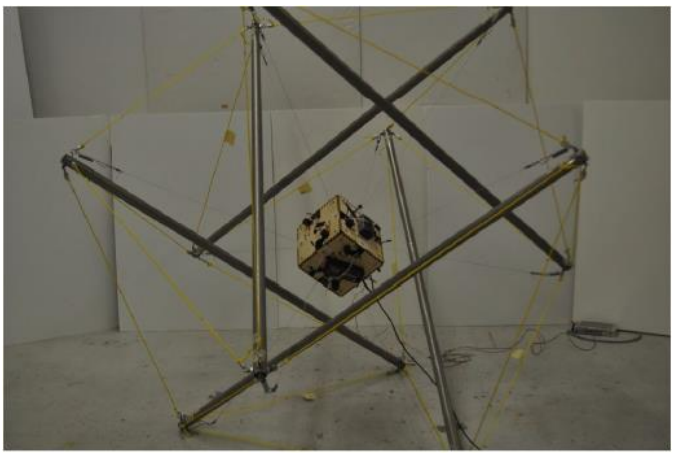

Fig. 1. Super Ball Bot (NASA Ames Research Centre) [5]

At first, tensegrities were used mainly in the art of sculpture and subsequently were introduced in architecture and civil engineering. In these areas, they have been used mainly due to their excellent load-bearing capacity / weight ratio, and the fact that these structures have a minimal area and are therefore able to withstand worse weather conditions is used to advantage in high-rise buildings. Over time they spread to robotics and space industry. By importing the drives that control the prestressing of the elements into tensegrity structures, the concept of mechatronic tensegrity was born, [2].

The deployable tensegrities are most suitable for creating manipulators. These are structures composed of individual modules (stages) that are arranged in series and together form a

tensegrity beam. A great advantage of these structures is the fact that the individual modules can change their length based on the choice of the initial lengths of the ropes. On the contrary, the disadvantage is the need for high prestressing of the ropes to achieve the required bending stiffness, which is a key feature for manipulators, see Fig. 2, [4].

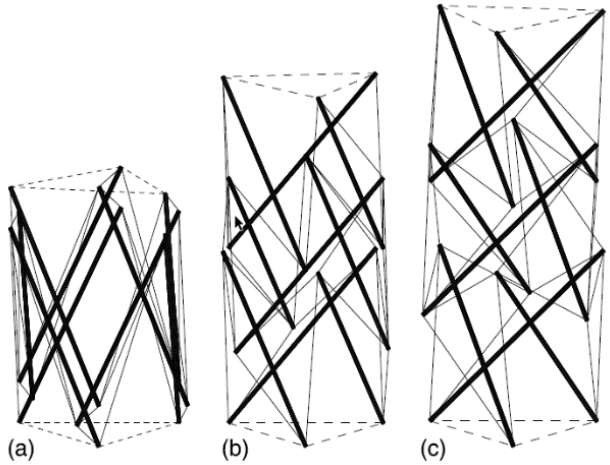

Fig. 2. Deployable tensegrity – 3 stages [3]

The design of individual concepts of planar manipulators can be described as a transition from a common serial robot to a complex tensegrity structure. The first concept (*classic*) is therefore a classic serial robot. In the second concept (*cross*), the drives in the revolute joints are replaced by a parallel connection of cables. The third concept (*tens_rev*) is class 3 tensegrity. This concept allows you to change the length of individual stages based on the choice of cable lengths. The fourth concept (*tens_fix*) reduces the number of cables needed to control the shape of stage by connecting bars into pairs. The last concept (*tens*) is then a complex tensegrity structure, see Fig. 3.

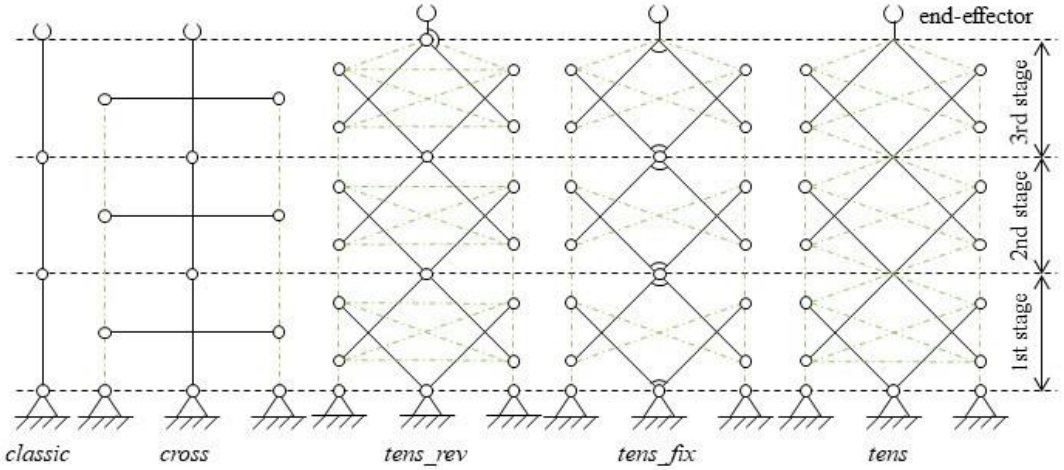

Fig. 3. Sequence of design of planar manipulators

Dynamic models of individual concepts were compiled with the Simscape environment of the program Matlab. This environment allows the direct application of models of physical blocks, which greatly simplifies the compilation of equations and the determination of dynamic properties.

The concept *tens_fix* was chosen for control design, because in contrast to complex tensegrity, the revolute joints between stages allows a greater range of motion and, compared to the concept of *tens_rev*, is less demanding on control. The actual length control was chosen for the system. The free length of cable is controlled by a PID controller based on the difference between the required and the measured length of cable.

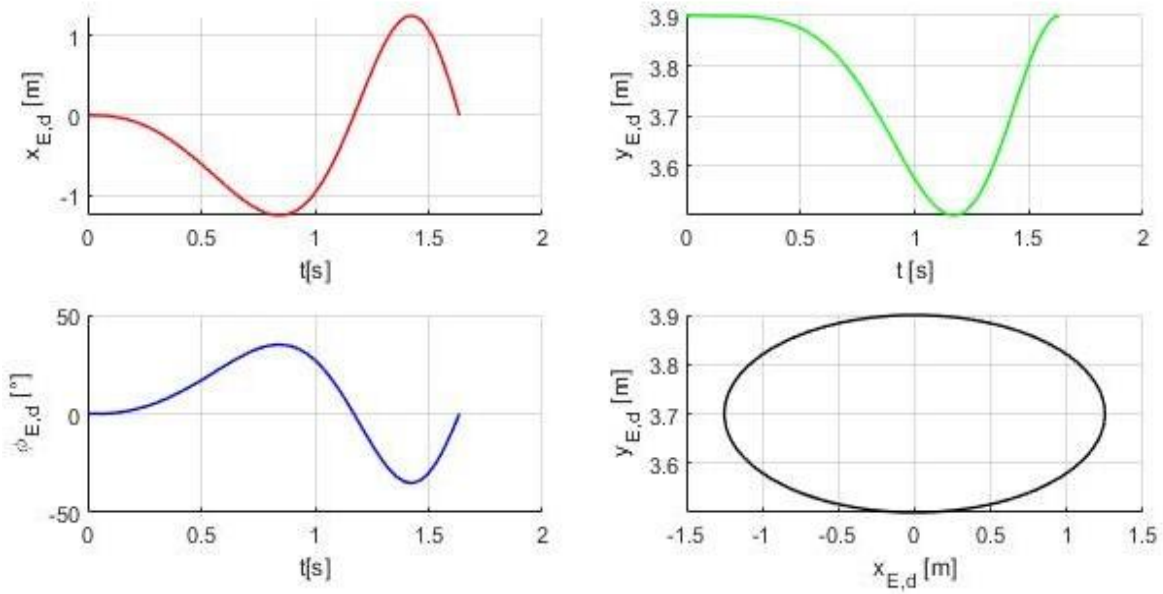

Fig. 4. Trajectory of end-effector E

To demonstrate and optimize the control, the trajectory of the end-effector E of a four-stages robot of the *tens_fix* type shown in Fig. 4 was used. The optimization parameters are then the proportional, integration and derivative gain (k_p, k_i, k_d) of the PID regulators. Due to the large range of parameters, a sensitivity analysis of individual parameters was first performed to determine the starting point of optimization. The target function is defined as the sum of the weight multiples of the position and angle deviations (e_E^x, e_E^y, e_E^ϕ). The *fmincon* function was used for the optimization itself. Fig. 5 shows the end-effector deviations of the optimized system.

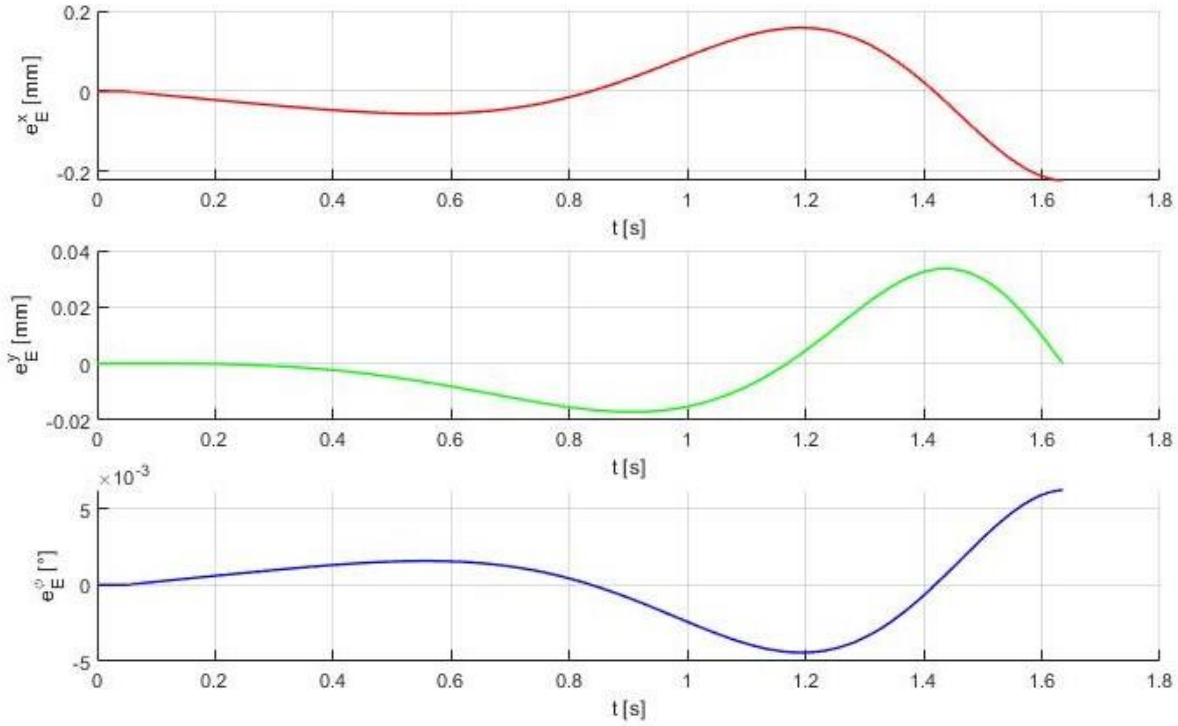

Fig. 5. End-effector deviations of optimized system

Acknowledgements

The work has been supported by the Czech Science Foundation project 20-21893S "Mechatronic tensegrities for energy efficient light robots" and partly by the project SGS19/156/OHK2/3T/12 "Mechatronics and adaptronics 2019" of Czech Technical University in Prague.

References

[1] Balon, A., Optimization and control of mechatronic tensegrity for robotics, master thesis, Czech Technical University, Prague, 2019. (in Czech)
[2] Skelton, R.E., Oliveira, M.C., Tensegrity systems, Springer, 2009. ISBN 978-0-387-74241-0
[3] Sultan, C., Skelton, R.E., Deployment of tensegrity structures, International Journal of Solids and Structures 40 (2003) 4637-4657.
[4] Sultan, C., Tensegrity deployment using infinitesimal mechanisms, International Journal of Solids and Structures 51 (2014) 3653-3668.
[5] SunSpiral, V., Agogino, A., Atkinson, D., Final report phase II, Super Ball Bot - structures for planetary landing and exploration for the NASA innovative advanced concepts (NIAC) program, NASA Ames Research Center, 2019.

COMPUTATIONAL MECHANICS 2021
36th conference with international participation
Srní
November 8 - 10, 2021

Implementation of a modified unified viscoplastic constitutive model

O. Havlíček[a], M. Bartošák[b]

[a]Department of Mechanics, Biomechanics and Mechatronics, Faculty of Mechanical Engineering, Czech Technical University in Prague, Technická 4, 16607 Prague 6, Czech Republic
[b]Department of Mechanics, Biomechanics and Mechatronics, Faculty of Mechanical Engineering, Czech Technical University in Prague, Technická 4, 16607 Prague 6, Czech Republic

A modified unified viscoplastic constitutive material model is proposed for simulating the temperature and time-dependent cyclic behaviour of the material SiMo 4.06. The constitutive model is based on the non-linear kinematic hardening rule of Chaboche, in which several features are added to incorporate strain rate sensitivity, the strain range dependency of the cyclic hardening, static recovery and mean stress evolution. In addition, continuum damage mechanics is incorporated into the constitutive model. This advanced constitutive model is numerically integrated and implemented into a finite element method analysis as well as into the stand-alone code to simulate the strain-controlled uniaxial low-cycle fatigue tests and the uniaxial creep tests.

1. Constitutive model

The constitutive model is based on previous version of this model [2]. The non-linear kinematic hardening rule of Chaboche with static recovery term and mean stress evolution can be expressed as follows:

$$\dot{\boldsymbol{\alpha}}_{\boldsymbol{i}} = \frac{2}{3} C_i \dot{\boldsymbol{\varepsilon}}^{\boldsymbol{pl}} (1 - D) - \gamma_i (\boldsymbol{\alpha}_{\boldsymbol{i}} - \boldsymbol{Y}_{\boldsymbol{i}}) \dot{p} (1 - D) - \gamma_{ri} [J(\boldsymbol{\alpha}_{\boldsymbol{i}})]^{m_i - 1} \boldsymbol{\alpha}_{\boldsymbol{i}} + \frac{1}{C_i} \frac{\partial C_i}{\partial T} \boldsymbol{\alpha}_{\boldsymbol{i}} \dot{T} \,. \quad (1)$$

To capture viscoplastic behaviour, a hyperbolic sine flow rule is chosen [1]

$$\dot{p} = \alpha \sinh\langle \beta f \rangle \,. \quad (2)$$

Strain range dependency of the cyclic hardening is achieved by introducing dependency of isotropic hardening parameter on the plastic strain memory surface radius. Then, continuum damage mechanics is incorporated into the constitutive model in order to simulate the tertiary creep strain responses and to predict fatigue damage evolution under uniaxial loading. Isotropic damage variable is evolved according to [3] as

$$\dot{D} = A \frac{(1 - e^{-q}) \sigma_{eq}^{p}}{q} e^{qD} \,. \quad (3)$$

The scalar isotropic damage model is coupled with the constitutive model through the effective stress relationship. This modified constitutive model has been numerically integrated and implemented into the finite element method analysis and experimentally validated against a broad set of fatigue, creep and fatigue-creep responses under isothermal temperature conditions. In the next section the development of a constitutive model is described for a stand-alone viscoplasticity code.

2. Stress return mapping

The numerical scheme used to integrate the differential equations is an implicit backward Euler method called the radial return method. The numerical scheme leads to a nonlinear scalar algebraic system of equations having scalar unknowns that are solved using a nested solution architecture that employs the gradient-based Newton-Raphson iteration method. Presented issues are related to constitutive model development for a stand-alone viscoplasticity code that introduces concepts related to stress return mapping, which requires stress corrections for the strain driven approach of the radial return method. The same concept is used when solving special case problems in structural analysis, such as plane stress problems. During structural analysis through the finite element method, local and global level numerical iterations are carried out simultaneously through a strain driven approach. In the strain driven approach, all components of strain are prescribed, and stress increments are calculated through local numerical integration for the chosen constitutive model. Global iteration then proceeds by solving the nodal force equilibrium.

In the stand-alone viscoplasticity model, where not all strains components are prescribed, stress correction terms are required. One of the classical examples is a uniaxial strain-controlled loading history. In such case, only one strain increment is prescribed, while the other five components of strain are unknown, but corresponding stress increments are known and equals to zero which is used to modify the numerical scheme according to [4]. A general equation for stress increment of radial return method can be expressed as:

$$\Delta\boldsymbol{\sigma} = \Delta\boldsymbol{\sigma}^{\boldsymbol{tr}} - 2G\Delta\boldsymbol{\varepsilon_p}\,, \tag{4}$$

$$\begin{bmatrix}\Delta\sigma_1\\0\\0\end{bmatrix} = \begin{bmatrix}k_1 & k_2 & k_2\\ k_2 & k_1 & k_2\\ k_2 & k_2 & k_1\end{bmatrix}\begin{bmatrix}\Delta\varepsilon_1\\\Delta\varepsilon_2\\\Delta\varepsilon_3\end{bmatrix} - 2G\begin{bmatrix}\Delta\varepsilon_{p1}\\\Delta\varepsilon_{p2}\\\Delta\varepsilon_{p3}\end{bmatrix}. \tag{5}$$

It should be noted that the elastic matrix is described here by general terms k_1 and k_2. Strain prescriptions $\Delta\varepsilon_2$ and $\Delta\varepsilon_3$ in elastic predictor are not known, hence unknown strain values are taken out and replaced by new trial strain values as follows:

$$\begin{bmatrix}\Delta\sigma_1\\0\\0\end{bmatrix} = \begin{bmatrix}k_1 & k_2 & k_2\\ k_2 & k_1 & k_2\\ k_2 & k_2 & k_1\end{bmatrix}\begin{bmatrix}\Delta\varepsilon_1\\\Delta\varepsilon_2^{tr}\\\Delta\varepsilon_3^{tr}\end{bmatrix} - 2G\begin{bmatrix}\Delta\varepsilon_{p1}\\\Delta\varepsilon_{p2}\\\Delta\varepsilon_{p3}\end{bmatrix} + \begin{bmatrix}k_2\\k_1\\k_2\end{bmatrix}(\Delta\varepsilon_2 - \Delta\varepsilon_2^{tr}) + \begin{bmatrix}k_2\\k_2\\k_1\end{bmatrix}(\Delta\varepsilon_3 - \Delta\varepsilon_3^{tr})\,. \tag{6}$$

New trial strain values correspond to the pure elastic loading and can be directly obtained from Hooke's law. The third and the fourth correction terms on the right side of Eq. (3) can be modified. By setting $\boldsymbol{q} = \boldsymbol{s} - \boldsymbol{a}$ and $J_q = J(\boldsymbol{s} - \boldsymbol{a})$ increment of plastic deformation can be expressed as

$$\Delta\boldsymbol{\varepsilon_p} = \frac{3}{2}\Delta p\,\frac{\boldsymbol{q}}{J_q}\,. \tag{7}$$

Stress update equation can be now derived from equations (3) and (4) in deviatoric form as

$$\boldsymbol{s} = \boldsymbol{s}^{\boldsymbol{tr}} - 2G\Delta\boldsymbol{\varepsilon_p} + \frac{\Delta p}{J_q}\boldsymbol{s_{cor}}\,. \tag{8}$$

Subtracting backstress from both sides of the equation (5) leads to the final equation (to simplify the equation, basic backstress without static recovery term and mean stress evolution term is used)

$$\boldsymbol{q} = \boldsymbol{s} - \boldsymbol{a} = \frac{\boldsymbol{s}^{\boldsymbol{tr}} - \sum_{i=1}^{N}\frac{\boldsymbol{a_{n,i}}}{1+\gamma_i\Delta p} + \frac{\Delta p}{J_q}\boldsymbol{s_{cor}}}{1+\frac{\Delta p}{J_q}\left(3G+\sum_{i=1}^{N}\frac{C_i}{1+\gamma_i\Delta p}\right)}\,. \tag{9}$$

The equation (6) is a non-linear equation because the correction term $\boldsymbol{s_{cor}}$ contains unknown $\boldsymbol{q = s - a}$ and is updated iteratively. This means that in the stand-alone code with the correction terms, convergence of $\boldsymbol{q}$ must be checked as well. After the whole numerical procedure is done, unknown strain components can be determined. The rest of the numerical scheme will proceed according to the standard method.

Stand-alone code has been created for this model to simulate the strain-controlled uniaxial fatigue and the stress-controlled uniaxial creep responses. Stand-alone codes have been incorporated into the optimization procedure based on least-squares method to determine material parameters of the model. Results were checked against the finite element method analysis.

3. Conclusion

The modified unified viscoplastic constitutive material model is proposed for simulating the temperature and time-dependent cyclic behaviour of the material SiMo 4.06. This advanced constitutive model is numerically integrated and implemented into a finite element method analysis as well as into the stand-alone code to simulate the strain-controlled uniaxial low-cycle fatigue tests and the uniaxial creep tests. Stand-alone codes have been incorporated into the optimization procedure to determine material parameters of the model.

Acknowledgement

The authors acknowledge support from the Grant Agency of the Czech Technical University in Prague, No. SGS21/150/OHK2/3T/12.

References

[1] Barrett, P.R., Hassan, T., A unified constitutive model in simulating creep strains in addition to fatigue responses of Haynes 230, International Journal of Solids and Structures 185-186 (2020) 394-409.
[2] Bartošák, M., Španiel, M., Doubrava, K., Unified viscoplasticity modelling for a SiMo 4.06 cast iron under isothermal low-cycle fatigue-creep and thermo-mechanical fatigue loading conditions, International Journal of Fatigue 136 (2020) 105566.
[3] Liu, Y., Murakami, S., Damage localization of conventional creep damage models and proposition of a new model for creep damage analysis, JSME International Journal Series A 41 (1) (1998) 57-65.
[4] Nazrul, I., Advanced constitutive model development for structural integrity analysis, Dissertation thesis, North Carolina State University, 2018.

COMPUTATIONAL MECHANICS 2021
36th conference with international participation
Srní
November 8 - 10, 2021

Eulerian-Lagrangian and Eulerian-Eulerian approaches for the simulation of particle-laden free surface flow

V. Heidler, O. Bublík, A. Pecka

NTIS – New Technologies for the Information Society, Faculty of Applied Sciences, University of West Bohemia, Univerzitní 8, 301 00 Plzeň, Czech Republic

This paper studies the Eulerian-Lagrangian and Eulerian-Eulerian approaches for the simulation of free surface flow with particles. The study of free surface flows with immersed particles is of high importance across various fields in industry, such as hydraulic, ocean, environmental engineering or casting, which this work is focused on. In the casting manufacturing process, the design of the casting mould is essential. Based on the geometry of the mould, inlets and outlets need to be positioned such that the molten material fills in the mould completely. Computational modelling becomes an efficient tool for predicting the casting process, where also fillers are embedded in molten material for the improvement of its mechanical properties.

To computationally resolve the free surface flow with immersed particles within a thin casting mould cavity, a computational grid with numerous cells is often required. Thus, the numerical simulation becomes expensive in terms of computational time and memory demands. In order to address these issues, the lattice Boltzmann method (LBM) has been chosen, as it is well suited for massive parallelization on various architectures while its algorithm is very efficient.

For the free surface tracking in simulations, a method similar to Volume of Fluid (VOF) method is employed. VOF is widely used in Navier-Stokes solvers and a very influential paper concerning VOF LBM is, e.g., [3, 5]. In our applications, the effect of the gaseous phase is negligible. For these reasons, the gaseous phase is ignored in this study.

For fluid-particle interaction, the particulate immersed boundary method (PIBM) [1] is adopted. It is similar to the traditional immersed boundary method (IBM), which only assumes the mesh resolution much smaller than the particle size and imposes velocity boundary condition on the particle surface. However, many applications including casting with fillers involve numerous tiny particles. Therefore, the PIBM, allows particles to be much smaller than grid resolution and the fluid-particle interaction behaviour is corrected by introducing the fluid-particle slip velocity.

In general, particles submerged in a fluid can be described using the Lagrangian or the Eulerian approach. In the Lagrangian approach, each of the particles has its own coordinates and its own equations of motion. In the case of the Eulerian approach, the particles are described statistically by a function of particle concentration, the time evolution of which is described by a convection-diffusion equation, see [4]. In Fig. 1, as an example of a comparative test case, the results obtained by Eulerian-Lagrangian and Eulerian-Eulerian LB schemes and the results taken from [2] are shown next to each other. The Reynolds number in this simulation is set to 1 000 and 5 000 particles are randomly distributed inside the three-dimensional cavity. The results are in very good agreement, but the Eulerian-Eulerian approach has one big advantage. The computational complexity does not depend on the number of simulated particles. In contrast, the computational complexity increases with the number of modelled particles in case of

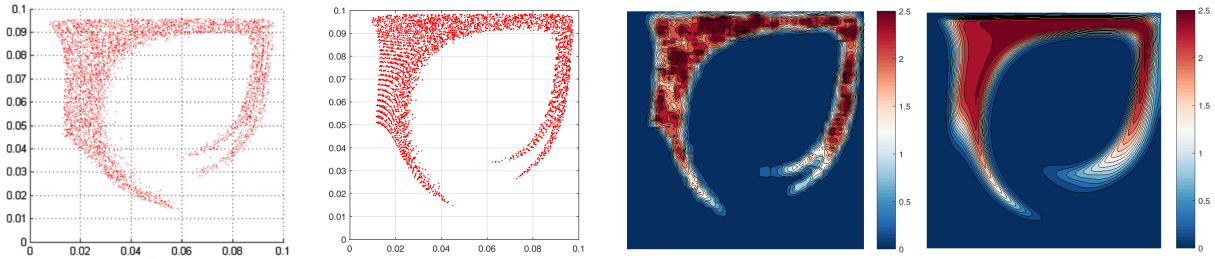

(a) (b) (c) (d)

Fig. 1. Distribution of particles within 3D cavity. Individual particles (a) are shown for the results taken from [2]. Both individual particles (b) and concentration (c) are shown for results by the Eulerian-Lagrangian LB scheme. Only concentration (d) is show in the case of the Eulerian-Eulerian LB scheme. In both cases, concentration is summed along the z-axis

the Eulerian-Lagrangian approach. This fact is important for simulations with many particles such as gravity casting with fillers.

A test case concentrating on more practical problems similar to those encountered in gravity casting with fillers is presented in Fig. 2. Here, the free surface is modelled as well. The reservoir on the top of the mould is filled by fluid with density $\varrho = 1000\,\mathrm{kg\,m^{-3}}$ and the kinematic viscosity $\nu = 10^{-4}\,\mathrm{m^2\,s^{-1}}$ and partially filled by evenly distributed particles (red color) with diameter $d_p = 2 \times 10^{-4}\,\mathrm{m}$ and density $\varrho_p = 5000\,\mathrm{kg\,m^{-3}}$. At time $t = 0$, the gate is removed and the fluid with the dispersed particles fills the mould as it is pulled by gravity downwards.

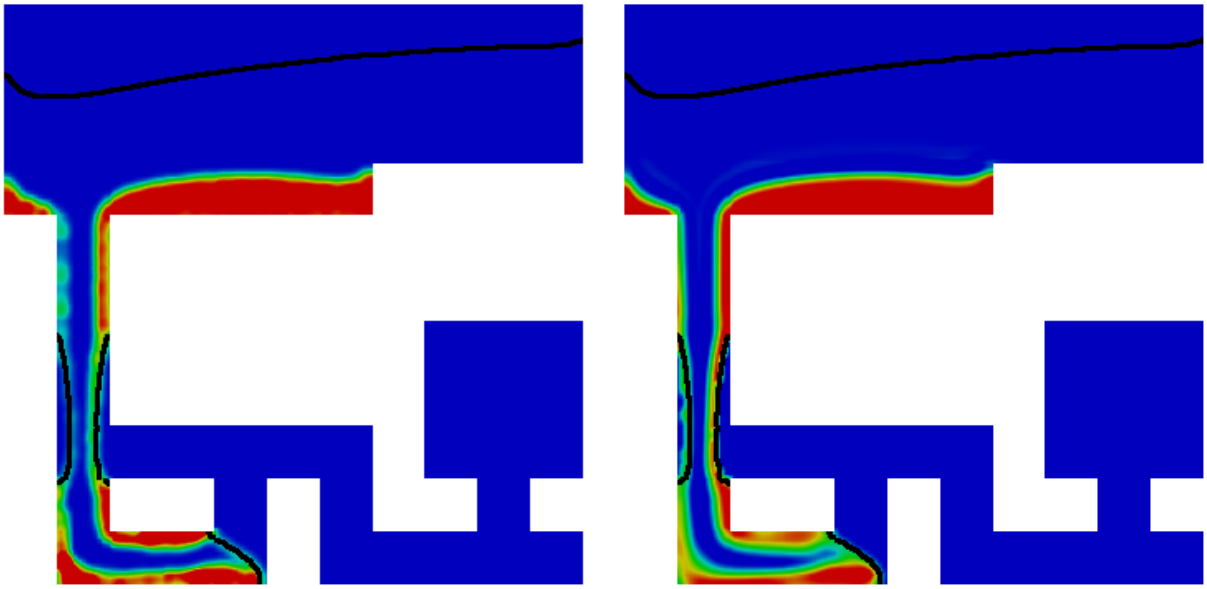

Fig. 2. Particle concentration obtained by the Eulerian-Lagrangian (*left*) and Eulerian-Eulerian (*right*) schemes at simulation time $t = 0.5\,\mathrm{s}$

In this work, Eulerian-Lagrangian and Eulerian-Eulerian lattice Boltzmann (LB) schemes were developed and compared. The main target of this work is to validate the Eulerian-Eulerian approach developed for the solution of the free surface flows with dispersed particles against the Eulerian-Lagrangian approach, considered as a reference solution. The solutions by the fully Eulerian LB scheme is more smeared but the agreement is more than satisfactory.

Acknowledgement

The authors appreciate the kind support of the student grant project SGS-2019-009.

References

[1] Habte, M. A., Wu, C., Particle sedimentation using hybrid lattice Boltzmann-immersed boundary method scheme, Powder Technology 315 (2017) 486-498.

[2] Safdari, A., Kim, K., Lattice Boltzmann simulation of solid particles behavior in a three-dimensional lid-driven cavity flow, Computers and Mathematics with Applications 68 (5) (2014) 606-621.

[3] Thürey, N., Physically based animation of free surface flows with the lattice Boltzmann method, Ph.D. Thesis, University of Erlangen–Nuremberg, Erlangen, 2007.

[4] Trunk, R., Henn, T., Dörfler, W., Nirschl, H., Krause, M. J., Inertial dilute particulate fluid flow simulations with an Euler-Euler lattice Boltzmann method, Journal of Computational Science 17 (2016) 438-445.

[5] Vimmr, J., Lobovský, L., Bublík, O., Mandys, T., Experimental validation of numerical approach for free surface flows modelling based on lattice Boltzmann method, Proceedings of the 6th European Conference on Computational Mechanics: Solids, Structures and Coupled Problems (ECCM 2018), Glasgow, 2020, pp. 2211-2222.

COMPUTATIONAL MECHANICS 2021
36th conference with international participation
Srní
November 8 - 10, 2021

Design of experimental transsonic axial compressor

D. Hermann, J. Klesa

[a] *Faculty of Mechanical Engineering, Czech Technical University in Prague, Technická 4, 160 00 Prague, Czech Republic*

1. Introduction

Axial compressors are a widely used today. This is principally due to their high efficiency and high compression in multi-stage arrangements. The requirement for a multi-stage arrangement to achieve a large pressure rise, making them complex and expensive relative to other designs (e.g., centrifugal compressors). Axial compressors are also sensitive to surging so it is necessary to operate these compressors under the correct operating conditions [2].

2. Blade profile

These are transsonic profiles for axial compressors designed by Jan Klesa [3] for a design Mach number of 0.8 (Fig. 1). The individual profiles are based on explicit geometric rules and are designed to have properties comparable to controlled diffusion airfoils (CDA). It is planned to use them for the design of a compressor for the secondary circuit of a gas-cooled nuclear reactor being developed under the KOBRA programme.

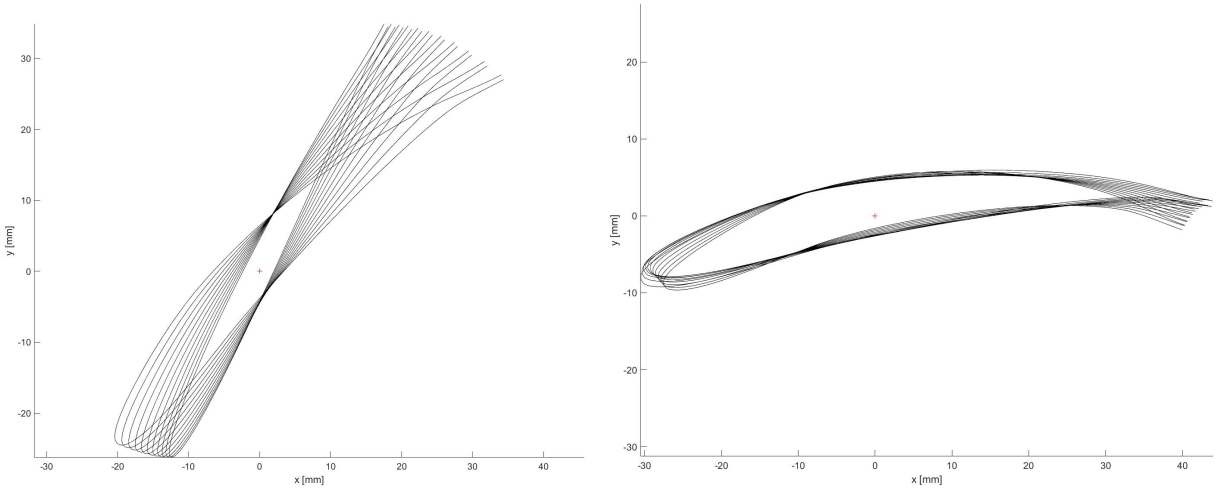

Fig. 1. Sections along the rotor blade height (*left*), sections along the stator blade height (*right*)

3. Structural compressor design

The experimental compressor will be designed as a single stage compressor and will be used to verify the characteristics of designed profiles. The compressor is driven by a 200 kW electric motor at 8000 rpm, and the rotor is supported by rolling ball bearing. The main design parameters are as follow: hub diameter 330 mm, shroud diameter 660 mm, mass flow 38.88 kg/s. The

rotor blades is composed of sandwich design consisting of a carbon composite with a foam core. The flanges will be of pre-impregnated unidirectional carbon fabric, the cover of pre-impregnated plain weave fabric.

4. CFD calculation

A model of the flow path was created to enable the creation of the mesh. The mesh was made up of unstructured tetrahedra and only on the surface of the blades was the mesh refined and structured to capture the boundary layer processes, Fig. 2. The total number of elements of the mesh is 1 265 390.

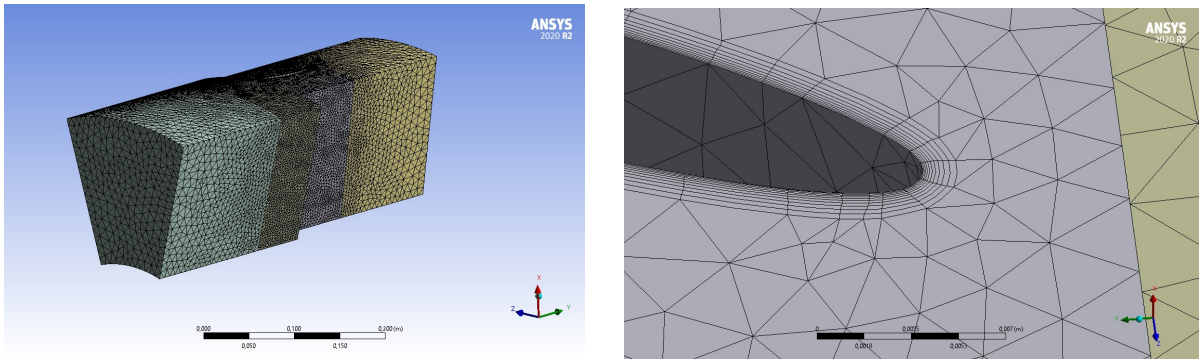

Fig. 2. View of the overall mesh (*left*), view of the detailed mesh on the stator leading edge (*right*)

For a single axial flow compressor the most commonly used the Mixing Plane Model [1]. The following parameters were used in the calculation: k-ω SST model, which is one of the most widely used models for simulating turbulent types of flow, ideal gas with Sutherland viscosity model as working gas. The inlet and outlet conditions correspond to the international standard atmosphere at 0 m altitude. A mixing plane were used to model the rotor-stator interface and the pressure-based solver for calculate a solution (Figs. 3 and 4).

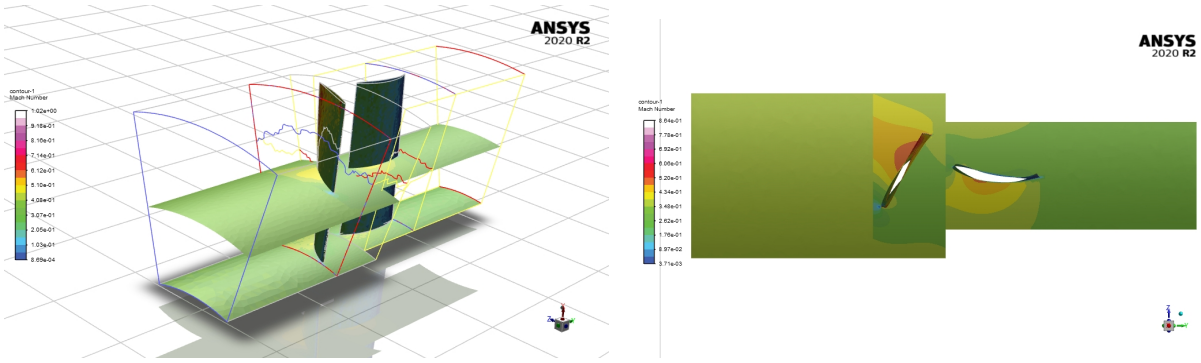

Fig. 3. Mach number distribution on the rotor blade, stator, hub and middle section (*left*), Mach number distribution on detailed middle section (*right*)

5. Conclusion

To explore the possibilities of use the new transsonic airfoil a single stage axial compressor was designed. A model of this compressor was computed using CFD solver and the flow do not exhibit undesirable phenomena such as pressure surges or flow separation at the blade surface.

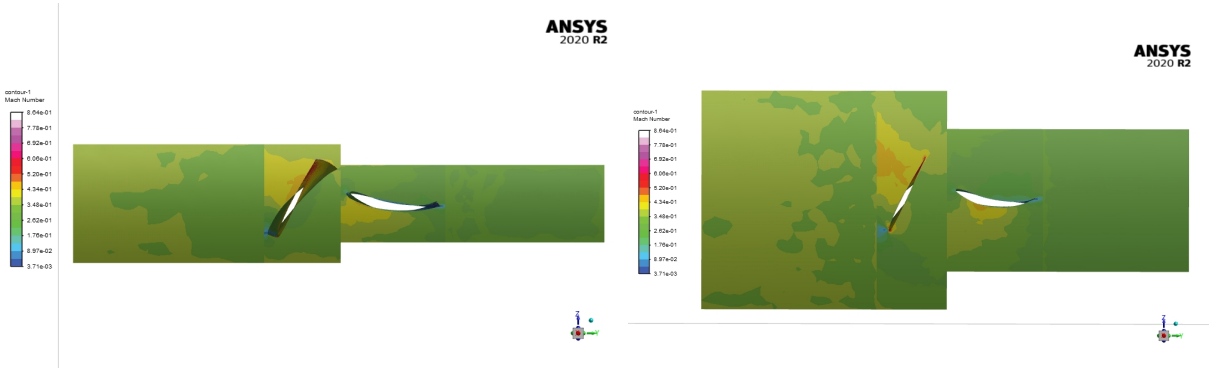

Fig. 4. Mach number distribution on detailed hub section (*left*), Mach number distribution on detailed shroud section (*right*)

Acknowledgement

This work was supported by the Technology Agency of the Czech Republic, project TK03030121 Conceptual Design of an Innovative Safety System for Gas-cooled Nuclear Reactors.

References

[1] ANSYS Inc., ANSYS Fluent tutorial guide, Release 17, 2016.

[2] Cumpsty, N. A., Compressor aerodynamics, Krieger, Malabar, 2004.

[3] Klesa, J., Aerodynamic design of transsonic compressor airfoil family, Proceedings of the 36th conference with international participation Computational Mechanics, Srní, University of West Bohemia, 2021.

COMPUTATIONAL MECHANICS 2021
36th conference with international participation
Srní
November 8 - 10, 2021

Form-finding of tensegrity structures based on defined topology and following semi-automatic creation of corresponding Simscape models

M. Hrabačka[a], R. Bulín[b]

[a] Department of Mechanics, Faculty of Applied Sciences, University of West Bohemia, Univerzitní 8, 301 00 Plzeň, Czech Republic
[b] NTIS – New Technologies for the Information Society, Faculty of Applied Sciences, Technická 8, 301 00 Plzeň, Czech Republic

Solving a problem of form-finding of a free-standing tensegrity structure means to determine spatial configuration of the structure based on defined topology and to determine members pre-stress forces. In most cases, it is also required that the final structure configuration meets the criteria of so called super-stability [3]. There are various suitable approaches for tensegrity form-finding that lead to stable configuration, see [1]. In this work, the Adaptive force density method (AFDM) presented by [2] is used. This method is further modified so that it is possible to assign altitude to arbitrary number of structure nodes.

In the first design stage, feasible force density vector $\mathbf{q}$ is searched for. The vector $\mathbf{q}$ consists of force densities $q_i = \frac{F_i}{l_i}$ of all members, F_i is an internal force in i-th member and l_i is its length. These force densities have to satisfy the necessary condition for super-stability and the non-degeneracy condition for free-standing structures. In d-dimensional space, they can be combined into one requirement: force density matrix $\mathbf{E} = \mathbf{E}(\mathbf{q}, \mathbf{C})$ [3], where $\mathbf{q}$ is a vector of force densities and $\mathbf{C}$ is a connectivity matrix defining topology, must have $d + 1$ zero eigenvalues and all other eigenvalues positive. Because the target is to get an explicit value of some eigenvalues, eigenvalue analysis and spectral decomposition of matrix $\mathbf{E}$ is applied. According to the condition mentioned above, some of detected eigenvalues λ_i are modified so a new set of eigenvalues λ_i^{mod} is created, eigenvectors $\mathbf{v}_i$ remain unchanged. Based on these sets λ_i^{mod} and $\mathbf{v}_i$, a new force density matrix $\overline{\mathbf{E}}$ can be found. When eigenvalues $\overline{\lambda}_i$ of the matrix $\overline{\mathbf{E}}$ are discovered, they probably will not be the same as pre-assigned set of eigenvalues λ_i^{mod} from the last step. But if these steps are repeated, difference between sets λ_i^{mod} and $\overline{\lambda}_i$ will fall to low values after a sufficient number of iterations. So if the difference falls below a specified tolerance, the new force density matrix $\overline{\mathbf{E}}$ is declared as the force density matrix $\mathbf{E}$ that meets the specified requirements.

In the second design stage, self-equilibrated configuration of the tensegrity is determined. By solving the system

$$\begin{bmatrix} \mathbf{E} & \mathbf{0} & \mathbf{0} \\ \mathbf{0} & \mathbf{E} & \mathbf{0} \\ \mathbf{0} & \mathbf{0} & \mathbf{E} \end{bmatrix} \begin{bmatrix} \mathbf{x} \\ \mathbf{y} \\ \mathbf{z} \end{bmatrix} = \mathbf{H}\mathbf{X} = \mathbf{0}, \tag{1}$$

where $\mathbf{x}, \mathbf{y}, \mathbf{z}$ are coordinates of all nodes in each direction, a super-stable configuration without possibility of controlling altitude of nodes can be discovered.

If specific altitude of some nodes is required, additional equations are added

$$\mathbf{A}\mathbf{z} = \mathbf{b}, \tag{2}$$

where matrix $\mathbf{A}$ (containing only zeros and ones) informs which nodes have pre-assigned altitude and vector $\mathbf{b}$ specify altitude of selected nodes. By combining systems (1) and (2), it can be written that

$$\begin{bmatrix} \mathbf{E} & \mathbf{0} & \mathbf{0} \\ \mathbf{0} & \mathbf{E} & \mathbf{0} \\ \mathbf{0} & \mathbf{0} & \mathbf{E} \\ \mathbf{0} & \mathbf{0} & \mathbf{A} \end{bmatrix} \begin{bmatrix} \mathbf{x} \\ \mathbf{y} \\ \mathbf{z} \end{bmatrix} = \widehat{\mathbf{H}}\mathbf{X} = \widehat{\mathbf{b}}. \tag{3}$$

This is the final system of equations that is numerically solved and the solution provides self-equilibrated configuration of the tensegrity.

Overall, outputs from the modified AFDM are coordinates $\mathbf{x}, \mathbf{y}, \mathbf{z}$ of all nodes and force densities $\mathbf{q}$ in all members.

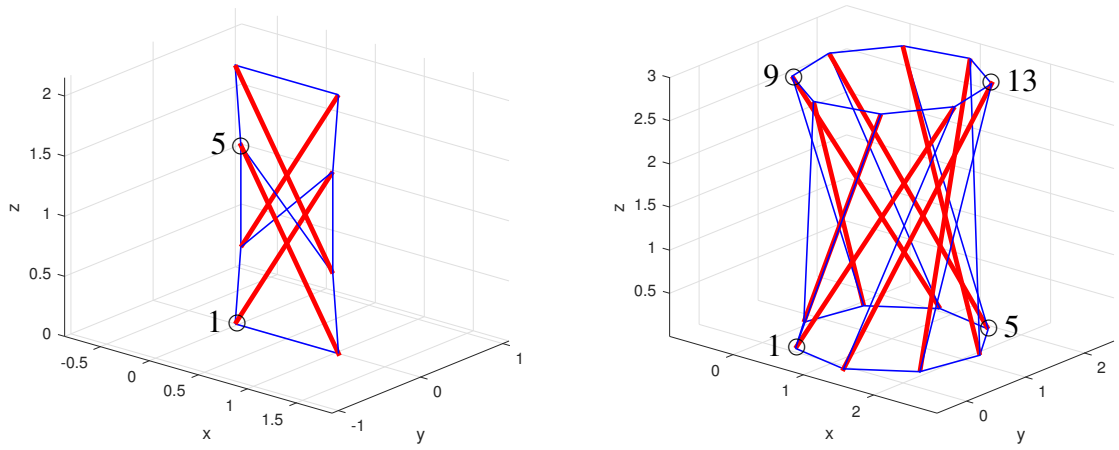

(a) a 2-D tensegrity

(b) a 3-D tensegrity

Fig. 1. Examples of super-stable tensegrity structures

In Fig. 1, two examples of tensegrity structures can be seen. Their configuration was determined by the modified AFDM. In case of the 2-D tensegrity in Fig. 1a, altitude equal to 0 in the node no. 1 and altitude equal to 1.5 in the node no. 5 was required. In case of the 3-D tensegrity in Fig. 1b, altitude equal to 0 in the nodes no. 1 and 5 and altitude equal to 3 in the nodes no. 9 and 13 was required at the same time. Resulting structures meet all requirements for altitude and super-stability (verified by a simulation).

Based on calculated force densities in structure members and coordinates of nodes, a model in the Simscape software (SIMULINK environment) is generated using MATLAB script. The program is able to compile a 2-D or a 3-D tensegrity model of any class but the tensegrity can only consist of 1-D elements (cables, struts). The core of the MATLAB script creating Simscape models consists of invocations of functions *add_block()* and *add_line()* that adds a specified SIMULINK-like block or connects existing blocks together.

Most important features of the resulting model in Simscape are these facts: struts are modelled as thin rigid cylinders, cables are massless – they represent one-sided viscoelastic forces between two nodes. It is intended to model a tensegrity as a structure lying on a flat surface, so the node with the lowest altitude is connected to the ground by a spherical joint, remaining nodes with the same altitude are connected to the ground by planar constraints, other nodes can move freely.

Fig. 2. Example of a Simscape model of a super-stable 3-D tensegrity

In Fig. 2, a visualisation of the Simscape model is depicted, it represents the same 3-D tensegrity as in Fig. 1b. The visualisation does not offer a possibility to show cables but struts can be observed clearly.

The whole methodology allows fast generation of stable spatial tensegrity computational models that can be further analysed from the viewpoint of mechanical properties, such as overall stiffness and modal properties. The resultant tensegrity structures usually reach good strength to weight ratio and they can be used as substructures of special robotic manipulators. On the one hand, described concept of the modified AFDM does not take the weight of members into account, which may be considered as a disadvantage. On the other hand, the structure consists only of thin struts and massless cables so deviation of total structure mass from originally considered massless state is relatively small. The essence of super-stable structures is that they remain stable even when a slight deviation of structure parameters occurs.

Acknowledgements

This research work was supported by project SGS-2019-009 of the Czech Ministry of Education, Youth and Sport, and by the Czech Science Foundation project number 20-21893S.

References

[1] Juan, S. H., Tur, J. M. M., Tensegrity frameworks: Static analysis review, Mechanism and Machine Theory 43 (2008) 859-881.

[2] Zhang, J. Y., Ohsaki, M., Adaptive force density method for form-finding problem of tensegrity structures, International Journal of Solids and Structures 43 (2006) 5568-5673.

[3] Zhang, J. Y., Ohsaki, M., Tensegrity structures: Form, stability, and symmetry, Springer, Tokyo, Japan, 2015.

COMPUTATIONAL MECHANICS 2021
36th conference with international participation
Srní
November 8 - 10, 2021

Aerodynamic wind tunnel testing of U-beams

S. Hračov[a], M. Macháček[a]

[a] *Institute of Theoretical and Applied Mechanics, Czech Academy of Sciences, Prosecká 76, 19000 Prague, Czech Republic*

The proposed paper presents the outcomes from the experimental aerodynamic testing of the slender beams with U-shaped cross section, which is typical e.g., for conveys, the bridge decks with the wind barriers or the footbridges with the railings. In particular, two sets of six U - beams having identical ratio of the along-wind to the across-wind dimension *B/D* = 2:1, but different porosity and depth of their U-shaped cross sections were analysed in order to determine their potential galloping susceptibility. The tests were carried out in the smooth flow conditions in the closed-circuit climatic wind tunnel of ITAM AS CR in Telč in the Czech Republic. The assessment of the proneness was performed based on the quasi-steady theory [3], i.e. on the analysis of a sign of a slope of the experimentally obtained transverse force coefficient, C_{Fy}, around the zero angle of the wind attack, α.

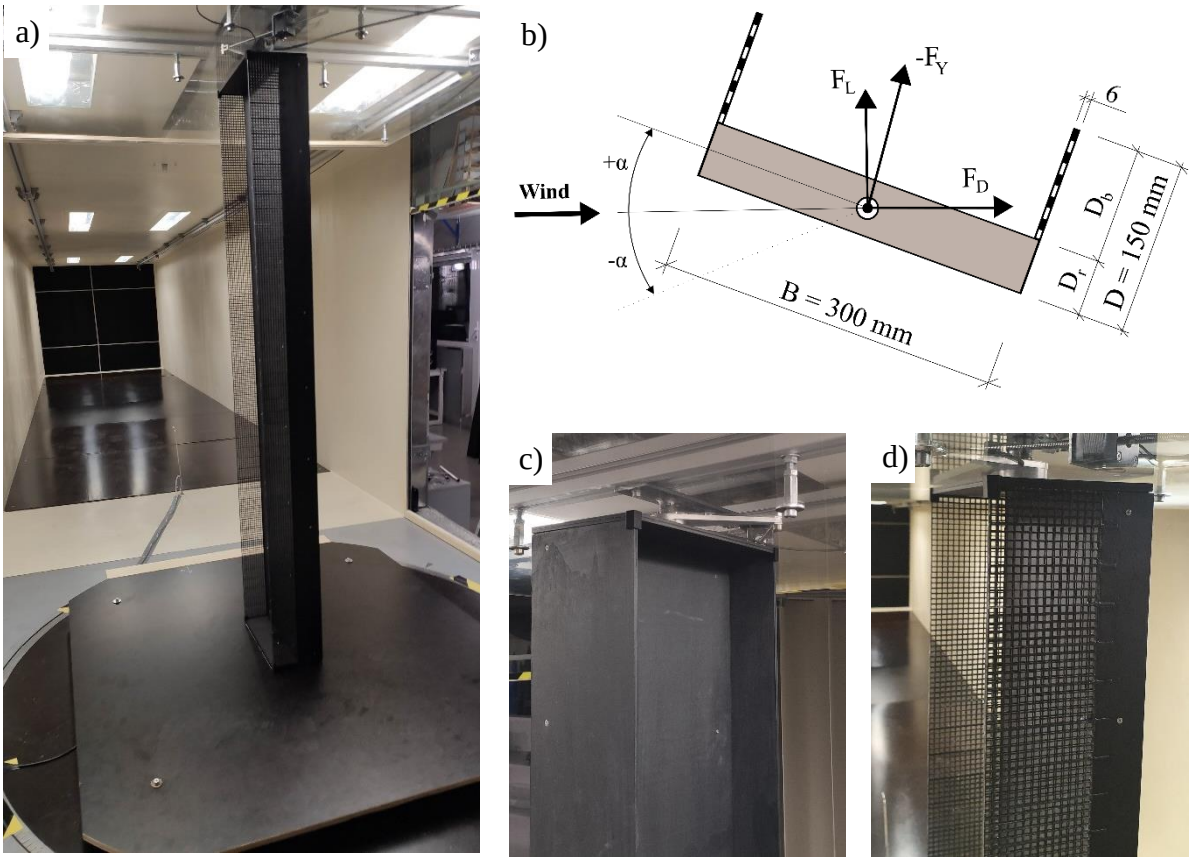

Fig. 1. (a) Photo of the porous U-shaped beam in the wind tunnel (B/D_r = 4:1, p= 75%), (b) Schema of the U-profile, (c) Snapshot of the non-porous U-profile (B/D_r = 4:1), (d) Snapshot of the U-profile (B/D_r = 6:1) with porosity p = 75%

All 160 cm long experimental specimens (beams) were assembled from a wooden rectangular prism and a pair of the plastic flanges. The basic geometry and dimensions of their U-shaped cross section are schematically depicted in Fig. 1b. The first set of six U-beams was constructed from the rectangular prism with B/D_r = 4:1, thus had the depth, D_b, equal to one-fourth of the width, B. For the second set of U-beams, which was characterized by D_b equal to one third of B, the rectangular prism with B/D_r = 6:1 was used. The individual U-beams in each set differed only in the level of the flange porosity. In total five levels of porosity ranging from 0 % to almost 100 % were analysed. The flanges were built from two plastic nets with certain degree of porosity that were glued onto the frontal and rear sides of a tiny plastic frame. All nets had an axial 7 mm square grid. For comparison purposes, also the rectangular prisms with side ratios B/D = 2:1, 4:1 and 6:1 and specimens with the attached frame only, i.e., without the nets, were tested.

All models were placed vertically into the measuring part of the aerodynamic test section of the wind tunnel, which is 1.9 m wide and 1.8 m high. The models were enclosed between wooden and plastic end-plates to enforce bidimensional flow conditions, see Fig. 1a. Two load cells ATI Industrial Automation sensors Mini 40 were used for measuring the aerodynamic drag and lift forces F_L and F_D caused on the bodies of the specimens by the wind load for the angles of wind attack, α, in the range from -15° to +15°. These sensors were fixed to the upper and lower ends of the specimens and to the specially designed synchronized rotation mechanisms, that enabled rotation of the specimens with the very small angular step, $\Delta\alpha = 0.2°$. Thus, the alternation of aerodynamic forces with the changing angle, α, can be detected very precisely. The data from the sensors were recorded for 60 seconds, which revealed as sufficient with respect of the ergodicity and stationarity of the process, with a sampling frequency f_s = 1000 Hz. All wind tunnel tests were conducted in a nominal smooth flow with minimal turbulence intensity around 1%. The independence of the aerodynamic force coefficients on the Reynolds number, Re, was successfully verified for wind velocity ranging from 4 ms^{-1} to 19 ms^{-1}. The tests were finally performed at a wind speed of about 14 m/s, i.e., corresponding to $Re = 2.8e^5$ normalized using along-wind dimension, B. Due to a higher blockage of the wind tunnel in the range of 7.9 % to 11.7 % depending on simulated angle of the wind attack, the corrections of the measured wind speeds, which was based on a comparison of the results of CFD simulations and measurements, were incorporated.

At first, the drag and lift coefficients, C_D and C_L, were evaluated from the mean values of the measured drag and lift forces, F_D and F_L, for all angles of wind attack according their definition, see e.g. [2]. The values of transverse force coefficient, C_{Fy}, were subsequently calculated from C_D and C_L based on the geometrical relations, see Fig. 1b or [2]. In Fig. 2 the obtained transverse force coefficient, C_{Fy}, is reported against the angle of attack for all analysed profiles. The upper graph of this figure is related to the set of beams with higher D_b, while the lower graph to the set of beams with lower D_b. All results are in these graphs normalized to the same height D = 150 mm.

The positive slope of C_{Fy} around zero angle of attack represents a necessary condition for galloping proneness of analysed profile [3]. The value of this slope corresponds also to the galloping stability parameter a_g [1], which is used for calculation of the onset galloping velocity. In engineering practise, the values of C_{Fy} are usually not explicitly determined as in this study and the coefficient a_g is calculated from the values of C_D and C_L according to formula

$$a_g = \frac{dC_{FY}}{d\alpha}\Big|_{(\alpha=0°)} = -\left(\frac{dC_L}{d\alpha} + C_D\right)\Big|_{(\alpha=0°)}. \quad (1)$$

This approach for evaluation of a_g was also adopted here. The value of the slope of C_L around zero angle was obtained by linear approximation of the values in the angular interval ranging from -1° to +1°. The only exception represented the beam with B/D_r = 6:1 and flange porosity

p = 75%, where only angular range from -0.5° to +0.5° was used. It must be noted, that a negative slope of the lift coefficient, C_L, around zero angle of the wind attack represents a necessary condition for possibility of the galloping proneness. The negative slope of C_L was determined for the rectangular prism with SR = 2, for all U-beams with flange porosity up to and including 75% and also for U-beam given by B/D_r = 4:1 and p = 90%. The values of the slope of C_L and C_D corresponding to the zero angle of wind attack are presented for all tested bodies in Table 1. Moreover, in this table also the galloping stability parameter, a_g, and the intervals of angles of attack around zero angle, $\Delta\alpha_{IP}$, for which C_{FY} has the positive slope, are given. Generally, the wider this interval is, the higher response of the body can be expected.

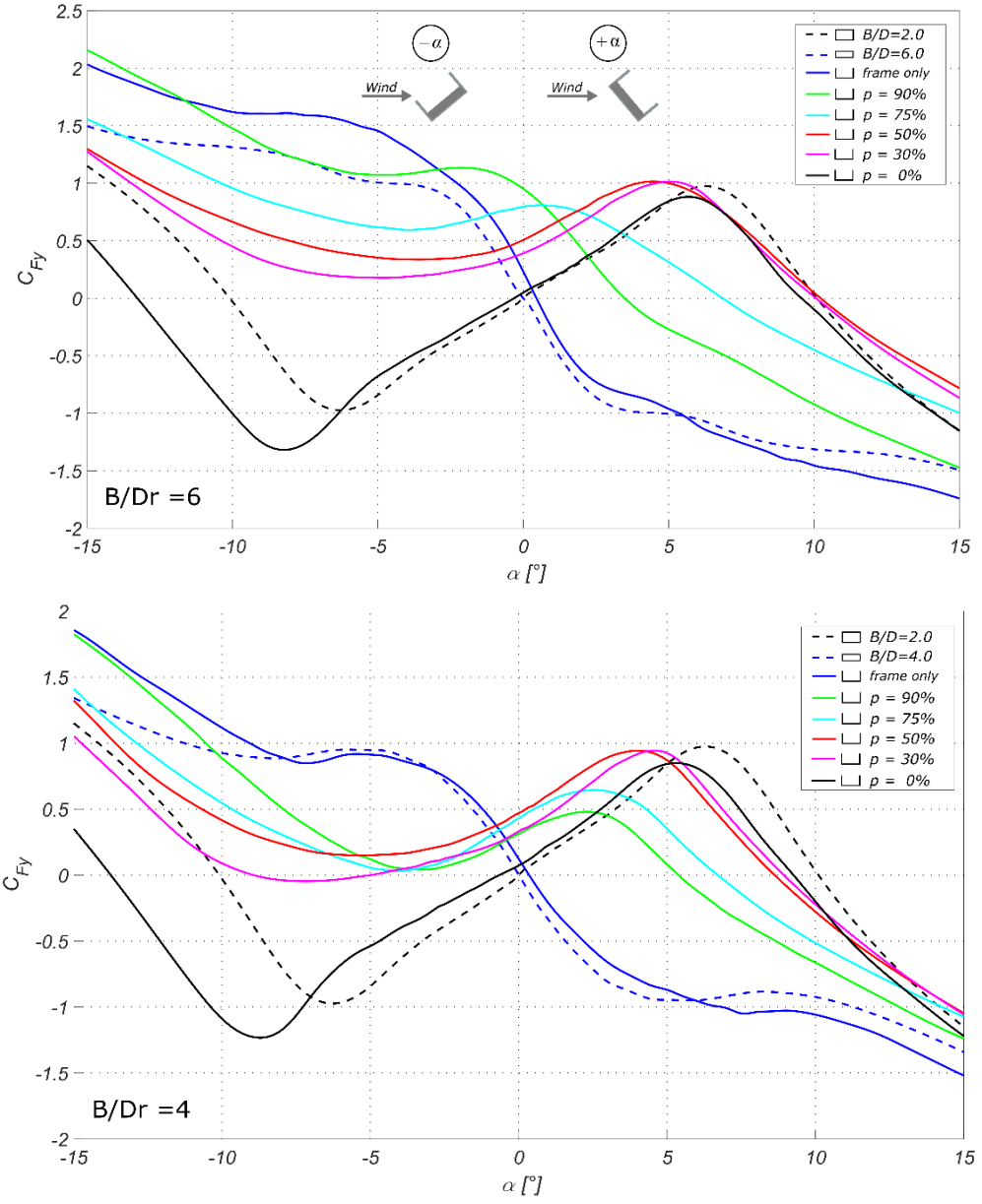

Fig. 2. The transverse force coefficient of the cylinders with rectangular and U-shaped cross-sections for various angles of wind attack

The analysis of the results showed the strong susceptibility of the rectangular prism with SR = 2 to the transversal galloping. The stability parameter, a_g, equal to very high value 9.81 was for this beam determined. Only slightly lower values of a_g were determined for U-beams with porosity up to and including 50 % regardless the depth, D_b, of their profiles. The onset galloping velocities for these U-profiles are expected to be very close.

Table 1. The aerodynamic parameters of tested profiles

Cross section	B/D [/]	B/Dr [/]	Porosity [%]	C_D (α=0°) [/]	$dC_L/d\alpha$ (α=0°) [/]	a_g [/]	$\Delta\alpha_{IP}$ [°]	$\langle\alpha_{IP-}; \alpha_{IP+}\rangle$ [°]
⊔	2	4	0	1.46	-8.94	7.48	14.0	⟨- 8.7; 5.3⟩
⊔	2	6	0	1.45	-9.60	8.15	13.8	⟨- 8.2; 5.6⟩
⊔	2	4	30	1.47	-8.26	6.79	11.6	⟨-7.1; 4.5⟩
⊔	2	6	30	1.49	-7.35	5.86	9.8	⟨-4.8; 5.0⟩
⊔	2	4	50	1.33	-8.66	7.33	9.4	⟨-5.3; 4.1⟩
⊔	2	6	50	1.42	-8.15	6.73	8.0	⟨-3.6; 4.4⟩
⊔	2	4	75	1.04	-8.60	7.56	6.6	⟨-4.1; 2.5⟩
⊔	2	6	75	1.04	-3.35	2.31	4.6	⟨-4.0; 0.6⟩
⊔	2	4	90	1.04	-7.53	6.48	5.6	⟨-3.4; 2.2⟩
⊔	2	6	90	0.94	9.42	-	-	-
⊔	2	4	frame	0.72	18.55	-	-	-
⊔	2	6	frame	0.52	26.92	-	-	-
□	2	2	0	1.48	-11.29	9.81	12.4	⟨-6.2; 6.2⟩
□	4	4	0	0.55	19.61	-	-	-
□	6	6	0	0.33	22.36	-	-	-

A more significant influence of D_b on a_g was identified only for U-beams with flange porosity higher than 50 %. While for lower D_b, i.e. B/D_r = 4:1, the coefficient a_g did not change substantially for all tested porosities, for lower D_b a significant reduction in a_g was observed for p = 75%. Finally, in the case of even higher porosity p = 90 % and lower D_b the profile can be considered as stable due to positive value of the slope of C_L. The positive slope of C_L and thus the resistance to galloping were also determined for rectangular prisms with SR = 4 and 6. The effect of the plastic frame onto the change of proneness to galloping of these rectangular cylinders was identified as minimal. The performed tests indicated that the interval, $\Delta\alpha_{IP}$, is decreasing with the increase in the flange porosity of U-profiles and with the increase in D_b. In the cases of non-porous U- profiles, this angular interval is even slightly wider than for rectangular prism with SR = 2.

The analysis of the results determined the beams with U-shaped cross sections with the side ratio SR = 2, depth D_b = *1/4 B* and flange porosity up to and including 90 % as potentially unstable from the point of view of transversal galloping. The proneness in terms of the expected value of critical wind velocity is almost in all cases comparable with the rectangular prism with SR = 2. In the case of U-beams with D_b = *1/3 B*, the susceptibility to galloping was determined for U-beams with porosity up to and including 75 %. However, for porosity equal to 75% a significant reduction of stability parameter affecting the value of onset galloping velocity was identified. The geometrically identical U-beams with porosities higher than 75% as well as the rectangular prisms with SR = 4 and 6 can be assumed as stable in terms of transverse galloping.

Acknowledgements

The kind support of Czech Scientific Foundation project No. 19-21817S and RVO 68378297 institutional support are gratefully acknowledged.

References

[1] Eurocode 1 – Actions on structures – Part 1-4: General actions –Wind actions.
[2] Hracov, S., Machacek, M., Susceptibility of U-profiles with different geometry and porosity to galloping, EASD Procedia EURODYN, 2020, pp. 621-630.
[3] Paidoussis, M.P., Price, S.J., de Langre, E., Fluid-structure interactions: cross-flow induced instabilities, Cambridge University Press, 2014.

COMPUTATIONAL MECHANICS 2021
36th conference with international participation
Srní
November 8 - 10, 2021

Numerical computation of stress relaxation of isotropic magnetorheological elastomer using fractional viscoelastic models

T. Huu-Nam[a], I. Petríková[a], B. Marvalová[a]

[a] *Faculty of Mechanical Engineering, Technical University of Liberec, Studentská 1402/2, 461 17 Liberec 1, Czech Republic*

Abstract

The paper presents numerical research on stress relaxation of isotropic magnetorheological elastomer (MRE) using fractional derivative viscoelastic models. The isotropic MRE has been fabricated by filling micro-sized carbonyl iron particles into silicone rubber. Effects of applied constant strain and magnetic field on short-term stress relaxation of isotropic MRE were carefully investigated by single- and multi-step relaxation shear tests using double-lap shear specimens. Three fractional viscoelastic models, namely, fractional Maxwell, fractional Kelvin–Voigt, and fractional Zener models were used to describe the stress relaxation response of isotropic MRE. Results showed that the fractional Kelvin-Voigt and Zener models were fitted well to the experimental data of isotropic MRE in both single- and multi-step stress relaxations. The calculated stress with long-term predictions for the isotropic MRE is in very good agreement with the measured one. Therefore, fractional Kelvin-Voigt and Zener models are applicable to predict the long-term stress relaxation of isotropic MRE.

1. Introduction

Magnetorheological elastomers (MREs) are regarded as smart composite materials because their mechanical and rheological properties can be controlled rapidly and reversibly by the application of an external magnetic field [1]. MREs have been prepared by filling micro-sized ferromagnetic particles into non-magnetic polymer matrices. The elastic and damping properties of MREs can be controlled in nearly real-time in response to changing external excitations [3]. With their controllable properties, MREs have been used in a broad range of engineering applications [5]. The viscoelastic properties of MREs have been extensively studied by experimental and analytical methods. The research on the stress relaxation of MREs has been carried out to determine their time-dependent rheological properties [7].

The stress relaxation behavior of polymer materials can be examined numerically using fractional viscoelastic models [4]. The fractional Maxwell, Kelvin–Voigt, and Zener models have been used to characterize viscoelastic behaviors of materials [2]. For this study, isotropic MRE was fabricated by dispersing micro-sized carbonyl iron particles (CIPs) into silicone rubber [6]. The stress relaxation behavior of isotropic MRE was examined by relaxation tests using double-lap shear specimens. Effects of constant strain level and magnetic field on short-term stress relaxation of isotropic MRE were investigated. The fractional Maxwell, Kelvin–Voigt, and Zener models were used to describe the stress relaxation response of the MRE.

2. Stress relaxation measurements

The stress relaxation of isotropic MRE was studied by single- and multi-step relaxation shear tests. The relaxation tests were conducted for double-lap shear samples with constant strains

changing from 5 to 20% and magnetic flux density (MFD) from zero to 0.58 T using the Instron Electropuls testing system. The shear test, MRE double-lap specimen, and electromagnet system were depicted in our earlier paper [6]. In the single- and multi-step relaxation tests for isotropic MRE, a strain rate of 1.0/s was applied in loading and unloading paths. The strains of 5, 10, 15, and 20% were applied for the single-step relaxation test at room temperature. For the multi-step relaxation test, step strains from 0 to 100% with a 20% strain interval were applied in the loading path, and then applied strains were reduced to zero with a 20% strain interval in the unloading path. The stress relaxation was recorded for 1000 s in the single-step relaxation test and 600 s for each step of the multi-step relaxation test.

3. Fractional viscoelastic models and numerical simulation

3.1. Fractional derivative viscoelastic models

Fractional derivative viscoelastic models, namely, fractional Maxwell, Kelvin–Voigt, and Zener models were used to deal with the stress relaxation behavior of the MRE. These models were built by different combinations of elastic spring and fractional-order dashpot (Fig. 1).

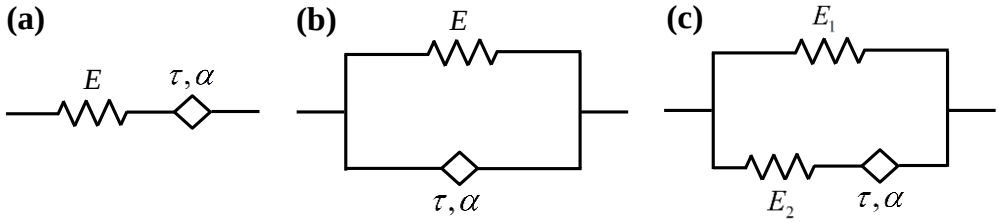

Fig. 1. Fractional derivative viscoelastic models: (a) fractional Maxwell model, (b) fractional Kelvin-Voigt model, and (c) fractional Zener model

The constitutive equations for the fractional Maxwell, Kelvin–Voigt, and Zener models [6] in the time domain are respectively written as follows:

$$\frac{d^{\alpha}\sigma}{dt^{\alpha}}+\frac{\sigma}{\tau^{\alpha}}=E\frac{d^{\alpha}\varepsilon}{dt^{\alpha}}, \tag{1}$$

$$\frac{d^{\alpha}\varepsilon}{dt^{\alpha}}+\frac{\varepsilon}{\tau^{\alpha}}=\frac{\sigma}{E\tau^{\alpha}}, \tag{2}$$

$$\frac{d^{\alpha}\sigma}{dt^{\alpha}}+\frac{\sigma}{\tau^{\alpha}}=\left(E_1+E_2\right)\frac{d^{\alpha}\varepsilon}{dt^{\alpha}}+\frac{E_1\varepsilon}{\tau^{\alpha}}, \tag{3}$$

where E, E_1, and E_2 is the elastic moduli of the springs, and τ is the relaxation time of the fractional dashpot, and α is the fractional parameter with value varying between 0 and 1 [2,6].

The stress relaxation moduli of fractional Maxwell, Kelvin–Voigt, and Zener models based on a Mittag–Leffler function kernel respectively are expressed as follows [6]:

$$G(t)=EM_{\alpha}\left(-\left(\frac{t}{\tau}\right)^{\alpha}\right), \tag{4}$$

$$G(t)=E\left[1+M_{\alpha}\left(-\left(\frac{t}{\tau}\right)^{\alpha}\right)\right], \tag{5}$$

$$G(t)=E_1+E_2M_{\alpha}\left(-\left(\frac{t}{\tau}\right)^{\alpha}\right). \tag{6}$$

3.2. Numerical simulation of MRE stress relaxation

The fractional Maxwell, Kelvin–Voigt, and Zener models were applied to study the stress relaxation behavior of isotropic MRE. Eqs. (4)–(6) were used to fit the relaxation modulus

measured by single- and multi-step relaxation tests. The fitting was done using the nonlinear least-squares method in Matlab. The model parameters fitted with the experimental data of the single-step stress relaxation are given in Table 1. The fitted and measured relaxation modulus at different constant strain levels and MFDs are presented in Fig. 2. A comparison of calculated and measured shear stress with the long-term prediction for the isotropic MRE is depicted in Fig. 3. The fittings of the relaxation modulus to the experimental data under various MFDs for the isotropic MRE in the multi-step stress relaxation are presented in Fig. 4.

Table 1. Fitting parameters of models with experimental data of single-step relaxation tests for isotropic MRE

Strain level	Fractional Maxwell model			Fractional Kelvin-Voigt model			Fractional Zener model			
	E	α	τ	E	α	τ	E_1	E_2	α	τ
0.05	1.92	0.052	4.61E-09	0.375	0.348	3.62E-01	0.371	0.51	0.309	8.14E-02
0.10	1.79	0.051	6.73E-09	0.370	0.346	2.91E-01	0.365	0.56	0.300	3.76E-02
0.15	1.79	0.051	4.95E-09	0.365	0.354	3.10E-01	0.357	1.19	0.269	9.08E-04
0.20	1.73	0.050	6.01E-09	0.364	0.372	3.34E-01	0.355	2.64	0.270	3.85E-05

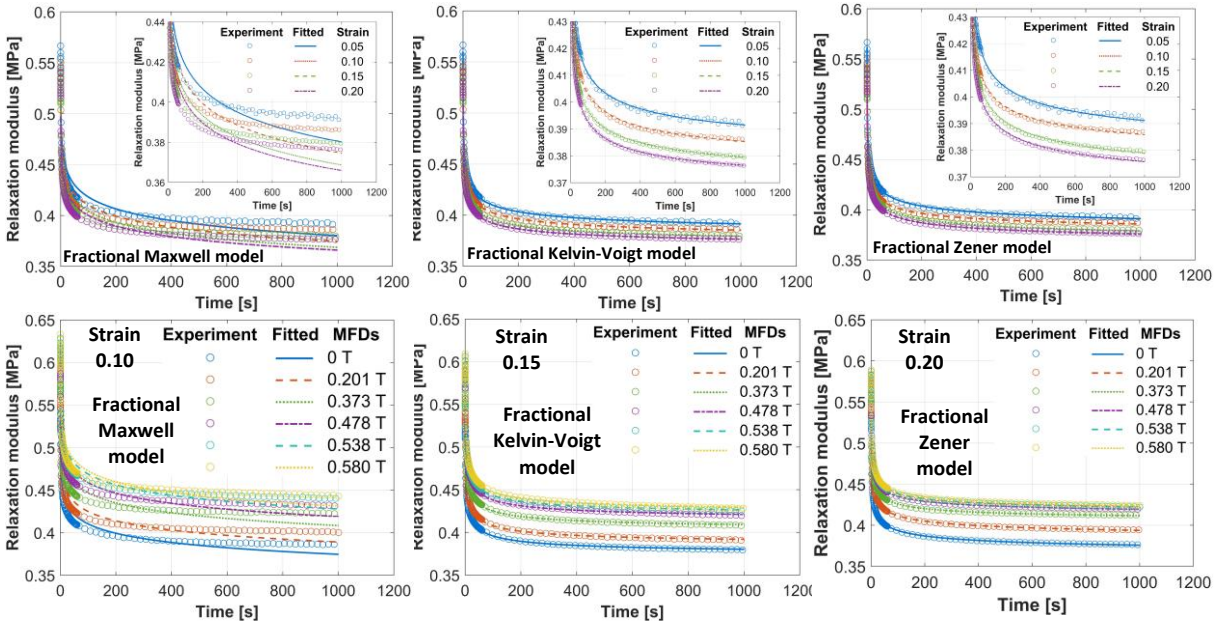

Fig. 2. Relaxation modulus (experimental and model fitted curves) of the isotropic MRE at different constant strain levels and various MFDs in the single-step stress relaxation

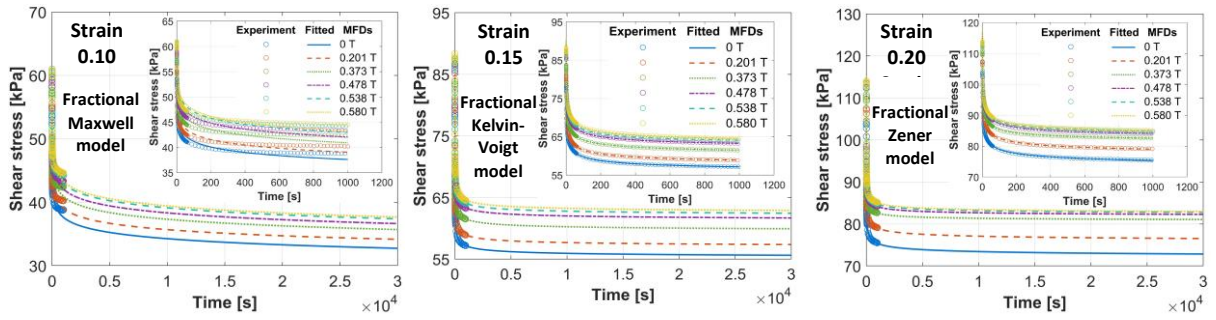

Fig. 3. Stress relaxation stress (experimental and model fitted curves) of the isotropic MRE under different MFDs in the single-step stress relaxation. The insert is a zoom of the first 1000 sec

The maximal differences between fitted curves of fractional Maxwell, Kelvin–Voigt, and Zener models and measured data for the relaxation modulus are 6.70%, 1.29%, and 1.02%, respectively. A very good agreement between experimental and fitted relaxation modulus of fractional Kelvin-Voigt and Zener models under different strain levels and MFDs is obtained.

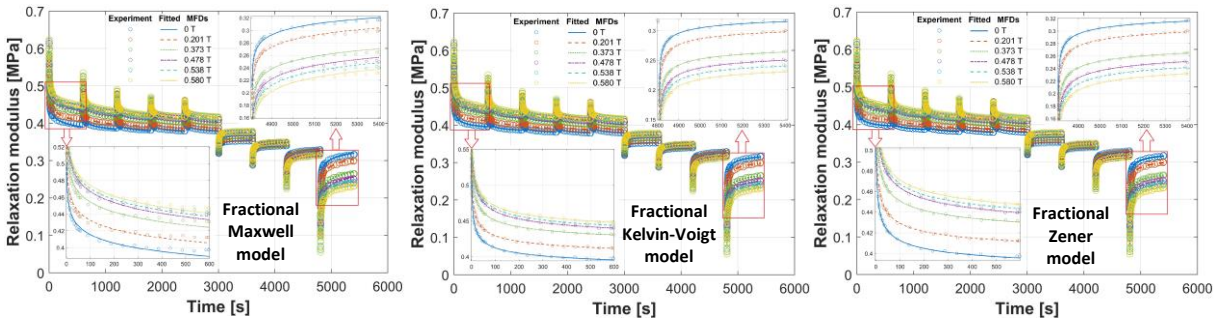

Fig. 4. Relaxation modulus (experimental and model fitted curves) of the isotropic MRE under different MFDs in the multi-step stress relaxation

4. Conclusions

The numerical studies on the shear stress relaxation of isotropic MRE made of silicone rubber and micro-sized CIPs using fractional derivative viscoelastic models have been conducted in this paper. The fractional Maxwell, Kelvin–Voigt, and Zener models were used to fit the experimental data of the isotropic MRE. The relaxation modulus and shear stress of the isotropic MRE were measured using single- and multi-step relaxation tests at different constant strains and magnetic fields. The simulated results showed that the fractional Kelvin-Voigt and Zener models were fitted well to the experimental data of the isotropic MRE under different strain constants and MFDs in both single- and multi-step stress relaxations. The maximal difference between measured and calculated relaxation modulus of the fractional Maxwell model is relatively large. The estimated stress with long-term predictions using fractional Kelvin-Voigt and Zener models for the isotropic MRE is in very good agreement with the measured one. In short, the fractional derivative Kelvin-Voigt and Zener models can be used to predict the long-term stress relaxation of the isotropic MRE.

Acknowledgments

This work was supported by the Ministry of Education, Youth and Sports of the Czech Republic and the European Union – European Structural and Investment Funds in the frames of Operational Program Research, Development and Education – project Hybrid Materials for Hierarchical Structures (HyHi, Reg. No.CZ.02.1.01/0.0/0.0/16_019/0000843).

References

[1] Bastola, A.K., A review on magneto-mechanical characterizations of magnetorheological elastomers, Composites Part B 200 (2020) 108348.
[2] Bonfanti, A., Kaplan, J.L., Charras, G., Kabla, A., Fractional viscoelastic models for power-law materials, Soft Matter 16(26) (2020) 6002–6020.
[3] Dargahi, A., Sedaghati, R., Rakheja, S., On the properties of magnetorheological elastomers in shear mode: Design, fabrication and characterization, Composites Part B 159 (2019) 269–283.
[4] Guo, X., Yan, G., Benyahia, L., Sahraoui, S., Fitting stress relaxation experiments with fractional Zener model to predict high frequency moduli of polymeric acoustic foams, Mechanics of Time-Dependent Materials 20(4) (2016) 523–533.
[5] Li, W.H., Zhang, X.Z., Du, H., Magnetorheological elastomers and their applications, in: P.M. Visakh et al. (Eds.), Advances in Elastomers I: Blends and Interpenetrating Networks, Springer, 2013, pp. 357–374.
[6] Nam, T.H., Petríková, I., Marvalová, B., Experimental characterization and viscoelastic modelling of isotropic and anisotropic magnetorheological elastomers, Polymer Testing 81 (2020) 106272.
[7] Qi, S., Yu, M., Fu, J., Zhu, M., Stress relaxation behavior of magnetorheological elastomer: experimental and modeling study, Journal of Intelligent Material Systems and Structures 29 (2018) 205–213.

COMPUTATIONAL MECHANICS 2021
36th conference with international participation
Srní
November 8 - 10, 2021

Subject-specific human body (sub-)models developed by morphing

L. Hynčík

New Technologies – Research Centre, University of West Bohemia, Univerzitní 8, 301 00 Plzeň, Czech Republic

Virtual biomechanical human body models contribute to designing safe and user-friendly products through virtual prototyping. Contemporary trends focus on personalized approach to implement safety systems, protective equipment and personalized health care for a specific person. Here a virtual prototyping plays an irreplaceable role. For designing personal protective equipment or personal tool and approaches in health care by virtual prototyping, subject-specific human body models seem to be a promising tool for personalized approach. As the person-specific model development is a complex task, the virtual human model of a generic body is used and adopted to the particular person. There are two basic approaches for developing a person-specific human body model, particularly scaling and personalization. Whilst scaling changes only the global dimensions (anthropometry, mass and stiffness) based on the general anthropometric parameters [3], personalization updates the local geometrical and biomechanical details of the particular human body segments [2]. Additional mesh morphing refines particular details of the segment discretized by a finite element mesh [4].

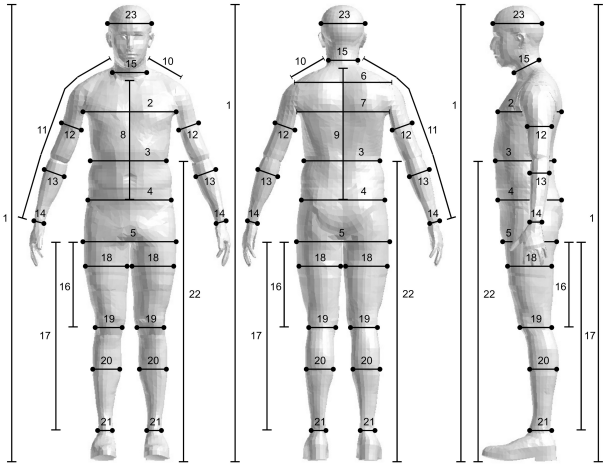

Fig. 1. Clothing industry dimensions

The personalization method upgrades the local dimensions by addressing the measured dimensions and so it develops a subject-specific virtual human body model. The presented algorithm benefits from the implementation of the clothing industry dimensions, see Fig. 1. The external body shape is personalized using polynomial functions to secure the continuous and smooth body surface, which is desired mainly for applications where the human body comes into contact with other subjects or external objects. We use polynomials of degree n_i^s in the

form

$$p_i^s(i) = \sum_{k=0}^{n_i^s} c_{ik}^s i^k \tag{1}$$

to interpolate the body shape along each spatial axis $i \in \{x, y, z\}$ where vector $\mathbf{c}_i^s = [c_{i0}^s, \ldots, c_{in}^s]$ contains the polynomial coefficients in spatial direction $i \in \{x, y, z\}$ for each body segment $s \in \{0, \ldots, 15\}$, when dividing the human body for 15 basic segments as shown in Table 1.

Table 1. Basic human body segments for personalization

Segment	Head	Neck	Thorax	Abdomen	Arm	Forearm	Palm	Thigh	Calf	Foot
Left	3	2	1	0	4	5	6	10	11	12
Right					7	8	9	13	14	15

The polynomial interpolation might suffer from inaccuracy and unrealistic overshoots in the polynomial shape if we interpolate incomparable values, which is why the scaling [3] is carried out in the first step before the personalization. Fig. 2 shows an example of the personalized human body model of a 45 years-old male with the height 176 cm and the weight 85 kg.

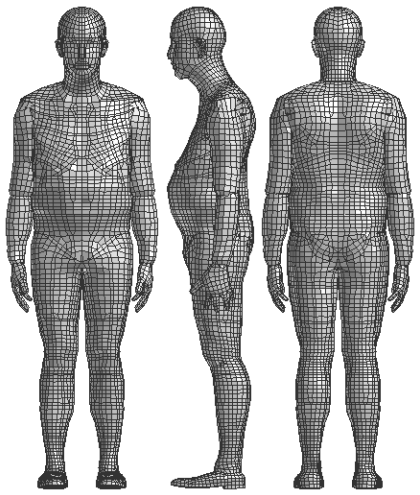

Fig. 2. Subject-specific human body model

Mesh morphing as one of the morphing approaches accommodates radial basis functions to interpolate function $f(\mathbf{X})$ at the point $\mathbf{X}$ having m corresponding landmarks on both the original (baseline) $\mathbf{X}_{Lj}$ and the target (morphed) $\mathbf{X}_{Tj}$ models, $j \in \{1, \ldots, m\}$ as [1]

$$f(\mathbf{X}) = p(\mathbf{X}) + \sum_{j=1}^{m} \lambda_j \varphi\left(\|\mathbf{X} - \mathbf{X}_j\|\right) + \alpha, \tag{2}$$

where $p(\mathbf{X})$ is a low order polynomial, λ_j, $j \in \{1, \ldots, m\}$, are the weighting coefficients, φ is the basis function and α is a constant, which we choose zero. A first order polynomial

$$p(\mathbf{X}) = [1, x, y, z]\,[c_0, c_1, c_2, c_3]^{\mathrm{T}} = \mathbf{X}\mathbf{c} \tag{3}$$

and the thin plate spline basis function $\varphi = r^2 \log r$ results in a smooth function $f(\mathbf{X})$ in Eq. (2) [2, 5]. Considering function $f(\mathbf{X}) = [x_{Ti}, y_{Ti}, z_{Ti}] = \mathbf{X}_{Ti}$ represents the target mesh

with n nodes, $i \in \{1, \ldots, n\}$, Eq. (2) can be written as

$$\mathbf{X}_{Ti} = \sum_{j=1}^{m} \lambda_j \varphi \left(\|\mathbf{X}_{Li} - \mathbf{X}_{Tj}\| \right) + \mathbf{X}_{Li}\mathbf{c}, \quad j \in \{1, \ldots, m\} \tag{4}$$

or in the matrix form as

$$\begin{bmatrix} \mathbf{A} & \mathbf{B} \\ \mathbf{B}^{\mathrm{T}} & \mathbf{0} \end{bmatrix} \begin{bmatrix} \boldsymbol{\lambda} \\ \mathbf{c} \end{bmatrix} = \begin{bmatrix} \mathbf{T} \\ \mathbf{0} \end{bmatrix}, \tag{5}$$

where

$$\mathbf{A} = A_{ij} = \varphi \left(r_{ij} \right) = r_{ij}^2 \log r_{ij} \tag{6}$$

is a $m \times n$ matrix containing the distances between the pairs of the baseline and the target landmarks $r_{ij} = \|\mathbf{X}_{Li} - \mathbf{X}_{Tj}\|, \forall i, j \in \{1, \ldots, m\}$,

$$\mathbf{B} = \begin{bmatrix} 1 & x_{L1} & y_{L1} & z_{L1} \\ \vdots & \vdots & \vdots & \vdots \\ 1 & x_{Lm} & y_{Lm} & z_{Lm} \end{bmatrix} \tag{7}$$

is a $m \times 4$ matrix containing the coordinates of the baseline model landmarks,

$$\mathbf{T} = \begin{bmatrix} x_{T1} & y_{T1} & z_{T1} \\ \vdots & \vdots & \vdots \\ x_{Tm} & y_{Tm} & z_{Tm} \end{bmatrix} \tag{8}$$

is a $m \times 3$ matrix containing the coordinates of the target model landmarks and $\mathbf{c}$ is a constant matrix. Solving Eq. (5) brings the matrix $\boldsymbol{\lambda}$ of size $m \times 3$ and the matrix $\mathbf{c}$ of size 4×3. Once they are determined, by assuming that the number of nodes in the baseline model is n, the coordinates of the nodes in target model $\bar{\mathbf{T}}$ (a matrix of size $n \times 3$) can be calculated as

$$\begin{bmatrix} \bar{\mathbf{T}} \\ \mathbf{0} \end{bmatrix} = \begin{bmatrix} \bar{\mathbf{A}} & \bar{\mathbf{B}} \\ \mathbf{B}^{\mathrm{T}} & \mathbf{0} \end{bmatrix} \begin{bmatrix} \boldsymbol{\lambda} \\ \mathbf{c} \end{bmatrix}, \tag{9}$$

where

$$\bar{\mathbf{T}} = \begin{bmatrix} \bar{x}_1 & \bar{y}_1 & \bar{z}_1 \\ \vdots & \vdots & \vdots \\ \bar{x}_n & \bar{y}_n & \bar{z}_n \end{bmatrix} \tag{10}$$

is a $n \times 3$ matrix containing the coordinates of the nodes in the target model,

$$\bar{\mathbf{A}} = \bar{A}_{ij} = \varphi \left(r_{ij} \right) = r_{ij}^2 \log r_{ij} \tag{11}$$

is a $n \times m$ matrix, where $i \in \{1, \ldots, n\}$ are the nodes in the baseline model, $j \in \{1, \ldots, m\}$ are the baseline model landmarks and

$$\bar{\mathbf{B}} = \begin{bmatrix} 1 & x_1 & y_1 & z_1 \\ \vdots & \vdots & \vdots & \vdots \\ 1 & x_n & y_n & z_n \end{bmatrix} \tag{12}$$

is a $n \times 4$ matrix containing the coordinates of all nodes in the baseline model. As the thin plate spline function is chosen, the coincident baseline and target landmarks ($\log r_{ij} \to -\infty$) contribute to the particular position in the matrix $\mathbf{A}$ by zero.

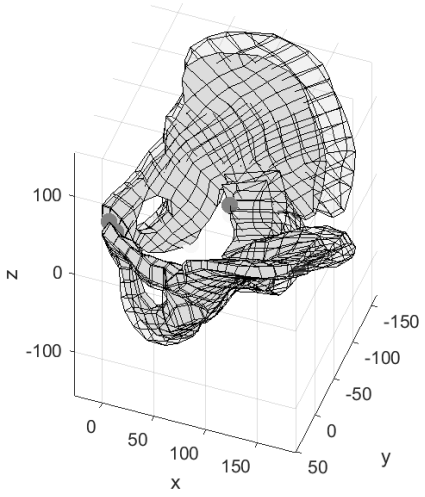

Fig. 3. Example of a morphed simple pelvic bone finite element model

Scaling is a convenient tool for creating generic human body models representing a population group for virtual prototyping, safety systems in mobility or designing personal protective equipment. Personalization is a sufficient tool for developing subject-specific human body models. For local segment refinement, the mesh morphing algorithm is an efficient tool to update the finite element mesh based on a set of chosen landmarks. Modern technologies enable personalized products to be designed, so if we want to address a subject-specific approach for protective equipment or personal tool and approaches in health care, personalization and morphing is a good solution for the subject-specific anthropometry.

Acknowledgement

This research was funded by the European Regional Development Fund-Project (grant number CZ.02.1.01/0.0/0.0/17_048/0007280).

References

[1] Carr, J. C., Fright, R., Beatson, R. K., Surface interpolation with radial basis functions for medical imaging, IEEE Transactions on Medical Imaging 16 (1) (1997) 96-107.

[2] Hwang, E., Hallman, J., Klein, K., Rupp, J. et al., Rapid development of diverse human body models for crash simulations through mesh morphing, SAE Technical Paper 2016-01-1491 (2016), doi: 10.4271/2016-01-1491.

[3] Hynčík, L., Čechová, H., Kovář, L., Bláha, P., On scaling virtual human models, SAE Technical Paper 2013-01-0074 (2013), doi: 10.4271/2013-01-0074.

[4] Liu, S., Beillas, P., Ding, L., Wang, X., Morphing an existing open source human body model into a personalized model for seating discomfort investigation, SAE Technical Paper 2020-01-0874 (2020), doi: 10.4271/2020-01-0874.

[5] Skala, V., A practical use of radial basis functions interpolation and approximation, Investigacion Operacional 37 (2) (2016) 1-8.

COMPUTATIONAL MECHANICS 2021
36th conference with international participation
Srní
November 8 - 10, 2021

Biomechanical comparison of five implants used to treat a supracondylar periprosthetic fracture of ostheoporotic femur

M. Jansová[a], T. Malotín[b], J. Křen[a], P. Votápek[c], L. Lobovský[a], L. Hynčík[d]

[a]*NTIS - New Technologies for the Information Society, Faculty of Applied Sciences, UWB in Pilsen, Technická 8, 301 00 Plzeň, Czech Republic*
[b]*Department of Orthopaedics and Traumatology, Faculty of Medicine of Charles University and Faculty Hospital in Plzeň, alej Svobody 80, 304 60 Plzeň, Czech Republic*
[c]*Department of Machine Design, Faculty of Mechanical Engineering, UWB in Pilsen, Univerzitní 22, 306 14 Plzeň, Czech Republic*
[d]*Department of Mechanics, Faculty of Applied Sciences, UWB in Pilsen, Technická 8, 301 00 Plzeň, Czech Republic*

The goal of the study is to assess the biomechanical properties of several implants used to treat a supracondylar periprosthetic fracture which rarely occurs mainly in ostheoporotic patients after total knee arthroplasty (TKR). The behaviour of ostheoporotic bone and implants under load is analysed by means of the finite element model.

The study extends the previous analysis [1] of four implants: Distal Femoral Nail (DFN), Angled Blade Plate (ABP), Dynamic Compression Screw (DCS), Less Invasive Stabilization System (LISS). Additionally, the Non-Contact Bridging (NCB) implant is considered and the change in the distance between the proximal and the distal surface of the fracture is assessed along with the displacement of the bone and stress distribution in implants under axial load and torque.

Both compact and spongy bone are modelled by 3D elements. The gap between the surfaces in the fracture line is 2 mm wide. The finite element models of femur with total knee replacement (TKR) and the implants are shown in Fig. 1.

Fig. 1. Frontal and lateral view of the model of femur with particular implants: TKR (green), the fracture (black), ABP (violet), DCS (light blue), NCB (dark blue), LISS (orange) and DFN (red)

The material parameters of the bone correspond to the ostheoporotic bone. Titanium alloy or stainless steel is used for the implants according to the manufacturers specifications. The TKR is made from Co-Cr-Mo alloy.

Two types of load were simulated – the uniaxial load and the torque. In case of the uniaxial load, a force of 800 N was applied on the centre of femoral head in the direction of mechanical axis. As for the torque, a moment of 5 Nm was applied on the centre of femoral head about the mechanical axis.

The von Mises stress distribution in the implants, the displacement of bone in all three main directions and the shortest distance in the fracture line were analysed for the five implants and the two loading conditions.

The axial load is the most evident in the sagittal plane. The bone bends ventrally in all implants, the least in case of DFN. The highest stress values are observed in the fracture area in case of DFN and below the most distally placed screw in the diaphysis in the other implants. The screws are loaded mainly in the area of contact with the compact bone.

For torque, the femoral head rotates ventrally and the greater trochanter dorsally in all cases. The femoral diaphysis twists around the mechanical axis with the values being significantly higher in case of NCB and LISS. The plate implants are loaded mainly in the middle area with no screws inserted, the DFN in the fracture area. The highest stress values are observed in LISS implant.

The proximal part of the fractured bone slides under axial load. The movement is mostly in frontal-distal direction in case of DFN. There is also a displacement in lateral direction in case of the other four implants and the overall displacement in the fracture line is almost double of the one observed with DFM implant. The bone rotates around the implant under torque. The way of rotation depends on the placement of the implant plate). The DFN is inserted inside the bone, therefore the bone rotates around its centre and the maximal movement is lower compared to the other implants in which the centre of rotation is placed significantly laterally.

The results show, that the DFN exhibits the best behaviour for the axial load as expected by the orthopaedic surgeons. However, the LISS and NCB implants do not prove to be the most suitable under torque. The analysis of the change in the distance between the proximal and the distal surface of the fracture under the load has revealed that the movement is more complex and should not be considered only as the change in the shortest distance.

Acknowledgements

The work was supported by the European Regional Development Fund-Project ‘Application of Modern Technologies in Medicine and Industry’ (No. CZ.02.1.01/0.0/0.0/17_048/0007280).

References

[1] Jansová, M., Malotín, T., Křen, J., Votápek, P., Lobovský, L., Hynčík, L., A comparative analysis of four implants used to treat a supracondylar periprosthetic fracture of ostheoporotic femur, Proceedings of Computational Mechanics 2019, Srní, 2019, pp. 80-81.

COMPUTATIONAL MECHANICS 2021
36th conference with international participation
Srní
November 8 - 10, 2021

Assessment of post-processing capabilities in selected software for topology optimization

O. Ježek[a,b], J. Kopačka[b], D. Gabriel[b]

[a] Faculty of Mechanical Engineering, Czech Technical University in Prague, Technická 4, 160 00 Prague 6, Czech Republic
[b] Institute of Thermomechanics, Czech Academy of Sciences, Dolejškova 1402/5, 182 00 Prague 6, Czech Republic

Abstract

Topology optimization (TO) has come to the fore in recent years, especially with the development of 3D printing. Finite element systems often include TO functionality based on either density-based or level set methods. In the case of the first-mentioned method, the results of TO are further processed into geometry suitable for additive manufacturing. However, current programs only include basic post-processing capabilities with minimal customization options. This paper will first briefly summarize the theoretical background of TO and post-processing methods. Next, selected commercial TO programs will be compared from the perspective of shape post-processing. The final part will be devoted to applying the level set method for shape post-processing of a topologically optimized industrial robot gripper.

1. Introduction

Topology optimization (TO) has become a popular method for designing innovative components in recent years. Its goal is to find the optimal distribution of the material in a design space based on predefined requirements and constraints. The popularity of this method has grown considerably with the development of 3D printing, and today it is incorporated in many finite element programs as well as in CAD software.

The seminal paper that laid the foundations for the development of topology optimization is considered to be the work of Bendsøe et al. [1]. Since then, the development of TO has taken several directions, and nowadays, many different methods can be found in the literature. An overview of known TO methods can be found e.g. in the review article [2]. Nevertheless, only two methods, *Density-based* and *Level-set*, can be considered the most widely used.

In this paper, we will first formulate the optimization problem of compliance minimization with a constraint on the volume fraction. Then, the two mentioned methods - SIMP and level set - will be introduced. Then, selected commercial TO programs will be compared in terms of shape post-processing. The main contribution of the paper lies in the use of the level set method to postprocess the results obtained by the SIMP method. The proposed procedure is demonstrated on a popular test example of the so-called Messerschmitt-Bölkow-Blohm (MBB) beam.

2. Compliance minimization using topology optimization

A typical topology optimization problem is to find a maximally stiff structure with respect to its loads and supports. The constraint is the volume fraction, i.e., a certain ratio between the volume

of the structure and the volume of the entire domain in which the optimization is performed. Such a problem can be described by minimizing an objective function c (strain energy) with a constraint on the volume fraction f, i.e.,

$$\begin{aligned} \min_{\rho}: \quad & c(\rho) = \mathbf{U}^T\mathbf{K}\mathbf{U} = \sum_{e=1}^{N} E_e(\rho_e)\mathbf{u}_e^T\mathbf{k}_0\mathbf{u}_e, \\ \text{subjected to}: \quad & V(\rho)/V_0 = f, \\ & 0 \leq \rho \leq 1, \end{aligned} \tag{1}$$

where $\mathbf{U}$ is the global displacement vector, $\mathbf{F}$ is the global stiffness matrix, $\mathbf{u}_e$ is the displacement vector of the element, k_0 is the stiffness matrix of the element with the corresponding Young's modulus, N indicates the total number of elements, $V(\rho)$ is the current volume of the material, and V_0 is the volume of the design domain.

2.1 Modified SIMP method

The SIMP method, which stands for Solid Isotropic Material with Penalization, belongs to the class of *Density-based* methods and is one of the most used in TO. It employs finite elements to describe the shape, where a fictitious density is assigned to each element. Note that this is not a real physical density but a kind of importance of the element in the system. This fictional density (referred to as the design variable in the optimization) assigns a modulus of elasticity to each element in the system.

The distribution of the material during optimization can produce a so-called checkerboard pattern, where the fictitious density changes in leaps and bounds between adjacent elements. To suppress this effect, filtering is used. This is a kind of averaging of the density values of adjacent elements using a weighting factor. The basic methods of filtering can be divided into density-based and sensitivity-based, cf. [3].

The result of the SIMP method is a scalar field of fictitious densities ρ, where each element is assigned constant fictitious density ρ_e. To obtain the shape, elements from a certain density threshold can be labeled as solid ($\rho = 1$), and elements with lower density can be labeled as void ($\rho = 0$). The density threshold is set to ensure that the volume fraction f is preserved. This removal of material produces sharp edges. If the component were made identical in shape to the element model, a large number of stress concentrator zones would be created. This should be avoided, and the model should be suitably modified so that these zones are smoothed, and the resulting stress concentrators are removed. To perform the actual smoothing, so-called shape post-processing is used. In the case of 2D objects, shape post-processing can be performed by simple sketching in CAD software. For more complex solids, it is necessary to use automated techniques.

2.2 Level set method

In the SIMP method, the design variables are element-dependent. The level set (LS) method [5], on the other hand, uses a level set function (LSF) to describe the shape. In the 2D case, the intersection of this function with the cutting plane produces the contour of the shape, i.e., the boundary between the solid and the void space. The height of the cut plane (level set) usually passes through zero ($\phi_{\text{plane}} = 0$). However, in special cases, its height can be changed, thus affecting the volume fraction f.

In order to use this method in topology optimization, it is necessary that the LSF evolves over "time" and that the shape of the optimized object changes gradually. The Hamilton-Jacobi equation is often used for this purpose.

Level set methods do not need post-processing. The LSF defines a clear boundary between solid and void material. An advantage is that this boundary is independent of the edges of the elements. The resulting geometry of the optimized object is therefore smooth.

3. Post-processing capabilities in selected software for TO

TO has become an integral part of many finite element systems. These systems usually use Density-based methods to obtain the optimal material distribution. The main advantage of these methods is their robustness. However, the results are not smooth enough, and also no clear transition between full material and empty space is given, Fig. 1. For this reason, shape post-processing of the results is required to obtain sharp and smooth geometry. For this purpose, commercial software uses very basic shape post-processing based on the density isocontour method with linear segment approximation. The results from this method are not of very high quality, and elements of the original finite element mesh are evident on the obtained geometry. Some software uses B-spline curve segments to smooth the geometry, but here the results are of much higher quality. Unfortunately, all available software offers little or no user customization in terms of shape post-processing.

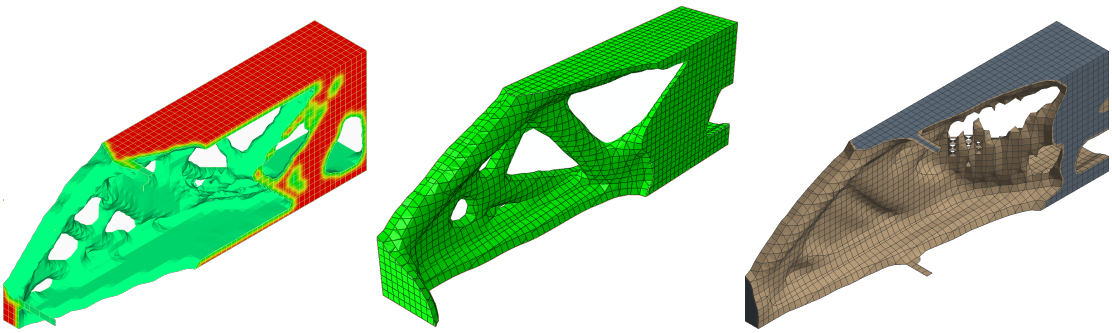

Fig. 1. Comparison of TO 3D MBB beam results performed in selected programs: results from FEMAP are on the left, Abaqus in the middle and Ansys on the right

4. Post-processing by the level set method

We propose to combine the two methods by constructing a level-set function for post-processing of the SIMP method results. First, the nodal values of the fictitious densities are calculated as the averages of the values of the adjacent elements. Next, by implementing radial basis functions (one radial basis function with height corresponding to the fictitious density is placed at each node of the mesh and then summing these functions), the LSF shape can be obtained. The intersection of this function with the cutting plane produces the contour of the object. The height of the cutting plane h can be used to modify the volume fraction f and also the shape of the object. A more detailed procedure is given in the work of [4]. The TO result using the SIMP method is shown in Fig. 2 (left). Subsequent shape post-processing using the LS method produced the result seen in Fig. 2 (right).

5. Conclusions

In the first section of this paper, a brief insight into topology optimization was given. Two main TO methods, SIMP and level set, were presented. The SIMP method belongs to the family of *Density-based* methods using finite element shape and fictitious densities to describe the shape. The Level-set method works on a different principle, using the LS function in combination with

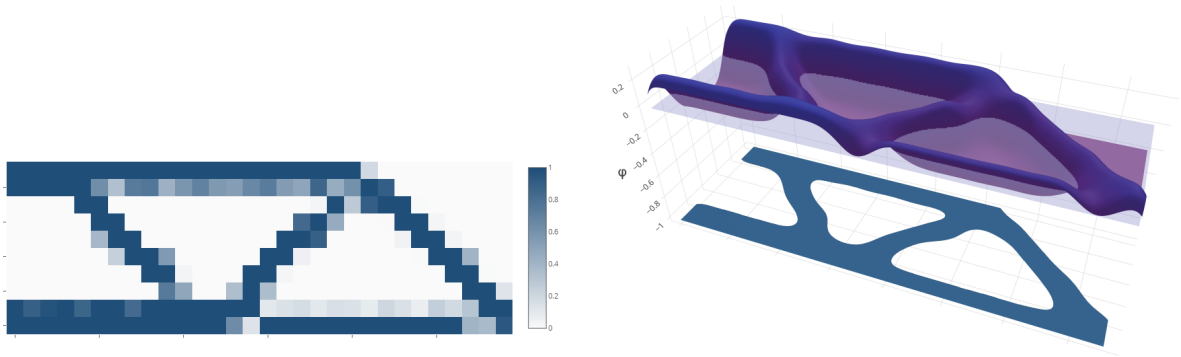

Fig. 2. The principle of the level set method on a 2D MBB beam problem

the cutting plane to describe the shape. In practice, the *Density-based* methods are preferred because of their robustness and the possibility to introduce new holes during optimization. On the other hand, the level-set method does not require shape post-processing. In the second part, the possibilities of shape post-processing within commercial programs were briefly discussed. Furthermore, a comparison of the selected programs was made on the 3D MBB beam. In the last part, the procedure of shape post-processing using the LS method was proposed. The construction of the LSF itself was performed using Radial Basis Functions combined with a fictitious density of node points of the finite-element mesh. By intersecting the cutting plane with the LS functions, a sharp transition between the solid and void material was achieved. It can be seen from Fig. 2 that a very good result was achieved.

Acknowledgements

The work was supported by the Technology Agency of the Czech Republic under grant No TN01000024/08 (National Competence Center-Cybernetics and Artificial Intelligence) - subproject "Automation and production system optimization" and the European Regional Development Fund under Grant No. CZ.02.1.01/0.0/0.0/ 15_003/0000493 (Centre of Excellence for Nonlinear Dynamic Behaviour of Advanced Materials in Engineering) within institutional support RVO:61388998.

References

[1] Bendsøe, M. P., Kikuchi, N., Generating optimal topologies in structural design using a homogenization method, Computer Methods in Applied Mechanics and Engineering 71 (2) (1988) 197-224.

[2] Sigmund, O., Maute, K., Topology optimization approaches: A comparative review, Structural and Multidisciplinary Optimization 48 (2013) 1031-1055.

[3] Sigmund, O., Morphology-based black and white filters for topology optimization. Structural and Multidisciplinary Optimization 33 (4–5) (2007) 401-424.

[4] Swierstra, M. K., Post-Processing of topology optimized results: A method for retrieving smooth and crisp geometries, Master Thesis, Delft University of Technology, 2017.

[5] van Dijk, N. P., Maute, K., Langelaar, M., Van Keulen, F., Level-set methods for structural topology optimization: A review, Structural and Multidisciplinary Optimization 48 (2013) 437-472.

COMPUTATIONAL MECHANICS 2021
36th conference with international participation
Srní
November 8 - 10, 2021

Structural health monitoring during white-noise vibration testing using total harmonic distortion

J. Karlíček[a], P. Steinbauer[a], V. Pawlik[a]

[a] *Faculty of Mechanical Engineering, Czech Technical University in Prague, Technická 4, 160 00 Prague, Czech Republic*

1. Introduction

Pursuing idle time and cost reduction in production plants, structural health monitoring (SHM), making possible to predict machines failures and thus providing possibility to improve maintenance planning, could be advantageous. In beginnings of development of SHM methods classical approaches using spectral analysis were mostly used. Basic methods are described e.g. in [1, 3]. Today, with large development of sensors and data acquisition SHM methods based on deep learning, artificial neural networks and other means for Big Data evaluation are on the rise. Review on deep learning methods is provided e.g. in [5].

In vibration testing sweep sine or white-noise excitation are commonly used. Novel ideas for structure's health evaluation during white noise excitation could be found in [2].

Total harmonic distortion (THD) expresses rate of harmonic components in output signal. THD is more often mentioned in connection with sound or electric signals, but its usage could be extended. In this article we present a method, which uses white-noise excitation during vibration testing and computation of THD to evaluate state of the testing assembly. As far as we know, THD is used for structural health evaluation solely while using sine sweep excitation like in [4]. Our goal is to continuously evaluate the state of the testing assembly to detect any kind of damage (loosened screws, hidden cracks, etc.), which may devaluate ongoing vibration test.

2. Total harmonic distortion

Proposed algorithm is based on computation of THD, which determines the ratio between fundamental frequency of excitation and its harmonic frequencies. Harmonic frequencies are the integer multiples of base frequency. THD is commonly calculated as

$$THD = \frac{\sqrt{A_2^2 + A_3^2 + A_4^2 + \cdots + A_n^2}}{A_1} * 100 \quad [\%],$$

where A_n is the amplitude of n-th harmonic frequency. A_1 is base frequency of excitation. In case, where excitation is in form of white-noise all frequencies in predefined interval are present in input signal, if measured window is long enough. This means that within the range of excitation each frequency could be considered as fundamental frequency as well as harmonic frequency of several previous fundamental frequencies and thus the amplitude consist of base excitation and harmonic components.

3. Algorithm

Before beginning of measurement several parameters are chosen or computed: frequency vector, which defines frequencies in which THD is computed, number of harmonic frequencies included in THD calculation, excitation limit frequency which is the maximum frequency present in white noise excitation, batch length of input accelerometer signal L, length of multiplying window W and number of overlapping samples M of two consecutive signal batches. Except the limit frequency, all parameters are subject of optimization. For better FFT performance parameters L, W, M are recommended to be chosen in form of m^2, where m is a positive integer.

Input signal from chosen accelerometer is processed in batches of length L. Each batch is multiplied by Blackman window and fast Fourier transformation (FFT) is performed to acquire spectral components of the signal. While computing THD fundamental frequency is the one from frequency vector defined at the beginning of the measurement but only frequencies larger than excitation limit frequency are used as harmonics in THD formula. That is for exclusion of base excitation component in corresponding amplitude. THD is thus computed for every frequency in defined frequency vector. Finally, average THD value for every batch is computed as output of this algorithm.

4. Experimental setup

Experimental setup consists of LDS V830 shaker with steel mounting plate, aluminium testing frame and tested component. Testing frame is mounted on steel plate and serves for attachment of tested component, which is in form of plastic container.

During experiment white-noise is generated using Polytech software and through amplifiers delivered as an input to the shaker. Three-axis accelerometers of IEPE standard (from B&K and PCB manufacturers) are attached to several parts of the assembly and their signal is processed by NI PXIe system with PXIe-4497 measurement card.

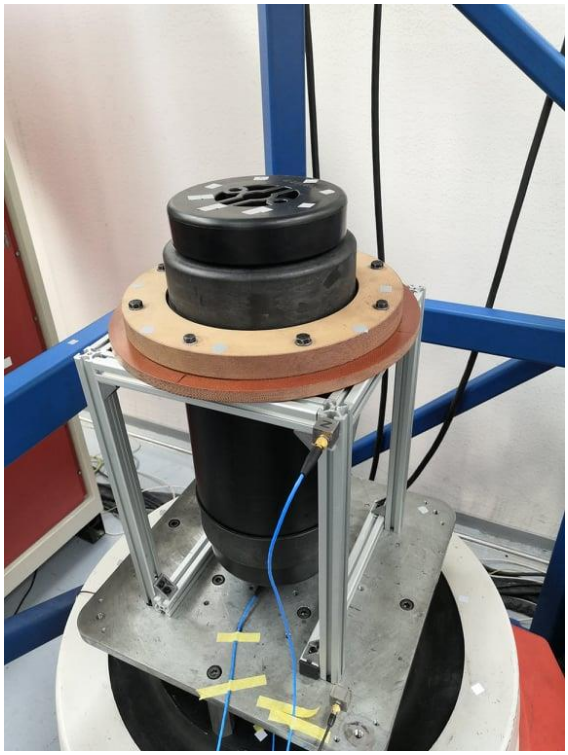

Fig. 1. Vibration testing assembly

5. Experimental results

For THD computation only vertical axis measurement of one accelerometer BK 4056 is used. White-noise with 10 m/s^2 prescribed acceleration and 10-2000 Hz frequency range is used for excitation. Sample rate for measurement is 100 kHz. Experiments are performed in 4 different configurations. They differ in assembly configuration and manner of simulated damage. The algorithm is used on premeasured data.

1st experiment: Fig. 2 - Only steel plate is mounted on shaker's armature. After 60 seconds of measurement two screws on the plate are tightened.

2nd experiment: Fig. 3 - Steel plate and aluminium testing frame are mounted on shaker's armature. After 60 seconds of measurement one screw on vertical beam of testing frame is tightened.

3rd experiment: Fig. 4 - Steel plate and aluminium testing frame are mounted on shaker's armature. After 60 seconds of measurement two screws on aluminium plate are tightened.

4th experiment: Fig. 5 - Complete testing setup (Fig. 1) is assembled (steel plate, aluminium testing frame and tested component). After 200 seconds of measurement one screw on vertical beam of testing frame is loosened.

Noticeable change in computed values are observed after tightening/loosening the screws in all scenarios.

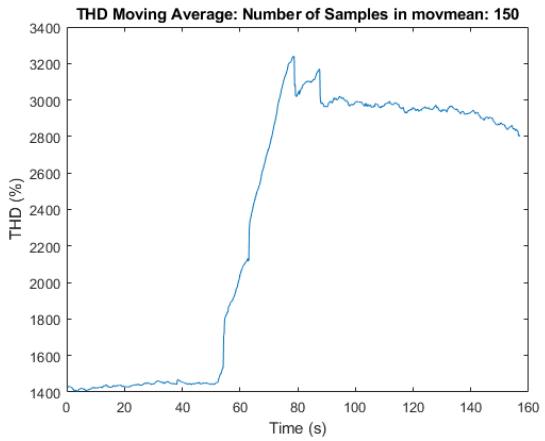

Fig. 2. Moving average of THD during 1st experiment

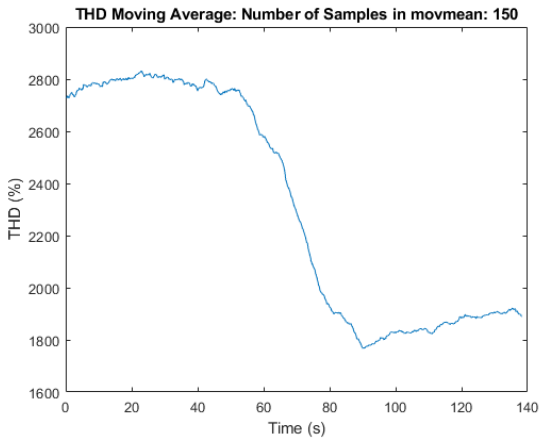

Fig. 3. Moving average of THD during 2nd experiment

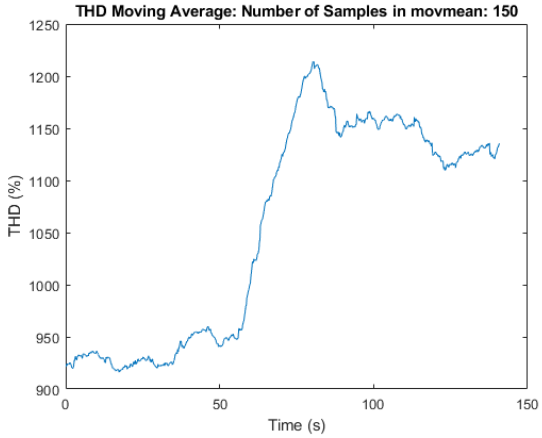

Fig. 4. Moving average of THD during 3rd experiment

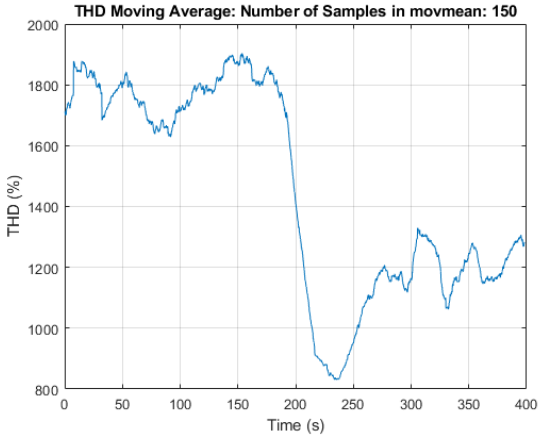

Fig. 5. Moving average of THD during 4th experiment

6. Conclusion

Method for SHM during vibration testing suitable for white-noise excitation is proposed. Based on several experiments noticeable changes in computed average THD values are observed. In four experiments it's 114%, 36%, 24%, 33% respectively.

Future work plan contains real-time implementation, other means of damaging the structure, using data from more accelerometers and axes while performing more experiments in different conditions. This work needs to be done to make the method robust and reliable, but first results seem to be promising.

Acknowledgements

This work has been supported by Student Grant Competition of CTU under project Modelling, control and design of mechanical systems 2019 No. SGS19/157/OHK2/3T/12 and by TACR project #TN01000071 National Competence Centre of Mechatronics and Smart Technologies for Mechanical Engineering (MESTEC).

References

[1] Broch, J. T., Mechanical vibration and shock measurements, Bruel & Kjaer. K. Larsen & Son, Soborg. 1984.
[2] Fan, G., Li, J., Hao, H., Vibration signal denoising for structural health monitoring by residual convolutional neural networks, Measurement 157, 2020.
[3] Miláček, S., Měření a vyhodnocování mechanických veličin, ČVUT, Praha, 2001. (in Czech)
[4] Minderhound, J., A Method for shaker validation, Webinar presentation of Vibration Research Corporation.
[5] Toh, G., Park, J., Review of vibration-based structural health monitoring using deep learning, Applied Sciences 10 (5) 2020.

COMPUTATIONAL MECHANICS 2021
36th conference with international participation
Srní
November 8 - 10, 2021

Practical notes on the evaluation of fatigue life of welded nodes of bus bodyworks

M. Kepka[a], M. Kepka jr.[a], R. Minich[a], P. Žlábek[a]

[a] *Faculty of Mechanical Engineering, University of West Bohemia in Pilsen, Univerzitní 8, 301 00 Plzeň, Czech Republic*

In order to calculate fatigue service life of structures and their parts operating under cyclic loads, one needs the following data: information on their fatigue strength and information on their service loads. In high-cycle fatigue scenarios, the main input data includes: S-N curve and service stress spectra for major operating modes. This input information must apply to the same (critical) cross-section of the component in question. It is normally found by measurement and testing. S-N curves are constructed from laboratory fatigue test data using statistical evaluation. Service stress spectra are obtained by analysing measured data during operation or so-called design stress spectra are used. Stress spectra are converted to fatigue damage using cumulative damage rules which have been proposed by various authors. Two basic approaches are available for evaluating [1].

Approach A: Using the relevant service stress spectrum and S-N curve parameters, the fatigue damage of a particular component or structural detail cross-section is calculated, and an estimate of its service life is obtained and compared to the desired life. This is the usual procedure.

Approach B: Based on the desired service life, pre-defined S-N curve parameters, and a design stress spectrum, the engineer determines maximum allowable service stress levels for a particular cross-section of a component or structural detail. The procedure is shown in Fig. 1.

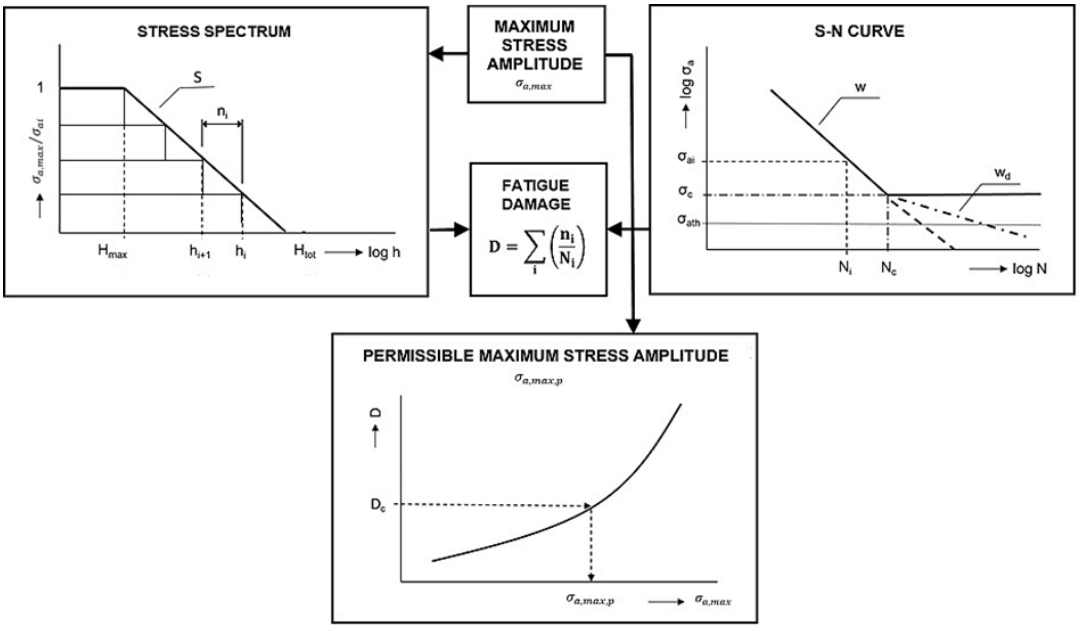

Fig. 1. Procedure to determine the permissible maximum stress amplitude $\sigma_{a,max,p}$

Case study A

The detail of interest was a severely stressed beam joint in the top corner of the door opening in the bus body shown in Fig. 2. The critical cross section was monitored by strain gauge T6.

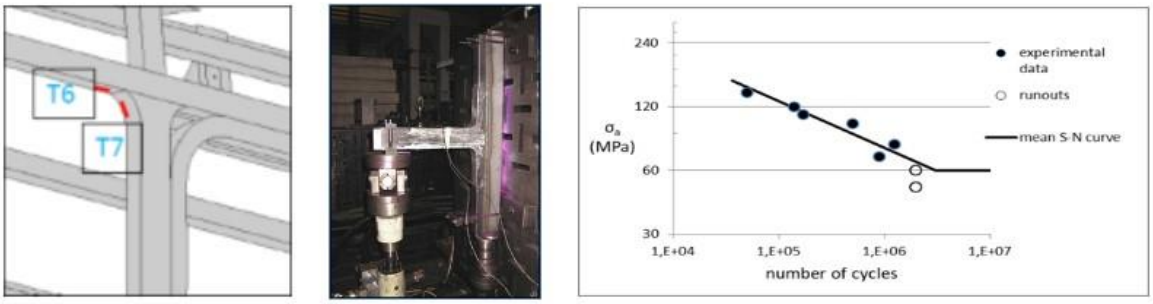

Fig. 2. Detail of interest, laboratory fatigue test and S-N curve

The test specimens were made from thin-walled welded closed profiles, which had 70×50 mm cross-section and 2 mm wall thickness and were made of S235JR steel. The critical cross-section of the joint was subjected to reverse bending load (the cycle stress ratio was $R = -1$).

The limit state was defined by the instant at which a macroscopic fatigue crack forms (1 to 2 mm). In all cases, fatigue cracks initiated in the transition zone of the fillet weld.

Statistical evaluation of the fatigue test data yielded the parameters of the mean S-N curve for the structural detail in the form

$$log\ (N) = 14.54 - 4.53 \cdot log\ (\sigma_a)\ ;\ \sigma_c = 60 \text{ MPa}.$$

During testing, the stresses acting on the critical cross-section were measured by strain gauges attached approximately 5 mm from the toe of the fillet weld. The measured values by strain gauges T6 can therefore be referred to as the equivalent structural stress.

In this case, the service stress-time histories were measured for a city bus riding on an irregular surface along a city route whose total length was $L_m \approx 40$ km. In a similar manner to representative urban traffic, the stress spectra on the test polygon were evaluated. The test polygon offers sections, tracks and roads with various longitudinal road profile and different surface quality. The measurement was repeated tree times with empty vehicle and three times with fully loaded vehicle. Total length of the measured route was $L_m \approx 35.5$ km. The signals were analysed in the frequency domain, and insignificant high frequencies were eliminated before using the rain-flow technique. In high-cycle fatigue of welded structures, the mean stress of the cycle does not play a major role. Therefore, only the one-parameter stress spectra $\sigma_{ai} - n_i$ were used for subsequent calculations.

Mostly the fatigue damage D is calculated using the linear cumulative damage rule. According to this rule, the limit state with respect to fatigue is reached (i.e. the fatigue life of the structural part is exhausted) when the following condition is met

$$D = \sum_i \frac{n_i}{N_i} = D_c,$$

where D is the fatigue damage caused by the stress spectrum imposed, n_i is number of cycles applied at the i-th level of stress with the amplitude σ_{ai}, N_i is limit life under identical loading (the number of cycles derived from the S-N curve for the part in question at the amplitude σ_{ai}) and D_{lim} is limit value of fatigue damage.

Various rules apply various boundary conditions to fatigue damage calculation. A schematic representation of these boundary conditions is shown in Fig. 3.

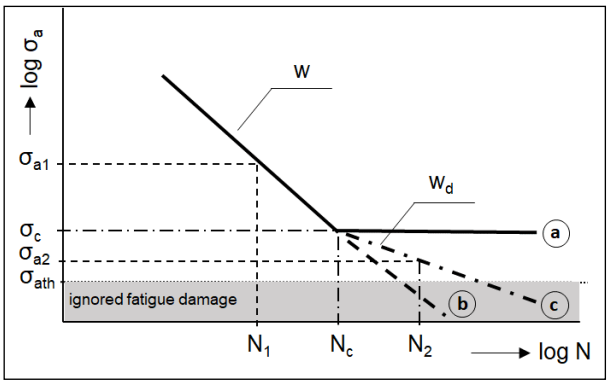

Fig. 3. Boundary conditions for calculating cumulative fatigue damage:
a - Palmgren-Miner original, b - Palmgren-Miner elementar, c – Haibach

In the present case, the Haibach-modified version of the Palmgren-Miner rule was chosen for calculating fatigue damage. The limit number of cycles Ni was determined as follows

$$\text{- } \sigma_{ai} \geq \sigma_c\text{:} \qquad N_i = N_c \cdot \left(\frac{\sigma_c}{\sigma_{ai}}\right)^{w},$$

$$\text{- } \sigma_{\text{ath}} < \sigma_{ai} < \sigma_c\text{:} \qquad N_i = N_c \cdot \left(\frac{\sigma_c}{\sigma_{ai}}\right)^{wd}.$$

Haibach recommends the exponent for the lower part of the S-N curve to be set as $w_d = 2w - 1$. In this study, the value was $w_d = 8$. The threshold stress amplitude for taking the fatigue damaging into account was given as $\sigma_{ath} = 0.5 \cdot \sigma_c$ in the present case. The limit value of fatigue damage was taken as $D_{lim} = 0.5$.

The computational estimate of service fatigue life (in kilometre run) is obtained from equation

$$L = (D_{lim} / D) \cdot L_m .$$

Table 1 provides predicted fatigue life for the service stress spectra and the spectra measured on the test polygon. The ratio of these predicted fatigue life is an estimation of the acceleration (shortening) of the driving fatigue test that could be achieved on the test polygon compared to normal vehicle operation.

Table 1. Estimation of acceleration factor of driving fatigue test

Empty vehicle	Real operation	Testing ground	Acceleration
L [km]	3,178,000	203,000	15.7

Loaded vehicle	Real operation	Testing ground	Acceleration
L [km]	4,309,000	337,000	12.8

Case study B

The structural nodes with and without reinforcement were tested and two materials (low carbon steel and stainless steel) were considered in this study, see schematic pictures of nodes A, B and C in Fig. 4. Statistical evaluation of the fatigue test data yielded the parameters of the S-N curve. The scatter of fatigue properties of assessed construction nodes was considered by British Standard BS 7608. In the present case, the Haibach-modified version of the Palmgren-Miner rule was chosen for calculating fatigue damage again. The maximum permissible stress amplitudes $\sigma_{a,max,p}$ were determined by the approach schematically shown in Fig. 1 and compared with the values calculated, Fig. 5.

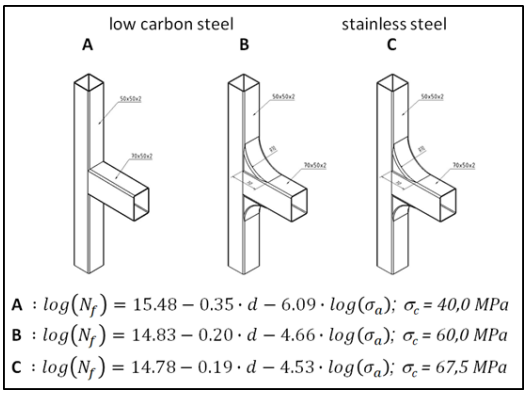

Fig. 4. Bodywork structural nodes and S-N curves

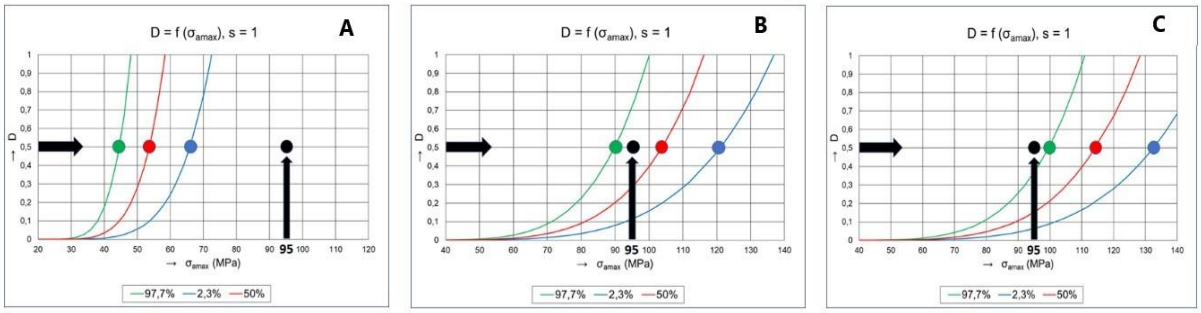

Fig. 5. Maximum calculated stress amplitude (black) and permissible values

Based on the case study, it is possible to formulate a clear conclusion. The structural node A does not absolutely meet the required service life. Even the structural node B does not achieve the required service fatigue life with sufficient reliability. Only the structural node C could be recommended because it meets the required service fatigue life with the usual design reliability (survival probability higher than 97.7%).

Acknowledgements

The work has been supported by the Technology Agency of the Czech Republic, research project Nr. FW01010386 “Research and development of articulated electric bus”.

References

[1] Kepka jr., M., Degradation of mechanical properties of cyclically loaded materials and structural nodes, dissertation thesis, University of West Bohemia, Faculty of Mechanical Engineering, Pilsen, 2021.

COMPUTATIONAL MECHANICS 2021
36th conference with international participation
Srní
November 8 - 10, 2021

Use of advanced kinematic hardening rules for prediction of multiaxial ratcheting

V. Klepač[a], S. Parma[a], H. P. Feigenbaum[b], R. Marek[a], J. Plešek[a], J. Svárovský[c]

[a] *Institute of Thermomechanics, Czech Academy of Sciences, Dolejškova 5, 180 00 Praha 8, Czech Republic*
[b] *Department of Mechanical Engineering of Northern Arizona University 15600 S. McConnel Dr. NAU bldg 69 Flagstaff, AZ 86001-5600*
[c] *Department of Mechanics, Biomechanis and Mechatronics,Faculty of Mechanical Engineering, CTU in Prague, Czech Republic*

Cumulation of plastic strain due to cyclic loading, so called ratcheting, experimentaly observed as Baushinger effect, is possible cause of problems in range of engineering applications. This phenomenon occurs during unsymmetric cyclic loading in structures such as facilities pipes, offshore structures, etc., whenever occasional overloads occur. This can cause problems of structures service, or even their failure. To capture physical process of multiaxial ratcheting (MR) evolution, wide range of advanced plasticity models was developed. In this work we are focused on phenomenon of non-linear kinematic hardening (KH). Models for capturing of KH are based on concept of multi-component backstress [1]. There are many of these models published. In this work we present a model of *Multicomponent Armstrong–Frederick with Threshold with r modification* (MAFTr) published in [2]. For reason of MR prediction on complex structures, the model is implemented into FE code Abaqus through UMAT subroutines coded in FORTRAN programming language.

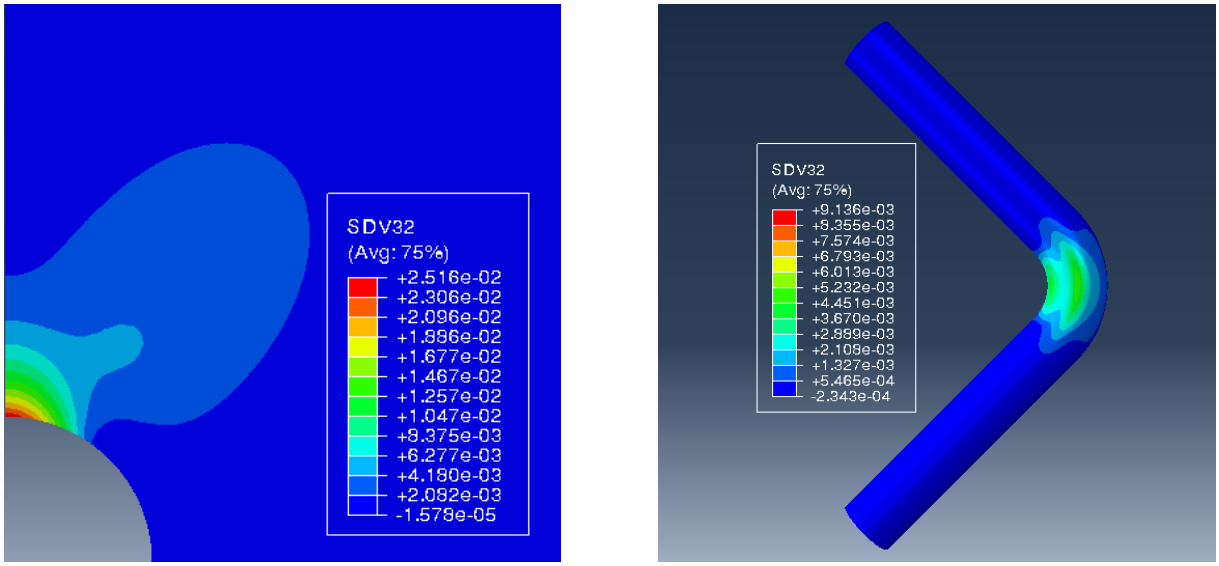

(a) (b)

Fig. 1. Numerical examples used to test performance of UMAT subroutine with implemented *MAFTr* model into Abaqus FE code

Table 1. Material parameters of MAFTr model [2]

a_{11} [−]	a_{12} [−]	a_{13} [−]	a_{14} [−]	a_{21} [MPa^{-1}]	a_{22} [MPa^{-1}]	a_{23} [MPa^{-1}]	a_{24} [MPa^{-1}]
225 353.7	12 123.0	3 004.0	56 338.0	0.05917	0.02199	0.004437	0.0591

Within the *MAFTr* model, an additive decomposition of small, rate independent strains is assumed as in $\boldsymbol{\varepsilon}_{\mathrm{tot}} = \boldsymbol{\varepsilon}_{\mathrm{pl}} + \boldsymbol{\varepsilon}_{\mathrm{el}}$. Elastic behavior of material follows Hooke's law in the form $\boldsymbol{\sigma} = \lambda \boldsymbol{I} \mathrm{tr}\boldsymbol{\varepsilon}_{\mathrm{el}} + 2\mu\boldsymbol{\varepsilon}_{\mathrm{el}}$, where $\boldsymbol{\sigma}$ is a stress tensor, λ and μ are Lamé elastic parameters and $\boldsymbol{I}$ is a unit second-order tensor. Hereafter, however, to keep the notion simple, we use Hooke's law in general form $\boldsymbol{\sigma} = \boldsymbol{C}\boldsymbol{\varepsilon}_{\mathrm{el}}$. Hence, further in this work, the term λ denotes exclusively the loading index. In this work we adpot classical von Mises yield criterion is used as

$$f = \sqrt{\frac{3}{2}} \left(\boldsymbol{s} - \boldsymbol{\alpha}\right) : \left(\boldsymbol{s} - \boldsymbol{\alpha}\right) - k^2. \tag{1}$$

Further we omit change in the isotropic hardening by keeping $\dot{k} = 0$. We adpot the associative flow rule, which may be written as

$$\dot{\boldsymbol{\varepsilon}}_{pl} = \lambda \frac{\partial f}{\partial \boldsymbol{\sigma}}. \tag{2}$$

The *MAFTr* KH rule reads

$$\bar{\boldsymbol{\alpha}}_i = a_{1i} \left\| \frac{\partial f}{\partial \boldsymbol{\sigma}} \right\| \left(\boldsymbol{n} - a_{2i} \left[r_i \boldsymbol{\alpha}_i + \left(1 - r_i\right) \left(\boldsymbol{\alpha}_i \boldsymbol{n}\right) \boldsymbol{n}\right]\right), i = 1, 2, 3, \tag{3a}$$

$$\bar{\boldsymbol{\alpha}}_4 = a_{14} \left\| \frac{\partial f}{\partial \boldsymbol{\sigma}} \right\| \left(\boldsymbol{n} - a_{24} \left[r_4 \boldsymbol{\alpha}_4 + \left(1 - r_4\right) \left(\boldsymbol{\alpha}_4 : \boldsymbol{n}\right) \boldsymbol{n}\right] \left\langle 1 - \frac{\overline{a}}{g\left(\boldsymbol{\alpha}_4\right)} \right\rangle \right), \tag{3b}$$

$$g\left(\boldsymbol{\alpha}_4\right) = \left[\frac{3}{2} \boldsymbol{\alpha}_4 : \boldsymbol{\alpha}_4\right]^{\frac{1}{2}}, \tag{3c}$$

$$r_i = \sqrt{\frac{3}{2} \boldsymbol{\alpha}_i : \boldsymbol{\alpha}_i} \sqrt{\frac{2}{3}} a_{2i}\,, \tag{3d}$$

where a_{1i}, a_{2i} and $\bar{a}$ are material parameters, and $\boldsymbol{n}$ denotes the unit norm of the yield surface. Parameter r_i is a weighting factor and evolves along the loading history.

The implementation via UMAT follows the scheme published in [5]. This algorithm is built on predictor-corrector method with radial return onto the yield surface. Implementation of *MAFTr* was verified by comparison with closed form solution

$$\alpha_i = \frac{1}{a_{2i}} - \left(\frac{1}{a_{2i}} - \alpha_i^0\right) \exp\left[-a_{1i} a_{2i} \sqrt{\frac{3}{2}} \left(\varepsilon_{cum} - \varepsilon_{cum}^0\right)\right], \tag{4a}$$

$$\alpha_4 = \left(\frac{1}{a_{24}} \pm \sqrt{\frac{2}{3}} \overline{a}\right) - \left(\frac{1}{a_{24}} \pm \sqrt{\frac{2}{3}} \overline{a} - \alpha_4^0\right) \exp\left[-a_{14} a_{24} \sqrt{\frac{3}{2}} \left(\varepsilon_{cum} - \varepsilon_{cum}^0\right)\right], \tag{4b}$$

derived for the case of uniaxial loading. To test performance of subroutines, two numerical examples were done. First one was planar plate with hole loaded by a pressure in single direction. Second one was simulation of elbow pipe preloaded by a pressure and cyclicly loaded by displacement according to experiment in [4]. These examples are depicted in Fig. 1.

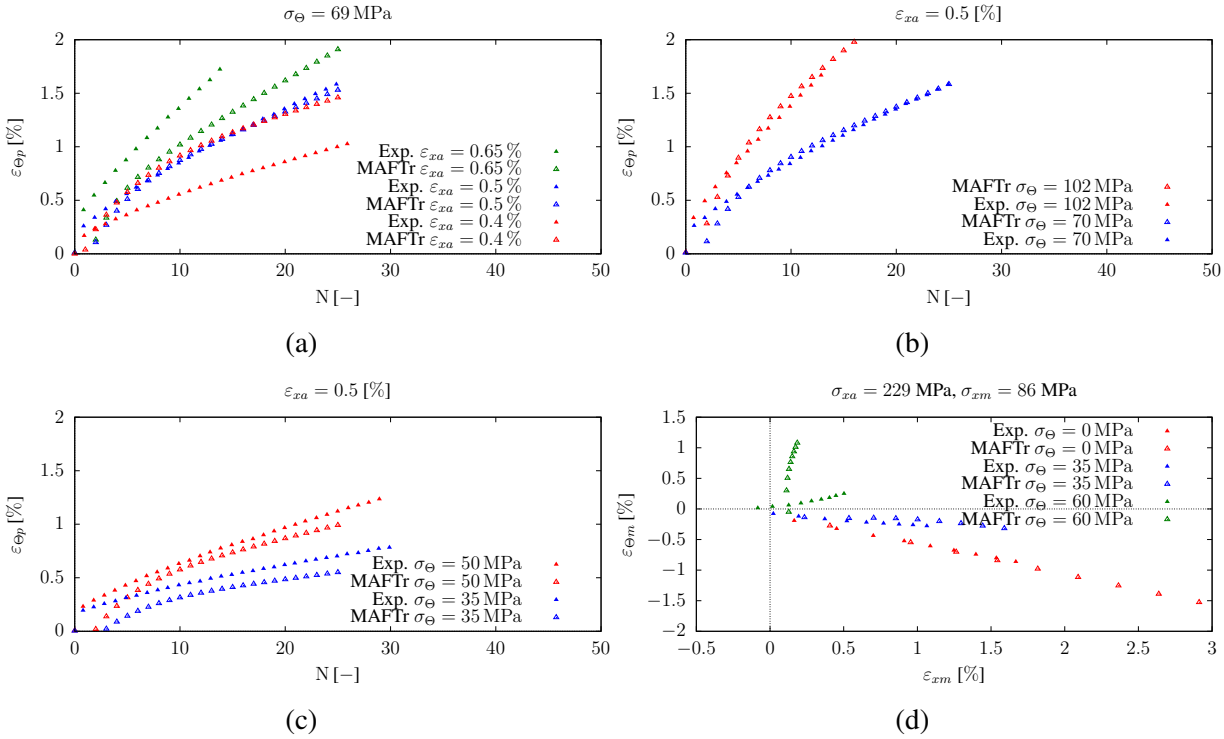

Fig. 2. Biaxial ratcheting predicted by MAFTr model and prediction of ratcheting as a function of number of cycles. Set of experimental data was meassured on CS 1026 published in [3]. Ratcheting simulations with previously estimated stress increment and their comparison with the experimental data are depicted in subfigures (a) – (d)

Prameters of *MAFTr* model were calibrated on experimental MR data published by Hassan et al. [3], reported in [2] and given in Table 1. With calibrated model, range of simulations of MR was performed. Results of some of them are depicted in Fig. 2. In Fig. 2(a), tests differ in amplitude of prescribed axial strain ε_{xa}. The evolution of ratcheting by FEA with implemented *MAFTr* model is underpredicted for $\varepsilon_{xa} = 0.65\,\%$, and overpredicted if $\varepsilon_{xa} = 0.4\,\%$. Accurate results were obtained for case of $\varepsilon_{xa} = 0.5\,\%$. To check importance of prescribed axial strain, tests with different load and preload stress were performed. Results of these set-ups are shown in Figs. 2(b) and 2(c). So far, less promising situation is depicted in Fig. 2(d), which shows evolution of ratio between circumferential mean strain $\varepsilon_{\Theta m}$ and axial mean strain ε_{xm}, when the specimen is preloaded by circumferential stress σ_{xm} and axial stress σ_Θ, and cyclicly loaded by axial stress σ_{xa}.

This work presented the use of advanced KH rule to predict multiaxial ratcheting by FEM. The departure between prediction and experimental data in Fig. 2(a) and its dependency on prescribed axial strain ε_{xa} leads to the need of study of calibration procedure. Hence, in future work, the identification of model parameters will be studied more deeply. Subsequentaly, evolution of ratcheting in complex structures, such as aforementioned elbow pipe [4], and its prediction by FEM in combination with advanced plasticity laws will be modeled.

References

[1] Chaboche, J. L., Dang-Van, K., Cordier, G., Modelization of the strain memory effect on the cyclic hardening of 316 stainless steel, Proceedings of the 5th International Conference on Structural Mechanics in Reactor Technology, Berlin, Germany, 1979, pp. 1-10.

[2] Dafalias, Y. F., Feigenbaum, H. P., Biaxial ratchetting with novel variations of kinematic hardening, International Journal of Plasticity 27 (4) (2011) 479-491.

[3] Hassan, T. Corona, E., Kyriakides, S., Ratcheting in cyclic plasticity, part II: Multiaxial behavior, International Journal of Plasticity 8 (2) (1992) 117-146.

[4] Hassan, T., Rahman, M., Bari, S.,Low-cycle fatigue and ratcheting responses of elbow piping components, Journal of Pressure Vessel Technology 137 (3) (2015) No. 031010.

[5] Marek, R., Plešek, J., Hrubý, Z., Parma, S.,Feigenbaum, H. P., Dafalias, Y. F., Numerical implementation of a model with directional distortional hardening, Journal of Engineering Mechanics 141 (12) (2015) No. 04015048.

COMPUTATIONAL MECHANICS 2021
36th conference with international participation
Srní
November 8 - 10, 2021

Aerodynamic design of transsonic compressor airfoil family

J. Klesa

Faculty of Mechanical Engineering, Czech Technical University, Karlovo náměstí 13, 121 35 Praha, Czech Republic

New family of transsonic compressor airfoils is being developed in the frame of KOBRA project. This project is focused on the development of new gas-cooled nuclear reactor and axial compressor is a part of the secondary system. Maximum Mach number based on intake velocity is assumed 0.8, which gives compromise between high stage pressure ratio and low loss coefficient. New airfoil family should have better performance that classical NACA 65 airfoils [2], but it should offer performance comparable with the Controlled Diffusion Airfoils (CDA) [1].

Airfoil shape is defined in an explicit way, i.e. like NACA 65 airfoils. This is the main difference in comparison with common CDA airfoils [5, 3, 4], where each airfoil have to be designed separately and optimised by means of CFD simulation. Explicit formulation of airfoil geometry brings several advantages, e.g., faster and easier blade design or less problems during blade assembly from separated airfoils.

Several chamber functions were tested during airfoil development (see Fig. 1):

1. combination of straight line and polynome, Fig. 1 (left),
2. mean line of NACA 6 airfoils for constant γ, Fig. 1 (middle),
3. mean line of NACA 6 airfoils for trapezoidal γ, Fig. 1 (right).

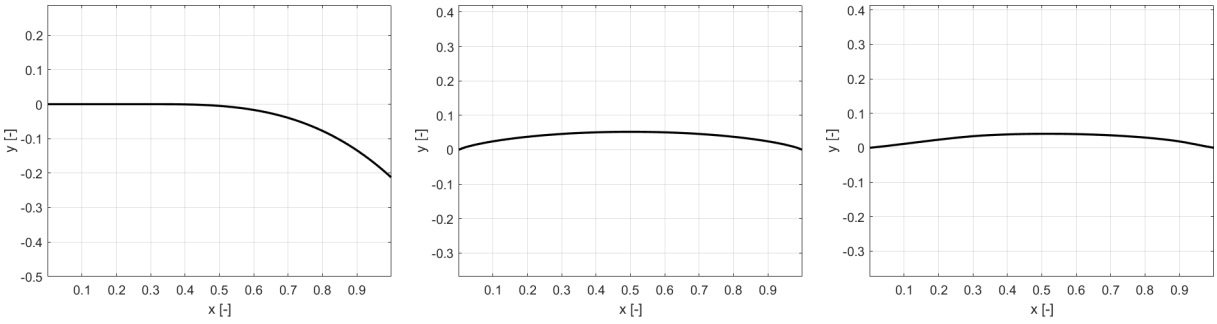

Fig. 1. Comparison of three mean curves used for the compressor airfoil development

Thickness function is based on the thickness function derived from the NASA supercritical airfoil SC(2)-1006. Thickness function is modified so that trailing edge thickness can be chosen according to the design requirements. Comparison of the original and modified thickness functions ca be seen in Figs. 2 and 3. Presented airfoils have third type of chamber function and intake angle 60° and Mach number 0.8. Airfoils characteristics will be analyzed by means of CFD in order to find design rules for cascade solidity, incidence and deviation angles.

The design procedure of the new airfoil family suitable for transsonic axial compressors is presented in this paper. These airfoils will be used for the compressor for nuclear reactor

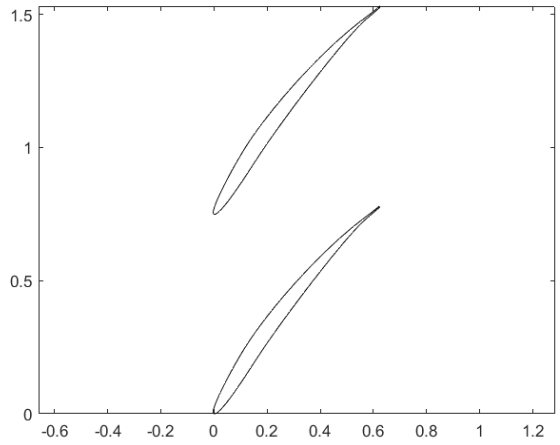

Fig. 2. Airfoil with unmodified thickness function for the intake angle 60° and Mach number 0.8

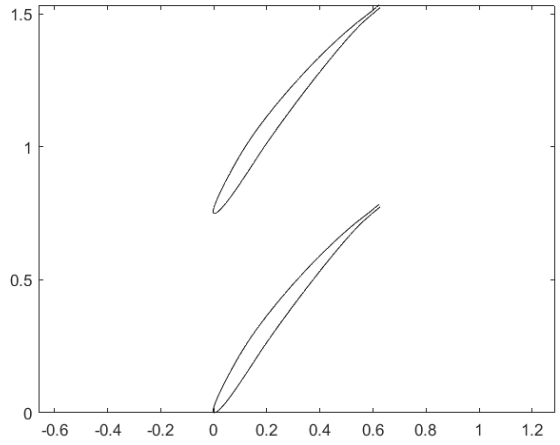

Fig. 3. Airfoil for the intake angle 60° and Mach number 0.8 with modified trailing edge, i.e. trailing edge thickness is 1% of the airfoil chord

cooling developed during the KOBRA project in the cooperation of Czech Technical University, Nuclear Research Institute and Czech Academy of Sciences. The aim is to develop airfoils which geometry is defined in explicit way and which have performance comparable with controlled diffusion airfoils (CDA), i.e. high stage pressure ratio and high polytropic efficiency is reached. Airfoil geometry is based on the mean curve and thickness distribution. Thickness distribution is modified so that prescribed trailing edge thickness is reached. Several mean curves are tested. Finally, the geometry of the airfoil family is presented.

Acknowledgement

This work was supported by the Technology Agency of the Czech Republic, project TK03030121 Conceptual Design of an Innovative Safety System for Gas-cooled Nuclear Reactors.

References

[1] Bräunling, W. J. G., Aircraft engines, Springer, Berlin Heidelberg, 2015. (in German)
[2] Cumpsty, N. A.,Compressor aerodynamics, Krieger, Malabar, 2004.

[3] Köller, U., Mönig, R., Küsters, B., Schreiber, H.-A., Development of advanced compressor airfoils for heavy-duty gas turbines: Part I – Design and optimization, Proceedings of the ASME 1999 International Gas Turbine and Aeroengine Congress and Exhibition, Indianapolis, USA, 1999, Paper No: 99-GT-095.

[4] Küsters, B., Schreiber, H.-A., Köller, U., Mönig, R., Development of advanced compressor airfoils for heavy-duty gas turbines: Part II – Experimental and theoretical analysis, Proceedings of the ASME 1999 International Gas Turbine and Aeroengine Congress and Exhibition, Indianapolis, USA, 1999, Paper No: 99-GT-096.

[5] Schnoes, M., Nicke, E., A database of optimal airfoils for axial compressor throughflow design, Numerical Heat Transfer 4 (8) (1989) 165-180.

COMPUTATIONAL MECHANICS 2021
36th conference with international participation
Srní
November 8 - 10, 2021

In vitro structured tree model of the peripheral vascular network

J. Kohút, J. Jagoš, M. Formánek, J. Burša

Faculty of Mechanical Engineering, Brno University of Technology, Technická 2896/2, 616 69 Brno, Czech Republic

1. Introduction

The heart provides pulsatile flow through arteries. In the cardiovascular system, arteries convey nutrient-rich and oxygenated blood to the tissues. Large arteries with a diameter reaching 25 mm gradually taper towards the periphery and branch into smaller arteries. Arterioles with a diameter less than 1 mm are followed by even smaller vessels, capillaries, where the exchange between the blood and tissue cells occurs. The focus of this study is on the arterial periphery and thus on the small arteries. It has been shown that their branching follows a certain order. They form a self-similar asymmetric structured tree, which can be described mathematically [2]. The parent vessel r_p, representing small artery, branches into two smaller arteries (r_{d_1}, r_{d_2}) with radii reduced by coefficients α and β, i.e.,

$$r_{d_1} = \alpha r_p \quad \text{and} \quad r_{d_2} = \beta r_p. \tag{1}$$

The branching is terminated with a minimum radius r_{min} corresponding to the radius of arterioles. The termination has its physiological meaning since the arterioles have approximately the same diameter to ensure even blood supply to organs. Minimum radius r_{min} is constant inside the tree but can vary with different structured trees representing individual organs [2].

The purpose of this work is to assemble a similar system *in vitro*. So far, previous phantom studies have incorporated only pure resistance or two-element Windkessel (2-WK) as an *in vitro* periphery [1], mostly represented by a needle valve and a compliance chamber. Thus, neglecting some of the characteristic features of the arterial periphery, e.g., fluctuations on the input impedance modulus and phase resulting from wave propagation and its reflections within the entire tree with most pronounced reflections at the capillary level. These shortcomings justify the rather smooth waveforms without higher frequency oscillations in phantom experimental measurements, for instance in [1]. Moreover, phase and modulus deviates from reality in both lower and higher frequencies for 2-WK, due to the absence of inertance and characteristic impedance of the root vessel respectively [3, 4]. Including the asymmetric structured tree model in *in vitro* studies as a boundary condition could improve the wave shapes and consequently the overall flow field behaviour (e.g., in an aortic or a carotid phantom).

2. Mathematical model

The wave propagation velocity in small arteries (considered as cylindrical) is much larger than the velocity of the blood flow dominated by viscous forces, leading to the analytical solution of axisymmetric Navier-Stokes equation in the form of pressure $P(x, \omega)$ and flow $Q(x, \omega)$ wave equations. In terms of electrical analogy, the vascular impedance $Z(x, \omega)$ is defined as a ratio

between these wave equations

$$Z(x,\omega) = \frac{P(x,\omega)}{Q(x,\omega)} = \frac{\frac{i}{cC}\left(C_2\cos(\frac{\omega x}{c}) - C_1\sin(\frac{\omega x}{c})\right)}{C_1\cos(\frac{\omega x}{c}) + C_2\sin(\frac{\omega x}{c})}. \tag{2}$$

Eq. (3) based on Eqs. (2) and (4) (from Poiseuille's equation) are the final equations used in the mathematical model [2]

$$Z(0,\omega) = \frac{\frac{i}{cC}\sin(\frac{\omega L}{c}) + Z(L,\omega)\cos(\frac{\omega L}{c})}{\cos(\frac{\omega L}{c}) + icCZ(L,\omega)\sin(\frac{\omega L}{c})} \quad \text{for} \quad x = 0,\ \omega \neq 0, \tag{3}$$

$$Z(0,0) = \lim_{\omega\to 0} Z(0,\omega) = \frac{8\mu l_{rr}}{\pi r^3} + Z(L,0) \quad \text{for} \quad x = 0,\ \omega = 0, \tag{4}$$

where Z is the impedance [kg.m^{-4}.s^{-1}], c is the wave propagation velocity [m.s^{-1}], $C = \frac{3Ar}{2Eh}$ is the compliance [m^2.Pa^{-1}], A is the cross-sectional area [m^2], h is the thickness [m], E is the Young's modulus [Pa], ω is the angular frequency [rad.s^{-1}], x is the axial coordinate [m], $C_{1,2}$ are the constants from general solution of differential equation [–], L is the length of the vessel [m], μ is the dynamic viscosity [Pa.s], l_{rr} is the length to radius ratio [–], and r is the internal radius [m]. The 1D mathematical model of a structured tree is closed with two boundary conditions. A bifurcation condition and a terminal boundary condition, which is determined by zero impedance or constant resistance

$$\frac{1}{Z_p} = \frac{1}{Z_{d_1}} + \frac{1}{Z_{d_2}} \quad \text{and} \quad Z(L,0) = 0,\ Z(L,\omega) = 0. \tag{5}$$

Indexes in this equation correlate with Eq. (1) [2].

The input impedance of the root vessel in the arterial tree includes the resistance of smaller arteries (zero frequency), total arterial compliance (lower frequencies), the characteristic impedance of the root vessel (higher frequencies), wave propagation, and the reflections in the system [4]. The purpose of this model is to describe the input impedance of the structured tree, i.e., the input impedance at the beginning of the root vessel. Since only the impedance at the termination r_{min} is known, the recursive algorithm is necessary to acquire the input impedance [2]. The results can be then validated against experimental measurements *in vitro*.

3. Experimental circuit

For validation of the mathematical model and other experimental measurements, the experimental circuit was assembled (see Fig. 1). The working fluid is moved from reservoir 1 by two-roller peristaltic pump 2, which generates the physiological waveform with specific rotational velocity profile per revolution (found iteratively). The pump is driven by a stepper motor controlled from the MATLAB/Simulink environment, with the usage of Simulink Desktop Real-Time's kernel and Humusoft's I/O device MF634. The circuit also comprises ultrasonic flow meter 3 and two relative pressure sensors 4 and 5 with a sampling frequency of 200 Hz (sufficient to capture the transient pressure waveform). The distance between the pressure sensors was set to 0.6 m, so the pressure loss Δp would be significant and thus measurable for every time step. The transient Δp profile was used to calculate (by pressure-time method) the instantaneous flow rate since the ultrasonic flowmeter provides only the mean flow rate. The evaluation units 6 and 7 serve for individual data collection. The root of the structured tree 8 is connected downstream to the rigid tube with the pressure sensors. The fluid exits the structured tree to the atmospheric pressure and back to reservoir 1. Because the *in vitro* tree is larger in size and less compliant, a slightly higher viscosity of working fluid (mixture of glycerin and water) was chosen in comparison with the real blood to ensure similarity with the *in vivo* impedance, i.e., constant

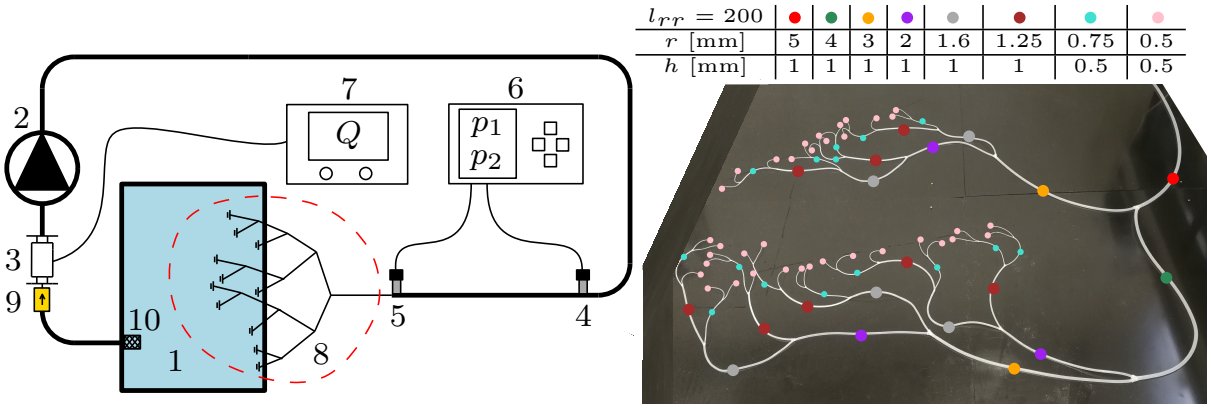

Fig. 1. The scheme of the experimental station for *in vitro* input impedance measurements: 1 – reservoir, 2 – peristaltic pump, 3 – ultrasonic flowmeter, 4 and 5 – pressure sensors, 6 and 7 – evaluation units of pressure and flow, 8 – structured tree (in detail on the right), 9 – non-return valve, 10 – suction filter

viscosity $\mu = 6$ mPa.s and density $\rho = 1126.8$ kg.m^{-3}.

The structured tree consists of small silicon tubes (60 Shore A), which are glued together to form the peripheral vascular site, in detail Fig. 1 (right). It was assumed that the deformations are very small since the maximal pressure in the tube is relatively low, 45 kPa. Therefore, only a few percentages (up to 10%) were included in the determination of E, corresponding to 4.8 MPa. The tube lengths and radii are scaled towards the periphery in a similar manner as can be found *in vivo*, see Eq. (1). To obtain a similar input impedance *in vivo*, the dimensions of the real model had to be scaled according to the limited dimensions and material properties of the commonly available silicon tubes (e.g., internal radii r, thickness h, and Young's modulus E).

The obtained variables from the evaluation units (i.e., the pressure waveform from sensor 5 and flow waveform) need to be transferred from the time-discrete domain to the discrete frequency domain. Doing so, the electrical analogy can be used once again as a simple ratio between the pressure and flow rate. Hence, the frequency-dependent input impedance of the arterial tree is evaluated and can be compared with the mathematical one.

4. Results and discussion

Analytical equations together with the recursive algorithm based on [2] were implemented into MATLAB R2020a. The analytical input impedance is a direct output of the algorithm (blue curve in Fig. 2). The measured waveforms (period $T = 1$ s) were decomposed into cosine waves with corresponding amplitude and phase using the Fourier series. Therefore, the *in vitro* input impedance modulus and phase could be obtained (red curve). Ten harmonics ($n = 10$) were sufficient to describe both waves. The higher the harmonics the smaller is the contained information in signals, which are subjected to noise. Resulting in significantly scattered values of input impedance modulus and phase in higher frequencies. It was mitigated by averaging the input impedance from analyzing multiple periods [4]. For further observation, the human brachiocephalic artery input impedance measured *in vivo* (green curve) [2] is also depicted.

The *in vitro* modulus $|Z_i|$ corresponds very well with the mathematical one, both qualitatively and quantitatively, Fig. 2 (left). Especially in lower frequencies, where the scatter is less pronounced. However, the r_{min} in the mathematical model had to be lowered by 20 %, because of the spread of the gluing into the smallest tubes in the *in vitro* model and thus reducing the internal radius, which led to a higher resistance. The deviation in higher frequencies can be caused by the averaging of multiple periods. Compared to *in vivo* curve, these modules are

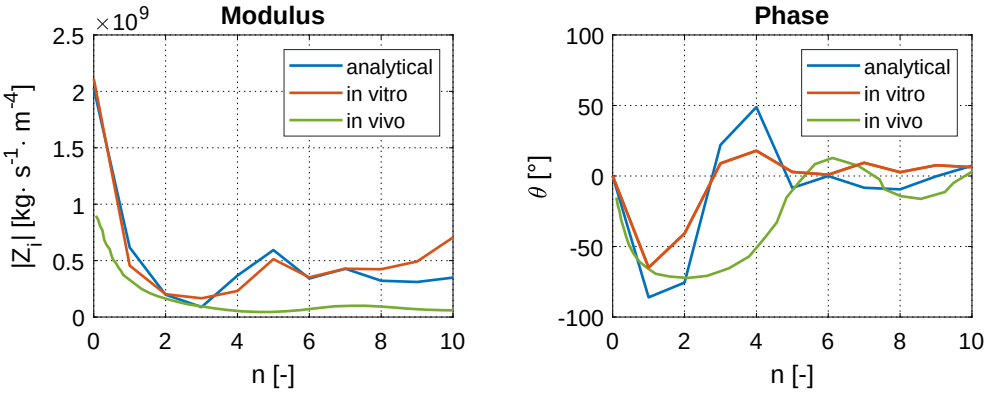

Fig. 2. Comparison of the input impedance modulus $|Z_i|$ and phase θ between *in vitro* experimental measurements (red) and analytical solution from mathematical model (blue), the green curve represents the *in vivo* input impedance of brachiocephalic artery [2], n stands for the number of the harmonics

significantly shifted to higher impedances. Mainly due to the differences in material properties between the arterial wall and 60 Shore A silicon, but also in viscosity and the individual tree geometries (l_{rr}, r_{min}, r, h, α and β).

The right graph represents the phase difference θ between pressure and flow wave for each harmonic. All curves exhibit similar behaviour. Under the lower frequencies, as the total compliance contributes, the phase is negative, i.e., the flow is leading pressure. With increasing frequency the phase becomes positive and then it oscillates to zero values. As the arteries in *in vivo* tree have smaller l_{rr} (around 50), the negative phase is more extensive (green curve).

There are also some facts that could not be described by the mathematical model. Such as a significant decrease in the bifurcation compliance due to the glued bonding between each tube and stepwise diameter reduction between the connected tubes. It may be a source of acceleration in wave propagation causing earlier and unwanted reflections, leading to phase and modulus discrepancies.

Despite all the mentioned limitations and inaccuracies, the overall behaviour of the *in vitro* input impedance is relatively close to the mathematical one. It would be worth improving the real model of the structured tree since the Young's modulus is still very high in comparison with the arterial one. Also, the glued bifurcations and connections between each tube should be eliminated. For example, casting the whole structured tree using the 3D printed moulds would be one option. Another method could be a 3D print of the lumen from wax and then immersion of the luminal model into the pre-mixed silicon with required Young's modulus. After heating the model, the wax would be blown out. Consequently, the *in vitro* and analytical curve would correspond considerably more to the *in vivo* one. Nevertheless, finding a reasonable agreement between the 1D mathematical model and *in vitro* experimental measurements provides an opportunity to design individual structured tree models representing different peripheral sites.

References

[1] Jebbink, E. G., Mathai, V., Boersen, J. T., et al., Hemodynamic comparison of stent configurations used for aortoiliac occlusive disease, Journal of Vascular Surgery 66 (2017) 251-260.

[2] Olufsen, M. S., Peskin, C. S., Kim, W. Y., Pedersen, E. M., Nadim, A., Larsen, J., Numerical simulation and experimental validation of blood flow in arteries with structured-tree outflow conditions, Annals of Biomedical Engineering 28 (2000) 1281-1299.

[3] Vlachopoulos, C., O'Rourke, M., et al., McDonald's blood flow in arteries, CRC Press, 2011.

[4] Westerhof, N., Stergiopulos, N., Noble, M. I., Snapshots of hemodynamics, Springer, 2010.

COMPUTATIONAL MECHANICS 2021
36th conference with international participation
Srní
November 8 - 10, 2021

Experimental based tuning of active absorber

K. Kraus[a], Z. Šika[a]

[a] *Department of Mechanics, Biomechanics and Mechatronics, Faculty of Mechanical Engineering, Czech Technical University in Prague Technická 4, Praha 6, 160 00 Prague, Czech Republic*

Vibration suppression takes place in many applications and enviroments. In various cases, for example in robotics and industrial enviroment [3], it might be convenient to use absorbers [1] to suppress vibrations of the main structure. Based on application, mass-spring absorber is attached to main structure in point of interest, tuned and actively driven if needed. In order to be able to actively tune and control absorber, some sort of sensors needs to be implemented in the main structure or in the absorber itself, such as accelerometers, encoders, geophones, etc. Depending on absorbers count and the nature of vibrations, various algorithms can be used to drive absorber's actuators, such as PID regulation, H-inf, LQR [4], Delayed resonator [2], etc. Nevertheless, besides mass and stiffness of the absorber, due to many kinds of bearings, usually some sort of damping takes place in the absorber. Lots of real cases of beraing damping are far from linear and thus burdens control algorithms. In this paper we are experimentally tuning real active absorber to be as much undamped (ideal) as possible, so it can be further controlled by superior algorithm.

An assembly MGV52 (Fig. 1a) is being used as actuated mass. It consists of AVM60-25 voice-coil actuator, linear ball bearing and built-in encoder. It has been further equipped with additional parts an external springs in order to get linear absorber with preloaded springs (Fig. 1b). dSpace computer is then used to read sensors and control voice-coil actuator through motor driver (Fig. 2a).

First of all, rough identification must take place in order to get basics characteristics, such as precise mass, stiffness and drive coefficient. Since this identification is based on measurement data from the control pc, ceratin delay of the loop between output and input of the pc (Fig. 2a) is also included among these characteristics. After that it is possible to more closely identify the damping function.

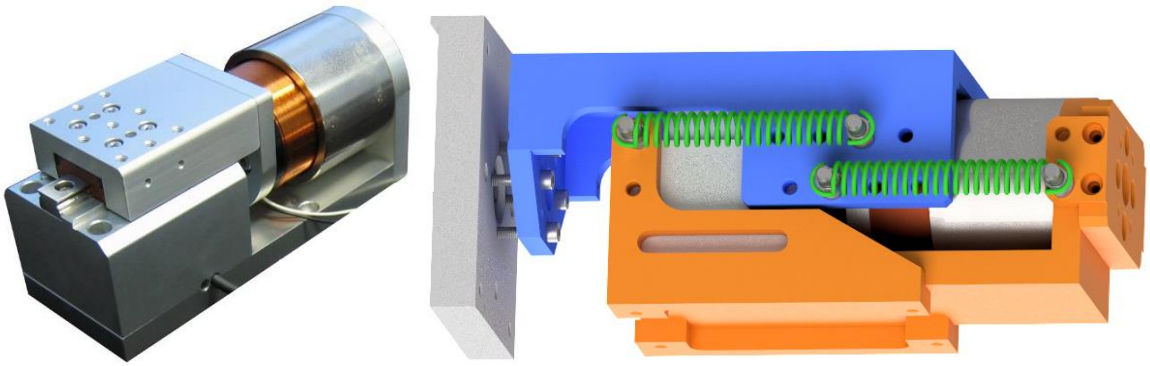

a) actuated mass with linear bearing b) mass-spring configuration

Fig. 1. Absorber design based on MGV52 assembly

Ordinary linear function (viscous damping) with Coulomb damping has been set as starting point. More and more non-linear functions has been added to identify its coefficients. In the end, this assembled function has been replaced with 1-D look-up table, ie. with discrete line with tunable points. Due to Coulomb characteristics included, parameter-points are more dense when close to zero speeds. Such a configuration is far better than linear model, but generally not satisfying enough.

Since voice-coil has been chosen as an active absorber's actuator for various advantageous reasons, there are more damping sources apart from bearings. Firstly, its closed-end design with one millimeter wide gap does not allow air to flow effortlessly in and out. Secondly, and more relevantely, electrical characteristic of magnet-coil coupling greatly depends on the mutual position. Therefore, parametrical 1-D look-up table must be at least 2-dimensional. Fig. 2b shows one of more precise idendifications of damping as a function of both, displacement and velocity of the absorber. It consists of more or less conventional coulomb-viscous area in low speeds and strokes, as well as of great fluctuations (with some sense of symetry) in areas of high strokes. This parametrical plane, when put into positive feedback, is then able to reduce relative damping of the absorber and retain its stability at the same time. Such an active system is then possible to be externaly excited as well as put it stop.

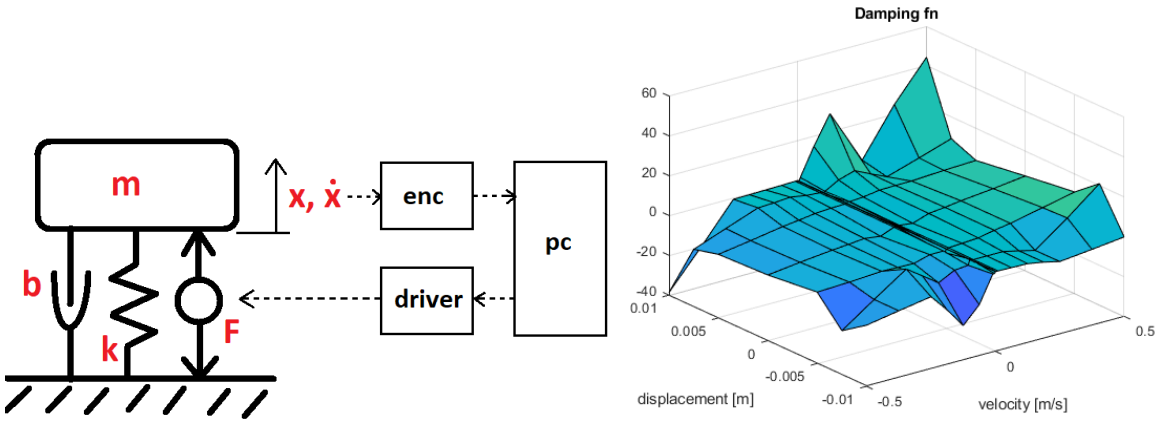

a) Control scheme b) Damping function included in algorithm

Fig. 2. Absorber control algorithm

Acknowledgements

The work has been supported by the Czech Science Foundation project GA21-00871S "Active non-collocated vibration absorption for robots and mechanical structures".

References

[1] Kraus, K., Šika, Z., Beneš, P., Krivošej, J., Vyhlídal, T., Mechatronic robot arm with active vibration absorbers, Journal of Vibration and Control 26 (13-14) (2020) 1145-1156.

[2] Olgac, N., Elmali, H., Hosek, M., Renzulli, M., Active vibration control of distributed systems using delayed resonator with acceleration feedback, The Journal of Dynamic Systems, Measurement, and Control 119 (3) (1997) 380-389.

[3] Olsson, T., Haage, M., Kihlman H., "Cost-efficient drilling using industrial robots with high-bandwidth force feedback," Robotics and Computer-Integrating Manufacturing 26 (1) (2010) 24-38.

[4] Šika, Z., Kraus, K., Beneš, P., Vyhlídal, T., Valášek, M., Active multidimensional vibration absorbers for light robots, Proceedings of the 5th Joint International Conference on Multibody System Dynamics, Lisbon, Portugal, 2018, pp. 1-12.

COMPUTATIONAL MECHANICS 2021
36th conference with international participation
Srní
November 8 - 10, 2021

Design of cooling system of power-electronics

M. Krejčová[a], L. Sova[a], M. Lermer[b]

[a] ZF Engineering, Univerzitní 53, 301 00 Plzeň, Czech Republic
[b] ZF Friedrichshafen AG, Werk Auerbach, Graf-Zeppelin-Straße 1, 91275 Auerbach, Germany

1. Introduction

The increasing pressure to produce electro and hybrid vehicles requires effective handling of power electronics. In the inverter, there is a printed circuit board (PCB) with chips belonging to power electronic kind. It means their power losses are in tens of watts each. These chips are MOSFETs or IGBTs (type of chip depends on specific hybrid application) usually. The produced heat causes thermal damage to the chips over lifetime and induces destruction of the whole inverter. Thus, it is necessary to design a cooling system for these chips very carefully.

Decreasing temperature is not the only objective the designer of the component needs to face in. Generally, there is also a requirement to have low pressure loss of the coolant medium as possible. It influences the efficiency of the complete system including pumps for circulation. However, these two demands are in contradiction against each other.

The last demand is to balance temperature in a chip row to avoid unwanted thermoelectric effects e.g., the Seebeck one [1].

2. Geometry model

The inverter model is for the calculation simplified to area around chips which need to be cooled by water-glycol mixture to reduce their temperature. The main parts of the model are inlet and outlet piping, housing, cooler body with pins pattern and chips. These parts are given. Due to some freedom in design, there is possible to modify pins pattern to match the above-mentioned demands.

The channel system is optimized to produce the maximal cooling performance with the lowest pressure loss respecting manufacturing restrictions, see Fig. 1.

3. Used software and simulation model

For the calculation FloEFD computation software (from Siemens) was used. Its big advantage is that it can be embedded to a CAD (Computer Aided Design) software – in this case to Creo Parametric. FloEFD uses an automatic cartesian mesh without any need to manually create invers geometry for area of fluid. It has three kinds of cell – solid, solid/fluid, and fluid. In the solid/fluid cells there is boundary layer based on the Prandtl boundary layer equations for a coarse mesh or Van Driest [2] approach for a fine mesh, [3].

The approach of FloEFD to creating a mesh is very fast and do not require time-consuming pre-processing of the geometry itself.

The important part of the simulation model is setting the simplified chip properties as a two-resistor component. It requires to define power-loss of the chip module and thermal resistance acquired from manufactures datasheet or measurement. In another words, chips produce heat

based on the power-loss and their thermal characteristic is described by thermal resistance, which is dependent on geometry and material properties as well as a manufacturing quality.

The simulation focuses on steady state. It produces the worst-case scenario of reaching maximum chip temperature and reduce calculation time.

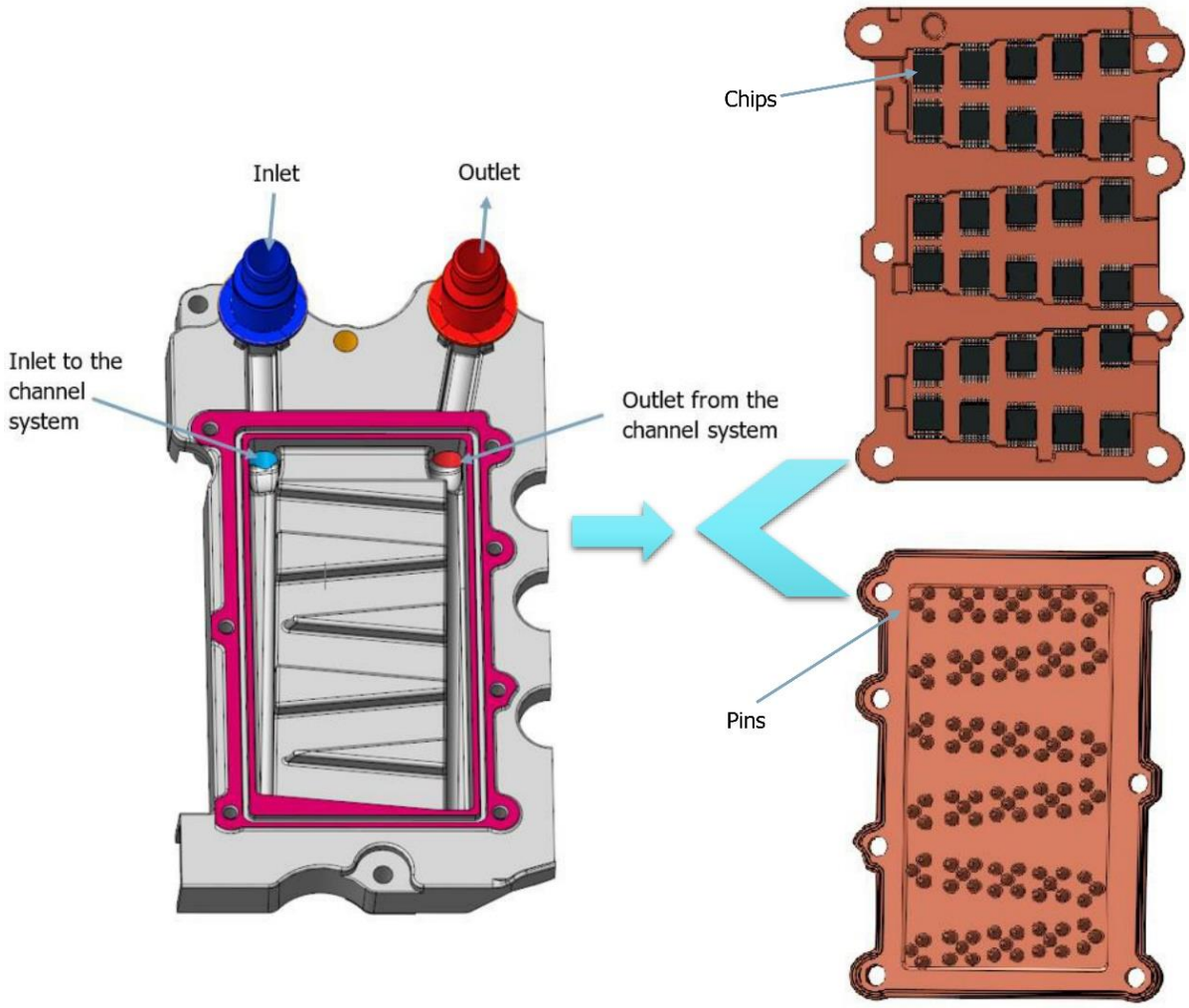

Fig. 1. Initial geometry of the model

4. Results

To obtain results for this contribution, 4 variants of the pins pattern were calculated. One with the original geometry and three improved versions of the pins pattern, see Fig 2.

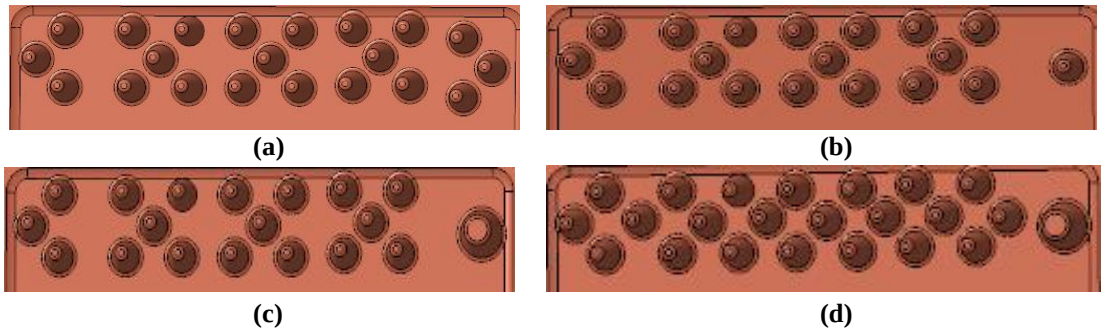

Fig. 2. Pins optimalization: (a) corresponds to initial geometry and thus Design 1, (b) it is Design 2, (c) corresponds to Design 3 and (d) to Design 4

In each geometrical variant 4 load cases (LCs) were set. There are distinguished by amount of the coolant entering to the system per minute and its temperature. The coolant temperature is identical to the ambient one. These load cases are as follows: 5 l/min @ 75°C (LC1), 10 l/min @ 75°C (LC2), 5 l/min @ 25°C (LC3) and 2 l/min @ -25°C (LC4).

The main observed effects of geometry changes are shown in Fig. 3. There is visible a percentual change in comparison to the original geometry. The higher percentage number at temperature means lower temperature and higher percentage number at pressure loss stands for lower pressure loss. It measures the benefits of the improvement.

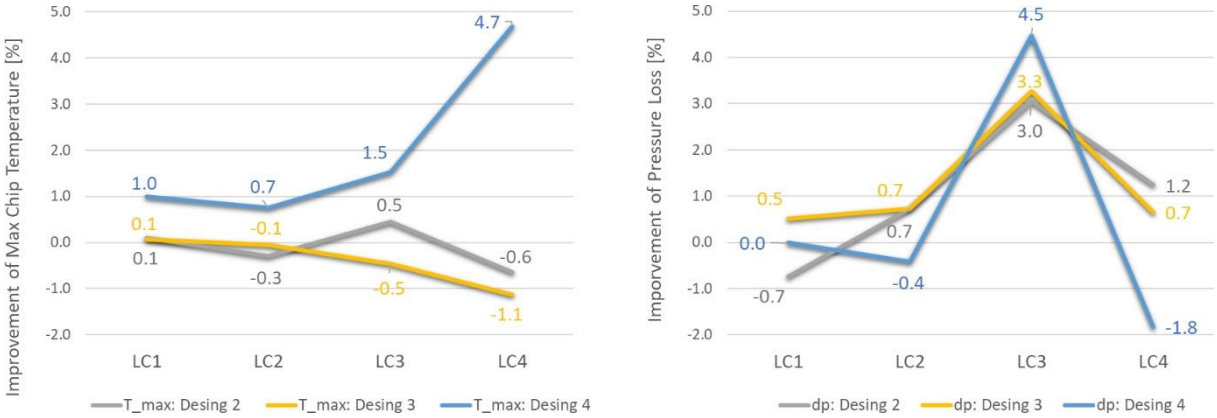

Fig. 3. Improvement of max chip temperature and pressure loss in %

5. Conclusion

Totally, 16 calculations were done. There were 4 geometrical variants and 4 load case scenarios for each geometry. The most feasible results are from the Design 4, where the first pin in a row is bigger than others and the pins are not only under the chips In this design the improvement of maximal chip temperature is up to 4.7 % depending on the load case. The negative impact on the pressure loss is still reasonable. However, the improvements of maximal chip temperature can look small it significantly decreases the risk of failure and increase the inverter lifetime and reliability.

References

[1] Kumar, A., et al., A review on fundamentals, design and optimization to high ZT of thermoelectric materials for application to thermoelectric technology, Journal of Electronic Materials 50 (2021) 6037-6059.

[2] Van Driest, E.R., On turbulent flow near a wall, Journal of Aeronautic Sciences 23 (11) (1956) 1007-1011.

[3] Simcenter FLOEFD™ for Creo® Technical Reference, Software version 2021.1, 2021.

COMPUTATIONAL MECHANICS 2021
36th conference with international participation
Srní
November 8 - 10, 2021

Vibration suppression using nonlinear control of active absorber

J. Krivošej[a], Z. Šika[a], K. Kraus[a]

[a] Faculty Faculty of Mechanical Engineering, CTU in Prague, Technická 4, 166 07 Praha 6, Czech Republic

Vibration suppression is still very demanding problem, specifically for fast and exact motion request demands. Extensive research in this filed shows mainly approaches based on linear models or their linearized forms in connection with a linearized absorber.

This paper deals with an active absorber mounted on a robotic arm which dynamics is generally nonlinear. A robot arm is considered nonrigid. The nonrigidity is considered as a flexible robot link which review is discussed and summarized in [4] and possible control algorithms of two-link flexible manipulators are summarized in [2]. The main considered properties of the robot arm are chosen as close as possible to the reality and a dynamic model of the robot arm is assembled. The modal and inertia properties are investigated using the finite element method (FEM). The simulation results are then used as inputs for a simplified dynamic model.

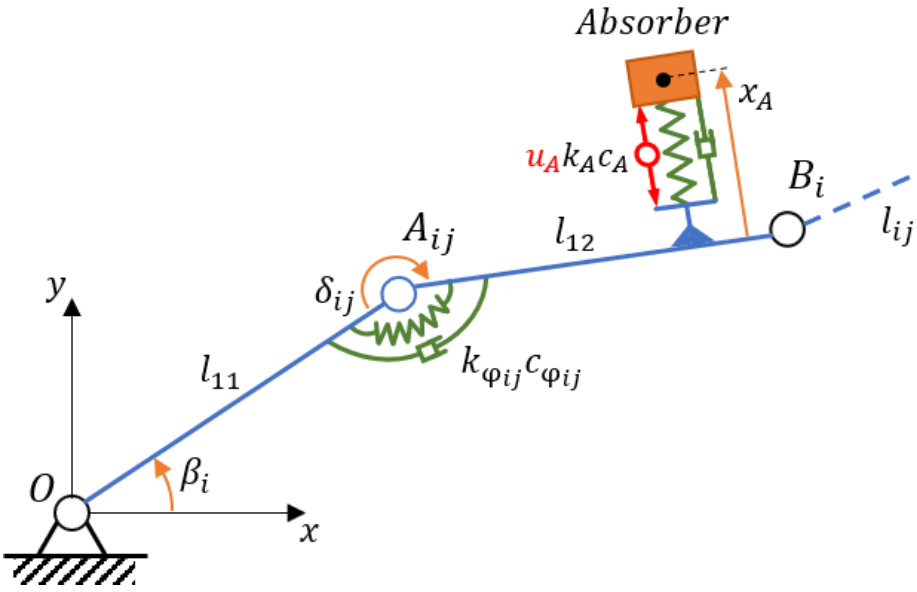

Fig. 1. A scheme of a flexible robot link with active absorber

A flexible robot link OB_i (or $B_{i-1}B_i$ for $i > 1$) is modeled as a rigid serial chain with joints A_{ij} with torsional spring $k_{\varphi ij}$ and damping $c_{\varphi ij}$. An active absorber is added as is shown in Fig. 1. The u_A, k_A and c_A are the active force, stiffness and damping of the absorber, respectively. The similar approach is shown in [1], where the joints A_{ij} are replaced by the two springs k_x and k_y.

The control scheme is based on the computed torque method (CTM) which uses the inverse dynamic to linearize the model of the robot. The inverse-dynamics procedure for flexible-robot manipulators is also used in [3] where its leads to driving forces associated with the deformation modes. This idea is similar in this paper, however, besides the driving forces the concept is

extended to the active absorber added to the structure. In connection with large motion demands the active absorber deals with the nonlinear dynamic of the robot arm. The investigated structure in this paper (Fig. 1 where $i, j = 1$) is considered in a few steps. Firstly, the rigid arm with fixed absorber inertia properties is considered as a starting point. For this structure the CTM method is optimized in control parameters which is taken as a default state of control performance. The simplified control scheme with the feedback linearization loop is shown in the Fig. 2. This procedure is tested for trajectories which represent fast and large motion request demands. Secondly, the robot arm is considered rigid with active absorber. This leads to performance comparison and searching for control law of the absorber with stability analysis. Finally, the robot arm is modelled flexible and considers the first deformation mode of the link.

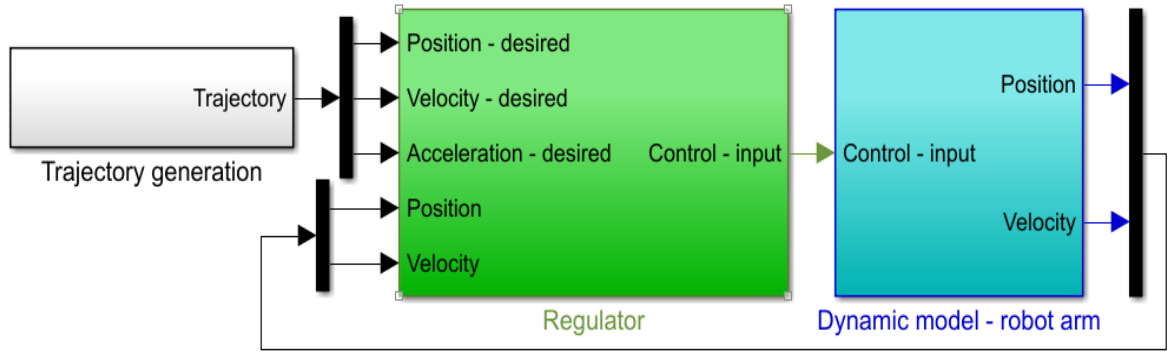

Fig. 2. Simulation scheme with CTM control strategy

In conclusion, the brief investigation to the flexible manipulator model in connection with the nonlinear control of active absorber is shown. The flexible robot link is considered and CTM control with the nonlinear control of absorber based on deformation modes is investigated.

The future work considers the extension of the deformation modes ($j > 1$). This should lead to the more complex adaptive control law of the absorber.

Acknowledgements

The work has been supported by the Czech Science Foundation project GA21-00871S “Active non-collocated vibration absorption for robots and mechanical structures” and by the project SGS16/208/OHK2/3T/12 "Mechatronics and adaptronics 2019" of CTU in Prague.

References

[1] Kraus, K., Šika, Z., et al., Mechatronic robot arm with active vibration absorbers, Journal of Vibration and Control 26 (13-14) (2020) 1145-1156.
[2] Lochan, K., Roy, B.K., Subudhi, B., A review on two-link flexible manipulators. Annual Reviews in Control 42 (2016) 346-367.
[3] Shabana, A.A., Bai, Z., Actuation and motion control of flexible robots: small deformation Journal of Mechanisms and Robotics 14 (2021) 1-41.
[4] Subedi, D., Tyapin, I., Hovland, G., Review on modeling and control of flexible link manipulators, Modeling, Identification and Control 41 (3) (2020) 141-163.

COMPUTATIONAL MECHANICS 2021
36th conference with international participation
Srní
November 8 - 10, 2021

Modelling approaches to the stress wave propagation in a cracked specimen

A. Kruisová, J. Kopačka, J. Kober

Institute of Thermomechanics, Czech Academy of Sciences, Dolejškova 5, 182 00 Prague 8, Czech Republic

Abstract

One of the essential tasks of non-destructive testing is to detect a crack in a specimen. It is well known that a component with a crack exposed to a harmonic excitation of a given frequency has a nonlinear response as a function of the excitation amplitude. The focus of this paper is the numerical modelling of this phenomenon using the finite element method with the consideration of the contact constraint at the crack interface. In addition to the nonlinear transient dynamic problem solved by explicit time integration, a more efficient procedure based on the harmonic balance method is developed. The results of numerical simulations are also compared with experimentally obtained data.

1. Introduction

Non-destructive testing is often used to detect defects in solids, but the commonly used linear ultrasonic techniques based on reflection, transmission, and scattering, are not sensitive to closed cracks. However, damaged solids, together with other microheterogeneous media such as rocks and concrete, containing such cracks, exhibit strong nonlinearities [3] when a resonant frequency depends on the amplitude of the ultrasonic signal. The underlying microscopic mechanism of these nonlinearities is still poorly understood [1], thus the numerical simulations are used to decode the effect of clapping or frictional contacts of the crack interfaces or the effect of the crack tip plastic zone. In addition, the comparison of numerical simulations with experimental results can provide internal parameters and thus the complete characterization of the defects.

Since the direct time integration method for computing the resonance of the sample is very time-consuming, the new method based on harmony balance has to be developed. In this work, we present this newly developed method and its comparison with direct time integration. Thus, only the effect of clapping of crack interfaces is studied here.

2. Formulation

The problem of wave propagation in an elastic specimen with a crack can be formulated as a linear elastodynamics problem with contact conditions. In particular, it is an initial boundary value problem where the governing equations are partial differential equations of hyperbolic type expressing the balance of linear momentum. For the spatial discretization, we use the finite element method, which leads to a system of nonlinear ordinary differential equations of

the form

$$\mathbf{M}\ddot{\mathbf{u}} + \mathbf{K}\mathbf{u} + \mathbf{f}_{\text{c}}(\mathbf{u}) = \mathbf{f}_{\text{ext}}(t), \tag{1}$$

where $\mathbf{M}$ is the mass matrix, $\mathbf{K}$ is the stiffness matrix, $\mathbf{f}_{\text{ext}}$ is the vector of external forces, $\mathbf{f}_{\text{c}}$ is the vector of contact forces and $\mathbf{u}$ is the vector of nodal displacements. Contact constraints are enforced by the so-called bi-penalty method [2].

The time discretization of the semi-discrete system (1) is preferably performed by the central difference method (CDM), which is particularly suitable for fast phenomena such as the wave propagation problem. In addition to the undeniable advantages of this method, such as simplicity and efficiency of numerical implementation, the main disadvantage of the CDM is the conditional stability, which dictates the maximum allowed time step size. In this work, we use the leapfrog variant of the CDM, whose integration scheme is

$$\mathbf{a}^n = \mathbf{M}^{-1}(\mathbf{f}_{\text{ext}}^n - \mathbf{f}_{\text{c}}^n - \mathbf{K}\mathbf{u}^n), \tag{2}$$

$$\mathbf{v}^{n+1/2} = \mathbf{v}^{n-1/2} + \mathbf{a}^n \Delta t, \tag{3}$$

$$\mathbf{u}^{n+1} = \mathbf{u}^n + \mathbf{v}^{n+1/2} \Delta t, \tag{4}$$

where the acceleration $\mathbf{a}^n \approx \ddot{\mathbf{u}}(n\Delta t)$, velocity $\mathbf{v}^{n\pm1/2} \approx \dot{\mathbf{u}}(n\Delta t \pm 1/2\Delta t)$, and displacement $\mathbf{u}^n \approx \mathbf{u}(n\Delta t)$ are obtained by integration at discrete time points $\{0, \Delta t, 2\Delta t \ldots, N\Delta t\}$. The system of equations is completed with initial and boundary conditions.

Zero displacement and velocity fields are often considered an initial condition, but this is not compatible with harmonic excitation. Therefore, there is a transient phase in the early stages of time integration before the system response stabilizes at the expected harmonic response. It necessitates considering a sufficiently long simulation time for the solution to transition to steady-state harmonic oscillation. In addition, the finite element mesh must be sufficiently fine to capture waves of the desired frequency correctly. All these limitations impose enormous time demands on the numerical solution.

A promising alternative that could reduce the described drawbacks of the direct time integration solution is the harmonic balance method (HBM) [4]. This method offers an alternative to time-domain methods for analyzing problems where a steady-state, periodic solution to the equation of motion is sought. The idea of this method is to represent the time history of the displacement function, $\mathbf{u}(t)$ by its frequency content, $\mathbf{U}(\omega)$, to obtain a set of equations for the corresponding frequencies (harmonics) and iteratively balance the related terms. Specifically, the displacements and forces are represented as truncated Fourier series with N harmonics

$$\mathbf{u}(t) \approx \sum_{n=1}^{N} \mathbf{U}_n e^{j(\omega_n t)}, \qquad \mathbf{f}_{\text{c}}(t) \approx \sum_{n=1}^{N} \mathbf{F}_{\text{c}}^n e^{j(\omega_n t)}, \qquad \mathbf{f}_{\text{ext}}(t) \approx \sum_{n=1}^{N} \mathbf{F}_{\text{ext}}^n e^{j(\omega_n t)}, \tag{5}$$

where $\mathbf{U}_n$, $\mathbf{F}_{\text{c}}^n$, $\mathbf{F}_{\text{ext}}^n$ are the vectors of Fourier coefficients. Substituting these expressions into the equation of motion, (1), and balancing the harmonic terms yields, for a harmonic n

$$\left(\mathbf{K} - (n\Omega)^2\mathbf{M}\right)\mathbf{U}_n = \mathbf{F}_{\text{c}}^n + \mathbf{F}_{\text{ext}}^n. \tag{6}$$

As the Fourier coefficients, $\mathbf{F}_{\text{c}}^n$, of the non-linear contact forces are functions of the displacements, equation (6) is non-linear and must be solved iteratively. This iteration process can be sketched as

$$\mathbf{U}(\omega_n)^{(k)} \xrightarrow{\text{FFT}^{-1}} \mathbf{u}(t)^{(k)} \rightarrow \mathbf{f}_{\text{c}}(t)^{(k+1)} \xrightarrow{\text{FFT}} \mathbf{F}_{\text{c}}(\omega_n)^{(k+1)} \rightarrow \mathbf{U}(\omega_n)^{(k+1)}. \tag{7}$$

While the CDM approach achieves steady-state solutions by direct time integration, the HBM solves systems of nonlinear equations. For large problems, HBM proves to be a more efficient approach.

3. Numerical example

As a numerical example, we studied a resonant frequency of a plate with the dimension of $100 \times 20 \times 8\,\mathrm{mm}^3$ with a V-shaped crack in the middle of the longest side of the sample. The crack length is half of the plate, and the aperture of the crack on the side of the plate is $1\,\mu\mathrm{m}$, see Fig. 1. Plate was made from 2024 aluminium alloy with Young's modulus of elasticity $E = 73.1$ GPa, Poisson's ratio $\nu = 0.33$ and density $\rho = 2.78$ g.cm^{-3}. The sample was modelled by 20×100 plane strain 4-node elements. The direct integration was provided by the central difference method with time step 7×10^{-8} s. Contact pairs were prescribed on the clapping crack interfaces, and the bi-penalty method was used to simulate the contact nonlinearity.

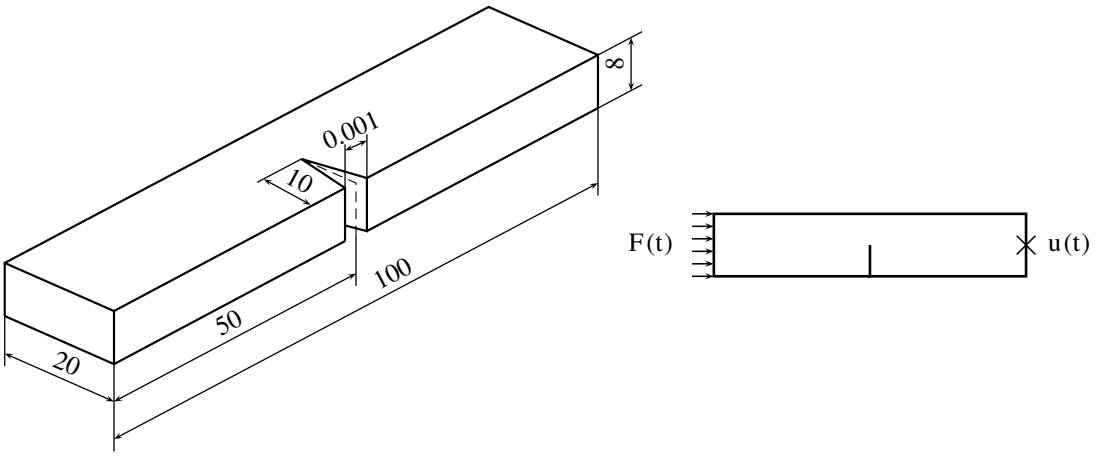

Fig. 1. Sample geometry (*left*) and loading (*right*)

During the first 10 ms of computation, on one side of the sample was applied force signal shown in Fig. 2 causing the longitudinal waves. It is the linear chirp signal with frequencies from 20 kHz to 23 kHz modified by the cosine-tapered window on the first and last sixths of the signal. Next 50 ms, the sample was already unloaded. The displacement in the longitudinal direction was captured in the middle of the opposite face to loading, see Fig. 3. After the fast Fourier transform (Fig. 4), the resonance frequency was stated (here, it is 21.978 kHz).

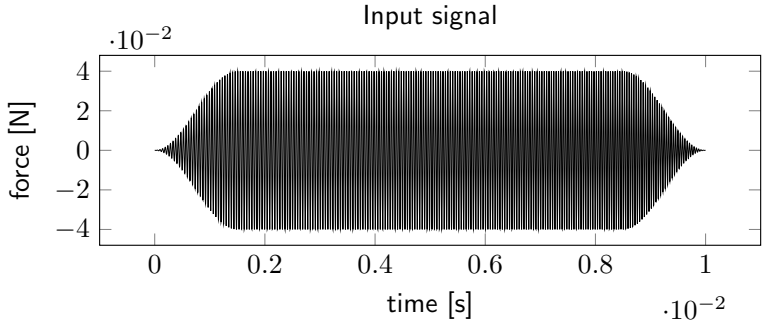

Fig. 2. Input loading signal is a chirp with frequency from 20 kHz to 23 kHz

4. Conclusions

The direct time integration method for the determination of the resonance frequency is time-consuming. On the other hand, the harmonic balance method proves to be more efficient, espe-

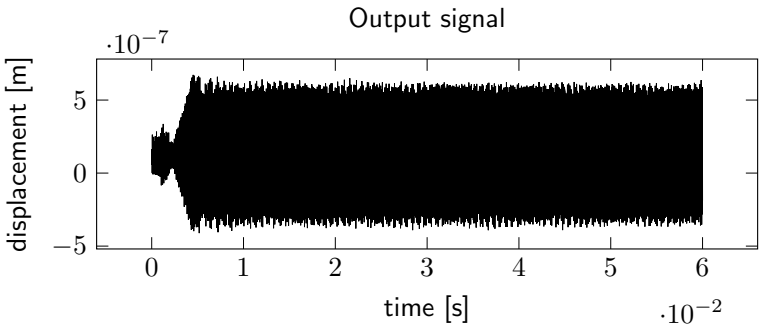

Fig. 3. Computed displacement

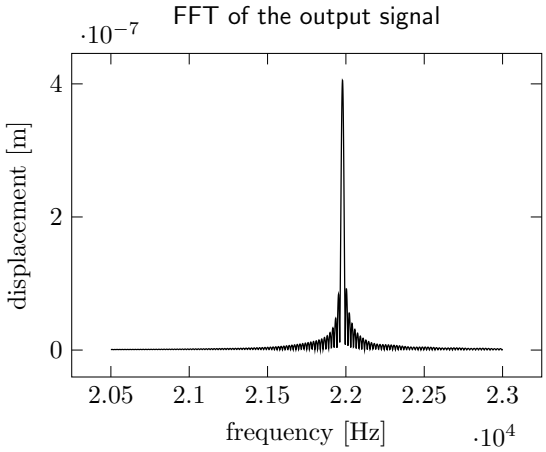

Fig. 4. Fast Fourier transform of the displacement signal

cially for large 3D problems with a fine finite element mesh. It is because the demanding time integration with a small time step is replaced by a sequence of iterative solutions of systems of nonlinear equations. Moreover, due to the orthogonality of the basis functions of the Fourier expansion, the process can be parallelized efficiently. The proposed methodology will be further employed to study the behavior of a crack subjected to harmonic excitation.

Acknowledgements

This research was founded by the Czech Science Foundation (grant number GA 19-142375) and institutional support RVO: 61388998.

References

[1] Gao, K., Rougier, E., Guyer, R. A., Lei, Z., Johnson P. A., Simulation of crack induced nonlinear elasticity using the combined finite-discrete element method, Ultrasonics 98 (2019) 51-61.

[2] González, J. A., Kopačka, J., Kolman, R., Park, K. C., Partitioned formulation of contact-impact problems with stabilized contact constraints and reciprocal mass matrices, International Journal for Numerical Methods in Engineering 122 (17) (2021) 4609-4636.

[3] Nazarov, V. E., Sutin, A. M., Nonlinear elastic constants of solids with cracks, The Journal of the Acoustical Society of America 102 (1997) No. 3349.

[4] von Groll, G., Ewins, D., The harmonic balance method with arc-length continuation in rotor / stator contact problems, Journal of Sound and Vibration 241 (2) (2001) 223-233.

COMPUTATIONAL MECHANICS 2021
36th conference with international participation
Srní
November 8 - 10, 2021

Influence of surface structure of composite on adhesive joint shear strength

J. Krystek[a], L. Horák[a]

[a] *Faculty of Applied Sciences, University of West Bohemia in Pilsen, Univerzitní 8, 301 00 Plzeň, Czech Republic*

This paper is focused on the experimental investigation of the shear strength of the adhesive joint of composites depending on the surface structure. The composite material was manufactured from carbon fibers and epoxy resin. VAP© technology was used. Two types of the surface structure were obtained. The joint shear strengths were determined by means of the lap-shear test according to the ASTM standard.

The composite plate was made in autoclave. Carbon fibers TENAX J IMS60 E13 24K and epoxy resin (L285+hardener 287) were used. Composite plate was consistered of 8 layers ($[0°, 90°, 45°, -45°]_s$).

Two types of the surface structure were created. The smooth surface was created by lamination to a smooth mold (aluminum plate). The rough surface was created by contact with the peel-ply fabric. Prismatic tapes were cut using water jet from the composite plate. The top layer of the tape had a 90° orientation relative to its longest side. Width of the tapes was w = 25 mm, thickness of the tapes was T = 2.3 mm and length of the tapes was l = 100 mm. The tapes were glued together in combinations of different surface structures (smooth-smooth, rough-rough and smooth-rough). Length of glued part was a_{lep} = 12,5 mm (Fig. 1). To ensure an even thickness of the adhesive, a special preparation tool was used [2]. An adhesive Scotch-Weld DP490 was used in this work.

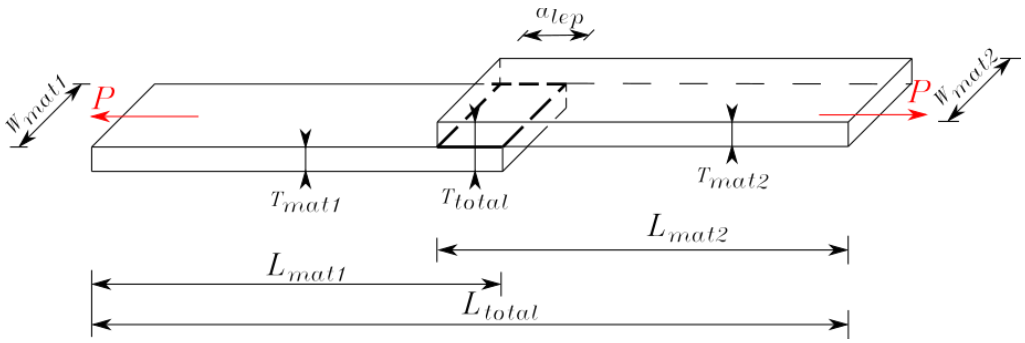

Fig. 1. Geometric parameters of specimen

A universal testing machine *Zwick/Roell Z050* was used. Specimens were loaded in the tension in the longitudinal direction according to standard ASTM D5868 [1]. The initial distance between the jaws of the machine was L_j = 112.5 mm. A uniaxial extensometer was used for measuring the elongation (gage length was L_0 = 80 mm). Self-locking jaws were used to clamp the sample, which allow mutual offset so that the loading takes place in the axis of the adhesive. The loading velocity of crosshead was v = 1 mm/min.

The force–displacement dependencies (Fig. 2) were obtained from the tensile test complying with ASTM D5868 [1]. The shear strength was calculated using

$$\tau = \frac{P_{\max}}{W \cdot a_{lep}}, \tag{1}$$

where $P_{\max}$ is maximum force, W is width of the specimen and a_{lep} is length of the glued part.

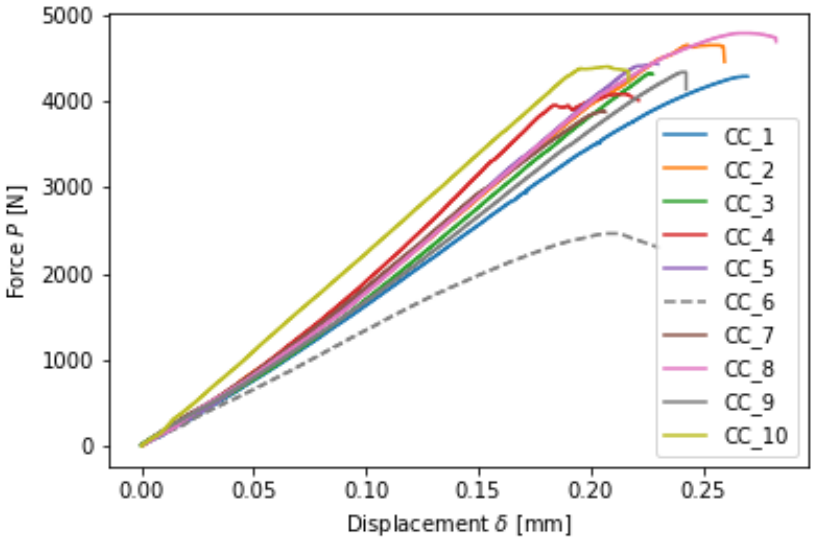

Fig. 2. Force–displacement dependencies

The shear strength was not affected by the surface structure. The influence of the surface structure on cohesive failure was found.

Acknowledgements

The work was supported from European Regional Development Fund-Project „Research and Development of Intelligent Components of Advanced Technologies for the Pilsen Metropolitan Area (InteCom)" (No. CZ.02.1.01/0.0/0.0/17_048/0007267) and by project SGS-2019-009.

References

[1] ASTM International, standard test method for lap shear adhesion for fiber reinforced plastic (FRP) bonding, Designation: ASTM D5868-01.

[2] Kalina T., Sedláček, F., Krystek, J., Determination of the influence of adherent surface on the adhesive bond strength, MATEC Web Conf. 157 (2018) 05012. https://doi.org/10.1051/matecconf/201815705012

COMPUTATIONAL MECHANICS 2021
36th conference with international participation
Srní
November 8 - 10, 2021

DoE analysis of the spherical joint friction torque

J. Kult[a]

[a] *VÚTS, a.s., Svárovská 619, 460 01 Liberec XI- Růžodol I, Czech Republic*

1. Introduction

The article deals with numerical modeling of friction properties of a spherical joint. The goal was to predict the key dimensions of the four spherical joint components in order to reach the target value of the friction torque. The Design of Experiment (DoE) method implemented in Ansys Design Explorer software was used to investigate the relationship between a set of four input parameters (contact overclosure values) and one output parameter (friction torque). The individual design points defined by the DoE method were solved using the FE method in Ansys Mechanical. The approximated response surface allows to predict the continuous values of the friction torque in the interval of interest. The workflow described in the article was used to find out the best combination of the part dimensions.

Friction torque describes the ability of the spherical joint to allow rotational movement thus the essential property of the joint. Very low torque values mean free play of the joint and result in fast wear while very high torque values mean unwanted resistance to rotational motion.

The friction torque is measured in two direction:

- rotation (about the pin axis) and
- tilting.

The friction torque is measured in two different conditions:

- static conditions (break-away torque): the torque is measured after a long period without movement
- dynamic conditions (running torque): the joint is moved over the entire range of motion just before the measurement.

The torque values in dynamic conditions and rotational direction are described in this article. The torque is calculated as a product of the friction force and the lever arm. The friction force is evaluated according to the simple Coulomb's law as a product of the normal force and the friction coefficient.

2. Input data and FE model description

The geometry of the spherical joint was simplified, small features were ignored and only a segment representing 1/16 of the full circle (i.e. 22.5°) was modeled. The simplified geometry was meshed with hexahedral elements (Fig. 1).

A linear elastic material model was used for the metal components of the spherical joint: steel pin, steel closing ring and aluminum body. Consequently, the stress values were checked and it was proved that they do not exceed the yield stress limit. The bearing is made of polyoxymethylen. An elastic-plastic material model based on measured curves was defined. Creep properties of the bearing were neglected.

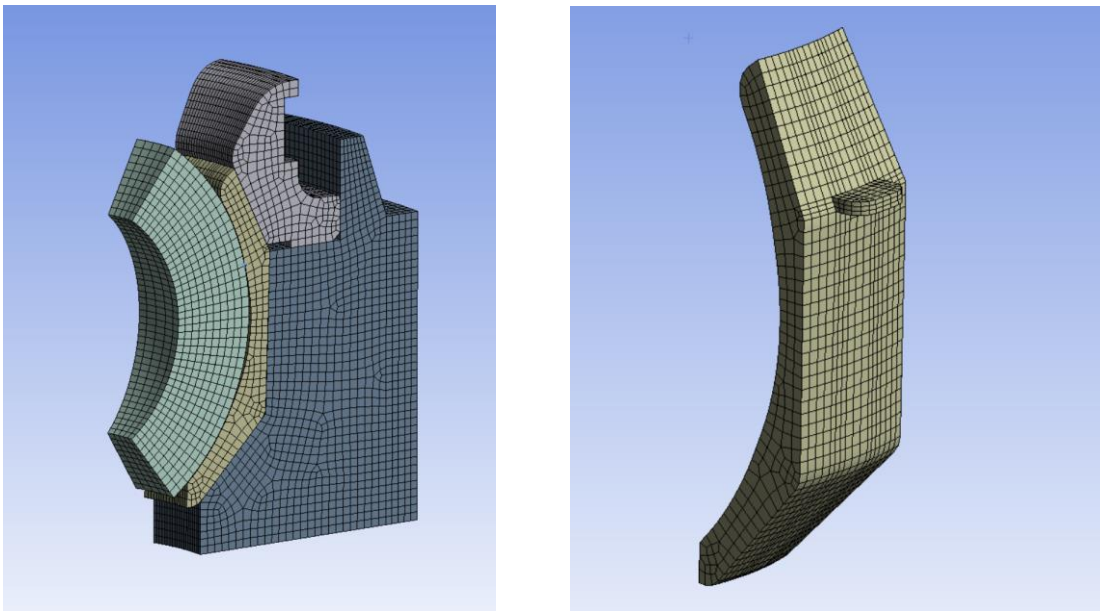

Fig. 1. Hexahedral mesh of the spherical join

There are four essential contact pairs defined between the spherical joint components:

1. pin – bearing (spherical shape)
2. bearing – closing ring (conical shape)
3. bearing – body I (cylindrical shape)
4. bearing – body II (conical shape)

Ansys Mechanical allows to define initial overclosure (penetration) of each contact pair as a parameter called offset [1].

The center of the pin was constrained in all direction in order to fix the structure. Symmetrical boundary conditions were defined on the trimmed faces of the joint segment. No external forces were applied to the structure. The assembly was loaded with internal forces coming out of the initial overclosure – the overclosure values of the four above listed contact pairs were four input parameters of the DoE analysis.

The main output of the FE analysis was friction torque in rotation. The torque was calculated as a product of the normal force, the friction coefficient [2] and the lever arm in each individual contact element of the contact pair "pin – bearing". Consequently the torque value of all elements was summed up.

3. DoE Analysis

The Design of Experiment (DoE) method implemented in Ansys Design Explorer software was used to investigate the relationship between the set of four input parameters (contact initial overclosure values) and one output parameter (friction torque of the contact pair "pin – bearing"). The combinations of input parameters (design points) were automatically created by Design Explorer in the user defined range using the central composite method. The approximated response surface allows to predict the values of the friction torque in the analyzed interval of interest.

4. Results

The first important result of the DoE analysis is the sensitivity chart (Fig. 2) describing the sensitivity of the output parameter (torque) on the four input parameters (contact pair offset).

The chart clearly shows that the first parameter (offset of the contact pair “pin – bearing”) is the most important of all four input parameters.

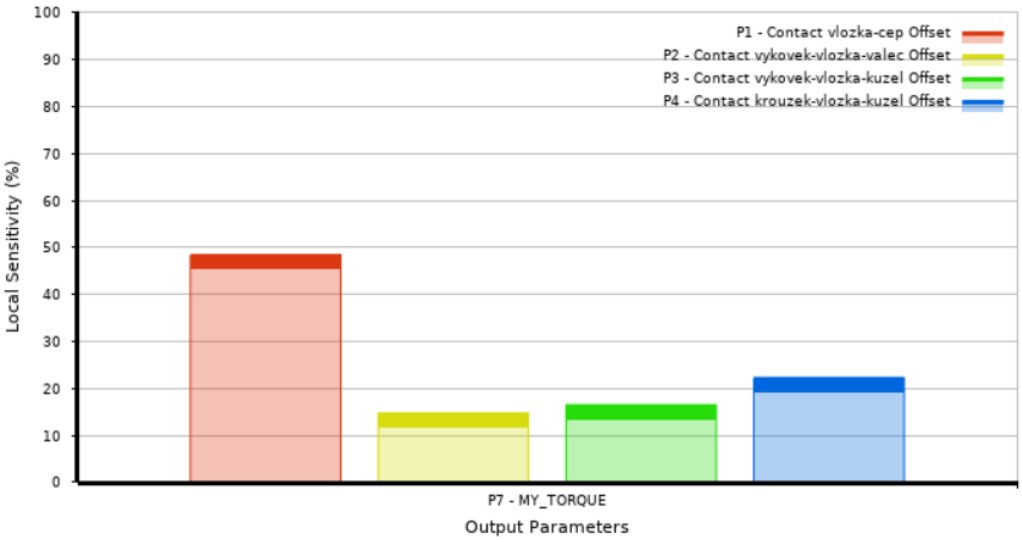

Fig. 2. Local sensitivity of the four input parameters (contact pair offset values)

The second useful result of the DoE analysis is the predicted torque value for any combination of the four input parameters in the analyzed interval. The approximated response surface is created based on the results of analyzed design points. The Design Explorer software is also able to find out combinations of input parameter values for a known target value of the output parameter.

5. Conclusion

The described workflow was used to identify the parameters with the highest sensitivity and to find out the best combination of the part dimensions needed to achieve the target value of the friction torque. The parameters with higher sensitivity represent dimensions which have stronger influence on the resulting torque therefore they request tighter manufacturing tolerances and stricter quality control in general.

Acknowledgements

This publication was supported by the Czech Ministry of Industry and Trade in the framework of the project The development of high-performance articulated ball-joint for aluminum safety chassis components, recipient: Strojmetal Aluminium Forging, s.r.o., other participants: VÚTS, a.s., SVÚM, a.s.

References

[1] Ansys Product Help, online documentation, revision 2020 R2.
[2] Pomp, N., Palasovics, N., Měření koeficientu tření kulového čepu, VÚTS, a.s., Liberec, 2020. (in Czech)

COMPUTATIONAL MECHANICS 2021
36th conference with international participation
Srní
November 8 - 10, 2021

Numerical study of the air flow around the U-profile

B. Ledvinková[a], S. Hračov[a], M. Macháček[a]

[a] *Institute of Theoretical and Applied Mechanics, Czech Academy of Sciences, Prosecka 809/76, 190 00 Prague 9, Czech Republic*

Our contribution deals with the 2D numerical study of the airflow around the bluff bodies represented by U-profiles and by rectangles having side ratios 2 and 4 and with the subsequent evaluation of the aerodynamic drag and lift coefficients needed for the determination of their proneness to the self-excited transverse galloping. Transverse galloping is a kind of the aeroelastic instability occurring at bluff cross-section bodies characterised by the large amplitude oscillations with the low frequency, perpendicular to the direction of the air flow. These oscillations emerge after the critical wind velocity is exceeded. The susceptibility of rectangles and U-profiles to the galloping was evaluated on the basis of the quasi-steady theory with the help of the den Hartog instability criterion in the proximity of the zero impact angle [1]

$$\left(\frac{dC_L}{d\alpha} + C_D\right) < 0, \tag{1}$$

where C_D is the drag coefficient, C_L is the lift coefficient and α is the angle of the attack.

The effect of the air flow impact angle α on aerodynamics characteristics needed in evaluation of the proneness of the body to the galloping was investigated by many authors. The dependence of the drag and lift coefficients for the rectangle with the side ratio SR=5 was measured by Mannini et al. [4]. Patruno et al. [6] investigated the effect of the impact angle on the drag and the lift coefficient for values α=0.1° and 4° both experimentally and by the Unsteady Reynolds averaged Navier-Stokes (URANS) and Large Eddy simulations (LES) for the rectangle with the same side ratio. Guissart et al. [3] presented experimental results and the results of URANS and DDES (Delayed Detached Eddy) simulations for the dependence of aerodynamics coefficients on the angle of attack for rectangle having side ratio SR=4. The flow around U-profiles was investigated experimentally and by CFD simulations by Strecha et al. [7].

The 2D Unsteady Reynolds averaged Navier-Stokes (URANS) simulations of the airflow around the bluff bodies were performed in this study using k-ω SST model [5]. URANS simulations are based on averaged continuity and Navier-Stokes equations, the k-ω SST model introduces two additional differential equations for the turbulence kinetic energy and the specific dissipation rate needed for the turbulence modelling. Due to the switching function k-ω SST model combines the Wilcox k- ω model suited for modelling of the flow in the viscous sublayer near the walls and the robustness of k-epsilon models in the free air flow. The Comsol Multiphysics software was used in our simulations.

The air flow around rectangles with side ratios SR=B/D =2 (30/15cm) and SR=4 (30/7,5cm) and around the U-profile with SR=2 (30/15cm) with the inner depth D_b equal to 7.5cm at different angles of attack was simulated see Fig 1. Subsequently, the drag and lift coefficients needed for den Hartog instability criterion were evaluated.

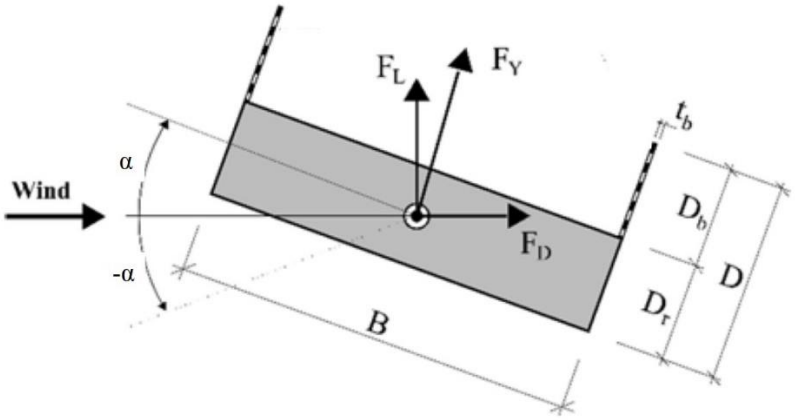

Fig. 1. U-profile layout (taken from [2])

The rectangles and the U-profile were placed into the larger square computational domain 15x15m in order to supress the blockage effect. The position of the rectangle/U-profile in the computational domain is apparent from Fig.2. The computational mesh consists of the structured and unstructured parts. The circle surrounding the rectangle/U-profile in Fig. 2 is filled with the unstructured mesh with finer resolution and the remaining computational domain with the unstructured mesh having the coarser resolution, cf. Fig. 2. The width of the first cell adjacent to the rectangle/U-profile wall was set to a value providing wall resolution $y^+ \approx 1$ for the most of the cells on the walls of the investigated bodies.

Due to the time demanding computations for the inlet flow velocity 14m/s used in the wind tunnel experiments [2], the velocity of the inlet flow was chosen in our simulations to be 2.8 m/s corresponding to Reynold's number Re = 2.7e4. This value was also used in similar studies [3,6]. The value of the turbulent intensity was considered to be 1% corresponding to the moderate turbulence level and the value of the turbulent length scale was set equal to 8.2e- 4m corresponding to the turbulence eddy viscosity ratio 1. The no slip boundary condition was assumed on the walls of the modelled body and the zero pressure was imposed at the outlet. The freestream was inclined at the range α = 0-9° in order to obtain the dependence of aerodynamic coefficients on the angle of wind attack, therefore the boundary condition at the top and the bottom wall of the computational domain was set to the open boundary.

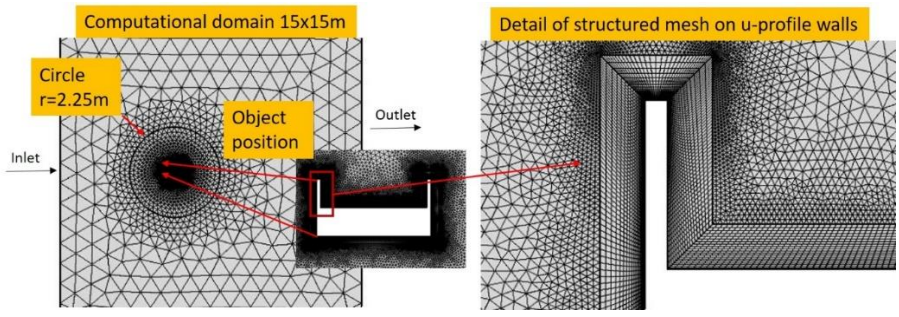

Fig. 2. Computational mesh used for URANS simulation

The values of the drag and the lift forces were evaluated by the integration of the *x*-and *y* components of the total stress force over all the walls of the investigated body, the effect of the angle of the attack was taken in the consideration coefficients. The drag and lift coefficients were calculated according to equations.

$$C_D(\alpha) = \frac{2F_D(\alpha)}{\rho U^2 D}\ , \tag{2}$$

$$C_L(\alpha) = \frac{2F_L(\alpha)}{\rho U^2 D} \quad , \tag{3}$$

where F_D and F_L are the drag and lift forces, ρ is the air density, U is the mean air velocity and D is the cross wind dimension.

The results of our simulations mapping the dependence of the drag and lift coefficients on the impact angle were compared with the experimental ones obtained by the static measurement in the wind tunnel [2] as demonstrated in Fig. 3.

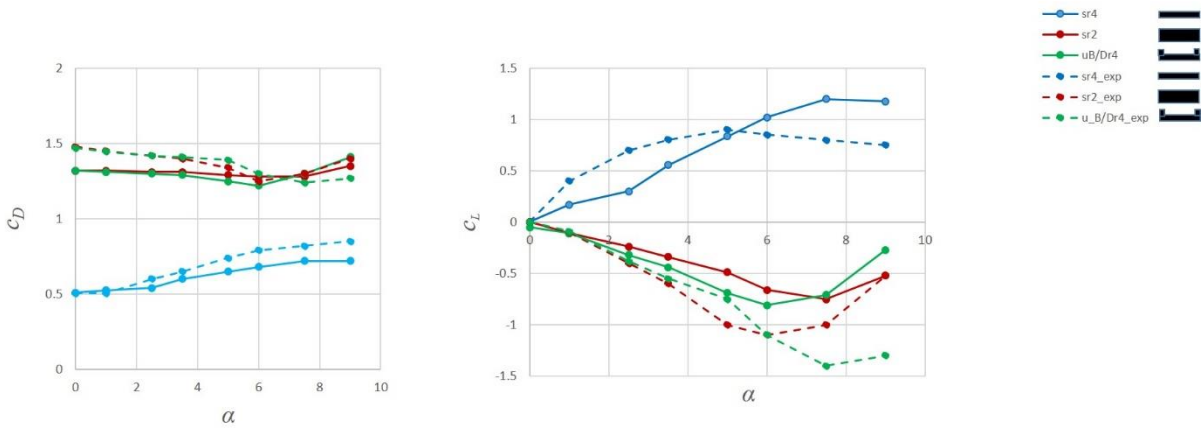

Fig. 3. Drag and lift coefficients- comparison of the results calculated by the k-ω SST model and values measured in the wind tunnel

The results of our simulations show qualitatively same trends for the drag and the lift coefficients depending on the impact angle for all analysed cross-sections as the experimental results obtained by the static measurement in the wind tunnel [2]. The calculated values of the drag coefficient have more monotonous character compared to measured ones. The calculated lift coefficient corresponds to its experimental value for all bodies with SR=2 only at small angles of wind attack. For angles higher than 5° the difference between experimental and numerical results is evident and is increasing with the increasing impact angle. The slope of the lift coefficient near the zero angle is positive or negative according to the experimental data, but for obtaining its more precise value needed for the evaluation to the proneness to the transversal galloping the simulations with smaller angle step near zero and with negative angles have to be done. The possible effect of the different Reynolds number used in measurements in the wind tunnel and in our simulations should be also taken in account.

The simulations of the U-profiles with porous barriers and their comparison with measured results are planned as the next step needed for the understanding of the proneness of U-profiles to the galloping.

Acknowledgement:

The kind support of Czech Scientific Foundation project No. 19-21817S and RVO 68378297 institutional support are gratefully acknowledged.

References

[1] Holmes, J.D., Wind Loading Structures, 3rd edition, CRC Press, 2018.

[2] Hracov, S., Machacek, M., Susceptibility of U-profiles with different geometry and porosity to galloping, EASD Procedia EURODYN, pp. 621-630.

[3] Guissart, A., Andrianne, T., Dimitriadis, G., Terrapon, V.E., Numerical and experimental study of the flow around a 4:1 rectangular cylinder at moderate Reynolds number, Journal of Wind Eng. and Ind. Aerodynamics 189 (2019) 289-303.
[4] Mannini, C., Marra, A.M., Pigolotti, L., Bartoli, G., The effects of free-stream turbulence and angle of attack on the aerodynamics of a cylinder with rectangular 5:1 cross section, Journal of Wind Eng. and Ind. Aerodynamics 161 (2017) 42-58.
[5] Menter, F.R., Two-equation eddy-viscosity turbulence models for engineering applications, AIAA Journal 32 (1994) 1598-1605.
[6] Patruno, L., Ricci, M., de Miranda, S., Ubertini, F., Numerical simulation of a 5:1 rectangular cylinder at non-null angles of attack, Journal of Wind Eng. and Ind. Aerodynamics 151 (2016) 146-157.
[7] Strecha, J., Steinrück, H., Dependence of the aeroelastic stability of a slender U-beam on the realised flow pattern, Proceedings in Applied Mathematics and Mechanics 14 (2014) 497-498.

COMPUTATIONAL MECHANICS 2021
36th conference with international participation
Srní
November 8 - 10, 2021

Computational modelling of pelvic ring osteosynthesis by minimally invasive fixation techniques

L. Lobovský[a], M. Marešová[a], T. Mandys[a], M. Salášek[a,b], J. Hluchá[a], T. Pavelka[b], J. Křen[a]

[a] *NTIS, Faculty of Applied Sciences, University of West Bohemia, Univerzitní 8, 301 00 Plzeň, Czech Republic*
[b] *Clinic for Orthopaedics and Traumatology of Locomotive Organs, University Hospital, alej Svobody 80, 304 60 Plzeň, Czech Republic*

There is a variety of osteosynthesis techniques for medical treatment of pelvic ring injuries available. The presented study focuses solely on sacral bone fractures and related minimally invasive fixation techniques. The techniques employing either of the following are considered: the transiliac internal fixator (TIFI), the transiliac plate (TP) or the iliosacral screw (ISS).

Although there are several experimental studies on stability of the above mentioned techniques, e.g. on TIFI in [2, 5] or on ISS and TP in [1, 3], a serie of newly performed in-house experiments is performed. The experimental campaign is designed so that a high repeatibility of the recorded experimental data is achieved. In order to do so, orthopaedic pelvic models made of solid foam [4] are employed and mounted in a dedicated metal stand so that no displacements nor rotations are allowed in acetabula.

A special attention is paid to treatment of unilateral transforaminal fractures with absence of other affiliated pelvic ring injuries. Cases with either linear or comminuted fracture zone are considered, Fig. 1. Each examined fixation technique is analysed using a fresh pelvic model which is first tested in an intact state. Then the fracture is created and the fixation applied. During the tests, pelves are subjected to compressive loading applied at the sacral base.

The experimental measurements serve as a basis for development and validation of the computational model. The computational model geometry is based on the computed tomography (CT) images of the experimentally tested pelves with the applied fixators. This allows for a precise positioning and orientation of the fixators within the computational model. The finite element (FE) computations reflect the experimental setup including the boundary conditions and the material properties.

The homogeneous isotropic linearly elastic material model is applied for both the solid foam pelves and the titanium fixators. The parameters of the solid foam material model are identified based on in-house tensile and compression tests. Nonlinearity in the foam's elastic response and its viscoelasticity are negligible.

Between the two bone parts along the fracture line, a surface to surface contact problem with friction is utilised. A volumetric computational mesh consists of approximately $300\,000$ tetrahedral elements. The geometry of all fixators is simplified to elementary three-dimensional geometric shapes, e.g. the screw threads are omitted and a cylinder with the effective diamater of the screw is applied instead. Movement of the screw within the insertion hole as well as the relative motion of the fixator parts are fully constrained.

The computational model is fine tuned using the experimental data. The numerical results confirm the same trends as observed in the experiments. The difference between the computa-

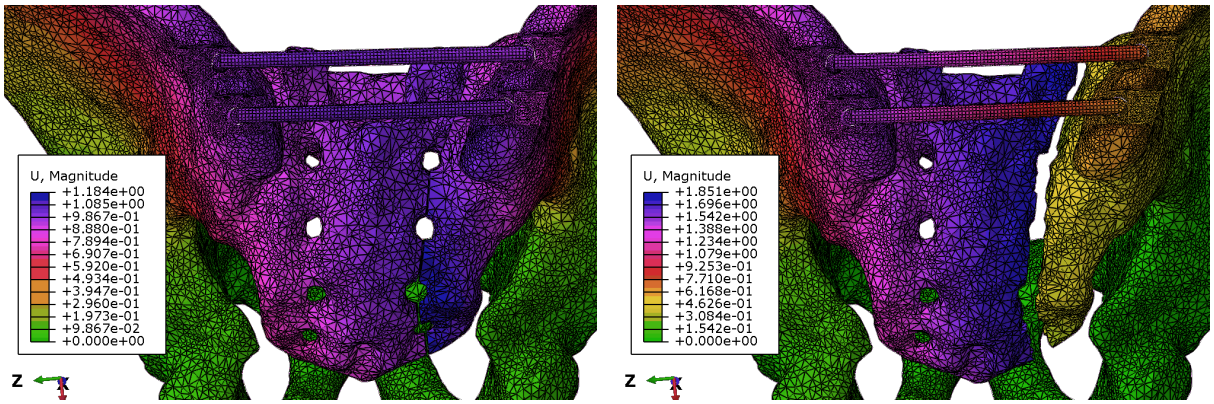

Fig. 1. Contour plot of displacement magnitude [mm] as computed by the FE model for dual TIFI fixation of linear transforaminal fracture (*left*) and transforaminal fracture with comminuted zone (*right*)

tional and the experimental data is in a range of percents. In case of the linear transforaminal fracture, a supraacetabular insertion of the selected fixator (TIFI or TP) provides superior stability of the pelvic structure. Opting for a dual fixation (either dual TIFI or dual TP) does not enhance the stability of the structure for the tested case. However, for the comminuted fracture zone, the differences between classical, supraacetabular and dual fixation techniques are insignificant. On the contrary, combination of supraacetabularly inserted TIFI or TP with ISS inserted into the first sacral joint significantly improves the mechanical stability of the treated pelvic ring for both linear and comminuted fractures.

A selection of the fixation technique influences not only stability of the pelvic ring fixation but also complexity and duration of the surgery, intraoperative blood loss and a level of risk of iatrogenic injuries. These other factors are not reflected within the study.

Acknowledgements

This work is supported by the European Regional Development Fund-Project "Application of Modern Technologies in Medicine and Industry" No. CZ.02.1.01/0.0/0.0/17_048/0007280.

References

[1] Berber, O., Amis, A. A., Day, A. C., Biomechanical testing of a concept of posterior pelvic reconstruction in rotationally and vertically unstable fractures, The Journal of Bone and Joint Surgery. British volume, 93-B (2) (2011) 237-244.

[2] Dienstknecht, T., Berner, A., Lenich, A., Zellner, J., Mueller, M., Nerlich, M., Fuechtmeier, B., Biomechanical analysis of transiliac internal fixator, International orthopaedics 35 (12) (2011) 1863-1868.

[3] Giráldez-Sánchez, M. A., Lázaro-Gonzálvez, A., Martínez-Reina, J., Serrano-Toledano, D., Navarro-Robles, A., Cano-Luis, P., Fragkakis, E. M., Giannoudis, P. V., Percutaneous iliosacral fixation in external rotational pelvic fractures. A biomechanical analysis, Injury 46 (2) (2015) 327-332.

[4] https://www.sawbones.com/full-male-pelvis-large-solid-foam-w-sacrum-1301.html

[5] Ueno, F. H., Pisani, M. J., Machado, A. N., Rodrigues, F. L., Fujiki, E. N., Biomechanical study of the sacroiliac fracture fixation with titanium rods and pedicle screws, Acta Ortopedica Brasileira 23 (3) (2015) 154-157.

COMPUTATIONAL MECHANICS 2021
36th conference with international participation
Srní
November 8 - 10, 2021

Generation of artificial vascular trees – constrained constructive optimization approach

V. Lukeš

Faculty of Applied Sciences, University of West Bohemia, Univerzitní 8, 301 00 Plzeň, Czech Republic

Modelling of blood perfusion in an organ usually requires having a suitable geometrical model of the vascular system embedded in the organ. The vascular structures identified in CT or MR scans often suffer from incompleteness, unreliability and are only available up to a certain vessel size. Constrained constructive optimization (CCO) techniques are able to generate artificial vascular trees that mimic the real structures and preserve their main features.

The artificial vascular tree models are generated in such a way to minimize the total blood volume inside the tree structure and to fulfil the physiological boundary conditions and constraints regarding flows and input/output pressures. The radii of branching vessels can not be arbitrary, to conserve flow through the tree, the branching law for vessel radii must be satisfied. The branching law contains the so-called flow exponent, by the choice of which we can achieve uniform shear stress on the vessel walls or minimize wave reflection of the pulse waves.

The algorithm published in [1] starts generating a tree with one root node and many leaves (terminal nodes), which are connected directly to the root at the beginning of the tree generation process. The leaf positions are placed randomly with the uniform distribution in a given volume, while the root position is usually defined as an input parameter to the algorithm. The generation process consists of relaxing, merging, and splitting steps which are repeated until a local optimization criterion is met. The above steps are done iteratively many times on each tree node to get the optimal branching (bifurcation, trifurcation, ...) at the nodes and to adjust the node positions. In order to get the optimum at the global level, the hierarchical iterations involving pruning and reconnecting steps, which lead to topological changes of the tree, are applied. See [1] for details.

Another CCO algorithm, published in [2, 5], starts with a root segment, representing the entry vessel to an organ, and repeatedly connects randomly placed terminal nodes to the existing tree structure. When a new leaf is created, the algorithm finds the appropriate existing vessel segment, minimizing a cost function, and connects the new leaf to that segment. The optimal position of the newly created bifurcation must be calculated to ensure given bifurcation rules and to minimize total intravascular volume. This "growing" approach produces binary vascular tree models while the algorithm [1] allows for multifurcations in the tree.

Artificial vascular trees are crucial for hierarchical modelling of tissue perfusion as discussed in [4]. The upper hierarchy of a generated tree, representing larger vessels in an organ, can be used for 1D computation of blood flow through the perfusion tree. The lower hierarchies, i.e. a wide range of small vessels, can be employed in calculations of tissue permeabilities which are involved in the complex multi-compartment models, see e.g. [3].

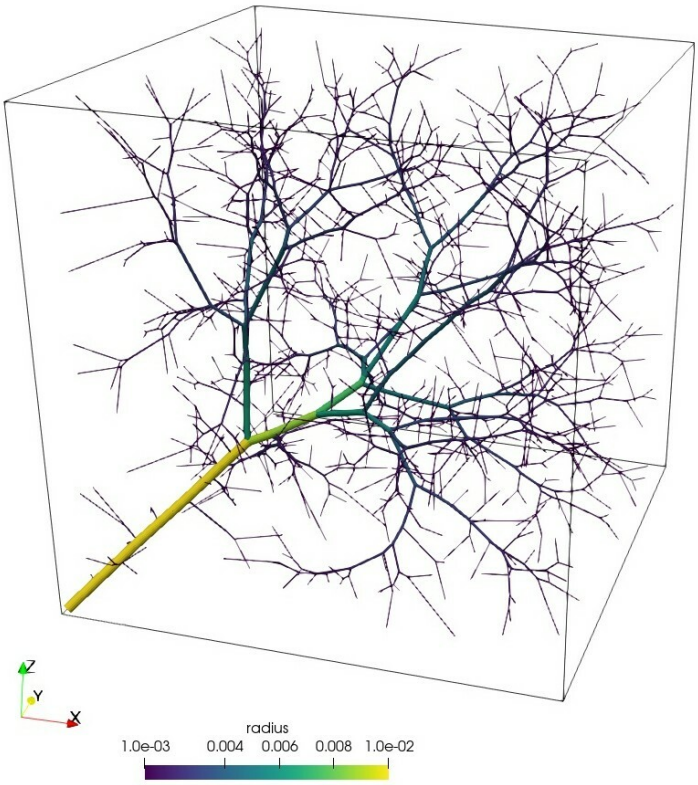

Fig. 1. Example of a generated vascular tree, 16×10^3 terminal segments (leaves)

Acknowledgement

The work was supported from European Regional Development Fund-Project "Application of Modern Technologies in Medicine and Industry" (No. CZ.02.1.01/0.0/0.0/17_048/0007280).

References

[1] Georg, M., Preusser, T., Hahn, H. K., Global constructive optimization of vascular systems, Technical Report: WUCSE-2010-11, Washington University in St. Louis, 2010.

[2] Karch, R., Neumann, F., Neumann, M., Schreiner, W., A three-dimensional model for arterial tree representation, generated by constrained constructive optimization, Computers in Biology and Medicine 29 (1) (1999) 19-38.

[3] Michler, C., Cookson, A. N., Chabiniok, R., Hyde, E., Lee, J., Sinclair, M., Sochi, T., Goyal, A., Vigueras, G., Nordsletten, D. A., Smith, N. P., A computationally efficient framework for the simulation of cardiac perfusion using a multi-compartment Darcy porous-media flow model, International Journal for Numerical Methods in Biomedical Engineering 29 (2) (2012) 217-232.

[4] Rohan, E., Lukeš, V., Jonášová, A., Modeling of the contrast-enhanced perfusion test in liver based on the multi-compartment flow in porous media, Journal of Mathematical Biology 77 (2) (2018) 421-454.

[5] Schwen, L. O., Preusser, T., Analysis and algorithmic generation of hepatic vascular systems, International Journal of Hepatology 2012 (2012) No. 357687.

COMPUTATIONAL MECHANICS 2021
36th conference with international participation
Srní
November 8 - 10, 2021

Finite element analysis of composite tubes with integrated loop technology joints

A. Malá[a], T. Zámečníková[a], M. Bartošák[a], B. Kropík[a], T. Ponížil[b], N. Schmidová[a], T. Mareš[a]

[a] *Faculty of Mechanical Engineering, Czech Technical University in Prague, Technická 4, 160 07 Prague 6, Czech Republic*
[b] *Compo Tech PLUS, spol. s r.o., Nová 1316, 342 01 Sušice, Czech Republic*

This paper presents Finite Element (FE) models of integrated loop technology joints. The composite tubes with integrated joints are developed in order to improve the connections of composite beams to achieve the continuous stress transfer through the connection, and in order to fulfil the strength and stiffness requirements. Therefore, FE models of composite beams with integrated joints have been created, also they have been compared with the experiments, which were performed in tension and compression loading. Due to the results of the experiments and the simulations of the first design of integrated loop joints (presented in [2] and [3]) the technology of the production has been changed.

The second generation has been developed and analysed by FE simulations. The differences between the first and second generation can be observed in Fig. 1 and Fig. 2. The pins (Fig. 2) are used for the manufacturing by fibre winding and placement technology. The pins allow the fibres to be placed in the area between the loops and the placement of fibres on tube body is more unified, without thin-walled areas near the integrated joint.

Fig. 1. First generation specimen

Fig. 2. Second generation specimen

The set of nine specimens (see Table 1) of the second generation has been numerically simulated in order to select the best of them for future manufacturing and experimental testing. They have been composed from four differently wound layers: SN (DEG), A1, A2 and Hoop (see the description below Table 1). Numerical models were created on the basis of the knowledge gained in modelling of the first generation. Damage represented by Inverse reverse factor (IRF) and the occurrence of local damage have been monitored. Based on these results four of the second generations specimens were selected for experimentally testing in tensile and compressive loading scenarios, namely SN02, SN07, SN08 and SN09. These specimens were provided with a glued composite tube, by which the FEM model of these components was extended.

The pair SN02 and SN08 has been selected for comparison of change of lay-up sequence (1st and 3rd layers are swapped) and the pair SN07 and SN08 has been selected to observe the effect of

wrapping the fibres around the joined tube. Specimen SN09 is without SN (0), which is replaced by another layer A1 because of technological requirements.

Table 1. Lay-up of second generations specimens

Specimen type	First area	Second area	Third area	Fourth area	Fifth area
SN_01	SN (45)	A1	Hoop	SN (0)	SN (45)
SN_02	SN (45)	A2	Hoop	SN (0)	SN (45)
SN_03	SN (60)	A1	Hoop	SN (0)	SN (60)
SN_04	SN (60)	A2	Hoop	SN (0)	SN (60)
SN_05	SN (30)	A1	Hoop	SN (0)	SN (30)
SN_06	SN (30)	A2	Hoop	SN (0)	SN (30)
SN_07	Hoop	A1	SN (45)	SN (0)	SN (45)
SN_08	Hoop	A2	SN (45)	SN (0)	SN (45)
SN_09	Hoop	A1	A1	SN (45)	SN (45)

SN ("DEG") – the body of the tube bounded by pins, when the fibres are placed in angles $\pm DEG_S$

A1, resp. A2 – wound ring around the tube in axial direction, whose fibres form the ILT joints. A1 fibres are wrapped with one more ring around the joined tube, A2 fibres are not.

Hoop – the body of the tube without the area near ILT joint when the fibres are placed at angle nearly 90°.

The comparison of experiment to numerical models has shown that the differences in displacements were about 20% to 60%. Therefore, the models were further modified. The connection between ILT joint and the glued tube was modelled as a bonded connection with a contact debonding function, the connections between pins and the glued tubes were modelled as contacts with the friction. The pins, which represented the boundary conditions and loading, were modelled as rigid. The FE model of strain gauges have been added on the tubes body. Due to added strain gauges in the model the evaluation was more accurate as shown in Table 2. Subsequently, more sophisticated methods of experimental displacement evaluation have been used, also they have been refined to be more accurate as a result of the knowledge of the numerical simulations.

Table 2. Displacements/deformations evaluation of FE models to experimental testing

	FEA percentage deviation to experiment [%]			
	displacement		deformation	
	TENSION	COMPRESSION	TENSION	COMPRESSION
SN_02	-20	-55	-6	-27
SN_07	-48	-55	-6	-29
SN_08	-28	-59	-13	-35
SN_09	-58	-53	-4	-19

The SN 09 specimen has been chosen as a technologically more advantageous variant of the variants. It summarizes the advantages of the composite windings of the previous types of components with integrated joints. The using of double A1 is chosen as the axial reinforcement. It is wound with a double layer SN (45) with angle of ± 45 ° and it is underlaid with the technological sublayer Hoop. The experiment and numerical simulation evaluation both found the critical places (see Fig. 3), where the failures have occurred. The differences in the behaviour of the models are evident from Fig. 4. According to the results, the SN 09 specimen can be chosen as the most suitable variant.

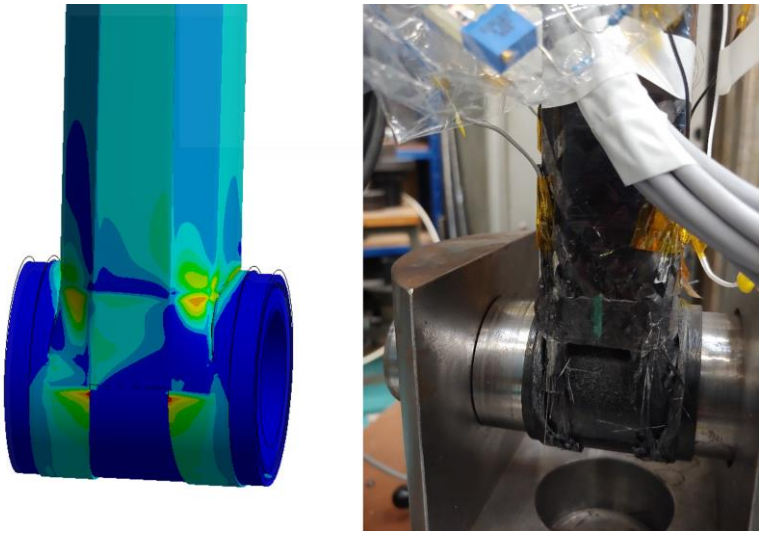

Fig. 3. SN 09: FE model – maximal principal stress (left) and experiment (damage in ILT joint) (right)

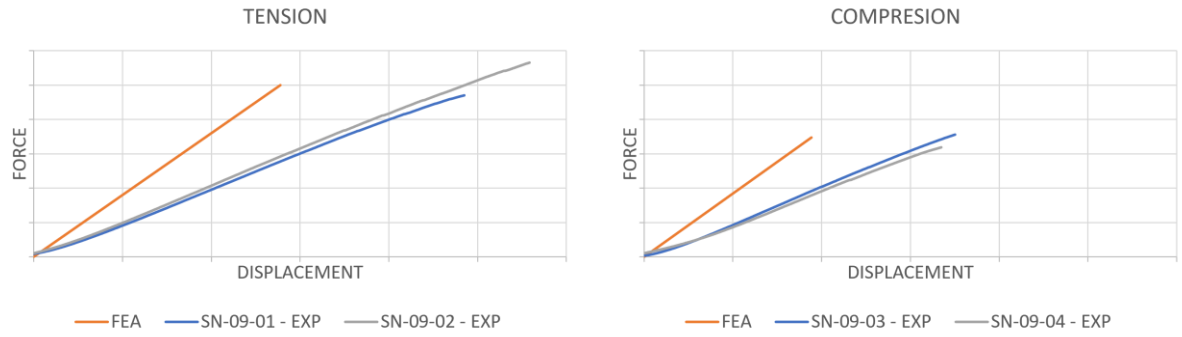

Fig. 4. Force/displacement curves for the specimen SN 09

The optimal variant, SN 09, has been also tested in the other loading scenarios, such as torsion, bending etc. These results will be published separately.

Acknowledgements

This work has been supported by project No. SGS21/151/OHK2/3T/12 of the Grant Agency of the Czech Technical University in Prague and by project No. TJ02000252 of the Technology Agency of the Czech Republic. Support of the Compo Tech PLUS company in development, manufacturing and testing of composite parts is also greatly acknowledged.

References

[1] ANSYS 19.2 Help.

[2] Malá, A. et. al, Finite element analysis of composite tubes with integrated loop connections, Proceedings of computational mechanics 2019 (2019) 114–116. http://hdl.handle.net/11025/36260

[3] Kropík, B. et al., Detection and monitoring of failures in cfrp specimens with integrated joints by acoustic emission method, Proceedings of the 27th Workshop of Applied Mechanics, 2019, pp. 20–23.

COMPUTATIONAL MECHANICS 2021
36th conference with international participation
Srní
November 8 - 10, 2021

Influence of potting geometry of inserts load-carrying capability in sandwich structure

T. Mandys[a], V. Laš[a], J. Krystek[a]

[a] *NTIS, Faculty of Applied Sciences, University of West Bohemia in Pilsen, Univerzitní 8, 301 00 Plzeň, Czech Republic*

Sandwich structure with honeycomb core is widely used in different structural applications in lightweight transportation systems such aerospace industries. Their main advantage is high specific stiffness-to-weight ratio in comparison to conventional materials such as aluminum alloys. The disadvantage of the sandwich structures is the inability of the direct mechanical attachment to other components that required the installation of the special types of fasteners. Threaded inserts bonded to the sandwich structure are universally used for the screws attachment with various other constructions components (brackets, holders, etc.). The load capability of the inserts is the main parameter for design and installation of the sandwich structure. This does not depend only insert type and geometry, but also on the geometrical conditions that are affiliated with the installation (bonding) of the inserts into the structure.

The load capability of the insert bonded into the composite sandwich structure was experimentally tested in case of the out-of-plane tensile pull-out test on the sandwich structure specimens in accordance of the ASTM standard [2]. The principle of the pull-out test is based on the tensile load of the insert over the screwed-in screw, when the upper face sheet of the sandwich specimen is pressed against the steel plate of the testing stand with the central hole with diameter of 80 mm. The two types of the blind inserts with inner threads M5 and M8 bonded into the composite sandwich specimens with the inner dimension of 110 x 110 mm and total thickness 30 mm were tested. The principle of the tensile pull-out experimental setup is shown in Fig. 1. The tested inserts made of titanium were located in the centre of the face sheets of the specimens. The sandwich structure consisted of the two face sheets made of 8 layers of unidirectional carbon prepregs (total thickness of the face sheets is 0.74 mm) and of 5056 aluminum alloy hexagonal type honeycomb core with cell size 3/16” and the thickness 0.001” of single walls.

The numerical simulations were used for the comparison. The numerical model of the sandwich structure with the insert was created in the FEM software Abaqus 6.13. The honeycomb hexagonal core was modeled as a homogenous structure. The individual parts of the sandwich structure and the bonded inserts were connected using tied constraints. The contact without friction was considered between the sandwich structure and the tested steel stand. The computational model was modeled as a quarter of tested specimen due to symmetry with added the appropriated boundary conditions. The computational model is shown in Fig. 2. The non-linear material models with damage were considered for the modeling of the main parts of the sandwich structure. The non-linear behavior of the face sheets was modeled by user defined material model designed by the authors and implemented into the commercial FEM software [1]. The material parameters of the individual parts of the sandwich structure were determined from the performed experimental tensile and compressive test on the separated materials specimens.

The results from numerical simulations were compared with the experimental data in the form of the force-displacement dependencies for the case of insert M5 and insert M8 as is displayed in Fig. 3 and Fig. 4 respectively. In the case of the M5 insert two variants of the potting were modeled in accordance with the fact observed due to experiment, when some specimens had not fully potted inserts at the bottom. This state was created due to incorrect bonding procedure and was manifested by a sharp decrease of the stiffness during loading. That is caused by immediate rupture of the adhesive in a weakened place at the interface of the bottom of the inserts and the honeycomb. The computational model shows a good agreement with the experimental data in the form of the force-displacement dependencies and in the damage which occurred in the sandwich structure with insert during the loading.

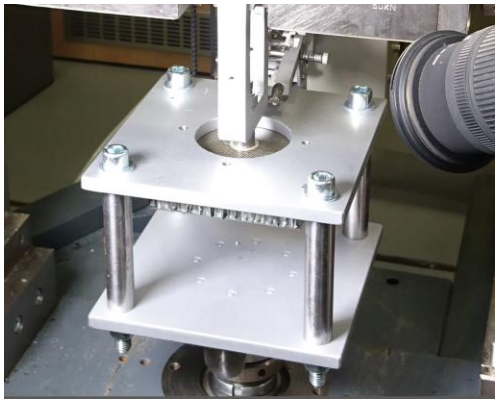

Fig. 1. Tensile pull-out test setup

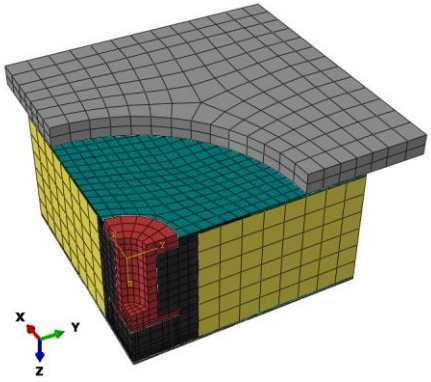

Fig. 2. The FEM mesh of the pull-out tensile test of the sandwich structure with the M8 insert

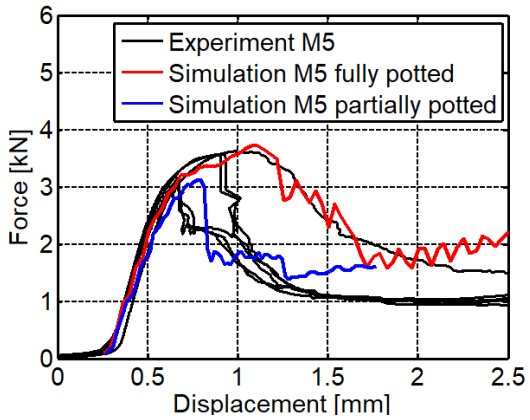

Fig. 3. The comparison of the force-displacement curves between the experiment and numerical simulation for the insert M5. Two types of the potting are compared – fully and partially potted state

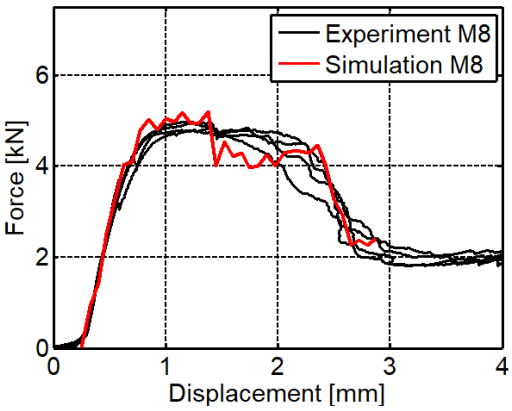

Fig. 4. The comparison of the force-displacement curves between the experiment and numerical simulation for the insert M8

The parametrical study based on the variation of levels of the potting radius r_p of the blind inserts with M5 and M8 thread was performed on the computational model of the sandwich structure in order to specify the possibilities of increase the load-carrying capability of the inserts. The size of the potting radius in the core can be affected by the application of the milling techniques in time of preparation of installation of the inserts in the sandwich structure. The potting radius r_p in the core is obviously equal to the inner radius of the installed insert r_i. The two other sizes of the potting radius in the parametrical study were considered as a 1.25 and 1.50 multiple of the inner insert radius r_i. The influence of the

potting radius and the total size of potting in accordance to the hexagonal honeycomb and relevant cell and the comparison of the force-displacement dependencies in case of variation of potting radius for the insert M5 are shown in Fig. 5, in Fig. 6 for the insert M8 respectively.

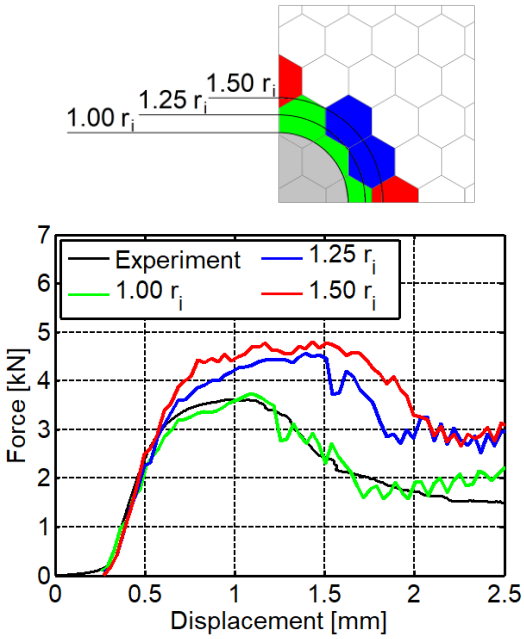

Fig. 5. The influence of the potting radius as a multiple of the inner radius r_i of insert M5 on the force-displacement dependencies

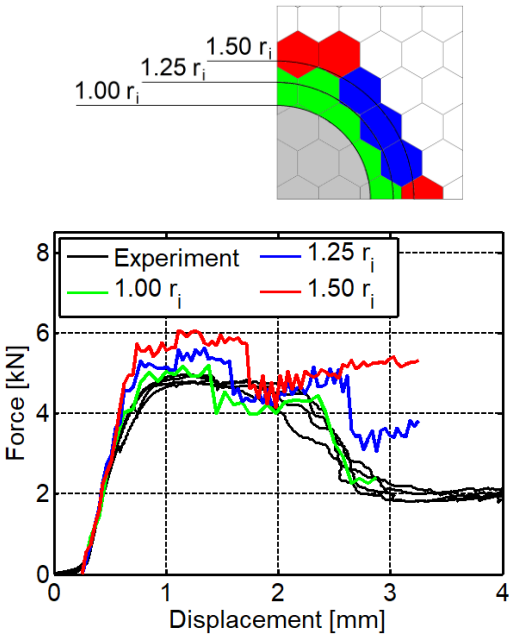

Fig. 6. The influence of the potting radius as a multiple of the inner radius r_i of insert M8 on the force-displacement dependencies

The variation of the potting radius in the hexagonal core showed an increase of the load-carrying capability of the insert potted into the sandwich structure. The most significant effect in the carrying capability was achieved for 1.25 multiple of the inner radius of the insert. The increase of the carrying capability was 19% for the insert M5 and 11% for the insert M8.

Acknowledgements

The work was supported from European Regional Development Fund-Project „Research and Development of Intelligent Components of Advanced Technologies for the Pilsen Metropolitan Area (InteCom)" (No. CZ.02.1.01/0.0/0.0/17_048/0007267) and from project SGS-2019-009 of the Czech Ministry of Education, Youth and Sports.

References

[1] Mandys, T., Kroupa, T., Laš, V., The non-linear sandwich structure model for low-velocity impact, Tehnical Gasette 27 (1) (2020) 5-11.

[2] Space engineering – Insert design handbook, Ecss-E-HB-32-22A, ESA Requirements and standards division, Netherlands, 2011.

COMPUTATIONAL MECHANICS 2021
36th conference with international participation
Srní
November 8 - 10, 2021

Modeling of large deformation of the foam part using LS-DYNA

O. Medůna[a], J. Kult[a], M. Šulc[a]

[a] *R&D Department of Computations and Modeling, VUTS, a. s., Svárovská 619, Liberec XI- Růžodol I, 460 01 Liberec, Czech Republic*

Our article deals with modeling large deformations during the drop test of the part made from expanded polypropylene (EPP). This work is related to simulations considered only static material tests [2] and measurements focused on a real drop test [3]. EPP foam is used for the damping part of the protective helmet. These helmets are usually tested to meet technical standards when the helmet is subjected to impact by a rigid punch (drop test). The numerical analysis was done using explicit FE method (solver LS-DYNA) so the full dynamic behavior of the tested structure is considered. Because the used foam material has a strongly nonlinear behavior and the dynamic loading does not have a constant speed, it was necessary to measure the stress-strain characteristics at different values of the strain rate. These curves were obtained by the dynamic tests using the Split-Hopkinson pressure bar method [1].

For accurate and repeatable results of dynamic material tests it is necessary to produce material specimens with high shape accuracy. The most important is the parallelism of the opposite surfaces of the cube that are subject to the load. At first, we tried to use cutting with a knife with cutting tool (guide for knife sliding) but the resulting surfaces of the cube were not exactly perpendicular/parallel to the others. Even with the guide, the cut was not straight. Grinding and/or sanding down was not effective too because there was no material removal. As our experience suggests, the only way how to get final 13 mm cube as a specimen is to use milling. The first step to the final specimen is prism creation by handsaw from the top longitudinal part of the helmet. This prism is machined to the final width of 13 mm. The last phase is cutting of the prism and the final milling to reach the third dimension of 13 mm (Fig. 1). The specimen is made so that its orientation during material testing corresponds to its original orientation on the entire foam part during the real drop test.

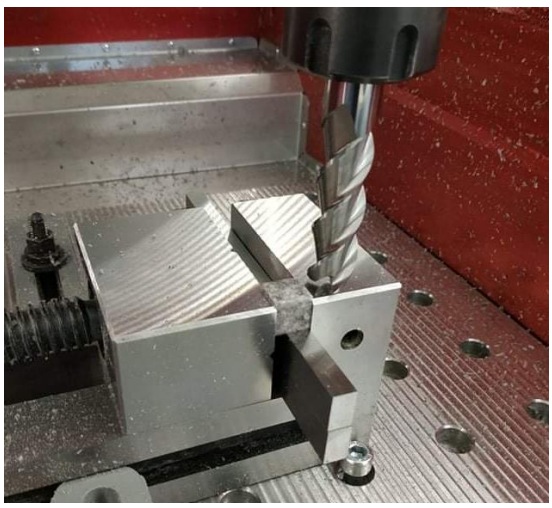

Fig. 1. Machining a foam specimen

To check and select the most accurately produced specimens, a 3D shape analysis was performed using laser scanning. Due to the structure of the foam material, which is not smooth, evaporating titanium powder was used to better scan the rough surfaces of the specimens. There is the selection of 10 specimens with a maximum parallelism deviation of 0.22 degrees as the result of the 3D analysis.

The foam specimens thus produced were loaded by impact Open Hopkinson Pressure Bar method (OHPB). Main parts of testing machine are two measurement bars (diameter 20 mm), each equipped with a foil strain-gauge (Fig. 2). First of these, the 1600 mm long incident bar works as an impactor. It is accelerated by an air cannon to the required impact velocity, its linear guidance ensures that a collision with the specimen occurs in a precisely defined position. A specimen is attached to the front of the second, transmission bar (1600 mm long). This procedure produces stress-strain characteristics under dynamic loading, in our case for two different strain rate values.

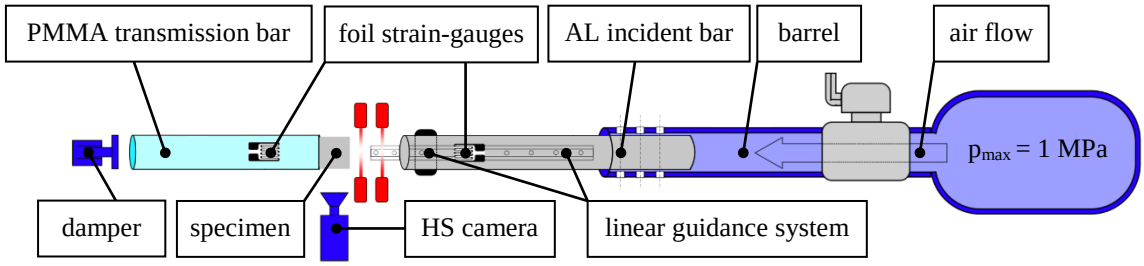

Fig. 2. Basic scheme of the OHPB testing machine

Standard configuration of the test machine consists of these two bars made from the same material – aluminum alloy (EN-AW-7075). In the case of tested EPP foam, too low force values measured during tests ($F < 100$ N) can be expected. Such low forces are difficult to measure with standard foil strain gauges. Therefore, it was necessary to use poly-methyl-methacrylate (PMMA) as the material for the transmission bar. This makes it possible to accurately measure forces, but signal evaluation requires the use of more complex techniques for decomposing deformation waves [1].

For the purposes of explicit numerical simulations, an FE mesh was created entirely of hexahedron elements. The original external and internal surfaces of the foam part were simplified by removing negligible details to obtain smoother surfaces. Such a geometry was divided into several volumes, each of which can be fully meshed with hexahedrons.

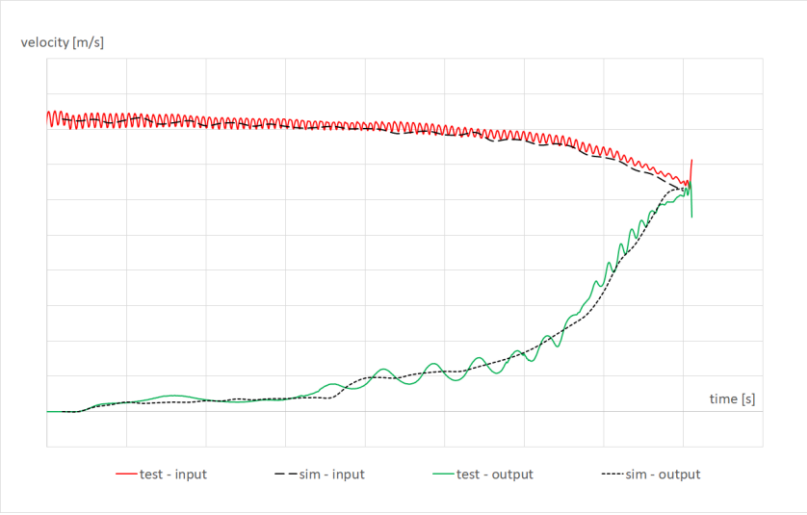

Fig. 3. Velocity of incident bar face (input) and transmission bar face (output) during the OHPB test – comparison between real test and its simulation

Numerical simulations of the drop test were performed using the LS-DYNA solver and the LS-PrePost software. For the EPP foam, the material model *MAT_FU_CHANG_FOAM (*MAT_83) was used. This model was defined using these material properties: material density, tensile modulus of elasticity, tensile stress cutoff, Poisson's ratio, stress-strain curves from uniaxial compression OHPB tests and static test. For good numerical stability and result accuracy it was necessary to prepare measured raw data before using them as input stress-strain curves in the simulation [4]. Before simulating the entire drop test, the foam material model was first validated using OHPB test simulation (Fig. 3).

The ERODING_NODES_TO_SURFACE type of contact has the possibility to keep contact even if some elements are eroded from the surface of the foam part due to high compression. Therefore, it is necessary to select nodes in the entire volume compressed by the punch, not just surface nodes.

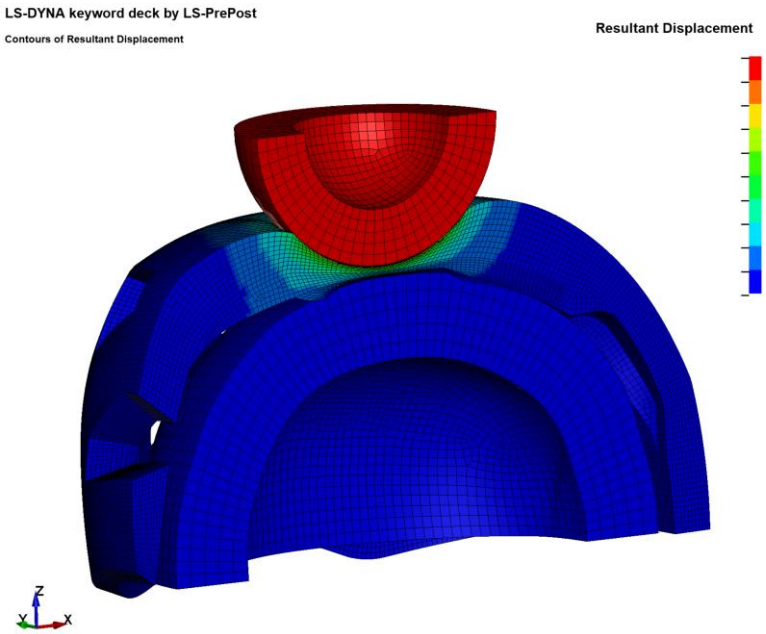

Fig. 4. Drop test simulation – displacement of the foam part

Acknowledgements

This publication was supported by the Ministry of Industry and Trade (MPO) within the framework of institutional support for long-term strategic development research organization - provider MPO, recipient VÚTS, a. s.

References

[1] Jiroušek, O., Testování mechanických vlastností EPP pěny, Ústav mechaniky a materiálů, Fakulta Dopravní, ČVUT, 2020. (in Czech)
[2] Medůna, O., Kult, J., Hisem, P., Pomp, N., Klouček, P., Protective helmet behavior under dynamic load, Proceedings of Computational Mechanics 2019, Srní, 2019.
[3] Pomp, N., Klouček, P., Force measurement during drop tests of helmets, VÚTS, a. s., Liberec, 2019.
[4] Serifi, E., Hirth, A., Matthaei, S., Müllerschön, H., Modelling of foams using MAT83 - Preparation and evaluation of experimental data, Proceedings of the 4th European LS-DYNA Users Conference, Ulm, Germany, 2003, pp. 59 – 72 (D – II).

COMPUTATIONAL MECHANICS 2021
36th conference with international participation
Srní
November 8 - 10, 2021

New test device design for static ferrofluid magnetic sealing

M. Molčan[a,b], P. Ferfecki[a,b], J. Zapoměl[b,c]

[a] *IT4Innovations, VSB - Technical University of Ostrava, 17. listopadu 2172/15, 708 00 Ostrava-Poruba, Czech Republic*
[b] *Department of Applied Mechanics, VSB - Technical University of Ostrava, 17. listopadu 2172/15, 708 00 Ostrava-Poruba, Czech Republic*
[c] *Institute of Thermomechanics, The Czech Academy of Sciences, Dolejškova 1402/5, 182 00 Praha 8, Czech Republic*

1. Introduction

Ferrofluids belong to the magnetically sensitive fluids which are in recent years used for industrial applications within sealings elements. This paper deals with essential theory and experimental results of the newly designed device for testing the static seal using a classical ferrofluid or a ferrofluid-based magnetorheological fluid.

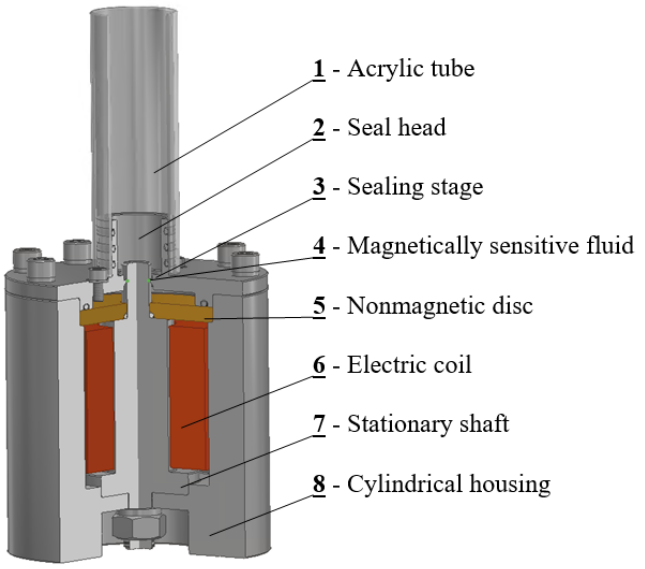

Fig. 1. Test device for the static magnetic fluid seal

A 3D schematic of the test device is shown in Fig. 1. The main parts of the proposed stand are a centre bored seal head (2) with a single stage sealing element (3) and a stationary shaft (7) with a thin layer of magnetically sensitive fluid (4) in between. The magnetic flux generated by the electric coil (6) passes through the body of the device and the layer of magnetically sensitive fluid (4). The cylindrical housing (8), stationary shaft (7), and seal head (2) are made of steel and the disc (5) is made of brass material. The electric coil has 341 turns of a copper conductor of 1.80 mm in diameter.

As resistance against the high- and low-pressure seal regions of the magnetically sensitive fluid depends on change magnetic induction, the electric current can be used to control the pressure difference. The critical pressure difference is defined as the maximum sealing pressure of the seal operating without leakage. The computation of the critical pressure difference Δp_{cr} in the layer of the magnetically sensitive fluid is based on assumptions [1], the derived ferrohydrodynamic Bernoulli equation, the magnetically saturated fluid, and neglection of the influence of the gravitational field

$$\Delta p_{cr} = M_s \cdot \Delta B_{max\text{-}min}. \quad (1)$$

M_s is the magnetization of the fluid and $\Delta B_{max\text{-}min}$ is the difference of the magnetic induction on both sides of the magnetically sensitive fluid layer.

The geometrical shape of the sealing stage was designed according to the results of the nonlinear magnetostatic analysis performed with utilisation of the finite element method.

Experimental analysis was focused on testing a magnetic field effect on the critical pressure value. The tested seal head contains one sealing stage with a radial seal gap of 0.15 mm filled with the ferrofluid volume of approximately 0.03 ml. If the residual magnetization of the test device (Fig. 2) was greater than 1 mT, the demagnetization process preceded the measurement. A very simple and efficient demagnetization procedure (see Fig.3) of the test stand, using a variable autotransformer (M10-522-20 250/8 2kVA MCP), was tested. In the initial phase of the experiment, the DC current source, generated by Agilent E3632A DC power supply, was connected to the electric coil, a ferrofluid was injected into the seal gap, and the water column in the acrylic tube was very slowly increased (Fig. 4). The experiment was stopped when leakage was detected.

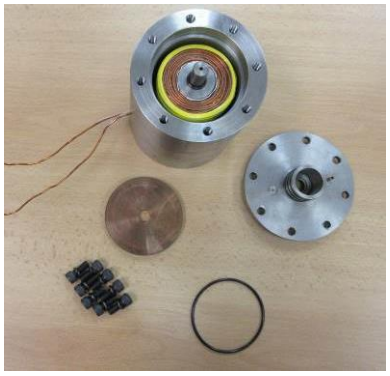

Fig. 2. Test device

Fig. 3. Assembly for the demagnetization

Fig.4. Measurement

The experiments were carried out with commercial EFH series-1 ferrofluid, manufactured by Ferrotec. This ferrofluid uses a light hydrocarbon as the carrier liquid, the volume of the magnetic particle concentration is 7.9%, the density is 1210 $kg \cdot m^{-3}$, the dynamic viscosity is 6 mPa·s (for 27°C), and the magnetization saturation is 35 $kA \cdot m^{-1}$.

The critical pressure values, listed in Table 1, are determined according to the measured water column height for the magnetic field intensity induced by the current 0.2 A. The mean value of the critical pressure difference is equal to 3884.3 Pa.

Table 1. Measured water column height/critical pressure values

Experiment number	Current 0.2 A
1	40.0 cm / 3916.9 Pa
2	40.5 cm / 3965.9 Pa
3	38.5 cm / 3770.1 Pa

2. Conclusion

The article presents preliminary experiment results of a newly designed device for testing the seal using a ferromagnetic fluid in static conditions for air and water environments.

Acknowledgements

This work has been supported by the grant project 19-06666S of the Czech Science Foundation, the doctoral grant VSB-TUO, reg. no. CZ.02.2.69/0.0/0.0/19_073/0016945 within the Operational Programme Research, Development and Education, under project DGS/TEAM/2020-033, and by the National Programme of Sustainability (NPU II) project "IT4Innovations excellence in science - LQ1602". Their help is gratefully acknowledged.

References

[1] Rosensweig, R.E., Ferrohydrodynamics, Dover Publications, Inc., Mineola, New York, 2014.

COMPUTATIONAL MECHANICS 2021
36th conference with international participation
Srní
November 8 - 10, 2021

Acoustic streaming of viscous fluid in a confining layer with vibrating walls – numerical simulations

F. Moravcová, E. Rohan

[a] *NTIS – New Technologies for the Information Society, Faculty of Applied Sciences, University of West Bohemia, Univerzitní 8, 301 00 Plzeň, Czech Republic*

Acoustic streaming (AS) is a non-intuitive phenomenon occurring in a high-intensity sound field. In general, AS is a quasi-stationary flow generated by a nonlinear acoustic wave propagating in a viscous fluid. This flow is produced due to inhomogeneities in a viscous fluid due to non-zero divergence of the Reynolds stress (due to the kinetic energy of the acoustic wave), or due to vibrating fluid-solid interface (effects of surface acoustic waves). It is observed at fluid boundary layers as the Rayleigh streaming due thermal and/or viscous phenomena, or in the bulk fluid as the high-frequency Eckart streaming. The so-called micro-streaming in the vicinity of channel walls can provoke cavitation associated with actions of microbubbles (cavitation microstreaming). Mathematical modelling of the AS was originated by Rayleigh (1884). Major pioneering contributions are due to Nyborg and Lighthill [1, 3] who established the fundamental framework for the nonlinear acoustic wave treatment using the perturbation theory.

In the present study, we explore the AS induced by the vibrating fluid-solid interface producing surface acoustic waves. For this, we consider laminar flows in vibrating channels, as shown in Fig. 1. A viscous barotropic fluid is considered, such that the adiabatic condition holds.

By pursuing the standard perturbation analysis, the flow field variables are decomposed into time-periodic components, representing the primary acoustic response, and the components representing the secondary quasi-stationary effects which can describe the acoustic streaming phenomenon. Besides the model arising due this perturbation analysis, we apply the standard approach of computational analysis by means of the relevant flow model, thus, providing direct numerical simulations (DNS) of the phenomenon. Open source software OpenFOAM is employed to solve both the types of the evolutionary boundary value problems.

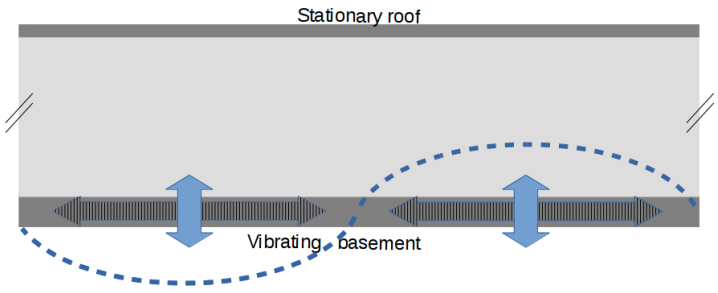

Fig. 1. Flow domain and boundaries conditions

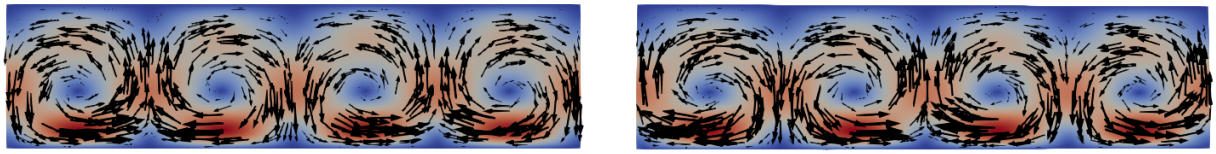

$\boldsymbol{U} \parallel \boldsymbol{n}$ $\qquad$ $\boldsymbol{U} \cdot \boldsymbol{n} = 0$

Fig. 2. Acoustic streaming due to vibrating wall Γ_w with normal (left) $U_1 = 0$, and tangential (right) $U_2 = 0$ displacement amplitude, see (3). Note the different vortex orientations

Flow in a confined 2D layer with vibrating walls We consider a 2D thin slab $\Omega =]0, L[\times]0, b[\subset \mathbb{R}^2$ representing a section of the infinite layer $]-\infty, +\infty[\times]0, b[$ occupied by a viscous barotropic fluid. Domain Ω is bounded by $\partial\Omega$ consisting of four parts Γ_w, Γ_0 and $\Gamma_\#$. The flow is induced by harmonic oscillations of the inferior wall $\Gamma_w = \{x \in \partial\Omega | x_2 = 0\}$, whereas fixed superior wall $\Gamma_0 = \{x \in \partial\Omega | x_2 = b\}$ is considered, cf. [2]. For practical reasons of the numerical simulations, periodic conditions are prescribed on the vertical boundary segments, $\Gamma_\# = \{x \in \partial\Omega | x_1 = 0, L\}$. The velocity vector $\boldsymbol{u}$, the density ρ and the pressure p satisfy the Navier-Stokes equations involving the mass and momentum conservation equations,

$$\begin{aligned} \partial_t \rho + \nabla.(\rho \boldsymbol{u}) &= 0 \ , \\ \partial_t (\rho \boldsymbol{u}) + \nabla.(\rho \boldsymbol{u} \otimes \boldsymbol{u}) &= -\nabla p + \nabla \cdot \boldsymbol{\sigma}^{vi}(\boldsymbol{u}) \ , \end{aligned} \tag{1}$$

where the viscous part of the stress $\boldsymbol{\sigma}^{vi}$ is defined using the viscosity coefficients μ and η. Thus, we may introduce operator $\hat{\mathcal{A}}(\boldsymbol{u})$, as follows

$$\hat{\mathcal{A}}(\boldsymbol{u}) := \nabla \cdot \boldsymbol{\sigma}^{vi}(\boldsymbol{u}) = \mu \nabla^2 \boldsymbol{u} + (\eta + \frac{1}{3}\mu) \nabla(\nabla \cdot \boldsymbol{u}) \ . \tag{2}$$

Besides the barotropic fluid, we may consider an incompressible fluid which yields $\hat{\mathcal{A}}(\boldsymbol{u}) = \mu \nabla^2 \boldsymbol{u}$.

The vibrations of the wall Γ_w are defined in terms of prescribed fluid velocity $\boldsymbol{v} = \boldsymbol{w}$,

$$\boldsymbol{w}(x, t) = \boldsymbol{U} \cos\left(\frac{2\pi x}{L}\right) \sin\left(\frac{2\pi t}{T}\right) , \tag{3}$$

where $\boldsymbol{U} = (U_1, U_2)$ is a given amplitude and T is the time period.

Although the fluid oscillates with frequency $\omega = 2\pi/T$ in the response to the vibrating wall, we are interested in the behaviour observed at a time scale much larger than the period T. For this, any quantity $q(x, t)$ is averaged to define $\overline{q}(x, t)$,

$$\overline{q}(x, t) := \langle q \rangle := \frac{1}{T} \int_t^{t+T} q(x, \tau) \mathrm{d}\tau \ . \tag{4}$$

Solution methods The flow equations (1) can be either solved directly (the DNS approach) or in a decomposed form [3] obtained due to the expansion of the state variables with respect to a perturbation parameter ϵ, such that

$$\begin{aligned} \boldsymbol{u}(\boldsymbol{x}, t) &= \epsilon \boldsymbol{u}_1(\boldsymbol{x}, t) + \epsilon^2 \boldsymbol{u}_2(\boldsymbol{x}, t) \ , \\ p(\boldsymbol{x}, t) &= p_0 + \epsilon p_1(\boldsymbol{x}, t) + \epsilon^2 p_2(\boldsymbol{x}, t) \ , \\ \rho(\boldsymbol{x}, t) &= \rho_0 + \epsilon \rho_1(\boldsymbol{x}, t) + \epsilon^2 \rho_2(\boldsymbol{x}, t) \ . \end{aligned} \tag{5}$$

The "zero order" variables labelled by $_0$ are constant in time, whereas the "first order" ones labelled by $_1$ are assumed to be T-periodic in time. Note that the equilibrium velocity is assumed to vanish ($\boldsymbol{u}_0 = 0$) and the equilibrium pressure p_0 and density ρ_0 are constants. Obviously, for an incompressible fluid, $\rho = \rho_0$. In other cases, we assume the wave propagation as an adiabatic process and employ the following barotropic approximation relating the pressure perturbation to the density perturbation through the sound speed c_0, see also [4]. By virtue of (5), the Taylor expansion of the pressure p in response to ρ yields

$$p_1 = c_0^2 \rho_1 \ , \ \ p_2 = c_0^2 \rho_2 + c_0 d_0 \rho_1^2 \ , \quad \text{where } c_0 = \sqrt{\left(\frac{\partial p}{\partial \rho}\right)_s} \ , \ \ d_0 := \left(\frac{\partial c_0}{\partial \rho}\right)_s \ . \tag{6}$$

Below the rescaled pressure $\hat{p_1} := p_1/\rho_0$ is employed.

Upon substituting (5) and (6) in (1) and pursuing the standard split according to orders in ϵ, two problems for the couples $(\hat{p_1}, \boldsymbol{u}_1)$ and $(\hat{p_2}, \boldsymbol{u}_2)$ are identified being governed by the following linear equations (here we consider the barotropic fluid) whereby the averaging (4) is applied,

$$\begin{aligned} &\partial_t \hat{p_1} + c_0^2 \nabla \cdot \boldsymbol{u}_1 = 0 \ , \qquad && \partial_t \bar{\hat{p}}_2 + c_0^2 \nabla \cdot \bar{\boldsymbol{u}}_2 = N \ , \\ &\partial_t \boldsymbol{u}_1 = -\nabla \hat{p_1} + \hat{\mathcal{A}}(\boldsymbol{u}_1) \ , \qquad && \partial_t \bar{\boldsymbol{u}}_2 = \boldsymbol{F} - \nabla \bar{\hat{p}}_2 + \hat{\mathcal{A}}(\bar{\boldsymbol{u}}_2) \ , \end{aligned} \tag{7}$$

see (2), where N and $\boldsymbol{F}$ are computed, as follows

$$N := -\left\langle \nabla . (\hat{p_1} \boldsymbol{u}_1) \right\rangle \ , \ \ \boldsymbol{F} := -\left\langle \nabla . (\boldsymbol{u}_1 \otimes \boldsymbol{u}_1) \right\rangle \ , \tag{8}$$

providing the driving forces for the acoustic streaming. For the incompressible case, the continuity equations in (7) are reduced to $\nabla \cdot \boldsymbol{u}_1 = 0$ and $\nabla \cdot \bar{\boldsymbol{u}}_2 = 0$. This decomposed form of the AS problem can be solved using any standard CFD computational tool. For this we employed the OpenFOAM to write our own solvers.

To illustrate the AS phenomenon, in Fig. 2 we depict the flow field $\bar{\boldsymbol{u}}_2$ in domain Ω. The steady state vortices are generated by vibrations of the lower edge in the normal direction, i.e., with an amplitude $\boldsymbol{U} = (0, U_2)$, see (3). Similar pattern is obtained for the tangential vibrations when $\boldsymbol{U} = (U_1, 0)$, whereby small differences between the barotropic and incompressible fluids were observed. In Fig. 3, the relative magnitude $|\bar{\boldsymbol{u}}|/u^*$ of the velocity obtained using the DNS method is displayed along a horizontal and a vertical sections located at $x_2/b = 0, 1/4, 1/2, 3/4$ and $x_1/L = 0, 3/8, 1/4$, respectively, whereby $u^* = \frac{1}{|\Omega|} \int_\Omega \bar{\boldsymbol{u}} d\boldsymbol{x}$. Quite similar curves are obtained while plotting the solution $\bar{\boldsymbol{u}}_2$ of the expanded problem (7). The difference $(|\bar{\boldsymbol{u}}| - |\bar{\boldsymbol{u}}_2|)/u^*$ between the two solutions is less than 5% (Fig. 4).

Remarks and perspectives The computational study reported very briefly in this paper enabled to reveal the Acoustic Streaming (AS) phenomenon in the context of numerical solution methods. Although the phenomenon has been studied and reported in the literature over past decades in various contexts, our intent is to study the AS in periodic scaffolds and to account for thermal and deformation effects which bring a two-way coupling between the first and second-order problems of the decomposed form, see (7).

Acknowledgements

The research has been supported by the grant project GACR 21-16406S of the Czech Science Foundation, and in a part by the European Regional Development Fund-Project "Application of Modern Technologies in Medicine and Industry" (No. CZ.02.1.01/0.0/ 0.0/17 048/0007280) of the Czech Ministry of Education, Youth and Sports.

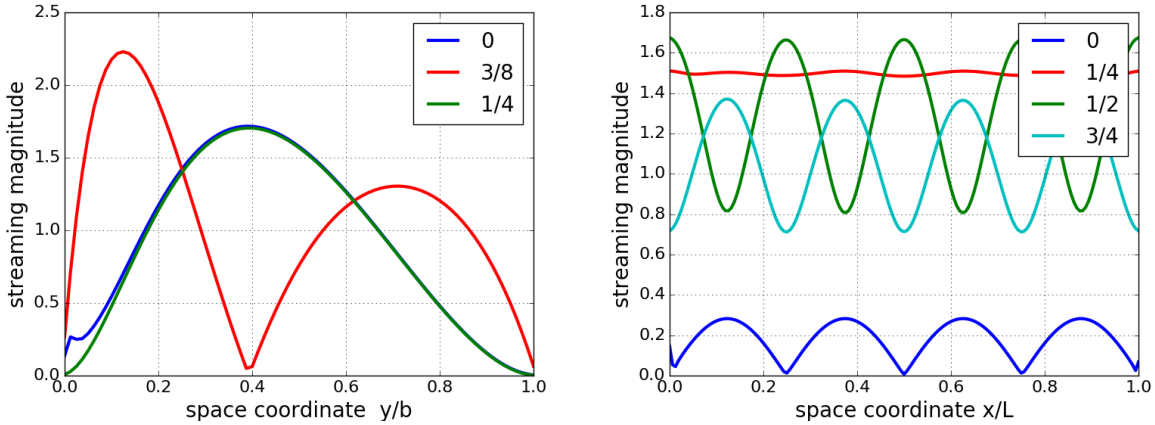

Fig. 3. Velocity magnitude $|\bar{\boldsymbol{u}}|/u^*$ along the vertical (*left*) and horizontal (*right*) line sections

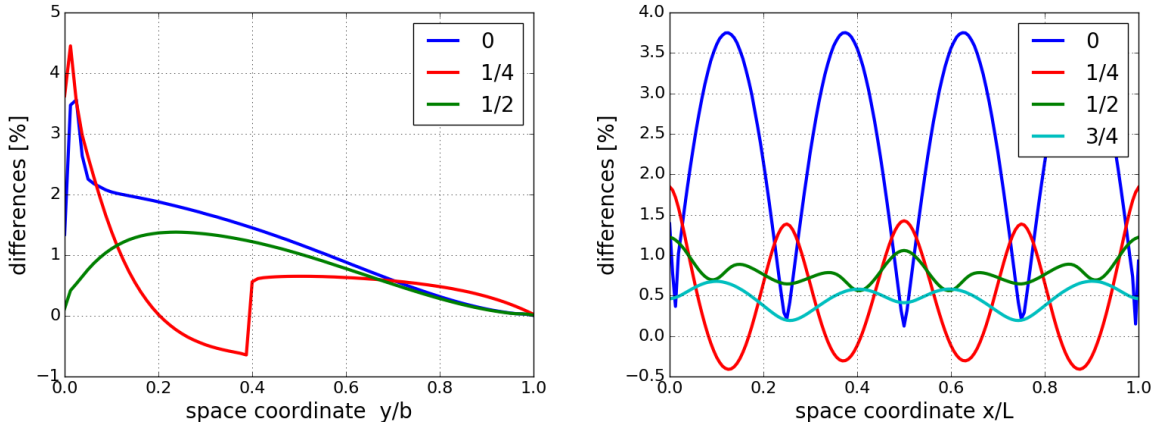

Fig. 4. Relative differences $(|\bar{\boldsymbol{u}}| - |\bar{\boldsymbol{u}_2}|)/u*$ between the direct and expansion resolution in %

References

[1] Lighthill, J., Acoustic streaming, Journal of Sound and Vibration 61 (3) (1978) 391-418.

[2] Loh, B.-G., Hyun, S., Ro, P. I., Kleinstreuer, C., Acoustic streaming induced by ultrasonic flexural vibrations and associated enhancement of convective heat transfer, The Journal of the Acoustical Society of America 111 (2) (2002) 875-883.

[3] Nyborg, W. L., Acoustic streaming due to attenuated plane waves, The Journal of the Acoustical Society of America 25 (1) (1953) 68-75.

[4] Wu, J., Acoustic streaming and its applications, Fluids 3 (4) (2018) No. 108.

COMPUTATIONAL MECHANICS 2021
36th conference with international participation
Srní
November 8 - 10, 2021

Control of modal properties of beam structures using the reinforcing core

M. Naď[a], L. Rolník[a], J. Lovíšková[b]

[a] *Faculty of Materials Science and Technology in Trnava, Slovak University of Technology in Bratislava, Ul. Jána Bottu 25, 917 24 Trnava, Slovak Republic*
[b] *Institute of Informatics, Slovak Academy of Sciences, Dúbravská cesta 9, 845 07 Bratislava 45, Slovak Republic*

The harmful effects caused by the occurrence of undesired vibrations in machines and various constructions have in many cases fatal consequences for their functionality and in extreme cases also for their structural integrity. In view of the need to eliminate these undesirable states that arise during operation, it is important to create conditions for modifying the modal properties of the relevant structural elements of the mechanical system.

The beam structures can be considered as basic structural elements applied in mechanical and civil structures. A very dangerous state occurs when these structures are exposed to inappropriate dynamic loading effects, which in unfavorable cases can cause their resonant state. One of the important tasks in structural design of the beam structures should be the ability to prevent or reduce the level of unwanted vibrations. The dynamical properties of the beam structures [1], [3], [6] are depended on their structures, geometrical parameters and material properties. The beam structures are usually made of homogeneous material these structures in many cases do not have the required dynamic properties.

Generally, we consider the beam structure (Fig.1) with rectangular cross section (b_0, h_0) and with hole along whole beam length L_0. The moving reinforcing core (cylinder shape) with diameter d_c is inserted into beam hole. The length L_c of inserted cylindrical core is less than the length beam structure ($L_c < L_0$).

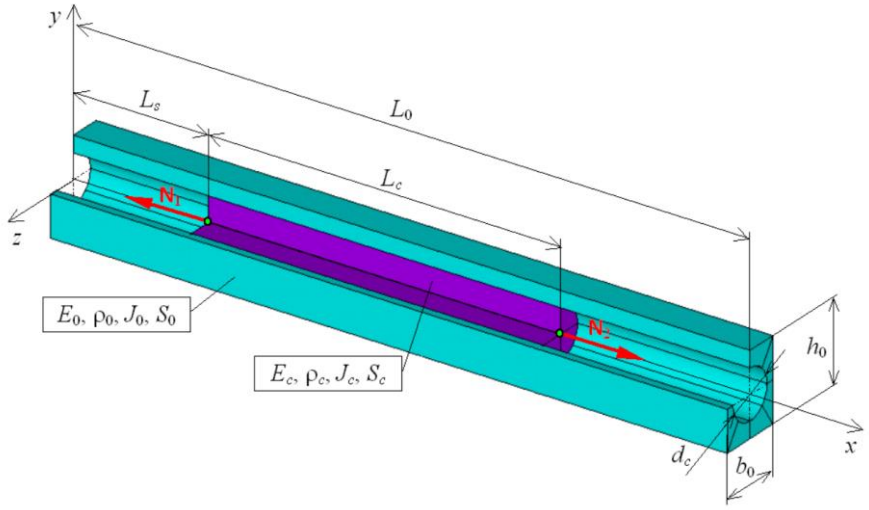

Fig. 1. General model of beam structure with inserted pre-stressed reinforcing core

On both end cross-section surfaces of the reinforcing core, the pre-stressed forces can be applied. Also the position of the inserted reinforcing core can be changed. Then the beam structure has three different structural fields. It is clear [4], [5], that the changing core

position, geometric parameters and material properties of reinforcing core and also prestressing forces, the induce the change in the distribution of mass and flexural stiffness of the modified beam structure, which subsequently causes a change in the modal properties.

The following assumptions [5] to the creation of mathematical model of the modified beam structure (Fig. 1) are considered:

- cross-section parts of the beam structure lie in plane perpendicular to the neutral x-axis,
- beam cross-sections before and during beam deformation is assumed as planar,
- cross-sections of beam profile and core are symmetrical with respect to both axes y, z,
- material properties of the beam structure parts are isotropic and homogeneous,
- perfect adhesion at the interface of beam-core is supposed.

The computational model describing the studied beam structure (Fig. 1) is based on the assumptions of the Euler-Bernoulli beam theory. The general equation [2] for bending vibrations of beam with axial pre-stressing forces acting on core, for each j^{th} segment of beam, can be written in the form

$$E_j J_j \frac{\partial^4 w_j(x_j,t)}{\partial x_j^4} - N_j \frac{\partial^2 w_j(x_j,t)}{\partial x_j^2} + \rho_j S_j \frac{\partial^2 w_j(x_j,t)}{\partial t^2} = 0, \tag{1}$$

where $w_j(x_j, t)$ is vibrating beam deflection.

For each segment in the beam structure, the flexural stiffness E_jJ_j and mass ρ_jS_j of the beam are constant. It must be noted that sign minus before force effect N_j is for a tensile load and sing plus is for a compression load.

By introducing the solution $w_j(x_j,t) = W_j(x_j)T(t)$, the equation (1) has following form

$$\overline{W}_j^{VI}(\xi_j) - \alpha_j^2 \overline{W}_j^{II}(\xi_j) - \beta_j^4 \overline{W}_j(\xi_j) = 0, \tag{2}$$

where parameters α_j and β_j are axpressed by

$$\alpha_j = \sqrt{\frac{N_j}{E_j J_j} L_0^2} \qquad \text{and} \qquad \beta_j = \sqrt[4]{\frac{\rho_j S_j}{E_j J_j} L_0^4 \omega_{0m}^2} \tag{3}$$

and ω_{0m} is natural angular frequency modified beam structure. dimensionless parameters are introduced in the form

$$\overline{W}_j(\xi_i) = \frac{W_j(x_j)}{L_0}, \qquad \xi_j = \frac{x_j}{L_0}, \qquad \xi_s = \frac{L_s}{L_0}, \qquad \xi_c = \frac{L_c}{L_0}. \tag{4}$$

By solving the eigenvalue problem $\lambda_{j,k}^4 - \alpha_j^2 \lambda_{j,k}^2 - \beta_j^4 = 0$ for j^{th} beam segment, the eigenvalues $\lambda_{j,k}$ ($k = 1 \div 4$) are obtained.

The solution of the equation (2), for j^{th} beam segment, has the following form

$$\overline{W}_j(\xi_j) = A_{j1}\cos(\eta_{j1}\xi_j) + A_{j2}\sin(\eta_{j1}\xi_j) + A_{j3}\cosh(\eta_{j2}\xi_j) + A_{j4}\sinh(\eta_{j2}\xi_j), \tag{5}$$

where $$\eta_{j1} = \sqrt{\frac{1}{2}\left[\sqrt{\alpha_j^4 + 4\beta_j^4} - \alpha_j^2\right]}, \qquad \eta_{j2} = \sqrt{\frac{1}{2}\left[\sqrt{\alpha_j^4 + 4\beta_j^4} + \alpha_j^2\right]} \tag{6}$$

and $A_{j1} \div A_{j4}$ are integration constants.

The boundary conditions for the clamped-free beam structure and for core position $\xi_s = 0$ are presented in Table 1. The intervals for dimensinless parameters ξ_j (j = 1,2) are defined as follows

$$\xi_1 \in \langle 0,\ \xi_c \rangle, \qquad \xi_2 \in \langle 0,\ 1 - \xi_c \rangle. \tag{7}$$

Table 1. Boundary conditions for beam structrure

$\xi_1 = 0$	$\overline{W_1}(\xi_1)\big\|_{\xi_1=0} = 0$
	$\overline{W_1}'(\xi_1)\big\|_{\xi_1=0} = 0$
$\xi_1 = \xi_c$	$\overline{W_1}(\xi_1)\big\|_{\xi_1=\xi_c} = \overline{W_2}(\xi_2)\big\|_{\xi_2=1-\xi_c}$
$\xi_2 = 1 - \xi_c$	$\overline{W_1}'(\xi_1)\big\|_{\xi_1=\xi_c} = -\overline{W_2}'(\xi_2)\big\|_{\xi_2=1-\xi_c}$
	$(1+\Delta_{EJ})\overline{W_1}''(\xi_1)\big\|_{\xi_1=\xi_c} = \overline{W_2}''(\xi_2)\big\|_{\xi_2=1-\xi_c}$
	$(1+\Delta_{EJ})\overline{W_1}'''(\xi_1)\big\|_{\xi_1=\xi_c} = -\{\overline{W_2}''(\xi_2) - \overline{N}\overline{W_2}'(\xi_2)\}\big\|_{\xi_2=1-\xi_c}$
$\xi_2 = 0$	$\overline{W_1}''(\xi_1)\big\|_{\xi_2=0} = 0$
	$\overline{W_2}'''(\xi_2)\big\|_{\xi_2=0} = 0$

$E_1J_1 = E_0J_0(1+\Delta_{EJ})$ $\rho_1S_1 = \rho_0S_0(1+\Delta_{\rho S})$ $N_1 = 0$	$E_2J_2 = E_0J_0$ $\rho_2S_2 = \rho_0S_0$ $N_2 = N$	$\overline{N} = \dfrac{NL_0^2}{E_0J_0}$

The modification parameters

$$\Delta_{EJ} = \frac{E_cJ_c}{E_0J_0} \quad \text{and} \quad \Delta_{\rho S} = \frac{\rho_cS_c}{\rho_0S_0} \tag{8}$$

characterize the proportional changes in the stiffness and mass properties of the beam caused by inserting the core, where E - Young modulus, ρ - density, S - cross-section area, J - second moment of area (subscript 0 is used for the basic beam structure and subscript c is used for the core). Parameter $\overline{N}$ represnts dimensionless axial prestressing force.

Substituting the solution $\overline{W}_j(\xi_j)$ from the equation (5) into the boundary conditions (Table 1), the frequency determinant is created. As a result of the solution of the frequency determinant, the modification function taking into account the changes in the mass and stiffness properties of the modified beam structure, induced by the prestressed core, is expressed. The modification function $f_{m\omega,k}(\overline{N}, \xi_c, \Delta_{\rho S}, \Delta_{EJ})$ for k^{th} vibration mode shape is defined as the ratio of natural angular frequency $\omega_{0m,k}$ of the modified beam structure to natural angular frequency $\omega_{0,k}$ of the unmodified beam structure

$$\frac{\omega_{0m,k}}{\omega_{0,k}} = f_{m\omega,k}(\overline{N}, \xi_c, \Delta_{\rho S}, \Delta_{EJ}). \tag{9}$$

The modification functions for the first two natural frequencies in dependency on the dimensionless length of core insertion for zero, tensile and compression dimensionless forces and for modification parameters $\Delta_{EJ} = 0.25, \Delta_{\rho S} = 0.25$ are shown in Fig.2. In the case of zero prestressing force, the modification function values are greater than 1.0 over the entire length of core insertion. The values of the first two natural frequencies of the modified beam structure increase proportionally to the length of core insertion. For the first natural frequency the values of modification function are greatest when the core is inserted in the half beam length and the growth is aproximately 10%. When the tensile force is acting at the core end,

the pre-stressed state is initialized in the first segment of beam and the first natural frequency of the beam structure increases by 25% when the core is inserted into 90% of the beam length. In the case of compressive force, a decrease in natural frequencies occurs when the core is inserted into an area that exceeds half the length of the beam structure (Fig. 2).

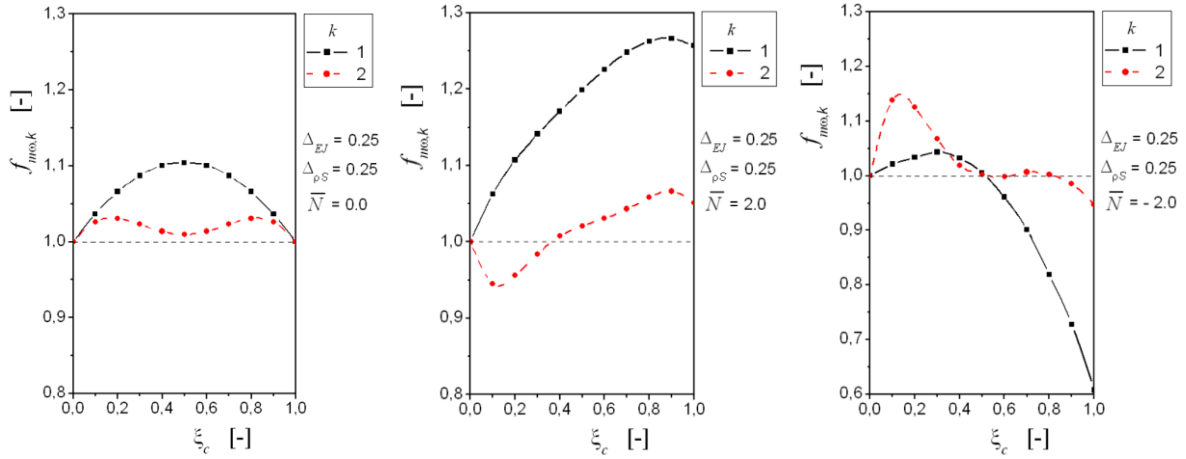

Fig. 2. Dependency of modification functions $f_{m\omega,k}$ (for the first two mode shapes k = 1,2) on core position ξ_c

The technique of structural modification leading to the change of modal properties (natural frequencies, mode shapes) of beam structures, which is based on applications reinforcing core inserted into beam body, its geometrical parametrs and materiál properties and also on prestressing forces acting on the core in the axial direction of the beam structures is presented in ths paper. By changing modification parameters $\overline{N}$, Δ_{EJ}, $\Delta_{\rho S}$, ξ_c is possible to achieve a appropriate modification of natural frequencies of the beam structure (Fig. 1), i.e.

$$\omega_{0m,k} = \omega_{0,k} f_{m\omega,k}(\overline{N}, \xi_c, \Delta_{\rho S}, \Delta_{EJ}) . \tag{10}$$

Presented beam structure modifications provide the possibilities leading to structural modification, ie. redistribution of beam spatial properties, which could be used to "tune" the modal properties of beam structures to the desired values and thus to eliminate the occurrence of resonant states.

Acknowledgements

The work has been supported by the grant project „EDU-MaTech" Interreg SK-CZ and by the research project KEGA 009STU-4/2021.

References

[1] Avitable, P., Twenty years of structural dynamic modification - A review (based on a paper presented at IMAC-XX), Sound and Vibration, 2003.
[2] Meirovitch, L., Analytical methods in vibrations, McMillan Company, London, 1987.
[3] Naď, M., Modification of modal characteristics of vibrating structural elements, Scientific Monographs, Köthen, 2010.
[4] Naď, M., Rolník, L., Čičmancová, L., Prediction of changes in modal properties of the Euler–Bernoulli beam structures due to the modification of its spatial properties, International Journal of Structural Stability and Dynamic 17 (9) (2017) (13 pages).
[5] Rolník, L., Structural dynamic modification of lathe tool body, PhD. thesis, Slovak University of Technology in Bratislava, Faculty of Materials Science and Technology, 2015.
[6] Ságа, M., Žmindák, M., Dekýš, V., Sapietová, A., Segľa, Š., Selected methods for the analysis and synthesis of mechanical systems, VTS ZU, Zilina, 2009. (in Slovak)

COMPUTATIONAL MECHANICS 2021
36th conference with international participation
Srní
November 8 - 10, 2021

Description of the quasi-periodic response caused by combined harmonic and random excitation

J. Náprstek, C. Fischer

Institute of Theoretical and Applied Mechanics of the Czech Academy of Sciences, Prosecká 76, 190 00 Prague, Czech Republic

Abstract

The generalized van der Pol equation exposed to combined harmonic and random excitation can exhibit a quasi-periodic response. The existence of this particular type of response depends on the detuning between the driving and resonance frequencies. The response is stationary for a "small" or "large" value of detuning. The contribution specifies in detail the detuning interval in which the quasi-periodic response occurs.

1. Introduction

When dealing with the frequency characteristics of real dynamic systems, such as those that appear in the dynamics of civil engineering structures, one encounter the phenomenon of the so-called frequency lock-in. It consists in the fact that for certain values of design parameters the change of the response does not correspond to the change of the frequency of the external excitation. For example, when examining the properties of a flow-induced movement of a body, the frequency of vibrations of the body caused by the separation of vortices is approximately proportional to the flow speed. However, once the flow velocity approaches the critical velocity, when the vortex separation frequency is close to the natural frequency of the body, the increase stops. The frequency of vibrations of the body remains constant in the non-zero vicinity of the resonant frequency, i.e. for a certain interval of values of the flow speed. If the flow velocity exceeds a certain limit with the next increase, the linear relationship between vibration frequency and flow velocity is restored.

This effect stems from the non-linear nature of the physical phenomenon. It is often described using the generalized van der Pol equation. In a state very close to resonance, the solution of this equation corresponds to a stable limit cycle. Large amplitudes of vibrations in this state affect the frequency of the vortex shedding, so that the excitation frequency is in fact fixed at the natural frequency of the structure.

The oscillation of the body in resonance is stationary and approximately harmonic. When the difference between the excitation and resonant frequencies increases, the vibrations of the body cease to be stationary and a quasi-periodic response occurs. It has two main components: the natural oscillation corresponding to the respective natural frequency, and the stationary forced oscillation. Their combination then cause the beating effect. The periods and amplitudes of the beating depend on the parameters of the system and on the difference between the natural and excitation frequencies. If the excitation frequency shifts from the natural frequency, i.e. the detuning increases, the period of beats shortens, because the influence of the auto-oscillating component of the response decreases. When this component disappears,

the response will be stationary again. Its frequency will correspond to the frequency of forced oscillation.

The assumption of a random additive component, which can represent turbulence effects in the flow, introduces uncertainty into the problem. Experimental studies show that the random component can be considered Gaussian, the spectral density corresponds to von Kármán's velocity spectrum [1]. Theoretical investigation of a combined deterministic and random excitation in the resonance case has been published by the authors [5]. The paper which permits a positive value of detuning is currently under preparation. This work presents several results of a numerical examinations of the mathematical model in the state close to resonance, when the additive random component contributes to forming of beats, and to a general non-stationary character of the response.

2. Mathematical model

The stochastic single-degree-of-freedom van der Pol oscillator with strongly nonlinear damping part, which is a very suitable model of the case described in Introduction, can be written as

$$\ddot{u} - (\eta - \nu u^2)\dot{u} + \omega_0^2 u \;=\; P\omega^2 \cos\omega t + h \cdot \xi(t), \tag{1}$$

where

$u = u(t)$	displacement $[\mathrm{m}]$,	$v = v(t)$	velocity $[\mathrm{m.s}^{-1}]$,
η, ν	parameters of the damping $[\mathrm{s}^{-1}, \mathrm{s}^{-1}\mathrm{m}^{-2}]$,	ω_0	eigen-frequency of the adjoint linear SDOF system,
ω	excitation frequency of the vortex shedding $[\mathrm{s}^{-1}]$,	$P\omega^2$	amplitude of the harmonic excitation force $[\mathrm{m.s}^{-2}]$,
h	multiplicative constant $[\mathrm{m.s}^{-2}]$,	$\xi(t)$	broadband weakly stationary Gaussian random process [1].

Eq. (1) characterizes the nonlinear vibration of an SDOF system modelling the reduced flutter as one of post-critical response types of an aeroelastic system. In general, this equation describes state when the total linear damping component drops below zero due to aeroelastic effects and only nonlinear effects stabilize.

3. Deterministic stationary case

The possible stationary solution to Eq. (1) in the vicinity of the resonance can be characterized using the harmonic balance approach. The procedure described in [3] assumes the solution in a harmonic form

$$u = U\cos(\omega t + \varphi)\,, \tag{2}$$

where the stationary amplitude U is given by

$$U^2\left(4\Delta^2 + \left(\eta - \frac{\nu}{4}U^2\right)^2\right) = \omega^2 P^2\,. \tag{3}$$

Stability of the admissible solutions can be assessed using two Routh-Hurwitz conditions

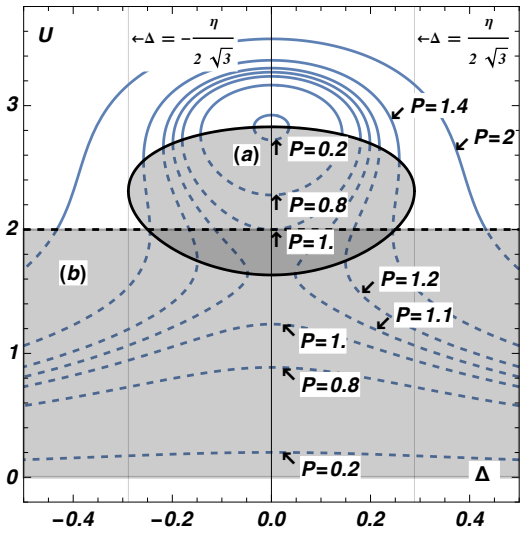

Fig. 1. Stationary amplitudes and instability areas

$$\text{(a)}\quad 64\Delta^2 + \left(4\eta - 3\nu U^2\right)\left(4\eta - \nu U^2\right) \geq 0\,, \qquad \text{(b)}\quad 2\eta - \nu U^2 \geq 0, \tag{4}$$

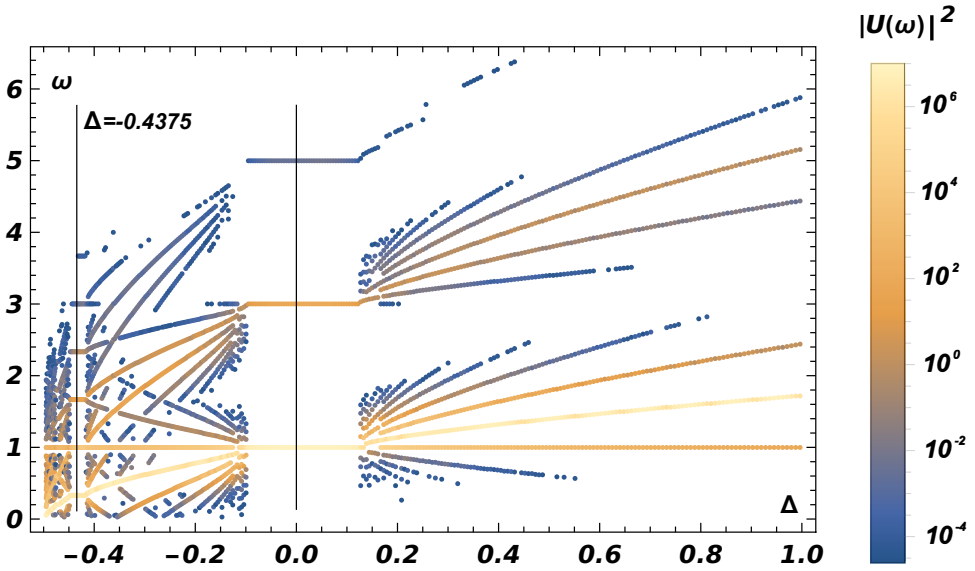

Fig. 2. Frequency characteristics of the response of Eq. (1). Abscissa: detuning Δ. Ordinate: angular frequency axis of the response. Colours: absolute values of dominant Fourier coefficients

where $\Delta = \frac{\omega_0^2-\omega^2}{2\omega} \approx \omega_0 - \omega$ and η is assumed positive. Fig. 1 shows the amplitudes U for various excitation levels $P = 0.2, \ldots, 2$ depending on detuning values Δ. The greyed areas show where the conditions (4) are violated. Values used: $\eta = 1, \nu = 1/2, \omega = 1$.

4. Deterministic non-stationary case

When the detuning exceeds limits given by the stability conditions (4), the stabilised response given by Eq. (1) forms non-stationary quasi-periodic time histories. The frequency characteristics of the response are visible in Fig. 2. All simulations were performed for a prescribed value of the excitation frequency and amplitude $\omega = 1, P = 1$. Thus, the varying detuning Δ on the horizontal axis in Fig. 2 represents in fact the system eigenfrequency ω_0. The dominant peaks of the periodogram for each value of ω_0 are plotted vertically. This way the ordinate represents the Fourier frequency of the response. The color intensity corresponds to absolute values of the dominant Fourier coefficients in a logarithmic scale. The stationary lock-in interval appears for $-0.1 \lessapprox \Delta \lessapprox 0.12$, although two super-harmonic components ($\omega = 3\omega_0, 5\omega_0$) are also clearly visible. Also the presence of a sub-harmonic resonance interval for $\Delta \approx -7/16$ (i.e., for $\omega_0^2 = 1/8$) indicates a complex behaviour of the nonlinear response. For theoretical explanation of such effects see [4]. It is worth noting that the curves corresponding to the individual peaks are linear when plotted as dependent on ω_0.

5. Random excitation

When the response of a system in deterministic case is of a quasi-periodic character, the random response is generally neither stationary nor ergodic. Consequently, it would prevent the application of procedures which are commonly used for evaluation of stochastic parameters along the time coordinate. However, the detailed parameters, e.g. stochastic moments, repeat in a cyclic regime. Consecutive quasi-periods are similar to those observed on synchronously running two or more parallel realizations of the response process. Such processes are called in literature cyclo-stationary processes. For further details on the topic, see [2].

Fig. 3 illustrates behaviour of the quasi-period length for an increasing intensity of the random component. Naturally, the variance of the period length for a low noise intensity is small

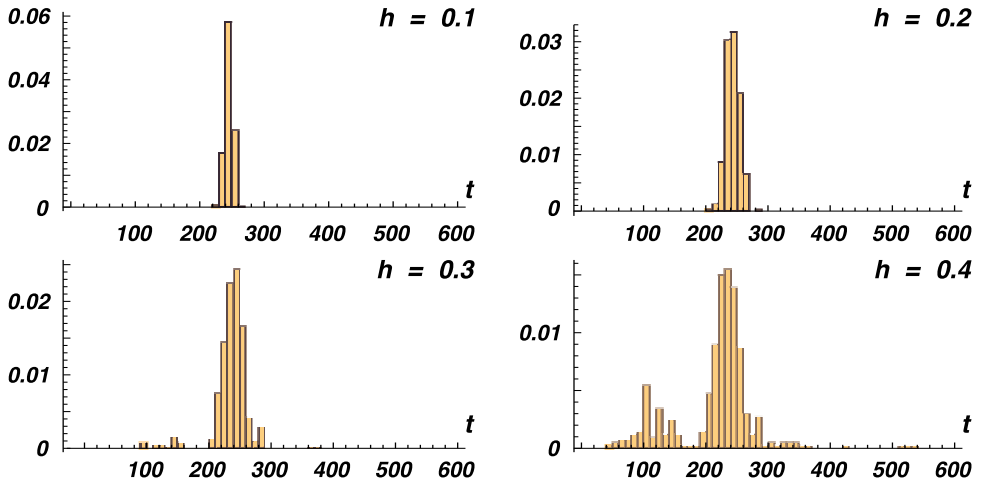

Fig. 3. Histograms of the quasi-period length for an increasing intensity of the random component

and increases proportionally to the noise. It appears, however, that an additional source of uncertainty is a limited possibility to detect the length of the quasi-period. Spurious quasi-periods appear for values of the parameter as low as $h = 0.3$; in the plot for $h = 0.4$ the character of the response changes significantly. A new peak appears in this case for periods of approximately half the original length. If the noise intensity increases further, the original quasi-period will no longer be recognizable in the histogram.

6. Conclusions

The lock-in regime can be significantly complicated when a random noise is considered in addition to a harmonic aeroelastic force. Despite of its complexity, this effect can be modelled using the single-degree-of-freedom van der Pol oscillator with a strongly non-linear damping part. As a beginning of a larger study, the beating quasi-periodic response type in the vicinity of the system eigen-frequency has been studied numerically. It has been shown that the coincidence of both frequencies provides a stationary response. For the response outside the lock-in regime, the complex behaviour has been examined. When random excitation is considered, the shape of the response PDF can qualitatively change due to values of the damping parameters and can exhibit local extremes which can emerge or disappear. Detailed analysis of both excitation components (harmonic, random) is apparently very important.

Acknowledgements

The kind support of Czech Science Foundation project No. 19-21817S and of the RVO 68378297 institutional support are gratefully acknowledged.

References

[1] Dyrbye, C., Hansen, S. O., Wind loads on structures. Wiley and Sons, Chichester, 1997.

[2] Gardner, W. A., Napolitano, A., Paura, L., Cyclostationarity: Half a century of research. Signal Processing 86 (2006) 639-697.

[3] Náprstek, J., Fischer, C., Analysis of the quasiperiodic response of a generalized van der Pol nonlinear system in the resonance zone. Computers & Structures 207 (2018) 59-74.

[4] Náprstek, J., Fischer, C., Super and sub-harmonic synchronization in generalized van der Pol oscillator, Computers & Structures 224 (2019) No. 106103.

[5] Náprstek, J., Fischer, C., Pospíšil, S., Trush, A., Modeling of the quasi-periodic galloping response type under combined harmonic and random excitation, Computers & Structures 247 (2021) No. 106478.

COMPUTATIONAL MECHANICS 2021
36th conference with international participation
Srní
November 8 - 10, 2021

Study of anharmonic vibrational properties in 3D crystals using molecular dynamics simulations

J. Očenášek[a]

[a] *New Technologies - Research Centre, University of West Bohemia in Pilsen, Univerzitní 8, 301 00 Plzeň, Czech Republic*

In classical theory, solids are elastic objects that obey Hooke's law, according to which the deformation (strain) of an object is proportional to the stress applied to it. However, if the deformations have wavelengths of the magnitude comparable to the interatomic distances, classical continuum elasticity fails quantitatively. A correct prediction of these nanoscale deformations can only be obtained by considering the atomic vibrations in the crystal lattice. A unit (quantum) of vibrational energy in crystal lattice is called phonon. In this paper, we present one of the few possible numerical approaches to phonon spectra estimation that is very general and allows the study of specific anharmonic features such as phonon softening.

The linear mass-spring chain model is a classical model of a one-dimensional crystal lattice with the potential to reveal the main principles of lattice dynamics, i.e., vibrational waves propagating through the lattice, where the isolated masses represent atoms. In this contribution, a linear mass-spring model is introduced and extended to provide an accurate 3D model of a ferroelectric barium titanate (BTO) crystal, with a perovskite structure, see Fig. 1.

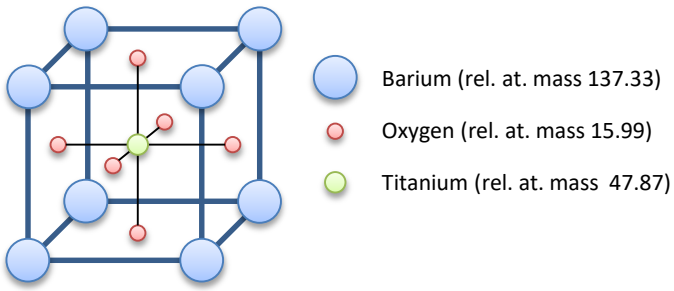

Fig. 1. Unite cell structure of barium titanate

Atomic forces in the BTO lattice were modelled by means of a shell model, which is a simple method for adding polarizability to the system. The shell model treats an atom as two coupled particles connected by a spring: (i) a core with positive charge, which holds the atomic mass of the atom, and (ii) a massless shell with negative charge. All cores and shells interact by Coulomb forces except the core and shell of the same atom. A short-range atomic pair interaction is set only between the shell particles. The short-range interaction was implemented as Born potential. The interaction scheme is given in Fig. 2, and model parameters were optimized in [3].

In order to correctly represent the possible states of the mechanical system at absolute temperature, a canonical ensemble NVT was set and thermalized by means of the Nosé–Hoover thermostat algorithm. This provides approximation of a system in thermal equilibrium with a Maxwell-Boltzmann statistics of the particles energy states.

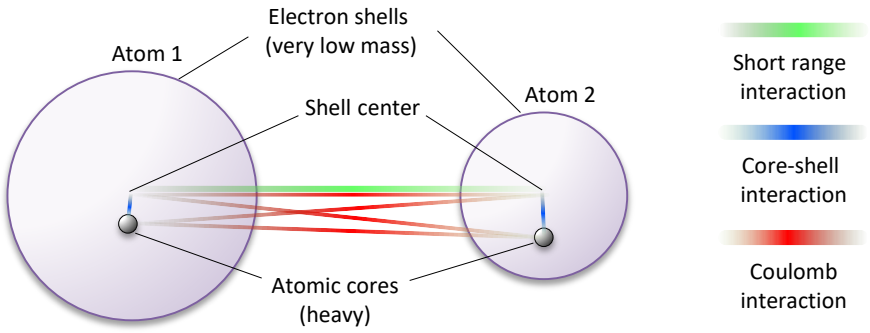

Fig. 2. Schematic representation of the core-shell model

This model, together with the classical molecular dynamics method (based on Newton´s equations of motion), is employed to numerically solve the trajectories of the atoms at a given temperature. Computer simulations were done using LAMMPS code [2]. Calculated atomic trajectories were then used to analyze the lattice vibrational properties and construct the phonon dispersion, i.e. to determine the wave frequencies present, the corresponding wavelength and the direction of propagation. The mathematical procedure involves autocorrelation of the Fourier transformed atomic velocities, details can be seen in [1]. Resulting phonon spectra for a selection of wave vectors (set of points at brillouin zone symmetry lines between [000] [001] and [½ ½ 0] wave vectors) is given in the Fig. 3. This method allows identification of all 12 optical modes and 3 acoustic modes of the spectra.

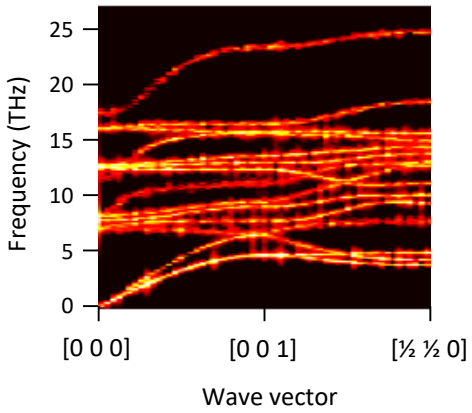

Fig. 3. Calculated phonon spectra at the low temperature (rhombohedral) BTO phase

Finally, specific anharmonic effects such as soft phonons, which are related to the phase transformation of the BTO crystal lattice at elevated temperatures, are discussed.

Acknowledgements

This work by was supported by The Ministry of Education, Youth and Sports under grant CEDAMNF CZ.02.1.01/0.0/0.0/15_003/0000358 (Czech Republic).

References

[1] Koukaras, E.N., Kalosakas, G., Galiotis, C., Papagelis, K., Phonon properties of graphene derived from molecular dynamics simulations, Scientific Reports 5 (2015) 12923.
[2] Plimpton, S., Fast parallel algorithms for short-range molecular dynamics, Journal of Computational Physics 117 (1995) 1-19.
[3] Vielma, J.M., Schneider, G., Shell model of $BaTiO_3$ derived from ab-initio total energy calculations, Journal of Applied Physics 114 (2013) 174108.

COMPUTATIONAL MECHANICS 2021
36th conference with international participation
Srní
November 8 - 10, 2021

Method of shifted order spectra – identification of spatial orders of electric machines

J. Otta[a], P. Macák[b]

[a] ZF Friedrichshafen AG, 88038 Friedrichshafen, Germany
[b] ZF Engineering Plzeň s.r.o., Macháčkova 24, 318 00 Plzeň, Czech Republic

1. Introduction

Hybrid and electric cars are becoming increasingly quiet, therefore the aspects of Noise, Vibration and Harshness (NVH) gained a very important role in the development of electric drives. One of the main excitation sources of the electric motors is the rotating magnetic field exciting radial eigenmodes of stator.

Typical processing of NVH measurement data can detect relevant time orders of the electric motor, see Fig. 1a, but is not able to identify the shape of the force-waves (spatial orders) acting in the air gap between stator and rotor. This paper presents a method for processing measured NVH data based on averaging of phase-shifted spectra of sensors located around stator to determine spatial orders of excitation forces.

2. Permanent magnet synchronous electric motor excitation

A typical permanent magnet synchronous electric motor (PMSM) contains stator and rotor. Stator consists of outer yoke, and teeth with windings. Alternating currents flowing in winding induce rotating magnetic field in stator. The magnetic field in the rotor is generated by permanent magnets, which follows the rotating field of stator [5] due to magnetic and reluctance torque.

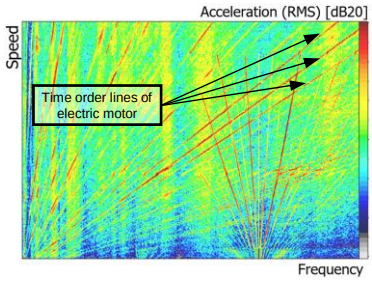

Fig. 1a. Typical Campbell diagramm of NVH measurement with highlighted time orders, [3]

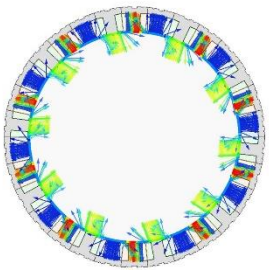

Fig. 1b. Example of forces acting on the stator of a PMSM

Harmonic forces that act in the air gap between stator and rotor, see example in Fig. 1b, can be decomposed as a sum of cosine waves [4]

$$f(\varphi,t) = f_0 + \sum_{s,n} f_{s,n} cos\left(s\varphi - n\omega t - \alpha_{s,n}\right), \tag{1}$$

where ω is angular velocity, s is space order (SO), n is time order (TO), φ is angular coordinate, $\alpha_{s,n}$ corresponds to phase offset and $f_{s,n}$ corresponds to the amplitude of the force-wave for time order n and spatial order s.

Wave direciton and count of waves around circumference define the number of spatial order *s*, see examples in Fig. 2. The time order *n* is a dimensionless quantity that expresses the ratio between excitation frequency and reference frequency, in this case rotor revolutions per second. Time order can be understood as a multiple of the spatial order *s* and the ratio of angular velocity of rotating SO wave to the angular velocity of rotor, cf. Fig. 2.

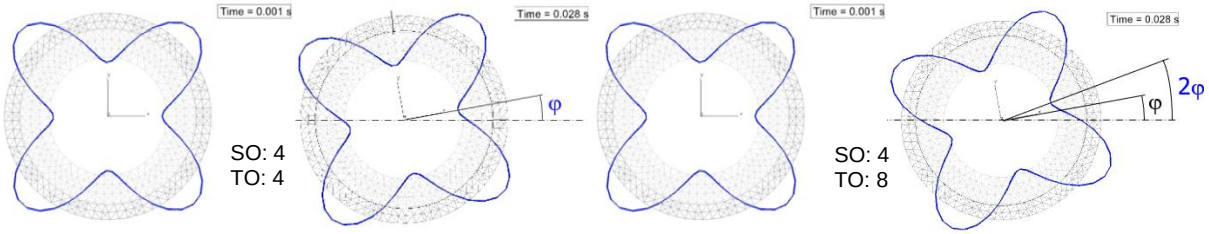

Fig. 2. Example of force waves for SO = 4 and TO = 4, 8

3. Method principle

NVH measurement, in which only one sensor is used in the vicinity of the stator, can detect TO but does not allow any distinction between different spatial orders. On the other hand, if multiple sensors are used, the evaluation of spatial orders could help to understand the system behaviour but does not allow the contributions of each SO to be quantified and identified, see Fig. 3. This is only possible if phases of the signals are processed each one by one.

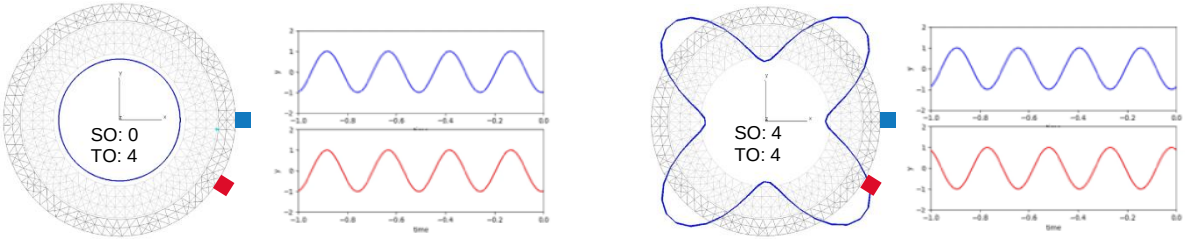

Fig. 3. Importance of the phase information for SO and TO detection. Deflection shape can be identified using phase information from more accelerometers only

3.1 Sensor placement, measurement

The sensors should be placed (ideally equidistantly) around the stator circumference in one plane perpendicular to the rotor, see Fig. 4. It is recommended to use 3D accelerometers or a set of 1D accelerometers measuring radial direction. The sensors can also be placed on a housing (or stator carrier) but only if the stator is connected to these parts by press-fit and not by discrete connections as bolts.

The NVH measurement is performed for a run-up with constant torque. The frequency domain accelerometer data are processed in the form of complex order cuts with given order bandwidth.

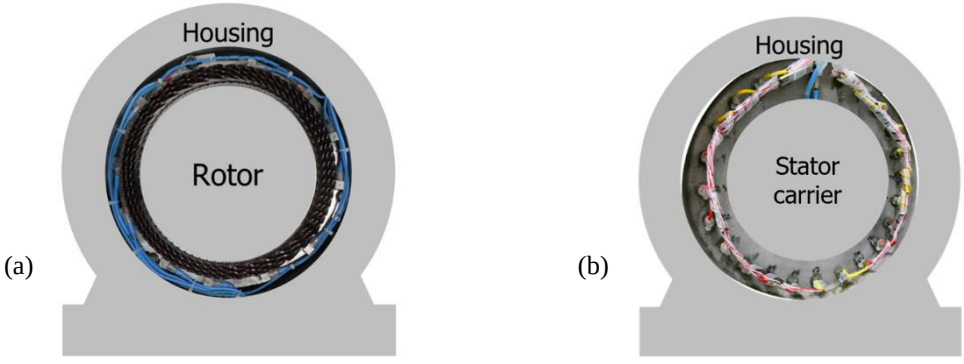

Fig. 4. Illustration of sensors placement on stator (a), stator carrier (b)

3.2 Data processing

The basic idea of the method can be illustrated on the example of stator deflection in time domain under harmonic excitation by spatial orders s = 1, 2 and 3, see Fig. 5.

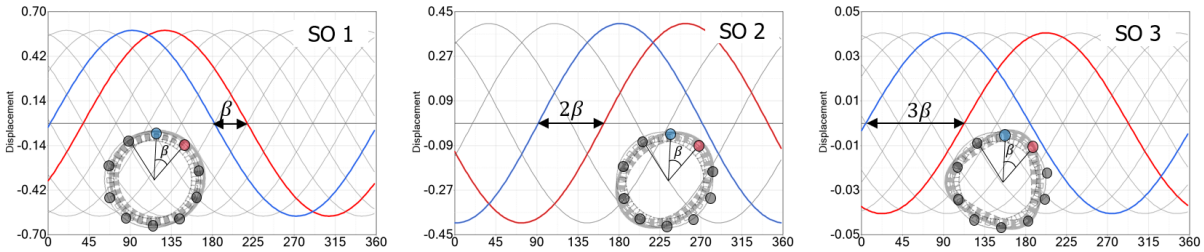

Fig. 5. Phase-shift of signals between 2 sensors in the time domain is product of spatial angle β between the sensors and SO number s = 0, 1, 2

Deformations are evaluated at equidistant positions in the time domain. The phase shift of the system response can be observed in dependence on the number of spatial order s and sensor angular coordinate β.

To evaluate the spatial order number s, the original sensor data are proportionally modified as follows [2]:

- The phase of the sensor signals is shifted by

$$\varphi = \varphi_0 + \beta s\,, \qquad \text{for } s = 0,\ \pm 1, \ldots, \frac{N}{2} - 1\,, \tag{2}$$

  where φ_0 is original measured phase angle, β stands for the spatial angle between the sensor and reference sensor (see Fig. 5), N is total count of the sensors, s is the number of the spatial order to be evaluated.

- Shifted order spectra $A_s(f)$ for each sensor position j w.r.t spatial order s are then arithmetically averaged (complex sum divided by number of sensors N) as

$$A_s(f) = \frac{1}{N}\sum_{j=1}^{N} a_j(f) e^{i\beta s}\,. \tag{3}$$

Maximal spatial order to be evaluated is limited by Nyquist-Shannon sampling theorem, [3]. Shifted average spectra (3) allows to identify, which spatial order is dominating in given frequency. Arithmetic sum of complex signals from all sensors are amplified, if their phases are same (or similar) and supressed if the phases differ, see Fig. 5. Therefore the dominance of shifted order spectrum $A_s(f)$ for some s among other spatial orders indicates that the highest contribution to the stator reponse comes from spatial order s.

4. Method testing and application

The method is illustrated on example of the FE model of single stator, see Fig. 6. The stator is excited by superimposed unit-force excitation by spatial order s = 0, 2, 3, 5. The system response in all 10 positions is presented in Fig. 6a. Data processed by (3) in Fig. 6b show that the peaks in the RMS data from all 10 sensors are dominated by spatial orders exactly at the eigenfrequencies corresponding to the radial eigenmodes of (oval shape, triangular shape, breathing shape).

Example of the method applied on the measurement data illustrates Fig. 7. Evaluation has been performed on an electric machine (PMSM, 3 phase, 30 slots, 10 pole pairs) with 24 uniaxial sensors located on the stator carrier, see Fig. 4b. The method of shifted order spectra has been applied to the fundamental time order of electric machine, i.e. n = 60.

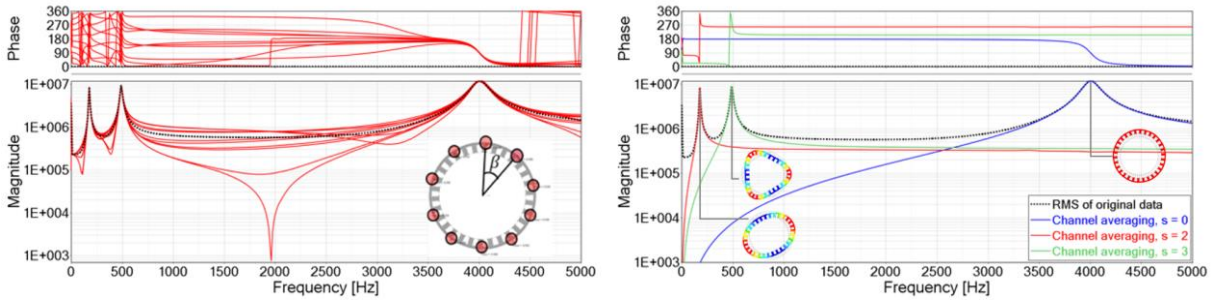

Fig. 6. (a) Original data, (b) results of shifted channel averaging

In a healthy machine, the root cause of vibrations for time order $n = 60$ is usually expected as a pulsating excitation by spatial order $s = 0$. Observed high contributions of spatial order $s = \pm 1$ can be explained by non-uniform magnetic pull caused by uneven magnetization or static eccentricity [3].

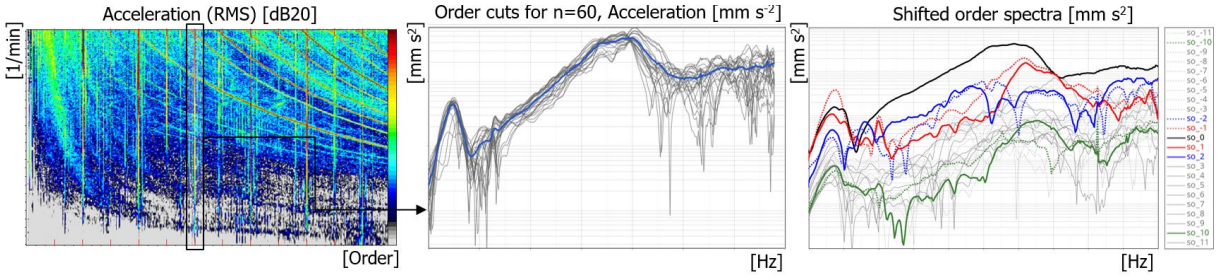

(a) (b) (c)

Fig. 7. Evaluation of shifted order spectra for electric motor with fault. (a) Campbell diagram with acceleration results for 1 given sensor, (b) order cuts for $n = 60$ for all sensors with their RMS curve, (c) evaluation of shifted order spectra for s, $-11 \leq s \leq 11$

5. Limitations

Method of shifted order spectra enables to identify the root cause of stator resonances in electric motors. The method has practical limitations in cases where stiffness of the measured area is not uniform or when there is no possibility to measure directly in one plane. In such cases a hybrid approach can be used that combines simulated transfer functions from stator teeth to the accelerometer positions with measured responses in the accelerometers.

Acknowledgements

The authors thank the ZF management for supporting their participation in the conference and in preparing this paper.

References

[1] Degrendele, K., Devillers, E., Le Besnerais, J., Advanced NVH measurement data processing of electric motors under electromagnetic excitations, Proceedings of Automotive Acoustics Conference, Wiesbaden, 2019.
[2] Otta, J., Shifted channel average for identification of measured electric spatial orders, ZF internal material, 2020.
[3] Otta, J., Kotnik, K., Giesler, J., Acoustics of E-drives basics, ZF internal material, 2020.
[4] Root, V., Investigation of active noise reduction on electrical machines with current harmonics, master thesis, University of Applied Sciences Würzburg-Schweinfurt, 2015. (in German)
[5] Schröder, D., Kennel, R., Electric drives - basics, Springer Vieweg, 2021. (in German)

COMPUTATIONAL MECHANICS 2021
36th conference with international participation
Srní
November 8 - 10, 2021

Development of composite element joining keel beam and aircraft fuselage

Z. Padovec[a], R. Sedláček[a], T. Zámečníková[a]

[a] *CTU in Prague, Faculty of Mechanical Engineering, Department of Mechanics, Mechatronics and Biomechanics, Technická 4, 160 00, Prague, Czech Republic*

Presented document deals with design, stress/strain analysis and testing of composite element used in aircraft for joining keel beam with fuselage. Nowadays this part is made from titanium because of electro-chemical corrosion which can occur when joining steel and composite material. Titanium T profile is manufactured from the block which is not economical because much waste material during machining. That´s why two composite elements of T and Y shape were designed. These profiles were manufactured from C/PPS fabrics with the use of thermoforming technology.

At first stiffness comparison of both composite profiles and titanium one was done. With the use of FE software Abaqus models were created and loaded with unit loading through the holes in the profile´s web, see Fig. 1. Many versions of the computation were done e.g., rigid vs. deformable plate, effective characteristics for composite profile vs. lay up characteristics, solid vs. continuum shell elements, etc… with the result that Y-profile is stiffer than T profile.

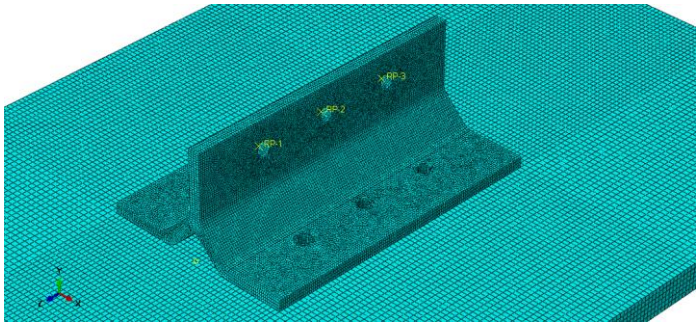

Fig. 1. Model of C/PPS Y profile

Next step was the proof that both profiles can transmit the real load of the component which was given to us from the manufacturer. Geometry of the models was the same as in stiffness analysis but just models with layered continuum shell elements were used for analysis. Real load of each reference point can be seen in Table 1. Results were compared with the use of failure index (FI) evaluated by strength theories for composites in Abaqus (max stress, max strain, Tsai – Hill, Tsai – Wu, ….). Failure index can be listed for each ply or as an envelope of worst cases through plies. FI according to Tsai – Hill theory for T – profile can be seen in Fig. 2.

Table 1. Comparison of deflection/rotation for designed versions

Reference point no.	F_x **[N]**	F_y **[N]**	F_z **[N]**
RP – 1	-276.1	-411.9	3 496.9
RP – 2	-345.6	-518.9	3 007.8
RP – 3	-168.0	-415.7	2 846.1

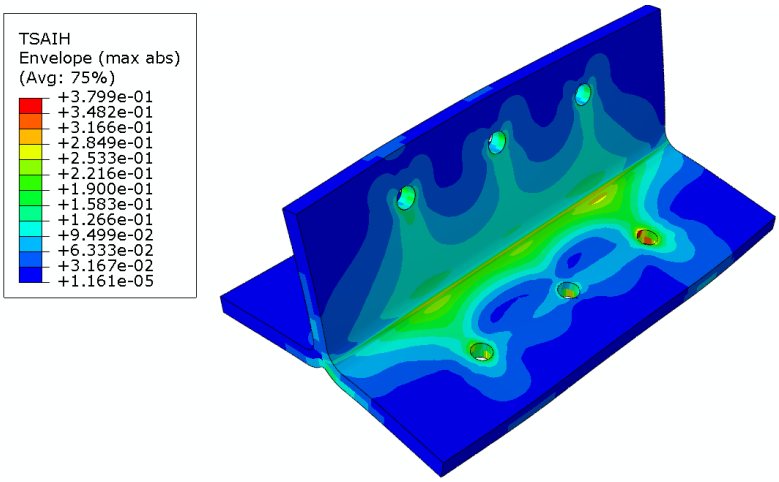

Fig. 2. FI acccording to Tsai-Hill theory for T – profile

For each tested case (T - profile and Y – profile joined with rigid/deformable plate) and each strength theory, FI was lower than 1 which means that the construction didn´t fail and it can withstand required load.

Then both profiles were experimentally tested on TIRA 2300 universal testing machine in our lab. The tensile load was applied through the screws in the web of the element jointed with the machine's jaws. The load was released just in the z direction, as shown in Fig. 3, left. The profiles were tested until total failure, but some of them were tested only until the first failure occurred (the first visible peak in the loading curve). Typical load curves for a T-profile and for a Y-profile are displayed in Fig. 3, right.

The profiles with the first failure were analysed using a CT scan and a microsection photo to find the failure area, see Fig. 4, left.

Because the real geometry of both profiles differs little bit from the ideal one, analysed by FEM in previous step, the new simulation of both profiles was carried out to analyse the location of the first failure and compare it with the failure area from CT scan mentioned above, see Fig. 4, right. The failure was interlaminar, so layered solid elements were used in the model to determine S33 stress. The first failure force of the experiment corresponds to S33=33 MPa, as calculated by FEM. The tensile strength in the 90° direction of the UD material is 39 MPa, according to the datasheet [3]. Even though it is not exactly the material used in the project, the agreement between simulation and experiment is quite good. The area of the failure from the CT scan is also in good agreement with the maximum stress area from the FE simulation.

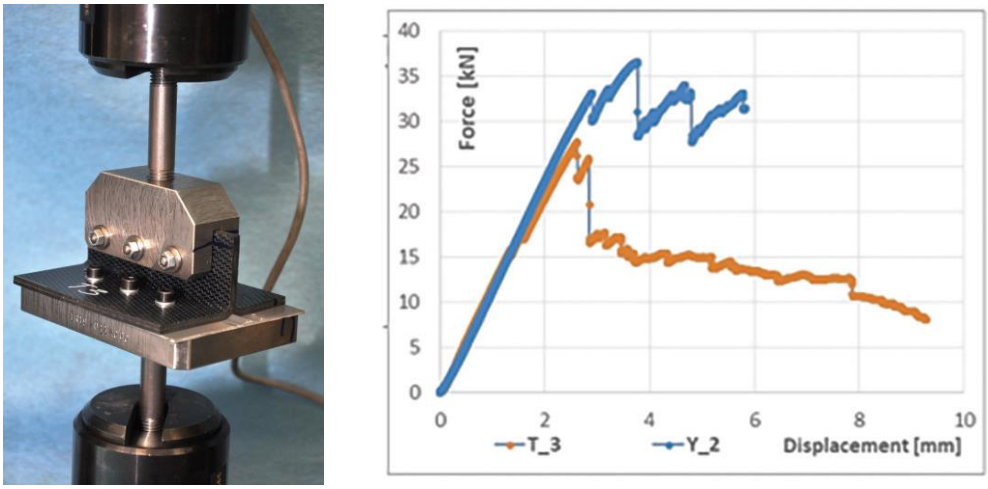

Fig. 3. T – profile loaded in tensile machine and typical loading curve for both tested profiles

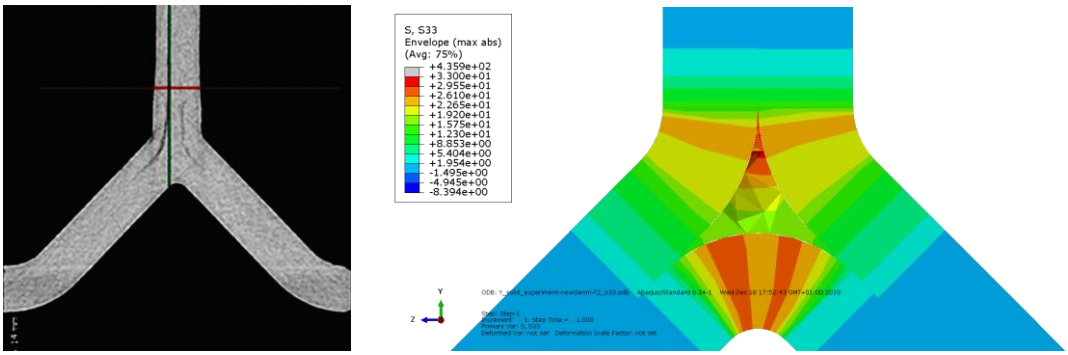

Fig. 4. First failure area evaluated from a CT scan and area with maximum stress from FEM [1]

Comparing the results from the T-profile experiment and from the Y-profile experiment (Fig. 4, right) shows that the first peak of the loading force (which is crucial for fatigue) in the tested T-profiles occurs at about 15 kN. In the Y-profiles, this peak is at about 29 kN, i.e., the improvement is almost twice as much as for the T-profile. T – profile weight 0.129 kg, Y – profile 0.127 kg. Compared with original titanium solution which weights 0.308 kg, it is around about 58 % weight saving [1].

The last step was the fatigue/lifetime tests which were conducted in the laboratory on three T profiles and three Y profiles. The *R* value was 0.1 and the frequency of the load was 5 Hz except for sample Y_03 with a frequency of 4 Hz. Sinusoidal type of signal and load control was used in the testing program. The experiment was performed using the Instron 40 kN hydraulic testing system. The selected loading levels were derived from the limit load, which was 5 910 N in the z direction – 100% meant loading up to the limit load level, 153% loading up to the ultimate load level, 200% loading up to twice the limit load level and 306% loading up to twice the ultimate load level. Once the sample was subjected to 1 000 000 cycles without failure, the experiment was stopped, and the sample was inspected by means of the ultrasonic testing method. The sample was then put aside for subsequent static testing aimed at proving whether a change had occurred in terms of the strength compared to the "virgin" samples that had been statically tested previously. The results and a description of the fatigue/lifetime test are provided in Table 2 [2].

Table 2. Lifetime results for the tested profiles

Sample	Load level	*F* [N]	Number of cycles *N* [-]	Result
T_01	100%	5 910	1 000 000	without failure
T_02	100%	5 910	1 000 000	without failure
T_03	153%	9 042	1 000 000	without failure
Y_01	153%	9 042	1 000 000	without failure
Y_02	200%	11 820	1 000 000	without failure
Y_03	306%	18 085	122 396	failure

Sample Y_03 was destroyed after 122 396 cycles following the destruction of the screws (after 83 407 cycles and 108 876 cycles), which were replaced both times. Moreover, the final failure (see Fig. 5) was also accompanied by the destruction of some of the screws.

The T-shaped samples and samples Y_01 and Y_02 survived the fatigue testing process, thus presenting the opportunity to perform static testing aimed at proving whether there had been a change in their behaviour. The static testing was conducted in a similar way to that described above. The comparison of these values with the values for the "virgin" samples (Fig. 6) indicated that the values were not significantly affected by the fatigue effect.

While fatigue/lifetime testing using a small number of tested samples provides some room for doubt, it must be stressed that the testing was performed at a high loading level of up to

1 000 000 cycles. All the T-shaped samples withstood the limit and ultimate upper loads without failure. Hence, the Y-shaped samples were tested directly up to the ultimate load, twice the limit load and twice the ultimate load, which is unusual for this type of construction.

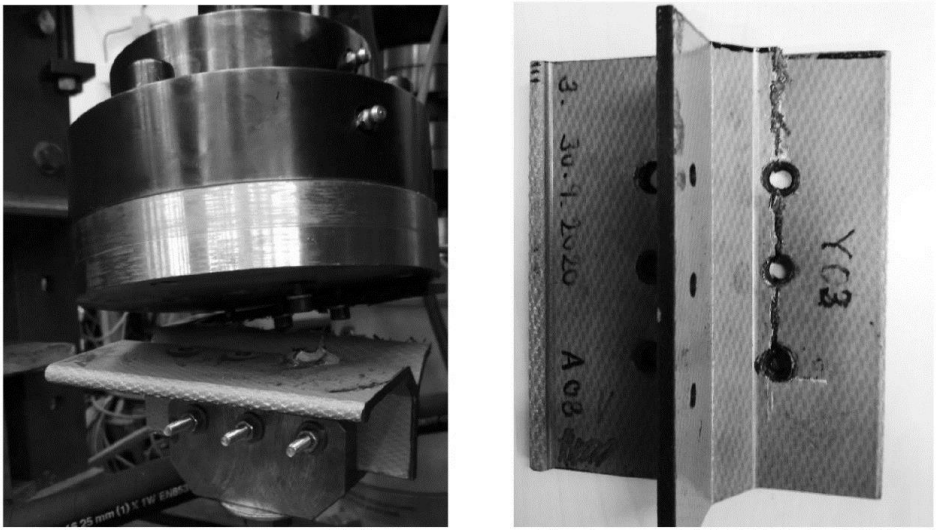

Fig. 5. Destroyed sample Y_03 after 122 396 cycles [2]

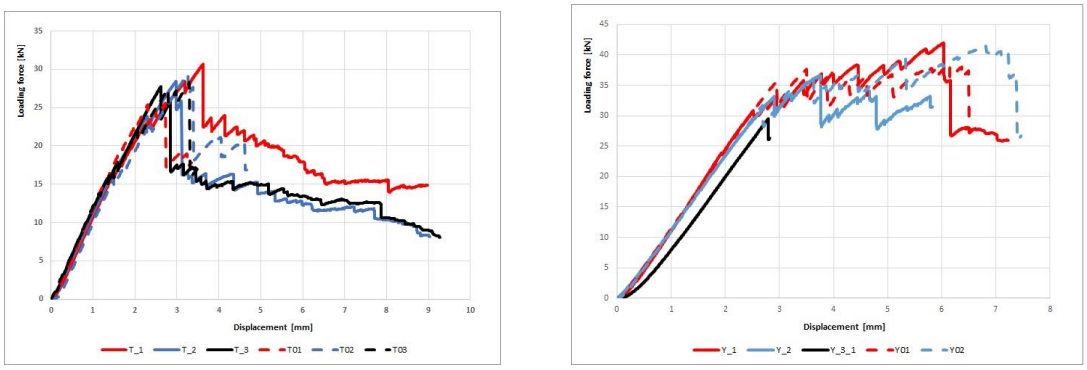

Fig. 6. Relationship between the loading force and the displacement for the tested T and Y profiles ("virgin" and after 1 000 000 cycles) [2]

The main aim was to determine the limits of the components. The destruction of the bolted joint occurred at twice the ultimate load level. These results exceeded the requirements for this type of construction. Moreover, the static testing of the samples after 1 000 000 cycles indicated the absence of the fatigue effect on the maximal loading force and force values, which corresponded with the first discontinuity in the loading diagram, compared with the "virgin" samples [2].

Acknowledgements

This work has been supported by project FV30033 of the Ministry of Industry and Trade of the Czech Republic and by the Grant Agency of the Czech Technical University in Prague, under grant No. SGS21/151/OHK2/3T/12.

References

[1] Křena, J., Padovec, Z., Sedláček, R., Zámečníková, T., A thermoplastic T-profile with effective lay-up on one shot, JEC Composite Magazine 135 (2020) 27 – 29.
[2] Padovec, Z., Křena, J., Sedláček, R., Zámečníková, T., The experimental and numerical analysis of optimized composite profiles for aircraft construction, Mechanics of Composite Materials (accepted).
[3] Toray Data Sheet for material Cetex® TC1100.

COMPUTATIONAL MECHANICS 2021
36th conference with international participation
Srní
November 8 - 10, 2021

Computational assessment of hinge deformation of the tilting sidewall of the truck body

P. Pavlata

Vision Consulting Automotive s.r.o., Rumunská 12, CZ – 120 00 Praha 2, Czech Republic

In the current era of forensic expertise in the field of transport and accident analysis, software (hereinafter sw) based on algorithms of Multi-Body-Systems (MBS) dominates for the solution of dynamic simulations (especially vehicle collisions). Representatives of such software in Europe are, for example, PC Crash or Virtual Crash. Both software excel in sophisticated graphics, which, unlike previously used analytical solutions with a number of complex equations, allow litigants to create a much more realistic picture of a court case solution, which otherwise often causes considerable difficulties for non-technical judicial staff. However, both of these software work mainly with rigid non-deformable bodies, which can often lead to incorrect results.

Fig. 1. Tipper body with spring mechanism, opened sidewall

The paper deals with the search for the mechanism of damage to the hinge of the tilting sidewall with the spring mechanism of the tipper body, Fig. 1, for the purposes of litigation between the vehicle operator and the body manufacturer. Although the problem could probably be solved using analytical procedures, in our case, a nonlinear variant of FEM with a PAM Crash solver is used to solve the dynamics of the body sidewall movement in the gravitational field. This approach, which is rarely used in similar cases, will provide the parties to the dispute with a completely objective view of the whole matter, while making it

possible to monitor the distribution of stresses and deformations in the sidewall at individual moments of tilting.

The applicant's view, which in the present case is the vehicle operator, supported by an expert opinion, states that the damage to the sidewall should have been due to the inertial effects of the bulk load (sand) on the body when the tipper (TATRA T-815) was driving in arcs.

Therefore, this load condition was also analyzed in two body loading modes, when on the one hand bulk material (sand of average humidity and density) was poured into the body at a pour angle of about 35°, Fig. 2A, up to a payload of 13.6 t. This case can be seen as one of the borderline cases where the sidewall of the body is loaded with sand to a minimum height of 35 cm. The second of the limit cases then represents the state when the sandy surface is aligned in the body to a rectangular cross-section, Fig. 2B. In this case, the sidewall is loaded with sand up to a max. height of 78 cm. If the height of 78 cm was exceeded (the total height of the sidewall is 90 cm), the payload of the vehicle would already be exceeded. The pressure distribution of the bulk cargo at the bottom of the body and the sidewall can be considered similarly to the hydrostatic pressure of liquids.

The following 3 operating states (modes) were analyzed, which are based on traditional empirical approaches:

1. standing in a gravitational field 1.0 g
2. driving in an arc of 0.3 g in a gravitational field of 1.0 g
3. tilting the sidewall in the gravitational field 1.0 g, Fig.3.

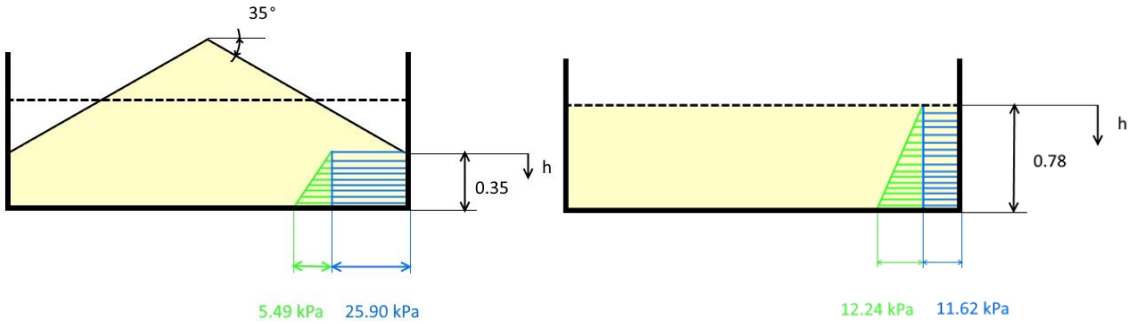

Fig. 2. Pressure distribution A) for a pour angle of 35 ° B) for a flat surface

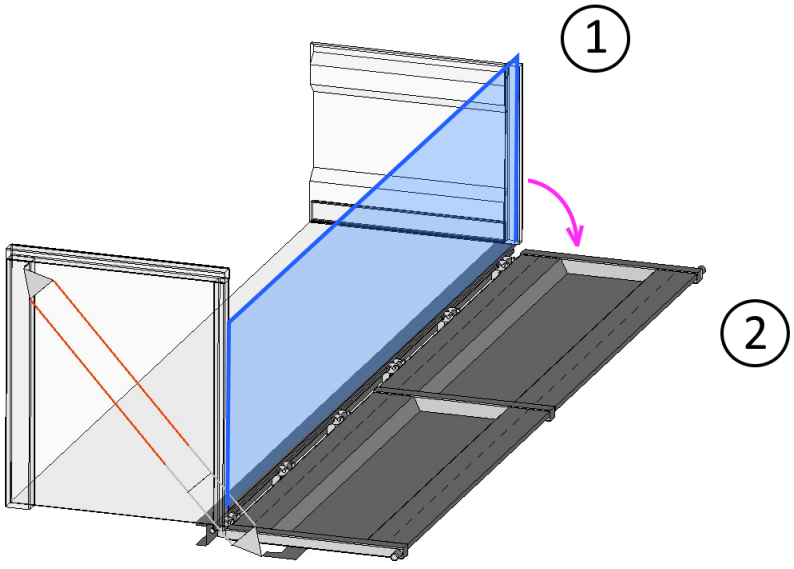

Fig. 3. The principle of the sidewall tilting

Modes 1 and 2 were chosen as conservative modes (depending on the distribution of the surface layer of sand on the body of the tipper). At the same time, in mode 2, conservative results are achieved with a relatively high acceleration factor of 0.3 g when driving in a curve, as it is clear that this limit value will only occur exceptionally in real traffic. For mode 2, friction between the loading area and the bulk load (sand) is not considered, which further increases the degree of conservatism of the results.

On the other hand, operating state number 3 - tilting of the sidewall is solved with an empty body, Fig. 3, when the sidewall is not loaded by any sand. The results can be seen as rather optimistic, when the dynamics of tilting the sidewall, especially in the lower position with stops will cause significantly less tension in critical places than in the case of a body loaded with sand. In real operation, the sidewall will be loaded by the own weight of the bulk load, which will increase the kinetic energy of the released sidewall at the moment of contact with the hinge stops and thus the stress in critical areas will reach significantly higher values.

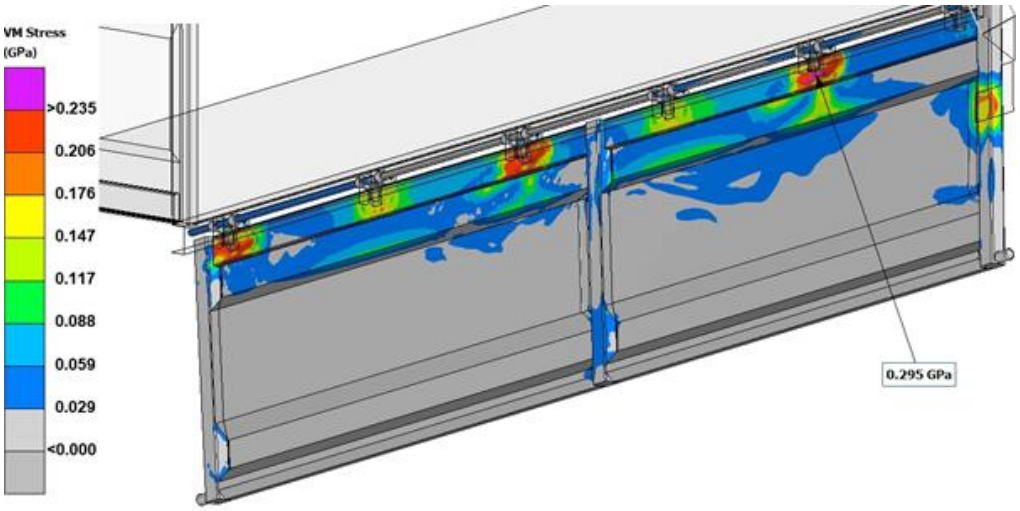

Fig. 4. Tilting of the sidewall in the gravitational field 1.0 g - residual stress, overall view from below, scale VM 0-235 MPa

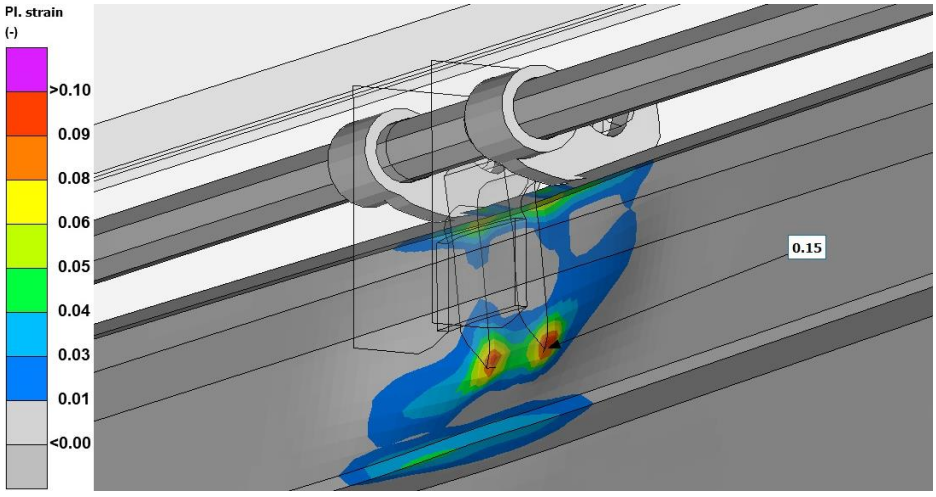

Fig. 5. Tilting of the sidewall in the gravitational field 1.0 g - moment at max. deformation - detail of the hinge with the highest plastic deformation, plastic deformation scale 0-10%

In the given task, in modes 1 and 2, negligible plasticization of the material was found in the places of the side hinges (max<0.5%). In the third mode, local plasticization of the material was found to reach a value of up to 15%, when the yield strength of the material used was exceeded in 5 of 6 hinges. Such behavior would, in the case of frequent repetition of the analyzed load, lead to the so-called low-cycle fatigue of the structure (up to a maximum of 10,000 similar cycles). However, in none of the critical points of the structure did there be a damage or fracture with a subsequent collapse of the sidewall.

Summary

FEM model of the assembly of the side of the body of the truck - tipper according to Fig. 1 assembled from approx. 234 thous. elements with a nominal size of 5 - 8 mm was analyzed for 3 selected load cases representing selected operating modes of a fully loaded vehicle, including the body sidewall tilting mode. The means of nonlinear FEM solver PAM-Crash Explicit v. 2019 were used for the analysis.

The used nonlinear solver and the used elasto-plastic material model make it possible to evaluate the behavior of the structure also above the yield point of the used metallic materials.

The aim of the analysis was to determine the stress distribution with the possibility to determine the places with maximum stress values and to assess the character of deformation in the places of attachment of the hinges of the sidewall of the vehicle body in individual operating modes.

The simulations of operating modes 1 and 2 did not show the occurrence of significant plastic deformations causing permanent deformation of the sidewall structure of the tipper. In operating mode 3 - tilting of the sidewall by free fall in the gravitational field, a stress of 415 MPa was found in the places of welding of the hinges to the lower profile of the sidewall due to the impact of the hinge, exceeding not only the yield strength of S235. The maximum plastic deformation found here reaches 15%. This operating mode can therefore be considered as the cause of damage to the body side.

The maximum values of stress and plastic deformation for individual operating modes are recorded in Table 1.

Table 1. Values of max. stress and max. plastic deformations found on the sidewall

Operating mode		max. VM stress	max. plast. deformation
		[MPa]	[%]
1.	stojící vozidlo v gravitačním poli 1.0 g	151	0
2.	průjezd obloukem 0.3 g v gravitačním poli 1.0 g	237	0.5
3.	spuštění bočnice v gravitačním poli 1.0 g.	415	15

COMPUTATIONAL MECHANICS 2021
36th conference with international participation
Srní
November 8 - 10, 2021

Control of the electrodynamic shaker with additional force sources

V. Pawlik, P. Steinbauer, J. Karlíček, P. Denk, K. Kraus, I. Bukovský

Faculty of Mechanical Engineering, CTU in Prague, Technická 4, 160 00 Praha 6, Czech Republic

In vibration testing, the device under test (DUT) is usually connected to an electrodynamic exciter using a fixture. The connection needs to be as rigid as possible, such that it influences the acceleration exposition spectrum as little as possible. However, if the fixture is too heavy, then a more powerful exciter is required to be able to deliver sufficient force to achieve the requested acceleration magnitude. The unwanted vibrations are often dealt with using an active vibration absorber, such as [2] or more specifically a delayed resonator [3]. The issue with such approaches is that mass is added to the device. One possible solution to this problem is to use a light fixture with additional actuators that compensate for vibrations of the fixture itself.

A 3D CAD model of a small plastic tank with a fixture was constructed from aluminium extrusions connecting it to the steel plate of the main vibration exciter. Then a simulation model was developed and then its order was reduced using modal reduction. The positions of the accelerometers and the action of the actuators are collocated. The assembly is shown in Fig. 1.

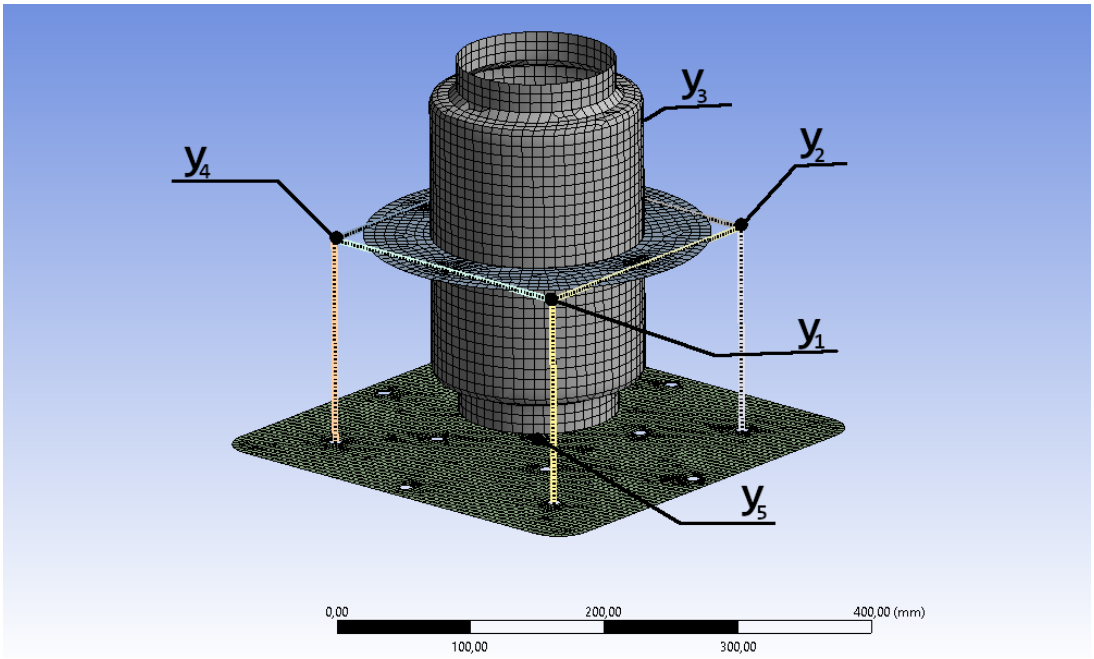

Fig. 1. DUT and the fixture. The positions of the accelerometers are marked – points y_1 to y_4 are located on top of the studs and the y_5 is located on the plate underneath the tank, which is suspended from the crossbars. The actuators points of action are collocated with the accelerometers

The control strategy is based on the adaptive inverse control [4] approach that utilizes an adaptive filter. In this work, this control strategy is realized using a Linear Neural Unit (LNU) with Levenberg–Marquardt (LM) learning algorithm, as described in [1].

The LNU input $\vec{x}$ consist of bias $x_0 = 1$ and delayed samples of the system output y_i

$$\vec{x}(t) = \begin{bmatrix} 1 & y_1(t-T) & \dots & y_1(t-n_yT) & y_2(t-T) & \dots & y_5(t-n_yT) \end{bmatrix}^T,$$

where $T = 0.01$ ms is sampling period and n_y is the number of samples from each output that are included. The output of the LNU is then given by

$$\vec{y}_{\mathrm{LNU}} = \vec{w}^T \vec{x},$$

where $\vec{w}$ is the vector of neural weights. The LM algorithm optimizes the cost function

$$\mathrm{MSE}_j = \frac{1}{l} \sum_{i=1}^{l} e_j(t_i)^2,$$

where l is the batch length and e_j is the jth component of

$$\vec{e}(t) = \vec{y_D} - \vec{y}_{\mathrm{LNU}},$$

which is the difference between the desired output $\vec{y}_D$ and the optimized system output $\vec{y}$. The goal is for the LNU to be the inverse of the controlled system, so in this case

$$\vec{e}(t) = \vec{u}(t - T_D) - \vec{y}_{\mathrm{LNU}}(t),$$

where $\vec{u}$ is the controlled system input and $T_D = \left\lfloor \frac{n_y}{2} \right\rfloor$ is the delay used to eliminate the issues with causality. The weights' updates are then calculated as

$$\vec{w}(k+1) = \vec{w}(k) + \Delta\vec{w}(k) = \vec{w}(k) + \left(\mathbb{J}^T\mathbb{J} + \mu\mathbb{I}\right)^{-1} \mathbb{J}^T\mathbb{E},$$

where

$$\mathbb{J} = \begin{bmatrix} \vec{x}(t) \\ \vdots \\ \vec{x}\left(t - T(l-1)\right) \end{bmatrix}$$

is the Jacobian matrix, μ is the learning coefficient, $\mathbb{I}$ is the identity matrix,

$$\mathbb{E} = \begin{bmatrix} e(t) \\ \vdots \\ e\left(t - T(l-1)\right) \end{bmatrix}$$

and l is the length of the mini-batch. This update is calculated for every l time step. The diagram of the system is shown in Fig. 2.

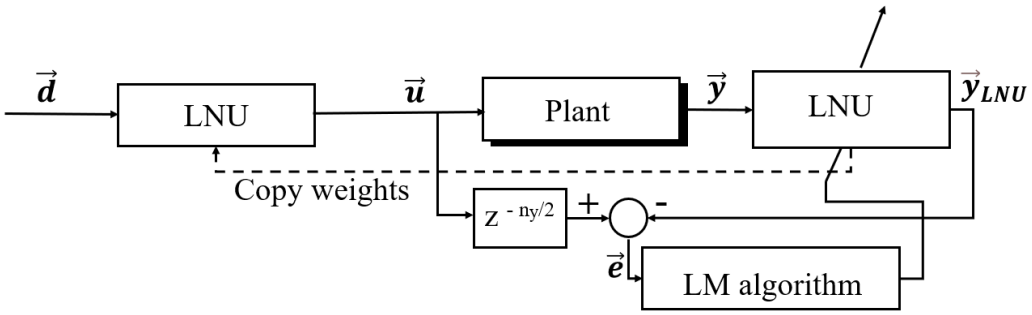

Fig. 2. Diagram of the control system. The LNU before the plant works as a controller. The LNU after the plant is learning the inverse of the plant and its weights. The weights are then used to update the controller LNU

The system has been simulated with parameters

$$\begin{aligned} n_y &= 200, \\ l &= 500, \\ \mu &= 0.1, \end{aligned}$$

and white noise with constant power spectral density in the frequency range 0 to 2000 Hz and with $d_{\mathrm{RMS}} = 1 \ \frac{\mathrm{m}}{\mathrm{s}^2}_{\mathrm{RMS}}$ as input. The same waveform was used for all inputs. The results of the simulation are shown in Fig. 3.

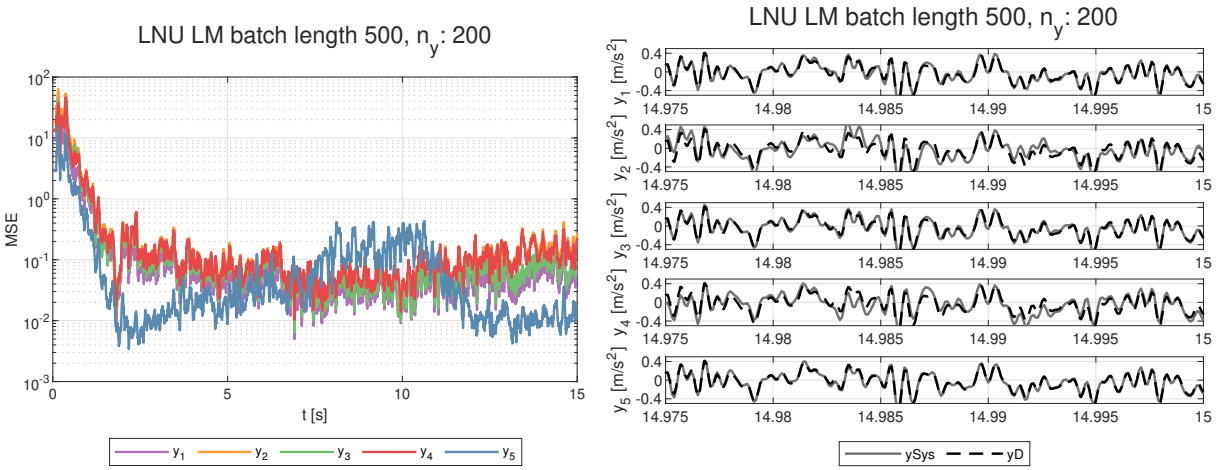

Fig. 3. (*Left*) The LNU is able to decrease the MSE significantly in the first 3 seconds; (*right*) the output acceleration follows the desired waveform

The simulation results are promising. Therefore, the following work will focus on the experimental evaluation of the algorithm on the specific real world test stand, which is currently being built.

Acknowledgements

The work has been supported by the project SGS19/156/OHK2/3T/12 “Mechatronics and adaptronics 2019” of Czech Technical University in Prague and TACR project #TN01000071 National Competence Centre of Mechatronics and Smart Technologies for Mechanical Engineering (MESTEC).

References

[1] Bukovský, I., Nonconventional neural architectures and their advantages for technical applications, Habilitation Thesis, Czech Technical University in Prague, 2012.

[2] Kraus, K., Šika, Z., Beneš, P., Krivošej, J., Vyhlídal, T., Mechatronic robot arm with active vibration absorbers, Journal of Vibration and Control 26 (13-14) (2020) 1145-1156.

[3] Šika, Z., Vyhlídal, T., Neusser, Z., Two-dimensional delayed resonator for entire vibration absorption, Journal of Sound and Vibration 500 (2021) No. 116010.

[4] Widrow, B., Walach, E., Adaptive inverse control: A signal processing approach, Reissue ed. IEEE Press series on power engineering. Piscataway NJ, Hoboken N.J. IEEE Press; Wiley-Interscience, 2008.

COMPUTATIONAL MECHANICS 2021
36th conference with international participation
Srní
November 8 - 10, 2021

Fluid-structure interaction algorithm for an elastic structure with large deformations

A. Pecka, O. Bublík

NTIS – New Technologies for the Information Society, Faculty of Applied Sciences, University of West Bohemia, Univerzitní 8, 301 00 Plzeň, Czech Republic

This contribution introduces a fluid-structure interaction (FSI) methodology where the structure is considered elastic. One of the main requirements for the FSI algorithm is a high level of modularity, meaning that the fluid and structure solvers are independent of each other and the meshes do not need to align on the fluid-solid interface. For this reason, a partitioned approach was adopted with the option of either weak or strong coupling.

Compressible Navier-Stokes equations in the arbitrary Lagrangian-Eulerian formulation are considered as the mathematical model for the fluid flow. The fluid dynamics is simulated using an implicit discontinuous Galerkin finite-element scheme with Newton's iterative procedure. The interior penalty method is used to approximate viscous fluxes. The discontinuous Galerkin solver is being developed by the authors of this contribution under the name FlowPro [1]. FlowPro is a multipurpose numerical software that solves system of hyperbolic and parabolic partial differential equations. The elastic structure is described by nonlinear equations of elastodynamics that allow for large deformations. The system is solved by an implicit finite-element scheme with Newton's iterative procedure. The finite-element structure solver is also a product of the authors of this contribution.

Since the fluid and structure meshes are mutually nonconforming on the fluid-solid interface, the aerodynamic stress tensors needs to be interpolated from the fluid mesh to the structure mesh. The interpolation is achieved by radial basis functions. Likewise, the displacement determined by the structure solver needs to be interpolated onto the fluid mesh on the fluid-solid interface. The interpolation is taken care of by the mesh-deformations algorithm, which is also based on radial basis functions.

The FSI algorithm is validated on the well-known Turek-Hron benchmark, which was first proposed in [2] and then again published in [3]. The benchmark consist of three FSI problems with a 2D incompressible laminar flow around a fixed cylinder with elastic cantilever embedded in the cylinder. The vortices that are shed from the cylinder excite oscillations in the cantilever. The geometric parameters are tabulated in Table 1 (left). The no-slip boundary condition is prescribed at the walls - the fixed cylinder, the elastic cantilever and the upper and lower walls. At the inlet on the left-hand side of the fluid domain, a parabolic velocity profile is prescribed as ${}^{\mathrm{f}}v_{\mathrm{in}}(y) = 35.69\,{}^{\mathrm{f}}\overline{v}_{\mathrm{in}}\,y\,({}^{\mathrm{f}}H - y)$ with mean inlet velocity ${}^{\mathrm{f}}\overline{v}_{\mathrm{in}}$. The outlet pressure is chosen such that the free-stream Mach number is 0.05 and thus the flow can be considered incompressible. The reason for the choice of an incompressible-flow benchmark for the compressible-flow solver is the lack of benchmarks for FSI problems.

The structure and fluid parameters found in Table 1 (right) are chosen such that for FSI1 the flow stabilises at the steady state, whereas FSI2 and FSI3 lead to periodic oscillations of

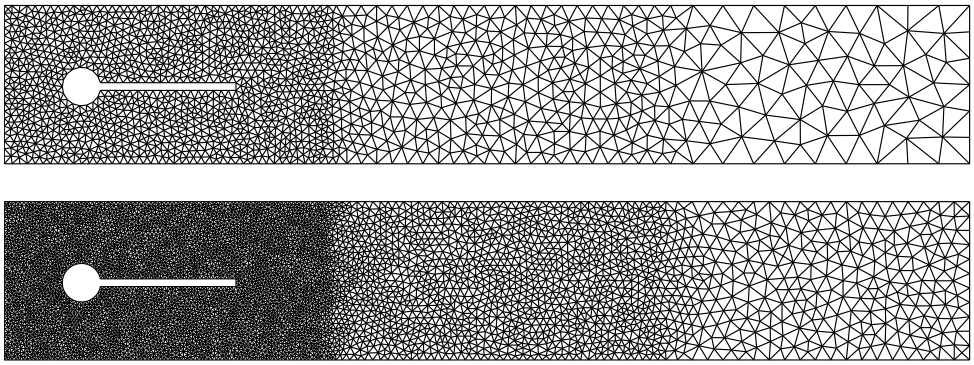

Fig. 1. Coarse mesh with size $h = 0.02\,\mathrm{m}$ and 3040 elements (*top*) and fine mesh with size $h = 0.01\,\mathrm{m}$ and 12 092 elements (*bottom*)

Table 1. Geometric parameters (*left*) and physical parameters (*right*)

	symbol	value [m]
channel length	${}^{\mathrm{f}}L$	2.5
channel height	${}^{\mathrm{f}}H$	0.41
cylinder centre	C	[0.2, 0.2]
cylinder radius	r	0.05
cantilever length	${}^{\mathrm{s}}L$	0.351 01
cantilever height	${}^{\mathrm{s}}H$	0.02
reference point	A	[0.6, 0.2]

symbol	units	FSI1	FSI2	FSI3
${}^{\mathrm{s}}\rho$	$\frac{\mathrm{kg}}{\mathrm{m}^3}$	10^3	10^4	10^3
${}^{\mathrm{s}}E$	$\frac{\mathrm{kg}}{\mathrm{m\,s}^2}$	$1.4 \cdot 10^6$	$1.4 \cdot 10^6$	$5.6 \cdot 10^6$
${}^{\mathrm{s}}\nu$	$\frac{\mathrm{kg}}{\mathrm{m\,s}^2}$	0.4	0.4	0.4
${}^{\mathrm{f}}\rho$	$\frac{\mathrm{kg}}{\mathrm{m}^3}$	10^3	10^3	10^3
${}^{\mathrm{f}}\mu$	$\frac{\mathrm{kg}}{\mathrm{m\,s}}$	10^{-3}	10^{-3}	10^{-3}
${}^{\mathrm{f}}\bar{v}_{\mathrm{in}}$	$\frac{\mathrm{m}}{\mathrm{s}}$	0.2	1	2
Re	-	20	100	200

the structure at a frequency close to the second lowest natural frequency of the structure. The added-mass effect occurs in the case for FSI1 and FSI3, where ${}^{\mathrm{s}}\rho = {}^{\mathrm{f}}\rho$. The added-mass effect is a numerical instability that occurs when the density of the structure is similar to or lower than the density of the fluid. FSI1, as it is a steady-state problems, does not cause significant stability issues, whereas FSI3 does. Therefore, subitarations need to be performed for FSI3, otherwise the solver would not converge. On the other hand, weak coupling is sufficient for FSI2.

In order to compare displacement of the structure, a reference point (point A) was chosen at the end of cantilever in the middle of its thickness. The displacement of the structure (at point A) for the FSI1, FSI2 and FSI3 benchmarks is shown in Table 2 and Figs. 2 and 3, respectively. FSI1 benchmark was performed with two different meshes, shown in Fig. 1, and different degrees of basis polynomials. The FSI2 and FSI3 benchmarks were performed with the finer mesh and cubic basis polynomials. An agreement with Turek and Hron benchmark in all the cases is indisputable. We can see that the y-component agrees better than the x-component, since the x-component of the amplitude is one order of magnitude lower than the y-component. A sequence of velocity fields during half a period is shown in Fig. 4 for FSI2 and FSI3 benchmarks.

Acknowledgements

The authors appreciate the kind support of the grant GA 20-26779S "Study of dynamic stall flutter instabilities and their cosequences in turbomachinery application by mathematical, numerical and experimental methods" of the Czech Science Foundation and of the student grant project SGS-2019-009.

Table 2. FSI1 benchmark: x and y components of displacement at point A. Values $2.2708 \cdot 10^{-5}$ m and $8.2086 \cdot 10^{-4}$ m are considered exact x and y components of displacement, respectively

h [m]	elements	order	d_x [m]	d_x error [%]	d_y [m]	d_y error [%]
0.02	3040	2	$1.995 \cdot 10^{-5}$	12.2	$6.709 \cdot 10^{-4}$	18.3
0.02	3040	3	$2.221 \cdot 10^{-5}$	2.2	$7.568 \cdot 10^{-4}$	7.8
0.02	3040	4	$2.253 \cdot 10^{-5}$	0.8	$8.004 \cdot 10^{-4}$	2.5
0.01	12 092	2	$2.112 \cdot 10^{-5}$	7.0	$7.467 \cdot 10^{-4}$	9.0
0.01	12 092	3	$2.252 \cdot 10^{-5}$	0.8	$7.863 \cdot 10^{-4}$	4.2
0.01	12 092	4	$2.271 \cdot 10^{-5}$	0.0	$8.024 \cdot 10^{-4}$	2.3

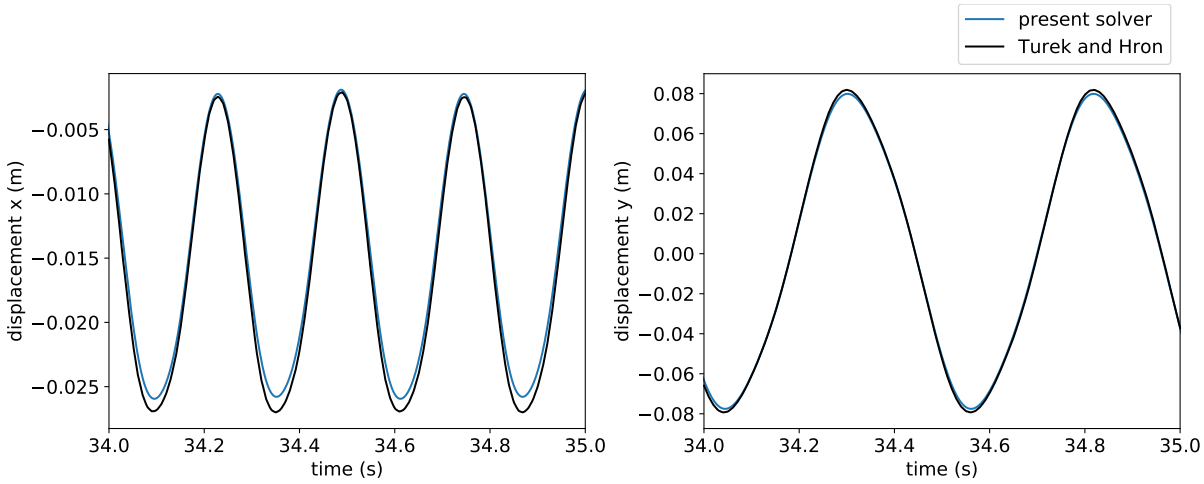

Fig. 2. FSI2 benchmark: displacement at point A

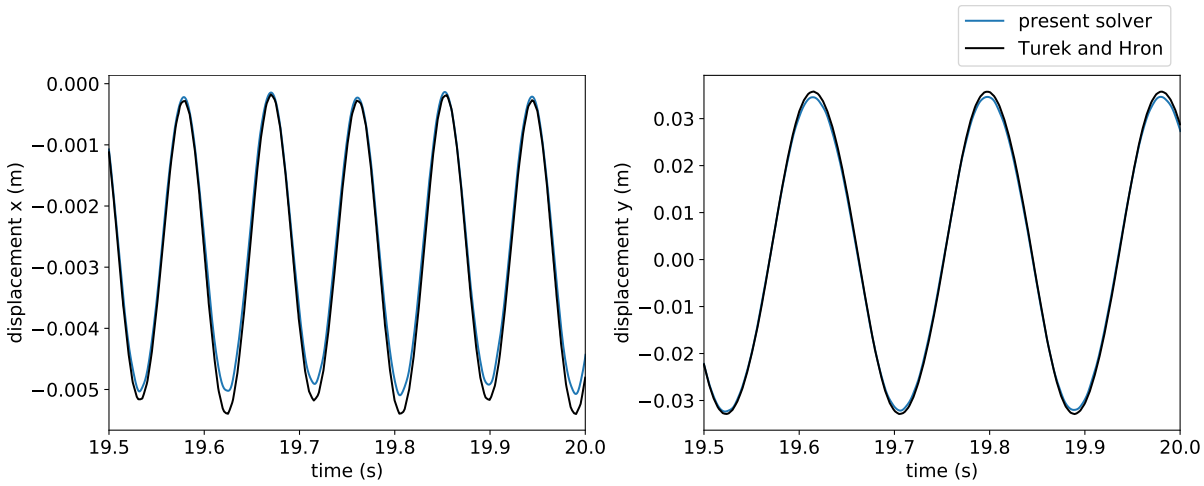

Fig. 3. FSI3 benchmark: displacement at point A

References

[1] Ondřej, B., Pecka, A., FlowPro [Source code], 2018. https://github.com/ondrabublik/FlowPro

[2] Turek, S., Hron, J., Proposal for numerical benchmarking of fluid-structure interaction between an elastic object and laminar incompressible flow. In: Fluid-Structure Interaction (edit.: H. J. Bungartz, M. Schäfer), Springer Berlin Heidelberg, 2006, pp. 371-385.

[3] Turek, S., Hron, J., Mádlík, M., Razzaq, M., Wobker, H., Acker, J., Numerical simulation and benchmarking of a monolithic multigrid solver for fluid-structure interaction problems with application to hemodynamics, Lecture Notes in Computational Science and Engineering 73 (2010) 193-220.

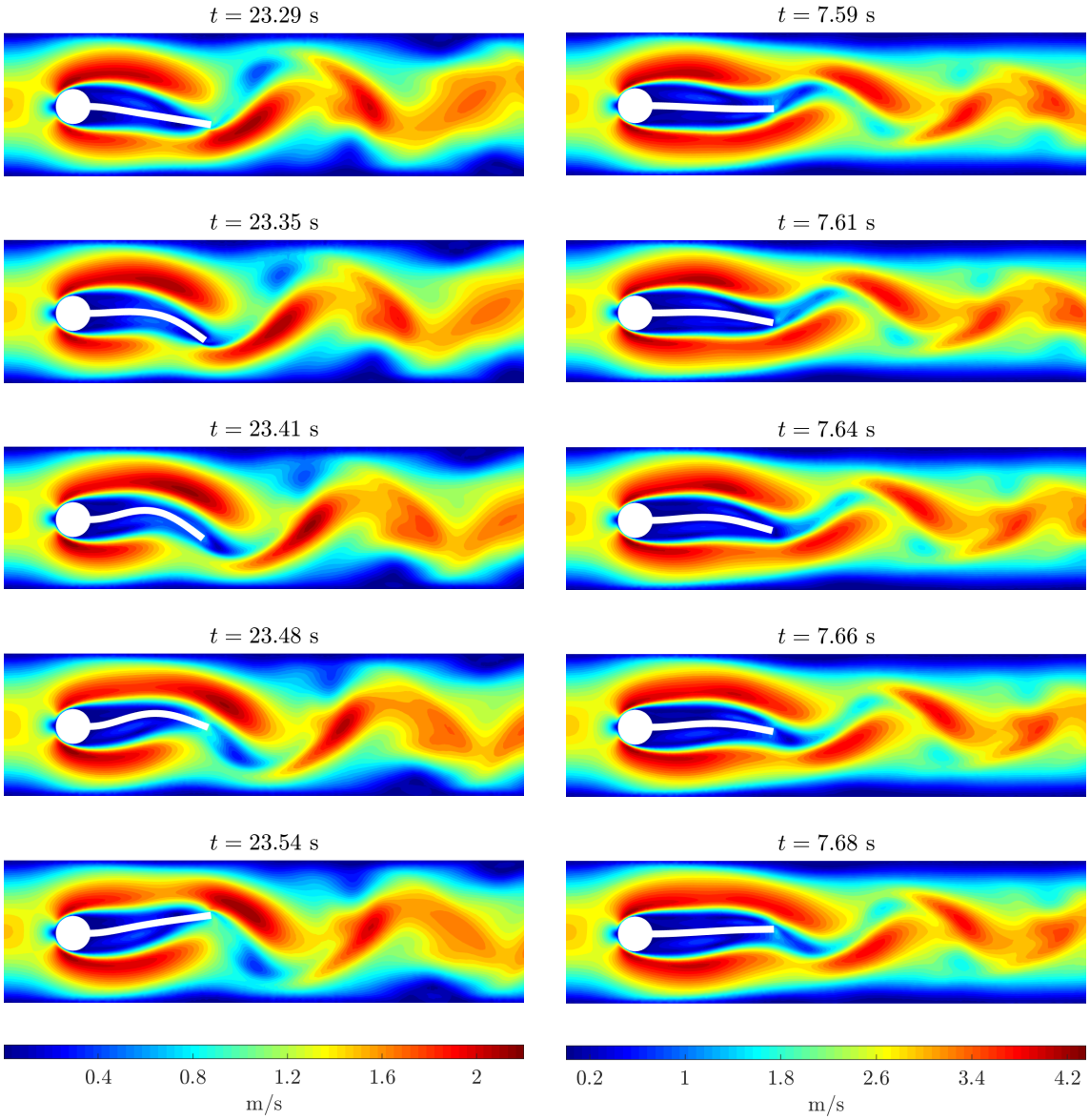

Fig. 4. Contours of velocity magnitude during half a period for the FSI2 (*left column*) and FSI3 (*right column*) benchmark

COMPUTATIONAL MECHANICS 2021
36th conference with international participation
Srní
November 8 - 10, 2021

Screw expander: The expansion solver

S. Plánička[a], Z. Rendlová[a], J. Švígler[a]

[a] *NTIS, Faculty of Applied Sciences, University of West Bohemia in Pilsen, Univerzitní 8, 301 00 Plzeň, Czech Republic*

The most efficient energies utilization will be essential in all fields of human activities in the nearest future. For the making use of waste heat, for example in small industrial facilities, the possibility of screw motors application was studied, where the tasks of our department were primarily to analytically describe the screw motor geometry and secondarily to solve the expansion of the working medium within. An introduction of initial ideas of the expansion process solver is the main object of presented conference paper.

Benefits of the analytical description of a screw engine working chambers geometry lie in their usability for possible modifications of the working chambers geometry design, which prospective impact on engine efficiency should be evaluate appropriately. Resultant power of torque produced in a screw engine by working medium could be used as a design evaluation criterion, this requires calculations of expansion phase thermodynamics and especially the solution of pressure in the working space during the screw engine working cycle. In order to handle aforementioned calculations effectively, utilization of complete CFD for simulations of fluid flow in a screw engine is almost impossible due to its extreme computational demands. More suitable approach to handle these tasks could be creation of an own simplified and computationally fast solver of expansion processes. Such program code should be coupled with the geometrical code to acquire input geometrical data and to calculate the resulting forces as an integral of the pressure acting on screws surfaces.

Let me note that the proposed screw engine was originally intended to work with an organic medium in organic Rankine cycle (ORC). Both the ORC with phase changes and the working medium with a low speed of sound required the development of a nontrivial flow solver with complex constitutive relationships. Later, the working gas has been changed to air, consequently entire working cycle of the engine was shifted to the area of superheated vapor of air (inlet pressure $p^{IN} \lesssim 15$ atm and interior temperature $t \in (-50; 200)$ °C). Detailed analyses of partial test cases carried out on simplified geometry of single working chamber (e.g. study of inertia effects, propagation of expansion waves, friction losses, turbulence effects etc.) showed that a simple zero-dimensional model based on the laws of the ideal gas isentropic processes is sufficiently accurate to capture the air expansion in working space. Additionally, to lubricate the compressor and to seal small gaps, a small amount of warm oil is injected together with the compressed air into the working space. The resulted model of the working medium expansion was developed taking into account the following assumptions:

- There are no leakage flow losses (idealized analytical geometry with perfect contacts).
- Behavior of air is described by the ideal gas law (this assumption is true and of sufficient accuracy under operating conditions).
- Expansion of gas is adiabatic (fast processes, without heat exchanges).
- Oil is taken as an incompressible fluid, which is separated from air (its volume reduces the working space volume free for air expansion).

- At one moment pressure has the same value in the entire working space (instantaneous propagation of pressure changes, without significant fluid flow).
- Pressurization of the working space is immediate (from the opening until the closing of the inlet port, the working space is pressurized to the inlet parameters values).

Following aforementioned simplifications, the fundamental part of the model, i.e. the equation of the expansion phase pressure, is described by a simple algebraic equation

$$p(V) = p^{IN} \left(\frac{V^{IN} - V_{oil}^{IN}}{V - V_{oil}^{IN}} \right)^{\gamma},$$

where V is volume of working space variable during the expansion, p is corresponding pressure, p^{IN} is inlet pressure, V^{IN} is volume of working space at the moment of inlet port closing, V_{oil}^{IN} is total volume of injected oil to working space and γ is heat capacity ratio of air. The algorithm based on this simplest model is very computationally fast and obtained results are sufficiently accurate if the above assumptions are valid. A similar models were used in some computational software commonly, see [1]. The solution of proposed model can be seen in Fig. 1 (red dashed line), considering the ideal geometry of chosen screw engine and inlet pressure p^{IN} = 2.992 bar. For comparison is there shown a blue line, which corresponds to the data measured using experimental stand operated at the same inlet pressure in Technical University of Applied Sciences in Amberg.

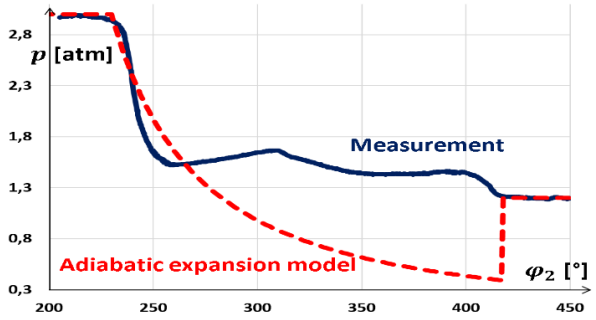

Fig. 1. Solution of the simplest 0-D model (red) in comparison with measurement data (blue)

After numerical experiments and followed by validation using experimental data, some shortcomings of the simplest 0-D model became apparent. The major inaccuracy of the presented model lies in the geometric representation, because our model considers strictly perfect contacts, but in general a leakage flow through gaps can occur and rapidly decrease the pressure gradient and accordingly negative affect efficiency of screw machines. The second imprecision of the basic model is unrealistic filling of the working space with compressed air, when the rapidly enlarging working space is still totally filled to the inlet pressure value through the closing inlet port. The third improper assumption of basic model is contained in approach of the adiabatic expansion of air. The experimental measurements on test stand clearly showed the significantly higher outlet temperature compared to predictions of the adiabatic expansion model. The only relevant explanation of such phenomenon may reside in air re-heating during the expansion process. The modified solver, which is able to handle with the all above-mentioned inconveniences will be detailed presented in the conference talk.

Acknowledgements

The institutional support of the Department of Mechanics is gratefully acknowledged.

References

[1] Stosic, N., Smith, I., Kovacevic, A., Screw compressors – mathematical modelling and performance calculation, Springer Berlin Heidelberg New York, 2005. ISBN-10 3-540-24275-9

COMPUTATIONAL MECHANICS 2021
36th conference with international participation
Srní
November 8 - 10, 2021

Calculation of stiffness and damping coefficients of hydrodynamic lemon-bore journal bearings

J. Pokorný[a], T. Návrat[a]

[a] *Institute of Solid Mechanics, Mechatronics and Biomechanics, Faculty of Mechanical Engineering, Brno University of Technology, Technická 2896, 616 69 Brno, Czech Republic*

1. Introduction

This paper deals with a calculation of stiffness and damping coefficients of the hydrodynamic lemon-bore journal bearings of the finite length. The hydrodynamic pressure distribution is described by the dynamic Reynolds equation solved using the finite volume method. The variable temperature in the circumferential and axial directions of the bearing is considered in the calculation resulting in changes of the lubricant viscosity and density. The proposed computational model involves the mixing of the lubricant, obtaining a steady-state solution of the pressure and temperature, and establishing the equilibrium position of the journal. Based on the small dynamic displacements of the journal from the equilibrium position, the stiffness and damping coefficients are determined. The results of these dynamic characteristics are presented in dependence on speed for the selected load of the particular lemon-bore bearing.

2. Theory

The position of the journal of the hydrodynamic bearing is given by the eccentricity e and the attitude angle ψ (Fig. 1). The journal is separated from the bearing bush by the lubricant film of the thickness h. There is the hydrodynamic pressure p in the lubricant film.

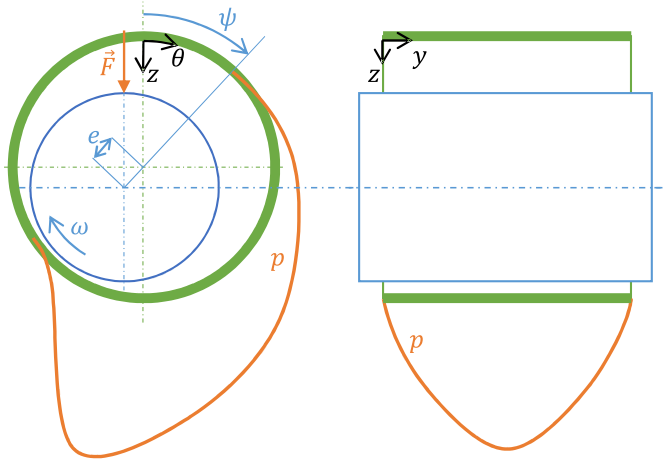

Fig. 1. Cylindrical hydrodynamic bearing in the static equilibrium position, the used coordinate system, [1]

The hydrodynamic pressure distribution is described by general Reynolds equation for dynamic lubrication

$$\frac{\partial}{R^2\partial\theta}\left(\frac{\rho h^3}{\eta}\frac{\partial p}{\partial\theta}\right)+\frac{\partial}{\partial y}\left(\frac{\rho h^3}{\eta}\frac{\partial p}{\partial y}\right)=6\left(U\frac{\partial(\rho h)}{R\partial\theta}+2\frac{\partial(\rho h)}{\partial t}\right), \tag{1}$$

where R is the journal radius, θ and y are the circumferential and axial coordinates, ρ and η are the lubricant density and viscosity, U is the sliding velocity and t denotes time, [3].

The two-dimensional temperature distribution T in the lubricant film, assuming the constant temperature across the film thickness with adiabatic boundary conditions, follows the energy equation [3]:

$$q_\theta\frac{\partial T}{R\partial\theta}+q_y\frac{\partial T}{\partial y}=\frac{\eta U^2}{J\rho c_p h}+\frac{h^3}{12\eta J\rho c_p}\left[\left(\frac{\partial p}{R\partial\theta}\right)^2+\left(\frac{\partial p}{\partial y}\right)^2\right], \tag{2}$$

where $q_\theta=\frac{Uh}{2}-\frac{h^3}{12R\eta}\frac{\partial p}{\partial\theta}$ and $q_y=-\frac{h^3}{12\eta}\frac{\partial p}{\partial y}$ are the flow rates, J is the mechanical equivalent of heat, and c_p is the specific heat of the lubricant. The Reynolds equation (1) and the energy equation (2) are solved using the finite volume method.

The cold lubricant is supplied from the reservoir as the bearing operates. Therefore, the mixing of the lubricant must be considered to determine the temperature change in the lubricant film [2]:

$$T_{1,n}=T_0+c_{mix}\frac{q_{2,n-1}}{q_{s,n}+q_{2,n-1}}\left(T_{2,n-1}-T_0\right), \tag{3}$$

where $T_{1,n}$ is the temperature at the leading edge of the nth lobe, T_0 is the lubricant supply temperature, c_{mix} is the mixing factor, $q_{2,n-1}$ is the exit flow at trailing edge of the upstream lobe and $T_{2,n-1}$ is its temperature, and $q_{s,n}$ is the side leakage of the lobe.

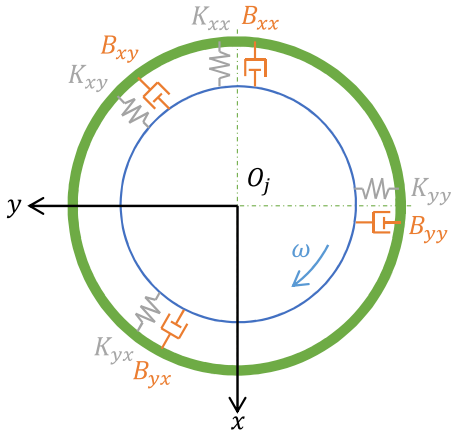

Fig. 2. Scheme of the hydrodynamic bearing stiffness and damping coefficients, [5]

Due to the temperature dependence of the viscosity and density of the lubricant, equation (1) is solved simultaneously with (2) and (3) until a steady-state solution is found. At the same time, the static equilibrium position of the journal is sought, resulting in the balance between the external load and the hydrodynamic pressure [4]. The stiffness and damping coefficients are determined using small dynamic displacements about this equilibrium position. The reaction forces of the lubricant film are functions of this small displacements:

$$\boldsymbol{f}=\boldsymbol{K}\,\boldsymbol{U}+\boldsymbol{B}\dot{\boldsymbol{U}}, \tag{4}$$

where $\boldsymbol{f}$ is the force response vector, $\boldsymbol{U}$ is the displacement excitation vector, $\dot{\boldsymbol{U}}$ is the velocity excitation vector, $\boldsymbol{K}$ and $\boldsymbol{B}$ are the stiffness and damping matrices both containing four coefficients (Fig. 2).

The central finite differences are used to establish these dynamic coefficients. The excitation of the journal is performed separately in two directions, with one direction half of the coefficients is obtained, with the other direction the rest [6].

3. Results

Results are presented for the lemon-bore bearing with parameters given in Table 1.

Table 1. Hydrodynamic lemon-bore bearing parameters

Journal radius	$R = 45mm$
Bearing length	$l = 63mm$
Radial clearance	$c = 0.075mm$
Preload	$\delta = 0.7$
External load	$F = 5\ 670N$ (average pressure $p_m = 1MPa$)
Rotational speed	$n = 2\ 000 \div 30\ 000rpm$
Lubricant type	oil TB 46
Lubricant supply temperature	45°C

Fig. 3 shows the static equilibrium position of the bearing for different rotational speeds. The direction of rotation is considered clockwise. The lubricant film thickness is not in scale; it was 50 times magnified. The maximum values of the pressure at $2000rpm$ and $30000rpm$ were $4.3MPa$ and $7.6MPa$, respectively. The minimum lubricant film thicknesses were $28\mu m$ and $69\mu m$ for these rotational speeds.

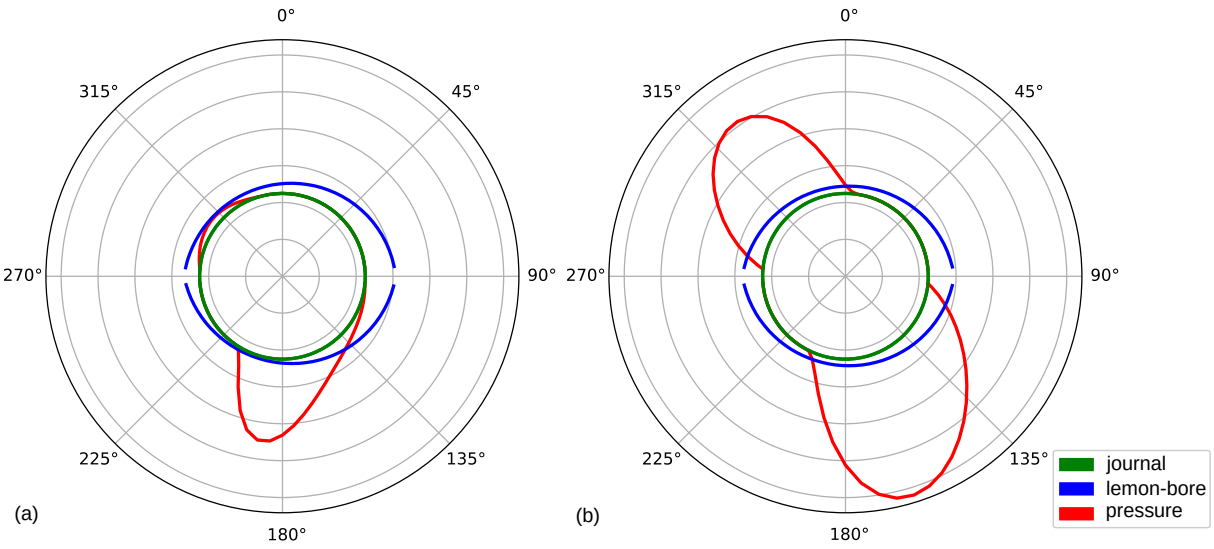

Fig. 3. Hydrodynamic pressure at the static equilibrium position: a comparison, $n = 2000rpm$ (a), $n = 30000rpm$ (b)

Fig. 4 (a) shows the hydrodynamic pressure distribution at $30000rpm$. The pressure is shown not only at the bearing mid-plane (Fig. 3 (b)) but across the entire length of the bearing. Fig. 4 (b) shows the comparison of the temperature change in the circumferential direction for different rotational speeds. Due to mixing, the temperature change at the leading edge of the lobes is not zero.

Fig. 5 shows the dependence of the stiffness and damping coefficients on the rotational speed. The coordinate system is indicated in Fig. 2. The direct stiffness coefficient in the load direction increases with speed while all the damping coefficients decreases. The cross-coupled damping terms have the same value. Although the cross-coupled stiffness coefficients have a destabilizing effect, it is much smaller than in the case of a plain cylindrical bearing. Therefore, lemon-bore journal bearings are used more than cylindrical.

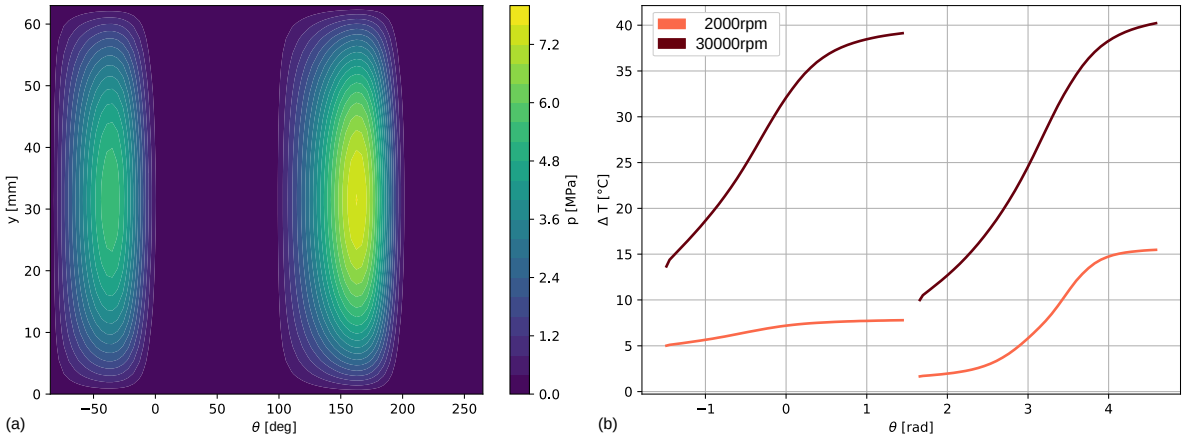

Fig. 4. Hydrodynamic pressure distribution at $30000rpm$ (a), Temperature change at the bearing mid-plane (b)

4. Conclusions

In the presented paper, the dynamic solution of the Reynolds equation was used to determine the stiffness and damping coefficients of the lemon-bore hydrodynamic journal bearing. The energy equation with lubricant mixing was coupled with the Reynolds equation to incorporate the temperature changes in the lubricant film. Thus, the variable viscosity and density of the lubricant were considered in the circumferential and axial direction of the bearing. Therefore, the steady-state solution of the static equilibrium position of the journal was obtained. Based on this position, the dynamic characteristics of the bearing were established. The speed dependence of these characteristics was presented for particular lemon-bore bearing.

The proposed approach can be recommended for determining the dynamic characteristics not only of lemon-bore bearings but also of plain journal bearings and other types of bearings with fixed geometry. It offers reasonable results within a short time. Further research might be focused on fixed-pad bearings or tilting-pad journal bearings.

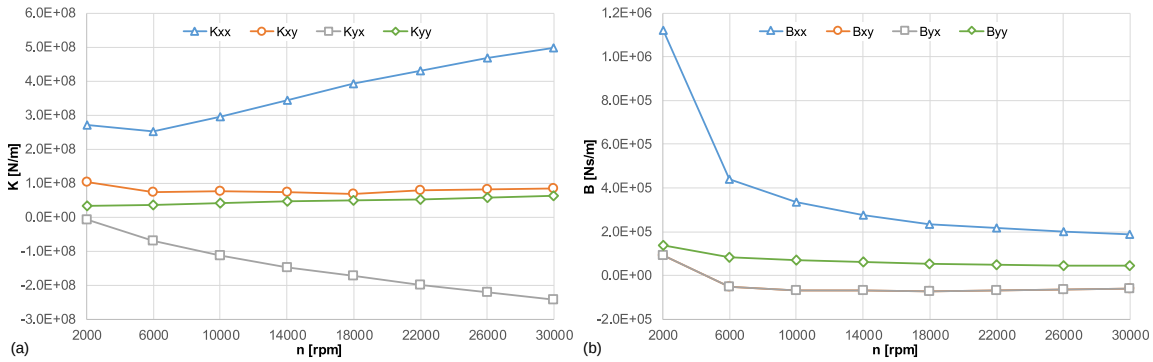

Fig. 5. Dynamic characteristics: a speed dependence, stiffness coefficients (a), damping coefficients (b)

References

[1] Harnoy, A., Bearing design in machinery: engineering tribology and lubrication, Marcel Dekker, New York, 2003.

[2] Heshmat, H., Pinkus, O., Mixing inlet temperatures in hydrodynamic bearings, Journal of Tribology 108 (1986) 231–244.

[3] Huang, P., Numerical calculation of lubrication: Methods and programs, John Wiley & Sons, Singapore, 2013.

[4] Pokorný, J., Calculation of static equilibrium position of hydrodynamic journal bearings, in: Zolotarev, I., Radolf, V. (Eds.), Engineering Mechanics 2019, Institute of Thermomechanics of the Czech Academy of Sciences, Svratka, 2019, pp. 291–294.

[5] San Andrés, L., Modern lubrication theory: Gas film lubrication, Notes 15, Texas, 2010.

[6] Tiwari, R., Rotor systems: Analysis and identification, 1st ed., CRC Press, Boca Raton, 2017.

COMPUTATIONAL MECHANICS 2021
36th conference with international participation
Srní
November 8 - 10, 2021

Research on the utilization of mechatronic tensegrities in robotics

P. Polach[a], Z. Šika[b], M. Hajžman[a], R. Bulín[a], P. Beneš[b], J. Zavřel[b]

[a] *New Technologies for the Information Society, European Centre of Excellence, Faculty of Applied Sciences, University of West Bohemia, Univerzitní 8, 306 14 Plzeň, Czech Republic*
[b] *Department of Mechanics, Biomechanics and Mechatronics, Faculty of Mechanical Engineering, Czech Technical University in Prague, Technická 4, 166 07 Praha, Czech Republic*

The basic research in the field of robotics is currently very intensive in many directions involving different new possibilities of artificial intelligence, as well as the improvement of mechanical and especially dynamic properties, both with new concepts of mechanical structures and the new concepts of their control. The most common robots today have the well-known serial structure. They have good ratio between the built-up space and the effective workspace. Their main disadvantages are typically the low effective stiffness, low damping and in particular, the unfavourable ratio between stiffness and mass. The parallel kinematic mechanisms (PKM) can be used as an alternative to serial ones with better stiffness, but worse built-up/usable space ratio, usually more complicated control and higher number of possible collisions within the workspace. In case of the redundantly actuated PKMs even the singular positions can be eliminated and other parameters of the mechanism can be improved as well. The cable driven variants of the PKMs combine principles of parallel kinematics with the usage of cables/fibres as links, which brings further advantages – namely the lightweightness, large range of motion, possibility of anti-backlash property, easy reconfiguration and even cheaper construction compared to traditional mechanisms.

(a)  (b) 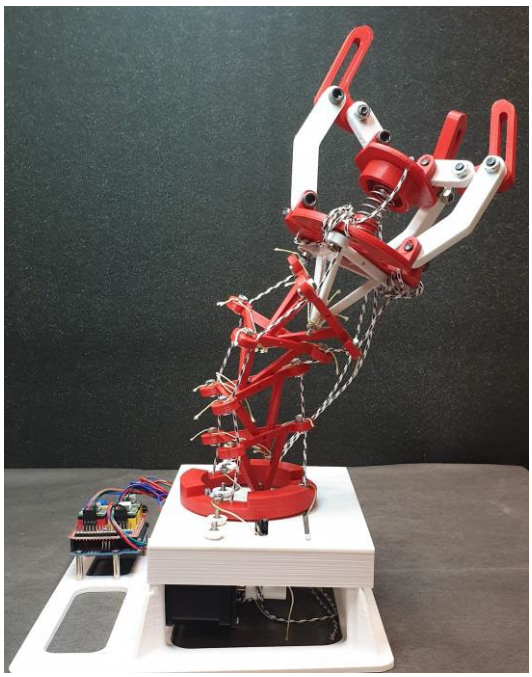

Fig. 1. (a) Example of tensegrity (Needle Tower located in Washington D.C., USA) – taken from [1]; (b) example of sophisticated parallel bio-inspired tensegrity robot HEDRA – taken from [6]

The important task of basic mechanical engineering research in robotics is to propose, investigate and optimize unconventional combinations of different structures and possibilities of their advanced control. Tensegrity (abbreviation of "tensional integrity") mechanisms, combining some serial and parallel aspects, can be taken as next qualitative level arising from cable mechanisms. The idea of tensegrity is one of the very interesting concepts of spatial structures, which is currently being investigated both in the sphere of civil engineering constructions and in the design of innovative reconfigurable mechanisms of the future. The tensegrity structures in a narrow sense are the structures composed from isolated (do not touch each other) members (usually rods or struts) in compression inside a net of prestressed tensioned members (usually cables, fibres or tendons) – see for example Fig. 1. A tensegrity configuration that has no contacts between its rigid bodies is a class 1 tensegrity system (see Fig. 2 and Fig. 3c), and a tensegrity system with as many as *k* rigid bodies in contact is a class *k* tensegrity system (see Fig. 3d). The basic step in the design phase of a functional tensegrity structure is to determine its equilibrium configuration, a process called as "form-finding" [1]. "Form-finding" is the search for new topologies and morphologies of tensegrity structures.

Although the original idea is not new [4], the current possibilities of mechatronics open a new intensive research field of their actively controlled and reconfigurable variants. The actuators deforming some members (rods or cables) on a tensegrity structure can be used to control its shape [7]. The robots TR-3 and TR-4 (see Fig. 2), based on the three-prism tensegrity structure, are analyzed in [2].

(a)  (b) 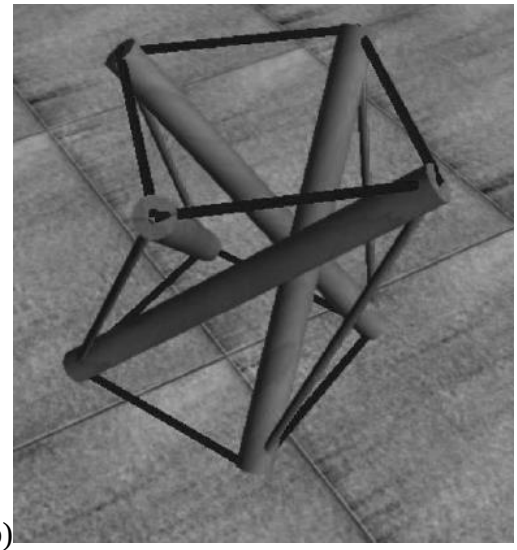

Fig. 2. (a) Robot TR-3, based on the three-prism tensegrity structure; (b) robot TR-4, based on the four- prism tensegrity structure – both taken from [2]

Tensegrity modelling and control tools have been developed, among others, by NASA Ames Research Center as an open source Tensegrity Robotics Toolkit (NTRT) [5]. Many control strategies (e.g. H_2 and H_∞ synthesis, genetic algorithms, the output-feedback linear parameter-varying) have been developed to treat locomotion of tensegrities (e.g. [2]). There are currently several demonstrators of the tensegrities either with active rods or active cables. Another realization of active cables uses e.g. piezoactuators or shape-memory alloys.

The replacement of classical serial robot by light active tensegrity mechanism can significantly improve its stiffness/mass ratio and bring completely new possibilities of controllability and observability by internal actuators and sensors. The great benefit of active tensegrities is that we can reach a high level of force control within the structure. The low authority control (vibration suppression) can be combined with the high authority motion control and force control. The possibility of temporary relaxation of potentially colliding

tendons can enlarge the reachable workspace. The nature of tensegrity mechanisms containing many springs or other pre-stressed components seems to be suitable for an interesting concept called as “eigenmotion” [3]. This control approach is based on a constant sum of kinetic and potential energy, e.g. pendulum like motion. With absence of external load and neglected energy dissipation this results in motion with zero energy consumption. These aspects associated with tensegrity robots are very promising, but have not yet been sufficiently investigated. Research on these topics is a key objective of or activities.

the goal of our activities is a complex basic research of a new type of hybrid serial-parallel mechanisms for robotics. These mechanisms will be composed of both rigid bodies and cable/fibre/tendon components. Such type of mechanisms can be characterized as mechatronic tensegrity. The challenge is to maximize overall mechanical and dynamic properties, especially collision free workspace, dexterity, calibrability, stiffness, damping and modal properties. Improving these features will be accomplished together by the optimization of mechanical structure of tensegrity mechanism itself and its advanced control. The ultimate goal is to increase operational accuracy and speed of the robots in large workspace and reduce their energy consumption.

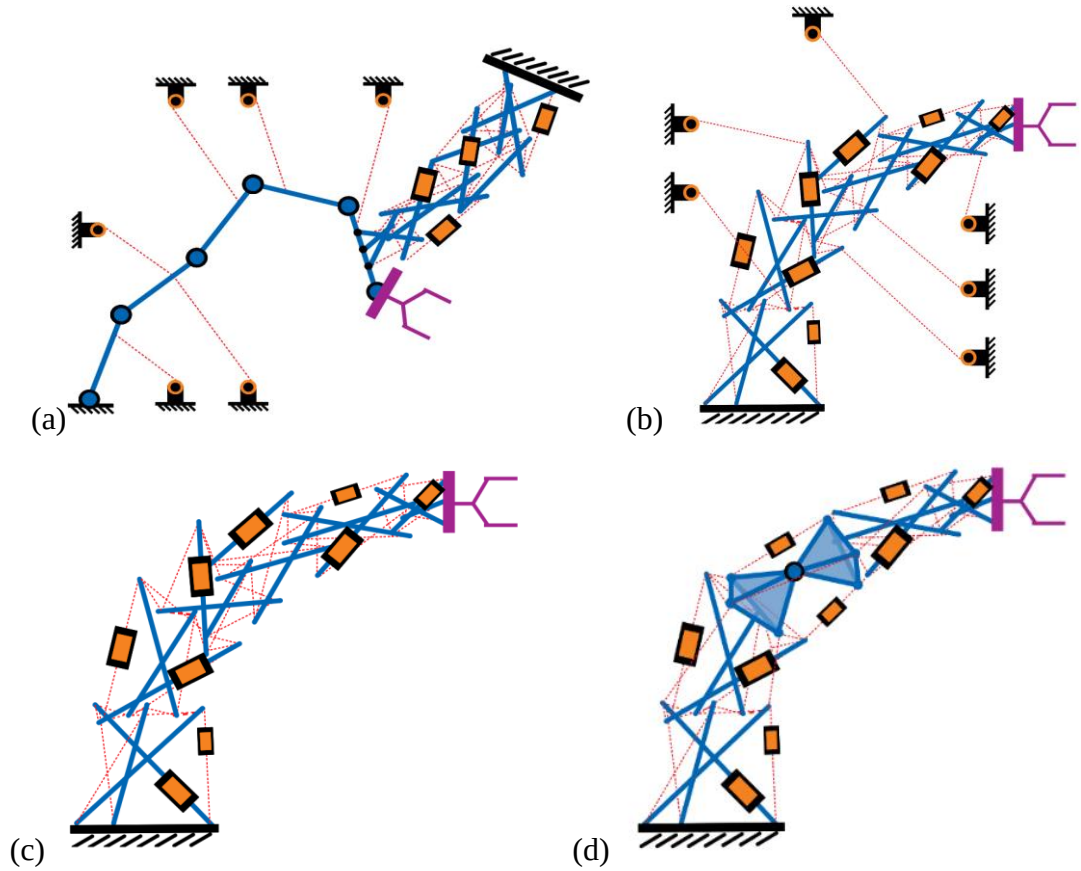

Fig. 3. Some concepts of robots with controlled tensegrity mechanisms: (a) Robot with additional cable drives and tensegrity, (b) tensegrity robot with additional cable drives, (c) robot created by tensegrity class 1 and (d) robot using tensegrity of higher class

The idea of active tensegrity usage for robots can be concretized in many ways. Some of possible concepts are in Fig. 3. First variant of more or less classical serial robot with additional cable drives and tensegrity is in Fig. 3a, tensegrity robot with additional cable drives is in Fig. 3b, robot created by tensegrity of class 1 in Fig. 3c and robot built using tensegrity of higher class in Fig. 3d. The tensegrity types of mechanisms have the potential to comprise strong points of both main robot types (serial, parallel) together, primarily the large workspace together with the favourable ratio between stiffness and mass. Important challenge is to use natural property

of tensegrity mechanisms with spring tendons to absorb potential energy. This property can be used for minimizing the energy consumption of tensegrity robot during its motion control. The optimized variants of tensegrity robots and their best control strategies will be tested on complex virtual models and partly also experimentally using a simplified demonstrator.

One of examples of a new robotic mechanism based on tensegrity robots and reconfigurable modular robots is the bio-inspired modular tensegrity robot with polyhedral parallel modules (HEDRA) [6]. An adaptive cable driven robotic gripper is designed and attached to the tensegrity manipulator for grasping objects in different shapes, weights, and sizes (see Fig. 1b). Consequently the particular objectives of our activities can be summarized as follows:

1. To investigate and optimize different variants of tensegrity mechanisms suitable for future light robots. The target is to use specific properties of tensegrity structures to maximize non-collision workspace, dynamic stiffness, controllability and observability at minimum mass.
2. To develop advanced motion and force planning strategies of the whole tensegrity structure fulfilling requested non-collision operations of end-effector together with minimization of energy consumption and other requests.
3. To investigate and develop optimum mechatronic solution of tensegrity robot with optimization of control algorithms, actuators and sensors in order to maximize robot performance. The low authority control (vibration suppression), high authority motion control and force control will be combined using special possibilities of tensegrities.
4. To build complex simulation models of most promising variants of investigated tensegrity robots, to evaluate mechanical and operational properties and test the control strategies.
5. To realize experiments with a proposed simplified demonstrators for verification of selected properties of a smart tensegrity mechanisms.

Acknowledgements

The paper has originated in the framework of solving No. 20-21893S project of the Czech Science Foundation entitled “Mechatronic tensegrities for energy efficient light robots”.

References

[1] Carreño, F., Post, M.A., Design of a novel wheeled tensegrity robot: a comparison of tensegrity concepts and a prototype for travelling air ducts, Robotics and Biomimetics 5 (1) (2018). https://doi.org/10.1186/s40638-018-0084-8

[2] Chandana, P., Valero-Cuevas, F.J., Lipson, H., Design and control of tensegrity robots for locomotion, IEEE Transactions on Robotics 22 (5) (2006) 944-957.

[3] Demeulenaere, B., Berkof, R.S., Improving machine drive dynamics: A structured design approach towards balancing, ASME Journal of Mechanical Design 130 (8) (2008), 082302.

[4] Jáuregui, V.G., Controversial origins of tensegrity, Proceedings of the International Association for Shell and Spatial Structures (IASS) Symposium, Universidad Politecnica de Valencia, Valencia, 2009, pp. 1642-1652.

[5] National Aeronautics and Space Administration (NASA), Tensegrity robotics, 2018. https://ti.arc.nasa.gov/tech/asr/groups/intelligent-robotics/tensegrity/NTRT/

[6] Ramadoss, V., Sagar, K., Sadiq Ikbal, M., Lugo Calles, J.M., Zoppi, M., HEDRA: A bio-inspired modular tensegrity soft robot with polyhedral parallel modules, Proceedings of the IEEE International Conference on Robotics and Automation (ICRA), 2020, arXiv:2011.14240.

[7] Skelton, R.E., Adhikari, R., Pinaud, J.-P., Chan, W., An introduction to the mechanics of tensegrity structures, Proceedings of the 40th IEEE Conference on Decision and Control, IEEE, Orlando, 2001, pp. 4254-4259.

COMPUTATIONAL MECHANICS 2021
36th conference with international participation
Srní
November 8 - 10, 2021

Inverse problem for nonlinear Gao beam and foundation

J. Radová, J. Machalová

Faculty of Science, Palacký University Olomouc, 17. listopadu 12, 779 00 Olomouc, Czech Republic

This contribution deals with the identification problem for a nonlinear beam and two types of foundation – an elastic deformable and perfectly rigid foundation. We study the nonlinear model beam known as a Gao beam that was published by Prof. D. Y. Gao in [1]. A small correction of the Gao beam model was presented in the recent paper [3]. On the basis of this correction the Gao beam model equation reads as follows

$$E\,I\,w^{IV} - E\,\alpha\,(w')^2\,w'' + P\,\mu\,w'' = f \qquad \text{in } (0,L), \tag{1}$$

where

$$\alpha = 3\,t\,b\,(1-\nu^2), \qquad \mu = (1-\nu^2), \qquad f = (1-\nu^2)\,q$$

and E is Young's elastic modulus, $I = \frac{2}{3}t^3 b$ denotes a constant area inertia moment of the cross-section, where $2t$ is a thickness, and b width of the beam. Further, the transverse displacement is denoted by w, ν is the Poisson ratio and q denotes the applied traversal load per unit length L of the beam. Finally, P stands for the constant axial force acting at the end point $x = L$. We shall distinguish two cases: $P > 0$ causing the compression of the beam and $P < 0$ causing its tension. The beam model needs to be completed by one of the following stable and unstable boundary conditions:

(B1) simply supported beam: $w(0) = w(L) = 0;\ w''(0) = w''(L) = 0,$

(B2) clamped beam: $w(0) = w'(0) = w(L) = w'(L) = 0,$

(B3) propped cantilever beam: $w(0) = w'(0) = w(L) = 0;\ w''(L) = 0,$

(B4) cantilever beam: $w(0) = w'(0) = 0;$

$$w''(L) = E\,I\,w'''(L) - \tfrac{1}{3}E\,\alpha\,(w'(L))^3 + P\,\mu\,w'(L) = 0.$$

Firstly, we consider the contact problem for the Gao beam situated above a perfectly rigid obstacle. The following analysis is restricted to the clamped Gao beam with the boundary conditions (B2), see Fig. 1. The gap between the beam and the foundation is defined by a function $g(x)$ and the contact force is denoted by $T(w)$. If $w(x) = g(x)$ at $x \in (0,L)$, then the beam is in a contact with the foundation at x and $T(w(x)) \geq 0$. If $w(x) > g(x)$ at $x \in (0,L)$, then there is no contact at x and thus $T(w(x)) = 0$. Therefore, Eq. (1) and the contact conditions on $(0,L)$ read as

$$E\,I\,w^{IV} - E\,\alpha\,(w')^2\,w'' + P\,\mu\,w'' = f + T(w) \qquad \text{in} \qquad (0,L), \tag{2}$$

$$\left.\begin{array}{ll} w & \geq g \\ T(w) & \geq 0 \\ (w-g)\,T(w) & = 0 \end{array}\right\} \quad \text{in } (0,L). \tag{3}$$

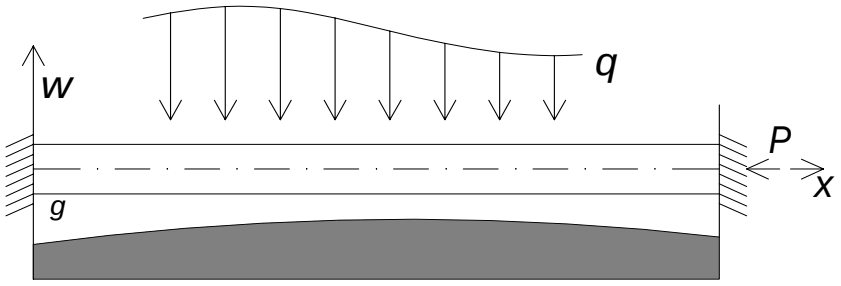

Fig. 1. Clamped beam situated above the foundation

The relations (3) are well known as the Signorini conditions. The variational formulation reads as follows

$$\begin{cases} \text{Find } w \in K \text{ such that} \\ a(w, v-w) + \pi(w, v-w) \geq \mathcal{L}(v-w), \qquad \forall v \in K, \end{cases} \tag{$\mathcal{P}_R$}$$

where

$$a(w,v) = \int_0^L EI w'' \, v'' \mathrm{d}x - \int_0^L P(1-\nu^2) w' \, v' \mathrm{d}x, \tag{4}$$
$$\pi(w,v) = \int_0^L E\, t\, b\, (1-\nu^2)(w')^3 v' \mathrm{d}x, \qquad \mathcal{L}(v) = \int_0^L (1-\nu^2)\, q\, v \, \mathrm{d}x$$

and the set K of admissible deflection is defined by

$$K = \{v \in V : v \geq g \text{ in } (0, L)\}, \tag{5}$$

where $V = H_0^2((0, L))$ is the space of admissible displacements.

Secondly, we consider the contact problem with an elastic deformable foundation, thus, i.e., the beam can penetrate into it in some parts of $(0, L)$. In this case, a contact force $T(w)$ is generated. We shall consider so called normal compliance model

$$T(w) = k_F \, b \, (1-\nu^2)(g-w)^+, \tag{6}$$

where $k_F > 0$ denotes the foundation modulus and $(u(x))^+ = \max\{0, u(x)\}$. The governing equation is given again by (2) with $T(w)$ defined by (6). The corresponding variational formulation is given by

$$\begin{cases} \text{Find } w \in V \text{ such that} \\ a(w, v) + \pi(w, v) - \kappa(w, v) = \mathcal{L}(v), \qquad \forall v \in V, \end{cases} \tag{$\mathcal{P}_D$}$$

where $a(w, v)$, $\pi(w, v)$ and $\mathcal{L}(v)$ are defined by (4),

$$\kappa(w,v) = \int_0^L k_F \, b(1-\nu^2)(g-w)^+ \, v \, \mathrm{d}x. \tag{7}$$

The solution of similarly problem as ($\mathcal{P}_D$), we can find in [2], where the contact problems for the Gao beam with elastic deformable foundation without the gap $g(x)$ were analyzed.

The main idea of the identification problem is to determine the material coefficients (E, ν) of the static Gao beam equation in the contact problem with an elastic deformable or rigid foundation by using an *optimal control approach*.

The identification problem is formulated as the minimization of a least squares cost functional depending on the solution to problems $(\mathcal{P}_R)$ or $(\mathcal{P}_D)$. The set of admissible parameters U_{ad} is defined by

$$\begin{aligned} U_{ad} := \{&p \in L^\infty((0,L)) \times L^\infty((0,L)) : \\ &0 < p_{\min} \le p \le p_{\max} < \infty \text{ in } (0,L), p|_{K_i} \in P_0(K_i) \times P_0(K_i),\ i = 1, \dots, r\}, \end{aligned} \tag{8}$$

where $p = (E, \nu)$ and $p_{\min}, p_{\max}$ are given vectors. We suppose that the interval $(0, L)$ is decomposed into mutually disjoint open intervals K_i, $i = 1, \dots, r$, i.e. $K_i \cap K_j = \emptyset, \forall i \neq j$, and $\langle 0, L\rangle = \bigcup_{i=1}^{r} \overline{K}_i$. Further $P_0(K_i)$ is the set of constant functions on the subintervals K_i. The cost functional $\mathcal{J} : U_{ad} \longrightarrow \mathbb{R}$ is defined by

$$\mathcal{J}(w(p)) = \frac{1}{2}\|w(p) - z\|^2, \tag{9}$$

where $\|\cdot\|$ is L^2-norm, z is a target deflection and $w(p)$ is a solution of the contact problem for Gao beam, see in [4]. Finally, the identification problem is formulated as follows

$$\begin{cases} \text{Find } p^* \in U_{ad} \text{ such that} \\ J(w(p^*)) = \min\limits_{p \in U_{ad}} J(w(p)), \\ \text{where } w(p) \text{ solves the contact problem} (\mathcal{P}_R) \text{ or } (\mathcal{P}_D). \end{cases} \tag{10}$$

Numerical solution of the minimization problem (10) is based on using the standard finite element method and discretization is composed of two parts. The first part is the discretization of the problems $(\mathcal{P}_R)$ and $(\mathcal{P}_D)$ that are solved by using the penalized method and nonsmooth Newton method. The second part concerns the discretization of the cost functional that is given by

$$\mathbf{J}(\mathbf{p}) = \frac{1}{2}\|\mathbf{S}\mathbf{w}(\mathbf{p}) - \mathbf{z}\|^2,$$

where $\mathbf{S}$ is the matrix representing the restriction mapping, $\mathbf{z}$ denotes the vector of given measured data and $\|\cdot\|$ is $L^2((0,L))$-norm. Finally, we obtain the nonlinear programming problem

$$\begin{cases} \text{Find vector } \mathbf{p}^* \in U_{ad} \text{ such that} \\ \mathbf{J}(\mathbf{p}^*) = \min\limits_{\mathbf{p} \in U_{ad}} \mathbf{J}(\mathbf{p}), \\ \text{where } \mathbf{w}(\mathbf{p}) \text{ solves the discretized problems } (\mathcal{P}_R) \text{ or } (\mathcal{P}_D). \end{cases} \tag{11}$$

The nonlinear problem (11) can be solved by the nonlinear conjugate gradient method and the gradient is computed by using so called adjoint state problem. For more information we refer to [5] and [4]. Finally, we state a numerical scheme for the nonlinear problem (11):

- Compute $\mathbf{w}^0(\mathbf{p}^0)$ for given $\mathbf{p}^0 := (\mathbf{E}^0, \boldsymbol{\nu}^0)$.
- Compute gradient $\mathbf{g}^0 = \mathbf{g}(\mathbf{p}^0)$ of $\mathbf{J}(\mathbf{p}^0)$ by using adjoint state problem.
- Let $\mathbf{d}^0 = -\mathbf{g}^0$.

For $k = 0, 1, 2, \cdots$ (until the stopping criterion is fulfilled)

1. Determine step length $\alpha^k > 0$ by using Wolfe conditions.
2. Set $\mathbf{p}^{k+1} = \mathbf{p}^k + \alpha^k \mathbf{d}^k$ and compute $\mathbf{w}^{k+1}(\mathbf{p}^{k+1})$.
3. Compute $\mathbf{g}^{k+1} = \mathbf{g}(\mathbf{p}^{k+1})$ by using adjoint state problem.
4. Compute $\beta^{k+1} = \dfrac{(\mathbf{g}^{k+1})^\top \mathbf{g}^{k+1}}{(\mathbf{g}^k)^\top \mathbf{g}^k}$.
5. Let $\mathbf{d}^{k+1} = -\mathbf{g}^{k+1} + \beta^{k+1}\mathbf{d}^k$.
6. Set $k = k + 1$.

Numerical computations were realized by using the mathematical software Matlab.

Acknowledgments

The authors gratefully acknowledge both the support by the grant IGA PrF IGA_PRF_2021_008 Mathematical Models of the Internal Grant Agency of Palacký University in Olomouc, Czech Republic and the Ministry of Education, Youth and Sports of the Czech Republic under the project CZ.02.1.01/0.0/0.0/17_049/0008408 Hydrodynamic design of pumps.

References

[1] Gao, D. Y., Nonlinear elastic beam theory with application in contact problems and variational approaches, Mechanics Research Communications 23 (1) (1996) 11-17.

[2] Gao, D. Y., Machalová, J., Netuka, H., Mixed finite element solutions to contact problems of nonlinear Gao beam on elastic foundation, Nonlinear Analysis: Real World Applications 22 (2015) 537-550.

[3] Machalová, J., Netuka, H., Comments on the large deformation elastic beam model developed by D.Y. Gao, Mechanics Research Communications 110 (2020) No. 103607.

[4] Radová, J., Machalová, J., Burkotová, J., Identification problem for nonlinear Gao beam, Mathematics 8 (11) (2020) No. 1916.

[5] Tröltzsch, F., Optimal control of partial differential equations: theory, methods, and applications, Graduate Studies in Mathematics Vol. 112, American Mathematical Society, 2010.

COMPUTATIONAL MECHANICS 2021
36th conference with international participation
Srní
November 8 - 10, 2021

Influence of mesh density on the analysis of textured journal bearings

J. Rendl, L. Smolík

NTIS – New Technologies for the Information Society, Faculty of Applied Sciences, University of West Bohemia, Univerzitní 8, 301 00 Plzeň, Czech Republic

The stability of a rotating system supported on a journal bearing can be improved by suitable texturing of the bearing shell. This contribution focuses on mathematical modelling of a textured bearing using the finite difference method and the study of mesh density impacts on static analysis results and estimated stability thresholds.

A simple 2 DoF rotor-bearing model with various texture layouts is analysed. Textures in all considered layouts are located in the replaceable bottom bearing shell to emphasise the influence of the texturing on the system stability compared to the plain bearing. The investigated texture layouts are depicted in Fig. 1a–d. The texture consists of dimples in regular grid (1 mm grid gap) produced by mechanical indentation with a steel ball of 1 mm diameter. The measured dimple profile is shown in Fig. 1e. Investigated bearing was designed with these parameters: inner diameter 37.933 mm, bearing length 20 mm and radial clearance 55 μm. Bearing is supplied by oil with dynamic viscosity 14 mPa.s through the circular bore of 5 mm diameter.

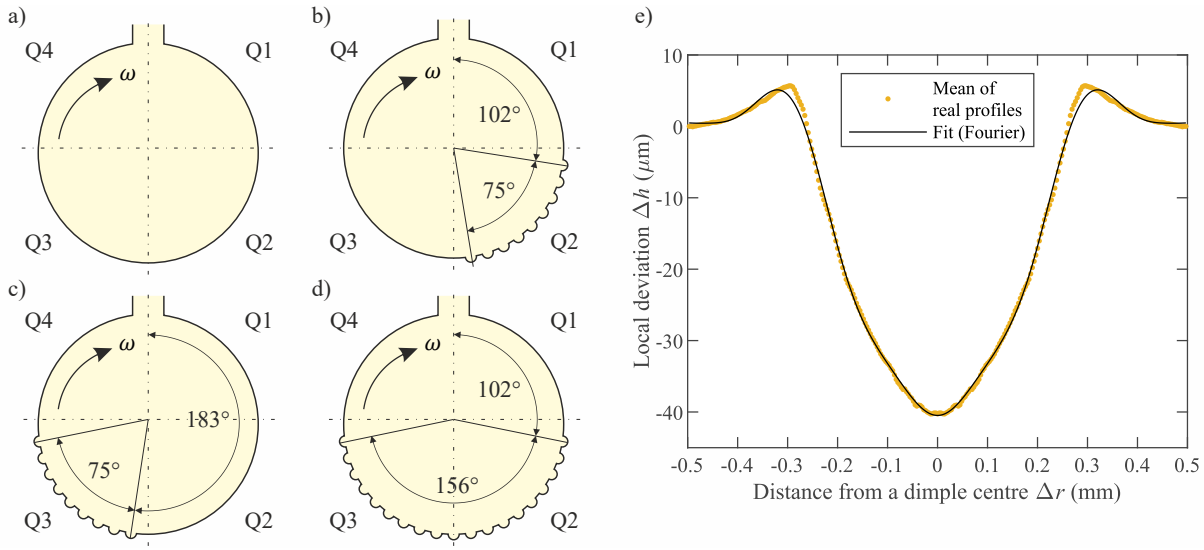

Fig. 1. Investigated bearing layouts: a) plain bearing, b) layout Q2 (26×19 dimples), c) layout Q3 (26×19 dimples), d) layout Q23 (53×19 dimples), e) measured dimple profile

The Reynolds equation [1, 4] governs the pressure field generated in a laminar flow of isoviscous incompressible Newtonian fluid. The film height is a sum of nominal gap h_{nom} of cylindrical bearing and local deviation Δh due to texture. The finite difference method [1] was employed in an in-house software for pressure field calculation and the hydrodynamic force

evaluation. The stability threshold speed assessment is then performed using the Routh-Hurwitz criterion described in [1].

The results of numerical simulations are affected by the utilised cavitation modelling approach and chosen computational mesh density defined as the number of nodes per mm^2. A mass-conserving cavitation modelling [3] approach (Elrod equation) is unsuitable for dense computational meshes because of memory restriction in regular workstations. The static equilibrium points calculated by utilising the Gümbel condition (G), which violates the conservation of mass [1, 4], are compared with those calculated using the mass-conserving Elrod equation (E) in Fig. 2a. Layout Q2 is used for the presented simulations. An in-house software solver uses a direct solution (Dir) for pressure field calculation and the Gümbel cavitation condition due to memory access restrictions. For verification of the obtained results, commercial software AVL Excite was used. This software employs the finite difference method and has a native multi-grid solver (MG) for pressure field solution with both Gümbel and Elrod cavitation models. Unfortunately, the total number of nodes for the numerical solution of the Elrod equation is restricted to ca. 4×10^5, which corresponds with the mesh density of 13×13 nodes per mm^2.

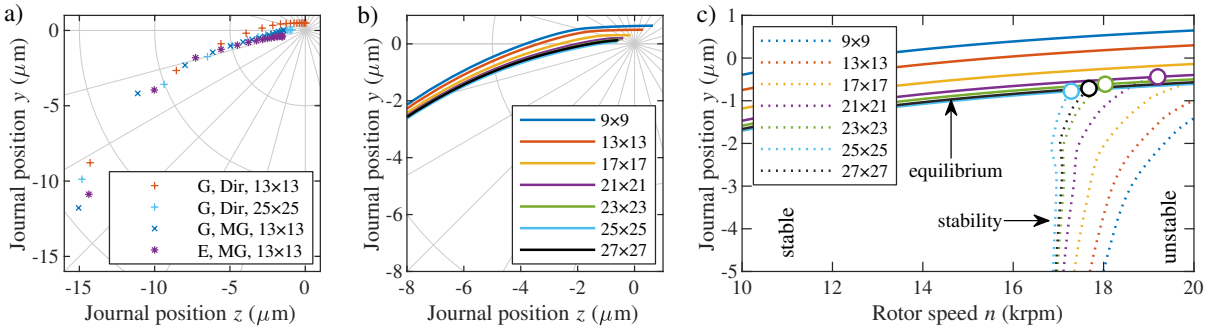

Fig. 2. Loci of equilibrium points for layout Q2: a) various numerical algorithms, b) various mesh densities, and c) threshold speeds (intersections of loci of equilibrium points with stability borderline denoted by ○) for various mesh densities; mesh density given in nodes per mm^2

The equilibrium points differ at higher eccentricities more significantly because of the numerical method rather than the cavitation model. The cavitation model influences the equilibrium points at lower eccentricities, but the results obtained on a dense mesh with the Gümbel condition are similar to the results of the mass-conserving cavitation model. Figs. 2b–c show the results calculated using the in-house software and various mesh densities from 9×9 to 27×27 nodes per mm^2. It is demonstrated on the static equilibrium points Fig. 2b and detected threshold speeds denoted by circles (intersection of equilibrium points and stability borderline) in Fig. 2c that coarse computational meshes predict different results. The results start to converge to limit values with the mesh density around 23×23 nodes per mm^2. Final mesh density 25×25 nodes per mm^2 was established as optimal concerning both computational accuracy and computational time costs.

Static equilibrium points for various texture layouts, bearing loads and relative supply pressures are depicted in Fig. 3. The textures in the third quadrant (layouts Q3 and Q23) affect the loci more significantly with the increased bearing load. However, the differences are also apparent for the lower nominal load. This behaviour is caused by the location of both texture and load-carrying pressure field in the third quadrant. On the contrary, the equilibrium points obtained for layout Q2 are almost at the same positions as in the plain journal bearing.

Threshold speeds for instability, which are deduced from linearised stiffness and damping coefficients in static equilibrium points, are compared in Fig. 4. Vertical axes in the individual

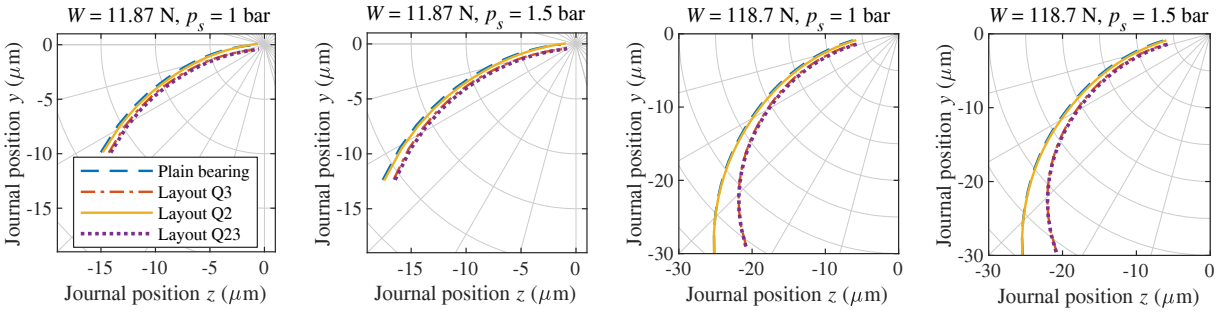

Fig. 3. Loci of equilibrium points for variou texture layouts, bearing loads and relative supply pressures

subfigures are depicted in a logarithmic scale for better clarity. The textures located in regions with high pressure gradients significantly impact the threshold speed in the case of lightly-loaded bearings. The threshold speed is then shifted from 17 krpm for the plain bearing to 19.7 krpm for layout Q2 and out of investigated speed range (i.e., above 20 krpm) for the case of layout Q23. On the other hand, threshold speed shifts only negligibly when the texture is located in the second quadrant of the lightly-loaded bearing. The differences between all layouts are also negligible when higher static load (0.15 MPa) is applied.

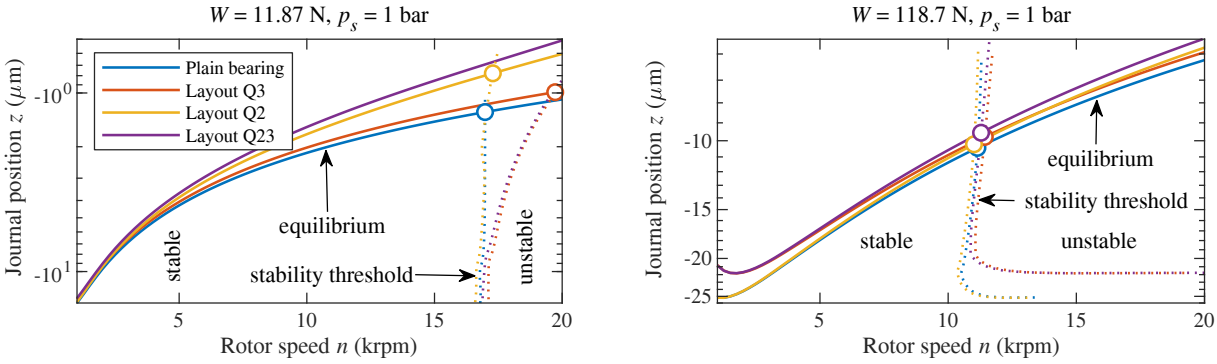

Fig. 4. Comparison of estimated threshold speeds for various texture layouts and bearing loads

Acknowledgements

This publication was supported by project SGS-2019-009 of Czech Ministry of Education, Youth and Sport. Results verification would not be possible without the AVL Excite software, which is available in the framework of the University Partnership program of AVL List GmbH and whose usage is greatly acknowledged.

References

[1] Dyk, Š., Rendl, J., Byrtus, M., Smolík, L. Dynamic coefficients and stability analysis of finite-length journal bearings considering approximate analytical solutions of the Reynolds equation, Tribology International 130 (2019) 229-244.

[2] Gropper, D., Wang, L., Harvey, T.J., Hydrodynamic lubrication of textured surfaces, Tribology International 94 (2016) 509-529.

[3] Qiu, Y., Khonsari, M. M., On the prediction of cavitation in dimples using a mass-conservative algorithm, Journal of Tribology 131 (4) (2009) No. 041702.

[4] Stachowiak, G. W., Batchelor, A. W., Engineering tribology, 4th edition, Butterworth-Heinemann, St. Louis, USA, 2013.

COMPUTATIONAL MECHANICS 2021
36th conference with international participation
Srní
November 8 - 10, 2021

Screw expander: Working chamber analysis to maximize transmitted torque

Z. Rendlová, S. Plánička, J. Švígler

Faculty of Applied Sciences, University of West Bohemia, Univerzitní 8, 301 00 Plzeň, Czech Republic

1. Introduction

A screw expander is a device that is structurally based on the principle of operation of a screw compressor. The main idea is to interchange the input of the screw compressor for the output and, while simultaneously changing the direction of rotation of the twin rotors, use the energy of the working medium to drive another device. In order to develop such a device and subsequently ensure its operation with the greatest possible efficiency, it is therefore necessary to know the working characteristics of a machine. These are affected not only by the thermodynamic parameters of the working medium, but also by the shape and volume of the working chamber, which changes during the working cycle.

2. Working chamber model

In the first step, it is necessary to describe the shape of the monitored working chamber. Since the working chamber is defined by the inner space of the compressor housing and the outer surface of the rotors, it is necessary to create an analytical description of the shape of both rotors, the male rotor and the female rotor. This description is based on knowledge of the shape of the female rotor profile in frontal plane which is performed using a series of analytical curves (for example, lines, arcs etc.). Depending on this description, the profile of the male rotor is created using the envelope principle [1]. Due to the fact that the axes of rotation of both rotors are fixed with respect to the inner space of the housing, their positions do not change during the working cycle. Considering two adjacent cuts that are perpendicular to the axis of rotation of the rotors shifted by distance Δl, the corresponding angle of rotation of the profiles can be determined. Then it is possible to determine the size of the cross-sectional area $A_{i,k}$, which corresponds to the working chamber for a given angle of rotation of the female rotor. For two adjacent slices at a distance of Δl, the the elementary volume $V_{i,k}$ is computed using

$$V_{i,k} = \frac{A_{i,k} + A_{i,k+1}}{2} \cdot \Delta l \,, \tag{1}$$

where A_i and A_{i+1} are working chamber areas in slices i and $i+1$, respectively. The index k represents chosen angle of rotation of female rotor from range $\varphi \in \langle 0,\, \varphi_5 \rangle$. The total volume V_k of working chamber is calculated as the sum of elementary volumes $V_{i,k}$ along total length of screws. The actual volume of the working chamber depends on the angle of rotation of the secondary rotor and changes with the angle of rotation, in particular in the case of a screw expander this volume increases.

3. Working cycle description

The operating cycle of the screw compressor can be divided into several phases. These phases can be defined with respect to the angle of rotation φ of the female rotor. In the first phase, the rotors are rotated from the reference position until the working chamber begins to form. This corresponds to the angle of rotation of the female rotor in the range $\varphi \in \langle 0\,, \varphi_1 \rangle$. Subsequently, the working chamber is formed in the range of the angle of rotation $\varphi \in \langle \varphi_1\,,\, \varphi_2 \rangle$. As soon as the angle of rotation becomes φ_2, the inlet port is opened and the working chamber is filled with the working medium (so-called filling phase). This phase takes place in the range of the angle of rotation $\varphi \in \langle \varphi_2\,,\, \varphi_3 \rangle$. Then, the inlet port is closed and the working chamber can be understood as an enclosed area into which the the specific amount of working medium has been introduced. Due to the rotation of the rotors, which occurs due to the action of the working medium on the surface of the rotors, the volume of the working chamber increases. Thus, the working medium in the working chamber expands (expansion phase). This phase takes place in the range of the angle of rotation $\varphi \in \langle \varphi_3, \varphi_4 \rangle$. Then there is a phenomenon when the working chamber no longer increases its volume and the angle of rotation varies within range $\varphi \in \langle \varphi_4\,, \varphi_5 \rangle$. Then the working medium leaves the space freely through the outlet port (exhaust phase).

4. Calculation of torque during the working cycle

Considering the elementary volume of working chamber given by two adjacent sections of the working chamber i and $i + 1$, the working media acts on the outer surfaces of the screws and on the inner surface of the housing. The pressure of working media is computed in isolated single working chamber with respecting of characteristics of working media at the inlet port. In the phase of expansion of the gas in the working chamber, the adiabatic law is respected. The aforementioned model of working medium expansion seems appropriate when a fast processes (adiabatic expansion of gas without heat exchanges) and an ideal geometry with ideal contacts (no leakage flow losses) are assumed [2].

5. Application

The described procedure was applied to a mass-produced B100 compressor produced by Atmos Chrást s.r.o. This compressor, the inversion of which is intended to obtain a screw expander, is equipped with rotors with a total length $l = 129.9\,\text{mm}$ and diameters of head circles $D_2 = 83.94\,\text{mm}$ for the female rotor and $D_3 = 106\,\text{mm}$ for the male rotor and the pitch angle $\gamma = 38.127°$. Both screws are mounted in the housing, the distance of the parallel axes of rotation of both screws is 73 mm, see Fig. 1. The working medium consisting of two separate phases, namely compressible gas (air) and incompressible liquid (oil).

6. Conclusion

In order to maximize the performance of the screw expander, an analysis of the working space was performed and the sizes of the surfaces on which the working medium acts were determined, thus generating a torque ensuring the rotation of the screws in the screw expander. From the performed analyzes, it seems advantageous to modify the screw profiles so that the active area on which the working medium acts is maximized while respecting the parameters of the housing. Another possible modification is to keep the existing tooth profiles of both rotors and insert screws with variable pitch angle into the housing.

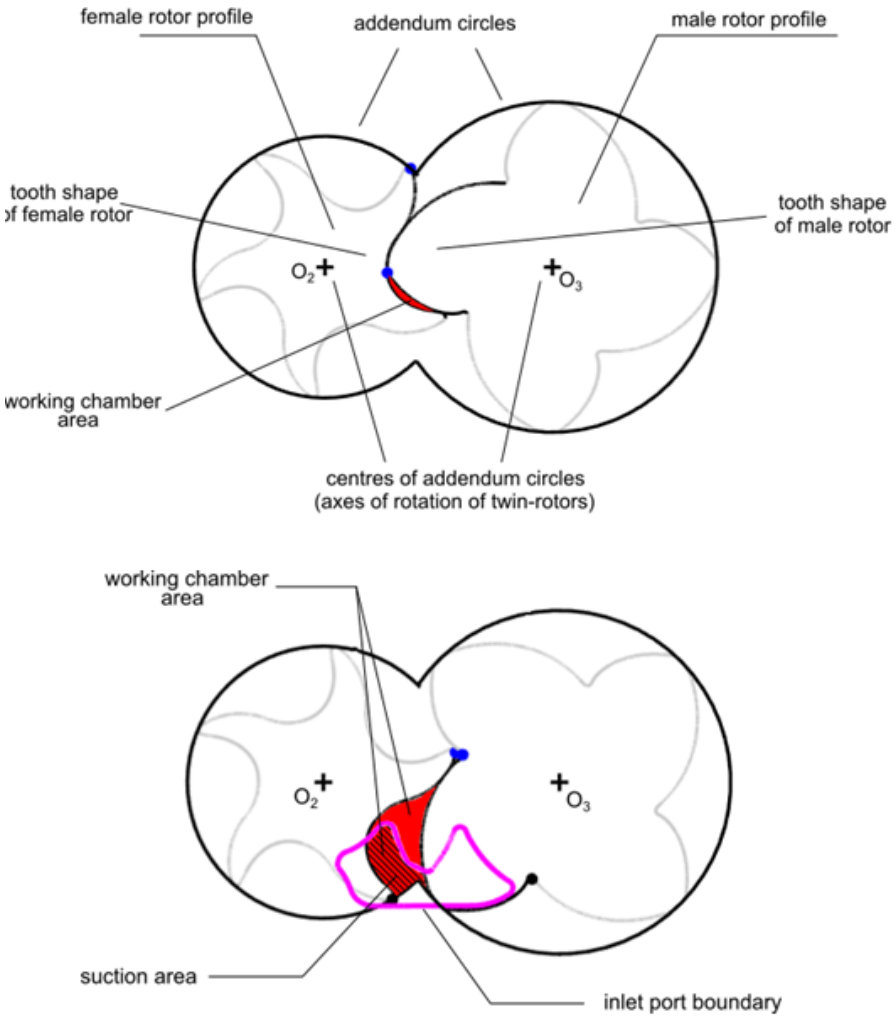

Fig. 1. Identification of the working chamber and the geometry of the suction opening for the selected angle of rotation of the female rotor

References

[1] Švígler, J., A treatise on the theory of screw machines, University of West Bohemia, Plzeň, 2010.

[2] Stosic, N., Smith, I., Kovacevic, A., Screw compressors: Mathematical modelling and performance calculation, Springer Berlin Heidelberg New York, 2005.

COMPUTATIONAL MECHANICS 2021
36th conference with international participation
Srní
November 8 - 10, 2021

Flow in poro-piezoelectric media induced by persitaltic deformation waves – homogenization approach

E. Rohan, V. Lukeš

NTIS – New Technologies for the Information Society, Faculty of Applied Sciences, University of West Bohemia, Univerzitní 8, 301 00 Plzeň, Czech Republic

We consider a fluid-saturated porous medium subjected to deformation waves which generate peristaltic driven flow. The deformation is actuated by piezoelectric elements periodically distributed in the structure and controlled locally by electrodes inducing the electrostatic field. The presented research is aimed to explore functionality of such metamaterial structures by in silico experiments. For this we employ a two-scale modelling approach based on the homogenization method [1] combined with the sensitivity analysis. We extend the homogenized model of the fluid-saturated piezo-poroelastic medium equipped with the controlling conductor networks [5] to describe the fluid-structure interaction respecting influence of the deformation of the micro-configuration.

The computational model arises from the homogenization of the fluid-saturated porous medium. To treat the large deformation phenomenon, we follow the Eulerian approach leading to the updated-Lagrangian incremental formulation in the two-scale setting [2, 3]. In the context of locally periodic structures, local cell problems are obtained which provide characteristic responses of the microstructures with respect to macroscopic strains, fluid pressure and electric potentials. Within the homogenization scheme introduced for the incremental fluid-structure interaction problem, the macroscopic nonlinearity of the device is captured using the first order expansions of the homogenized coefficients with respect to macroscopic variables [6], cf. [4]. For this, the sensitivity analysis approach is employed. We present examples of microstructures and results of the simulations as the proof of concept aimed at designing smeared peristaltic pumps in a bulk medium.

The heterogeneous periodic structure of the two-phase medium is constituted by a piezoelectric skeleton interacting with a viscous fluid saturating the pores in the skeleton. The structure characterized by the pore size $\ell^\varepsilon \approx \varepsilon$, where the parameter $\varepsilon \to 0$ is related to the asymptotic analysis leading to a model of the homogenized fluid saturated piezo-poroelastic medium.

Micromodel In the piezoelectric (PZ) solid, the Cauchy stress tensor $\boldsymbol{\sigma}^\varepsilon$ and the electric displacement $\vec{D}^\varepsilon = (D_i^\varepsilon)$ depend on the strain tensor $\boldsymbol{e}(\boldsymbol{u}^\varepsilon) = (\nabla \boldsymbol{u}^\varepsilon + (\nabla \boldsymbol{u}^\varepsilon)^T)/2$ defined in terms of the displacement field $\boldsymbol{u}^\varepsilon = (u_i^\varepsilon)$, and on the electric field $\vec{E}^\varepsilon = \nabla \varphi^\varepsilon$ defined in terms of the electric potential, $E_i^\varepsilon = \partial_i^x \varphi^\varepsilon$, such that

$$\begin{aligned} \boldsymbol{\sigma}^\varepsilon(\boldsymbol{u}^\varepsilon, \varphi^\varepsilon) &= \mathbb{A}^\varepsilon \boldsymbol{e}(\boldsymbol{u}^\varepsilon) - \underline{\boldsymbol{g}}^T \vec{E}^\varepsilon(\varphi^\varepsilon) \,, \\ \vec{D}^\varepsilon(\boldsymbol{u}^\varepsilon, \varphi^\varepsilon) &= \underline{\boldsymbol{g}}^\varepsilon \boldsymbol{e}(\boldsymbol{u}^\varepsilon) + \boldsymbol{d}^\varepsilon \vec{E}^\varepsilon(\varphi^\varepsilon) \,, \end{aligned} \tag{1}$$

where $\mathbb{A}^\varepsilon = (A_{ijkl}^\varepsilon)$ is the elasticity fourth-order symmetric positive definite tensor of the solid, where $A_{ijkl} = A_{klij} = A_{jilk}$, the deformation is coupled with the electric field through the 3rd

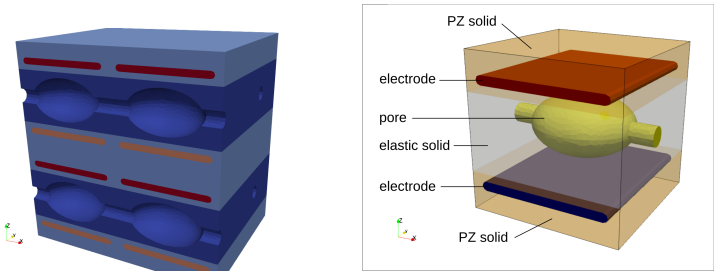

Fig. 1. The periodic microstructure with two electrodes (*left*); the representative unit cell Y (*right*)

order tensor $\underline{\boldsymbol{g}}^\varepsilon = (g^\varepsilon_{kij})$, $g^\varepsilon_{kij} = g^\varepsilon_{kji}$ and $\boldsymbol{d}^\varepsilon = (d^\varepsilon_{kl})$ is the permittivity tensor. The skeleton includes also conducting elastic parts (electrodes) constituting equipotential surfaces. Obviously tensors $\underline{\boldsymbol{g}}^\varepsilon$ and $\boldsymbol{d}^\varepsilon$ vanish in these electrodes which are used to control deformation of the PZ solid, thus, modifying the shape of the pores saturated by an incompressible viscous fluid characterized by the viscosity $\mu^\varepsilon = \varepsilon^2\bar{\mu}$. The fluid flow in the pores is governed by the linearized Navier-Stokes equations. On the fluid-solid interface, standard interaction conditions are prescribed guaranteeing continuity of the velocities and traction stresses of the two-phase medium.

In order to account for the localized electric field control inducing steep electric potential gradients $\approx 1/\varepsilon$, a proper scaling of the PZ material parameters must be considered when passing to the limit $\varepsilon \to 0$, as suggested in [5], such that

$$\underline{\boldsymbol{g}}^\varepsilon(x) = \varepsilon\bar{\underline{\boldsymbol{g}}}\,, \quad \boldsymbol{d}^\varepsilon(x) = \varepsilon^2\bar{\boldsymbol{d}}\,. \tag{2}$$

Homogenized model The limit macroscopic equations obtained for $\varepsilon \to 0$ involve the homogenized coefficients expressed in terms of the characteristic responses which are obtained upon solving the so-called local problems imposed in the representative cell Y, comprised of the solid and fluid parts, see Fig. 1.

The homogenization procedure leads to a model describing the fluid flow in the deforming PZ-poroelastic medium situated in the macroscopic domain $\Omega \subset \mathbb{R}^3$. Due to the non-stationary characteristic flow response , the hydraulic permeability $\boldsymbol{K}^H$ depends on time and constitutes the dynamic Darcy law governing the fluid seepage. The scaling (2) leads to a macroscopic model of a porous medium with a modified constitutive law involving the macroscopic potentials $\bar{\varphi}^k$, $k = 1, \ldots, \bar{k}$ which provide a control handle. The model is represented by following system of equations imposed in a time-space domain, $x \in \Omega$, $t > 0$, involving the macroscopic fields, the displacements $\boldsymbol{u}$, the fluid seepage velocity $\boldsymbol{w}$, and the pore fluid pressure p satisfying

$$\begin{aligned}
&\bar{\rho}\ddot{\boldsymbol{u}} + \rho_f\dot{\boldsymbol{w}} - \nabla\cdot\boldsymbol{\sigma}^H(\boldsymbol{u},p) = \boldsymbol{0}\,,\\
&\qquad \text{where} \quad \boldsymbol{\sigma}^H(\boldsymbol{u},p) = \mathbb{A}^H\boldsymbol{e}(\boldsymbol{u}) - p\boldsymbol{B}^H + \sum_k \boldsymbol{H}^k\bar{\varphi}^k\,,\\
&\boldsymbol{B}^H : \boldsymbol{e}(\dot{\boldsymbol{u}}) + M^H\dot{p} + \nabla\cdot\boldsymbol{w} = \sum_k Z^k\dot{\bar{\varphi}}^k\,,\\
&\qquad \text{where} \quad \boldsymbol{w} = -\int_0^t \boldsymbol{K}^H(t-\tau)[\nabla p(\tau,\cdot) + \rho_f\ddot{\boldsymbol{u}}(\tau,\cdot)]\mathrm{d}\tau\,,
\end{aligned} \tag{3}$$

whereby the voltage potentials $\bar{\varphi}^k(t,x)$, $k = 1, \ldots, k^*$ are assumed to be known functions of time t and macroscopic position x. This model involves homogenized coefficients $\mathbb{A}^H, \boldsymbol{B}^H$,

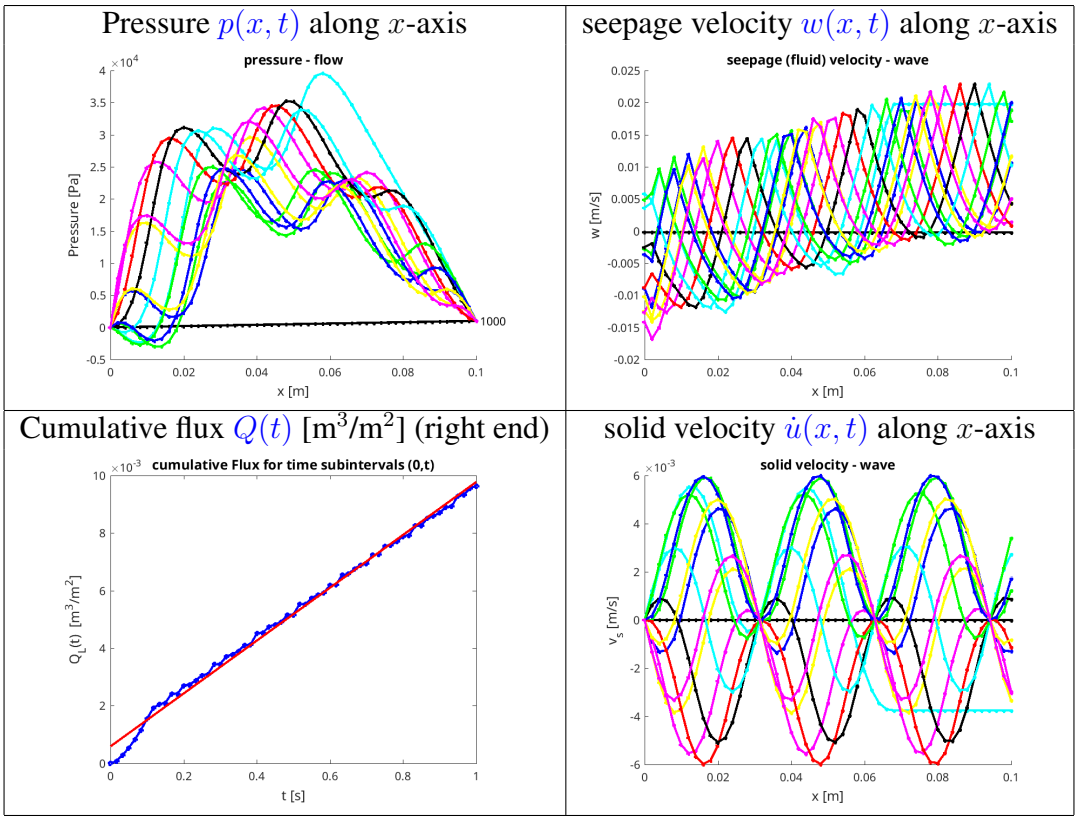

Fig. 2. Characterization of the peristaltic flow in the 1D continuum due the PZ actuation controlled by electric field

$\boldsymbol{K}^H$, M^H, $\underline{Z}$, $\boldsymbol{H}$, further denoted by $\mathbb{H}$ in a generic sense. The inertia effects are pronounced by the terms involving effective densities $\bar{\rho}$ and ρ_f, and also by the dynamic permeability.

Geometrical nonlinearity Since the peristaltic flow is driven by the pore deformation, it is crucial to capture the influence of the deformation on the permeability and other effective model parameters, though it is derived using the linear kinematics framework. As a compromise between the linear modelling leading to model (3) and a fully nonlinear treatment, cf. [2], we suggest to apply the approach proposed in [6] which is based on the domain method of the shape sensitivity analysis of the characteristic responses defining homogenized coefficients $\mathbb{H}$. This enables to introduce perturbed coefficients $\tilde{\mathbb{H}}(\boldsymbol{e}(\boldsymbol{u}), p, \{\bar{\varphi}^k\})$ using the first order expansion formulae which have the generic form applicable to each of the homogenized coefficients,

$$\tilde{\mathbb{H}}(\boldsymbol{e}(\boldsymbol{u}), p) = \mathbb{H}^0 + \delta_{\boldsymbol{e}}\mathbb{H}^0 : \boldsymbol{e}(\boldsymbol{u}) + \delta_p \mathbb{H}^0 p + \sum_k \delta_{\varphi,k}\mathbb{H}^0 \bar{\varphi}^k \ . \tag{4}$$

Although the two-scale problem becomes nonlinear, for a periodic initial configuration all the characteristic responses and the sensitivities are computed for the unperturbed cell Y, thus, independently of the macroscopic solutions.

Numerical illustration To illustrate capability of the material to transport the fluid against the pressure slope, a 1D macroscopic model was considered, whereby the effective material parameters are computed for a 3D microstructure, see Fig. 1, where the skeleton is made of the piezoceramic PZT-5 material. In this example we neglect the inertia effects. A pressure slope $\Delta p = \bar{p}_2 - \bar{p}_1 > 0$ is prescribed, which defines the boundary conditions $p(0,t) = \bar{p}_1$ and

$p(L,t) = \bar{p}_2$ of the 1D homogenized continuum. The reduced 1D model of a prism obtained from (3) due to the symmetry assumptions involves displacement $u = u_1$, seepage $w = w_1$, strain $e(u) = e_{11}(u) = u'$ and voltage φ being functions of (x,t), whereby the prime $()'$ denotes d/dx. Noting that the total stress $\sigma = -\bar{p}_2$ is constant, the following equations hold

$$\begin{aligned} \sigma := Ae(u) - pB + H\varphi &= -\bar{p}_2 \ , \\ M\dot{p} + w' + Be(\dot{u}) &= Z\dot{\varphi} \ , \\ w = -\tilde{K}p' \ , \quad \text{where } \tilde{K}(e,p,\varphi) &= K_0 + \partial_e K_0 e + \partial_p K_0 p + \partial_\varphi K_0 \varphi \ . \end{aligned}$$

Upon eliminating $e(u)$, we obtain the following equation for $p(x,t)$ to be solved for a given the electric potential wave $\varphi(x,t)$,

$$C\dot{p} - (K_0 + \partial_e K_0 A^{-1}\sigma + K_p p + K_\varphi \varphi)p'' + (K_p p' + K_\varphi \varphi')p' = F\dot{\varphi} \ ,$$

where

$$\begin{aligned} C = M + BA^{-1}B \ , \quad F = Z + BA^{-1}H \ , \\ K_p = \partial_e K_0 A^{-1}B + \partial_p K_0 \ , \quad K_\varphi = \partial_e K_0 A^{-1}H + \partial_\varphi K_0 \ . \end{aligned}$$

In Fig. 2, the response is depicted in terms of pressure $p(x,t)$, the fluid seepage velocity $w(x,t)$, the bulk material velocity $\dot{u}(x,t)$ and the cumulative flux $Q(t) = \int_0^t w(0,\tau)\mathrm{d}\tau$ which reveals the pumping effect. The pressure slope was $\bar{p}_2 - \bar{p}_1 = 10^3$ Pa.

Conclusions and perspectives Respecting the geometrical nonlinearity by virtue of the solution-dependent homogenized coefficients of the model is crucial to capture the performance of the peristaltic pump, i.e., a "smart structure" transporting the fluid against the flux due to the pressure gradient. Several issues to be explored in the further research include the control through the potential $\varphi(x,t)$, fully collapsible pores, and the influence of the acoustic wave propagation.

Acknowledgements

The research has been supported by the grant projects GACR 19-04956S and GACR 21-16406S of the Czech Science Foundation, and in a part by the European Regional Development Fund-Project "Application of Modern Technologies in Medicine and Industry" (No. CZ.02.1.01/0.0/0.0/17 048/0007280) of the Czech Ministry of Education, Youth and Sports.

References

[1] Cioranescu, D., Damlamian, A., Griso, G., The periodic unfolding method in homogenization, SIAM Journal on Mathematical Analysis 40 (4) (2008) 1585-1620.

[2] Lukeš, V., Rohan, E., Homogenization of large deforming fluid-saturated porous structures, http://arxiv.org/abs/2012.03730, 2020.

[3] Rohan, E., Modelling large deformation induced microflow in soft biological tissues, Theoretical and Computational Fluid Dynamics 20 (4) (2006) 251-276.

[4] Rohan, E., Sensitivity strategies in modelling heterogeneous media undergoing finite deformation, Mathematics and Computers in Simulation 61 (3-6) (2003) 261-270.

[5] Rohan, E., Lukeš, V., Homogenization of the fluid-saturated piezoelectric porous media, International Journal of Solids and Structures 147 (2018) 110-125.

[6] Rohan, E., Lukeš, V., Modeling nonlinear phenomena in deforming fluid-saturated porous media using homogenization and sensitivity analysis concepts, Applied Mathematics and Computation 267 (2015) 583-595.

COMPUTATIONAL MECHANICS 2021
36th conference with international participation
Srní
November 8 - 10, 2021

Fractional-order model of the Cajal-like interstitial cell

J. Rosenberg, M. Krejčová

NTIS – New Technologies for the Information Society, Faculty of Applied Sciences, University of West Bohemia, Univerzitní 8, 301 00 Plzeň, Czech Republic

1. Introduction

A simple model of the Cajal-like interstitial cells (IC-LC) based on Faville's model [3], see [9]. The comparison of this simulation with the published experimental results [5] has shown the qualitative similarity. The next step in improving this model can be the usage of the fractional-order derivative. The reason is that this derivative can take into account also the history of the whole process. A lot of papers dealing with this topic exist, e.g., [7, 10, 11]. Mainly, this approach is applied to Huxley-Hodgkin (H-H) or FitzHugh-Rinzel (FH-R) neuron model. As the main drawbacks of the models with integer-order derivatives have been stated

1. Dielectric losses in the membrane have been ignored [11].
2. The membrane capacitance has been assumed to be ideal [11].
3. The memory effect is not taken into account [7, 10].

This paper is devoted to missing software development and use it for IC-LC modelling. Here, we try to use fraction-order derivative, not on the conductance but on fluxes [7] or only on the membrane potential like in [11].

2. Short explanation of the fractional derivative

A lot of fractional derivative definitions exist. Here, we introduce the Gruenwald-Letnikov derivative [8]: The derivative of the order 1 and 2 is defined by

$$\frac{\partial}{\partial t} f(t) = \lim_{h \to 0} \frac{f(t) - f(t-h)}{h} \tag{1}$$

and

$$\frac{\partial^2}{\partial t^2} f(t) = \lim_{h \to 0} \frac{f'(t) - f'(t-h)}{h^2} = \lim_{h \to 0} \frac{f(t) - 2f(t-h) + f(t-2h)}{h^2}, \tag{2}$$

respectively.

The generalization on the n-derivative where n is an integer is then

$$\frac{\partial^n}{\partial t^n} f(t) = \lim_{h \to 0} \frac{1}{h^n} \sum_{j=0}^{n} (-1)^j \binom{n}{j} f(t - jh). \tag{3}$$

Without restriction that n be an integer we can define the Gruenwald-Letnikov derivative

$$D^q f(t) = \lim_{h \to 0} \frac{1}{h^n} \sum_{j=0}^{\infty} (-1)^j \binom{q}{j} f(t - jh). \tag{4}$$

For the binomial coefficients, it is necessary to use the Gamma function Γ:

$$\binom{q}{j} = \frac{\Gamma(q+1)}{\Gamma(j+1)\Gamma(q-j+1)}. \tag{5}$$

The meaning of the fractional derivative is not easy to define until now. Maybe, the simplest explanation can be found in [6]:

When q is non-integer then the derivative depends not only on the value of the function $f(t)$ at time t but also on previous values -– this property is called memory. In [6], the so-called Laplacean interpretation is shown. We suppose, the quantity $Y(t)$ depending on the previous values of the function $f(t)$

$$Y(t) = \int_0^t \frac{(t-\tau)^{q-1}}{\Gamma(q)} f(\tau) d\tau. \tag{6}$$

Now, we apply the Caputo derivative on both sides of this equation and the result is

$$D_C^q Y(t) = f(t). \tag{7}$$

Therefore, the memory is obtained in the fractional derivative. A general non-linear fractional system can be written as

$$D^q \mathbf{x} = \mathbf{f}(\mathbf{x}), \tag{8}$$

where $q = [q_1, q_2, \ldots, q_n]^T$ for $0 < q_i < 2, (i = 1, 2, \ldots, n)$ and $x \in \mathbb{R}^n$.

We use the algorithm and code published in [4] for numerical solutions.

3. Short explanation of the stability conditions

According to theorem 4.6 in [8], system stability is given as follows: "When we consider the incommensurate fractional-order system (FOS) $(q_1 \neq q_2 \neq \ldots \neq q_n)$ and suppose that m is the least common multiple of the denominators, u_i's of q_i's, where $q_i = v_i/(u_i;)v_i, u_i \in \mathbb{Z}^+$ for $i = 1, 2, \ldots, n$ and we set $\gamma = 1/m$. The system is asymptotically stable if

$$\mid arg(\lambda) \mid > \gamma \frac{\pi}{2} \tag{9}$$

for all roots λ of the following equation

$$\det(diag([\lambda^{mq_1} \lambda^{mq_2} \ldots \lambda^{mq_n}]) - \mathbf{J}) = 0, \tag{10}$$

where $\mathbf{J} = \dfrac{\partial f}{\partial x}$." For the stability analysis, we could not find the code and therefore spatial code was developed.

4. Fractional-order model of IC-LC

The whole model of IC-LC was described in detail in [9]. It has the form

$$d^q \mathbf{x} = \mathbf{f}(\mathbf{x}; \mu), \tag{11}$$

where $\mathbf{x} = [c, cer, v, w, cmt]$. Parameters c, cer, and cmt are Ca2+ concentrations (M) in the cytoplasm, in ER, and in MT, respectively. Variable v is the membrane potential (mV) and w is the dimensionless help variable. Function $f(x)$ is a vector of the right-side, see [9]. Whereas μ is the vector of control parameters. Like in [9], we use as control parameters the conductance of the voltage-operated calcium channel GCa $\mu\mathrm{M}/(\mathrm{mV} \cdot \mathrm{s})$ and the reverse potential of

the sodium/calcium exchanger zNaCa (mV). This is given with the Goldman-Hodgkin-Katz equation and the Nernst equations [1]

$$zNaCa = \frac{RT}{F}\left(4\ln\frac{|\ Na\ |_e}{|\ Na\ |_i} - \ln\frac{|\ Ca\ |_e}{|\ Ca\ |_i}\right), \tag{12}$$

where R is the gas constant, T absolute temperature, and F Faraday constant. They can be influenced by either nimodipine or change of external Na concentration, respectively. Experiments published in [2] show the decrease of $[Na]_e$ from 130 to 13 mM doubles the frequency of spontaneous Ca2+ oscillations.

To analyze this model, we have used the developed code which allows us to solve commensurate and incommensurate FOS, find its equilibrium points and solve their properties.

As an example, we show the influence of q on the period of the spontaneous oscillation of IC-LC which can be compared with the experiments [5]. In Fig. 1, the situation is set for $GCa = 0.001$ and $zNaCa = -60$. All other data are the same as in [9]. In Fig. 1a, integer-order derivatives are used. In Fig. 1b, there is set $\mathbf{q} = [1\ 1\ 0.95\ 1\ 1]$. The decrease of $\mathbf{q}$ lowers the frequency of the spontaneous oscillations.

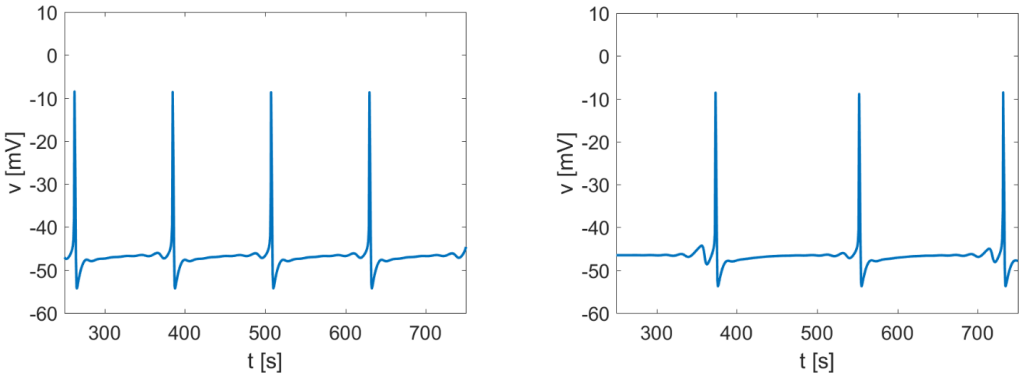

(a) $\mathbf{q} = [1\ 1\ 1\ 1\ 1]$ (b) $\mathbf{q} = [1\ 1\ 0.95\ 1\ 1]$

Fig. 1. Influence of fractional derivate order $\mathbf{q}$ for $GCa = 0.001$ and $zNaCa = -60$

Another example is the modelling of the influence of zNaCa change. In Fig. 2, we can see the situation for $zNaCa = -59$ with the integer-order derivative (Fig. 2a) and with $\mathbf{q} = [1\ 1\ 0.8\ 1\ 1]$ (Fig. 2b). Again, we can see that it is possible to obtain the result comparable with the experiments by changing $\mathbf{q}$.

In all cases, the calculation starts from the equilibrium point. The stability condition in Eq. (8) is not fulfilled. It means, the situation is $|\ \arg(\lambda)\ |_{min} = 0.7129$ and $\gamma\frac{\pi}{2} = 1.579$ in Fig. 2a.

5. Conclusion

The developed software allows the simulation of the spontaneous oscillation of IC-LC using the fractional-order derivative and the stability on the incommensurate systems. The comparison with the experimental results shows the positive influence of this derivative. In further work, we will focus our attention on further parameters tuning and finding the chaotic regions which can correspond with some pathological effects.

Acknowledgements

The work was supported from European Regional Development Fund-Project "Application of Modern Technologies in Medicine and Industry" (No. CZ.02.1.010.00.017_0480007280).

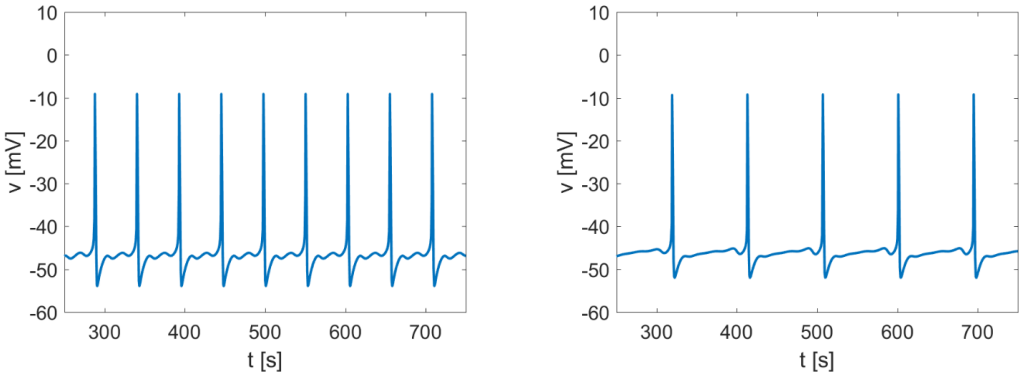

(a) $\mathbf{q} = [1\ 1\ 1\ 1\ 1]$ (b) $\mathbf{q} = [1\ 1\ 0.8\ 1\ 1]$

Fig. 2. Influence of fractional derivate order $\mathbf{q}$ for $GCa = 0.001$ and $zNaCa = -59$

References

[1] Altamirano, F., Eltit, J. M., Robin, G., Linares, N., Ding, X., Pessah, I. N., Allen, P. D., López, J. R., Ca2+ influx via the Na+/Ca2+ exchanger is enhanced in malignant hyperthermia skeletal muscle, Journal Biological Chemistry 289 (27) (2014) 19180-19190.

[2] Bradley, E., Hollywood, M. A., Johnston, L., Large, R. J., Matsuda, T., Baba, A., McHale, N.G., Thornbury, K. D., Sergeant, G. P., Contribution of reverse Na+-Ca2+ exchange to spontaneous activity in interstitial cells of Cajal in the rabbit urethra, The Journal of Physiology 574 (2006) 651-661.

[3] Faville, R. A., Pullan, A. J., Sanders, K. M., Smith, N. P., A biophysically based mathematical model of unitary potential activity in interstitial cells of Cajal, Biophysical Journal 95 (2008) 88-104.

[4] Garrappa, R., Numerical solution of fractional differential equations: A survey and a software tutorial, Mathematics 6 (2) (2018) 1-23.

[5] Kim, S.-O., Jeong, H.-S., Jang, S., Wu, M.-J., Park, J. K., Jiao, H.-Y., Jun, J. Y., Park, J.-S., Spontaneous electrical activity of cultured interstitial cells of Cajal from Mouse urinary bladder, The Korean Journal of Physiology & Pharmacology 17 (6) (2013) 531-536.

[6] Matlob, M. A., Jamali, Y., The concepts and applications of fractional order differential calculus in modeling of viscoelastic systems: A primer, Critical Reviews in Biomedical Engineering 47 (4) (2019) 249-276.

[7] Mondal, A., Sharma, S. K., Upadhyay, R. K., Mondal, A., Firing activities of a fractional-order FitzHugh-Rinzel bursting neuron model and its coupled dynamics, Scientific Reports 9 (2019) No. 15721.

[8] Petras, I., Fractional-order nonlinear systems modeling, analysis and simulation, Higher Education Press, Beijing and Springer-Verlag Berlin Heidelberg, 2011.

[9] Rosenberg, J., Štengl, M., Byrtus, M., Simple model of the Cajal-like interstitial cell and its analysis, Applied Mechanics and Materials 821 (2016) 677-684.

[10] Teka, W., Stockton, D., Santamaria, F., Power-law dynamics of membrane conductances increase spiking diversity in a Hodgkin-Huxley model, PLoS Computational Biology 12 (3) (2016) No. e1004776.

[11] Wardhan, H., Gupta, A., Chowdhury, S. R., Modified Hodgkin-Huxley model using fractional differential equation, Proceedings of the 47th Asilomar Conference on Signals, Systems and Computers, Conference Grounds, Pacific Grove, 2013.

COMPUTATIONAL MECHANICS 2021
36th conference with international participation
Srní
November 8 - 10, 2021

Pitfalls and myths when designing from composite materials

M. Růžička[a], O. Uher[b], V. Kulíšek[a]

[a] *Department of Mechanics, Biomechanics and Mechatronics, Faculty of Mechanical Engineering, Czech Technical University in Prague, Technická 4, Praha 6, Czech Republic*
[b] *CompoTech Plus s.r.o., Nová 1, Sušice, Czech Republic*

1. Introduction

Designers, computational engineers and technologists of mechanical equipment consider with responsibility many requirements and apply a number of criteria in designing and assessing the loading capacity of particular components of machines. Most machines and equipment designed in the last two centuries were made of metals. Their physical and mechanical properties can be generally considered as isotropic. For centuries design processes were developed and design know-how accumulated. The view, however, remained unchanged – it worked with metals and established itself in the minds of designers - "isotropic thinking". This view, unfortunately, predominates until now, when we can design parts with a controlled orientation of the load-bearing components, for example fibres or structural elements.

The rapid outset of development and use of composite materials in the last decades of the previous century caught the designers as well as the technologists unprepared to change their way of thinking. However, the designer who uses composite materials (we will here focus on long fibre composites used for primary structures and principal structural elements) is provided with a much broader range of structural options, [1]. Today we already know that the mere substitution of a metallic material with a composite is not enough. Often good application results were not obtained even with optimized designs of composite components which replaced the original one in the remaining all-metallic structure. And this is when then the discussed "myths about composites" started to appear.

The optimized properties and effectivity of fibre composites and implementation of their "academic advantages" can be fully applied only in an absolutely new and comprehensive structural design. This paper should help the traditional designer to gain courage to apply new composite materials, to get rid of thinking in the "isotropic dimension" and not succumb to uninterpretable myths which often accompany composite applications.

2. Can be composite structures so strong and tough as traditional metallic ones?

Indeed, such results in the history of the development and use of composites were arrived at by a number of companies, since by the mere replacement of the metallic material the required equivalents were not reached, e.g. stiffness and strength, [2]. Table 1 gives a comparison of selected physical and mechanical properties and prices of most current classical materials and basic types of fibres (HS – high strength, HM – high modulus, UHM – ultra high modulus fibres) and matrices most frequently used for the construction of long fibre composite structures, [3-5]. This table shows the known fact, that e.g. glass fibres have a potential to equal aluminium alloys in the longitudinal Young modulus E_x and also in strength. Carbon fibres reach in these parameters even much higher values than e.g. high strength steel. A bonus brought by composites is considerably lower specific mass ρ

compared with metals. If for example we should design a beam (here according to Fig. 1 with a rectangular profile $b \times h$) with a given bending stiffness k and concurrently minimize its mass, we would have to choose a material with the lowest ρ/E ratio), as follows from Equation 1.

Table 1. Comparison of selected physical and mechanical properties and material prices

Material	Density	Longitudinal Modulus	Transverse Modulus	Shear Modulus	Ultimate Strength Tension (T) Compresion (C)	Relative Price
	ρ	E_x	E_y	G_{xy}	R_m	P
	kg.m^{-3}	GPa	GPa	GPa	MPa	€/kg
Steel	7850	210	210	80	500…2000	0.5
Aluminum alloys	2690	71	71	27	360…470	1.9
Ductile Iron	7100	169	169	66	500…800	1.3
Gray Iron	7100	130	130	51	55 (T) 140 (C)	1.5
Mineral Casting	2400	40	40	15	12 (T) 120 (C)	2...5
Standard Carbon fibre	1760	230	40	60	3550	10
HS Carbon f.	1800	310	15	50	5550	40
HM Graphite f.	2120	350	6	10	3800	50
UHM graphite f.	2170	780	5	20	4200	60
E-Glass	2580	78	78	30	3450	2
S-Glass	2460	87	87	38	4580	15
Aramide Fiber	1440	110	5	12	3600	25
Epoxide matrix	1200	3...4.5	3...4.5	1.6	70 (T) 180 (C)	12

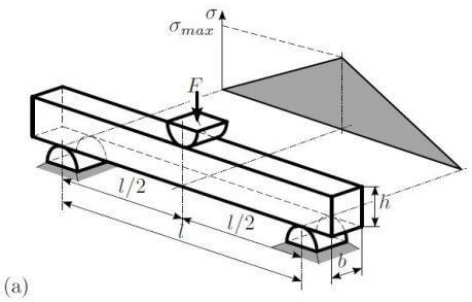

Fig. 1. Configuration of the specimen for the three-point bending test

$$J = \frac{1}{12} b \cdot h^3 = \frac{h^2}{12} A; \quad k = \frac{48\ EJ}{l^3}; \quad m = A \cdot L \cdot \rho = \frac{1}{4} k \cdot l \cdot \frac{\rho}{E} \tag{1}$$

3. Are composite structures expensive in relation to new benefits?

The value of the ratio ρ/E can even be by one order more appropriate for a carbon composite than for steel. On the contrary in other quantities given in the table, namely the shear elastic modulus G or the relative price, composite fibres seemingly cannot compete with metals. The utility properties and price of a composite component are specified by a more comprehensive combination of factors, namely optimum structure, used semiproducts and technology of their processing, selection of the type and orientation of the fibres in the structure, their part by volume and a number of other parameters. This gives a broad range of application of sophisticated procedures (analytical and numerical methods and optimizations) how to obtain various concepts which differ from one another which can observe the required criteria on a different level. The range of the covered parameters is e.g. in Table 2, which shows the

properties of five types of laminates made of various types of carbon fibres with various layer orientations. The table shows a theoretical example how to alternate types of fibres and orientations in a such a way that the resulting stiffness moduli can reach equivalence with those of classical materials (even in shear stiffness), or to reach even considerably higher stiffness parameters (e.g. by applying UHM fibres).

As the comparison of relative prices in Table 2 shows, the use of composites will lead to higher material costs. In a comprehensively conceived, e.g. all-composite concept, or in a specially designed composite structure, the newly gained utility properties must prevail over the purchase costs. For example, the temperature stability of dimensions can be reached by using layers with a zero thermal expansion coefficient or the effect of the thermal source can be eliminated by a structure of layers with low thermal transmittance. Such designs would be difficult to put into practice by application of the classical "metallic design". We often use the possibility to increase eigenfrequencies, and to increase damping of the composite structure (e.g. machine tool slides). The low masses of structures of e.g. manipulators, makes it possible to increase the dynamics of motions and thus to increase the cycle time on production lines with a consequent rapid returnability of costs. Further by applying sufficiently tough and long composite shafts the structure can be simplified and its cost reduced (less bearings in the supports of long rotating drives and in couplings between individual sections of the long shaft). A lot of other examples of the effective use of composites can be mentioned.

Table 2. Comparison of properties and prices of classical materials and typical carbon laminates

Material	Density	Longitudinal Modulus	Transverse Modulus	Shear Modulus	Thermal expansion	Thermal conductivity	Relative Price
	ρ	E_x	E_y	G_{xy}	α_x	λ_y	P
	$kg.m^{-3}$	GPa	GPa	GPa	$10^6.K^{-1}$	$W.m^{-1}.K^{-1}$	€/kg
Steel	7850	210	210	80	13	50	0.5
Aluminum alloys	2690	71	71	27	22	205	1.9
Gray-iron	7050	169	169	66	10	55	1.5
HS C/E: Unidirectional	1550	203	8,2	4.3	0.9	0.5	20
HS C/E: 0/90	1550	106	106	4.3	3.1	2.8	20
UHM C/E: Unidirectional	1750	470	4.8	3	-1.1	10	60
UHM C/E: 0/90	1750	237	237	3.6	-0.4	195	60
UHM C/E: 45/-45	1750	13.8	13.8	118			60

4. How can we improve the weakest link in the composite structure – joints?

In complicated equipment there is only a small change that the entire structure could be an all-composite one or in "one piece". Usually we must count with a composite-metal or composite-composite "interface" or "join" the composite component with other elements of the structure. Even in classical metallic structures it holds that most joints (whether screwed, riveted, pressed-on or welded) cause local concentration of deformation and stress and are potential points for the creation of fatigue cracks (e.g. during cyclic loading) or locally weaken the point even for static loads. However even the best optimization of the composite structure can be ineffective, if the designer is not able to tackle with the transfer of load over the composite-metal or composite-composite interface. The development of various types of production technologies was accompanied by the development of various types of joints (mechanical joining – screwing, riveting, gluing and their combinations). The development of new types of glues makes it possible to design sufficiently strong joints. Composites with a

thermoplastic matrix can be joined also by welding. Special "composite" methods of joining are developed, e.g. so-called stitching (multi-pin joining or z-pinning) of a 3D composite fabric, etc. So-called integrated joints can also be included in the assortment of specific joints of wound composite structures. They utilize load bearing longitudinal fibre bundles to create e.g. an assembly eye which embraces another composite or metallic component as shown in Figure 2. Also these joints are characterized by high strength and life.

(a) (b)

Fig. 2. Finite-element model (a); real part of the integrated composite joint at the end of a carbon fibre composite rod (b)

5. Conclusion

The portion of new types of materials including composites in mechanical engineering will even in future surely grow. What is important for their functional application and reliable operation is the profound knowledge of their properties and inventive utilization of their potential in connection with sophisticated designing and production technologies. Also important is a correct balance-sheet of their use from the aspect of the entire life cycle of the structure. Only then will deep-rooted myths begin to disappear, myths which more likely represent the traditional views of designers including the discussed "isotropic thinking".

Acknowledgements

This publication was created within the project Center for Advanced Aeronautical Technologies, Reg. No. CZ.02.1.01 / 0.0 / 0.0 / 16_019 / 0000826, which is co-financed by the European Regional Development Fund through the Operational Program Research, Development and Education. The authors would like to thank the Technology Agency of the Czech Republic for supporting of one part of this research with the projects No. FW01010450.

References

[1] Ashby, M.F., Material selection in mechanical design, Butterworth-Heinemann, Oxford, 1999.

[2] Tsai, S.W., Strength and life of composite, Department of Aeronautics and Astronautics, Stanford University, Stanford, United States of America, 2008, pp. 1-672.

[3] Mitsubishi Chemicals, Pitch-based Carbon Fiber DIALEAD. Japan: Mitsubishi Chemical Corporation, (2019-06-28). https://www.m-chemical.co.jp/en/products/departments/mcc/cfcm/product/1201229_7502.html

[4] Nippon graphite fiber corporation, Granoc yarn XN series, Japan: Nippon graphite fiber corporation, (2018-01-13), pp. 1-2. http://www.ngfworld.com/dcms_media/other/skill_skill02.pdf

[5] Toray industries, Inc. Torayca carbon fibres, Japan: Toray industries, Inc., 2005 (2019-03-12), pp. 1-3. http://www.torayca.com/en/download/pdf /torayca.pdf

COMPUTATIONAL MECHANICS 2021
36th conference with international participation
Srní
November 8 - 10, 2021

Planar and spatial active absorbers for entire vibration suppression

Z. Šika[a], K. Kraus [a], Z. Neusser[a], J. Krivošej[a], T. Vyhlídal[a]

[a] *CTU in Prague, Faculty of Mechanical Engineering, Technická 4, 160 00 Praha 6, Czech Republic*

Vibration plays an important role in many engineering applications and often needs to be eliminated. These problems occur with machine tools, where vibrations can affect the workpiece surface quality, with turbine rotors for different applications, in precise instruments such as electron microscopes, deep space telescopes, particle detectors, etc. Vibration compensation is a big task also in control of flexible robots [4], considering classical serial industrial robots, micromanipulation assembly lines (e.g., in microchip production), or high precision surgery robots.

The idea of passive vibration absorber connected to the primary mechanical structure to suppress its vibrations is known and patented for approximately one hundred years. The main benefit of this passive approach is that no (or minimal) energy needs to be exerted to damp the oscillations. The active versions of vibration absorption concept (Fig. 1) however significantly improve its efficiency. There is a lot of ways of control algorithm design. One specific alternative is a Delayed Resonator (DR) approach [2], [6], [7] – an active vibration absorber with delayed feedback from the position, velocity or acceleration measurements. Subsequently, applying delayed feedbacks, the physical absorber is turned to the ideal absorber at the given frequencies. For many such systems the vibration-affected parts of the structure are also the most inaccessible for a variety of reasons. For example, we cannot place an active vibration absorber at the tip of the cutting tool in machining or at the end-point of micro-manipulator of a surgery robot. This leads to the usage of non-collocated vibration absorption concept [3].

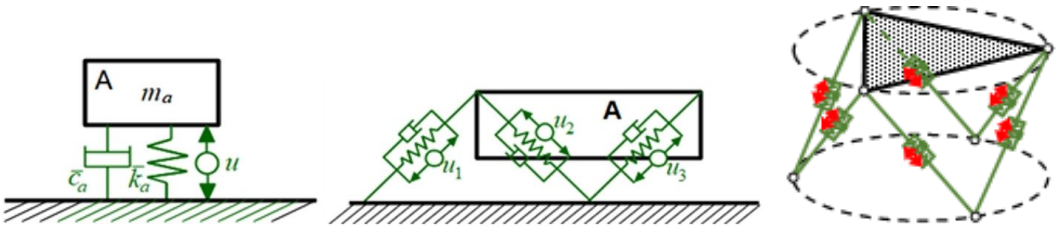

a) 1 DOF active absorber [5] b) 3 DOF active planar absorber [5] c) 6 DOF active spatial absorber

Fig. 1. Active absorbers of different dimensionality

In the case of application of active absorbers to planar or spatial robots and manipulators, the basic question is whether it is more efficient to use several 1 DOF (Fig. 1 a)) absorbers, or one compact planar or spatial variant (Fig. 1 b), c)). Investigation of this question shows, that one multi-DOF absorber typically needs less mass in total to achieve the same absorption ability than multiple 1-DoF absorbers do. One multi-DOF absorber also seems more advantageous given that we have one removable compact device for various directions and modes. The multi-DOF active absorber is generally considered in the form

$$\mathbf{M}\ddot{\mathbf{X}}_a(t) + \bar{\mathbf{C}}\dot{\mathbf{X}}_a(t) + \bar{\mathbf{K}}\mathbf{X}_a(t) = \mathbf{L}\mathbf{U}(t), \tag{1}$$

where $\mathbf{U} = [u_1, u_2, \ldots, u_n]^T$ is vector of action forces, and $\mathbf{L}$ provides the projection of the action forces to the absorber coordinates. By introducing the set of delayed feedback rules, the active absorber is transformed from (1) to a time delay system of retarded type with *n* delays

$$\mathbf{M}\ddot{\mathbf{X}}_a(t) + \bar{\mathbf{C}}\dot{\mathbf{X}}_a(t) + \bar{\mathbf{K}}\mathbf{X}_a(t) + \sum_{i=1}^{n} \mathbf{G}_i \mathbf{X}_a(t-\tau_i) = 0\,. \tag{2}$$

For the final use on a robotic arm moving in a workspace, the basic control law must be formulated as position-dependent. This applies to delayed resonators as well other ways [7].

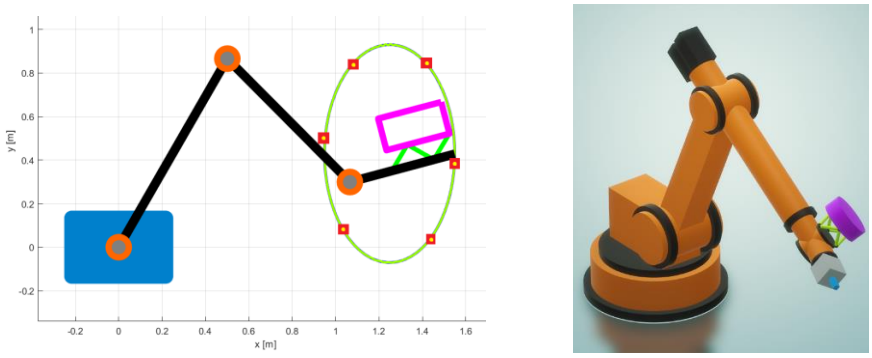

a) planar variant [1] b) spatial variant

Fig. 2. Compact multi-DOF active absorbers on serial robots

The position sensors (incremental encoders) parallel with voice-coils are considered for relative motion sensing in the multi-DOF absorbers cases. The main advantage over accelerometers is lower noise and direct collocation between measurement and active force. The voice-coils are considered for actuators, since they are easily capable of dozens of millimeters motion. Above all, however, compared to piezoactuators, they have zero initial stiffness between moving bodies, thus the eigenfrequencies can easily be tuned by parallel springs. A final absorber design is a multi-criteria optimization task, involving the structural, stability and implementation aspects.

Acknowledgements

The work has been supported by the Czech Science Foundation project GA21-00871S “Active non-collocated vibration absorption for robots and mechanical structures”.

References

[1] Kraus, K., Šika, Z., Beneš, P., Krivošej, J., Vyhlídal, T., Mechatronic robot arm with active vibration absorbers, Journal of Vibration and Control 26 (13-14) (2020) 1145-1156.
[2] Olgac, N., Holm-Hansen, B., A novel active vibration absorption technique: delayed resonator, Journal of Sound and Vibration 176 (1994) 93-104.
[3] Olgac, N., Jenkins, R., Time-delayed tuning of vibration absorbers for non-collocated suppression, American Control Conference (ACC) (2020) 1381-1386.
[4] Shabana, A.A., Bai, Z., Actuation and motion control of flexible robots: small deformation problem, Journal of Mechanisms and Robotics (2022.) 1-41.
[5] Šika, Z., Vyhlídal, T., Neusser, Z., Two-dimensional delayed resonator for entire vibration absorption, Journal of Sound and Vibration 500 (2021) 116010.
[6] Valášek, M., Olgac, N., Neusser, Z.. Real-time tunable single-degree of freedom, multiple-frequency vibration absorber, Mechanical Systems and Signal Processing 133 (2019) 106244.
[7] Vyhlídal, T., Anderle, M., Bušek, J., Niculescu, S., Time-delay algorithms for damping oscillations of suspended payload by adjusting the cable length, IEEE/ASME Trans Mechatron 22 (5) (2017) 2319-2329.

COMPUTATIONAL MECHANICS 2021
36th conference with international participation
Srní
November 8 - 10, 2021

Behaviour of the rail load parameter B defined by the standard EN 14363

J. Šlapák

Faculty of Transport Engineering, University of Pardubice, Studentská 95, 532 10 Pardubice, Czech Republic

1. Introduction

The mechanical system of railway vehicle running on the rails is a very complicated system with many bodies and also degrees of freedom. Probably the vehicle/track interaction is the most important part of this system and the forces acting on wheel/rail contact area are the most watched quantities of the whole mechanical system. This is confirmed, for example, in standard EN 14363 [1] which deals with testing and simulation of railway vehicles for their approval. Vertical wheel forces, lateral guiding forces or their combination are the main quantities used in this standard. Among other things, the standard describes the conditions for testing of rail load during railway vehicle running.

This paper is focused on the evaluation methods of a rail load according to the standard EN 14363. The standard takes into account the fundamental forces acting on wheel/rail contact area for evaluation of the rail load. For this evaluation, the limit values of quantities and test conditions are defined. But the standard also mentions the new quantities and parameters for this evaluation. These parameters that will be discussed in this paper are

- quasi-static rail load parameter $B_{a,qst}$,
- maximum rail load parameter B_{max}.

The other two parameters listed in the standard are the maximum guiding force and the rail surface damage parameter.

In order to determine the behaviour of the rail load parameters, multi-body simulations of railway vehicle running can be performed then it is possible to export and process records of required quantities.

2. Rail load evaluation according to EN 14363

Standard EN 14363 [1] defines the assessed quantities for running behaviour of railway vehicles. The quantities are used for evaluation of the vehicle/track interaction and describe the dynamics of the wheel/rail contact. It is possible to obtain reference values of these quantities as an output of multi-body simulations.

One of the fields covered by the standard is the evaluation of the track load. The assessment quantities are monitored and evaluated. For the evaluation of the rail load, the quasi-static guiding force Y_{qst}, quasi-static vertical wheel force Q_{qst} and maximum vertical wheel force Q_{max} are considered in this standard. The values of all these quantities are compared with their limit values. Both are listed in Table 1. The standard [1] sets the limit value for quasi-static

Table 1. Assessment quantities and their limit values for rail load evaluation according to the standard EN 14363 [1]

Assessment quantity	**Limit value**
quasi-static guiding force Y_{qst}	60 kN
quasi-static vertical wheel force Q_{qst}	145 kN for $P_{F0} \leq 225$ kN 155 kN for 225 kN $< P_{F0} \leq 250$ kN
maximum vertical wheel force Q_{max}	MIN(90 kN + Q_0; 200 kN) for vehicle speed $\leq$ 160 km/h

vertical wheel force $Q_{a,qst}$ under the condition of axle load P_{F0} value, which is defined as

$$P_{F0} = Q_1 + Q_2, \tag{1}$$

where Q_1 and Q_2 are vertical wheel forces of one wheelset. The limit value of maximum vertical wheel force Q_{max} is defined as smaller value of the two options mentioned. The sign Q_0 represents static vertical wheel force. This limit value only applies to vehicle speeds of 160 km/h or less. Higher vehicle speeds are not considered in this paper.

According to the ERA technical document [2], the values of quasi-static guiding force Y_{qst} are normalized by the relation

$$Y_{R,qst} = Y_{qst} - \left(\frac{10500}{R} - 30\right), \tag{2}$$

where R is the curve radius. This applies to curves of very small radii. However, for a curve radius of 350 m, the value calculated according to Eq. (2) is the same as the value without normalization.

According to the informative Annex J of the standard [1], the task of these quantities (see Table 1) is to control the following phenomena:

- rail internal fatigue, due to bending stresses in the rail,
- abrasive wear of rail,
- surface fatigue of the rail top due to high contact force,
- failure of fastening components due to high lateral forces or torsion moment.

However, it turns out that the quantities are not able to sufficiently represent these phenomena. This is the reason, why the additional parameters have been used in some countries. The additional parameters are following:

- maximum guiding force Y_{max},
- quasi-static and maximum rail load parameter B_{qst}, B_{max},
- track loading assessment quantity (Y/Q).

All these parameters are evaluated only for the outer rail in the curves.

The rail load parameters B were designed in the context of the demand for better evaluation of bending stress of rails. This two parameters are defined according to the standard [1] as

$$B_{qst} = |Y_{qst}| + 0.83 \cdot Q_{qst}, \tag{3}$$

$$B_{max} = \left(|Y| + 0.91 \cdot Q\right)_{max}. \tag{4}$$

For example in the standard UIC 518 [3], the quasi-static rail load parameter B_{qst} is defined as

$$B_{qst} = |Y_{qst}| + 0.83 \cdot Q_{qst} + \left[67.5 - \left(30 + \frac{10500}{R}\right)\right], \tag{5}$$

where R is the curve radius. However, for the purposes of this paper, the Equation 3 will be used.

3. Simulation conditions

Simulations of the railway vehicle running were performed in the computer program SIMPACK. A conventional passenger vehicle with 4 axles was considered. In order to obtain different values of the rail load parameter, the values of the vehicle body weight M and the longitudinal stiffness of the secondary spring k_{x2} (stiffness on one side of the bogie) were changed. The specific values of these quantities are listed in Table 2.

For the simulations, a curved track with a radius of 350 m was used. The cant of $D = 150$ mm and the cant deficiency of $I = 130$ mm were considered. This mean that the vehicle speed of $v = 25.3$ m/s was set. In order to consider a real model of the track, reference track irregularities were used and a model of a elastic track foundation was created.

Table 2. Considered vehicle parameters for the simulations

vehicle body weight M	**longitudinal stiffness** k_{x2}
40 tons	0.5 kN/mm
50 tons	1.0 kN/mm
60 tons	1.5 kN/mm
70 tons	2.0 kN/mm

4. Simulation results

The quasi-static rail load parameter B_{qst}, the quasi-static guiding force Y_{qst} and the quasi-static vertical wheel force Q_{qst} were evaluated for the different vehicle design conditions listed in Table 2. These values were calculated as the mean values of the time records of these quantities on a 300 m long curved track.

Dependences of all these quantities on longitudinal stiffness of secondary suspension on one side of bogie for different values of vehicle body weight are shown in Fig. 1. These quantities are calculated and plotted only for the first outer wheel of the vehicle. The black lines shown in the graphs indicate the limit values of the stated quantities. The limit value of the rail load parameter B_{qst} was calculated according to Eq. (3) where the limit values of guiding and vertical forces were set, therefore:

$$B_{qst,lim} = |Y_{qst,lim}| + 0.83 \cdot Q_{qst,lim}, \tag{6}$$

$$B_{qst,lim} = |60| + 0.83 \cdot 145 = 180.35\ kN. \tag{7}$$

Fig. 1 shows that the behaviour of the rail load parameter B_{qst} is similar to the behaviour of the vertical wheel force Q_{qst}. The best examples of the behaviour of the rail load parameter are the vehicle design with the highest values of longitudinal stiffness k_{x2} and the vehicle body weight of 40 and 50 tons. Because vehicles with these conditions meet the requirement of the rail load parameter B_{qst} but do not meet the requirement of guiding force Y_{qst}. Therefore, these

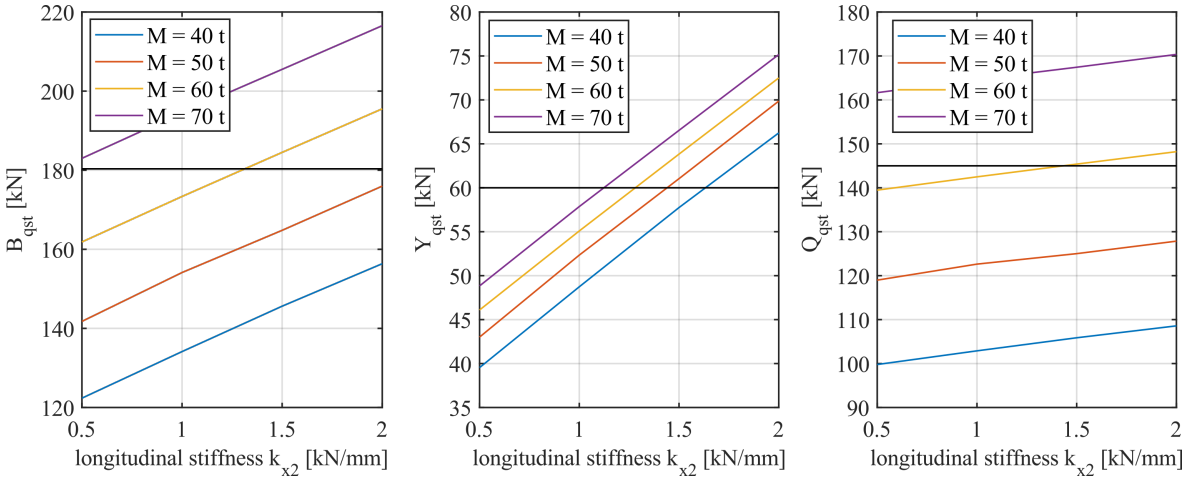

Fig. 1. Dependence of the rail load parameter B_{qst} (*left*), guiding force Y_{qst} (*middle*) and vertical wheel force Q_{qst} (*right*) on longitudinal stiffness k_{x2} of the secondary suspension for different vehicle body weights; the black lines represent limit values

vehicles do not comply according to the original evaluation method, but they comply according to the new method of evaluation, which uses the combined quantity B_{qst}.

It can be considered that a vehicle with a vehicle body weight of 65 tons and a longitudinal stiffness of secondary suspension $k_{x2} = 0.5$ kN/mm will not meet the requirement of vertical wheel force Q_{qst} but will meet the requirements in terms of rail load parameter B_{qst}.

5. Conclusion

As described above, the rail load parameter B_{qst} allows, under the specific conditions, the approval of vehicles that do not meet one of the original requirements, i.e. the vertical wheel force or the guiding force. This situations are stated in the standard [1] but there is no explanation or example of this behaviour. Therefore, the results of this paper confirm the assumption of this standard.

The second aspect is the dynamic effect of the vehicle on the rails and the rail loads. The requirements of guiding force and vertical wheel force are stricter and safer. The option of the rail load parameter offers the approval of vehicles that do not meet one of the original requirements. Therefore, the safety of using the rail load parameter needs to be further investigated.

Acknowledgement

This work was supported by the scientific research project of the University of Pardubice No. SGS_2021_010.

References

[1] EN 14363:2016+A1:2018. Railway applications – Testing and simulation for the acceptance of running characteristics of railway vehicles – Running behaviour and stationary tests, Brusel, European Commitee for Standardization, 2018.

[2] Running dynamics: Application of EN 14363:2005 – Modifications and clarfications, 3.0. European Railway Agency (ERA), 2014.

[3] UIC 518: Testing and approval of railway vehicles from the point of view of their dynamic behaviour – Safety – Track fatigue – Ride quality, 4th Edition, International Union of Railways (UIC), 2009.

COMPUTATIONAL MECHANICS 2021
36th conference with international participation
Srní
November 8 - 10, 2021

Effects of journal and housing roundness errors on dynamics of journal bearings

L. Smolík

Faculty of Applied Sciences, University of West Bohemia, Univerzitní 8, 301 00 Plzeň, Czech Republic

1. Introduction

In real applications, out-of-roundness errors affect profiles of both rotating journal and stationary bearing housing. The overall errors are random but can be decomposed to macroscopic surface waviness and microscopic surface roughness [3]. The errors on the bearing housing are stationary in a coordinate system fixed to the housing [1]. The errors on the journal, however, cause the bearing gap to be time-variant [3, 5]. The errors can vary in individual cross-sections, which further complicates the model [2]. In general, the surface waviness of the journal with the i-th wave number induces journal movement at the frequency which is i-th multiple to the journal rotating speed [3, 5]. On the other hand, the surface waviness of the bearing housing does not induce super-harmonic vibrations. However, it influences the stability, load capacity and friction coefficient of the bearing [1]. Interestingly, state-of-the-art literature does not deal with the interaction of the waviness of both journal and housing surfaces.

2. Methods

Let us assume a rigid journal of effective mass m, which rotates at *constant* angular speed ω and is supported on a journal bearing. If the angular misalignment of the journal is negligible, its motion is described by the equation

$$\begin{bmatrix} m & 0 \\ 0 & m \end{bmatrix} \begin{bmatrix} \ddot{y} \\ \ddot{z} \end{bmatrix} = -\iint\limits_{(s,\,x)} \begin{bmatrix} p\,\cos\left({}^{s}/_{r_s}\right) \\ p\,\sin\left({}^{s}/_{r_s}\right) \end{bmatrix} \mathrm{d}s\,\mathrm{d}x, + \begin{bmatrix} U\,\omega^2\,\cos\left(\omega\,t\right) \\ U\,\omega^2\,\sin\left(\omega\,t\right) \end{bmatrix} + \begin{bmatrix} -m\,g \\ 0 \end{bmatrix},$$

where $y = y(t)$, $z = z(t)$ are lateral displacements and s, x are circumferential and axial coordinates related to the bearing shell of nominal radius r_s. Function $p = p(s,\, x,\, t)$ describes the hydrodynamic (HD) pressure generated in the oil film due to the relative motion of the journal to the shell, U is the static unbalance of the journal, and g is the gravitational acceleration.

An exact form of an equation governing the HD pressure depends on simplifying assumptions. For the laminar flow of an isoviscous incompressible Newtonian fluid in a bearing gap with smooth surfaces, the governing Elrod equation reads [4]

$$\frac{\partial}{\partial s}\left(\frac{\theta\,h^3}{12\,\mu}\,\frac{\partial p}{\partial s}\right) + \frac{\partial}{\partial x}\left(\frac{\theta\,h^3}{12\,\mu}\,\frac{\partial p}{\partial x}\right) = \frac{\omega\,r_j}{2}\,\frac{\partial\left(\theta\,h\right)}{\partial s} + \frac{\partial\left(\theta\,h\right)}{\partial t},$$

where $\theta = \theta(s,\, x,\, t)$ is a fill ratio, which is unknown in areas where $p \leq 0$, and is equal 1 otherwise. Constants μ, r_j are the oil dynamic viscosity and the nominal journal radius, respectively, and $h = h(s,\, t)$ characterizes the bearing gap. The geometry of a profile affected by

roundness errors can be described with the use of the Fourier transform [3]. After neglecting terms dependent on the square of eccentricity e^2, the bearing gap can be approximated with

$$h \approx c_r - e\cos\left({}^{s}\!/_{r_s} - \phi\right) - \sum_{i=2}^{N} \Delta_{s,i} \cos\left[k_{s,i}\left({}^{s}\!/_{r_s} - \gamma_{s,i}\right)\right] - \sum_{i=2}^{N} \Delta_{s,i} \cos\left[k_{j,i}\left({}^{s}\!/_{r_s} - \gamma_{j,i} - \omega\, t\right)\right],$$

where c_r is the radial clearance and eccentricity e and attitude angle ϕ are shown in Fig. 1. Parameters $k_{s,i},\ k_{j,i}$ are shell and journal wave numbers, respectively, $\Delta_{s,i},\ \Delta_{j,i}$ are magnitudes of the i-th waves (harmonic components) and $\gamma_{s,i},\ \gamma_{j,i}$ are phase shifts of the i-th wave.

3. Results

Vibration due to the interaction of waviness of both journal and housing surfaces is analysed in this section. In a real system, the Fourier transform of roundness errors describes the bearing gap with a sum of many waves. To simplify the interpretation of the results, only combinations of one wave at the journal profile with one wave at the shell profile are tested. Both waves have the same magnitude – 15 % of the radial clearance – and the phase shifts are neglected for simplicity. The resulting responses of the system with parameters introduced in Table 1 are shown in Figs. 2 and 3. The response is analysed in the interval $\langle 1,\ 3\rangle\ s$ using the fast Fourier transform (FFT). Hence, the transient response to the initial conditions is omitted.

The bearing in a reference state, i.e. with no surface waviness, is susceptible to a period-doubling, which is apparent as a response at $0.5X$. The period-doubling is magnified by the static unbalance and often precedes the oil-induced instability or is forced by this instability. The shell waviness can suppress the period-doubling with wave numbers $k_s = 2,\ 3,\ 4$. In the case of $k_s = 5$, the bearing is presumably unstable with a dominant response at $0.47X$.

The period-doubling motion is allowed also if the shell is circular ($k_{s,i} = 0$) and the journal is elliptic ($k_j = 2$). The journal waviness with higher wave numbers attenuates the period-doubling motion. However, the journal waviness excites super-harmonic vibrations at the frequency equal to $k_j\,\omega$. The highest magnitude is reached if $k_j = 2$ and decreases with increasing wave number k_j. The journal waviness with $k_j = 5$ induces almost no vibrations.

Some journal and shell waviness combinations tend to magnify the super-harmonic vibrations, with the most prominent being $k_j = 2$ with $k_s = 3$. The shell waviness with odd wave numbers magnifies the induced vibrations more than waviness with even wave numbers.

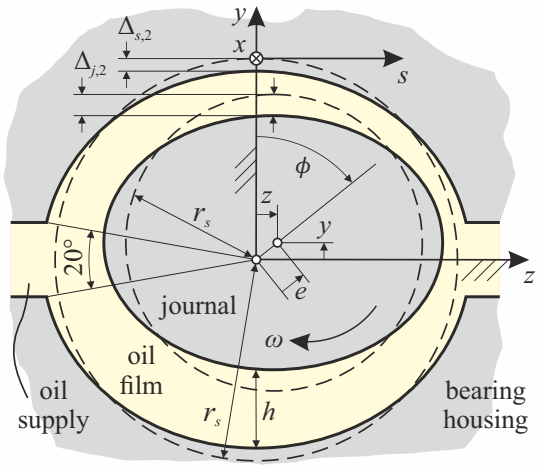

Fig. 1. Scheme of a tested bearing

Table 1. Parameters of the tested bearing

Parameter	*Unit*	*Value*
bearing diameter	[mm]	70
bearing length	[mm]	70
radial (half) clearance	[μm]	79.8
wave magnitude $\Delta_{j,i}$	[% of c_r]	15
wave magnitude $\Delta_{s,i}$	[% of c_r]	15
test speed	[rpm]	6000
static load	[N]	1000
oil viscosity	[mPa s]	12.3
supply pressure	[bar]	1.5
ambient pressure	[bar]	0

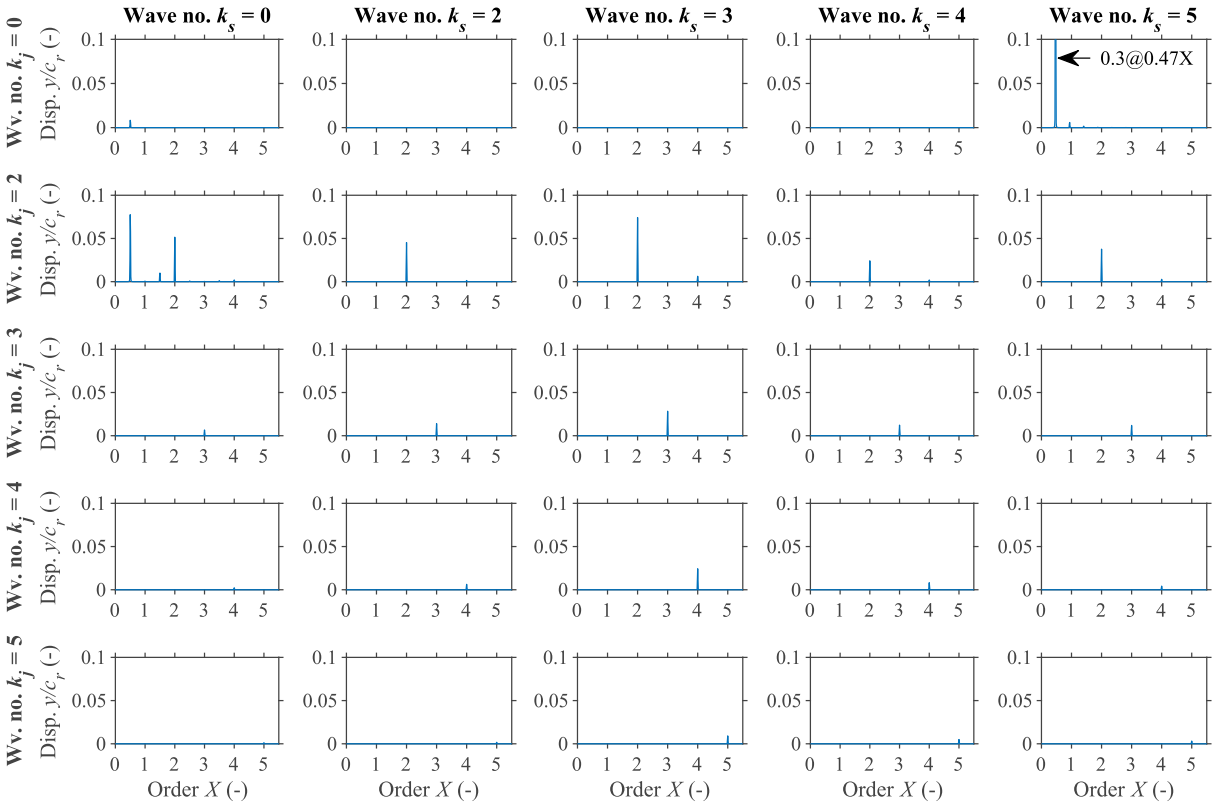

Fig. 2. Frequency spectra of vertical displacements of a perfectly balanced journal

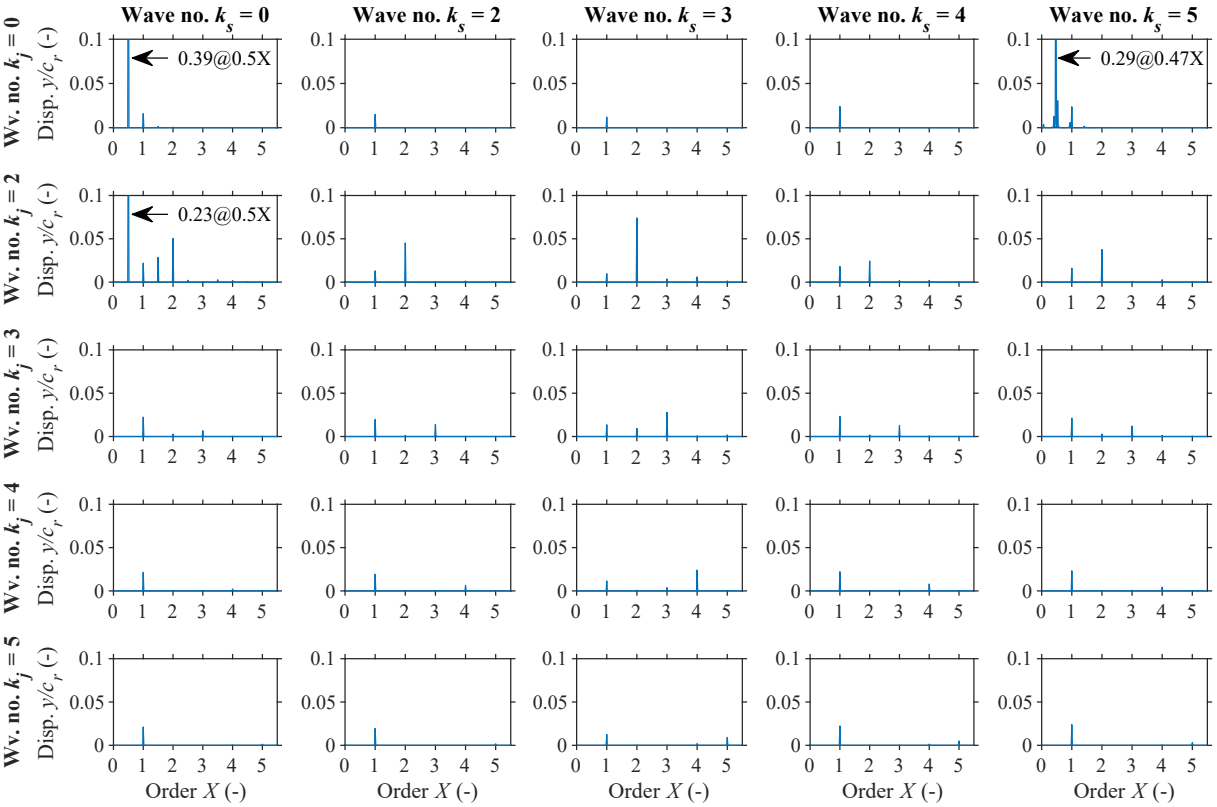

Fig. 3. Frequency spectra of vertical displacements of an unbalanced journal ($U = 217\,\mathrm{g\,mm}$)

The static unbalance has only a negligible influence on the super-harmonic vibrations. However, it affects the speed at which period-doubling bifurcations occur and the speed at which the system loses its stability.

4. Conclusions

This work presents results of simulations for the journal bearing with roundness errors of both journal and shell profiles, which are introduced as surface waviness. Various combinations of one wave at the journal profile and one wave at the shell profile are analysed in the concrete.

It is demonstrated that the waviness of the rotating surface induces super-harmonic vibration at a frequency equal to multiple of wave number k_j and angular speed ω. Although the waviness of the stationary surface does not excite any super-harmonic vibration, waves with odd wave numbers magnify the vibration induced by the rotating surface. The highest magnification has been found for the combination of stationary wave $k_s = 3$ and rotating wave $k_j = 2$. Interestingly, the rotating unbalance affects the super-harmonic vibration due to the surface waviness only negligibly. Furthermore, the waviness of the stationary surface influence the period-doubling bifurcations and stability of the system. However, a more detailed description of these effects would require a more comprehensive study.

Acknowledgement

Simulations would not be possible without the AVL Excite software, which is available in the framework of the University Partnership program of AVL List GmbH and whose usage is greatly acknowledged.

References

[1] Hassan, E. R., Effect of surface waviness on the hydrodynamic lubrication of a plain cylindrical sliding element bearing, Wear 223 (1-2) (1998) 1-6.

[2] Li, B., Zhou, D., Ogrodnik, P., Xu, W., Effect of journal cylindricity error with saddle or drum distribution on the performance of hydrodynamic journal bearing systems, Proceedings of the Institution of Mechanical Engineers, Part J: Journal of Engineering Tribology 234 (7) (2020) 1092-1105.

[3] Li, B., Zhou, D., Xu, W., Zhang, Y., Effect of random roundness error on the stability of a hydrodynamic journal bearing system – part I: Theoretical study, Advances in Mechanical Engineering 11 (4) (2019) 1-17.

[4] Lorenz, N., Offner, G., Knaus, O., Thermal analysis of hydrodynamic lubricated journal bearings in internal combustion engines, Proceedings of the Institution of Mechanical Engineers, Part K: Journal of Multi-body Dynamics 231 (3) (2017) 406-419.

[5] Xu, W., Ogrodnik, P.J., Li, B., Zhang, H., Gao, S., Effect of journal out-of-roundness on stability of a symmetric hydrodynamic journal bearing system. Part 1: Theoretical analysis, Proceedings of the Institution of Mechanical Engineers, Part J: Journal of Engineering Tribology 229 (11) (2015) 1347-1358.

COMPUTATIONAL MECHANICS 2021
36th conference with international participation
Srní
November 8 - 10, 2021

Numerical and experimental investigation of the flow field in five blade linear cascade in subsonic flow

P. Šnábl[a], S. Chindada[a], O. Bublík[b], P. Procházka[a], C. S. Prasad[a]

[a] *Institute of Thermomechanics of the CAS, v. v. i., Dolejškova 1402/5, 182 00 Praha 8, Czech Republic*
[b] *Faculty of Applied Sciences, University of West Bohemia, Univerzitní 8, 301 00 Plzeň, Czech Republic*

In large steam turbines, last stage blades are very long and must be designed very thin and with no shroud to minimize the centrifugal force which leads to low eigenfrequencies and low structural damping. In this case, aero-elastic damping plays important role on last stage bladed disc's dynamics. Three major aero-elastic issues found in turbomachinery as described in [2] are forced response, non-synchronous vibrations, and flutter. Flutter is an unstable, self-excited vibration resulting from coupling between the structural vibrations and unsteady aerodynamic forces. It is clear that this unstable behaviour must be avoided and predictions of flutter behaviour need to be performed during design stage of the turbine.

An experimental blade cascade with five NACA 0010 profiles with one degree of freedom (rotation) has been built in the Institute of Thermomechanics to study flutter phenomenon. The schematic picture of the cascade is shown in Fig. 1 and it is described in [1].

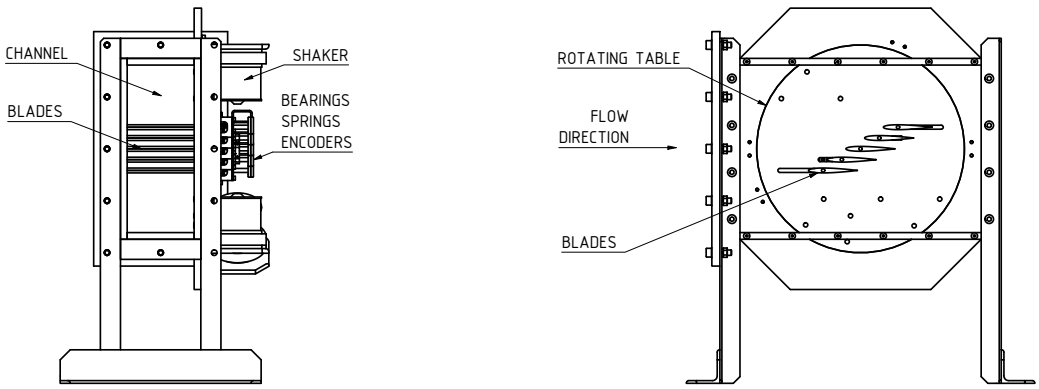

(a) front view (b) side view

Fig. 1. Assembly of the blade cascade

Laser *New Wave Research Pegasus PIV* and high speed camera *Vision Research Phantom* were used for PIV measurement of the flow field in the experiment. The results were compared with calculations in Ansys Fluent and in FlowPro.

Ansys Fluent is well-known commercial software that is used for simulation of flow, turbulence, heat transfer and reactions. 2D model of the cascade was simulated using compressible flow with K-ω SST turbulence model. The fluid parameters correspond to air, turbulent intensity was set to 0.05% and viscosity ratio was set to 1. The velocity inlet was prescribed at the inlet and the value of static pressure was prescribed at the outlet.

FlowPro is a multipurpose open-source CFD software designed for complex fluid flow simulations. The current version of the numerical software is capable of solving for example the system of Euler equations, Navier-Stokes equations, shallow water equations or equations of ideal magnetohydrodynamics. 2D model of the cascade was simulated using the incompressible fluid flow model together with Spalart-Allmaras turbulence model. The fluid parameters correspond to air, boundary conditions were set the same as in Fluent. The second order method in space and time was used.

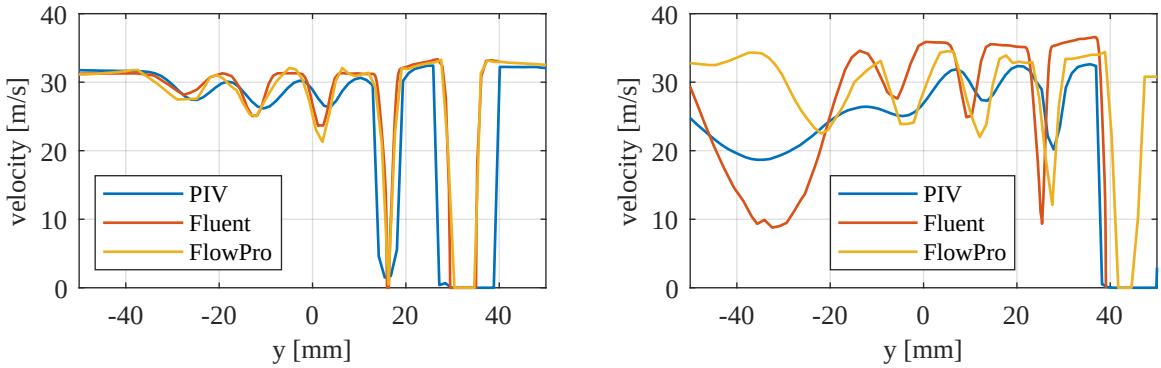

(a) angle of attack of the cascade $0°$

(b) angle of attack of the cascade $-8°$

Fig. 2. Comparison of flow velocities from the experiment (PIV) and calculations (Ansys Fluent and FlowPro) in the vertical plane placed 100 mm from the leading edge of the middle blade

Fig. 2 shows streamwise velocity in vertical plane placed 100 mm downstream from the leading edge of the middle blade. Results from the experiment are compared with the results from both Ansys Fluent and FlowPro for two angles of attack of the cascade, $0°$ and $-8°$. While the calculated results for $0°$ in Fig. 2a correspond well with the measured ones in terms of wake vertical position y and velocities in the wake, the results for $-8°$ in Fig. 2b look very different. Especially the wake region behind the first blade (the region with low velocity on the left side of the graph). There, the results from Ansys Fluent show similar position of the wake but the velocity gradient between the wake and surrounding flow is much higher. Interestingly, the result from FlowPro is different both from experiment and Ansys Fluent result. The wake is positioned higher in the y coordinate and is more narrow. There is an ongoing research to discover the reasons of those discrepancies in the results and to tune the simulations that will simulate also the cases with dynamic movement of the blades and the flutter phenomenon.

Acknowledgement

This research is supported by the research project of Czech science foundation No. 20-26779S "Study of dynamic stall flutter instabilities and their consequences in turbomachinery application by mathematical, numerical and experimental methods".

References

[1] Šnábl, P., Pešek, L., Prasad, C. S., Bula, V., Cibulka, J., Experimental setup and measurement for evaluation of blade cascade stall flutter instability, Proceedings of the 27th International Congress on Sound and Vibration, 2021.

[2] Waite, J. J., Physical insights, steady aerodynamic effects, and a design tool for low-pressure turbine flutter, Department of Mechanical Engineering and Materials Science, Duke University, 2016.

COMPUTATIONAL MECHANICS 2021
36th conference with international participation
Srní
November 8 - 10, 2021

Support of the numerical mechanics in the clarification of the mysterious death of Jan Masaryk

J. Špička[a], M. Čermák[c], T. Bońkowski[a,b], R. Kroft[b], J. Vychytil[a]

[a] *New Technologies - Research Centre, University of West Bohemia, Univerzitní 8, 301 00 Plzeň, Czech Republic*
[b] *Faculty of Applied Sciences, University of West Bohemia, Univerzitní 8, 301 00 Plzeň, Czech Republic*
[c] *Freelance investigator*

1. Introduction

This work describes political, social and historical situation in the Czechoslovakia in the year 1948, when the body of dead minister of foreign affair was found on the courtyard of the Černín Palace. His death is still unclear and several investigations were done. We are going to summarize them and point out some important features. In the 2019, the new investigation has begun after the new initiative documents containing newly discovered information. This document includes the numerical calculations and new measurements bringing some new aspects into the complex documentation. This initiative was supported by the UWB and their laboratories. The work here presents an application of the basic analytical mechanics and simple numerical calculations with the human body model, but applied in the forensic analysis. Although the fact, that only the elementary mechanics was used, the results can totally change the overview on this breakpoint of our modern history.

2. State of the art

Jan Masaryk was a son of the first president of Czechoslovakia, Tomáš Garrigue Masaryk. He worked as a politic and diplomat, he was an ambassador of ČSR in London in years 1925-1938, minister of foreign affair in the exile goverment as well in the first three governments after 1945, including the so called Klement Gottwald's government (1946-1948). In the morning of the March 10^{th} 1948, his body was found under the window of his flat on the courtyard of the Černín Palace. He laid on his back, more than 2 meters far from the wall and laterally shifted out of the window. The political situation in that time was very complicated, and this led to very uncommon process of investigation of his death: Murder, Unfortunate Accident or Suicide??. There is number of books focused on this topic, e.g., [2, 3, 5].

Investigations:

- **1948 (StB): Suicide**. Only a few hours after the body was found, there were an official statement: suicide, even before the autopsy.
- **1968–1969 (General Prosecutor's Office): Unfortunate Accident or Suicide.** This investigation was interrupted on the 10.11.1969 by the command of the General Prosecutor after the arrival of Soviet Union army.

- **1993–1996 (J. Havel): Forced suicide**. The first investigation dealing with the uncommon final position of the body (far from the wall, out of the window) [1], but this investigation was deferred.

- **2001–2003 (UDV + prof. Strauss): Murder**. Based on the biomechanical expertise of prof. Strauss, the investigation was closed as a murder, murderer is unknown. The expertise said that Jan Masaryk was unambiguously thrown out from the window (by external loading: one or more attacker). Such conclusion was done based on the final position of the body and concluded with the fact, that it is not possible to reach such position only with "own effort", the suicide jump.

- **2019**: There were some new evidences of this case: the new audio record and a technical analysis of the fall. Based on these two initiatives, the new investigation has been open in 2019 and closed in 2021 with the support of new data presented in this paper.

3. Technical data

Final position of the body: There is a lack of photo documentation of the body (only 5 photos of the body exist). There is also a official sketch of the criminal office from the 11.3.1948. The sketch contains the draw and dimensions, which are not very consistent. To validate the data, and found out the correct position, we have done several measurements inside the Černín Palace (courtyard, window, building, inside the flat, position of the body etc.), see Fig. 1.

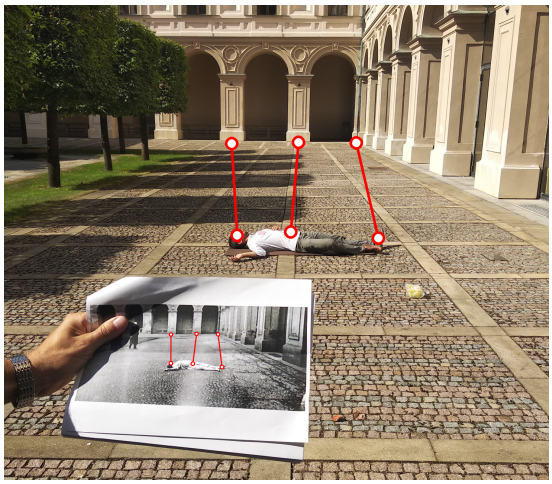

Fig. 1. Reconstruction of final position of the body

The criminal sketch defines the position of the body to be 2.3 m and 2.9 m from the wall, respectively and 13.1 m from the edge of the building. The first dimension (2.3 m) is the distance of the first impact of left heel, while the second dimension is the final position of the heel, see Fig. 2. Note there is an evident rearward motion of the body after the first contact with the ground. The lateral position of the body is 13.1 m from the building and with the support of the photos and own measurement, this distance indicates, that body was not found under the window, but approximately 1.6 m from its vertical axis.

Injury and cause of the death: Authors used only the data from the original autopsy report from prof. Dr. Hájek (1948). This document indicates, that Jan Masaryk was alive, when he forsook the ledge/window and he fell symmetrically on his heels, pelvis and back, see Fig. 3, absent the body rotation.

Witnesses: Even the fact, there are a lot of witnesses, we have decided not to take them into account, since they might be influenced with the circumstance of their acquisition, or might changed during the time. Our goal was to use only *hard facts*, to use the new technologies and to go further logically, systematically and technical precisely.

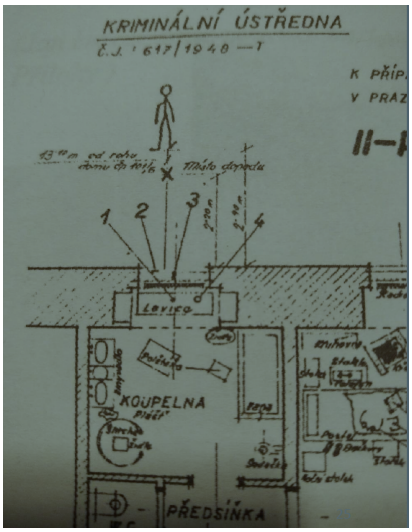

(a) official sketch from the criminal office, 1948

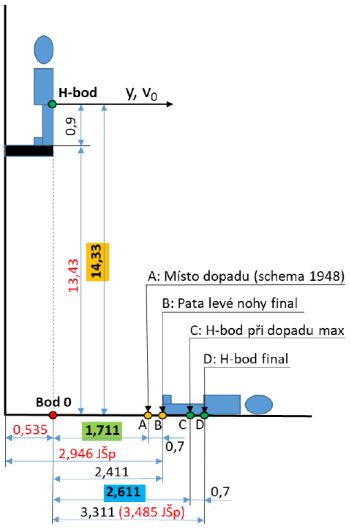

(b) on suite measurement + original data

Fig. 2. Position of the body

4. Support of the mechanics

Since the final position of the body is known (the official criminal sketch and our new measurement), and since the initial position is known (ledge of the window), it is only an example of classical mechanics, to calculate, how much force, acceleration or initial velocity the body needs, to reach the final position. The simply theory of oblique throw as well as the numerical analysis with the human body model Virthuman was used.

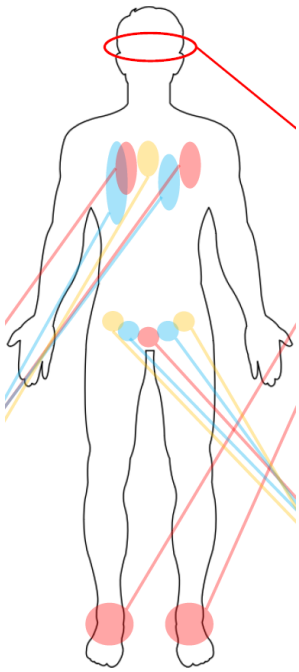

Fig. 3. Injuries sustained by Jan Masaryk

Laboratory measurement: Since the initial conditions (acceleration or velocity) required for the model of Jan Masaryk (his weight and height) are known, the conclusion, if he could do the jump by himself seems to be a simply task. However, the data of the dynamics of a real human jump is not very well known. There are some data measured by prof. Strauss in [4], but the results contain some irregularities, that forced us, not to used them. In order to get a real data of the human jump, the laboratory measurement was done in the laboratory the University of West Bohemia. The experimental testing of the rear jump from the ledge was done with set of volunteers. Each of them jumped several times, with four level of effort (normal jump, normal jump with hand, maximum jump and spontaneous fall). The testing subject has an accelerometer fixed close to his H-point and performed a rear jump from the model of the ledge. The results of the measurement is acceleration curve of a volunteer, see Fig. 4, from which the initial values of acceleration and velocity can be identified.

5. Conclusion

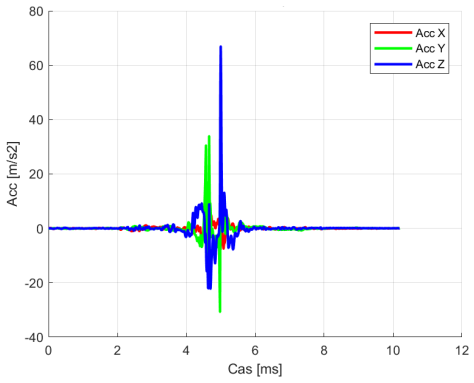

Fig. 4. Acceleration of the volunteer

Based on a newly discovered information, with the great help of the new technologies (accelerometer, simulation software, Virthuman etc.), the authors Čermák and Špička decided to submit the initiative to open a new investigation of Jan Masaryk case. The initiative was delivered to the Municipal Public Prosecutor's Office in Prague at October 10^{th} 2019 and then on the October, 21^{st}, the Public Prosecutor has opened the new investigation. This investigation was officially closed in 2021 with the support of this study and with the similar results. Murder, suicide, forced suicide or unfortunate accidents are all possible scenarios and it cannot be clarified until some new evidences would be discovered. However, the error from last investigation was corrected.

Acknowledgement

The result was financially supported with internal research project of University of West Bohemia SGS-2019-002: Biomechanical models of human body, biological tissues and biomechanical processes with application in industry and medicine.

References

[1] Havel, J., Death of Jan Masaryk by the view of criminalist. In the shadow of reflection and light of the document, Lípa, 1998. (in Czech)

[2] Jandečková, V., Case of Jan Masaryk: New view. Confession of murder and secret investigation process of StB from 1950-1951, 2015. (in Czech)

[3] Košatík, P., Kolář, M., Jan Masaryk – The true story, Albatros Media a.s., 2016. (in Czech)

[4] Strauss, J., Porada, V., Theory of forensic biomechanics, University of finance and administration, 2017. (in Czech)

[5] Sum, A., Lesák, J., Šedivý, Z., Boháč, L., Pravda, I., Kocián, J., Kalous, J., Jan Masaryk thoughts about his death, Úřad dokumentace a vyšetřování zločinu komunismu, Praha, 2005. (in Czech)

COMPUTATIONAL MECHANICS 2021
36th conference with international participation
Srní
November 8 - 10, 2021

Identification of viscoelastic material properties using the analysis of waves propagated in thin rods

J. Šulda[a], V. Adámek[a], R. Kroft[b]

[a] *Department of Mechanics, Faculty of Applied Sciences, University of West Bohemia, Univerzitní 8, 301 00 Plzeň, Czech Republic*
[b] *NTIS – New Technologies for the Information Society, Faculty of Applied Sciences, University of West Bohemia, Technická 8, 301 00 Plzeň, Czech Republic*

This work deals with the identification of material parameters of a thin prismatic viscoelastic homogeneous rods. The first part of this paper discusses transient waves in a viscoelastic 1D medium and presents the relations describing the acceleration of a rod in the space-time domain for specified boundary conditions and for different types of axial load. Subsequently, experiments performed on rods of various material properties, which verify the correctness of the derived solution, are presented in the next part. The following paragraph describes the procedure of material properties identification, which is implemented in the Matlab environment and uses a built-in optimization function and an algorithm of numerical inverse Laplace transform (NILT). Finally, the results of the optimization are analysed and discussed.

Rheological viscoelastic discrete models, which contain serial or parallel connections of elastic and viscous elements, are most often used to describe stresses and strains in viscoelastic solids (see [3]). The generalized Zener model (GZM) is used in this work, as it can represent simpler models in limit cases (see [2]). The relation describing acceleration of a viscoelastic rod of length l, the behavior of which is characterized by GZM, can advantageously be derived in the Laplace domain. Considering the zero initial conditions and the boundary conditions which describe free-free rod, the Laplace transform $A(x,p)$ of the rod acceleration depending on the longitudinal coordinate x and the variable $p \in \mathbb{C}$ can be written as

$$A(x,p) = \frac{\Sigma_0(p) C_0(p) p \cosh \dfrac{px}{C_0(p)}}{E^*(p) \sinh \dfrac{pl}{C_0(p)}}. \tag{1}$$

The complex function $\Sigma_0(p)$ is the Laplace transform of applied axial loading, $C_0(p)$ characterizes the complex wave velocity and $E^*(p)$ represents the complex modulus.

To verify the relation (1), the measurement of the non-stationary response of thin rods of 4 different materials was performed. These were both typically viscoelastic materials, namely acetal copolymer POM-C and polycarbonate PC1000, and typically elastic materials, such as steel and aluminium. The rods were loaded at one end with $Brüel\ \&\ Kjær\ Miniature\ Impact\ Hammer - Type\ 8204$ and the acceleration was measured using $Brüel\ \&\ Kjær\ Miniature\ DeltaTron^{®}\ Accelerometer - Type\ 4519$ at the other end. The signals from the impact hammer contained noise which was filtered out by applying a rectangular window on a part with the requested pulse. If the noise influences the pulse itself, the individual points were interpolated and scaled to the original maximum, if necessary.

To obtain the acceleration $a(t)$ from relation (1) in time domain, a Matlab code based on the NILT algorithm was created. This program calculates $A(x, p)$ for given material and geometric properties at required complex points p and for all x in the first phase. In the next step, the NILT algorithm taken from work [1] and based on the fast Fourier transform and the ε-algorithm accelerating the convergence of infinite series is applied. This procedure provides the response in time domain. Due to the high efficiency of the described method, the same core is used also for solving the inverse problem of material parameters identification. This parametric optimization has been solved using the standard Matlab fuction $fmincon$. It works with the target function f_c, which expresses the deviation from the measured acceleration, as follows

$$f_c = \left| \frac{(\mathbf{a}_E - \mathbf{a}_A)\mathbf{W}(\mathbf{a}_E - \mathbf{a}_A)^T}{\mathbf{a}_E \mathbf{W} \mathbf{a}_A^T} \right|. \tag{2}$$

The vectors $\mathbf{a}_A$ and $\mathbf{a}_E$ denote the analytically and experimentally determined acceleration vectors, respectively, and $\mathbf{W}$ is the diagonal weight matrix, which is identity in this case. In order to make the optimization precedure effective, the analysis of the target function f_c was performed. It is clear from Fig. 1, which presents the target function for two-parametric Maxwell model, that f_c is more sensitive to the modulus of elasticity E than to the normal viscosity λ and that it has several local minima in the area of interest. Since the $fmincon$ function is not able to find the global minimum without the known approximate values of the optimal parameters, the $GlobalSearch$ object was used in the program. It founds an approximate location of the global minimum in the specified domain. In addition, the created program is divided into three phases, which will speed up the optimization process. In the first phase, the $GlobalSearch$ object and the problem structure $createOptimProblem$ defining the task are created using the $fmincon$ method. Using the run function it starts an algorithm to find the approximate position of the global minimum while changing all moduli of elasticity contained in the rheological model. In the second phase, this algorithm is repeated for normal viscosities. Finally, the aproximate results are refined by running the $fmincon$ function itself with the starting parameters found in the first two phases.

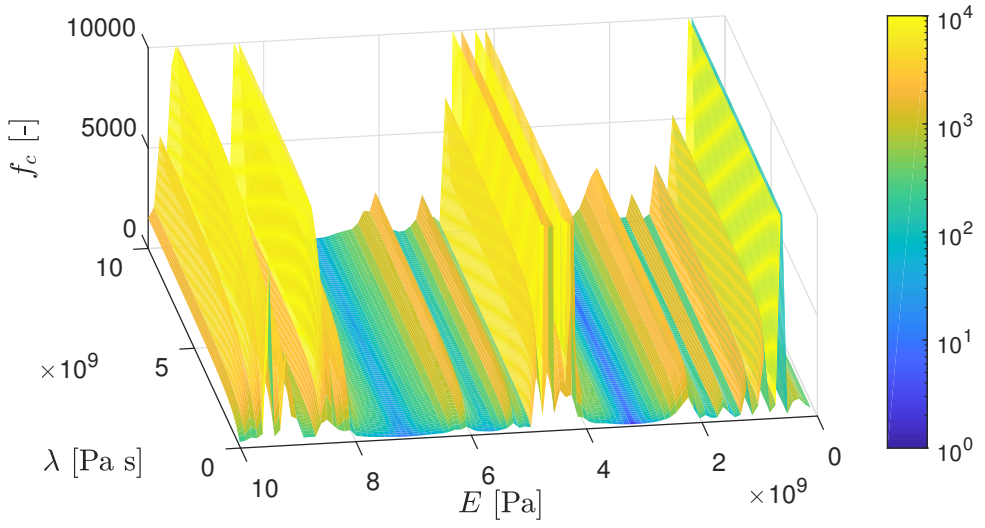

Fig. 1. Target function f_c in the considered domain of optimized parameters

As proved by performed computations, the developed code is very effective and gives reliable results for all the above-mentioned materials with low demands on computational time. Fig. 2a shows the comparison of the acceleration calculated analytically using the optimized

material parameters with the measured rod response. It can be seen that the curves have formally the same courses and that the wave speed and the dissipation of energy (i.e., damping) is well preserved in the whole studied time interval. The comparison of the responses for the elastic and viscoelastic model with the real data measured for aluminium is shown in Fig. 2b. It is clear that it is advantageous to include viscosity also for modeling of transient waves in "pure" elastic materials like aluminium because of non-negligible attenuation observed in the measured response for longer times.

In the first part of this work, the response of a viscoelastic thin rod to transient axial loading is derived for generalized Zener model in the Laplace domain. Then, due to an efficient algorithm for numerical inverse Laplace transform, this procedure is implemented into a program for the identification of material parameters making the use of experimental data. Finally, the correctness and the precision of obtained results were proved by the comparison of measured rods responses and the responses calculated using found optimized parameters.

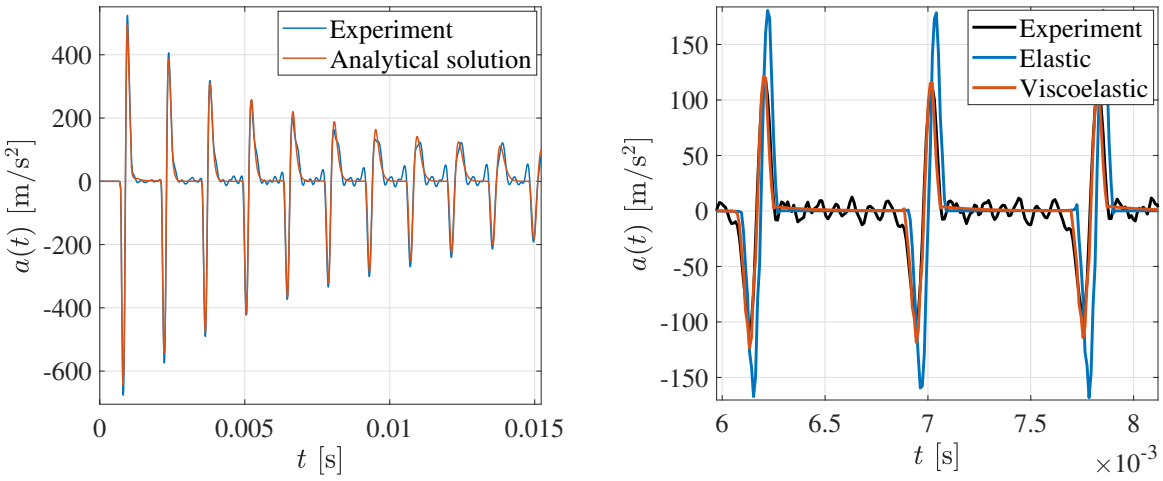

(a) response of PC1000 rod using viscoelastic GZM model

(b) response of aluminium rod using elastic and viscoelastic GZM model

Fig. 2. Comparison of calculated accelerations with measured data

Acknowledgements

The publication was supported by the project SGS-2019-009 and by the grant GA 19-04956S.

References

[1] Brančík, L., Programs for fast numerical inversion of Laplace transforms in Matlab language environment, Proceedings of the 7th MATLAB Conference, Prague, 1999, pp. 27-39.

[2] Sobotka, Z., Rheology of materials and engineering structures, Elsevier, 1984.

[3] Wang, L. L., Foundations of stress waves, Elsevier, Kidlington, 2007.

COMPUTATIONAL MECHANICS 2021
36th conference with international participation
Srní
November 8 - 10, 2021

On mathematical models of airflow in a glottal channel model periodically closed by flow induced vocal folds vibration

P. Sváček

Czech Technical University in Prague, Faculty of Mechanical Engineering, Dep. of Technical Mathematics, Czech Republic

1. Introduction

In this paper a two-dimensional mathematical model of human voice creation is addressed. Voice production is a complex process involving airflow induced vibrations of (elastic) vocal folds, [10]. The vibrations of the vocal folds generate a sound source, which is modified by the acoustic resonances of vocal tract cavities. The vocal folds oscillations appear at the so-called phonation onset which is basically a flutter type of instability. The phonation onset is characterized by certain airflow rate and a certain prephonatory vocal folds position, see [3, 4]. During the phonation a higher flow rates causes vibrations with increasing amplitudes, which leads to collisions of the vocal folds and to the closure of the glottis.

Consequently, the mathematical modelling of phonation process is challenging task: it needs to address the flow field, the structural deformation as well as acoustics, see e.g. [6, 11]. As the fundamental sound source is significantly influenced by the vocal folds contacts, this phenomena needs to be addressed properly in the model. This is rather difficult as it needs to be included not only to the structural model as impact forces but also to the fluid model, where it influences the geometrical domain deformation with possible topological changes as well as the artificial boundary conditions.

As the airflow velocity in the human glottal region is lower than 100 m/s, the air flow is modelled by the incompressible Navier-Stokes equations. The acoustic part can be modelled by an acoustic model, [9]. The addressed problem is a problem of fluid-structure interaction, where a simplified model of the elastic structure is used, [3, 5]. The attention is paid to the problem of glottis closure. This is realized by a modification of the computational domain, use of an artificial porous media subdomain and a suitable modification of the inlet boundary condition. The described mathematical model is discretized with the aid of the stabilized finite element method and numerical results are shown.

2. Mathematical model

First, we consider a simplified two dimensional model of the computational domain during the phonation onset phase, i.e., in the case of vocal folds are vibrating with only small amplitudes. The two-dimensional computational domain Ω_t for the fluid flow is considered as shown in Fig. 1. In this case the boundary of the computational domain consists of fixed or deformable walls denoted as Γ_{Wt} (it corresponds to the vibrating vocal folds with its upper $\Gamma_{Wt,up}$ and lower part $\Gamma_{Wt,down}$ as well as the other fixed walls Γ_{Wf} and the inlet Γ_I and the outlet Γ_O part of the boundary.

The air flow in the computational domain Ω_t is modelled as incompressible fluid flow described by the system of the incompressible Navier-Stokes equations (cf. [2]) written in the ALE form (cf. [7])

$$\frac{D^{\mathcal{A}}\boldsymbol{u}}{Dt} + ((\boldsymbol{u} - \boldsymbol{w}_D) \cdot \nabla)\boldsymbol{u} = \operatorname{div} \boldsymbol{\tau}^f,$$
$$\nabla \cdot \boldsymbol{u} = 0, \tag{1}$$

where $\boldsymbol{u} = (v_1, v_2)$ is the vector of fluid velocity, $\boldsymbol{\tau}^f = (\tau_{ij}^f)$ is the fluid stress tensor given as $\boldsymbol{\tau}^f = -p\mathbb{I} + 2\nu\boldsymbol{D}$, $\boldsymbol{D}$ is the symmetric gradient tensor $\boldsymbol{D}(\boldsymbol{u}) = \frac{1}{2}(\nabla\boldsymbol{u} + \nabla^T\boldsymbol{u})$ with components $d_{ij} = \frac{1}{2}(\frac{\partial u_i}{\partial x_j} + \frac{\partial u_j}{\partial x_i})$, p denotes the kinematic pressure (i.e. the pressure divided byt the constant fluid density) and $\nu > 0$ is the constant kinematic fluid viscosity. In order to take into account the deformation of the computational domain Ω_t the Arbitrary Lagrangian-Eulerian method is used. In this case by $\mathcal{A}_t$ the ALE mapping is denoted, which maps the reference configuration $\Omega_{ref} = \Omega_0$ onto the current configuration Ω_t at any time $t \in [0, T]$, $\boldsymbol{w}_D$ denotes the domain velocity (i.e. the velocity of the point with a fixed reference), and $\frac{D^{\mathcal{A}}\boldsymbol{u}}{Dt}$ is the ALE derivative, i.e. the derivative with respect to the reference configuration Ω_{ref}.

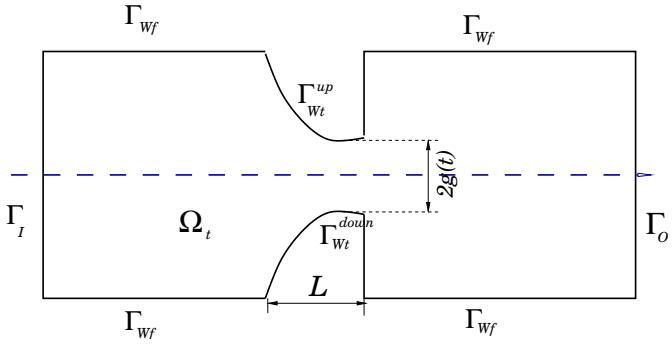

Fig. 1. The computational domain Ω_t with the boundary parts representing the (deformable and undeformable) walls, the inlet and the outlet. The domain is shown in a symmetric configuration with the dashed line showing the axis of symmetry

At the boundary $\partial\Omega_t^f$ of the computational domain formed by mutually disjoint parts $\partial\Omega_t^f = \Gamma_I \cup \Gamma_O \cup \Gamma_{Wt}$, the following boundary conditions are prescribed:

$$\begin{aligned}
&\text{a)} \quad \boldsymbol{u} = \boldsymbol{w}_D \text{ on } \Gamma_{Wt},\\
&\text{b)} \quad \frac{1}{2}(\boldsymbol{u}\cdot\boldsymbol{n})^{-}\boldsymbol{u} - \boldsymbol{n}\cdot\boldsymbol{\tau}^f = \frac{1}{\varepsilon}(\boldsymbol{u} - \boldsymbol{u}_I) \text{ on } \Gamma_I,\\
&\text{v)} \quad \frac{1}{2}(\boldsymbol{u}\cdot\boldsymbol{n})^{-}\boldsymbol{u} - \boldsymbol{n}\cdot\boldsymbol{\tau}^f = p_{ref}\boldsymbol{n} \text{ on } \Gamma_O,
\end{aligned}$$

where $\boldsymbol{n}$ denotes the unit outward normal vector to $\partial\Omega_t^f$, $\boldsymbol{u}_I$ is a prescribed inlet velocity, p_{ref} is a reference pressure value ($p_{ref} = 0$ in what follows), $\varepsilon > 0$ is a penalization parameter and α^- denotes the negative part of a real number α. Let us emphasize that at Γ_{Wf} the domain velocity equals zero $\boldsymbol{w}_D = 0$, whereas at the moving wall Γ_{Wt} the domain velocity $\boldsymbol{w}_D$ is equal to the velocity of the surface. The boundary condition (2c) weakly imposes the Dirichlet boundary condition $\boldsymbol{u} = \boldsymbol{u}_I$ using the penalization parameter $\varepsilon > 0$.

2.1 Vocal fold vibrations

The elastic deformation of the vibrating vocal fold is described using a simplified model with two degrees of freedom, i.e. the displacements $w_1(t)$ and $w_2(t)$ of the masses m_1 and m_2,

respectively (see Fig. 2). These displacements are governed by the equation of motion (see [3] for details)

$$\mathbb{M}\ddot{\boldsymbol{w}} + \mathbb{B}\dot{\boldsymbol{w}} + \mathbb{K}\boldsymbol{w} = -\boldsymbol{F}, \tag{2}$$

where $\mathbb{M}$ is the mass matrix of the system, $\mathbb{K} = \mathrm{diag}(k_1, k_2, k_4, k_5)$ is the diagonal stiffness matrix of the system characterized by spring constants k_1, k_2, and $\mathbb{B} = \varepsilon_1\mathbb{M} + \varepsilon_2\mathbb{K}$ is the matrix of the proportional structural damping, ε_1, ε_2 are the constants of the proportional damping. The mass matrix is given by

$$\mathbb{M} = \begin{pmatrix} m_1 + \frac{m_3}{4} & \frac{m_3}{4} & 0 & 0 \\ \frac{m_3}{4} & m_2 + \frac{m_3}{4} & 0 & 0 \\ 0 & 0 & m_4 + \frac{m_6}{4} & \frac{m_6}{4} \\ 0 & 0 & \frac{m_6}{4} & m_5 + \frac{m_6}{4} \end{pmatrix}, \tag{3}$$

where m_1, m_2, m_3 are the three masses shown in Fig. 2 (left) for the lower part of the vocal fold model and m_4, m_5, m_6 are the three masses shown in Fig. 2 (right) for the upper part of the vocal fold model. The vector $\boldsymbol{F} = \boldsymbol{F}_{imp} + \boldsymbol{F}_{aero}$ consists of the impact forces $\boldsymbol{F}_{imp}$ and the aerodynamical forces $\boldsymbol{F}_{aero} = (F_1, F_2, F_4, F_5)^T$.

The aerodynamical forces are evaluated as surface integrals from the aerodynamical quantites computed in the fluid part of the model, i.e. by the (kinematic) pressure p and by the gradient of the flow velocity $\boldsymbol{u} = (u_1, u_2)$. The displacement of the surface Γ_{Wt}^{down} is determined in terms of w_1, w_2, and it is used as boundary condition for the displacement of any point of the computational domain Ω_0^{ref} onto the domain Ω_t. Similarly the displacement of the surface Γ_{Wt}^{up} is determined in terms of the displacements w_4, w_5.

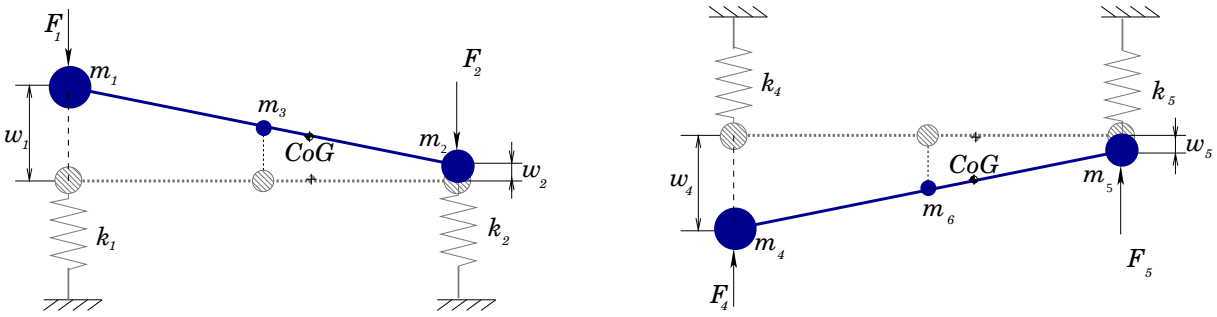

Fig. 2. The aeroelastic model of the down part (*left*) and the upper part (*right*) of the vocal fold

2.2 Contact problem

In order to model the contact of the vocal folds the flow of the air is approximated on a modification of the computational domain still denoted by Ω_t, which is formed of the original fluid domain Ω_t^f and of the part of the domain Ω_t^P, which is the part of the domain Ω_t assumed to be occupied by vocal folds. In practical problem it is realized by determination of the gap $2g(t)$ between the two vocal folds. In case when $g(t) \geq g_{min} > 0$ no modification of the computational domain is needed (here g_{min} a suitable minimal gap threshold). For the case $g(t) \leq g_{min}$, the displacements of the boundary parts Γ_{Wt}^{up} and Γ_{Wt}^{down} is modified, which leads to artificially created fictitious porous media domain Ω_t^p. The flow in Ω_t^P is then governed by the modified equations

$$\frac{D^{\mathcal{A}}\boldsymbol{u}}{Dt} + ((\boldsymbol{u} - \boldsymbol{w}_D) \cdot \nabla)\boldsymbol{u} + \sigma_P \boldsymbol{u} = \mathrm{div}\, \boldsymbol{\tau}^f,$$

where the coefficient σ_P corresponds to the artificial permeability P of the fictitious porous media. This approach can be also understand as penalization, see [1].

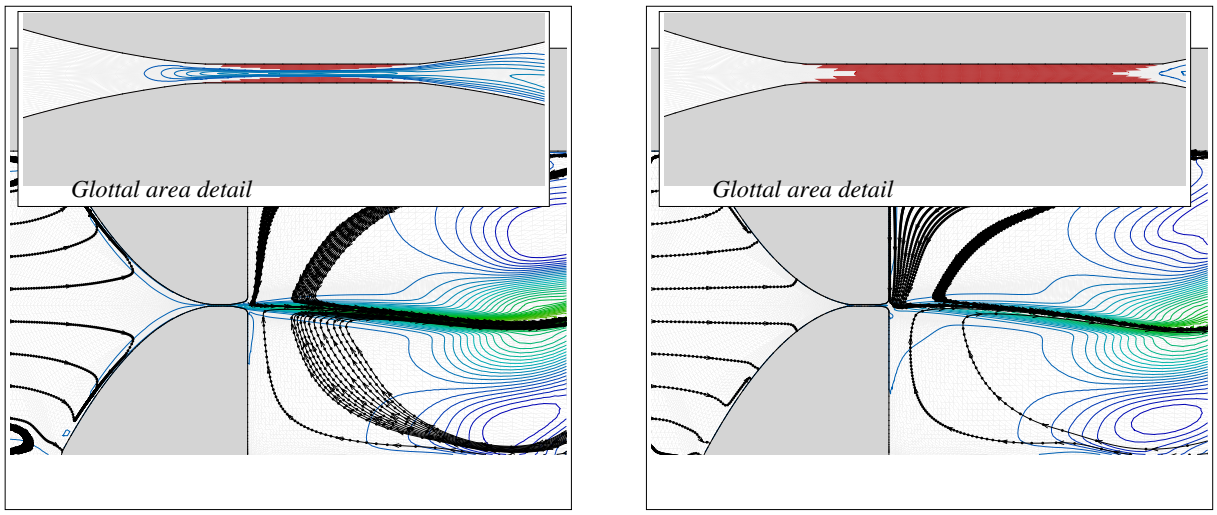

Fig. 3. The flow velocity distribution in the computational domain during two time instants for the case corresponding to post-flutter simulation from [8]

Acknowledgment

This work was supported by the *Czech Science Foundation* under the *Grant No. 19 - 04477S*.

References

[1] Angot, P., Bruneau, C. H., Fabrie, P., A penalization method to take into account obstacles in incompressible viscous flows, Numerische Mathematik 81 (1999) 497-520.

[2] Feistauer, M., Mathematical methods in fluid dynamics, Longman Scientific & Technical, Harlow, 1993.

[3] Horáček, J., Šidlof, P., Švec, J. G., Numerical simulation of self-oscillations of human vocal folds with Hertz model of impact forces, Journal of Fluids and Structures 20 (6) (2005) 853-869.

[4] Horáček, J., Švec, J. G., Aeroelastic model of vocal-fold-shaped vibrating element for studying the phonation threshold, Journal of Fluids and Structures 16 (7) (2002) 931-955.

[5] Ishizaka, K., Flanagan, J. L., Synthesis of voiced sounds from a two-mass model of the vocal coords, The Bell System Technical Journal 51 (1972) 1233-1268.

[6] Link, G., Kaltenbacher, M., Breuer, M., Döllinger, M., A 2D finite element scheme for fluid-solid-acoustic interactions and its application to human phonation, Computation Methods in Applied Mechanical Engineering 198 (2009) 3321-3334.

[7] Nomura, T., Hughes, T. J. R., An arbitrary Lagrangian-Eulerian finite element method for interaction of fluid and a rigid body, Computer Methods in Applied Mechanics and Engineering 95 (1992) 115-138.

[8] Sváček, P., Horáček, J., Numerical simulation of glottal flow in interaction with self oscillating vocal folds: Comparison of finite element approximation with a simplified model, Communications in Computational Physics 12 (3) (2012) 789-806.

[9] Šidlof, P., Zörner, S., Hüppe, A., A hybrid approach to computational aeroacoustics of human voice production, Biomechanics and Modeling in Mechanobiology 14 (2015) 473-488.

[10] Titze, I. R., The myoelastic aerodynamic theory of phonation, National Center for Voice and Speech, U.S.A., 2006.

[11] Valášek, J., Kaltenbacher, M., Sv'aček, P., On the application of acoustic analogies in the numerical simulation of human phonation process, Flow Turbulence Combust 102 (2019) 129-143.

COMPUTATIONAL MECHANICS 2021
36th conference with international participation
Srní
November 8 - 10, 2021

Development of autonomous experimental setup to investigate directional distortional hardening under biaxial loading

J. Svárovský[a,b], S. Parma[a], J. Štefan[a], C. Ciocanel[c], H. P. Feigenbaum[c], V. Klepač[a,b], R. Marek[a], J. Plešek[a]

[a] *Institute of Thermomechanics of the Czech Academy of Sciences, Dolejškova 1402/5, 182 00 Prague, Czech Republic*
[b] *Faculty of Mechanical Engineering, Czech Technical University in Prague, Technická 4, 160 00 Prague, Czech Republic*
[c] *Mechanical Engineering Department, Northern Arizona University, 15600 S. McConnell Dr. NAU, Flagstaff, AZ 86001-5600, USA*

This paper describes the experimental determination of yield surfaces (YS) in a cold drawn steel. YS bounds the elastic domain in the stress space. By reaching the surface, plastic strains occur and the YS changes in the position, size and/or shape. This phenomenon is referred as strain hardening. In the field of phenomenological plasticity theory, the elementary mechanisms of strain hardening are kinematic hardening *(translation of YS)* and isotropic hardening *(uniform expansion of YS)*. However, it has been experimentally proven that other processes such as distortion, rotation, and/or affine deformation are usually present and affect the shape of the YS [1, 3, 5].

Directional distortional hardening (DDH) is a well known mechanism of strain hardening. It is characterized by the YS developing a region of a high curvature in the direction of loading and a flattening at the rear part of the YS, Fig. 1. The yield function of the DDH model proposed by Feigenbaum and Dafalias in 2008 [2] is as follows

$$f = (\boldsymbol{s} - \boldsymbol{\alpha}) : \boldsymbol{\mathcal{H}} : (\boldsymbol{s} - \boldsymbol{\alpha}) - k^2 = 0, \tag{1}$$

where $\boldsymbol{s}$ is the deviatoric stress tensor, $\boldsymbol{\alpha}$ is the back-stress tensor, and k is the size of YS. $\boldsymbol{\mathcal{H}}$ is a fourth order tensor-valued internal variable used to model distortion. The tensor $\boldsymbol{\mathcal{H}}$ distinguishes this model from classical concept of isotropic and kinematic hardening. This model is thermodynamically consistent and was employed to model and predict multiaxial ratcheting, as reported by Welling et al. [4].

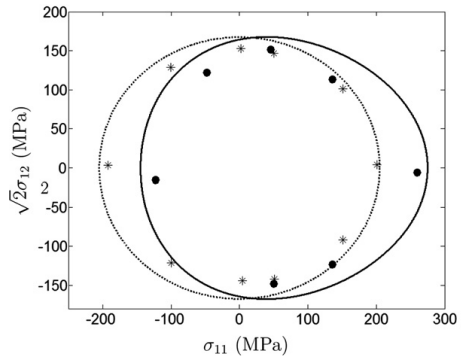

Fig. 1. DDH model for initial and subsequent YS; figure adopted from reference [2]

The aim of the experimental work is to develop a fully automated method for tracing YS with the ability to flexibly vary keys parameters such as specimen dimensions, stress rates, system of probing paths, etc. The experimental setup to capture the YS consists of an axial-torsional universal hydraulic testing machine by Instron company, a biaxial extensometer, and a desktop computer with software for data evaluation and machine control. Methods for tracing initial YS were developed in two separate softwares – Wavematrix2 (WM) and Labview 2017 (LV). Although the proprietary Instron WM software proved it's suitability for automated procedure for capturing yield surfaces [3], LV shows much more promise in terms of advanced parametrization. The results obtained from both software proved to be consistent and therefore only results acquired by LV are presented. The measurements were carried out on the thin-walled tubular specimens.

The YS tracing method consists in capturing a series of yield points according to a yield condition in the form of effective plastic strain

$$\varepsilon_{\text{eff}} = \sqrt{\left(\varepsilon^{\text{tot}} - \frac{4F}{\pi\left(D^2 - d^2\right)E} - \varepsilon^{(0)}\right)^2 + \frac{1}{3}\left(\gamma^{\text{tot}} - \frac{16DT}{\pi\left(D^4 - d^4\right)G} - \gamma^{(0)}\right)^2}, \qquad (2)$$

where ε^{tot} and γ^{tot} are total axial and shear strain respectively. The fractions in this equation are the elastic axial and shear strains, writen in terms of force, F, torque, T, outer diameter, D, inner diameter, d, and elastic moduli, E and G; $\varepsilon^{(0)}$ and $\gamma^{(0)}$ are the offsets. The specimen is subjected to a stress-controlled loading from the centrepoint at zero stress until the yield condition is reached and, consequently, unloaded back to the origin. This process is called probing. In the current measurement, the order and number of probes were chosen in accordance with Dietrich and Kowalewski [1]. More detailed information about the methodology can be found in [3, 5]. The results evaluated by the application developed in graphical programming software Labview are shown in Fig. 2. The stress space with the factor of $\sqrt{3}$ multiplying the shear was chosen so that the von Mises model would lead to a circular shaped YS.

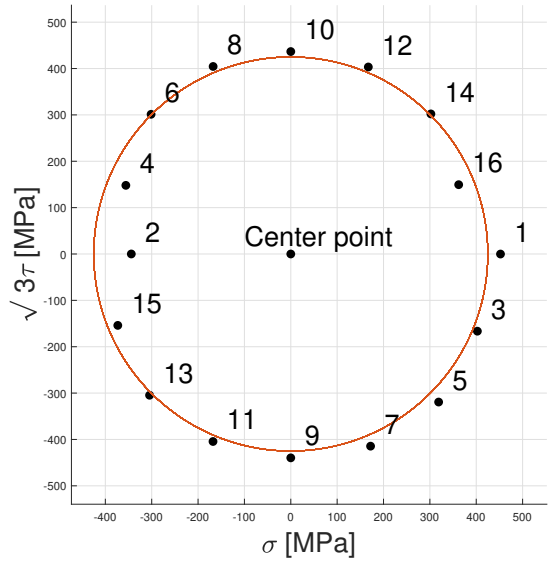

Fig. 2. Yield points measured with the experimental setup with comparison of von Mises yield surface in Axial stress – Shear stress space

The experimental results (in Fig. 2) show promising agreement with the von Mises yield surface model. A possible reason for the lower yield point (2) in the compressive loading direction is the manufacturing history, due to the fact, that the specimen used is made of cold drawn steel. Outlying points (4, 15, 16) violate the assumption of convexity of the YS. Therefore, the effect of cyclic strain hardening *(probing effect)* and the effect of automatic continuous least square regression for determination of the elastic moduli are being examined. The method is under further development.

Acknowledgements

This work was supported by the Ministry of Education, Youth and Sports under grant No. CZ.-02.1.01/0.0/0.0/15_003/0000493, Centre of Excellence for Nonlinear Dynamic Behaviour of Advanced Materials in Engineering (CeNDYNMAT), and grant No. LTAUSA18199, Advanced Phenomenological Models of Plasticity and Phase Transformations in Modern Engineering Materials, by US ARL under grant No. W911NF-19-1-0040, and by the Czech Science Foundation under grant No. GA19-03282S, Influence of Complex and Cyclic Loading Modes on Lifetime of Machine Parts Made by Additive Manufacturing.

References

[1] Dietrich, L., Kowalewski, Z. L., Experimental investigation of an anisotropy in copper subjected to predeformation due to constant and monotonic loadings, International Journal of Plasticity 13 (1-2) (1997) 87-109.

[2] Feigenbaum, H. P., Dafalias, Y. F., Directional distortional hardening in metal plasticity within thermodynamics, International Journal of Solids and Structures 44 (22) (2007) 7526-7542.

[3] Štefan, J., Parma, S., Marek, R., Plešek, J., Ciocanel, C., Feigenbaum, H. P., Overview of an experimental program for development of yield surfaces tracing method, Applied Sciences 11 (16) (2021) No. 7606.

[4] Welling, C. A., Marek, R., Feigenbaum, H. P., Dafalias, Y. F., Plesek, J., Hruby, Z., Parma, S., Numerical convergence in simulations of multiaxial ratcheting with directional distortional hardening, International Journal of Solids and Structures 126-127 (2017) 105-121.

[5] Wu, H. C., Yeh, W. C., On the experimental determination of yield surfaces and some results on annealed 304 stainless steel, International Journal of Plasticity 7 (8) (1991) 803-826.

COMPUTATIONAL MECHANICS 2021
36th conference with international participation
Srní
November 8 - 10, 2021

Virthuman application for family safety in highly automated vehicle's frontal crash

A. Talimian[a], J. Vychytil[a]

[a] *New Technologies Research Center, University of West Bohemia in Pilsen, Univerzitní 8, 301 00 Plzeň, Czech Republic*

Abstract

Highly automated vehicles' occupants will have more comfortableness because common interior elements such as steering wheel will not be existing anymore. It provides extra room to change their seats' location for sitting in either Face-to-Face or Living Room configuration. This study compares occupants' injury index in non-standard configurations with a standard one. A frontal crash is modelled by Low- and high-speed crash acceleration's pulses. Virthuman models in different ages and genders are chosen for modelling occupants in a simplified schematic of an autonomous vehicle's interior. Numerical simulations elaborate that there are no noteworthy changes for Rear-row occupants in non-standard seating configurations rather than a standard one in a low-speed crash. Moreover, at a high-speed crash scenario, non-standard seating configurations can decrease injury indexes for Front-row occupants' Head & neck and Rear row occupants' Legs.

1. Introduction

By the end of the first quarter of the twenty-first century, it is expected that fully automated safety features are seen in most of the vehicles on roads [4]. Vehicle's interior is going to be changed in consequence and some elements such as steering wheels will not exist anymore. Occupants shall have such flexibility to rotate/relocate their seats freely in a vehicle's interior. New seating configurations provide a comfortable long-travel for passengers.

Passengers' seats in almost all of the private vehicles have been facing to the front windshield. We name it standard seating configuration. Whenever the front row seats are rotated 180^{o} one can say occupants sit in Face-to-Face seating configuration. If occupants' seats in lately mentioned configuration rotate 30^{o} inward it is called Living Room seating configurations. Participants who attended in a study have shown their interests in non-standard seating configurations [3]. It was acceptable from their point of view to have extra restrains if occupants are allowed non-standard seating configurations.

A crash is unavoidable in some occasions if the automated driving system (ADS) may not work precisely. One may wonder how safe is these non-standard seating configurations for occupants in comparison with the standard one? For doing crash tests it is possible to use Post-mortem human subjects (PMHS) but keeping them in good conditions for a long time is difficult. On the other hand, full-scale anthropomorphic dummies lose their measurements' accuracy after several tests. Henceforth, Finite Element human body models have been introduced to overcome these limitations but simulation's time is an important matter. For reducing computation's time hybrid models such as Virthuman have being developed [2]. Virthuman model itself, which possesses a decent capability to present different ages and

genders in crash scenarios. It is made on a Multi-Body-System basis and able to evaluate body injuries regarding kinematic values and loads on some certain nodes/joints. It has worth to mention that Virthuman does not model tissues, muscles, brain, etc. None of these bodily injuries is considered by the algorithm for evaluating injury indexes.

For the present study, we ran simulations in the Virtual Performance Solution environment, PAMCRASH module. Bodies are fastened by three-points seat belts with standard materials to seats made by Polyurethane foam (PUR). The test was done for two crash acceleration pulses [5] in the frontal direction. Finally, by the help of an embedded algorithm [1] in the software for Virthuman, models' injury indexes are assessed for body's parts. In consequence, bodies' Injury indexes in non-standard seating configurations are compared with standard one for three dominant bodies' parts.

2. Simulation

Four Virthuman models were located in a simplified interior of an autonomous vehicle Fig. 1. Man (50th percentile male, 35-45 years old) and girl (50th percentile female, 10-11 years old) models were located in the front row. Rear row occupants were a boy (53rd percentile male, 6-7 years old) and woman (52nd percentile female, 30-35 years old). Three-point seat belts were the only elements which restrict bodily motion. Models' feet were not affixed to the interior's bottom. An extra cushion was added to common seat's cushion for the boy model. A two-step simulation was planned for doing a crash test. At first, bodies fall from rest slightly above seats meanwhile seat belts' retractors pull back them to affix on seats. Then seatbelts are locked. Secondly, the crash acceleration pulse [5] is applied to bodies and seats as well as the vehicle's interior.

Fig. 1. Seating configurations in a highly automated vehicle

3. Injury assessment

A post-processing algorithm is available for evaluating Virthuman's injury indexes [1]. It collects injury index of the body's parts according to their degree of injury at the current time. Therefore, a particular segment's degree of injury is its worst injury's degree in the time interval from the beginning to the current time step. Colour evaluation according to the degree of injury is returned by four basic levels according to EuroNCAP consumer rating. A small degree of injury or none is given by *Good*. An injury level can be either *Acceptable* or *Marginal*. However fatal injuries are presented by *Poor* level because make a serious degree of injuries Fig. 2. Head's injury index is evaluated by the Head Injury Criterion. Bending moment, as well as shear and tension forces of upper neck's joints, are used for injury index of a model's neck. Injury of the model's thorax is determined based on ribs' deflection and parts' Viscous Criterion. Compression and pubic forces are important parameters to

investigate index of injury for abdomen and pelvis respectively. Femurs, knees and tibiae' injury indexes are related to compression force and moments in these parts.

Here we divide Virthuman's body parts to three dominant sections: a) Head & Neck, b) Trunk (thorax, abdomen and pelvis), c) Legs (femurs, knees and tibiae). Each sections' injury index is its the worst injury's degree of its parts. For instance, in Head & Neck case if Neck's injury index is Acceptable but Head's injury index is Poor, the section's final assessment is Poor.

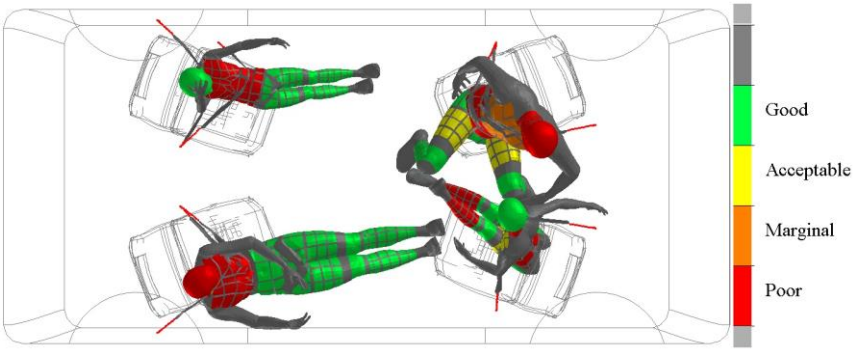

Fig. 2. Body part's injury indexes evaluation, (Living Room at 30 km/h)

Body sections' injury index in non-standard seating configurations is compared with the standard one. Safety of body's section in a seating configuration is worse than another one if its injury index is increased. On the other hand, whenever a section's injury index is decreased, the safety of body's section is improved Fig 3.

Fig. 3. Injury indexes' changes evaluation

Injury indexes comparisons per body sections are given in Table. 1 for two crash speeds. In where no sign is put in the table it means no changes were seen between two seating configurations from the body section's injury index point of view.

4. Discussion

Occupant's safety in non-standard seating configuration for highly automated vehicles was compared with standard seating configuration from an injury index point of view. Three sections of a model's body (Head & neck, Trunk and Legs) were considered for injury indexes evaluation. Simulation's data were collected for two impact pulses in a frontal crash direction. Results have not been validated against experimental tests which keep the study's topic open for further investigations.

Returning to numerical results for low-speed crash (30 km/h), because models' feet were not affixed to interior's bottom, the chance of legs' injury for front-row occupants (Girl and Man) is increased. Besides changing the orientation of Man's seat in Face-to-Face and living Room seating configurations causes its head hit to seat's headrest and experiencing a rotation on its neck respectively. These events increased the Head & neck section's injury index. On the other hand, man's trunk in Face-to-Face seating configuration hits to its seat's back and will not be in contact with shoulder belt. Therefore its injury index is decreased. All in all

non-standard seating configurations are not as safe as the standard one for front-row occupants (Girl and Man).

Based on simulation's outcome for high-speed crash (50 km/h) Face-to-Face seating configurations can improve Head & neck's safety of occupants who sit in front of the vehicle's interior (Girl and Man). Furthermore, it is expected rear-row passengers (Boy and Woman) have a safer condition in Living Room seating configuration from the legs' injury index point of view.

Table 1. Injury index comparison between seating configurations

		Boy			**Girl**			**Woman**			**Man**		
		Head & neck	*Trunk*	*Legs*	*Head & neck*	*Trunk*	*Legs*	*Head & neck*	*Trunk*	*Legs*	*Head & neck*	*Trunk*	*Legs*
30 km/h	*Face-to-Face vs. Standard*						✗				✗	✓	✗
	Living Room vs. Standard						✗				✗		✗
50 km/h	*Face-to-Face vs. Standard*				✓						✓		
	Living Room vs. Standard			✓						✓			✗

Acknowledgements

This work was supported by the European Regional Development Fund-Project "Application of Modern Technologies in Medicine and Industry" No. CZ.02.1.01/0.0/0.0/17_048/0007280.

References

[1] ESI, Virthuman Postprocessing Manual (VPS Explicit MBS Model, Model Version 1.1) Rev. 1, 2016.

[2] ESI, Virthuman User's Manual (VPS Explicit MBS Model, Model Version 1.1) Rev. 1, 2016.

[3] Jorlöv, S., Bohman, K., Larsson, A., Seating positions and activities in highly automated cars–a qualitative study of future automated driving scenarios, The International Conference on the Biomechanics of Impact (IRCOBI), 2017.

[4] NHTSA, Automated vehicles for safety, 2017. Available from https://www.nhtsa.gov/technology-innovation/automated-vehicles-safety#topic-road-self-driving

[5] Vezin, P., Bruyere-Garnier, K., Bermond, F., Verriest, J.P., Comparison of hybrid III, Thor-α and PMHS response in frontal sled tests, Stapp Car Crash Journal 46 (2002) 1-26.

COMPUTATIONAL MECHANICS 2021
36th conference with international participation
Srní
November 8 - 10, 2021

Dynamic mode decomposition and its application to the flutter analysis

J. Valášek, P. Sváček

Faculty of Mechanical Engineering, Czech Technical University in Prague, Karlovo nám. 13, Praha 2, 121 35

In this paper the dynamic mode decomposition (DMD) method is introduced. It is a data-driven and model-free method which decomposes a given set of signals to DMD modes and associated DMD eigenvalues, [2, 4]. Thus it offers a very interesting alternative to the proper orthogonal decomposition (POD) and similar methods usually used for the low-rank representation of the high-dimensional data. The advantage of DMD is better physical interpretation of the decomposition as the DMD modes have monofrequency content and the complex DMD eigenvalues provide the frequency as well as the growth/decay rate of particular mode, [4]. Moreover the DMD has solid theoretical underpinnings given by the Koopman operator, [2]. The disadvantage of DMD is a relative ambiguity of DMD mode selection which are not sorted as in the case POD decomposition, [1]. Finally an application example of the DMD analysis to the numerical simulation of flutter vibrations is presented.

DMD theory In the beginning let us assume that we study dynamical system of the form

$$\frac{\partial \mathbf{x}}{\partial t} = \mathbf{f}(\mathbf{x}, t, \mu), \tag{1}$$

where $\mathbf{x}(t) \in \mathbb{R}^n$ is a state vector at time t, μ represents parameters of the system and function $\mathbf{f}(\cdot)$ is generally nonlinear. Further we denote $\mathbf{x}_k = \mathbf{x}(t_k)$ as solution of Eq. (1) at time instant t_k (for example assuming $t_k = k \cdot \Delta t$). The states $\mathbf{x}_k$ are typically very large and they can arise from the spatial discretization of a partial differential equation or they can be collected from measurements of the dynamical system. Next we have got a data set $\mathcal{D}$ consisting of $\mathcal{D} = \{\mathbf{x}_1, \ldots, \mathbf{x}_N\}$ for which we would like to find low-dimensional representation.

The DMD method is based on the matrix $\mathbb{A}$ describing time development of the system in the form

$$\mathbf{x}_{k+1} = \mathbb{A}\mathbf{x}_k, \qquad k \in \{1, \ldots, N-1\} \tag{2}$$

as best fit in least-square sense, i.e., minimizing

$$\sum_{k=1}^{N-1} ||\mathbf{x}_{k+1} - \mathbb{A}\mathbf{x}_k||_2. \tag{3}$$

It is now clear from Eq. (2) that the DMD actually locally linearizes the original system (1), [2]. Quite interestingly, the DMD method can be theoretically viewed as the finite-dimensional approximation of the Koopman operator. The Koopman operator is a linear, infinite-dimensional operator that precisely represents the nonlinear operator of the dynamical system with finite dimension, [2].

The dynamics of system (1) (or more accurately the dynamics hidden in the data set $\mathcal{D}$) is given by the DMD matrix $\mathbb{A}$. The key to it (and the key of the DMD) is to perform the

eigendecomposition of matrix $\mathbb{A}$ to eigenvalues λ_i and eigenvectors $\mathbf{\Phi}_i$. Then the analyzed state-space trajectory (given by $\mathcal{D}$) can be reproduced according to the formula

$$\mathbf{x}(t_{k+1}) = \mathbf{x}_{k+1} \approx \mathbb{A}^k \mathbf{x}_1 = \sum_{i=1}^{N-1} \mathbf{\Phi}_i \exp(\omega_i \, t_k) \, b_i, \tag{4}$$

where ω_i are approximate continuous-time eigenvalues given by $\omega_i = \ln(\lambda_i)/\Delta t$ and $\mathbf{b} = (b_i)$ are the initial coefficients of mode participation for each DMD mode, i.e., $\mathbf{b} = \mathbf{\Phi}^\dagger \mathbf{x}_1$ with † notation of pseudo-inverse. The real and the imaginary part of ω_i provides us information about the exponential growth/decay rate and the frequency content of the particular mode, respectively, see [4].

In practice the DMD matrix is replaced by the projection of the matrix $\mathbb{A}$ onto first r left-singular vectors obtained by singular value decomposition (SVD) and corresponding to the biggest r singular values of $\mathbb{A}$, i.e., by matrix $\tilde{\mathbb{A}}$. Then also the summation in formula (4) is typically restricted to $M \ll r$, i.e., it is enough to choose a few dominant DMD modes (here M modes) acceptably representing the system dynamics, [2].

In next paragraph we shortly present the numerical simulation on which results the DMD was applied.

FSI simulation Numerical simulation of flow-induced vibration of vocal folds (VFs) with the full channel configuration was conducted with in-house solver described in [5]. The VF geometry and simulation parameters are based on article [5]. Particularly, the constant time step Δt is chosen as $4 \cdot 10^{-5}$ s and the inlet velocity $v_{\text{in}} = 1.98$ m/s is prescribed with the aid of penalization parameter $\epsilon = \frac{1}{2000}$ s/m. Such choice of the inlet velocity together with the penalization parameter exceeds the critical flutter velocity estimated to be $v_{\text{crit}} \approx 1.9$ m/s, [6].

Fig. 1 shows the VF displacement recorded at the top point of bottom VF. The gradual increase of vibration amplitude can be observed when the increase in last 0.05 s has obviously the exponential character typical for flutter phenomenon. At time instant $t = 0.2956$ s the simulation failed due to too distorted computational fluid mesh. This is a big disadvantage of ALE method and an open issue for the simulation of healthy human phonation.

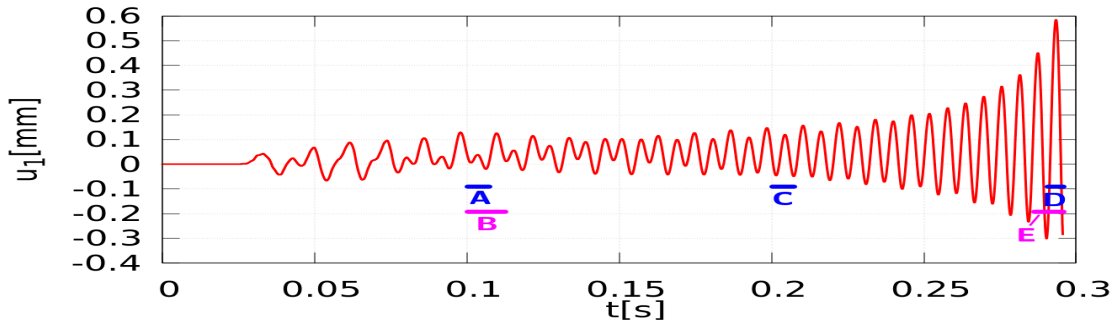

Fig. 1. VF displacement in x-direction monitored at point $S = [4.99; -0.505]$ mm. Five different time intervals are chosen for the application of DMD, marked by letters A-E

DMD application Here we apply the DMD on the numerical approximation of structural displacements $\mathbf{u}_h$ only. We choose 5 time intervals of 150 or 300 time steps covering the one or two periods of the most dominant frequency, see Fig. 1. The SVD is truncated such that all singular values greater than 10^{-3} are kept. The DMD mode with the highest mode participation measured as $z_i = |\sum_{k=1}^{N-1} \exp(\omega_i \, t_k) \, b_i|$ is chosen together with the DMD modes satisfying $z_i > 0.1 \cdot z_{\max}$, see [1].

The data sets from five different time intervals as shown in Fig. 1 are chosen. The DMD decomposition is performed for each of them and the chosen statistics are listed in Table 1. In all cases the DMD mode with frequency ≈ 168 Hz is present, in cases A, B, D is the dominant one. In cases B and E the highest contribution is associated with the mode representing asymmetry of the solution and having significant growth rate and rather unimportant frequency content. Formula (4) can be also used for the future state prediction for choice $k > N$. Employing this DMD feature the DMD prediction can be compared with the numerical solution in the cases A, B, C. The L^2 norm of the error e_{pred} of the DMD prediction for $k = N + 150$ (i.e., at the future 150^{th} time step) against the simulation is listed in the fifth column of Table 1. The reasonable agreement is achieved in case C, cases A and B fit well the given data sets but the correct prediction would need to better represent the interplay of two natural eigenmodes in the training data set. Similar problematic behaviour exhibits prediction in case E where the dominant DMD mode has too large growth rate which extrapolation gives wrong prediction clearly visible by eye. Omitting this dominant mode with excessive growth rate leads to an expectable DMD prediction.

Table 1. Five different data sets are analyzed by the DMD. The third column shows number of selected DMD modes. The error e_{pred} can not be computed in cases D and E as there is no simulation results to compare with

interval	time steps	# DMD modes	ω of the dominant mode	$e_{\text{pred}} \cdot 10^{-3}$
A	150	6	$5.81 + 168.5 \cdot 2\pi \cdot i$	1.3096
B	300	6	$53.2 + 5.8 \cdot 2\pi \cdot i$	1.2364
C	150	4	$9.8 + 168.5 \cdot 2\pi \cdot i$	0.47357
D	150	5	$65.69 + 167.3 \cdot 2\pi \cdot i$	'small'
E	300	5	$1000.5 + 101.5 \cdot 2\pi \cdot i$	'big'

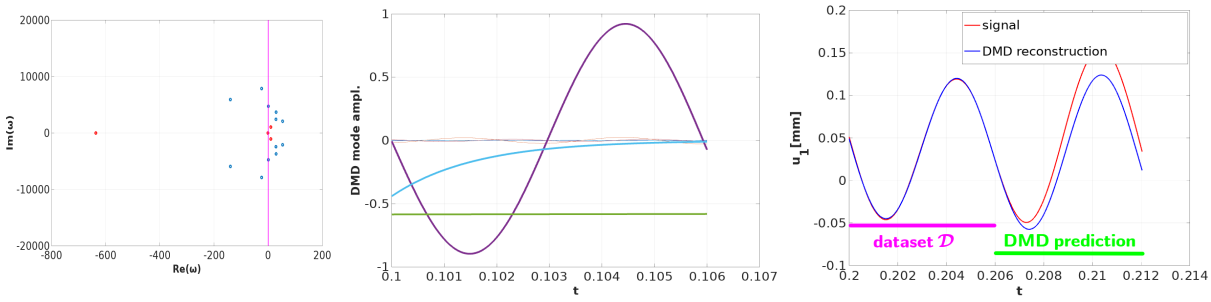

Fig. 2. (*Left*) DMD approximation of continuous-time eigenvalue spectrum. Vertical magenta line is the imaginary axis, i.e., stability boundary. The selected eigenvalues are highlighted by red circles. (*Middle*) Time behaviour of DMD mode participation coefficients (i.e., amplitudes). Three bold lines represents four selected DMD modes as the complex conjugated modes have the same real part of time behaviour. (*Right*) Comparison of the original displacement and the DMD prediction at point S. The state-space trajectory is reconstruction in time interval $0.2 - 0.206$ s (i.e., it is the data set) and the trajectory is predicted by the DMD based on Eq. (4) in time interval $0.206 - 0.212$ s. *All results concern case C*

Figs. 2 and 3 show more details about the DMD analysis for case C. The mentioned graphs for other cases are similar. Interestingly, the DMD mode with frequency ≈ 168 Hz is different from eigenmodes obtained by modal analysis. Its frequency lies between the second and the third natural eigenfrequency (155.8 Hz and 179.9 Hz) suggesting it is a vibration pattern arisen by merging of these two eigenmodes as it is typical for flutter phenomenon, see [7].

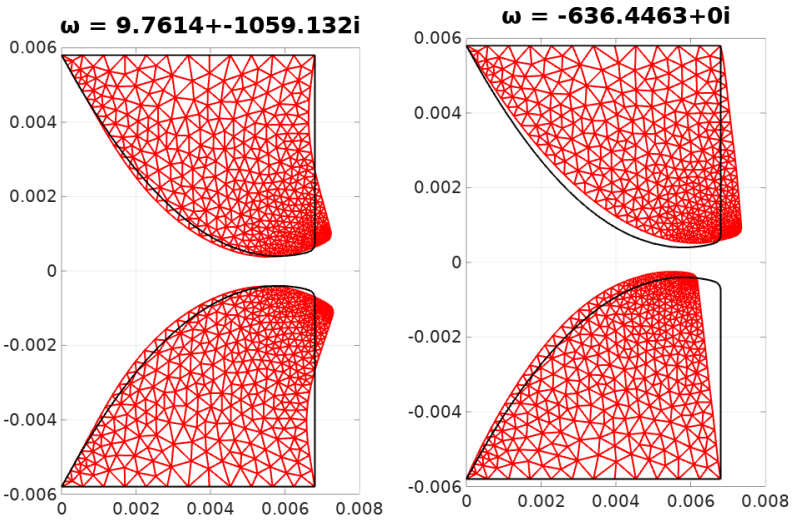

Fig. 3. Two selected DMD modes in case C. The *left* DMD mode has significant growth rate and frequency content 168.45 Hz. The relevance of the *right* DMD mode rapidly decaying with time as $Re(\omega) \ll 0$ and it has no frequency content, i.e., it helps to reconstruct the simulation asymmetry in the given data set only

Conclusion The DMD method is very interesting allowing us to uncover dynamics of given system without deep knowledge of it. The data set which it tries to reconstruct can be obtained by measurements or simulations. Therefore the DMD method has reached a lot of attention and many improvements of it have been developed, see e.g. [3]. Here it was applied on the flow-induced vocal fold vibrations. The presented analyses show that DMD can not be used as the all-able black-box but rather a little parameter tuning is needed.

Acknowledgements

Authors are grateful for support provided by *Grant No. GA19-04477S* of Czech Science Foundation and by *Grant No. SGS19/154/OHK2/3T/12* of the CTU in Prague.

References

[1] Kou, J., Zhang, W., An improved criterion to select dominant modes from dynamic mode decomposition, European Journal of Mechanics-B/Fluids 62 (2017) 109-129.

[2] Kutz, J. N., Brunton, S. L., Brunton, B. W., Proctor, J. L., Dynamic mode decomposition: Data-driven modeling of complex systems, Society for Industrial and Applied Mathematics, 2016.

[3] Noack, B. R., Stankiewicz, W., Morzyski, M., Schmid, P. J., Recursive dynamic mode decomposition of transient and post-transient wake flows, Journal of Fluid Mechanics 809 (2016) 843-872.

[4] Tu, J. H., Rowley, C. W., Luchtenburg, D. M., Brunton, S. L., Kutz, J. N., On dynamic mode decomposition: Theory and applications, Journal of Computational Dynamics 1 (2) (2014) 391-421.

[5] Valášek, J., Sváček, P., Horáček, J., On suitable inlet boundary conditions for fluid-structure interaction problems in a channel, Applications of Mathematics 64 (2) (2019) 225-251.

[6] Valášek, J., Sváček, P., Horáček, J., The influence of penalization inlet boundary condition on the stability boundary, Proceedings of the conference Computational Mechanics 2019, Srní, University of West Bohemia, 2019, pp. 212-215.

[7] Zhang, Z., Neubauer, J., Berry, D. A., Physical mechanisms of phonation onset: A linear stability analysis of an aeroelastic continuum model of phonation, The Journal of the Acoustical Society of America 122 (4) (2007) 2279-2295.

COMPUTATIONAL MECHANICS 2021
36th conference with international participation
Srní
November 8 - 10, 2021

Influence of an atmosphere at an airplane flutter velocity

J. Valenta[a], A. Kratochvíl[a]

[a] *Department of Aerospace Engineering, Faculty of Mechanical Engineering, Center of Advanced Aerospace Technology, Czech Technical University in Prague, Technicka Street 4, 16607, Prague 6, Czech Republic*

An airplane flutter is self-excited harmonic oscillation of a structure. It occurs without any warning and leads to destruction within a second. Flutter is cause by interaction of inertia, stiffness and aerodynamic forces. There have to be also considered a feedback between force and deformation of structure during mathematical analysis of a problem. A flutter analysis is an analytical process aimed at determination a velocity of flutter occurrence. A mathematical model for flutter analysis is based on airplane modal parameters obtained from ground vibration test of made prototype, mass and geometrical characteristic. A producer of airplane has to proof that each prototype of the airplane is free from flutter up to certain velocity given by airworthiness requirements. The minimal flutter velocity is usually related to a maximal airplane velocity referred as design velocity "V_D" multiplied by a safety coefficient, which is specified by airworthiness requirements of given category, it usually has the value of 1,2.

The flutter analysis is the most usually carried out for standardized atmosphere condition given by International Standard Atmosphere (next as ISA) model where model parameters such as a pressure, a temperature, a density, and a viscosity of the Earth's atmosphere change over a wide range of altitude. The ISA model works with a hypothetical standard day condition where all parameters represent averages of all over the planet location and all year seasons. It does not take in account actual meteorological situation or atmospheric conditions.

To determine variations in atmosphere parameters, the MIL-HDBK-310 is used. In this handbook is climatic data for use in engineering analyses. The atmospheric envelope model is chosen. This model consists climatic data of extremes at each altitude regardless of the location and time at which occurs. Therefore these envelopes are suitable for objects flying horizontally, see [1].

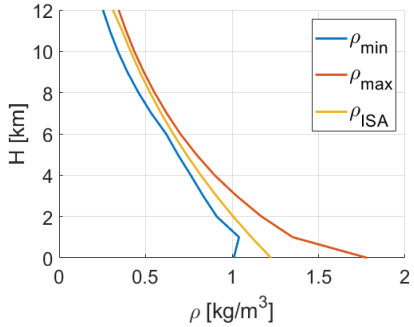

Fig. 1. Density at altitude

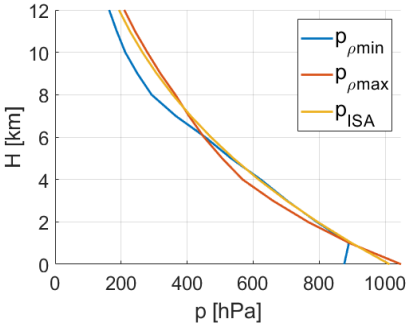

Fig. 2. Pressure at altitude

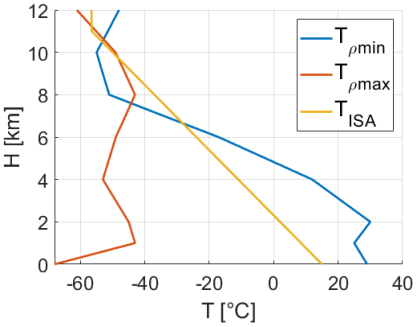

Fig. 3. Temperature at altitude

In used calculation model, the changing parameter of atmosphere is air density. Therefore, the extremes of density is used from handbook. Fig. 1 contains extremes of density at altitudes while Fig. 2 and Fig. 3 shows pressures and temperatures that occurs at this densities.

Three calculations method for determine a speed of flutter is used. 2D model uses unsteady aerodynamic load represented by Strip Theory and Theodorsen thin oscillation airfoil in ideal non-compressible flow. This model works with two-dimensional model. Therefore, the correction on finite span is made in 3D model. The third model is Double lattice method. This method uses thin oscillating surfaces in ideal compressible flow. The finite span is considered at this method, see [2].

The input data is taken from flutter analysis of airplanes which was performed at Department of Aerospace Engineering, Faculty of Mechanical Engineering, Czech technical university in Prague. The four cases of flutter are analysed as shown below.

Table 1. Analysed flutter cases

ID	Airplane	Flutter type
ID1	UFM-13 Lambada	tailplane, low-frequency mode
ID2	VIA NG4 LSA	tailplane, high-frequency mode
ID3	H55	wing, low-frequency mode
ID4	H55	wing, high-frequency mode

Calculations are performed for altitudes from zero to twelve km with one km step at true air speed (next as TAS). In Fig. 4 are shown v-d (velocity - negative logarithmic decrement) and v-f (velocity - frequency) diagrams for third case calculated by 2D method at 6 km. In v-d diagram we can find velocity at which flutter occurs. It is when negative logarithmic decrement reaches zero value. Then is read frequency for flutter velocity from v-f diagram. In this diagram is shown which modes interact with each other and causing flutter.

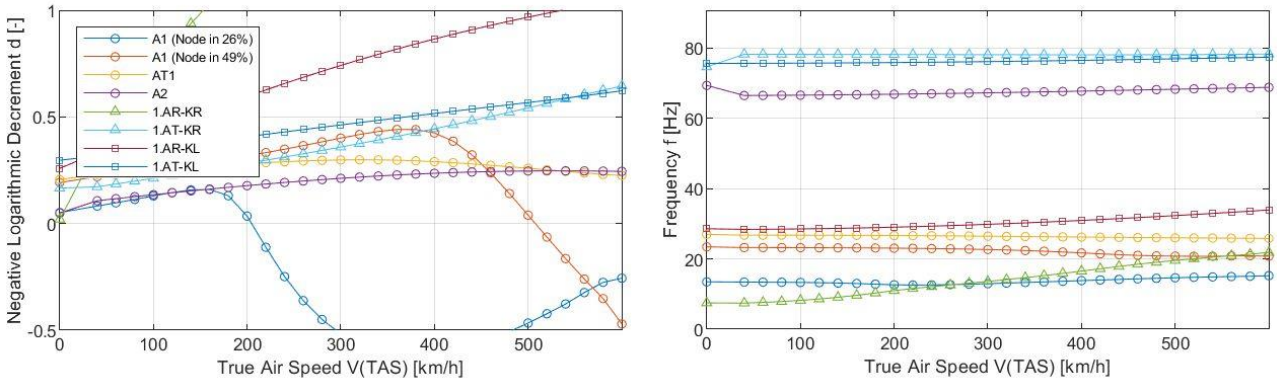

Fig. 4. ID3-MSA-2D, v-d v-f diagrams at 6km

From diagrams is read flutter velocities and frequencies for each altitude and from this values the graphs bellow is made.

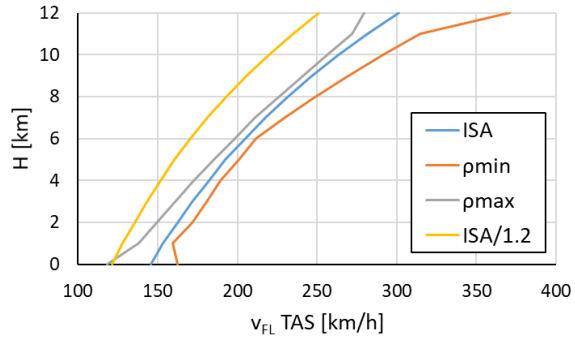

Fig. 5. ID3-2D, flutter velocity at altitude

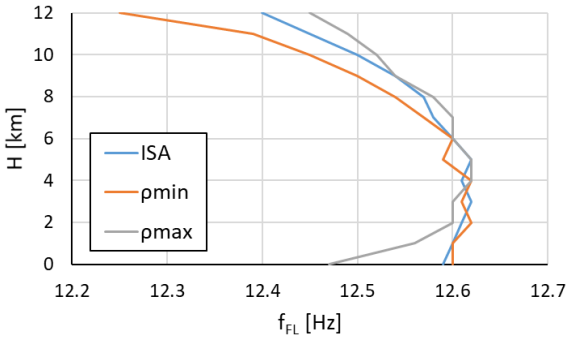

Fig. 6. ID3-2D, flutter frequency at altitude

Yellow curve in Fig. 5 shows limit values of flutter velocity for each altitude. This values is obtained by divining the ISA values by safety coefficient of 1,2. At the shown case is considerable reserve for higher altitudes, but for sea level the flutter velocity for maximal air density dropped below limit curve. This drop is not marginal and for DLM method, which should be more accurate, is this case ok. This is shown in the next figures. The curves of flutter frequency in Fig. 6 is different than in Fig. 8. This is given by differences in used computational models.

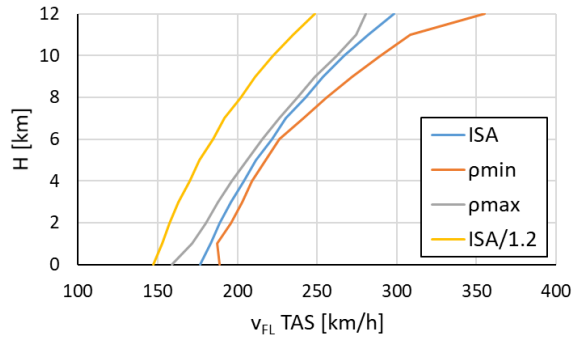

Fig. 7. ID3-DLM, flutter velocity at altitude

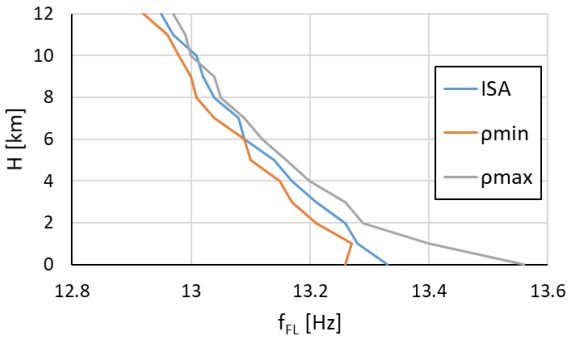

Fig. 8. ID3-DLM, flutter frequency at altitude

Acknowledgements

The work has been supported by the grant project Aeroelastic optimization of aircraft composite structures (SGS20/162/OHK2/3T/12).

References

[1] Global climatic data for developing military products, MIL-HDBK-310, United States Department of Defense, 1997.

[2] Slavík S., Weigl K., Flutter calculation model with isolated modal characteristics of control surfaces for small sport airplanes, Czech Aerospace Proceedings (Journal for Czech Aerospace Research), Czech Aerospace Manufacturers Association / ALV, Prague, No. 2, 2008.

COMPUTATIONAL MECHANICS 2021
36th conference with international participation
Srní
November 8 - 10, 2021

Innovative active head restraint system in car: Virtual prototyping and safety assessment

J. Vychytil[a], J. Špička[a], J. Hluchá[b], L. Kovář[b], P. Moravcová[c], K. Bucsuházy[c]

[a] *New Technologies – Research Centre, Univerzitní 8, 301 00 Plzeň, Czech Republic*
[b] *MECAS ESI, s.r.o., Brojova 16, 326 00 Plzeň, Czech Republic*
[c] *Transport Research Centre, Líšeňská 33a, 636 00 Brno, Czech Republic*

The risk of a fatal or serious injury of an occupant occurring in a side impact is higher than with other types of impact. Whereas the front and rear parts of a vehicle provide deformation zones that absorb part of an impact, the lateral parts of a car have minimal space for the absorption of energy during impact. Traumatic brain injuries incurred in lateral impact are more severe than those resulting from non-lateral impact [1]. Most currently used head restraints are unable to protect the head and cervical spine during oblique and lateral collisions or during vehicle rotation or rollover. Therefore, we describe the development and testing of a new active head restraint system. Its size is comparable to commonly used head restraints. The expanding frame has an arched shape and is equipped with a failsafe that activates the head restraint during a collision. It should absorb the abrupt movement of the occupant by deploying a padded element on each side of the occupant's head, see Fig. 1.

The finite element (FE) model of the head restraint system is developed including all relevant parts and containing more than 24,000 elements in total. The head restraint model is implemented within an FE model of a passenger vehicle. We consider a fully deformable model of a small car, including its interior. Side windows are not considered in these impact scenarios, though the vehicle model is equipped with a side airbag. The model is evaluated with regard to the injury assessment of the driver and is composed of more than 470,000 elements. It is fully validated for the impact scenarios.

The occupant is represented via the Virthuman model. Its basic skeleton is formed from of a "multi-body structure" (MBS). The surface of the model, on the other hand, is divided into a set of segments that are connected to the skeleton via nonlinear springs and dampers, which represent deformations of soft tissues. The model is formed from 263 rigid bodies in total. It is easy to position and enables fast calculations. Its biofidelity is confirmed e.g. in [3]. Virthuman models are scaled to account for diverse anthropometry of occupants from the 1st percentile female up to 99th percentile male. Namely, 18 different anthropometric types are considered. Standard seating position is considered with respect to the EuroNCAP procedure [2]. The head restraint is adjusted for each Virthuman model to obtain the correct position. The occupant is belted with a standard 3-point belt without pre-tensioning. Moreover, four different out-of-positions (OOP) are considered to assess potential risk from the deployment of the paddings itself. It includes leaning of the head towards the window and the passenger as well as rotations of whole body to both left and right sides.

Five collision scenarios are considered based on EuroNCAP protocols. Pole side impact

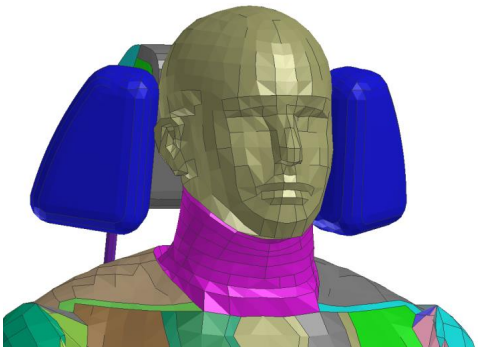

Fig. 1. Numerical model of an occupant (35-year-old male of the 99th percentile) with the restraint system at the active state

is a perpendicular impact of the vehicle to the rigid pole with the diameter of 254 mm at the velocity of 29 km/h. In the oblique pole side impact, the impact angle is 75 degrees and the impact velocity is 32 km/h, see [2]. These impact are considered at both driver and passenger side of the vehicle. Finally, the far-side impact as defined by the EuroNCAP is considered.

Safety assessment of the head restraint system and its virtual prototyping is done in three steps [4]. The results are evaluated with regards to the head and neck injury criteria. Standard injury criteria are considered as defined by the EuroNCAP testing protocols [2]. In the first step, 50th percentile male driver in a standard seating position is considered in four impact scenarios. Including of both inactive and activated state of the head restraint system leads to the total number of 8 simulations. The results suggest increase of occupant safety especially for the pole side impact. Based on the results, first steps of virtual prototyping are made in terms of deployment time as well as increasing the deployment angle.

Second step includes testing with various anthropometric types with improved head restraint system. All 18 representatives are considered in standard seating positions. Consideration of both side and oblique pole impact for all anthropometric types together with the impact at the passenger side for selected representatives leads to the total number of 96 simulations. The results suggest increase of the overall safety for variety of anthropometric types. However, some design changes are favourable in order to increase safety for particular extreme cases (such as 1st percentile female). Namely, additional foam and fabric are proved to be sufficient.

Finally, OOP are tested in all five impact scenarios leading to the total number of 17 simulations. Here, 50th percentile male is considered as an occupant. The model of head restraint is improved as described in two previous steps. Results of these simulations suggest that no injury of the occupant is caused by the deployment of the head restraint system itself.

Safety assessment and the process of virtual prototyping suggest potential benefit of the active head restraint system in terms of reducing occupant injury risk. It may represent a cheaper alternative to airbags. Also, this system might be a solution for passive safety in future mobility (autonomous vehicles) where the application of standard passive safety elements might be problematic.

Acknowledgements

This article was produced with the financial support of the Ministry of Transport within the program of long-term conceptual development of research organizations. The work was also supported by the European Regional Development Fund-Project “Application of Modern Technologies in Medicine and Industry” (No. CZ.02.1.01/0.0/0.0/17_048/0007280).

References

[1] Bazarian, J. J., Fisher, S. G., Flesher, W., Lillis, R., Knox, K. L., Pearson, T. A., Lateral automobile impacts and the risk of traumatic brain injury, Annals of Emergency Medicine 44 (2) (2004) 142-152.

[2] EuroNCAP, Oblique pole side impact testing protocol, Version 7.0.2, Nov. 2015.

[3] Vychytil, J., Manas, J., Cechova, H., Spirk, S., Hyncik, L., Kovar, L., Scalable multi-purpose virtual human model for future safety assessment, SAE Technical Paper (2014) 2014-01-0534.

[4] Vychytil, J., Hlucha, J., Kovar, L., Kostikova, M., Moravcova, P., Bucsuhazy, K., Innovative active head restraint system in a car: Safety assessment with virtual human body model, SAE Technical Paper (2020) 2020-01-0979.

COMPUTATIONAL MECHANICS 2021
36th conference with international participation
Srní
November 8 - 10, 2021

A high order discontinuous Galerkin method for fluid-structure interaction

O. Winter[a,b], P. Sváček[a,b]

[a] Dept. of Instrumentation and Control Engineering, Faculty of Mechanical Engineering, Center of Advanced Aerospace Technology, Czech Technical University in Prague, Technicka Street 4, 166 07, Prague 6, Czech Republic
[b] Dept. of Technical Mathematics, Faculty of Mechanical Engineering, Czech Technical University in Prague, Charles Square 13, 120 00, Prague 2, Czech Republic

1. Introduction

Many important scientific and engineering problems require analysis of fluid-structure interaction (FSI). For example, aeroelastic flutter can produce large and potentially destructive vibrations in aircraft [7], turbines [1], and other structures [3] or biological applications such as study of fluid flow inside human vocal tract [5]. The presented study deals with a high order discontinuous Galerkin method for fluid-structure interaction.

2. Mathematical model

The model consists of the Navier-Stokes equations governing the motion of a compressible fluid flow coupled to a rigid body dynamics, i.e., a movement of a structure, described by a second order ordinary differential equation. Arbitrary Lagrangian Eulerian (ALE) method is used to treat the deformable domain. The viscous gas dynamics in computational domain $\Omega_t \subset \mathbb{R}^2$ for any $t \in (0,T), T > 0$ is described by the Navier-Stokes equations, see e.g. [2]. The Navier-Stokes equations written in the conservative form reads

$$\begin{aligned}
&\frac{\partial}{\partial t}(\varrho) + \sum_{i=1}^{2} \frac{\partial}{\partial x_i}(\varrho v_i) = 0,\\
&\frac{\partial}{\partial t}(\varrho v_i) + \sum_{j=1}^{2} \frac{\partial}{\partial x_j}(\varrho v_i v_j + p\delta_{ij}) = \sum_{j=1}^{2} \frac{\partial}{\partial x_j}(\tau_{ij}), \quad \text{for } i = 1,2,\\
&\frac{\partial}{\partial t}(\varrho E) + \sum_{j=1}^{2} \frac{\partial}{\partial x_j}(\varrho v_j E + v_j p) = \sum_{j=1}^{2} \frac{\partial}{\partial x_j}(-q_j + v_i \tau_{ij}),
\end{aligned} \tag{1}$$

where ϱ is the fluid density, p is the pressure, v_1, v_2 are the velocity components of the velocity vector $\boldsymbol{v}$, and E is the total energy. The components of the viscous stress tensor $\boldsymbol{\tau}$ and the heat flux $\boldsymbol{q}$ are given by

$$\tau_{ij} = \mu \left(\frac{\partial v_i}{\partial x_j} + \frac{\partial v_j}{\partial x_i} - \sum_{k=1}^{2} \frac{2}{3} \frac{\partial v_k}{\partial x_k} \delta_{ij} \right) \tag{2}$$

and

$$q_i = \frac{\mu}{\mathrm{Pr}} \frac{\partial}{\partial x_i} \left(E + \frac{p}{\varrho} - \sum_{j=1}^{2} \frac{1}{2} v_j v_j \right), \tag{3}$$

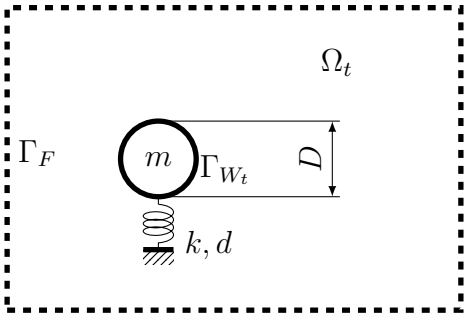

Fig. 1. Sketch of the computation domain Ω_t

where μ is dynamic viscosity and Pr, assumed to be constant $\mathrm{Pr} = 0.72$, is the Prandtl number. For an ideal gas, the pressure p has the form

$$p = (\gamma - 1)\varrho \left(E - \frac{1}{2} \sum_{i=1}^{2} v_i v_i \right), \tag{4}$$

where γ is the adiabatic gas constant, γ is set to 1.4 in presented study. Imposed boundary conditions are either free-stream at the far field, or adiabatic no-slip conditions at the boundaries of the structure, i.e., $\boldsymbol{v}|_{\Gamma_{W_t}}$ is equal to the velocity of the structure. System (1) is supplemented with suitable initial conditions.

The motion of the structure in the one-direction is modeled by the second-order differential linear equation, i.e.,

$$m\ddot{h} + d\dot{h} + kh = L, \tag{5}$$

where m is the oscillating mass of the system, d and k denote the mechanical damping and stiffness of the oscillator unit, respectively, h is the displacement of the oscillator and L is the force exerted by the fluid on the structure in the transverse direction, see Fig 1. Fluid flow model (1) is coupled with the rigid body model (5) via L in the following manner, i.e.,

$$L = -l \int_{\Gamma_{W_t}} \sum_{j=1}^{2} (\tau_{2j} - p\delta_{2j}) n_j \, dS, \tag{6}$$

where l is the depth of the structure, $\boldsymbol{n} = (n_1, n_2)$ is the unit outer normal to $\partial\Omega_t$ on Γ_{W_t} (pointing into the structure). System (5) is supplemented with initial suitable initial conditions.

3. Numerical approximation

The fluid flow model is discretized using a high-order discontinuous Galerkin formulation with triangular grid elements and nodal basis functions and the domain movement is taken into account with aid of arbitrary Lagrangian-Eulerian method, see e.g. [7]. Following standard procedure for DG discretization of second-derivatives, first the auxiliary gradient variable $\boldsymbol{g}$ is introduced, and then governing equations are rewritten as the system of first order equations, i.e.,

$$\frac{\partial}{\partial t}(\boldsymbol{u}) + \nabla \cdot \boldsymbol{F}^i(\boldsymbol{u}) - \nabla \cdot \boldsymbol{F}^v(\boldsymbol{u}, \boldsymbol{g}) = \boldsymbol{0}, \tag{7}$$

$$\nabla \boldsymbol{u} = \boldsymbol{g}, \tag{8}$$

where $\boldsymbol{u} = [\varrho, \varrho v_1, \varrho v_2, \varrho E]^T$ is the solution vector, $\boldsymbol{F}^i$ is inviscid flux given as

$$\boldsymbol{F}^i(\boldsymbol{u}) = \begin{bmatrix} \varrho v_1 & \varrho v_2 \\ \varrho v_1 v_1 & \varrho v_2 v_1 \\ \varrho v_1 v_2 & \varrho v_2 v_2 \\ (\varrho E + p) v_1 & (\varrho E + p) v_2 \end{bmatrix} \tag{9}$$

and $\boldsymbol{F}^v$ is viscous flux given as

$$\boldsymbol{F}^v(\boldsymbol{u}, \boldsymbol{g}) = \begin{bmatrix} 0 & 0 \\ \tau_{11}(\boldsymbol{g}) & +\tau_{12}(\boldsymbol{g}) \\ \tau_{21}(\boldsymbol{g}) & +\tau_{22}(\boldsymbol{g}) \\ -q_1(\boldsymbol{u}) + v_1\tau_{11}(\boldsymbol{g}) + v_2\tau_{21}(\boldsymbol{g}) & -q_2(\boldsymbol{u}) + v_1\tau_{12}(\boldsymbol{g}) + v_2\tau_{22}(\boldsymbol{g}) \end{bmatrix}. \tag{10}$$

The inviscid fluxes are computed using Roe's method [6], and the numerical fluxes for the viscous terms are chosen according to the compact discontinuous Galerkin (CDG) method [4]. The computational domain Ω is discretized by the computational mesh with elements $\mathcal{T}_h = \{K\}$. The solution $(\boldsymbol{u}, \boldsymbol{g})$ is sought in $[V_h^p]^4$ and $[V_h^p]^{4\times 2}$, respectively, where $V_h^p = \{v \in L^2(\Omega), v|_K \in P^p(K), \forall K \in \mathcal{T}_h\}$ with P^p being the space of polynomial functions of degree at most $p \geq 1$ on K. The semi-discrete DG formulation is expressed as: find $\boldsymbol{u}_h \in [V_h^p]^4$ and $\boldsymbol{g}_h \in [V_p^h]^{4\times 2}$ such that for all $K \in \mathcal{T}_h$

$$\begin{aligned} \int_K \frac{\partial \boldsymbol{u}_h}{\partial t} \cdot \boldsymbol{\varphi} + \int_K (\boldsymbol{F}^i(\boldsymbol{u}_h) - \boldsymbol{F}^v(\boldsymbol{u}_h, \boldsymbol{g}_h)) : \nabla \boldsymbol{\varphi} - \\ - \int_{\partial K} (\boldsymbol{F}^i(\boldsymbol{u}_h) - \boldsymbol{F}^v(\boldsymbol{u}_h, \boldsymbol{g}_h)) \cdot \boldsymbol{\varphi} = \boldsymbol{0}, \quad \forall \boldsymbol{v} \in [P^p(K)]^4, \end{aligned} \tag{11}$$

$$\int_K \boldsymbol{g}_h : \boldsymbol{\psi} + \int_K \boldsymbol{u}_h \cdot (\nabla \cdot \boldsymbol{\psi}) - \int_{\partial K} (\boldsymbol{u}_h \otimes \boldsymbol{n}) : \boldsymbol{\psi} = \boldsymbol{0}, \quad \forall \boldsymbol{\psi} \in [P^p(K)]^{4\times 2}. \tag{12}$$

Fluxes in Eqs. (11) and (12) are modified according to the ALE method, see e.g. [7]. All integrals in Eqs. (11) and (12) are integrated using high-order Gaussian quadrature rules. Time integration is done with aid of a high-order Runge-Kutta (RK) method.

4. Numerical results

To validate the high-order scheme, we considered a test problem consisting of flow-induced vibration of a circular cylinder, where the cylinder is allowed to move in vertical direction, see Fig. 1. The far field fluid has velocity $\boldsymbol{v} = (1, 0)\,\mathrm{m/s}$, density $\varrho = 1\,\mathrm{kg/m^3}$, Mach is equal to 0.2, and a Reynolds number with respect to diameter D is equal to 100. The constants chosen for this problem were $D = 1\,\mathrm{m}$, $m = 1\,\mathrm{kg}$, $k = 0.64\,\mathrm{N/m}$, $d = 10^{-3}k\,\mathrm{Ns/m}$, and $l = 1\,\mathrm{m}$. Fig. 2 shows position h of the cylinder during the computation. Numerical solutions for two cases of our discontinuous Galerkin scheme (RK2-DG1 – second order RK method, first order of polynomials, RK4-DG3 – fourth order RK method, third order of polynomials) are compared to finite volume approximation on very fine grid these solutions indicate very good converge of our scheme.

Acknowledgements

This work was supported by the Grant Agency of the Czech Technical University in Prague (SGS19/154/OHK2/3T/12). Authors acknowledge support from the ESIF, EU Operational Programme Research, Development and Education, and from the Center of Advanced Aerospace Technology (CZ.02.1.01/0.0/0.0/16_019/0000826), Faculty of Mechanical Engineering, Czech Technical University in Prague.

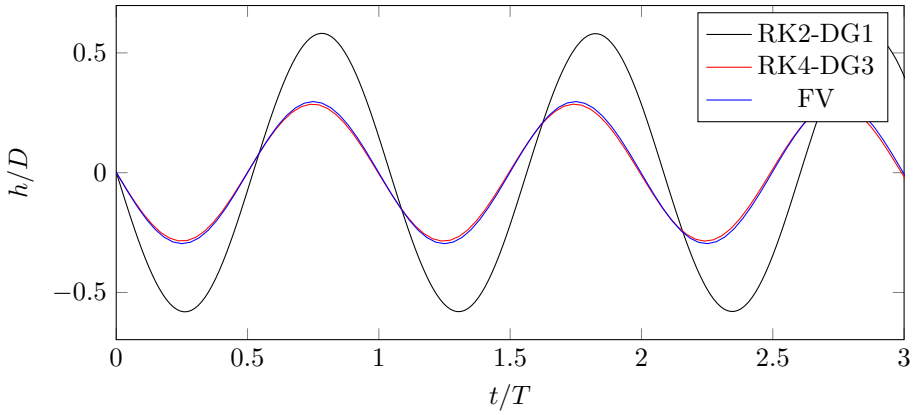

Fig. 2. Position of the cylinder h during selected time period

References

[1] Badur, J., Bryk, M., Accelerated start-up of the steam turbine by means of controlled cooling steam injection, Journal of Energy 173 (2019) 1242-1255.

[2] Blažek, J., Computational fluid dynamics: Principles and applications, Elsevier, 3rd edition, 2015.

[3] Hoseini, S. S., Najafi, G., Ghobadian, B., Akbarzadeh, A. H., Impeller shape-optimization of stirred-tank reactor: CFD and fluid structure interaction analyses, Chemical Engineering Journal 413 (2021) No. 127497.

[4] Peraire, J., Persson, P. O., The compact discontinuous Galerkin (CDG) method for elliptic problems, SIAM Journal on Scientific Computing 30 (4) (2008) 1806-1824.

[5] Sváček, P., Horáček, J., FE numerical simulation of incompressible airflow in the glottal channel periodically closed by self-sustained vocal folds vibration, Journal of Computational and Applied Mathematics 393 (2021) No. 113529.

[6] Toro, E. F., Riemann solvers and numerical methods for fluid dynamics, Springer, 3rd edition, 2009.

[7] Winter, O., Sváček, P., On numerical simulation of flexibly supported airfoil in interaction with incompressible fluid flow using laminar-turbulence transition model, Computers & Mathematics with Applications 83 (2021) 57-73.

COMPUTATIONAL MECHANICS 2021
36th conference with international participation
Srní
November 8 - 10, 2021

Problematics of curved laminated composites

J. Žák

Technická univerzita v Liberci, Fakulta strojní, Studentská 1402/2, 461 17 Liberec, Czech Republic

1. Introduction

The use of composite materials on textile machines is a matter of decades. As the demands on the quality of the final product increase, so do the demands on the precision of the parts that are directly involved in the fabric creation. In our paper we deal with the issue of production of the so-called batten for the DIFA weaving machine, which is intended for the production of 3D textiles, the so-called DIstance FAbric.

2. Problem analysis

The existing VEGA weaving machine was used as the basis for the construction of the DIFA loom, from which the basic components were taken over. However, it soon became apparent that while the precision with which existing parts are made is sufficient for weaving *ordinary* fabric, it will be necessary for the DIFA machine to change the technology of their production in order to reduce shape imprecisions.

The above mentioned batten on the VEGA and DIFA machines basically consists of a metal (steel made) tube and four C/E composite plates, which are glued to the tube (see Fig. 1). The tube represents the main element supporting the bending loads, the composite plates form a kind of clamps into which other textile technology devices are fixed, such as weft picking nozzles, various sensors and especially the reed and, in the case of the DIFA machine, also the supports for so called pulling bar. The whole then forms a two-hole profile, extremely stiff in torsion. The reed and the rail for the pulling bar must be very precisely positioned with respect to other devices, the main criterion here being their parallelism.

As can be seen from Fig. 1, the clamps are formed by a curved laminated plate. It is laminated from unidirectional plies of carbon/epoxy prepreg. In order to achieve sufficient bending and torsional stiffness, only the plies at angles of 90 (in the plane of section) and ± 45 degrees are comprised in the stacking sequence, see Fig. 2. The sequence is symmetrical according to the assumption that the resulting part will not twist due to the change in temperature during the cool down after curing. This assumption turned out to be wrong, so we profited of a major change of the batten conception (consisting in the change of principle of static balancing) to redesign the clamps.

3. Design of clamps

As can be seen from Fig. 1, the new clamps are similar in shape, only the dimensions differ. A further difference then consists in the different way the clamps are loaded: in DIFA loom the inertial forces of the reed do not sufficiently compensate the force of the weaving resistance. Both of these facts were taken into account when designing the new stacking sequence of the

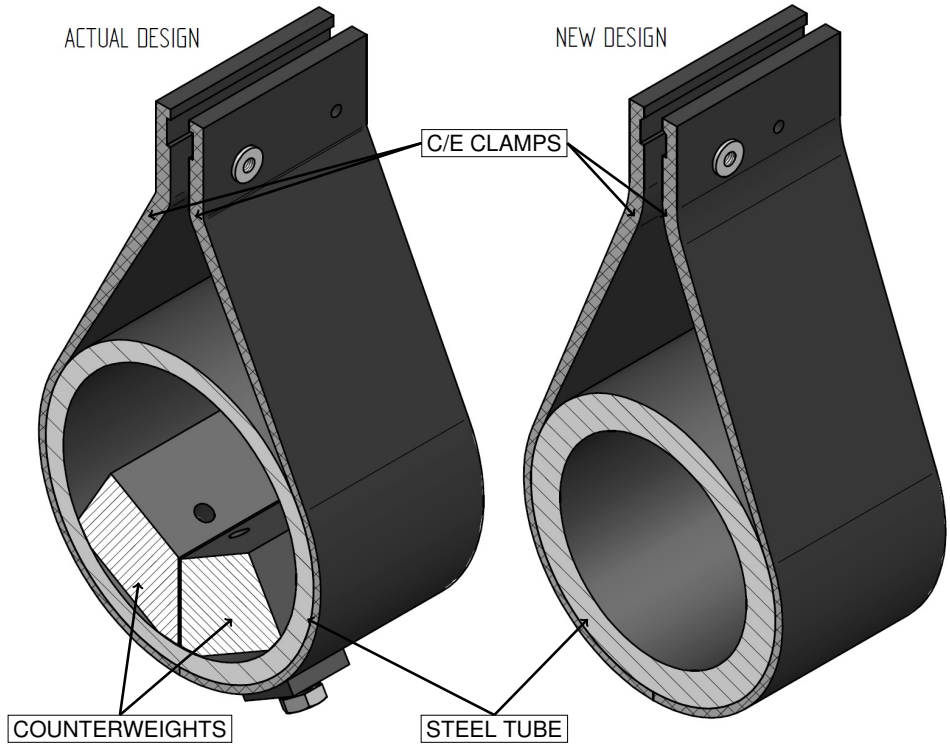

Fig. 1. Section of the batten

plies. The stacking sequence was then determined using classical lamination theory to meet the requirements for strength and stiffness of the batten. While a supposedly *non twisting* symmetric sequence was found we were aware from the beginning of its temperature dependent twisting behavior.

4. Modified classical lamination theory

Let's have the basic equation of a thin plate behavior (we are using annotation as used by [1])

$$\left| \begin{array}{c} \mathbf{N} \\ \mathbf{M} \end{array} \right| = \left| \begin{array}{cc} \mathbf{A} & \mathbf{B} \\ \mathbf{B}' & \mathbf{C} \end{array} \right| \cdot \left| \begin{array}{c} \varepsilon_{\mathbf{0}} \\ \kappa_{\mathbf{0}} \end{array} \right| - \Delta T \cdot \left| \begin{array}{c} \langle \alpha \cdot \mathbf{E} \cdot \mathbf{h} \rangle \\ \langle \alpha \cdot \mathbf{E} \cdot \mathbf{h^2} \rangle \end{array} \right|,$$

where $\varepsilon_{\mathbf{0}} = [\varepsilon_{0,x}, \varepsilon_{0,y}, \gamma_{0,xy}]'$, $\kappa_{\mathbf{0}} = [\kappa_x, \kappa_y, \kappa_{xy}]'$, $\langle \alpha \cdot E \cdot h \rangle$ and $\langle \alpha \cdot E \cdot h^2 \rangle$ being the terms of thermal expansion. In this relation the index 0 refers to the deformations of neutral surface.

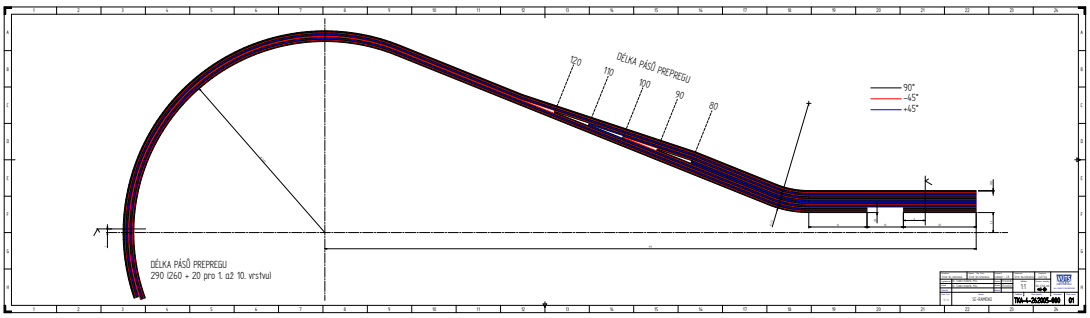

Fig. 2. Stacking sequence of the clamp

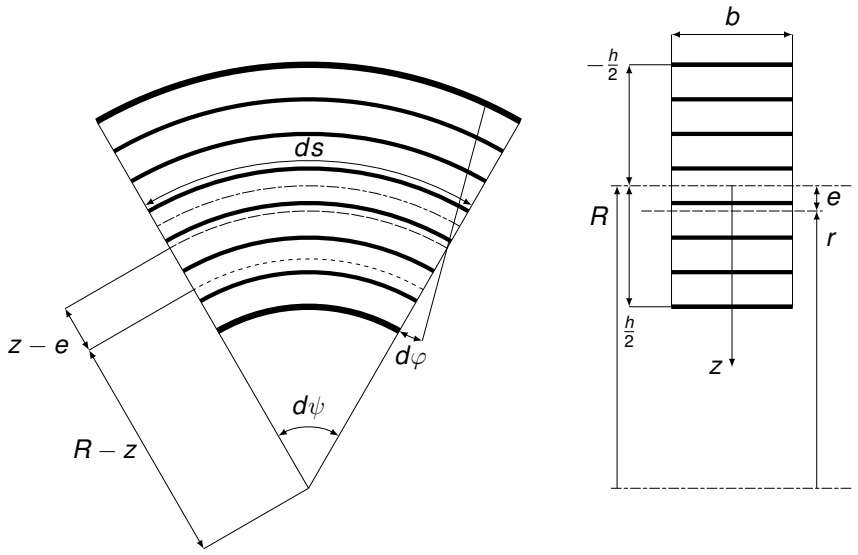

Fig. 3. Kinematics of a curved laminated plate

For a flat plate the terms of sub matrices $\mathbf{A}$, $\mathbf{B}$ and $\mathbf{C}$ are defined using the above mentioned classical theory as follows (see [1]);
per example

$$A_{11} = \sum_{k=1}^{K} \int_{h_{k-1}}^{h_k} \overline{E_{11k}} \cdot dz,$$
$$B_{11} = -\sum_{k=1}^{K} \int_{h_{k-1}}^{h_k} \overline{E_{11k}} \cdot z \cdot dz,$$
$$C_{11} = \sum_{k=1}^{K} \int_{h_{k-1}}^{h_k} \overline{E_{11k}} \cdot z^2 \cdot dz,$$

where K is total number of plies and z is distance from the neutral surface as given by the definition of ε by Kirchhoff's theory. The terms representing the thermal expansion are defined by

$$\langle \alpha \cdot E \cdot h \rangle_x = \sum_k \overline{\alpha \cdot E_{1,k}} \cdot (h_k - h_{k-1}) \text{ etc.}$$

Note: these relationships were used to determine the stacking sequence with respect to the required mechanical properties of the clamps.

The latter relations are based on the kinematics of a thin plane plate using Kirchhoff's theory. If we use the kinematics of a curved plate (see Fig. 3) to derive them, these relations get the following form

$$A_{11} = \sum_{k=1}^{K} \int_{h_{k-1}}^{h_k} \overline{E_{11k}} \cdot \tfrac{dz}{1-\frac{z}{R_x}},$$
$$B_{11} = -\sum_{k=1}^{K} \int_{h_{k-1}}^{h_k} \overline{E_{11k}} \cdot z \cdot \tfrac{dz}{1-\frac{z}{R_x}},$$
$$C_{11} = \sum_{k=1}^{K} \int_{h_{k-1}}^{h_k} \overline{E_{11k}} \cdot z^2 \cdot \tfrac{dz}{1-\frac{z}{R_x}},$$

It is clear from the form of the integrand in the above integrals that even for a symmetric stack-

ing sequence, the members of submatrices $\mathbf{B}$ will not necessarily vanish. It follows that for such a curved laminated plate a coupling occurs between the thermal expansion in the membrane direction and the change in its curvature.

5. Solution of the problem

Although it is theoretically possible to find such a stacking sequence that the members of the submatrices $\mathbf{B}$ are zero, it is practically impossible to meet the requirements for the resulting stiffness of the clamps at the same time. Therefore, we chose an alternative solution to solve the batten problem. There are 2 variants of clamps to be produced, *left* and *right* or *odd* and *even*. These two designs differ in the positions of the layers at ± 45 degrees, where the plies under $+45$ degrees in the *left* clamp are replaced by plies under -45 degrees in the *right* one and vice versa. The twist of these *mirror twins* due to thermal expansion should be inverse. By combining two pairs of *left* and *right* clamps on one tube (see Fig. 4), we obtain an untwisted batten. The price for this is an uneven distribution of the clamping force of the reed.

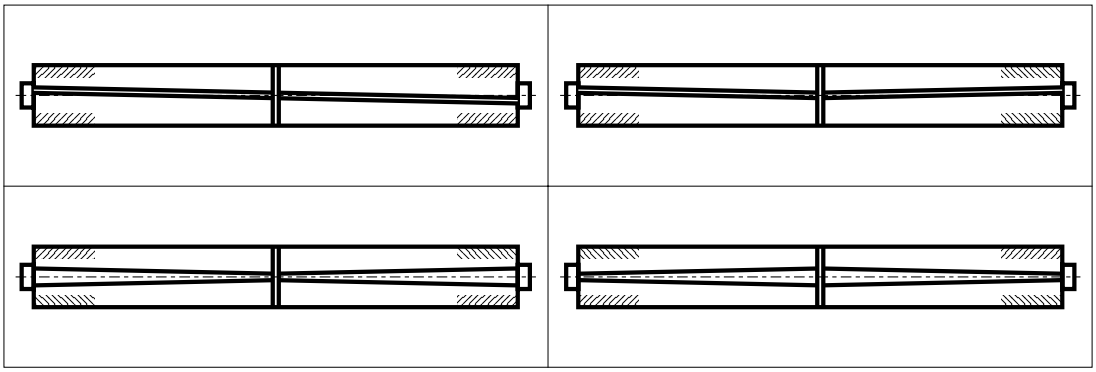

Fig. 4. Combinations of clamps; the current design is top left, the preferred new one is bottom right

6. Conclusion

Using the classical lamination theory, we were able to determine the origin of the clamps twisting as well as the practical impossibility of a *clean* solution. We also verified these calculations using FEM. The solution was to change the technology at the cost of increasing the production costs due to more complex logistics.

References

[1] Gay, D., Composite materials, 3rd Edition. Hermes, Paris, 1991. (in French)

COMPUTATIONAL MECHANICS 2021
36th conference with international participation
Srní
November 8 - 10, 2021

Comparison of analytical methods and FE models to calculate the stiffness of a wound composite beam

T. Zámečníková[a], T. Mareš[a], V. Kulíšek[a], B. Kropík[a]

[a] *Czech Technical University in Prague, Faculty of Mechanical Engineering, Department of Mechanics, Biomechanics and Mechatronics. Technická 4, 166 07 Praha 6, Czech Republic*

1. Introduction

The aim of this work is the search for a new analytical method of calculating the stiffness of the wound composite beams with the circular cross-section. The FE models and several analytical calculations were performed for chosen geometry of the composite beam and all results are compared to experimental data. The experiment of three-point bending on fibre-reinforced composite beams with four different composite lay-ups was done and the stiffness was calculated. The comparison of a new semi-analytical method with the known analytical methods of stiffness calculation and FE models are introduced in this paper.

Composite beams are very variable not only in their shape or cross-section, but also in the layup of the composite material from which they are made. This creates a number of variables that we must take into account when calculating their deformation. It is well known that the available methods for calculating the deformation of composite materials do not provide relevant results for all possible types and shapes of composite beams. It turns out that these methods differ in the results for the same case of a composite beam or are too complex for the initial design of the part. Also, the results of these methods differ from a possible experiment. Analytical, semi-analytical, and numerical methods are known for calculating the deformation of composite beams. The comparison of Timoshenko's and Bernoulli's method of bending calculation, the method of calculation using ABD matrices, the use of statistical mechanics, and the numerical method of finite elements were chosen as the basis for this work. All these methods were applied to an embedded composite beam with an inter-circular cross-section. The aim of this work is to find out in which specific cases the mentioned methods of calculating the effective stiffness of composite beams are valid for the general composition of the composite material.

2. Analytical methods to reach the equivalent stiffness modulus of the composite beam

2.1 The stiffness matrix and the compliance matrix

The Hooke's law contains the stiffness matrix $\boldsymbol{S}$.

$$\boldsymbol{\sigma} = \boldsymbol{S} \cdot \boldsymbol{\varepsilon} \quad , \tag{1}$$

The modulus of elasticity E is expressed for each layer separately by means of the stiffness matrix in the main coordinate system of the composite material $O(L, T, T')$. An orthotropic material is considered. [1] To express the equivalent modulus of elasticity in the main coordinate system of the whole beam $O(x, y, z)$, it is possible to use the stiffness matrix $\boldsymbol{S_{xy}}$ or an inverse matrix the compliance matrix $\boldsymbol{C_{xy}}$. The stiffness matrix $\boldsymbol{S_{xy}}$ is expressed by the

following transformation (3) to the coordinate system $O(x, y, z)$ and the compliance matrix $\boldsymbol{C_{xy}}$ is inverse to it (2).

$$\boldsymbol{C'_{xy}} = \boldsymbol{S'_{xy}}^{-1}, \tag{2}$$

$$\boldsymbol{S'_{xy}} = \boldsymbol{T_{xy}} \cdot \boldsymbol{S} \cdot \boldsymbol{T'_{xy}}. \tag{3}$$

The modulus of elasticity in the direction of the beam axis E_x can be obtained from the compliance matrix $\boldsymbol{C'_{xy}}$, and also from the stiffness matrix $\boldsymbol{S'_{xy}}$. The element S'_{11} is used from stiffness matrix $\boldsymbol{S'_{xy}}$ and element C'_{11} is used from compliance matrix $\boldsymbol{C'_{xy}}$. The usage of the stiffness matrix $\boldsymbol{S'_{xy}}$ represents the upper estimate of the equivalent stiffness, the use of the compliance matrix $\boldsymbol{C'_{xy}}$ the lower estimate of the stiffness of the composite beam. In the results section, their arithmetic mean is also used.

2.2 Calculation of equivalent elasticity modulus E_{eq} by Classical Laminate Theory

To calculate the deflection of a composite beam with a circular cross-section using method from [1] the following equation is used

$$\begin{bmatrix} \boldsymbol{N} \\ \cdots \\ \boldsymbol{M} \end{bmatrix} = \begin{bmatrix} \boldsymbol{A} & \vdots & \boldsymbol{B} \\ \cdots & \vdots & \cdots \\ \boldsymbol{B} & \vdots & \boldsymbol{D} \end{bmatrix} \begin{bmatrix} \boldsymbol{\varepsilon^{\circ}_m} \\ \cdots \\ \boldsymbol{k} \end{bmatrix}, \tag{4}$$

The force loading of the beam can be expressed using the elements of the matrix $\boldsymbol{A}$ [2]. The stress of a composite material using Hooke's law is expressed. To obtain the stress relationship, it is necessary to divide this expression by the total thickness of the composite material t.

$$\sigma_1 = \frac{N_1}{t} = \frac{1}{t}\left(A_{11} - \begin{bmatrix} A_{12} & A_{16} \end{bmatrix} \cdot \begin{bmatrix} A_{22} & A_{26} \\ A_{62} & A_{66} \end{bmatrix}^{-1} \cdot \begin{bmatrix} A_{21} \\ A_{61} \end{bmatrix}\right) \cdot \boldsymbol{\varepsilon^{\circ}_1} \ . \tag{5}$$

The equivalent modulus of elasticity is expressed by the following relation.

$$E_{eq} = \left(A_{11} - \begin{bmatrix} A_{12} & A_{13} \end{bmatrix} \cdot \begin{bmatrix} A_{22} & A_{23} \\ A_{32} & A_{33} \end{bmatrix}^{-1} \cdot \begin{bmatrix} A_{21} \\ A_{31} \end{bmatrix}\right) \cdot \frac{1}{t} \ , \tag{6}$$

2.3 Statistic method for bending stiffness calculation

This method is based on an analogy to statistical mechanics. According to statistical mechanics, the (probable) energy of the system $\langle E \rangle$ is equal to the negatively taken derivative of the logarithm of the partition function Z, according to a parameter called thermodynamic beta (β)

$$\langle E \rangle = -\frac{\partial \, lnZ}{\partial \, \beta} \ , \tag{7}$$

where the partition function can be obtained by a relation

$$Z = \sum_i e^{-\beta E_i} \ . \tag{8}$$

The energy of the system is obtained by following formulas.

$$\langle E \rangle = -\frac{\partial kZ}{\beta} \qquad \beta = \frac{1}{k_B T} \tag{9}$$

In this analogy leading to the determination of bending (and similarly shear) stiffness, we consider a micro-state as a set of stiffnesses of individual layers calculated according to any mutually different method. The total bending stiffness, *EJi*, corresponding to a given micro-state is given by the sum of the stiffnesses of all layers. Each micro-state has an energy equal

to the total potential energy of the beam. For example, when considering a symmetrical three-point bending

$$E_i = \Pi = U - F \cdot u = -\frac{1}{2} F \cdot u = -\frac{1}{2} F \cdot \frac{Fl^3}{48(EJ)_i} \tag{10}$$

The partition function *Z* expressed in this way is subjected to a numerical derivative according to equation (9) and we obtain the (assumed, average) energy of the beam $\langle E \rangle$. Backwards, from the relation for the total potential energy of the beam (10) we calculate the effective bending stiffness of the beam

$$(EJ)_{effective} = -\frac{F^2\, l^3}{96\langle E \rangle} \tag{11}$$

2.4 A new semi-analytical method

A new semi-analytical approach is based also on the Classical Laminate Theory and tries to calculate the equivalent stiffness of the beam with the combination of the tensile and bending stiffness matrix elements. The assumption for this theory is that the geometry of the composite beam with circular cross-section combines the tensile and bending loading of the material of composite beam. The combination of the elements of matrix ***A*** and matrix ***D*** (4) is used in a superposition of the stiffnesses.

$$(EJ)_{equivalent} = (EJ)_{A_{11}} + (EJ)_{D_{11}} \tag{12}$$

3. Experiment

Composite wound tubes with an inner diameter of 26 mm and 50 mm were selected as specimens. The tests were performed for four composite layups and two lengths of the composite beams. Three types of fibers were used for all composite layups. Three-point bending tests were performed on a FPZ 100/1 machine. Supports with a span of 200 mm and 400 mm for tubes with a diameter of 26 mm were used for the tests. The spans of the supports for tubes with an inner diameter of 50 mm were 400 mm and 600 mm. The beams were loaded with force through the strap. The deflection was measured with an extensometer and strain with a strain gauge. The sensors were placed in the centre of the beam under the load member.

Groups of six pieces from each combination of fibers, composite layup, and support span were tested. The average value of the equivalent stiffness EJ_{eq} was evaluated. All sample types were modelled by available FEM methods and the equivalent stiffness was calculated. All the mentioned analytical methods were also used to calculate the equivalent stiffness. A comparison of these values is shown in the following section.

4. Results

The results show the deviations of the individual methods from the experimental data in percentages. The equivalent stiffness of EJ_{eq} beams is compared. The results of two lay-ups Typical [90 °, 0 °, ± 30 °] in Fig. 1 and Diagonal [90 °, ± 45 °] in Fig. 2 of a composite beam with diameters of 26 mm and 50 mm made in several different fibre types are given here. The average stiffness (EJ_mean in the figures) obtained from the matrix S' and C' shows a good agreement with the experiment, but this method predicts higher stiffness compared with experimental data. The Statistical Mechanics has good agreement with the experimental data for the diameter of 50 mm in both lay-ups. It shows that this method fits good in cases of thin-walled beams. The new semi-analytical approach shows the constant deviations less than 25% from experimental data in all cases of specimens. These results are on the safety side of the calculation in most cases compared to the experimental data.

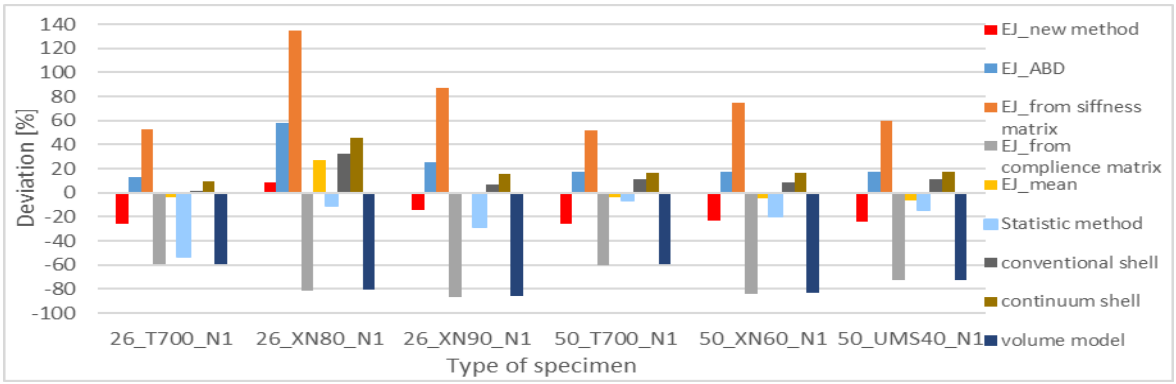

Fig. 1. The deviation from the experiment of equivalent stiffness for beams with Typical layup [90°, 0°, ±30°]

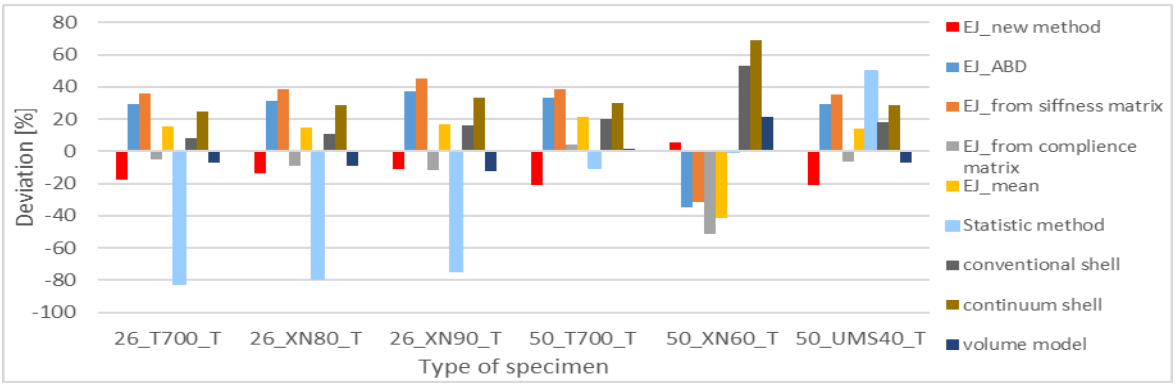

Fig. 2. The deviation from the experiment of equivalent stiffness for beams with Diagonal layup [90°, ±45°]

5. Conclusion

None of the methods described above gives sufficiently accurate predictions of the stiffness of experimentally tested beams. There is still a noticeable problem where the results of different methods approach different results of the beam equivalent stiffness.

From the performed comparison, methods with the appropriate results are selected. The new semi-analytical approach reached a good agreement with experimental data in all composite lay-ups. The method based on statistic mechanics reached a good conformity in cases with diagonal lay-ups. A method based on the mean of an upper and lower estimate of the stiffness of the composite lay-up seems to be almost equally suitable, but with the deviation that predicts the greater stiffness than the experiment. In terms of computational complexity, the proposed approaches are less demanding than the FE method and are therefore suitable for fast usage for the preliminary design. The numerical optimization of these approaches is also possible.

Acknowledgement

The work has been supported by the research project of Students grant agency CTU SGS21/151/OHK2/3T/12.

References

[1] Laš, V., Mechanics of composite materials, 2nd edition, ZČU, Pilsen, 2008. (in Czech)
[2] Zavřelová, T., Analysis of composite beam bending, Diploma thesis, ČVUT. Prague, 2015.

COMPUTATIONAL MECHANICS 2021
36th conference with international participation
Srní
November 8 - 10, 2021

The fuzzy approach for investigation of the steady-state response of rotors excited by loading effects of uncertain magnitude

J. Zapoměl[a,b], P. Ferfecki[a,c], M. Molčan[c]

[a] *Faculty of Mechanical Engineering, VŠB-Technical University of Ostrava, 17. listopadu 15, 708 00 Ostrava, Czech Republic*
[b] *Institute of Thermomechanics, Czech Academy of Sciences, 182 00 Praha, Dolejškova 5, Czech Republic*
[c] *IT4Innovations National Supercomputing Center, VŠB-Technical University of Ostrava, 17. listopadu 15, 708 00 Ostrava, Czech Republic*

Behavior of rotors depends on their geometric shape and composition, materials they are manufactured of, and on their loading and interactions with the environment and other bodies. All these factors are described by a number of parameters, the values of some of them can be uncertain.

Several approaches making it possible to treat this problem have been developed. Among them there are:

- the worst scenario method,
- the fuzzy number approach,
- the probabilistic approaches.

Application of each of these approaches requires to define uncertainty of the input parameters. The worst scenario method requires to know only the interval of values, which the uncertain quantities can acquire. The probabilistic approach utilizes mostly the Monte Carlo method. It is based on knowledge of the probability density function related to each uncertain quantity and requires corresponding generators of the random numbers.

The fuzzy approach assumes that the uncertain quantities take values from some intervals. Then the degree of membership, the magnitude of which is between 0 and 1, is assigned to all of them. This manipulation is based on experience. Some rules and recommendations how to determine the degree of membership can be found in [4]. The following solution consists in performing the interval analysis for all values of uncertain quantities, the degree of membership of which is equal or greater than the chosen one (the same for all uncertain parameters). This gives intervals of values of resulting parameters. Their degree of membership is equal or greater than the chosen one. The fuzzy number approach makes it possible to consider credibility of the obtained results. More details on fuzzy sets and fuzzy numbers can be found in [1], [3-5], [9].

The fuzzy number approach was applied in different fields of mechanics. Moens and Vandepitte [2] used a fuzzy finite element procedure to analyze the uncertain frequency-response function of damped structures, Vaško et al. for frequency analysis [8], Ságа et al. [6] for analysis of vibration of vehicles with uncertain parameters, and Vaško and Ságа [7] for damage prediction of mechanical structures. This paper deals with analysis of the steady state response of a rotor supported by nonlinear hydrodynamic bearings.

The investigated rotor is rigid. At both its ends it is supported by the hydrodynamic bearings. The rotor is loaded by its weight, by a force acting perpendicularly to its axis, and is excited by the imbalance. The whole system can be considered as symmetric. Scheme of the rotor is depicted in Fig. 1.

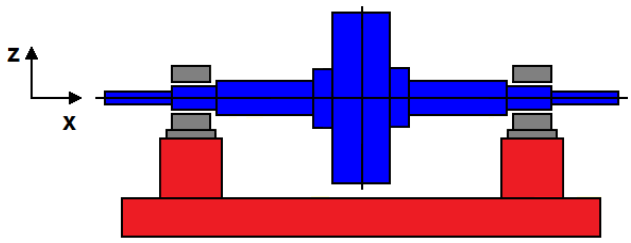

Fig. 1. The studied rotor system

In the computational model the rotor was considered as absolutely rigid and the hydrodynamic bearings were represented by force couplings. The Reynolds equation and computational integration of the obtained pressure distribution were applied to determine the bearing forces. The trigonometric collocation method was used to determine the rotor steady state response.

The mass of the rotor was 426 kg, the length/diameter of the bearing hole were 120/100 mm, the oil viscosity was 0.004 Pas, and the rotor rotated at the speed of 300 rad/s. Eccentricity of the rotor center of mass was assumed to be 30 ± 30 μm and magnitude of the horizontal (acting in the positive direction of axis y) and vertical (acting in the negative direction of axis z) components of the stationary force 2400 ± 72 N and 3600 ± 108 N, respectively.

The task was to find out if maximum displacement of the rotor from the axis connecting the centers of the bearing holes does not exceed 185 μm.

The steady state orbit of the rotor center determined for the most probable values of the uncertain parameters can be seen in Fig. 2. The history of the rotor radial displacement during one rotor revolution is depicted in Fig. 3. The analysis shows that the maximum radial displacement of the rotor center is 181 μm. It implies the allowable value of 185 μm is not exceeded.

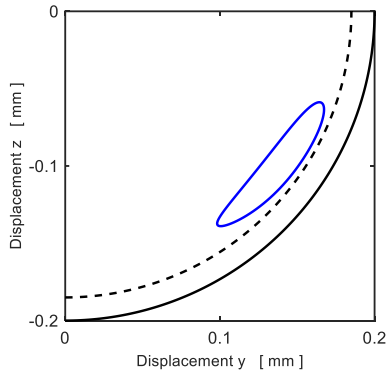

Fig. 2. Orbit of the rotor for the most probable magnitude of loading

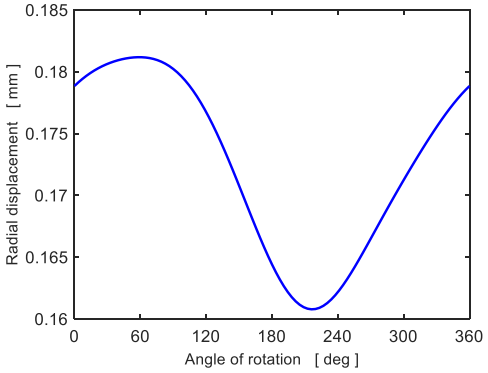

Fig. 3. History of the rotor radial displacement during one rotor revolution

In the next analysis the fuzzy number approach was applied. The membership function (Fig. 4) for the eccentricity is assumed to have a triangular shape (the probability of the lower and higher values goes down). The membership function for the components of the stationary force is estimated to be rectangular (the same probability for all assumed values), which implies the degree of membership of all possible values of the stationary force is 1.

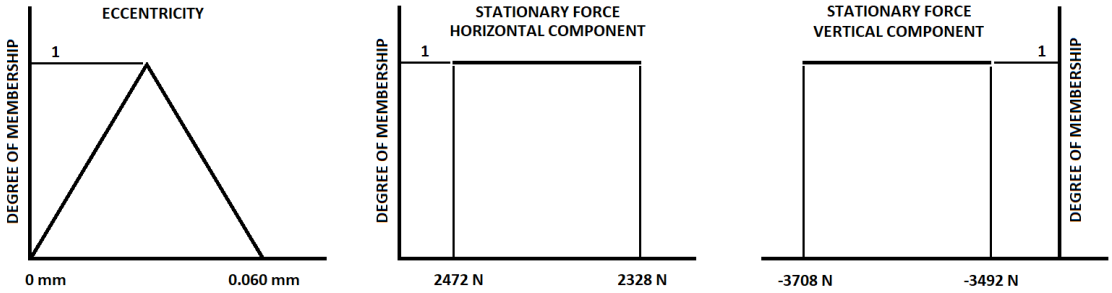

Fig. 4. The membership functions

Six levels of the membership function related to the eccentricity of the rotor center of mass was chosen. Consequently, the corresponding values of the eccentricity were determined. The values related to the uncertain force components were specified by uniform dividing the interval of the assumed magnitudes in 4 parts. The interval analysis was done for all combinations of the values specified for the individual uncertain parameters. Each analysis arrives at the value of the radial displacement of the rotor center. Its degree of membership corresponds to the lowest degree of membership of each component of the uncertain input parameters combination.

The performed analysis shows that membership function of the rotor radial displacement has the shape close to trapezoidal (Fig. 5). Fig. 6 depicts intervals of the rotor radial displacements for several membership levels.

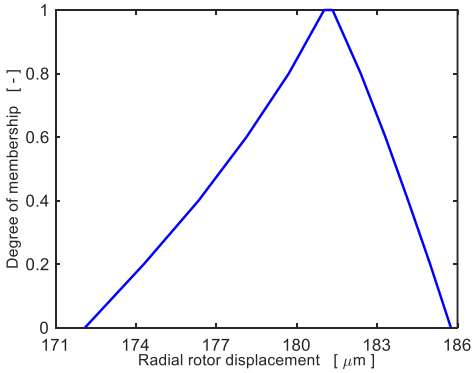

Fig. 5. The membership function of the radial displacement of the rotor center

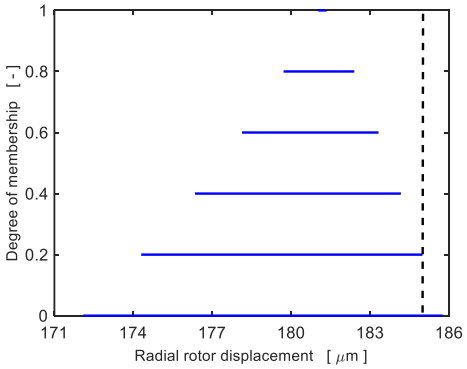

Fig. 6. Determined intervals of the rotor radial displacement for different degrees of membership

The interval related to the degree of membership of 0 corresponds to the worst case. The ratio of lengths of intervals corresponding to the chosen degree of membership and the degree of 0 can be considered as the degree of credibility, with which the results were obtained (Table 1). The allowable value of the rotor radial displacement is not exceeded for the results obtained with the degree of credibility of 78.2 %. This corresponds to the degree of membership 0.2.

Table 1. Degree of membership and credibility

Degree of membership	Degree of credibility
1.0	2.3 %
0.8	19.7 %
0.6	38.0 %
0.4	57.3 %
0.2	78.2 %
0.0	100.0 %

The approach for analyzing the systems with uncertain parameters based on application of the fuzzy numbers has some advantages. It does not require knowledge of the probability density function of uncertain parameters and corresponding random numbers generators. If the number of uncertain parameters is not large, the number of performed simulations can be considerably lower than those if the Monte Carlo method were applied.

Acknowledgements

This work was supported by the grant projects 19-06666S and LQ1602 (NPU II).

References

[1] Gupta, M.M., Yamakawa, T., Fuzzy computing: Theory, hardware and applications, North-Holland, Amsterdam, 1988.
[2] Moens, D., Vandepitte, D., A fuzzy finite element procedure for the calculation of uncertain frequency-response function of damped structures: Part 1 - Procedure, Journal of Sound and Vibration 288 (2005) 431-462.
[3] Novák, V., Fuzzy množiny a jejich aplikace, SNTL, Praha, 1990. (in Czech)
[4] Novák, V., Základy fuzzy modelování, BEN – Technická literatura, Praha, 2000. (in Czech)
[5] Ságа, M., Dekýš, V., Vaško, M., Some aspects of probability and possibility theories for numerical analysis of uncertain mechanical systems, Acta Mechanica Slovaca 14 (4) 92-101.
[6] Ságа, M., Letrich, M., Kocúr R., An analysis of yehicle vibration with uncertain system parameters, Komunikácie, 2005.
[7] Vaško, M., Ságа, M., Application of fuzzy structural analysis for damage prediction considering uncertain S/N curve, Applied Mechanics and Materials 4 (20) (2013) 21-29.
[8] Vaško, M., Ságа, M., Dekýš, V., Contribution to numerical analysis of uncertain mechanical systems using probability and possibility theory, Advances in Mechanisms Design: Proceedings of TMM 2012, Springer Science & Business Media, 2012, pp. 263-269.
[9] Zimmermann, H.-J., Fuzzy set theory – and its application, Kluwer Academic Publishers, Boston, 1996.

COMPUTATIONAL MECHANICS 2021
36th conference with international participation
Srní
November 8 - 10, 2021

Trajectory planning for tensegrity structures

J. Zavřel[a], Z. Šika[a], V. Halamka[a]

[a] *Faculty of Mechanical Engineering, Czech Technical University in Prague, Technická 4, 160 00 Praha, Czech Republic*

Tensegrities are structures composed of tensile and compressive elements or other objects. Tensegrities are usually composed of cables and struts, which can also transmit the force in both directions [4]. These elements are connected to each other and may be joined by more complex objects. The position is also related to the distribution of bodies in trajectory planning [1].

When considering a planar structure, each body has three degrees of freedom. The position of the end-effector, and possibly its orientation is required. For a three-body structure (three stages, Fig. 1) including the end-effector body, we get in total 9 degrees of freedom. Determining the three degrees of freedom for end-effector leaves 6 coordinates of the bodies that we can choose. There are thus an infinite number of configurations to choose from. Determining the positions of the remaining bodies is often approached by choosing a trajectory to place the bodies between the end-effector and the base frame uniformly. The limitation may then be the available space or the collision of the bodies and cables. However, this approach does not necessarily lead to a good solution, and so the design is often supplemented by optimizing some of the key features. The optimization criterion is often the stiffness at the end-effector or dexterity [5]. Closely related to these properties is the distribution of the cables and their prestressing. Since a redundant number of cables is used, it is also possible to work with the choice of cable prestressing. By prestressing cables it is possible to influence the resulting stiffness of the structure [2], [3].

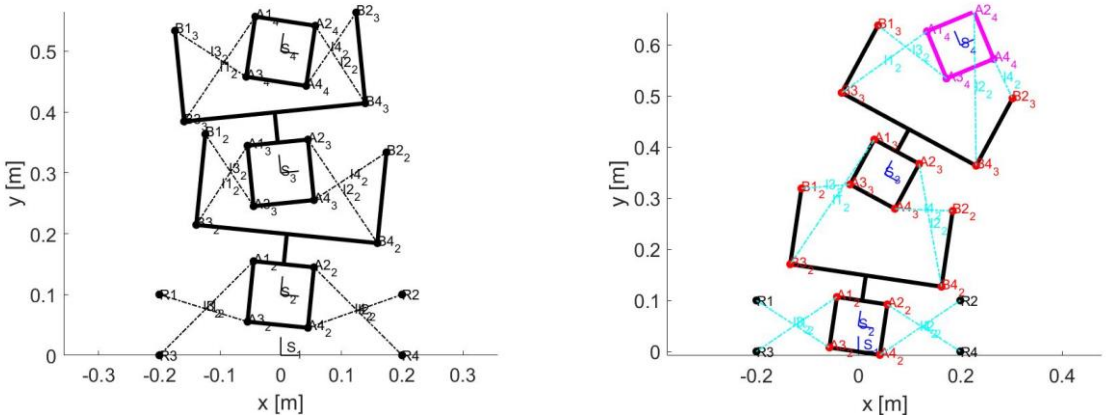

Fig. 1. The initial position of the tensegrity structure (left) and the common position (right)

To find the forces in the cables in a defined position, the dynamic equations of the bodies are used, from which the required forces for the dynamic equilibrium of the system are solved. Due to the redundant number of cables, this problem is also ambiguous. One approach to solving the problem is to choose the forces in the form of prestresses in the redundant cables and calculate the forces of the other cables from the dynamic equilibrium of the system. The

best option is then determined for different combinations of prestresses in the cables, for example by finding the configuration with the minimum of maximum of all cable forces. However, the equilibrium may also yield negative forces in the cables where a such configurations are not allowed. Another possibility for designing forces in cables is to use constrained optimization. However, this optimization is not suitable for a higher number of parameters due to its time consuming nature. Another option is to use SVD decomposition for the dynamic equilibrium equations of the whole tensegrity system. The number of equations is redundant and we have the possibility of using a redundant number of parameters to influence the result.

The modelled tensegrity structure (Fig. 1) consists of three stages, where one is an end-effector whose position is prescribed. The system contains a total of 12 cables at 9 degrees of freedom. Thus, there are a total of 3 redundant cables. A heuristic method is used to distribute the bodies as they move along the trajectory, with optimization of the forces in the cables along with analysis of the system dynamics equations using singular value decomposition method

$$m_i \ddot{x}_{1i} = \sum_{j=1}^{8} F_{ji}\, \overrightarrow{e_{ji}} \cdot \overrightarrow{e_x}\,,$$
$$m_i \ddot{y}_{1i} = \sum_{j=1}^{8} F_{ji}\, \overrightarrow{e_{ji}} \cdot \overrightarrow{e_y} - m_i g\,,$$
$$I_{S_i} \ddot{\varphi}_i = \sum_{j=1}^{8} \overrightarrow{r_{ji}} \times F_{ji}\, \overrightarrow{e_{ji}}\,,$$

where the m_i is the mass of the i-th body, I_{S_i} is the moment of inertia, $\ddot{x}_{1i}, \ddot{y}_{1i}$ accelerations of the center of gravity and $\ddot{\varphi}_{1i}$the angular accelerations, $F_{ji}$the corresponding force in the cable, e_{ji}, e_x and e_y unit vectors of cables and world frame axes. The dynamics equations for the i-th body are based on the free body diagram (Fig. 2). The resulting forces in the cables determined by the different methods are strongly dependent on the given structure configuration and the chosen prestress in the cables. The results of the different approaches verified the possibility of using the methods to design the move along the trajectory for redundantly actuated tensegrity structures.

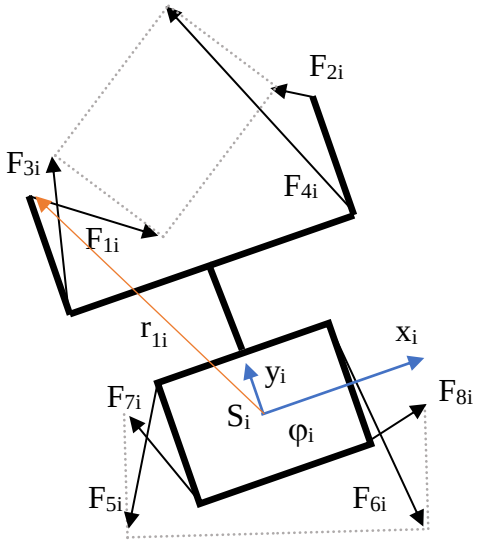

Fig. 2. The action of forces on the i-th stage

Acknowledgement

The research is supported by the Czech Science Foundation project No GA20-21893S "Mechatronic Tensegrities for energy efficient light robots ".

References

[1] Balon, A., Optimization and control of mechatronic tensegrity for robotics, master thesis, Czech Technical University, Prague, 2019. (in Czech)

[2] Skelton, R.E., de Oliveira, M., Tensegrity systems, Springer-Verlag US, 2009.

[3] Skelton, R.E., et al., An introduction to the mechanics of tensegrity structures, in Proceedings of the 40th IEEE Conference on Decision and Control, Orlando, 2001, pp. 4254-4259.

[4] Snelson, K., The art of tensegrity, International Journal of Space Structures 27 (2012) 71-80.

[5] Šika, Z., et al., Calibrability as additional design criterion of parallel kinematic machines, Mechanism and Machine Theory 50 (2012) 48–63.

COMPUTATIONAL MECHANICS 2021
36th conference with international participation
Srní
November 8 - 10, 2021

Modelling of nuclear fuel assemblies vibration in mutual interaction

V. Zeman, Z. Hlaváč

NTIS – New Technologies for the Information Society, Faculty of Applied Sciences, University of West Bohemia, Univerzitní 8, 301 00 Plzeň, Czech Republic

1. Introduction

The coolant pressure pulsations generated by the main circulation pumps in the coolant loops are one of the main sources of reactor excitation [1]. The vibrations of the VVER 1000-type reactor and its components caused by the coolant pressure pulsations was investigated in previous authors' research works on a linearized model of the reactor [2]. This model was later modified by the effect of the friction-vibration interactions in the reactor core barrel (CB) couplings with clearances [4]. The fuel assemblies (FAs) vibration without mutual interaction respecting new knowledge about excitation by coolant pressure pulsation measured at NPP Temelín [3] was published in [5]. The aim of the paper is to present an approach to the modelling of chosen FA vibration inside the reactor core with the possibility of interaction with the surrounding FAs.

2. A concept of modelling the FAs dynamic behavior

The general idea of the method is based on two-stage modelling concept depicted in Fig. 1. The first stage model represents the global nonlinear model of the reactor and the second stage model is model of the FAs group composed of the reference fuel assembly FA_i surrounded by up to six fuel assemblies FA_j (see Fig. 2).

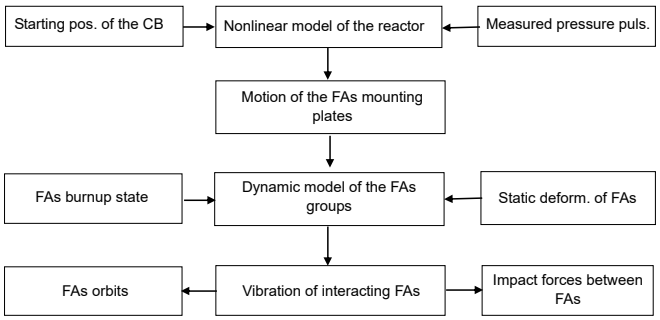

Fig. 1. A concept of modelling the FAs dynamic behavior

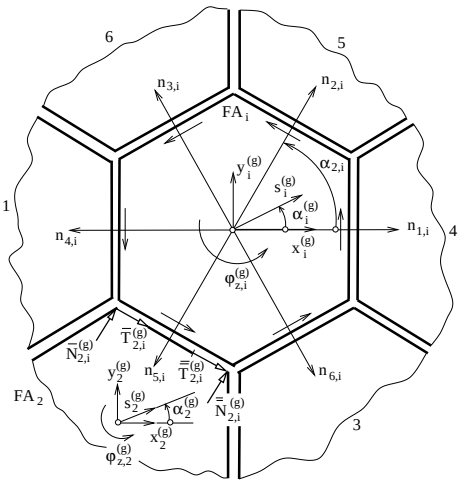

Fig. 2. A group of the FAs within the reactor core

Movement of FA mounting plates investigated on a global reactor model is the source of the FAs kinematics excitation. Interactions between FA_i and FA_j may arise as a result static deformation FAs. Static deformations are described by horizontal displacements $s_i^{(g)}$ and

$s_j^{(g)}$, $j \in \{1,\dots,6\}$ of the FA centers at the level of the spacer grids $g = 1,\dots,8$ from an ideal position. The directions of FAs static deformation are described by angles $\alpha_i^{(g)}$ and $\alpha_j^{(g)}$.

Contact of load-bearing skeleton of interacting hexagonal FAs can be assumed in the area of the vertices of the angles at the level of the spacer grids (Fig. 2). Which pair of vertices of the FA_j and FA_i angles on the contact line will be active depends on the relative transverse displacements. Relative displacements in the direction of the contact normal $n_{j,i}$, $j = 1,\dots,6$ of the vertices pairs on the common contact line can be described in the form

$$\bar{n}_{j,i}^{(g)}=s_j^{(g)}\cos(\alpha_{j,i}-\alpha_j^{(g)})-s_i^{(g)}\cos(\alpha_{j,i}-\alpha_i^{(g)})+(x_j^{(g)}-x_i^{(g)})\cos\alpha_{j,i}+(y_j^{(g)}-y_i^{(g)})\sin\alpha_{j,i}-h(\varphi_{z,j}-\varphi_{z,i}), \quad (1)$$

$$\bar{\bar{n}}_{j,i}^{(g)}=s_j^{(g)}\cos(\alpha_{j,i}-\alpha_j^{(g)})-s_i^{(g)}\cos(\alpha_{j,i}-\alpha_i^{(g)})+(x_j^{(g)}-x_i^{(g)})\cos\alpha_{j,i}+(y_j^{(g)}-y_i^{(g)})\sin\alpha_{j,i}+h(\varphi_{z,j}-\varphi_{z,i}), \quad (2)$$

where $\alpha_{j,i}$ are the angles of the contact normals and h is the half length of one contact line. Relative displacements of both pairs in the marked directions of the contact line are

$$t_{j,i}^{(g)}=s_j^{(g)}\sin(\alpha_{j,i}-\alpha_j^{(g)})-s_i^{(g)}\sin(\alpha_{j,i}-\alpha_i^{(g)})+(x_j^{(g)}-x_i^{(g)})\sin\alpha_{j,i}-(y_j^{(g)}-y_i^{(g)})\cos\alpha_{j,i}-\sqrt{3}h(\varphi_{z,j}-\varphi_{z,i}). \quad (3)$$

Rigid plate bodies of the FAs load-bearing skeleton (spacer grids parts of the angles in width at the rims) perform a spatial motion arround the statically deformed FAs described by vector of generalized coordinates

$$\boldsymbol{q}_j = [\dots, x_j^{(g)}, y_j^{(g)}, z_j^{(g)}, \varphi_{x,j}^{(g)}, \varphi_{y,j}^{(g)}, \varphi_{z,j}^{(g)}, \dots]^T \in R^{330},\ j = 1,\dots,6,\ g = 1,\dots,8 \quad (4)$$

and $\boldsymbol{q}_i$ respectively. Index g indicates the order of spacer grids. Transverse coordinates $x_i^{(g)}$, $y_i^{(g)}$, $z_i^{(g)}$, $y_j^{(g)}$ and torsion coordinates $\varphi_{z,i}^{(g)}$, $\varphi_{z,j}^{(g)}$ of the load-bearing skeleton affect the total (static and dynamic) relative displacements at possible contact points, see equations (1) – (3).

The contact forces between the interacting FAs, due to the mounting transverse clearances δ between neighboring FAs, have an impact character. Normal components $\bar{N}_{j,i}^{(g)}$ and $\bar{\bar{N}}_{j,i}^{(g)}$ of contact forces on one contact line and at the level of the grid g (see Fig. 2 for $j = 2$) can be written in the form

$$\bar{N}_{j,i}^{(g)} = k_C(n_{j,i}^{(g)} - \delta)H_1(n_{j,i}^{(g)} - \delta)H_2(t_{j,i}^{(g)})\,, \bar{\bar{N}}_{j,i}^{(g)} = k_C(n_{j,i}^{(g)} - \delta)H_1(n_{j,i}^{(g)} - \delta)H_2(-t_{j,i}^{(g)})\,, \quad (5)$$

where k_C is the contact stiffness between angles of the load-bearing skeleton. A necessary condition for the activation of any of the 96 normal contact forces (for $j = 1,\dots,6$ and $g = 1,\dots,8$) is a positive argument of the Heaviside function H_1. A sufficient condition is at the same time a positive argument of the Heaviside function H_2, which decides on the activation of one of the pairs of normal contact forces on the same contact line. Activated normal contact forces generate friction forces

$$\bar{T}_{j,i}^{(g)} = f(\dot{t}_{j,i}^{(g)})\bar{N}_{j,i}^{(g)} \text{ or } \bar{\bar{T}}_{j,i}^{(g)} = f(\dot{t}_{j,i}^{(g)})\bar{\bar{N}}_{j,i}^{(g)}\,. \quad (6)$$

The friction coefficient $f(\dot{t}_{j,i}^{(g)})$ is approximated by smooth function on the resulting sliding velocity $\dot{t}_{j,i}^{(g)}$ [4].

3. Mathematical model of the FAs group within the reactor core

The mathematical model of the group of seven FAs (see Fig. 2) can be written in the form

$$\mathrm{diag}[\boldsymbol{M}_{PS},..,\boldsymbol{M}_{PS}]\begin{bmatrix}\ddot{\boldsymbol{q}}_i\\ \ddot{\boldsymbol{q}}_1\\ \vdots\\ \ddot{\boldsymbol{q}}_6\end{bmatrix}+\mathrm{diag}[\boldsymbol{B}_{PS},..,\boldsymbol{B}_{PS}]\begin{bmatrix}\dot{\boldsymbol{q}}_i\\ \dot{\boldsymbol{q}}_1\\ \vdots\\ \dot{\boldsymbol{q}}_6\end{bmatrix}+\mathrm{diag}[\boldsymbol{K}_{PS},..,\boldsymbol{K}_{PS}]\begin{bmatrix}\boldsymbol{q}_i\\ \boldsymbol{q}_1\\ \vdots\\ \boldsymbol{q}_6\end{bmatrix}=\begin{bmatrix}\boldsymbol{f}_i^{KE}\\ \boldsymbol{f}_1^{KE}\\ \vdots\\ \boldsymbol{f}_6^{KE}\end{bmatrix}+\begin{bmatrix}\sum_{j=1}^{6}\boldsymbol{f}_{j,i}^{C}\\ \boldsymbol{f}_{i,1}^{C}\\ \vdots\\ \boldsymbol{f}_{i,6}^{C}\end{bmatrix}, \quad (7)$$

where $\boldsymbol{M}_{PS}$, $\boldsymbol{B}_{PS}$, $\boldsymbol{K}_{PS}$ are the matrices of mass, damping and stiffness of one linearized FA. The kinematic excitation vectors $\boldsymbol{f}_i^{KE}$ and $\boldsymbol{f}_j^{KE}$ differ in cooordinates describing the position of their axes in the reactor core. Vectors of contact forces $\boldsymbol{f}_{j,i}^{C}$ and $\boldsymbol{f}_{i,j}^{C}$, $j = 1, \ldots, 6$, $g = 1, \ldots, 8$ are expressed by means of normal componnets $\bar{N}_{j,i}^{(g)}$, $\bar{\bar{N}}_{j,i}^{(g)}$ and friction forces $\bar{T}_{j,i}^{(g)}$, $\bar{\bar{T}}_{j,i}^{(g)}$. If, based on the calculation of the arguments of the Heaviside functions H_1 and H_2 in (5), the normal components are not activated at any spacer grid level, the corresponding vectors $\boldsymbol{f}_{j,i}^{C}$ and $\boldsymbol{f}_{i,j}^{C}$ are zero.

The dimension of global vectors of generalized coordinates of all FAs in a group (specifically $7 \cdot 330 = 2310$) is too large. Therefore, it is expedient to use the modal reduction of generalized coordinates of individual FAs. If the reference FA_i is not surrounded by any of the FA_j or if contact with any of the FA_j can be excluded, corresponding block line in model (7) is deleted.

4. Result of numerical simulations

To demonstrate the presented method, dynamic response of the three configurations of hexagonal FA_2 and FA_5 (see Fig. 3) statically deformed in the shape of a "banana" applied in the VVER 1000-type reactor was analysed. Dynamic orbits of the reference FA_i centers in a short time interval at the level of the spacer grids 4, 5 for the configuration of Fig. 3b, they are shown in Fig. 4. The normal components of the impact forces between reference FA_i an surrounding FA_2 and FA_5 at the level of spacer grids 4 and 5 are shown in Figs. 5 and 6. The analysis of the different configurations of statically deformed FAs shows a large change in the dynamic behavior of interacting FAs.

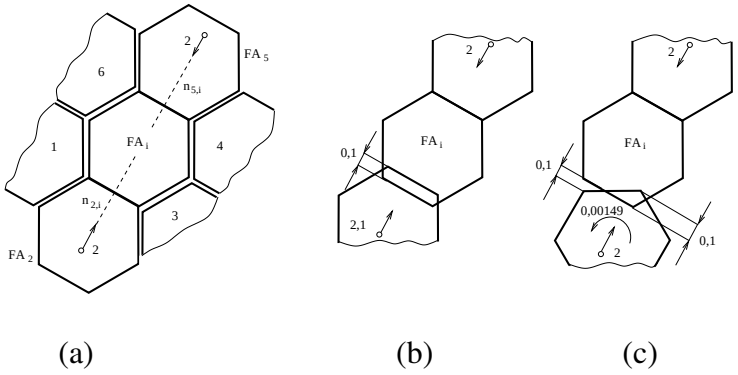

Fig. 3. Selected configurations of the statically deformed FA_2 and FA_5 (in mm) at the level of the grids 4 and 5

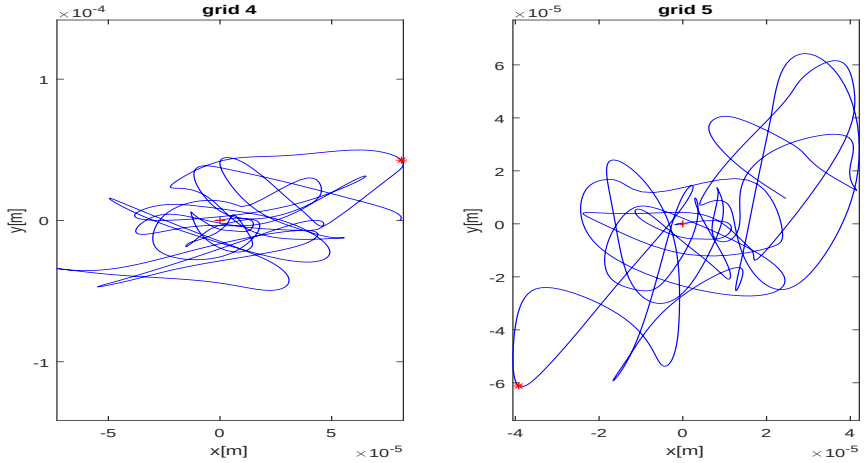

Fig. 4. Dynamic orbits of the reference FA_i centers at the level of grids 4,5 (+ origin, * extreme)

Acknowledgements

This work was developed under the research project Fuel cycle of NPP coordinated by Nuclear Research Institute Řež, a.s.

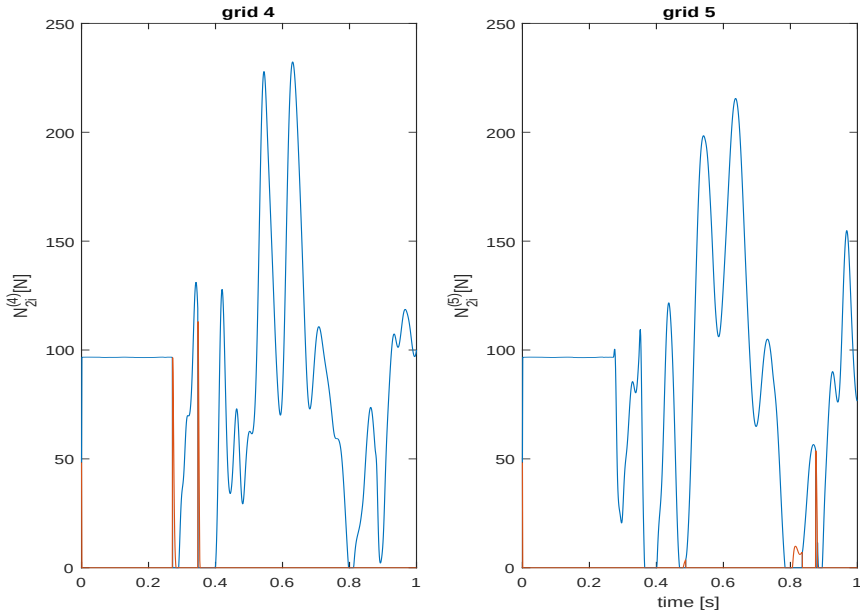

Fig. 5. Normal components of the impact forces between FA_i and FA_2 ($\bar{N}$ red, $\bar{\bar{N}}$ blue)

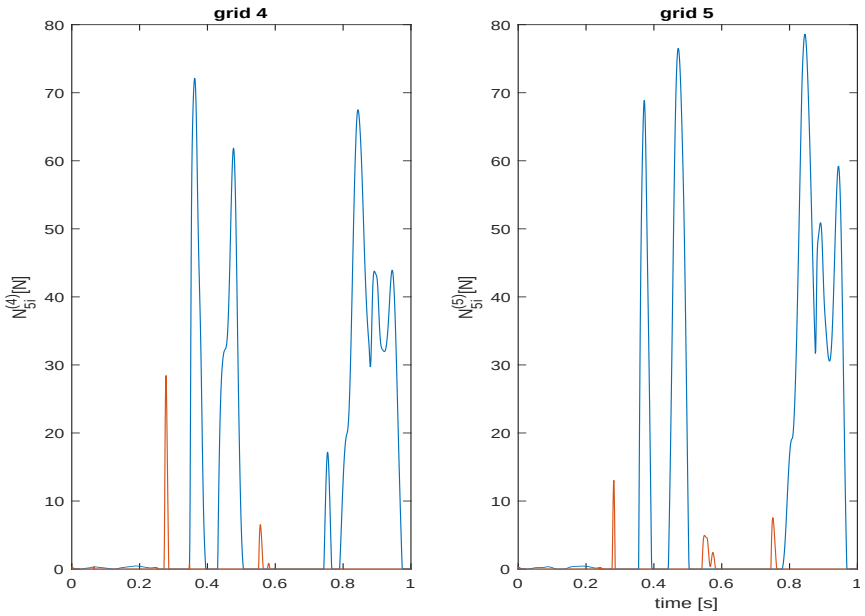

Fig. 6. Normal components of the impact forces between FA_i and FA_5 ($\bar{N}$ red, $\bar{\bar{N}}$ blue)

References

[1] Cheong, J. S., An analytical prediction on the pump-induced pressure pulsation in a pressurized water reactor, Annals of Nuclear Energy 27 (15) (2000) 1373-1383.

[2] Hlaváč, Z., Zeman, V., Vibration of nuclear fuel assemblies. Modelling, methods, applications, LAP Lambert Academic Publishing, Saarbrucken, 2013.

[3] Stulík, P., Bém, M., Machek, J., Dyk, Š., Zeman, V., Hlaváč, Z., Mechanical behaviour of the nuclear fuel, its monitoring and validation using process measurement, Research Report, ÚJV Řež, a.s., 2020. (in Czech)

[4] Zeman, V., Dyk, Š., Hlaváč, Z., Two-stage modelling of hexagonal fuel assemblies vibration considering mechanical nonlinearities, Progress in Nuclear Energy 138 (2021) No. 103825.

[5] Zeman, V., Hlaváč, Z., Modelling of the friction-vibration interactions in reactor core barrel couplings, Applied and Computational Mechanics 12 (2) (2018) 193-212.